SCHüRMANN, L W

THE KRUIDFONTEIN CARBONATITE COMPLEX, SOUTH AFRICA: GEOLOGY, PETROLOGY, GEOCHEMISTRY AND ECONOMIC POTENTIAL

DPhil UP 1999

Digitised by the Department of Library Services in support of open access to information, University of Pretoria, 2021

The Kruidfontein Carbonatite Complex, South Africa: Geology, Petrology, Geochemistry and Economic potential

by

Louis Willem Schürmann

submitted in partial fulfilment of the requirements for the degree

of

DOCTOR OF PHILOSOPHY

in the

Faculty of Science,

UNIVERSITY OF PRETORIA

JANUARY 1999

Digitised by the Department of Library Services in support of open access to information, University of Pretoria, 2021

ABSTRACT

The Kruidfontein Carbonatite Complex (1243 ± 171 Ma) is an example of an intracontinental caldera system which is related to carbonatite activity and mineralisation. It had a two-stage history, beginning with a cone-building period of predominantly nephelinitic pyroclastics and ignimbrites followed by cauldron subsidence. The second stage was carbonatitic in nature, and was also followed by cauldron subsidence. Today, the eroded volcano comprises an approximately circular carbonatitic inner zone, surrounded by an outer zone of silicate pyroclastics. The cauldron subsidence contributed to the preservation of the inner zone carbonatite sequence. Structures related to the caldera formation are radial and ring faults, along with several mineral occurrences and potential ore deposits.

The soil geochemistry, together with the high-resolution radiometric survey, depict several positive anomalies throughout the inner and outer zones. Of these the following are important: (a) the ferruginous lapilli tuff unit in the eastern and northeastern part of the inner zone; (b) the northern part of the inner zone associated with vents (characterised by vent breccia and proximal debris flow deposits, carbonatite dykes, plugs and faults), and (c) an area towards the southern boundary of the inner zone, characterised by dykes, vents and associated breccia and debris flow deposits. The anomalous Au, Pb and Zn levels are mainly associated with vent breccia and secondary ferruginisation. The strong Ba anomaly occurs in zones of fenitisation and displays a degree of structural control. Also notable is the correlation between high Ba values and the presence of calcite-carbonatite and fluorite-calcite-carbonatite dykes and barite-fluorite veins.

No Bouguer high is present on the Complex, suggesting that no buried high-density body is present in depth. The structure of the Complex, however, is clearly delineated by the high-resolution magnetic survey. A pronounced magnetic anomaly is situated along the northern boundary of the inner zone, the extent of which is limited to the assumed position of the caldera-collapse fault. In addition a north-south section derived from magnetic data across the Complex indicates gently-dipping rocks in the south, whereas in the north the magnetic zone is almost vertical. Anomalously high fluorite contents are present along the southern boundary of the inner zone. Here, the inward dipping altered carbonatite rocks are replaced by fluorite mineralisation.

Core from the KD01 borehole, drilled in the NE part of the inner zone has revealed great detail about the carbonatitic pyroclastic sequence. The sequence is dominated by ash fall and ash flow tuffs. With the exception of a unit 32 m below the top of the borehole, the sequence has been replaced by a fine-grained intergrowth of potassium feldspar, ankerite and chlorite. This was followed by a period of veining characterised by intergrown, very fine-grained chlorite, apatite, anatase and pyrite. The earlier feldspar-ankerite-chlorite assemblage has been overprinted by apatite, followed by fluorite crystallisation. Both minerals occur either as euhedral crystals or as small, scattered grains. The latest alteration to affect the rock was the introduction of calcite, which has caused some fine-scale brecciation and some replacement of the pre-existing mineral assemblage. One unit of the borehole core contains ash grains with exceptionally well-preserved primary textures, including quench microphenocrysts, and less abundant vesicles and larger phenocrysts. There are also groups, or "clots" of tiny microphenocrysts, which have not previously been observed in carbonatite lavas. These ash grains have erupted as droplets of lava of calcite-carbonatite and silicate, and formed an ash deposit containing some altered silicate lava fragments. The primary mineralogy of the droplets has been completely masked by late Sr-bearing calcite, chlorite and apatite. The latest stage of mineralisation is represented by anatase, apatite, chlorite and pyrite.

Digitised by the Department of Library Services in support of open access to information, University of Pretoria, 2021

Carbon and oxygen isotope patterns point to three major stages of development of the inner zone of the Complex:

- Stage one involves carbonatite magma with a H_2O-CO_2 vapour phase which originated by fractionation at 700°C in a closed system with a H_2O/CO_2 molar ratio of 0.5.

- The second stage of the development is recorded by a shift to higher $\delta^{18}O$ values without major changes in the $\delta^{13}C$ values in the intrusive carbonatitic dykes and in part of the carbonatitic ash flow tuffs. This second stage is the cause of secondary alteration at an estimated temperature of approximately 150°C. The isotopic characteristics of the alteration fluid could be determined as $\delta^{18}O_{H_2O}$ = 1.2‰ and $\delta^{13}C_{CO_2}$ = -3.8‰, and its possible origin is thought to be a hydrothermal fluid which introduced isotopically light C from the deep subvolcanic source and mixed with high $\delta^{18}O$ ground water that had equilibrated at about 150°C.

- The third stage is characterised by siderite mineralisation, with the concomitant precipitation of fluorite. Siderite appears to be younger than the other carbonates and can thus be assumed to have formed at or below 150°C. The late nature of the siderite mineralisation is substantiated by a negative correlation between the whole-rock carbonate $\delta^{18}O$ values and the modal siderite content. By applying the siderite/water and siderite/CO_2 fractionation factors of Carothers et al. (1988), the C and O isotope composition of the siderite-precipitating fluid was found to be approximately $\delta^{13}C_{CO_2}$ = -8.0‰ and $\delta^{18}O_{H_2O}$ = -1.4‰. From these findings it is concluded that siderite in the Kruidfontein Complex is likely to have been precipitated by a late-stage Fe-bearing hydrothermal fluid, depleted in ^{18}O and ^{13}C. Carbon was probably provided by a deep-seated source within the subvolcanic region, whereas Fe was leached from rocks through which the hydrothermal fluid passed. The siderite mineralisation and concomitant fluorite formation most probably took place during progressive cooling of the Kruidfontein Carbonatite Complex, as can be deduced from the positive correlation between the $\delta^{18}O$ and $\delta^{13}C$ values of siderite.

Digitised by the Department of Library Services in support of open access to information, University of Pretoria, 2021

UITTREKSEL

Die Kruidfontein Karbonatiet Kompleks (1243 ± 171 Ma) is 'n voorbeeld van 'n intrakontinentale kaldeira-stelsel wat verband hou met karbonatietaktiwiteit en mineralisasie. Die geskiedenis daarvan het in twee stappe verloop, en het begin met 'n periode waartydens 'n keël opgebou is, hoofsaaklik uit nefelinitiese piroklastika en ignimbriete, en wat toe gevolg is deur kuilvormige insakking. The tweede stap was karbonatities van aard en kuilvormige insakking het weereens daarop gevolg. Vandag bestaan the geerodeerde vulkaan uit 'n naastenby sirkelvormige karbonatitiese binnesone, omring deur 'n buitesone van silikaatpiroklastika. The kaldeira-vorming het bygedra tot die bewaring van die karbonatiet-opeenvolging van die binnesone. Strukture wat in verband staan met die vorming van die kaldeira is radiale en ringverskuiwings, saam met verskeie mineraalvoorkomste en potensiële ertsafsettings.

Die grondgeochemie, saam met die hoë resolusie radiometriese opname bring verskeie positiewe anomalieë in the binne- en buitesones aan die dag. Hiervan is die volgende van belang: (a) die ysterbevattende lapillitufeenheid in the oostelike en noordoostelike deel van die binnesone; (b) die noordelike deel van die binnesone wat geassosieer in met vroeëre vulkaanpype (gekenmerk deur pypbreksie en proksimale puinvloei-afsettings, karbonatietgange, -proppe en verskuiwings) en (c) 'n gebied in die rigting van die suidelike grens van die binnesone wat gekenmerk word deur gange, pype en geassosieerde breksie en puinvloei-afsettings. Die anomale vlakke van Au, Pb en Zn is hoofsaaklik met breksie en sekondêre verystering geassosieer. Die sterk Ba-anomalie kom in sones van fenitisasie voor en vertoon 'n mate van struktuurbeheer. Opmerklik is ook die korrelasie tussen hoë Ba-waardes en die teenwoordigheid van kalsiet-karbonatiet- en fluoriet-kalsiet-karbonatietgange en bariet-fluorietare.

Geen Bouguer-hoog is op die Kompleks nie, wat daarop dui dat geen liggaam met 'n hoë digtheid in diepte aanwesig is nie. Die struktuur van die Kompleks word egter duidelik deur die hoë-resolusie magnetiese opname omlyn. 'n Duidelike magnetiese anomalie kom langs die noordelike grens van die binnesone voor. Die verbreiding van die anomalie is beperk tot die veronderstelde posisie van die kaldeira se instortingsverskuiwing. Verder dui 'n noord-suid profiel, afgelei van magnetiese data oor die Kompleks, op lae wat effens na die noorde hel in die suide, terwyl in die noorde die magnetiese sones feitlik vertikaal is. Anomaal-hoë fluorietinhoude is langs die suidelike grens van die binnesone teenwoordig. Hier word die binnewaarts-hellende, veranderde karbonatietgesteentes vervang deur fluorietmineralisasie.

Boorkern uit die KD01 boorgat in die noordoostelike deel van die binnesone het baie besonderhede aangaande die karbonatitiese piroklastiese opeenvolging aan die lig gebring. Die opeenvolging word oorheers deur asrëen- en asvloeituwwe. Met die uitsondering van 'n eenheid wat 32 m onder the bokant van die boorgat is, is die opeenvolging vervang deur 'n baie fynkorrelrige vergroeiing van chloriet, apatiet, anataas en piriet. Die vroeëre veldspaat-ankeriet-chloriet-versameling is deur apatietvervanging gewysig, wat weer gevolg is deur fluorietkristallisasie. Beide minerale kom as of euëdriese kristalle of klein, verspreide korrels voor. Die laaste verandering van die gesteente was die toevoeging van kalsiet wat 'n mate van kleinskaalse breksiëring veroorsaak het asook 'n mate van vervanging van die reeds bestaande mineraalversameling. Een eenheid van die boorkern bevat askorrels met buitengewoon goed bewaarde primêre teksture, insluitende mikrofenokriste en meer seldsame gasblasies en groter fenokriste. Daar is ook groepe of segregasieklonte van klein mikrofenokriste wat nog nie voorheen in karbonatietlawas opgemerk is nie. Hierdie askorrels het uitgebars as druppeltjies lawa van kalsiet-karbonatiet en silikaat, en het 'n asneerslag met veranderde silikaatlawafragmente gevorm. Die primêre mineralogie van die druppels is geheel en al verdoesel deur laat-gevormde Sr-bevattende kalsiet, chloriet en apatiet. Die laaste stadium van mineralisasie word verteenwoordig deur anataas, apatiet, chloriet en piriet.

Digitised by the Department of Library Services in support of open access to information, University of Pretoria, 2021

Koolstof- en suurstof-isotoopgegewens wys op drie belangrike ontwikkelingstadiums van die binnesone van die Kompleks:

- ❒ die eerste stadium behels karbonatietmagma met 'n H_2O-CO_2 gasfase wat deur fraksionering by 700°C ontstaan het in 'n geslote sisteem met 'n H_2O/CO_2 molêre verhouding van 0.5.

- ❒ die tweede stadium van die ontwikkeling word verteenwoordig deur 'n verskuiwing na hoër $\delta^{18}O$-waardes sonder opmerklike veranderings in die $\delta^{13}C$-waardes van die intrusiewe karbonatitiese gange en gedeeltelike verandering van die karbonatitiese asvloeituwwe. Hierdie stadium is die oorsaak van die sekondêre verandering by 'n beraamde temperatuur van benaderd 150°C. Die isotoopkenmerke van die veranderingsvloeistof kon bepaal word as $\delta^{18}O_{H_2O}$ = 1.2‰ en $\delta^{13}C_{CO_2}$ = -3.8‰ en die moontlike oorsprong daarvan is waarskynlik dié van 'n hidrotermale vloeistof wat isotopies ligte C vanuit die diep subvulkaniese bron ingevoer het en met hoë-$\delta^{18}O$ grondwater wat by ongeveer 150°C ge-ekwilibreer het, vermeng het.

- ❒ die derde stadium word gekenmerk deur siderietmineralisasie met gepaardgaande presipitering van fluoriet. Dit kom voor asof die sideriet jonger is as die ander karbonate en dus kan aangeneem word dat dit by of onderkant 150°C gevorm het. Die gedagte van die laat-vorming van die siderietmineralisasie word verstewig deur 'n negatiewe korrelasie tussen die heelgesteente-waardes vir karbonaat-$\delta^{18}O$ en die modale siderietinhoud. Deur die fraksioneringsfaktore van Carothers et al. (1988) vir sideriet/water en sideriet/CO_2 toe te pas, is bevind dat die koolstof- en suurstof-isotoopsamestelling van die siderietpresipiterende vloeistof benaderd $\delta^{13}C_{CO_2}$ = -8.0‰ en $\delta^{18}O_{H_2O}$ = -1.4‰ was. Uit hierdie bevindings word tot die slotsom gekom dat sideriet in die Kruidfontein Kompleks heelwaarskynlik deur 'n laatstadium, Fe-bevattende hidrotermale vloeistof verarm in ^{18}O en ^{13}C, gepresipiteer is. Koolstof is moontlik verskaf deur 'n diepliggende bron binne die subvulkaniese gebied, terwyl Fe uit die rotse waardeur die hidrotermale vloeistof beweeg het geloog is. Die siderietmineralisasie en gepaardgaande fluorietvorming het waarskynlik tydens progressiewe afkoeling van die Kruidfontein Kompleks plaasgevind, soos afgelei kan word uit die positiewe korrelasie tussen $\delta^{18}O$- and $\delta^{13}C$-waardes van sideriet.

Digitised by the Department of Library Services in support of open access to information, University of Pretoria, 2021

CONTENTS

Digitised by the Department of Library Services in support of open access to information, University of Pretoria, 2021

Digitised by the Department of Library Services in support of open access to information, University of Pretoria, 2021

Digitised by the Department of Library Services in support of open access to information, University of Pretoria, 2021

FIGURES

Digitised by the Department of Library Services in support of open access to information, University of Pretoria, 2021

Digitised by the Department of Library Services in support of open access to information, University of Pretoria, 2021

Digitised by the Department of Library Services in support of open access to information, University of Pretoria, 2021

Digitised by the Department of Library Services in support of open access to information, University of Pretoria, 2021

Digitised by the Department of Library Services in support of open access to information, University of Pretoria, 2021

Digitised by the Department of Library Services in support of open access to information, University of Pretoria, 2021

Digitised by the Department of Library Services in support of open access to information, University of Pretoria, 2021

Digitised by the Department of Library Services in support of open access to information, University of Pretoria, 2021

Digitised by the Department of Library Services in support of open access to information, University of Pretoria, 2021

Digitised by the Department of Library Services in support of open access to information, University of Pretoria, 2021

Digitised by the Department of Library Services in support of open access to information, University of Pretoria, 2021

Digitised by the Department of Library Services in support of open access to information, University of Pretoria, 2021

Digitised by the Department of Library Services in support of open access to information, University of Pretoria, 2021

TABLES

Digitised by the Department of Library Services in support of open access to information, University of Pretoria, 2021

Digitised by the Department of Library Services in support of open access to information, University of Pretoria, 2021

1. INTRODUCTION

A carbonatite is a magmatic rock composed of more than 50 % carbonate minerals (the most abundant being calcite and dolomite/ankerite). Carbonatites are temporally and spatially associated with alkaline rocks such as nepheline syenites, nephelinites, phonolites and ijolites, and thus belong to alkaline rock provinces (e.g. Pilanesberg Alkaline Province) (Verwoerd, 1964; Heinrich, 1966; Tuttle and Gittins, 1966; Bailey, 1993). However, carbonatites are not necessarily spatially associated with the alkaline silicate rocks, and can occur as separate intrusions. Geochemically carbonatites are characterised by high Nb, Sr, Ba, and rare-earth element contents (Gold, 1963; 1966; Woolley and Kempe, 1989), and by an initial $^{87}Sr/^{86}Sr$ ratio of 0.702 to 0.705 (Barker, 1996). Currently known carbonatite ages range from Precambrian to Recent, examples being the Phalaborwa Complex dated at 2.06Ma (Reischmann, 1996) and Oldoinyo Lengai, which is still an active carbonatite volcano.

Carbonatite complexes vary greatly in both shape and size and this variability is assumed to be a function of the level to which they have been exposed by erosion, regional tectonic activity and the original intrusive or extrusive form. The majority, however are elliptical to circular in plan. Carbonatite complexes may be volcanic (consisting of lavas, tuff and agglomerate) such as Oldoinyo Lengai (Tanzania), subvolcanic (comprising composite carbonatite plugs, cone sheets and radial and ring dykes, agglomerates, subvolcanic breccias and fenitised country rocks) such as Napak (Kenya) and Chilwa Island (Malawi),or plutonic (dunite, pyroxenite, gabbro, ijolite, nepheline syenite and composite carbonatite) such as Fen (Norway), Oka (Canada), Spitskop, Phalaborwa, Nooitgedacht and Glenover (South Africa, Fig. 1.1), Shawa (Zimbabwe) and Lueshe (Democratic Republic of Congo). A common feature of carbonatite complexes is the partial or complete envelope of fenite (altered country rocks) along the periphery.

In 1996, Barker described the phenomenon of carbonatite volcanism as “plagued by a lack of examples”, an observation also mentioned by Church and Woolley (1995). The latter authors referred to the fact that of approximately 350 documented carbonatite occurrences in the world, only 25 to 30 are regarded as volcanic or subvolcanic. This is also true in Southern Africa where of 43 occurrences, only four, namely the Derdepoort, Melkfontein, Goudini and Kruidfontein Carbonatite Complexes, are known to be extrusive in nature.

Carbonatites as a group contain the highest concentrations of the rare-earth elements of all igneous rocks and are particularly enriched in light rare-earth elements (LREE, i.e. La to Sm). The rare-earth elements can occur as discrete minerals, or can be dispersed in the principal carbonatite carbonates, viz. calcite and dolomite-ankerite, or in phosphates, viz. apatite. Rare-earth element mineralisation in carbonatites can be magmatic, hydrothermal or supergene (Mariano, 1989a, 1989b; Schürmann and Harmer, 1998). Plutonic and subvolcanic carbonatite complexes are characteristically composed of several episodes of magmatic intrusion with the rare-earth element concentrations increasing progressively and reaching their

Digitised by the Department of Library Services in support of open access to information, University of Pretoria, 2021

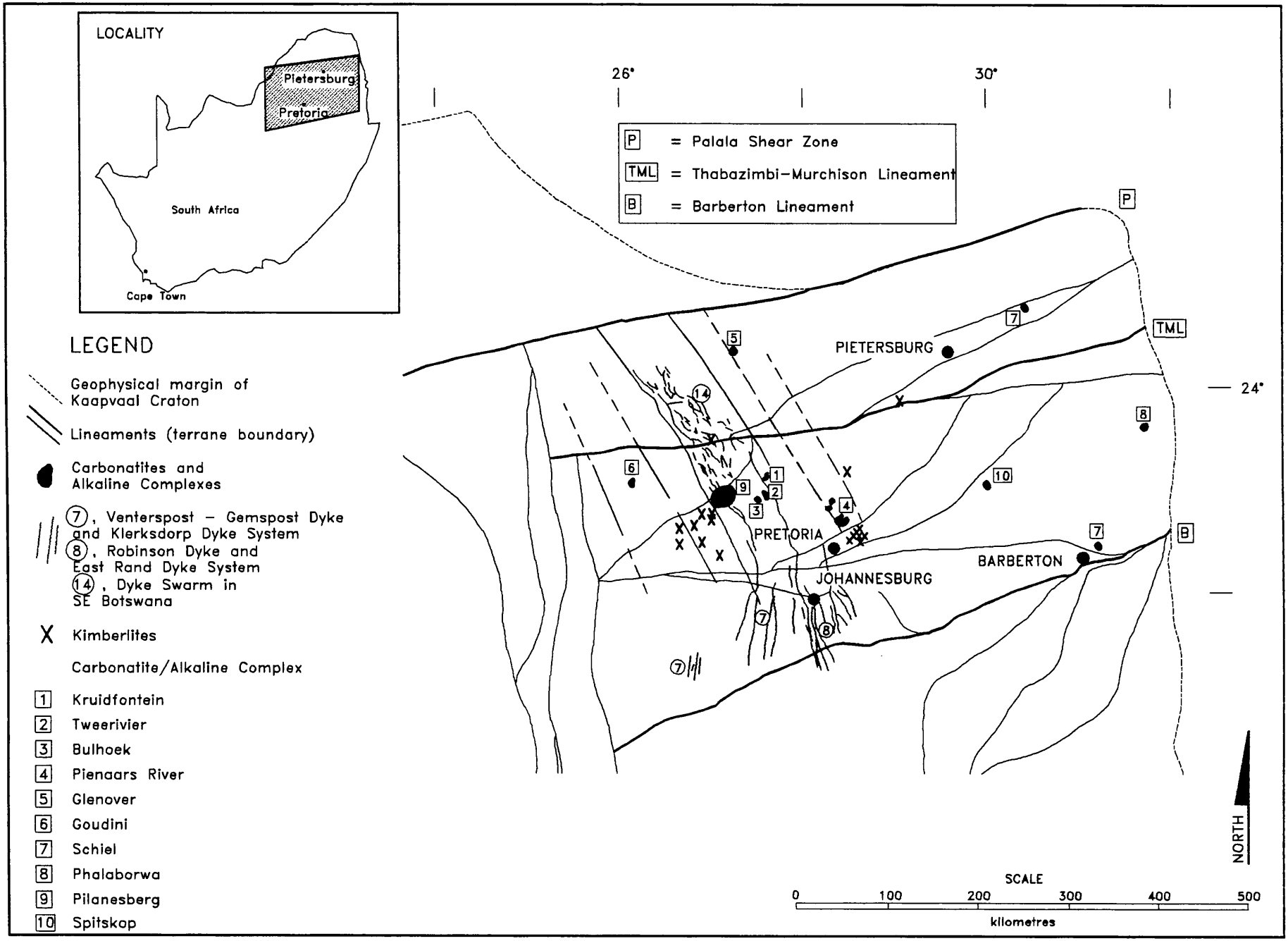

Figure 1.1 Localities of Palaeo- and Mesoproterozoic carbonatites, South Africa.

Digitised by the Department of Library Services in support of open access to information, University of Pretoria, 2021

highest levels in the youngest intrusions. Primary rare-earth minerals are rare and are generally only found in the youngest intrusive carbonatite in such a complex. The Mountain Pass Carbonatite in Colorado, U.S.A. is the only known example of an economic rare-earth element deposit where bastnaesite and parisite have been concentrated through primary magmatic processes (Mariano, 1989b).

The principal carbonates in carbonatites are relatively soluble and during hydrothermal activity their contained rare-earth elements are dissolved, thus leading to the subsequent precipitation of hydrothermal rare-earth minerals. Apatite, a widespread accessory phase of carbonatites, also contains appreciable rare-earth elements which are commonly remobilised by hydrothermal fluids. The nature of these secondary, hydrothermal rare-earth minerals is a function of both the range of accessory minerals present in the carbonatite and the nature of the volatile species comprising the hydrothermal fluid (Mariano, 1989b and Jones et al., 1996). Ancylite [$(Ce,La,Sr,Ca)_2(CO_3)_2(OH,H_2O)$], parisite [$Ca(Ce,La,Nd)_2(CO_3)_3F_2$], bastnaesite [$(Ce,La)CO_3F$] and synchysite [$Ca(Ce,La,Nd)(CO_3)_2F$] occur in the absence of phosphates, whereas monazite [$(Ce,La,Nd,Th)PO_4$] or britholite [$(Ce,Ca)_5(SiO_4,PO_4)_3(OH,F)$] are present where the P activity is high. Hydrothermal rare-earth element mineralisation in carbonatites typically occurs as fine-grained polycrystalline aggregates in veinlets or interstitial fillings, commonly associated with minerals like barite, fluorite, hematite, strontianite, quartz and sulphides. During chemical weathering of carbonatites, preferential leaching of Ca and Mg from carbonate minerals leads to the concentration of the less mobile elements, in particular the rare-earth elements and Sr in the residual soil. In this way laterite enriched in rare-earth elements, can develop on carbonatites, even where the parent rocks are devoid of primary rare-earth minerals. The most common supergene rare-earth minerals are members of the crandallite group [$(Ca,Sr)Al_3(PO_4)(PO_3OH)(OH)_6$], monazite, bastnaesite, parisite and synchysite (Mariano, 1989b).

The Kruidfontein Carbonatite Complex, which is situated 160 km north-northwest of Pretoria (Fig. 1.2), is a well-preserved Mesoproterozoic caldera structure, located along the northwest striking regional fault on the western side of the Crocodile River Fragment, an inlier of deformed Transvaal Supergroup rocks within the acid and mafic rocks of the Bushveld Complex (Hartzer, 1989). The Transvaal Supergroup in the Crocodile River Fragment consists of a pre-Black Reef sedimentary succession (limestone, shale and volcanic rocks), shale and quartzite of the Black Reef Formation, limestone, dolomite and banded iron formation of the Chuniespoort Group and shale and quartzite of the Pretoria Group.

The topography on the farms Kruidfontein 139JQ, Doornkloof 141JQ and Elandsfontein 23JQ is mountainous and essentially comprises an inner mountain range surrounded by an outer range and this has resulted in an annular drainage pattern. The area falls within the semi-arid summer rainfall region and receives an average of 375 mm of rain per annum. Temperatures range from 8 to 32 °C in winter and between 17 and 44 °C in summer.

Digitised by the Department of Library Services in support of open access to information, University of Pretoria, 2021

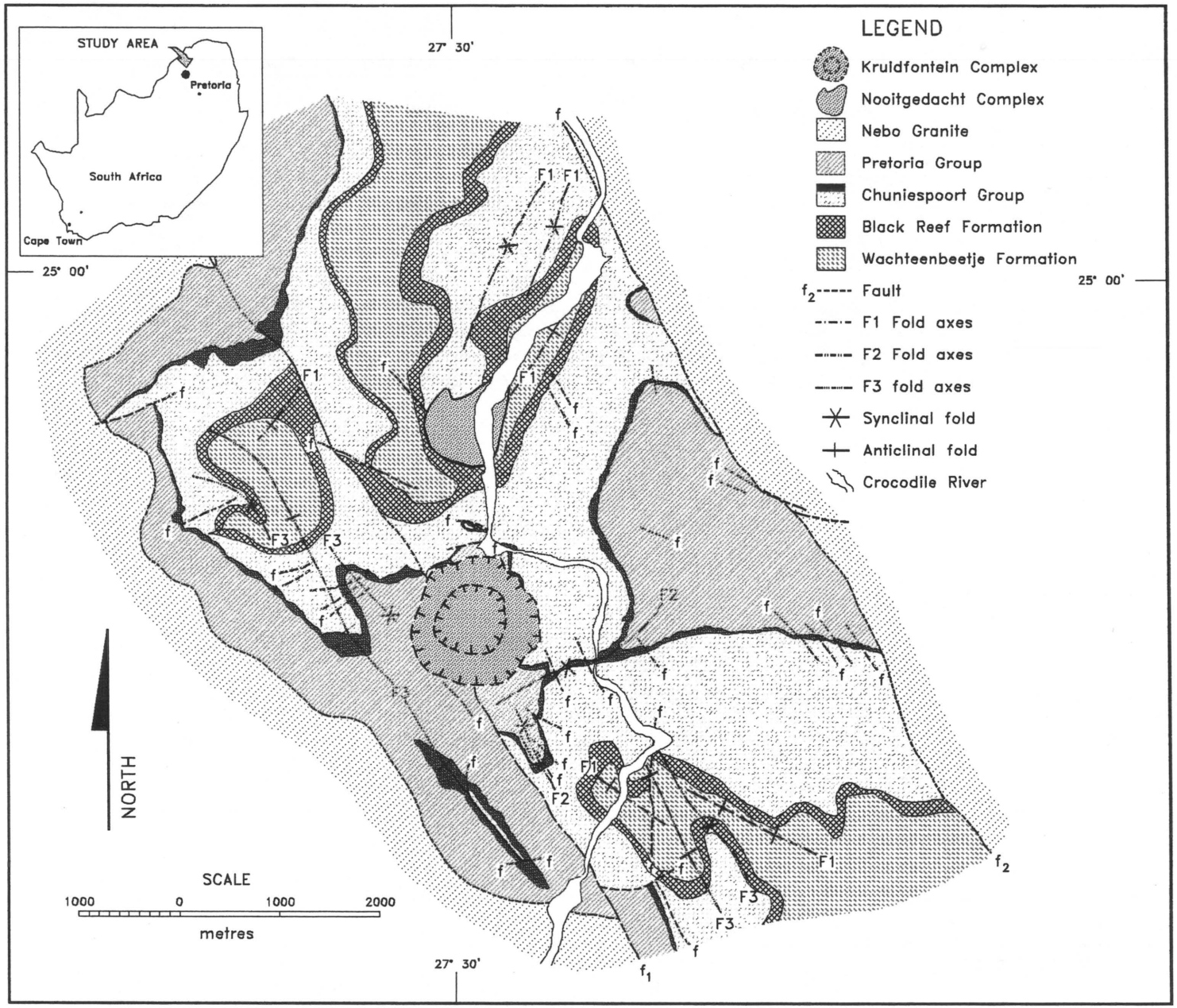

Figure 1.2 Regional geology of the Crocodile River fragment (modified after Hartzer, 1994), showing the localities of the Kruidfontein and Nooitgedacht Carbonatite Complexes.

Digitised by the Department of Library Services in support of open access to information, University of Pretoria, 2021

2. AIM OF THIS INVESTIGATION

In 1992 an extensive national study was initiated by the Mineral Resources Division of the South African Council for Geoscience to determine the economic potential of all carbonatites and alkaline complexes in South Africa. The more important aims of this national study were to classify these complexes in terms of their mode of occurrence, structure, mineralisation and genesis, and to investigate the possible occurrence of high-technology raw materials (especially rare-earth elements and their minerals) in them.

The Kruidfontein Carbonatite Complex was the first to be studied in detail for the following reasons:

- it was assumed that volcanic carbonatites would be potential targets due to associated late-stage alteration and possible economic mineralisation;
- none of the earlier studies of the Kruidfontein Carbonatite Complex had attempted to determine the overall economic potential of the Complex;
- none of these studies had focussed on the nature of the alteration and mineralisation processes, and;
- the Council for Geoscience had acquired borehole core and basic geophysical and geochemical data, enabling this detailed study to be undertaken.

The aim of this investigation is to determine the economic potential of the Kruidfontein Complex based on:

- the geology, structure, geophysical signature and soil geochemistry of the Complex;
- the characterisation of the carbonatite sequence represented in borehole core (holes KD01, KD02 and KD03);
- the nature of alteration and mineralisation by applying techniques such as petrography and cathodoluminescence, and to support this with a mineral chemistry study of related mineral phases using electron microprobe analysis;
- the characterisation of the geochemistry of the carbonatite sequence with the use of whole rock major- and trace-elements, including rare-earth elements;
- stable carbon and oxygen isotope systematics for the inner zone sequence of the Complex in an attempt to provide supporting evidence for the alteration and hydrothermal mineralisation processes.

Digitised by the Department of Library Services in support of open access to information, University of Pretoria, 2021

3. PREVIOUS WORK

During the past century a number of investigations have been carried out on the Kruidfontein Complex, one of three carbonatitic bodies in the Crocodile River Fragment. These investigations include the studies of Humphrey (1909), Hall (1932), Groeneveld (1948), Fockema (1949), Truter (1949), Verwoerd (1956; 1963; 1967), Clarke (1989), Clarke and Le Bas (1990), Clarke et al. (1991) and Pirajno et al. (1995).

Humphrey (1909) identified the Complex by the presence of red felsite and feldspathic volcanic breccia, which were not conformable with the surrounding banded ironstone and rocks of the lower Pretoria Group. This discordant relationship was later confirmed by Fockema (1949), who identified other rock types such as porphyritic basalt, trachyte, syenite, volcanic breccia and acid lava. The carbonatite was thought to be a large xenolith of dolomitic limestone. According to Truter (1949), there was doubt that the carbonatite was a large xenolith of dolomitic limestone, and suggested a "hydrothermal carbonatitic origin" (Verwoerd, 1967).

An initial reconnaissance radiometric survey followed by an airborne scintillometer survey on the Kruidfontein Carbonatite Complex were carried out in 1955 by Anglo-Transvaal Consolidated Investment Corporation Ltd. A surface scintillometer survey was also conducted by Verwoerd (1956). In 1967 the Kruidfontein Carbonatite Complex was described by Verwoerd as having an outer zone consisting of acid volcanics and subordinate intermediate lavas, and an inner zone consisting of metacarbonatite.

In most of the studies cited above, reference was made to fluorite mineralisation, and some of anomalous radiometric readings could be related to fluorite mineralisation. This prompted Metallgesellschaft S.A. (Pty) Ltd., to undertake an exploration program during 1970 and 1971. This program comprised geological mapping, sampling, trenching and drilling. The aim was to assess the viability of the fluorite veins and fluorite-bearing sövite bodies in the southern and southwestern portions of the inner zone. They concluded that the veins were too narrow and that the sövite bodies were too small to be of economic significance.

In 1972 Southern Sphere Mining and Development Company (Pty) Ltd conducted a soil and rock sampling program in an attempt to delineate additional fluorite and base metal anomalies. Although the fluorite potential seemed to be promising, that of the base metal potential appeared to be low. Due to an improvement in the fluorite and rare-earth-element markets during 1979, Southern Sphere Mining and Development Company (Pty) Ltd recommenced the exploration program. Initial emphasis was placed on evaluating certain anomalies by drilling and the fluorite mineralisation in the southwestern part of the inner zone proved better than expected. A large (2.8 Mt) tabular replacement deposit consisting mainly of fluorite (up to 28% CaF_2) was subsequently discovered.

More recent work (1989) was carried out by FOSKOR (Pty) Ltd, who initiated a geological mapping and

Digitised by the Department of Library Services in support of open access to information, University of Pretoria, 2021

soil sampling program on the inner and outer zones of the Complex. The results revealed a gold anomaly in the northwestern part of the inner zone. Although some results were encouraging, activities were terminated. Volcanological, petrological and geochemical studies were carried out by Clarke (1989) and Clarke and Le Bas (1990) in which they confirmed that the Kruidfontein Complex is a collapsed carbonatitic caldera structure, filled with silicate pyroclastics (outer zone) and carbonatitic bedded volcaniclastic rocks (inner zone). Studies carried out on pumice fragments suggest that phonolitic and carbonatitic magmas were present during the cauldron subsidence stage of evolution of the Complex. Pirajno et al. (1995), using the work of Clarke (1989), Clarke and Le Bas (1990) and Clarke et al. (1991), and results from FOSKOR (Pty) Ltd as background information, focused on the gold enrichment in the northeastern part of the inner zone. Despite the limited data they made the tentative conclusion that the gold became concentrated within the weathered carbonatitic pyroclastics under oxidising conditions.

Digitised by the Department of Library Services in support of open access to information, University of Pretoria, 2021

4. ACKNOWLEDGEMENTS

Technical information provided by FOSKOR (Pty) Ltd. regarding the following is gratefully acknowledged:

- the baseline and grid system used for soil sampling and other surveys;
- the positions and analyses of soil samples collected for the geochemical exploration;
- the results of geophysical surveys, comprising magnetic and radiometric methods;
- results of a drilling program, including the supply of the core samples and some relevant analyses;
- Lex Geraghty, formerly of FOSKOR (Pty) Ltd., who introduced me to the geology of the Kruidfontein Carbonatite Complex.

The Management and staff members of the Council for Geoscience are thanked for their continued interest and help, especially the staff of the XRD (Maria Atanasova), XRF (Corlien Cloete, Jansie Truter), microprobe (Dr. Deon de Bruin, Carel Janse van Vuuren and Annebie Wentzel) and stable isotope (Dr. Uwe Horstmann) laboratories. Special thanks is due to Frances Wall and Dr. Chris Hayward of the Department of Mineralogy, Natural History Museum, London, for their assistance with SEM and cathodoluminescence work respectively. Prof. C.P. Snyman is thanked for his support and guidance. His helpful suggestions were invaluable.

I thank Karin, Chantelle, Monique and my parents for their support and encouragement during this study.

Digitised by the Department of Library Services in support of open access to information, University of Pretoria, 2021

5. METHODS OF INVESTIGATION

5.1 Mapping

As the inner (and economically interesting) zone of the Kruidfontein Carbonatite Complex is more or less elliptical in plan, with the major axis east-west, an irregular hexagonal base line system was used by FOSKOR (Pty) Ltd. for survey purposes. This system is tied in with the south African Lo system, using 27°E as central meridian. Each side of the hexagon is 1.4 kilometre in length, the northern one along the boundary between Boschkop 138JQ and Kruidfontein 139JQ (Fig. 5.1). Compass traverses, 100m apart, in both directions perpendicular to these base lines were used as sampling lines. Samples spacing was 20 metres on each of these lines.

For regional reconnaissance sampling the complex was divided into Area 1 and Area 2 by a north-south bisecting line of the hexagon (Fig. 5.1). Both these areas were further subdivided by the east-west bisecting line of the hexagon, so that Area 1 comprised a northern Block 1 and a southern Block 2. Similarly Area 2 was subdivided into a northern Block 3 and a southern Block 4.

For the purpose of detailed mapping the Council for Geoscience superimposed a square grid pattern on the regional sampling pattern (Fig. 5.1). Eleven base lines in a north-south orientation and nine in an east-west orientation (in both cases 500 m apart) were inserted, resulting in reference blocks numbered A to J in an east-west and 1 to 8 in a north-south direction. These reference blocks were used for accurate reference.

5.2 Soil sampling

Before the Kruidfontein geochemical exploration project was initiated, an orientation survey was carried out to determine what sampling method, sample size, sampling depth and size fraction would be most suitable to achieve the maximum contrast in the geochemical landscape. Ultimately the sampling scheme was based on the topography and the known form, size, geology and structure of the Complex. The orientation survey also included a limited amount of geological mapping and rock sampling along a traverse intersecting the maximum number of rock types. Samples were taken of every rock type, zone of alteration, vein and dyke. Three to five samples of each rock type, varying in mass from 1 to 5 kg were collected.

In order to select the elements to be analysed, all samples were analysed semi-quantitatively by means of XRF spectrometry for the trace elements Ba, F, Mn, Ag, Cu, Pb, Zn, As, Hg and by fire-assay for Au. The elements that gave the highest contrast in the different rock types were chosen, namely Au, Ba, Mn, Pb and Zn.

Digitised by the Department of Library Services in support of open access to information, University of Pretoria, 2021

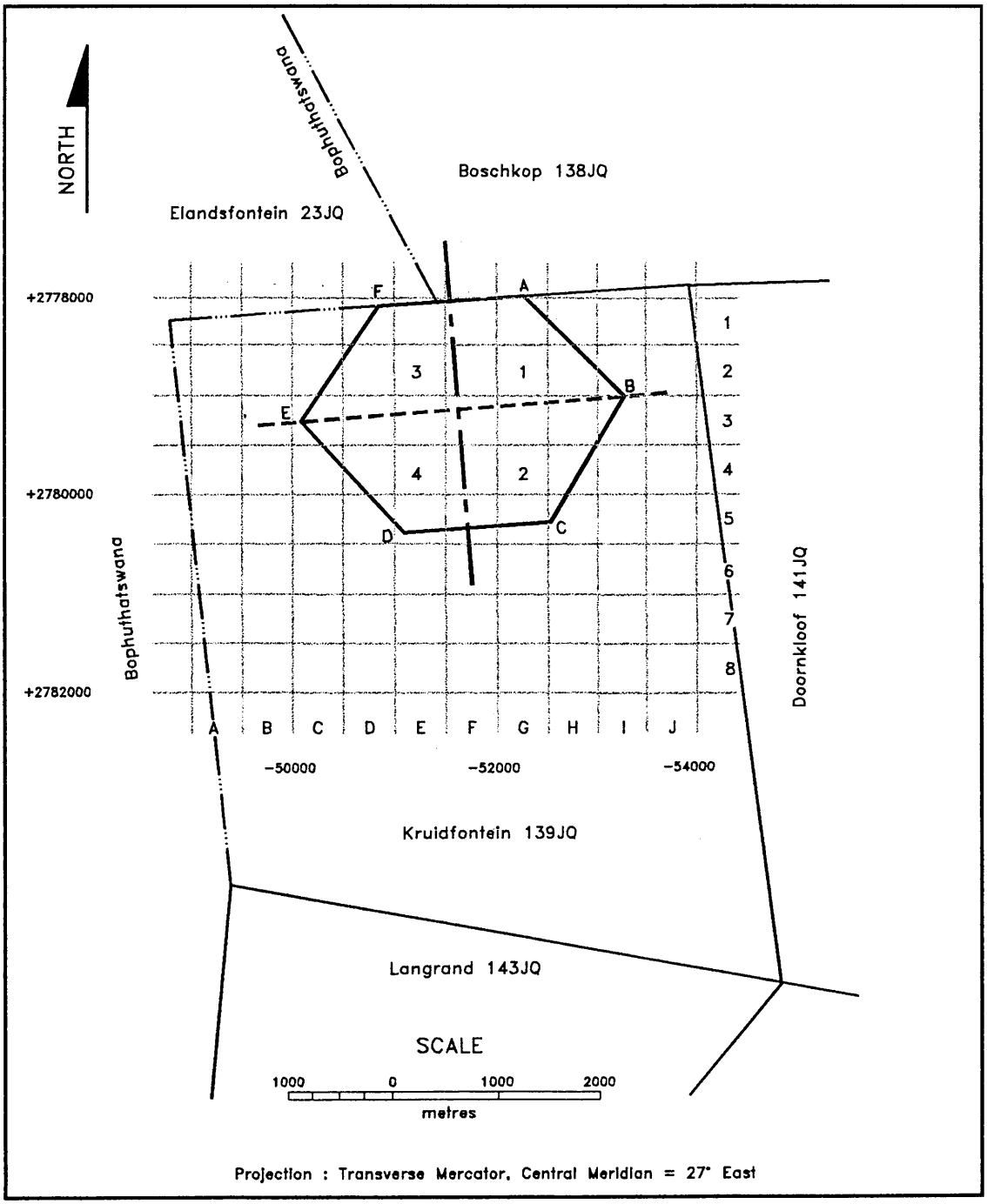

Figure 5.1 Map depicting farm boundaries, hexagonal base line system, divided by a north-south bisecting line. A square grid pattern is superimposed on the study area for the purpose of detailed mapping. Note that the blocks are labelled alpha numerically for easy reference.

Digitised by the Department of Library Services in support of open access to information, University of Pretoria, 2021

On the basis of the orientation survey, the following decisions were made:

- a grid pattern of sampling lines 100 metres apart, with sampling points every 20 metres, giving a grid 20 x 100 metres would be used;
- the grid pattern would be laid out radially across the inner and outer zones of the Complex, based on the hexagonal base line system;
- soil samples would be taken at 25 to 30 cm depth;
- the -80 mesh sieve fraction (-177µm) would be analysed for Au, Ba, Mn, Pb and Zn.

During the soil sampling program a total of 8762 soil samples were taken over the whole project area of 1779 hectares: 1170 and 2750 samples from Blocks 1 and 2 of Area 1 and 1578 and 3264 samples from Block 3 and 4 of Area 2 respectively. The samples were sieved in the field and sealed in plastic sample bottles. The possible effect of topography on the nature of the samples was noted. All samples were analysed by the FOSKOR chemical laboratories. The Au determinations were carried out by fire assay and subsequent atomic absorption spectroscopy, giving a detection limit of 10 ppb. The remaining element concentrations were determined using X-Ray Fluorescence techniques (detection limits for Ba, Mn, Pb and Zn being 0.05 wt%, 0.1 wt%, 20 and 50 ppm respectively).

The results were plotted on 1:25 000 scale field maps after the threshold values had been determined statistically.

5.3 Geophysical methods

Carbonatite complexes can be identified by means of magnetic and gravity surveys as well as regional geochemical and radiometric surveys as their physical properties and trace element content normally differ from those of the surrounding rocks. Magnetic and gravity techniques were therefore used in the exploration of the Kruidfontein Carbonatite Complex in an attempt to determine the presence of magnetic and/or more dense rock types in depth, and thus to obtain an indication of the possible structure. Geochemical results were used to correlate radiometric eK_2O, $eThO_2$ and eU_3O_8 values with the known lithology, alteration products and possible mineralisation.

5.3.1 Regional magnetic and gravity surveys

As part of its national geophysical reconnaissance program, the Council for Geoscience of South Africa did a series of aeromagnetic surveys at an altitude of 150±50 m with a flight line spacing of 1 km and an estimated sample spacing of 100 m. The navigation was carried out by means of radar beacons. The aeromagnetic data were recorded by means of a Scintrex Cesium Vapor magnetometer.

Digitised by the Department of Library Services in support of open access to information, University of Pretoria, 2021

The gravity measurements used in this study form part of the regional gravity data base of the Council for Geoscience. Gravity readings were taken on a rudimentary grid system at approximately 3 km spacing, based on available roads. Station altitudes were determined by using drift-coupled barometers, resulting in an elevation reading within 3 m of the true value. Gravimeter drift was kept to a minimum by implementing thermostatically controlled Lacoste-Romberg instruments, the drift of which were monitored every 12 hours with respect to a base station. Thus the cumulative error in the theoretical gravity values due to spatial positioning and gravimeter drift was some 6 milligal. Since the survey area has no substantial topography differences the Bouguer gravity data have not been corrected for topography.

5.3.2 High-resolution radiometric survey

The Chemtron Model G111A gamma-ray spectrometer was used for the regional radiometric survey. This spectrometer is capable of counting the rate of gamma ray emission by potassium and by specific daughter isotopes of uranium and thorium simultaneously in three separate channels, as well as the total emission in a fourth channel. The rate of gamma ray emission is a function of the concentration of the daughter isotopes. Channel drift is electronically corrected using the energy peaks of an internal source as reference.

As the gamma radiation caused by the disintegration of specific daughter isotopes within the multiple decay chain of two of the above three elements is measured, constant initial isotopic ratios of the specific parent elements (e.g. ^{238}U and ^{235}U) is assumed, as well as chemical equilibrium between the parent and each element in the decay chain. Since the various parent and daughter elements have different physical and chemical properties, disequilibrium could result from selective leaching or similar processes (Basson, 1979). Consequently spectrometer readings are given as "equivalents" of the parent isotope to account for possible disequilibrium e.g. eK_2O, eU_3O_8 and $eThO_2$.

The spectrometer detects gamma radiation by the fluorescence caused by the interaction of gamma radiation on specific crystals. The fluorescence is detected by a photocathode coupled to a photomultiplier tube. The magnitude of a pulse caused by a gamma ray is directly proportional to the energy of the gamma ray absorbed by the crystal. As the energy of the gamma rays is characteristic of the specific disintegrating nuclide, differentiating the different energy levels allows identification of the disintegrating nuclide (Basson, 1979). The number of pulses received by the photomultiplier tube is proportional to the concentration of the source. This count rate is also affected by the

Digitised by the Department of Library Services in support of open access to information, University of Pretoria, 2021

geometry of the source "visible to the detector". Readings within a pit would thus be greater than those on a flat surface by virtue of geometry. Gamma radiation is also readily absorbed and factors such as the instrument height and depth of the source material below the surface would affect the sensitivity.

The gamma-ray spectrometer was initially calibrated at the high concentration pads at Pelindaba. The calibration constants were determined by the Atomic Energy Corporation. These calibration constants resulted in many negative eK_2O values, presumably due to the high concentrations in the calibration pads. Recalibration at low concentration pads was therefore done at Lanseria. The resulting calibration matrix was very similar to that of Pelindaba.

The final calibration matrix is thus:

eK_2O (%)	=	3.0756 (K) - 5.0225(U) + 1.8389 (Th)
eU_3O_8 (ppm)	=	22.6632 (U) - 24.6275 (Th)
$eThO_2$ (ppm)	=	46.62 (Th) - 8.2463 (U)

Where (K) = counts per second in the potassium channel; (U) = counts per second in the uranium channel; and (Th) = counts per second in the thorium channel.

The radiometric survey was carried out along the regional sampling lines which were 100 metres apart, and perpendicular to the hexagonal base line system surveyed around the inner zone of the Kruidfontein Carbonatite Complex (Fig. 5.1). The radiometric readings were taken at 20 metre intervals along each line.

5.3.3 High-resolution magnetic survey

The earth has a natural magnetic field, the strongest component of which is the internal field now presumed to be due to the relative rotation of iron-enriched material at the core-mantle boundary. This field can be measured at any point on the earth's surface as a vector. There are four types of magnetic materials based on their response to an external magnetic field namely: diamagnetic, paramagnetic, ferrimagnetic and ferromagnetic.

Ferromagnetic and ferrimagnetic minerals are the only ones which have an appreciable influence upon the earth's magnetic field. The inducing field **H** causes the magnetic alignment of ferrimagnetic and ferromagnetic minerals in a rock mass to produce an induced field **M** that is proportional to **H**. The proportionality factor δ (the so-called

Digitised by the Department of Library Services in support of open access to information, University of Pretoria, 2021

magnetic susceptibility) is determined by the amount and distribution within the rock of magnetic minerals like magnetite, native iron, titanomagnetite, pyrrhotite and ilmenite. As magnetite is more than 1000 times more abundant than the total of the other magnetic minerals, the magnitude of **M** is for all practical purposes proportional to the magnetite content of the formation. One would therefore expect that a high value of the measured total magnetic field would give a direct indication of the magnetite content of the underlying rocks, but there are some complicating factors:

- the ambient magnetic field of the earth is a vector field and, in the vicinity of the Kruidfontein complex, this vector has a strength of 29000 nT and an inclination (i.e. a deviation from horizontal) of 60° in a declination (i.e. deviation from geographic north) of 17° west. In practice there will be two vector fields which have to be added vectorially - the background field caused by the earth's magnetic field (**H**) and a dipole-shaped field induced in the rock-body (**M**). The resultant of these two fields is conventionally called **B**. Most proton magnetometers measure the absolute magnitude of **B** only. So under normal circumstances, the magnitude of the measured field in South Africa will generally have a low value to the south of a magnetic body and a high value to the north of it, with the body itself directly below the crossover point.
- most magnetite-rich rocks have been exposed to magnetic fields with completely different orientations compared to that of the present field, and they may have retained some of this remanent induced magnetic field. This fact leads to ambiguity-remnant magnetism at some time or other which must also be incorporated in the interpretation. This incorporation can only be accomplished by determining the approximate strength and orientation of this remanent field of the rock-body by the techniques used in palaeomagnetic studies, and for this oriented rock samples, taken by means of non-magnetising drilling equipment, are required.

A proton precession magnetometer (Geometrix G8469G) was used in this survey, since this type of instrument can be transported easily and can be read rapidly. The principle of these instruments depends on nuclear magnetic resonance, in which a spinning hydrogen ion, which has its own magnetic dipole moment, executes a precession motion at a frequency directly proportional to the applied magnetic field. Initially the ions of a H-rich fluid are aligned by a strong artificial field, which is switched off to allow the H ions to realign themselves to the ambient magnetic field of the earth, and causing them to precess at a frequency which is measured and converted to the strength of the earth's

Digitised by the Department of Library Services in support of open access to information, University of Pretoria, 2021

field.

The same grid used for the radiometric survey was also used for the ground magnetic survey. Normally, a base station would be set up in order to correct for diurnal drift caused by changes in the magnetosphere, but no base station corrections have been made in this study.

5.4 Drilling

FOSKOR (PTY) LTD initiated a drilling program after several geochemical anomalies had been identified in the soil sampling program. The most important target generated by the geochemical exploration is the ferruginous lapilli tuff unit (2H) in the northeastern part of the inner zone (Fig. 5.2). As the elliptical outcrop pattern of the rocks of the inner zone of the Complex suggests centroclinal dips of about 30°, percussion boreholes were drilled at outward inclinations of 60° to a depth of 61 m. Samples were collected at 1 metre intervals, split and packed for analysis. Sections A - B and C - D (Fig 5.2) are based on these results.

After completion of the percussion drilling program three diamond drill holes were sunk in the northeastern part of the Kruidfontein Complex to penetrate the volcaniclastic sediments of the inner zone (boreholes KD01 to KD03) (Schürmann, 1992a; 1992b; 1992c; 1993). KD01 and KD02 are inclined and perpendicular to the layering, whereas KD03 is vertical.

5.5 Laboratory techniques

The drill core of boreholes KD01, KD02 and KD03 were cut lengthwise in two perpendicular directions by means of a diamond saw. One of the quarters formed in this way was sampled every five metres over a length of approximately 40cm. Each sample is representative of a specific lithologic unit at a certain depth. All the samples were submitted for X-ray diffraction, X-ray fluorescence spectrometry, high-performance ion chromatography and detailed petrography (including cathodoluminescence). Details of other analyses are given in Table 5.1.

5.5.1 Major- and trace-elements

Both major- and trace-elements were analysed on a Philips PW1400 XRF Sequential Spectrometer with a Rh anode side-window X-ray tube housed at the Council for Geoscience, South Africa. Major-elements, excluding Na_2O, were analysed on fusion disks prepared from 1.5 g of sample and 6 g Johnson and Matthey Spectroflux 100B. The software package NBSGSC (Tao et al., 1985) was used to set up the calibration for each oxide and for data reduction.

Digitised by the Department of Library Services in support of open access to information, University of Pretoria, 2021

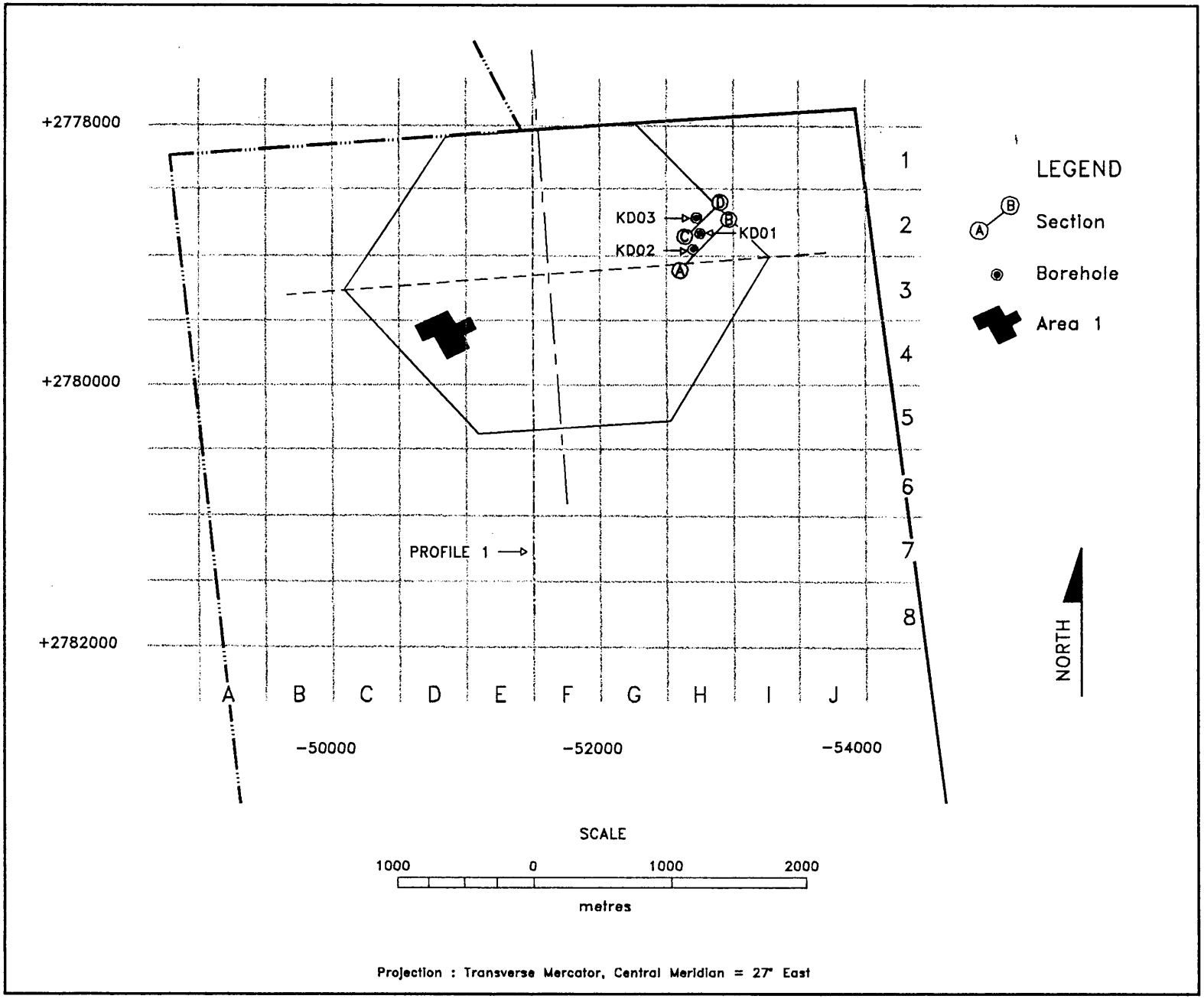

Figure 5.2 Locality map showing (a) the north-south magnetic profile 1; (b) borehole positions (KD01, KD02 and KD03); (c) sections (A-B and C-D); and (d) Area 1 (principle area of fluorite mineralisation).

Digitised by the Department of Library Services in support of open access to information, University of Pretoria, 2021

Trace-element and Na_2O analyses were carried out using powder briquettes. Calibration was based on the technique described by Willis (1989). FeO was determined by titration. CO_2 was analysed with a LECO CS244 apparatus by heating the sample in a stream of pure and dry oxygen. The combustion or dissociation products (CO_2 and water) were measured by absorption of the formed carbon dioxide in the near infrared region, and the CO_2 content is listed separately from loss on ignition (L.O.I.).

5.5.2 Rare-earth elements

Rare-earth element (REE) analyses were carried out on a Dionex Series 2000i/SP Ion Chromatograph, housed at the Council for Geoscience, South Africa. The separation of transition and alkali metals was achieved on-line, eliminating the necessity of an earlier separation step. First, the alkali and alkaline earth metals are eluted with ammonium acetate, followed by the elution of the transition metals with hydrochloric acid. Separation of the rare earths is accomplished by gradient elution with an oxalic-diglycolic system, followed by complexing with *PDCA* and photometric detection in the visible wavelength range (Le Roux and Watkins, 1990). The relative error in the rare-earth element determination is estimated at ± 6% (using the NBS-688 International standard).

5.5.3 Stable carbon and oxygen isotopes

Twenty-one samples from the inner zone of the Kruidfontein Complex were analysed for their carbon and oxygen isotopic composition. X-ray diffractograms showed the carbonate species of this sample set to be calcite, dolomite, ankerite and siderite with up to 3 carbonate species occurring in one sample. Whole-rock carbonate data were obtained by reaction with 100% H_3PO_4, using a modified technique after McCrea (1950) and Rosenbaum and Sheppard (1986). Depending on the dominant carbonate phase, calcite-rich samples were reacted at 25°C and dolomite/ankerite-rich samples at 50°C, for 20 to 24 hours, and siderite-rich samples at 150°C for 1 to 1.5 hours (Rosenbaum and Sheppard, 1986).

Whole-rock carbonate data would reflect a mixture of their carbonate phases. Because a physical mineral separation was not practical, multi-carbonate samples were treated using the sequential-reaction technique described by Al-Aasm et al. (1990). Because of the slower reaction with H_3PO_4 of dolomite and ankerite, and the still slower reaction of siderite, when compared to calcite, it is possible to collect separate batches of CO_2 from the carbonate phases of a reacted bulk sample. Following Al-Aasm et al. (1990) samples containing calcite and dolomite/ankerite and/or siderite were reacted at 25°C for one hour and the extracted gas labelled calcite. Immediately thereafter these samples were equi-

Digitised by the Department of Library Services in support of open access to information, University of Pretoria, 2021

Table 5.1 Summary of samples taken from the KD01 core and techniques applied.

SAMPLE	DESCRIPTION	C/O ISOTOPES	Energy-dispersive electron microprobe / Wavelength-dispersive electron microprobe				
			chlorite	carbonates	feldspar	fluorite	apatite
KD011	Lapilli tuff						
KD012	Layered ash tuff			✪	✪		✪
KD013	Lapilli tuff	●					
KD014	Layered ash tuff						
KD015	Green ash tuff						
KD016	Green ash tuff	●	✪	✪			✪
KD017	Altered brown ash tuff						
KD018	Altered brown ash tuff						
KD019	Altered brown ash tuff	●	✪	✪	✪		✪
KD110	Pyroclastic breccia						
KD111	Lapilli tuff	●	✪	✪		✪	✪
KD112	Altered brown ash tuff						
KD113	Altered brown ash tuff	●					
KD114	Altered brown ash tuff						
KD115	Altered brown ash tuff			✪			
KD116	Altered brown ash tuff	●					
KD117	Altered brown ash tuff			✪	✪		
KD118	Altered brown ash tuff	●					
KD119	Altered brown ash tuff		✪		✪		
KD120	Altered brown ash tuff						
KD121	Altered brown ash tuff		✪	✪	✪	✪	
KD122	Altered brown ash tuff	●					
KD123	Altered brown ash tuff						
KD124	Altered brown ash tuff	●			✪		
KD125	Altered brown ash tuff						
KD126	Altered brown ash tuff						
KD127	Altered brown ash tuff						
KD128	Altered brown ash tuff			✪			
KD129	Altered brown ash tuff						
KD130	Altered brown ash tuff	●	✪		✪	✪	
KD131	Altered brown ash tuff			✪			
KD132	Altered brown ash tuff						
KD133	Altered brown ash tuff	●	✪	✪	✪		

Digitised by the Department of Library Services in support of open access to information, University of Pretoria, 2021

SAMPLE	DESCRIPTION	C/O ISOTOPES	Energy-dispersive electron microprobe / Wavelength-dispersive electron microprobe				
			chlorite	carbonates	feldspar	fluorite	apatite
KD134	Altered brown ash tuff	●		✪			✪
KD135	Dark ash tuff, calcite and fluorite		✪	✪			
KD136	Dark ash tuff, calcite and fluorite						
KD137	Altered brown ash tuff						
KD138	Altered brown ash tuff	●	✪				
KD139	Altered brown tuff				✪		
KD140	Altered brown tuff		✪				
KD141	Massive fluorite and calcite	●					
KD142	Massive fluorite and calcite	●		✪			
KD143	Massive fluorite and calcite						
KD144	Altered brown tuff						
KD145	Altered brown tuff						
KD146	Altered brown tuff	●	✪	✪			
KD147	Altered brown tuff	●	✪	✪			
KD148	Altered brown tuff						
KD149	Altered brown tuff						
KD150	Altered brown tuff						

librated at 50°C for 30 minutes and the evolved gas discarded. The reaction was continued and dolomite/ankerite was subsequently decomposed at 50°C overnight.

Calcite, dolomite and ankerite were reacted at 25°C where siderite was also present in the sample and siderite was subsequently reacted at 50°C. Reaction times stretched from a few hours to several days, allowing enough time between two extractions to discard any CO_2 which could have been contaminated by previously generated CO_2 (Al-Aasm et al., 1990).

Phosphoric acid / carbonate fractionation factors used in the extraction procedures at various temperatures were 1.01025 at 25°C for calcite (Friedman and O'Neil, 1977, corrected from Sharma and Clayton, 1965), 1.01178 at 25°C and 1.01065 at 50°C for dolomite, 1.011741 at 25°C and 1.010609 at 50°C for ankerite, and 1.010461 at 50°C and 1.00771 at 150°C for siderite (all after Rosenbaum and Sheppard, 1986).

Digitised by the Department of Library Services in support of open access to information, University of Pretoria, 2021

The analyses of the liberated CO_2 gas were performed on a Finnigan MAT 251 triple collector gas-source mass-spectrometer. The C and O isotope ratios are reported in the common δ notation in ‰ relative to PDB (VPDB) for C, and to SMOW (V-SMOW) for O using an internal standard, calibrated against NBS-19. The reproducibility of an internal standard, analysed routinely, is better than ±0.1‰. All samples were done in duplicate; the difference between two aliquots of a sample was < 0.1‰ for calcite and the whole-rock carbonate samples, and <0.2‰ for dolomite, ankerite and siderite, from the sequential extractions. Calculated whole-rock carbonate $\delta^{13}C$ and $\delta\ ^{18}O$ values from sequentially reacted carbonates, are in reasonable agreement with the whole-rock analyses, underlining the applicability of the sequential-reaction technique.

5.5.4 X-ray diffraction

X-ray diffractometry was used to determine the mineralogy of samples from whole rock powders. Philips PW1050 and Siemens D5000 X-ray diffractometers (both with secondary monochromators) were used with Co Kα and Cu Kα radiation respectively, generated at 40 kV and 40 mA. XRD traces were qualitatively evaluated with DIFFRAC AT software, allowing comparison with ICDD (International Centre for Diffraction Data, 1992) files. Selected peak heights were taken as a semi-quantitative measure for the minerals present.

5.5.5 Cathodoluminescence

Cathodoluminescence was carried out at the Department of Mineralogy of the Natural History Museum, London, United Kingdom, using a CITL Mk. 4 cold-cathode instrument operated at beam conditions of 15kV and 300 μA and with a vacuum of 0.1Torr. These readings are measured within the control unit of the cathodoluminescence (CL) equipment; readings of beam conditions at the sample are not possible. The electron beam impinges upon about 100 mm^2 of the sample, which gives an approximate power density at the sample of 0.045 Wmm^{-2}. The CL vacuum chamber was mounted on a Leitz LM DM microscope, which is adapted especially for CL, with no accessories, beam-splitters or prisms within the light path. This enables almost 100% of the light emitted by the sample during CL to reach the oculars or the camera, with the only absorption occurring within the lenses and the lead-glass window of the vacuum chamber. Lenses used were Leitz Fluotar long working distance X5, X10 and X20 and a Nikon ELWD X40. Photomicrographs were taken in transmitted light using a Wild Leitz MPS 52 camera and Wild Leitz MPS 46 automatic camera control unit, with 400 and 1600 ASA Provia Fujichrome daylight slide film, corrected for tungsten light by means of a blue daylight filter. Exposure times for CL photomicrographs were typically 20-45 seconds, 20-90

Digitised by the Department of Library Services in support of open access to information, University of Pretoria, 2021

seconds and 120-150 seconds for X32, X80 and X320 magnifications respectively.

Cathodoluminescence takes place when primary excitation is by a beam of electrons, the cathode being the source of the electrons (Marshall, 1988). Luminescence in carbonates is mainly caused by trace elements in solid solution (Machel, 1985). Other causes, however, are (a) distorted crystal surfaces and cracks; (b) distorted internal structures between mosaic and intergrown crystals; (c) inhomogeneities of composition (between different parts of a crystal); (d) impurities in surface sites and interstitial lattice sites; and (e) charge displacements due to abnormally ionised or abnormally sized atoms and separated cation-anion pairs (Gies, 1976; Nickel, 1978; Marfunin, 1979). Other applications of cathodoluminescence microscopy are: (a) rendering fabrics visible which are not visible by standard petrographic microscopy (Sippel and Glover, 1965; Richter and Zinkernagel, 1981); (b) identifying and interpreting "cement sequences" or matrixes of replacement or rocks of diagenetic origin (Meyers, 1974); and (c) interpreting the trace element content of minerals, and of the formational fluids responsible for alteration, mineralisation, replacement and cementation.

Other general applications of cathodoluminescence are summarised as follows (Mariano et al., 1973; Mariano and Ring, 1975; Mariano, 1978; Marshall, 1978; 1988):

- determining the distribution of different minerals. Calcite and dolomite usually show differences in luminescence, where under more conventional petrographic methods, they seem similar;
- fine-grained minerals (like calcite, dolomite or apatite) or minerals in narrow vein filling are immediately distinguishable under CL;
- variations in the luminescent emission from different portions of the same mineral grain can indicate different generations or different conditions of formation;
- the colour of the luminescence of a particular mineral can be ascribed to the trace element content of the mineral;
- different luminescent properties of mineral examples of the same species could indicate that they have formed under different conditions, or may have formed from different sources.

The recording of emitted luminescence can be observed visually or recorded by spectrometer. Visually the effect is described as "bright", "dull" or "non-luminescent". The colour description, like the intensity, is dependent on the visual perception of the investigator. This problem is eliminated by the use of a spectrometer which measures the

Digitised by the Department of Library Services in support of open access to information, University of Pretoria, 2021

emission spectra. As an example, the specific wavelength of 590 nm is characteristic of Mn^{2+} activated luminescence in calcite.

Trace elements that promote active luminescence are Mn^{2+}, Pb^{2+}, several REE, Cu^{2+}, Zn^{2+}, Ag^{+}, Bi^{+} and probably Mg^{+} (Machel, 1985). The increase in luminescence intensity slows down above a certain activator concentration. Quenchers (elements like Fe^{2+}, Ni^{2+} and Co^{2+}) have an opposite effect, and lead to a low intensity of luminescence due to the absorption of most of the excitation energy and the generated transition energy without emitting radiation.

5.5.6 Electron microprobe analyses

Electron microprobe analyses of fluorite and apatite were made by using a Cameca SX50 WDS and a Hitachi S2500 EDS (housed at the Department of Mineralogy, Natural History Museum, London, United Kingdom). Analyses required lower kV values (15 kV, and 10 to 20 nA) and a defocused elecron beam (spot size of 5 to 25 µm). Typical detection limits for REE (wt% oxide) were 0.15, while for other elements it was 0.05 wt %. A JEOL 733 Superprobe (housed at the Council for Geoscience, Pretoria, South Africa) was also utilised for EDS analyses, with beam conditions of 15 kV and 15 nA and with spot diameters of 1 to 5 µm.

Digitised by the Department of Library Services in support of open access to information, University of Pretoria, 2021

6. REGIONAL SETTING OF THE KRUIDFONTEIN CARBONATITE COMPLEX

The Kruidfontein Carbonatite Complex is situated 160 km north-northwest of Pretoria (Fig. 1.2) on the farms Kruidfontein 139JQ, Doornkloof 141JQ and Elandsfontein 23JQ (Fig. 5.1). The Complex of Middle Proterozoic age, and with a caldera structure, is located along the northwest striking regional fault on the western side of the Crocodile River Fragment, an inlier of deformed Transvaal Supergroup rocks within the acid and mafic rocks of the Bushveld Complex (Hartzer, 1989). The Transvaal Supergroup in the Crocodile River Fragment consists of a pre-Black Reef, predominantly sedimentary succession (dolomite, shale, quartzite, conglomerate and volcanic rocks) (Wachteenbeetje Formation), shale and quartzite of the Black Reef Formation, dolomite, limestone and banded iron formation of the Chuniespoort Group and shale and quartzite of the Pretoria Group (Table 6.1).

The Rooiberg Group occurs towards the east of the Fragment while the Karoo Supergroup is represented by outliers towards the south. Several alkaline and carbonatite complexes occur within the Fragment such as the Buffelskraal, Nooitgedacht and Kruidfontein Complexes, while the Tweerivier, Bulhoek North and Bulhoek South Complexes are present in the Bushveld Granite, south-southeast of the Crocodile River Fragment. The pre-Black Reef succession of predominantly sedimentary rocks with minor volcanics was named the Wachteenbeetje Formation by Hartzer (1994) who correlated it with pre-Black Reef successions in the Transvaal basin such as the Wolkberg Group, the Bloempoort Formation and possibly even the Pniel Group. Some controversy still exists as to whether the Wachteenbeetje Formation should be considered as the upper part of the Ventersdorp Supergroup or as the lower part of the Transvaal Supergroup. The Transvaal Supergroup from the Black Reef Formation upwards (including the carbonate rocks of the Chuniespoort Group) to the shales of the Silverton Formation has been completely preserved within the Crocodile River Fragment, the only exception being the Penge Formation, the upper part of which has been eroded prior to the deposition of the Pretoria Group. The thicknesses of the Black Reef Formation and the lower carbonate units, especially the Oaktree Formation are noticeably greater than those preserved along the margin of the Transvaal basin.

In general the structure of the Crocodile River Fragment can be described as a large anticlinorium (Fig. 1.2). This anticlinorium is believed to be the result of interference between northwest to southeast and northeast to southwest striking folds, which are thought to have formed during three different phases of deformation (Hartzer, 1989). Two prominent, north-northwest striking faults (f1 and f2), marked by breccia, form the eastern and part of the western margins of the anticlinorium. The southern part of the Crocodile River Fragment is dominated by a large overturned anticline, marked by outcrop of the Black Reef Formation (Hartzer, 1994). The distribution of the Black Reef Formation and the various carbonate units in this area emphasises the extent of refolding and overfolding. Parasitic and interference folding have led to severe thickening of the carbonate sequence in places, especially the Oaktree and Monte Christo Formations. The northern part of the Crocodile River Fragment is characterised by north-east striking folds

Digitised by the Department of Library Services in support of open access to information, University of Pretoria, 2021

with curved axial plains. The structure is further complicated by the intrusion of the Buffelskraal and Nooitgedacht Complexes in the centre of the anticlinorium. Their development was responsible for radial thrusting and faulting around the centres of intrusion (Hartzer, 1989).

Table 6.1 Lithostratigraphic subdivision, lithology and approximate thicknesses of the formations in the Crocodile River Fragment (modified after Hartzer, 1994).

THICKNESS (m)	FORMATION	LITHOLOGY	SUBGROUP OR GROUP		SUPERGROUP	COMPLEX
		Nepheline syenite, ijolite, carbonatite, nephelinite				Kruidfontein Nooitgedacht Buffelskraal
100 80 90 10 190 695 3 to 50	Silverton Daspoort Strubenkop Dwaalheuwel Hekpoort Timeball Hill Rooihoogte	Shale Quartzite Shale Quartzite Andesite Shale, quartzite Conglomerate, quartzite, shale		Pretoria Group	Transvaal Supergroup	
141	Penge	Banded iron formation		Chuniespoort Group		
195 410 320 810 360	Frisco Eccles Lyttelton Monte Christo Oaktree	Dolomite, limestone Dolomite, chert Limestone, dolomite Dolomite, chert Limestone, dolomite	Malmani Subgroup			
280	Black Reef	Conglomerate, quartzite, shale				
1560	Wachteenbeetje	Shale, quartzite, dolomite, conglomerate, volcanics				

The emplacement of the Kruidfontein Complex in the centre of the Crocodile River Fragment caused local overfolding and thrusting. The southwestern part of the fragment is separated from the main body by the f1-fault and comprises the prominent Langrand anticline, which is part of a series of anti- and synclines, striking parallel to the main fault. Towards the north, the series of folds culminates in a dome, accentuating the influence of interference folding (Fig. 1.2).

Tectonically, the present features of the Crocodile River Fragment are the result of a complex interaction between regional deformation and the emplacement of the Bushveld Complex. Hartzer (1994) ascribed the initial folding to regional deformation along well-established and long-lived structural directions on the Kaapvaal Craton. Interference folding led to a series of domes and basins. Regional deformation was followed by the emplacement of the mafic rocks of the Bushveld Complex through a feeder zone believed to be located between the western edge of the Crocodile River Fragment and the western outer margin of the Transvaal basin. The Fragment acted as a physical barrier to the intruding mafic rocks, restricting

Digitised by the Department of Library Services in support of open access to information, University of Pretoria, 2021

them from spreading towards the central part of the Transvaal basin. The subsequent emplacement of the acid phase of the Bushveld Complex took place at higher levels and covered the central part of the Transvaal basin, including the Crocodile River Fragment. Petrographic evidence shows that deformation was initiated before the metamorphism associated with the intrusion of the Bushveld Complex.

Therefore, the structural deformation history of the Crocodile River Fragment can be summarised in the following phases (Hartzer, 1994) (Fig. 1.2):

- ❑ the first stage of folding (D1) was around a north-west trending axial plain and occurred in the northern part of the Crocodile River Fragment.
- ❑ the second stage of deformation was around a north-eastern trending axial plain and is manifested as the central synclinal structure. These deformational events were associated with Archaean lineaments and Transvaal folding respectively.
- ❑ the third stage of folding had a similar attitude to the first and was around an axial plain toward the north-west. This folding is manifested by the interference pattern on the nose of the anticlinal structure in the southern part of the Crocodile River Fragment.
- ❑ the final stage of deformation was associated with the two north-west striking regional faults. These faults are younger than the Bushveld Complex since they transgress rocks of both the Transvaal Supergroup and the Bushveld Complex. The displacement along the regional fault which forms the eastern boundary of the Crocodile River Fragment (f2, also known as the Crocodile River fault) is of the order of 3000 to 4000 metres in the south, decreasing northwards. Both these faults are major regional structures and the western one can be joined to the eastern fault of the Brits Graben.
- ❑ the emplacement of the Bushveld Complex accentuated the existing deformation and also led to low- to medium grade metamorphism of the rocks of the Transvaal Supergroup.
- ❑ after the emplacement of the Bushveld Complex deformation was locally enhanced by the emplacement and extrusion of the alkaline-carbonatite complexes.

The Kruidfontein Complex was emplaced on the western northwest striking regional fault (f1) and is clearly younger than the fault. The latter could have been a zone of weakness which controlled the eruption of the complex, thus showing similarities with the carbonatites of the East African Rift System. However, the Crocodile River Fragment represents a horst (Verwoerd, 1963), which is also a manifestation of tensional stress.

Digitised by the Department of Library Services in support of open access to information, University of Pretoria, 2021

7. GEOLOGY OF THE KRUIDFONTEIN CARBONATITE COMPLEX

7.1 Petrographic classification of carbonatites and pyroclastic rocks

Verwoerd (1967) mapped the Kruidfontein Complex in terms of bedded and non-bedded metabeforsite and sövite, rhyolite and younger and older pyroclastic breccia. Some of these terms have genetic connotations, and FOSKOR (Pty) Ltd. therefore attempted a descriptive classification of the pyroclastic rocks based on the presence or absence of bedding, the presence or absence of macroscopically visible clasts, the grain size, the sorting and whether the larger clasts were matrix- or clast-supported. However, in this classification distinctions were made between proximal (>20 mm in diameter) and distal (< 20 mm in diameter) debris flows in which the clasts are matrix-supported, and vent breccia which is clast-supported. These terms obviously have genetic connotations, and furthermore, no additional criteria have been given for the designation of pyroclastic breccias as vent breccia, proximal debris flow or distal debris flow.

In 1981 a descriptive nomenclature and classification of pyroclastic rocks were recommended by the IUGS Subcommission on the Systematics of Igneous Rocks (Schmid, 1981). The clast size categories are the same as the well known Wentworth classification used for sedimentary rocks, and are based on powers of 2 in millimetres (Table 7.1).

Table 7.1 Classification of pyroclastic rocks (after Schmid, 1981).

DOMINANT CLAST SIZE (mm)	PYROCLAST	CONSOLIDATED PYROCLASTIC ROCK
64 mm and larger	Bomb: mainly juvenile, rounded Block: may be accidental, angular	Agglomerate (rounded pyroclast) Pyroclastic breccia (angular pyroclasts)
2 mm to 64 mm	Lapillus: rounded or angular	Lapilli tuff
1/16 mm to 2 mm	Ash grain	Coarse ash tuff
smaller than 1/16 mm	Volcanic dust	Fine ash tuff

The rock names may be modified by means of suitable adjectives e.g. bedded, well sorted, clast-supported, etc. Tuffisite is an intrusive breccia consisting of angular to rounded clasts of the country rocks in a tuffaceous matrix varying in grain size from lapilli to dust.

Other definitions used are as follows (Schmid, 1981):

- *pyroclasts* "are individual crystals, crystal fragments, glass fragments, and rock fragments generated by disruption or during subsequent transport.." ;
- *bomb* "is a pyroclast with a mean diameter commonly exceeding 64 mm. Its shape is ellipsoidal, discoidal, or irregular..";

Digitised by the Department of Library Services in support of open access to information, University of Pretoria, 2021

- *block* "is a pyroclast with a mean diameter exceeding 64 mm, whose commonly angular to subangular shape indicates that during its formation is was in a solid state.";
- *lapilli* "are pyroclasts of any shape, with mean diameters of 2 to 64 mm.";
- *ash grains* "are pyroclasts with mean diameters smaller than 2 mm".

According to Streckeisen (1979) carbonatites contain more than 50 % by volume of carbonate minerals, and the following major classes are distinguished:

- calcite-carbonatite: sövite (coarse-grained) and alvikite (medium- to fine-grained)
- dolomite-carbonatite : beforsite
- ferrocarbonatite, consisting mainly of iron-rich carbonate minerals.

The presence of minor minerals is indicated by adjectives (e.g. an apatite-bearing sövite contains less than 10 % by volume of apatite) or by mineral names as prefixes (e.g. an apatite-sövite contains more than 10 % by volume of apatite). According to Woolley and Kempe (1989), a prefix to carbonatite (e.g. calcite-carbonatite instead of sövite) can be used. A compound name indicates that another mineral, apart from a carbonate mineral, is present (e.g. fluorite-calcite-carbonatite).

7.2 Lithological subdivision of the Kruidfontein Complex

7.2.1 The outer zone

Verwoerd (1967) subdivided the outer zone into the younger pyroclastic breccia, ignimbrite and older pyroclastic breccia, all of which contain xenoliths and/or protuberances of quartzite and/or banded iron formation. The rocks of the outer zone are clearly more siliceous than the rocks of the inner zone and are not carbonatites (Fig. 7.1: see folder). These lithological units have no bedding and therefore the centroclinal dip of these rocks is only assumed by analogy to the dip of the surrounding country rocks. The terms younger and older pyroclastic breccia therefore do not necessarily indicate any genetic time constraint as assumed by Verwoerd (1967), but merely that the older pyroclastic unit is situated in the distal part of the outer zone, that is along its periphery.

7.2.1.1 Older pyroclastic breccia unit

In the outcrop on Kruidfontein 139JQ (Fig. 7.1: see folder) the older pyroclastic breccia is difficult to distinguish from the younger pyroclastic breccia. Verwoerd (1967) made the distinction on the basis that the older pyroclastic breccia was darker than the younger pyroclastic breccia on the farm Boschkop 138JQ. This distinction does not apply to the outcrop on Kruidfontein 139JQ. During this study

Digitised by the Department of Library Services in support of open access to information, University of Pretoria, 2021

the older pyroclastic breccia on Kruidfontein 139JQ was distinguished from the younger pyroclastic breccia by the fact that its blocks vary in diameter from 64 mm to 100 mm. The older pyroclastic breccia also weathers to a yellow-orange colour (Fig. 7.1: 1A, 1B, 2A, 2B, 3A, 4A, 4B, 5B, 6B, 6C, 7B, 7C, 7D, 7E, 7F, 7H, 7I, 8D and 8E) except where obvious alkali metasomatism has taken place. The blocks in the older pyroclastic breccia are subrounded to subangular, poorly sorted and matrix supported, and consist of a variety of lithic fragments: quartzite, shale and banded iron stone (derived from the Transvaal supergroup); syenite and nephelinite genetically related to possible intrusive and extrusive phases of the Complex and gabbro and granite (derived from the Bushveld Complex).

In outcrop, the matrix has been removed preferentially by selective weathering, so that the blocks and lapilli protrude on the weathered surface. Vesicles were found within the matrix as well as in some of the volcanogenic pyroclasts. The matrix contains lapillus-size volcanogenetic and lithic ejecta, ash grains, subordinate crystals and black, elongated glass shards (1 to 2 mm in diameter). These shards have been pseudomorphosed by chlorite. The large angular blocks and lapilli vary greatly in appearance and include quartzite, banded ironstone, granite, and a range of black felsitic to rhyolitic lapilli.

Although scattered quartzite and banded ironstone clasts occur throughout the older pyroclastic breccia, they are concentrated in the vicinity of large protuberances of similar material. The blocks and lapilli of granite occur throughout the older pyroclastic breccia unit, and are coarse-crystalline, with euhedral to subhedral pink potassium feldspar (3 to 4 mm in diameter) and interstitial quartz. Black and fenitised tephra are the most abundant, and although they are found throughout the outcrop area, an increase in concentration is prominent near the contact with the ignimbrite unit in the southern portion of the study section. Several varieties of the black clasts can be identified in the field: massive green-black material is probably chloritised mafic material such as basalt which has been identified as flows north of the Kruidfontein Complex, layered grey-green to black material resembles chloritised shale, and black biotite-rich clasts was referred to as biotite schist by Verwoerd (1967). Smaller lapilli of purple fluorite, hematite (limonite) and calcite are common, and their characteristic mode of occurrence as alteration products or as void filling, implies neoformation.

Digitised by the Department of Library Services in support of open access to information, University of Pretoria, 2021

7.2.1.2 Ignimbrite unit

The ignimbrite unit (Fig. 7.1: 1I to 7G and 7F to 3A) generally occurs between the younger and older pyroclastic breccia and shows transgressive relations to both of them (e.g. 7C and 4B). It therefore appears to be the youngest of the three units. It is distinguished from the two pyroclastic breccias by its more uniform appearance, as it only contains sporadic angular to lenticular lapilli of devitrified glass, rock and crystal fragments and flattened and welded pumice (fiamme) in a matrix of glass shards (1 to 3 mm in diameter), largely pseudomorphosed by chlorite. Some of the rock fragments represent pinkish fenite. The overall colour of the ignimbrite varies from pinkish through orange to brick-red.

7.2.1.3. Younger pyroclastic breccia unit

The younger pyroclastic breccia (Fig. 7.1) is generally finer grained with an average clast size of 10 to 20 mm and should actually be called a lapilli tuff. However, blocks of up to 500 mm in diameter have been found in places. The younger pyroclastic breccia unit has a more siliceous appearance than the older pyroclastic breccia, possibly due to metasomatism, and upon weathering forms a smooth surface on which the lapilli are firmly cemented by the matrix (Fig. 7.1: 2B to 1F, 2J to 6G and 6F to 3B). The lapilli essentially consist of red fenite and black gabbro, but lesser quartzite and banded ironstone are also common. Fluorite, hematite and calcite are common replacement minerals within the clasts.

7.2.1.4 Country rock

Quartzite outcrops are limited to the outer zone of the Kruidfontein Complex (Fig. 7.1: 2A, 2B, 3B and 4B), and occurs within all three units. The largest outcrop of the quartzite is on the inner slope of the western part of the outer zone (3B). Smaller lenses of quartzite also occur towards the south and south-east of the mapped area (Fig. 7.1). Recrystallisation of the quartz grains is visible on a macroscopic scale. The composition of the quartzite ranges from almost orthoquartzitic to arkosic. The quartzite is usually massive but cross-bedding does occur; secondary brecciation is common, especially near the contact with the volcanic sequence, and it therefore seems likely that the quartzite outcrops represent country rocks of the Transvaal Supergroup which have been displaced and disrupted during the emplacement of the Kruidfontein Complex.

The conglomerate found in the outer zone of the Kruidfontein Complex contains

Digitised by the Department of Library Services in support of open access to information, University of Pretoria, 2021

pebbles of jasper, suggesting that it belongs to the Pretoria Group. Inclusions of banded ironstone of the Penge Formation are common within the outer zone (Fig. 7.1: 1H, 1I and 1J). It would therefore seem that the conglomerate most probably belongs to the Bevets Conglomerate Member of the Rooihoogte Formation which immediately overlies the Penge Formation.

7.2.2 The inner zone

The inner zone of the Kruidfontein Complex consists of tuffs interbedded with volcanic breccias (Fig. 7.1). The beds dip inwards at more than 50° at the margin, but the dip becomes shallower (an average of 20°) towards the middle of the inner zone. The different rocks alternate rapidly, both parallel and perpendicular to the strike, so that the units have a very erratic distribution and cross-cutting relationships and interfingering are present. Consequently the total thickness of the inner zone is unknown.

In general, the tuffaceous sediments consist of massive and bedded units. In places the massive units contain abundant, poorly sorted, angular to sub-angular clasts which are matrix supported. The majority of the clasts are lithic fragments. The matrix consists of fine-grained feldspar and recrystallised, fine-grained carbonate minerals. The modal percentage of feldspar varies from 0% to 20%. Tabular crystals of primary calcite are also present. Replacement of the carbonate by fluorite is wide-spread.

The massive tuff units are interbedded with laminated tuff which can be parallel and/or cross-stratified. The thicknesses of these units vary from a centimetre to several metres. The bedded tuff consists of fine-grained carbonates, and in this regard is similar to the matrix of the massive units. Many of the bedded sequences were subjected to soft-sediment deformation, such as slumping, dewatering and loading (leading to the disruption and contortion of the bedding), indicating that the sediment had been water-saturated.

7.2.2.1 Ash tuff

This unit is characterised by the virtual absence of large clasts and consists of fine ash grains and dust. The massive, non-bedded tuff units (Fig. 7.2) display brown surfaces. The fresh surfaces are usually light grey, but a dark grey chloritised unit, containing Fe- and Ti-oxides and sporadic bombs, blocks and lapilli occurs in places on the northern slope of the inner zone (Fig. 7.1: 1D, 1E and 1F) (Fig. 7.3).

Digitised by the Department of Library Services in support of open access to information, University of Pretoria, 2021

Figure 7.2 Fine-grained, light to dark brown, massive ash tuff. Large clasts are absent.

Figure 7.3 A rounded, elongated volcanic bomb (approximately 100 mm in diameter) imbedded in brown, massive ash tuff.

Digitised by the Department of Library Services in support of open access to information, University of Pretoria, 2021

The bedded tuff units are characterised by fine laminations, 1 to 2 mm in thickness (Fig. 7.4). The units are approximately 2 m thick. More siliceous units with a blue to greyish colour contain pyrite grains of approximately 1 mm in diameter.

The layering is predominantly tabular with lamina of low-angle cross-bedding (Fig. 7.5). Features characteristic of soft-sediment deformation include contorted bedding (Fig. 7.6), mud-volcanoes, due to compaction and dewatering (Fig. 7.7) and dewatering ripples (Fig. 7.8). Asymmetrical ripples (Fig. 7.9) indicate deposition in a shallow-water, low-energy environment (Reading, 1978). Volcanic bombs are rare in this unit. Beds of lapilli tuff with lapilli of up to 20 mm occur sporadically (Fig. 7.10). The lapilli which vary in colour from light brown to red, consist of carbonates, K-feldspar and Fe-oxides.

7.2.2.2 Pyroclastic breccia

The central part of the inner zone is composed mainly of pyroclastic breccia. Away from the central breccia body at the highest point in the Complex (Fig. 7.1: 2F, 3G, 3E and 2E), the breccias become interbedded with tuffs. The contacts between the breccias and the tuffs vary from sharp to gradational. Crude stratification can be recognised according to (a) clast size and (b) the matrix support. The type of clasts includes:

- ❑ lithic and vesiculated fragments of juvenile origin (altered nephelinite, ijolite and basalt);
- ❑ blocks of tuffaceous material (bedded to massive tuff, lapilli tuff and breccia); and
- ❑ clasts of surrounding country rocks (quartzite, shale, granite and mafic rocks).

The clasts are angular to subangular, with sizes varying from 50 to 500 mm. The breccias can be clast or matrix supported. The matrix consists mainly of fine-grained carbonates, K-feldspar, chlorite and Fe-oxides.

The coarse pyroclastic breccia is characterised by average block sizes of greater than 64 mm (Fig. 7.11). An estimate of the maximum block size was not attempted due to the limited exposure. The blocks consist mainly of red K-feldspar and resemble rhyolite (Fig. 7.12). Layered and massive lapilli are common (Fig. 7.13); many of these have been carbonatised. Blocks of earlier

Digitised by the Department of Library Services in support of open access to information, University of Pretoria, 2021

Figure 7.4 Bedded ash tuff units (approximately 1 to 2 metres thick) characterised by very fine layering. The rock has a composition similar to that of the massive ash tuff units.

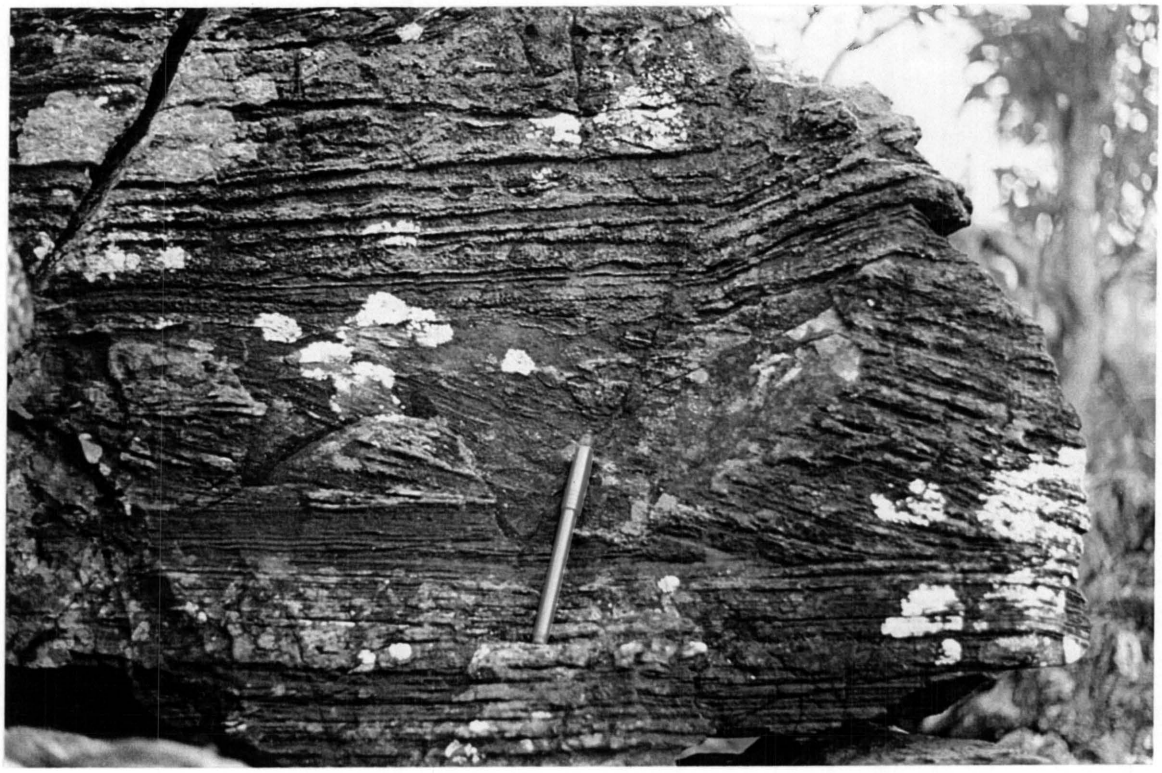

Figure 7.5 Parallel and cross-stratified beds with varying bed thicknesses in an ash tuff deposit. Note the yellow to white lichens.

Digitised by the Department of Library Services in support of open access to information, University of Pretoria, 2021

Figure 7.6 Disruption and contortion of the bedding of a bedded ash tuff unit due to post-depositional processes such as slumping, dewatering or loading.

Figure 7.7 Mud-volcano, due to compaction and dewatering, disturbing the fine-scale bedding in an ash tuff unit.

Digitised by the Department of Library Services in support of open access to information, University of Pretoria, 2021

Figure 7.8 Small scale, irregular dewatering ripples (1 mm in height) in the bedded ash tuff, indicating subaqueous deposition and subsequent dewatering.

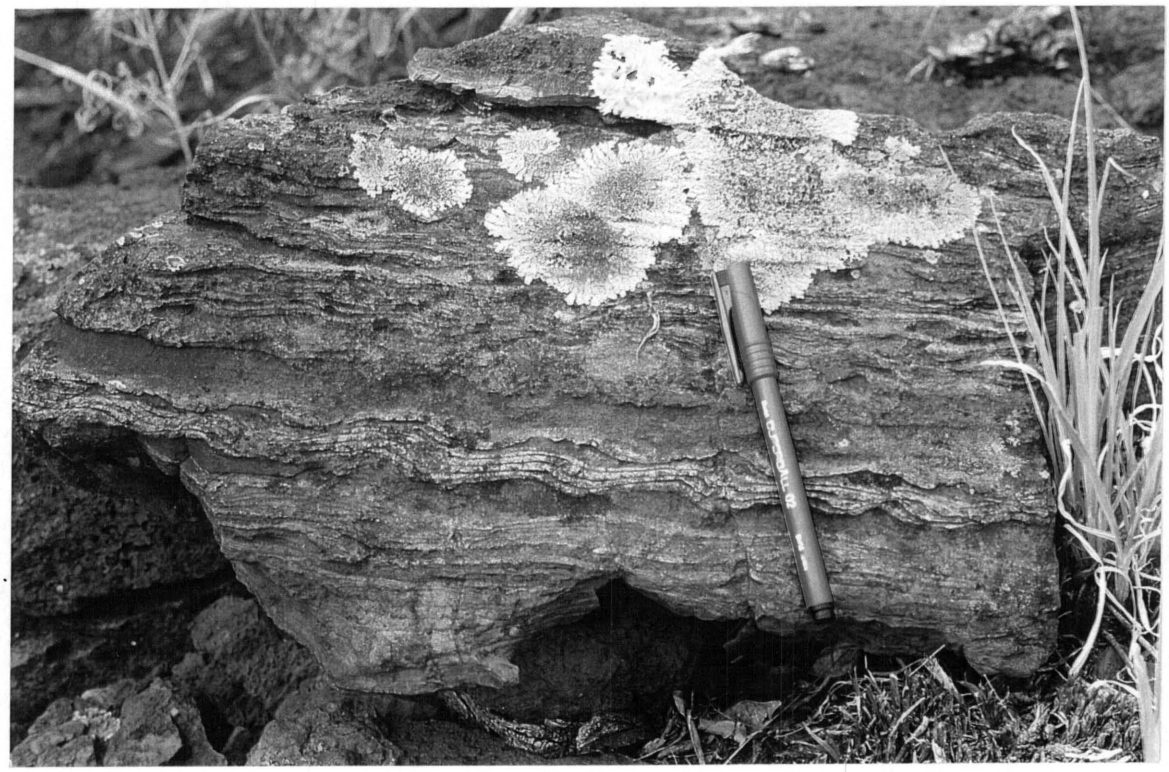

Figure 7.9 Asymmetrical ripples (ripple units varying from 1.5 to 5 cm in width) in massive tuff, suggesting deposition in shallow water. Grey mottles under the top portion of the outcrop are lichens.

Digitised by the Department of Library Services in support of open access to information, University of Pretoria, 2021

Figure 7.10 Rounded to deformed lapilli (up to 20 mm in diameter), brown to reddish in colour, in irregular beds of less than 1 metre thick.

Figure 7.11 Pyroclastic breccia characterised by an average clast size of greater that 64 mm.

Digitised by the Department of Library Services in support of open access to information, University of Pretoria, 2021

Figure 7.12 Large clasts in pyroclastic breccia (below the pen) consisting mainly of metasomatised material.

Figure 7.13 Layered and massive angular clasts (approximately 10 to 60 mm in diameter) in a clast-supported lapilli tuff.

Digitised by the Department of Library Services in support of open access to information, University of Pretoria, 2021

pyroclastic breccia are also present, and many of these have been chloritised in the central portion, whereas the rim is characterised by red K-feldspar and Fe-oxide, apparently formed as a result of potassium metasomatism (Fig. 7.14).

The matrix of the pyroclastic breccia is typically grey, and consists of fine-grained carbonate and sporadic, disseminated fluorite. Where fluorite-calcite-carbonatite dykes are present, the matrix of the breccia has been recrystallised. In places veins of tuff-like material occur within this unit, and although they seem to replace the matrix, they are interpreted as tuffisite. Pyroclasts contained in these veins are therefore thought as having been emplaced as a result of gas streaming.

7.2.2.3 Lapilli tuff

The lapilli tuff contains clasts with an average size of less than 64 mm and more than 10 mm in diameter (Fig. 7.15). The majority of the clasts are approximately 10 mm in diameter, and the larger ones are angular. Large bombs of 500 mm in diameter have nevertheless been noted.

The lapilli vary from angular to sub-rounded and are comprised of red K-feldspar, pre-existing carbonate breccia, older tuff and subordinate granite, syenite, quartzite and banded ironstone. The finer lapilli tuff is matrix supported and is interpreted as a debris flow deposit (lahar) (Fig. 7.16). The matrix consists of carbonate in various stages of recrystallisation, and in places contains disseminated to pervasive fluorite.

Graded bedding in the rock is poorly developed, and both upward fining and upward coarsening units can be found, suggesting suspension deposition in an aqueous environment and prograding fans of debris flows over fine-grained out-wash deposits respectively. Thin-bedded units are common, but bedding is only poorly developed (Fig. 7.17). Different episodes of ash deposition are manifested by fine ash tuff layers overlain with sharp contacts by coarse debris-flow deposits (Fig. 7.18).

7.2.2.4 Ferruginous lapilli tuff

The ferruginous lapilli tuff unit in the northwestern part of the inner zone (Fig. 7.1: 2H) was studied by means of drilling program of percussion boreholes down to depths of 61 m at inclinations of 60° towards the rim of the inner zone, based on

Digitised by the Department of Library Services in support of open access to information, University of Pretoria, 2021

Figure 7.14 Large (120 mm in diameter), chloritised clasts (greenish-blue) with characteristic red rims.

Figure 7.15 Clast-supported lapilli tuff with subangular clasts generally less than 40 mm in diameter.

Digitised by the Department of Library Services in support of open access to information, University of Pretoria, 2021

Figure 7.16 Matrix-supported tuff, thought to be a debris flow deposit (lahar). The clasts are mostly angular and display poor sorting.

Figure 7.17 Poorly defined layering in a distal debris flow, displaying angular, matrix-supported clasts.

Digitised by the Department of Library Services in support of open access to information, University of Pretoria, 2021

Figure 7.18 The sharp contact between an underlying ash tuff layer and a 1.20 m thick, faintly bedded debris flow deposit.

Digitised by the Department of Library Services in support of open access to information, University of Pretoria, 2021

the inferred centroclinal dip of the beds.

The ferruginous lapilli tuff contains clasts of which the majority are approximately 10 mm in diameter. The lapilli vary from angular to sub-rounded and are comprised of red K-feldspar and pre-existing carbonate breccia. The matrix consists of iron-rich carbonate in various stages of recrystallisation, and contains hematite, chlorite and disseminated fluorite. Any structures like bedding have been partly destroyed by the ferruginisation.

7.2.2.4.1 Section A - B

Section A - B (Figs. 5.2 and 7.19), based on the drilling results, can be described as follows: The dominant rock type is lapilli tuff with iron-enrichment at the SW and NE ends of the section. The ferruginous nature of the lapilli tuff in the NE is ascribed to syngenetic or diagenetic ferruginisation, whereas that of the SW is related to a fault zone, which is also characterised by chloritisation and relatively high gold values. Several carbonatite dykes and sills were also intersected at the extremities of the section.

7.2.2.4.2 Section C - D

Section C - D (Figs. 5.2 and 7.19) is more representative of the NE portion of the ferruginous lapilli tuff. As in section A - B the lower contact of the ferruginous lapilli tuff was not intersected.

7.2.2.5 Intrusive carbonatite

Carbonatite dykes and plugs are restricted to the inner zone of pyroclastic breccia, lapilli tuff and ash tuff. The dykes generally strike northwest with northeast and north as subordinate strike directions. They have sharp contacts with the wall-rock and in some cases display chilled, fine-grained margins. In places they form stringers of 10 to 120 mm thick, which invade the host rock as a network (Fig. 7.20). Several of the thick (>2 metres) dykes (Fig. 7.21) contain high concentrations of fluorite which seems to be a primary constituent of the carbonatite. The thicker dykes contain xenoliths of host rock varying from 10 mm up to several metres in diameter. Secondary fluorite is present as a replacement of the tuffaceous host rock, probably due to late stage fluids emanating from the carbonatite.

Digitised by the Department of Library Services in support of open access to information, University of Pretoria, 2021

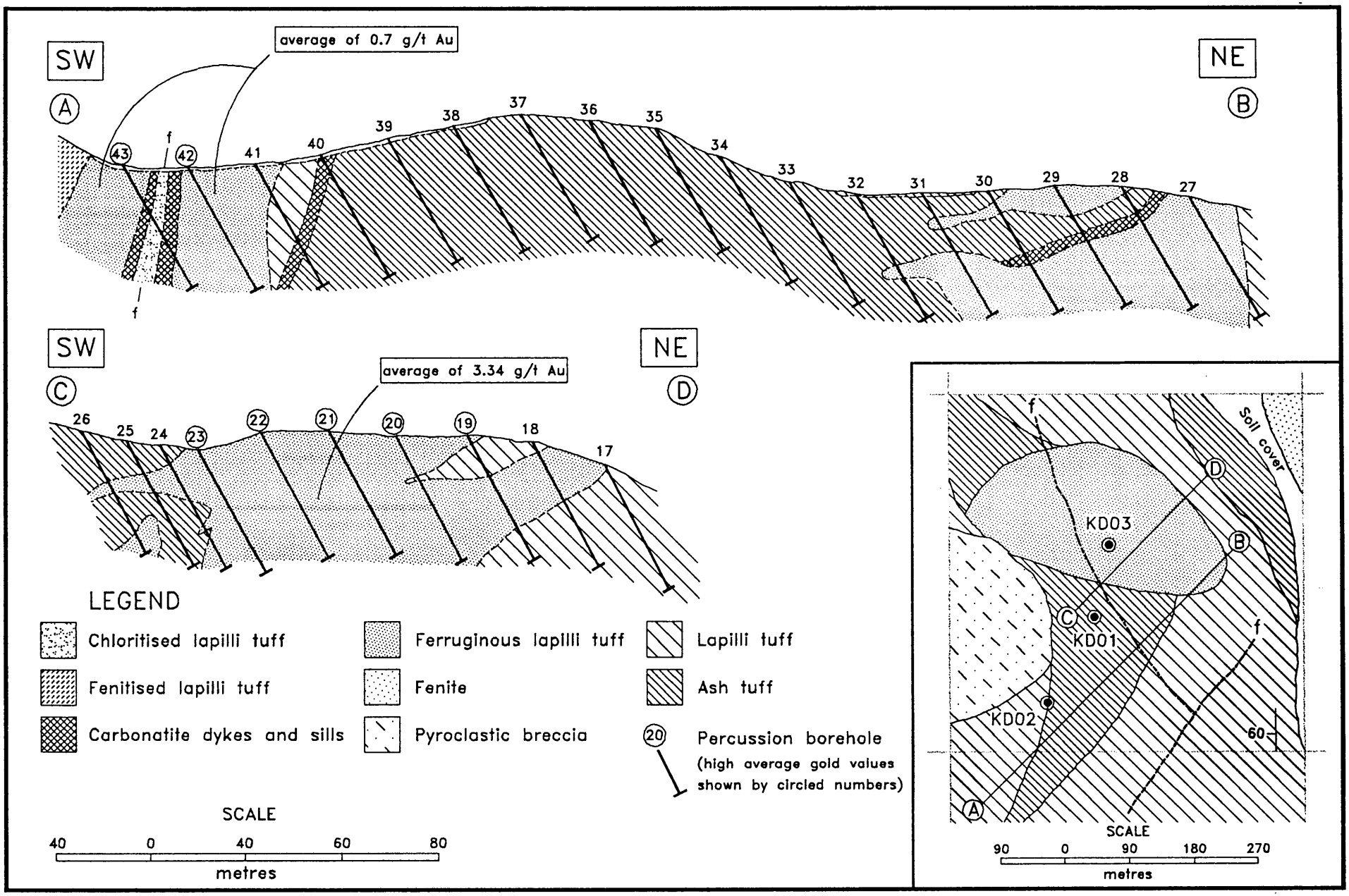

Figure 7.19 Sections A-B and C-D drilled across the ferruginous lapilli tuff unit, northeastern part of the inner zone (see Fig. 5.2 for section localities).

Digitised by the Department of Library Services in support of open access to information, University of Pretoria, 2021

Figure 7.20 Anastomosing stringers (10 to 120 mm in thickness) of fine-grained carbonatite (greyish white) in fine-grained ash tuff (yelowish bown).

Figure 7.21 Irregular carbonatite dyke (in places more than 2 m thick) intruded into brecciated ash tuff.

Digitised by the Department of Library Services in support of open access to information, University of Pretoria, 2021

The carbonatite dykes are fine- to medium-grained, and according to Clarke (1989), three groups of intrusive carbonatite are present in the inner zone, namely (a) sövites (medium-grained), (b) alvikites (fine-grained) and (c) fluorite and/or barite veins. In this study the latter group is not considered as carbonatite, although it is closely associated with the carbonatite.

The sövite (calcite-carbonatite) dykes are light coloured, and consist of 70-90% calcite, 10-15% fluorite, 5-10% quartz, 5-10% iron oxides and less than 1% accessory minerals such as apatite. The alvikite group (also calcite-carbonatite) is purple to brown in colour, and contains less calcite (60-70%), and more fluorite (10-30%) than the sövite. Iron oxides are also present (5-10%), together with apatite and pyrite as accessory minerals.

7.3 Alteration types

7.3.1 Fenitisation

This fenite was originally called a rhyolite by Verwoerd (1967). Although the presence of vesicles and apparent flow-banding could suggest that this unit is an altered rhyolite, the presence of macroscopic clasts like coarse ash grains and lapilli suggests that it is a tuff. Patches of secondary light and dark pink feldspar thus indicate albitisation and potassium metasomatism respectively (Clarke, 1989; Clarke et al., 1991), which are typical of a fenite in a carbonatite environment.

Evidence of potassium metasomatism is sporadically present throughout the inner and outer zones in the form of replacement, which may be pervasive, affecting pyroclastic rocks as a whole. However, often only the coarser pyroclasts are affected. Potassium metasomatism can also result in veins cutting across the layering. The most extensive outcrop of fenite forms an arc parallel to the bedding in the southeast of the inner zone (Fig. 7.1: 2I to 4E).

7.3.2 Chloritisation

Chlorite is a common alteration product and is especially well developed in the north western sector of the inner zone (Fig. 7.1: 1D, 1E, 2C and 2D). The chlorite is stratabound and is especially concentrated in tuff containing Fe- and Ti-oxides.

The "andesite" unit mapped by Verwoerd (1967) (Fig. 7.1: 6E, 6F and 6G) is also regarded as chloritised ignimbrite. Fiamme are readily recognised in this altered, welded pyroclastic breccia.

Digitised by the Department of Library Services in support of open access to information, University of Pretoria, 2021

7.3.3 Ferruginisation

Ferruginisation is fairly common in all the rock units, but only two major areas within the inner zone (Fig. 7.1: 2H and 1E) are highly ferruginised. The ferruginised material has a bluish hue, indicating a fairly high manganese content.

Although the ferruginisation can be associated with regional structures in some instances, that in the outer zone is generally associated with the occurrences of banded ironstone within the pyroclastic breccia and tuff units.

7.4 Mineralisation

Previous exploration on the farm Kruidfontein 139JQ was concentrated on the fluorite occurrences of the Complex: in 1970 by Metallgesellschaft AG, and from 1972 to 1976 and again during 1979 by the Southern Sphere (Pty) Co. Ltd..

7.4.1 Fluorite

Fluorite mineralisation is restricted to the inner zone (Crocker et al. 1988; Clarke, 1989), especially in the southwestern part (Fig. 7.1: blocks 3C, 3D; 4C, 4D; 5C, 5D and 6C, 6D). What is regarded as primary mineralisation is closely associated with the alvikite dykes. Several exposures extend for as much as 500 metres along strike with an average width of 10 metres. Fluorite occurs as disseminated grains throughout the carbonatite dykes, and also as fine-grained fluorite partly replacing pyroclastic breccia and tuff, so that the original fabric of these rocks is still evident (Fig. 7.22).

Anastomosing calcite-fluorite veins in tuff units (Fig. 7.23) and composite dykelets consisting of fluorite-bearing carbonatite and a central calcite vein rich in tuff fragments (Fig. 7.24) are generally found in the southern and southwestern part of the inner zone.

7.4.1.1 Replacement deposits and disseminated fluorite

The main economic concentration of disseminated fluorite is located in pyroclastic rocks on the southwestern boundary of the inner zone (Figs. 5.2 and 7.1: 3C, 3D; 4C, 4D; 5C, 5D and 6C, 6D) and extends for approximately 3.5 kilometres along strike. The dip of this stratiform body is variable, but it generally is towards the northeast at low angles (Fig. 7.25). Based on drilling by Southern Sphere Co. Ltd., resources of 2.5 Mt at 28% CaF_2 or 30 Mt at 15% CaF_2 have been proven.

Digitised by the Department of Library Services in support of open access to information, University of Pretoria, 2021

Figure 7.22 Irregular fluorite stringers in lapilli tuff.

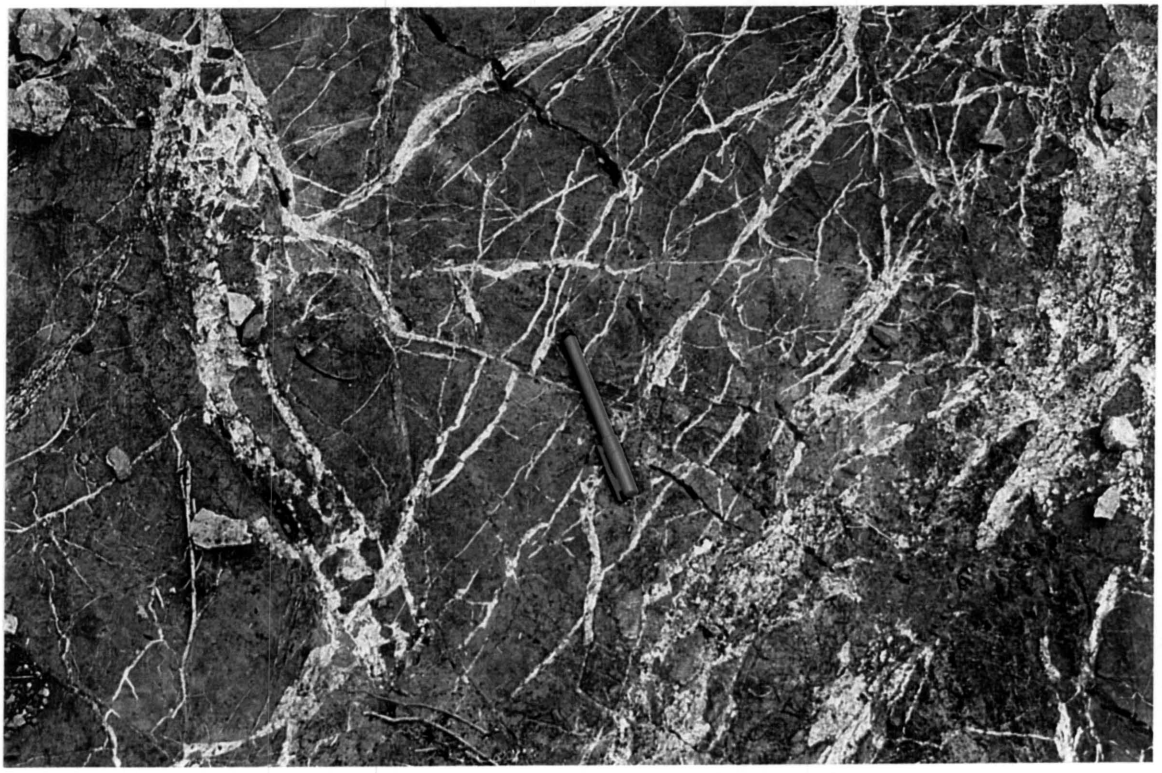

Figure 7.23 Anastomosing calcite veins in an ash tuff.

Digitised by the Department of Library Services in support of open access to information, University of Pretoria, 2021

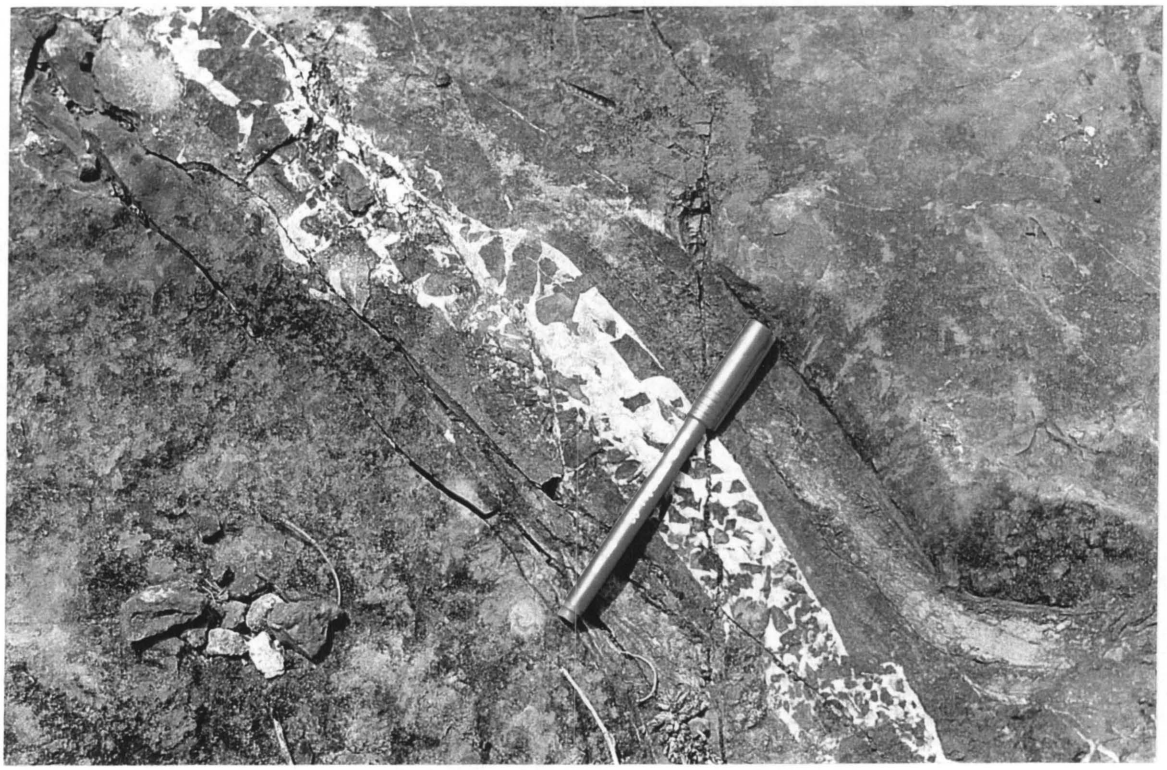

Figure 7.24 Composite dykelet (approximately 10 cm wide) of fluorite-bearing carbonatite, cut by a calcite vein with abundant fragments of ash tuff.

Digitised by the Department of Library Services in support of open access to information, University of Pretoria, 2021

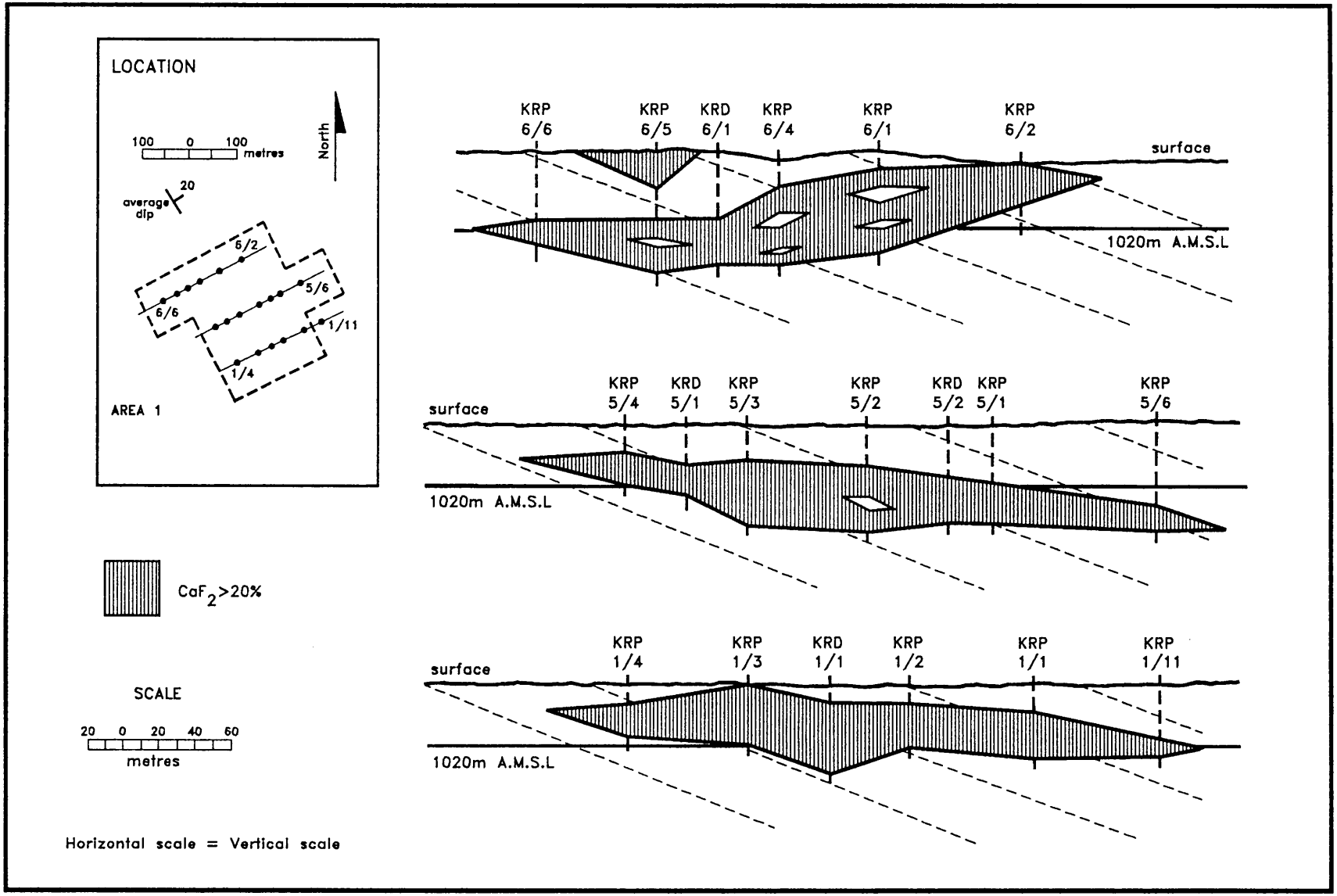

Figure 7.25 Sections showing the fluorite mineralisation across Area 1 (see Fig. 5.2) as estimated from percussion drilling results (Southern Sphere data, after Clarke, 1989).

Digitised by the Department of Library Services in support of open access to information, University of Pretoria, 2021

The ore body was formed mainly by replacement, the fluorite having pseudomorphosed both the matrix material and pyroclasts to varying degrees. The texture of the ore is therefore controlled by the texture of the original host rock. However, subordinate filling of open spaces in the host rock also took place. Southern Sphere Mining and Development Co., in a preliminary report, described the following fluorite-ore textures: (a) wavey or crenulated texture (common of replacement deposits and assumed to be also indicative of fluorite deposition in open spaces as fluorine-rich fluids percolated through the rock); (b) "oolitic texture", comprising interstitial, fine-grained, bluish-purple fluorite enclosing white, spheroidal to sub-rounded calcitic- to dolomitic concretions; (c) nodular texture, consisting of a fluorite matrix which appears to cement large (10 to 200 mm) carbonate grains; (d) pseudo-lapilli texture, described as the replacement of lapilli by fluorite; and (e) microcrystalline texture which consists of irregular, microcrystalline fluorite veinlets.

7.4.1.2 Fluorite-rich carbonatite dykes

Primary fluorite is an important constituent of the calcite-carbonatite (sövite) and calcite-fluorite-carbonatite (alvikite) dykes. These dykes contain an average of 10% CaF_2, but in some occurrences fluorite becomes a major constituent with concentrations varying between 15 and 50% CaF_2 (Crocker et al., 1988; Clarke, 1989).

Fluorite is interstitial with respect to calcite, and vug fillings and veinlets are also common. Two replacement textures can be observed (Clarke, 1989): (a) the replacement of calcite by ankerite, typically seen in fluorite-poor portions of the mineralised carbonatite dykes; and (b) the replacement of calcite in calcite-ankerite rock by purple fluorite ultimately giving a rock composed of ankerite and fluorite only.

7.4.1.3 Fluorite-barite veins

Fluorite-barite veins are related to fractures and existing veins. These fine- to coarse-grained veins vary in thickness from 2 mm to 200 mm.

7.5 Diamond drilling results

With percussion drilling the general dimensions of the ferruginous lapilli tuff unit were determined. One shortcoming of the percussion drilling program, however, was that the borehole depths were limited to 61 metres, so that the dimensions of the ferruginous lapilli tuff unit could not be

Digitised by the Department of Library Services in support of open access to information, University of Pretoria, 2021

ascertained.

Therefore, three diamond drill holes were used to penetrate the pyroclastic sediments of the inner zone in the northeastern part (Fig. 5.2) of the Complex (boreholes KD01 to KD03) (Schürmann, 1992a, 1992b, 1992c, 1993). KD01 and KD02 are inclined and perpendicular to the layering, whereas KD03 is vertical.

7.5.1 Borehole KD01

The KD01 succession was regarded to represent a combination of altered and generally fresh material. The succession was subdivided into four units, according to the lithology. These four units are the upper ash flow unit (interbedded lapilli and ash tuffs and pyroclastic breccia), the pyroclastic breccia and ferruginous ash fall units (interbedded, dark brown tuff and breccia), and the lower ash flow unit (dark, altered and mineralised lapilli and ash tuffs) (Fig. 7.26).

7.5.1.1 Upper ash flow unit

The first 15 m of the upper ash flow unit consists of ash tuff units (0.2 to 1.0 m thick) with interbedded, matrix-supported lapilli tuff layers (Fig. 7.26). The lapilli tuff contains rounded to angular clasts, 5 to 30 mm in diameter, and are rimmed in places. In places the lapilli tuff is dark with angular, matrix-supported fragments. Some of the lapilli tuff layers consist of an upper, matrix-supported part, which grades into a clast-supported base. Several agglutinated lapilli tuff units are also present. Fine-grained tuff with a dark green colour is present, displaying sharp upper and lower contacts. The matrix is rich in K-feldspar. The ash tuff is fine-grained, banded with some small, subangular particles.

From the depth of -15 m to a depth of -29.50 m the sequence consists mainly of lapilli tuff, pyroclastic breccia and several interlayered green tuff layers and mineralised veins. The breccias are matrix-supported and have variable pyroclast size ranges, and most probably represent pyroclastic flows. Clasts range in size from 60 to 100 mm in diameter, and vary from angular to rounded. Some units contain well-rounded clasts with feldspar-rich rims. Most of the breccia units contain fragments of lapilli tuff resembling that of the pyroclastic sequence of the outer zone, and less common dark, medium-grained, altered nephelinitic tephra. Most of the breccias have been feldspathised to some degree: initially only the matrix is affected and in more advanced stages the whole rock has been replaced so that clasts can only be recognised with

Digitised by the Department of Library Services in support of open access to information, University of Pretoria, 2021

difficulty. Veins of feldspar and calcite are common, often associated with fluorite, which also fills voids in the breccia.

The basal part of the upper ash flow unit consists of a tuff layer which displays no clear bedding. It is composed of grains, up to 1.5 mm in diameter, cemented by secondary calcite, feldspar and chlorite. Larger (5 to 10 mm), elongated and flattened nephelinitic lapilli are also present. The intensely altered zones are related to joints, and are orange to dark yellow in colour and from 0.2 to 4.7 m in thickness. They include clay layers of 10 to 20 cm thick which grade into intensely feldspathised zones. Contacts of these zones of intense alteration with the surrounding rock are quite sharp.

7.5.1.2 Lapilli tuff unit

The lapilli tuff unit represents a sequence of brown tuff and interlayered breccia (depths from -29.50 to -65.00 m) (Fig. 7.26). The contact between this and the overlying unit is masked by a 15 to 20 cm wide alteration zone with a clay core. The top third of the unit is dominated by altered brown tuff and the lower part by lapilli tuff. Individual beds tend to be relatively thick (approximately 0.6 to 3 m). The brown tuff is fine-grained with no macroscopically visible clasts and is generally massive, but locally it shows laminations of 1 to 2 mm in thickness. These laminations may indicate that the ash was deposited in water. This is corroborated by other sedimentary structures like channel structures and ripple marks.

The lapilli tuff consists of angular, poorly sorted, black red to green clasts, the average size of which is less than 40 mm. Thin ash tuff lamina are interbedded within some of the lapilli tuff layers. A description of a collection of pyroclasts is as follows:

- irregular, broken-up veins of fluorite, red K-feldspar and secondary calcite;
- irregular clasts, approximately 20 mm in diameter, consisting of fluorite and secondary calcite;
- clasts of rounded to angular fluorite;
- irregular, angular (and deformed) clasts of fine-grained dark-green (chloritised) material, hosting inclusions of oxides and minor sulphides;
- vesiculated fragments of nephelinitic rocks.

Digitised by the Department of Library Services in support of open access to information, University of Pretoria, 2021

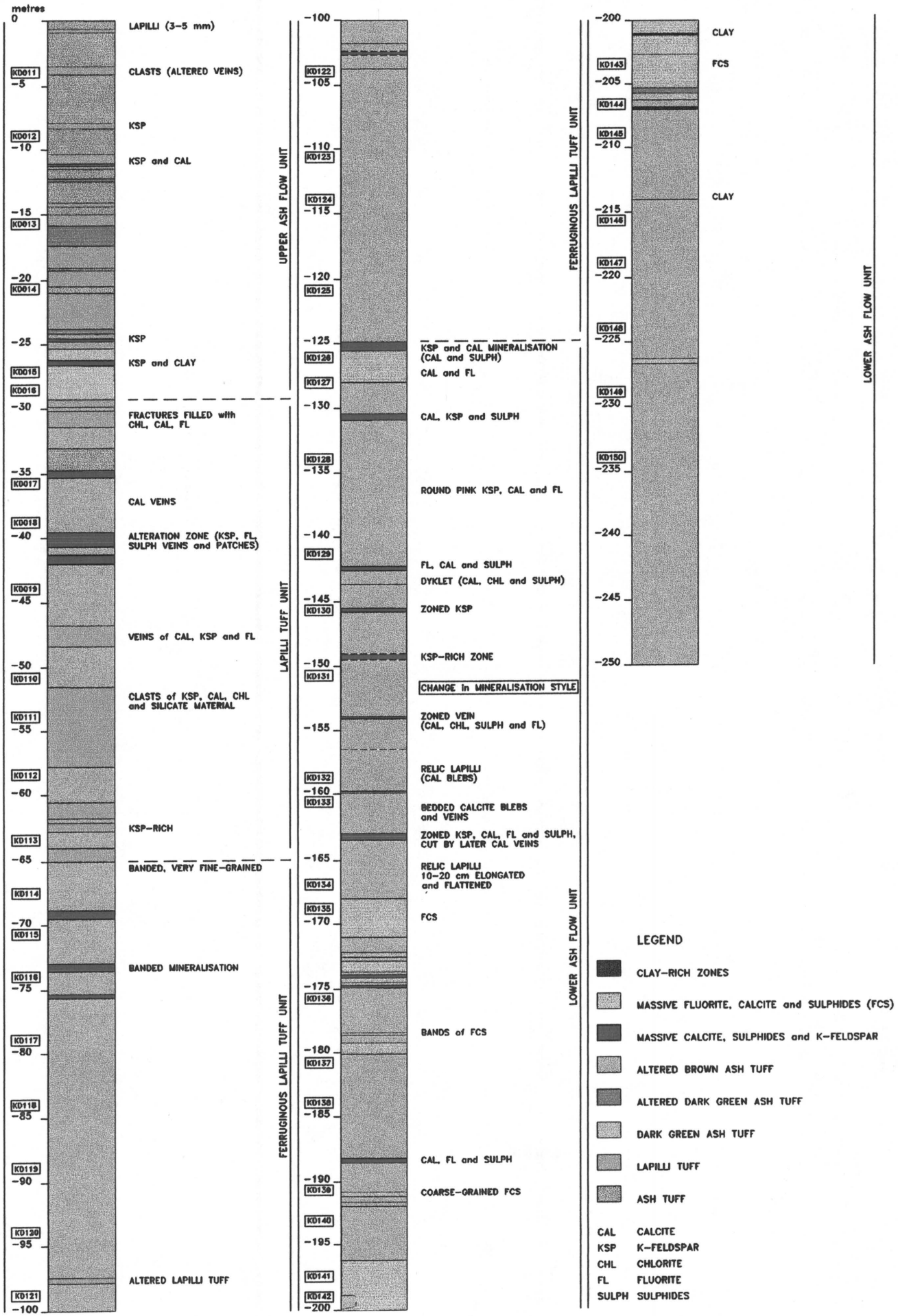

Figure 7.26 Detailed description of borehole KD01 drilled in the northeastern part of the inner zone (see Fig. 5.2 for the borehole localities).

Digitised by the Department of Library Services in support of open access to information, University of Pretoria, 2021

The significance of these various types of pyroclasts is the fact that juvenile deposits (vesiculated fragments from the inner zone and nephelinitic material from the outer zone) and closely associated mineralisation (fluorite, calcite and sulphides) were reworked to produce new lapilli tuff deposits. The matrix material is usually secondary, fine-grained, grey to green carbonate (calcite and dolomite), containing disseminated fluorite and sulphides.

Two joint systems (perpendicular and quasi-parallel to the core respectively) occur throughout the unit and are filled by vein material of fluorite, secondary calcite and sulphides. Jointing is more prominent between the top of the unit (at -29.70 m) and to -37.70. The host rock of the veins is dark brown and the joint filling varies from 1 cm to 10 cm in width.

The tuff is fine-grained and contains occasional calcite and feldspar veins in the upper 8 metres of the unit. From -38.00 m in depth there is a 2.5 m thick K-feldspar-rich zone with thin layers of less altered tuff. The tuff contains layers of mm-sized particles, brecciated and K-feldspar-rich zones and veins separated by relatively unaltered zones. Sulphides or their oxidised relics occur in places. Fluorite lenses, 10 mm in diameter, and irregular fluorite fillings occur at a few levels.

7.5.1.3 Ferruginous lapilli tuff unit

Below -65.00 m in depth (Fig. 7.26), the sequence is dominated by variably mineralised dark brown and red-brown ash tuff. Sporadic relic lapilli, layers and discordant patches of relatively unaltered tuff, indicate that this unit probably represents ferruginised pyroclastics originally similar to the upper ash flow and lapilli tuff units.

The upper part of this unit is massive, with ill-defined, welded fabrics. Its colour varies from dark grey, through green to brownish-purple, the latter being due mainly to the high modal percentage of siderite and hematite. Minor clasts consisting of K-feldspar, calcite and chlorite are present, and display varying degrees of deformation (undeformed to flattened).

7.5.1.4 Lower ash flow unit

The lower ash flow unit is present from a depth of -125.00 m to the end of the hole and consists of brown ash tuff similar to that of the overlying ferruginous

Digitised by the Department of Library Services in support of open access to information, University of Pretoria, 2021

lapilli tuff unit, except that several mineralised layers are present (Fig. 7.26). The tuff is a massive, poorly sorted rock with clasts consisting of K-feldspar and chlorite.

The mineralised zones are found sporadically between -125.0 m and -206.0 m and consist of: (a) medium- to coarse-grained calcite together with sulphides (pyrite) and K-feldspar, with less altered red-brown tuff as host rock (mainly from -125.0 m to -164.0 m, with minor occurrences at depths of -174.50 m and -198.0 m); and (b) medium- to coarse-grained fluorite and calcite together with pyrite and galena (mainly from -169.0 m to -206.0 m, with thick zone at -125.0 m).

7.5.1.5 Dykes

Dykes of carbonatite, grey to white in colour, cut across the volcaniclastic rocks, and are steeply dipping. Anastomosing dykes and veins of carbonatite occur at several localities in the lower ash flow unit. These dykes often have coarse centres and fine-grained margins, and display flow lines parallel to the contacts. Also present are several dyke-like bodies of calcite with subordinate fluorite and sulphides. They display marginal alteration zones of chlorite, fluorite and calcite.

7.5.2 Borehole KD02

Borehole KD02 was drilled 150 metres southwest of KD01 with the aim of defining the lateral extent of the ferruginous lapilli tuff unit. The intersected sequence consists mainly of pyroclastic breccia, lapilli tuff and ash tuff (Fig. 7.27). The upper 40.0 m of the core is characterised by grey to light-brown lapilli tuff with clasts of up to 40 mm, consist of K-feldspar, chlorite and black shale.

From -40.0 m down to a depth of -86.0 m pyroclastic breccia was intersected. The highly angular clasts (the average clast size is greater than 64 mm) are mainly metasomatised brick red material, although layered and massive carbonate clasts are also common. The matrix material is of fine-grained grey carbonate containing disseminated fluorite.

From -86.0 m the sequence consists mainly of lapilli tuff. Interbedded ash tuff layers were intersected from -128.0 m to -139.0 m, from -177.0 m to -194.0 m, and pyroclastic breccia units between -206.0 m and -220.0 m. The ferruginous lapilli tuff unit (from -223 to -308 m) has a dark, red-brown colour and displays graded bedding - coarse at the bottom and fine at the top, suggesting suspension settling in an aqueous environment.

Digitised by the Department of Library Services in support of open access to information, University of Pretoria, 2021

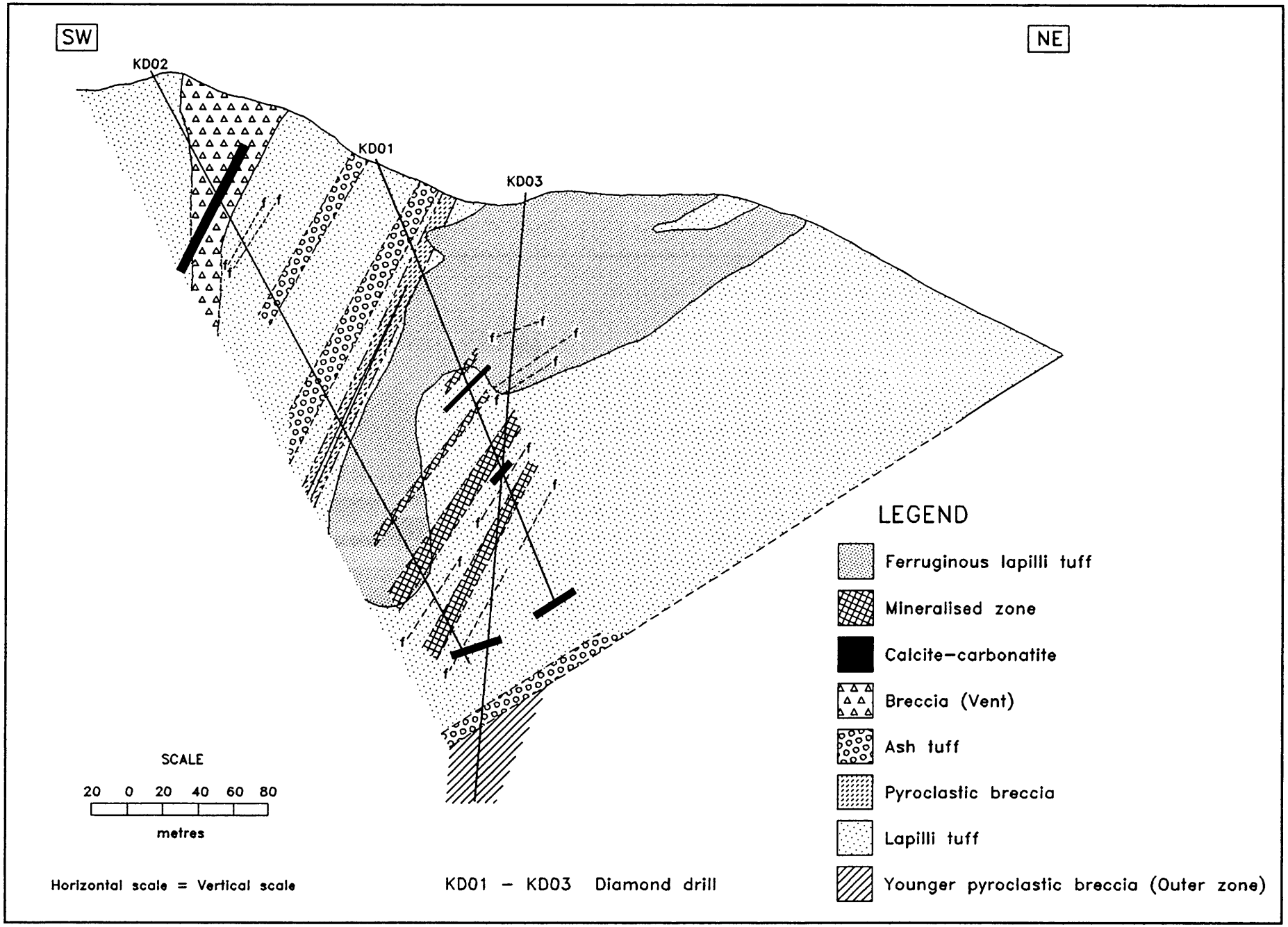

Figure 7.27 KD02-KD01-KD03 section across the ferruginous lapilli tuff unit in the northeastern part of the

Digitised by the Department of Library Services in support of open access to information, University of Pretoria, 2021

Fluorite mineralisation is observed as disseminated grains in the carbonatite dyke intersected at a depth of -71.0 m in the pyroclastic breccia, as fluorite veins at a depth of -50.0 m and as clast replacements in the pyroclastic breccia. Sulphide mineralisation mainly consisting of pyrite was observed in an oxidised zone at a depth of -82.0 m, and as fresh sulphides in a carbonatite dyke at a depth of -354.0 m.

7.5.3 Borehole KD03

Borehole KD03 was drilled vertically to determine the extent of the ferruginous lapilli tuff unit in depth (Fig. 7.27). Most of this sequence (down to -285.0 m) consists mainly of lapilli tuff with interlayered ash tuff units, carbonatite dykes and mineralised zones. The upper part (0.0 m to -103.0 m) consists of ferruginous lapilli tuff. Below the ferruginous lapilli tuff unit, lapilli tuff hosts several mineralised zones at depths between -120.0 and -140.0 m and -171.4 and -185.7 m. These zones consist of medium- to coarse-grained calcite and fluorite, pyrite and galena.

An important aspect of this borehole is that it intersects the contact between the inner and outer zones of the Complex at a depth of 294.0 m. The first 10.0 m of the outer zone consists of ash tuff with intercalated pyroclastic breccia.

Digitised by the Department of Library Services in support of open access to information, University of Pretoria, 2021

8. SOIL GEOCHEMISTRY AND GROUND RADIOMETRIC SURVEY

Assuming equilibrium within the radioactive decay chain of the relevant parent isotopes, a ground radiometric survey should give an indication of the distribution of K, U and Th. However, the equivalent radiometric concentration (determined by gamma-ray spectrometer) is generally much higher than the chemically determined concentrations, based on seven samples (Fig. 8.1). This may be ascribed to one or more of the following:

- ❑ disequilibrium within the uranium and thorium decay chains;
- ❑ the depth of the soil cover and sample geometry at the measuring point; and
- ❑ the representativeness of the sample used for chemical analysis, assuming the latter to be properly standardised.

Despite these problems the total radiometric count, and the eK_2O, $eThO_2$ and eU_3O_8 values will be used as an indication of the distribution of the radionuclides as a whole and of the relevant elements. A statistical analysis of the elements analysed in the soil sampling program is summarised in Table 8.1, and illustrated by means of the frequency histograms (Figs. 8.2, 8.3 and 8.4).

Table 8.1 Summary of the statistical analysis of the soil sample set.

VARIABLE	Au (ppb)	Pb (ppm)	Zn (ppm)	Mn (ppm)	Ba (ppm)
Sample population	3378	7742	8414	8411	8404
Average	19.2	39.4	160.9	2700.0	1418.3
Median	10	30	150	2400	1200
Mode	10	20	130	2200	900
Geometric mean	15.3	30.9	145.9	2380.9	1224.3
Variance	420.5	1258.4	5187.6	2.0×10^6	1.5×10^6
Standard deviation	20.5	35.5	72.0	1424.5	1227
Standard error	0.35	0.40	0.79	15.64	13.39
Minimum	10	10	10	70	200
Maximum	480	410	780	14200	23000
Range	470	400	770	14130	22800
Lower quartile	10	20	110	1730	900
Upper quartile	20	40	200	3330	1600
Interquartile range	10	20	90	1600	700
Skewness	8.3	3.6	1.4	108	7.4
Kurtosis	137	18	5	6	81
Threshold	40	75	230	4000	2600

Digitised by the Department of Library Services in support of open access to information, University of Pretoria, 2021

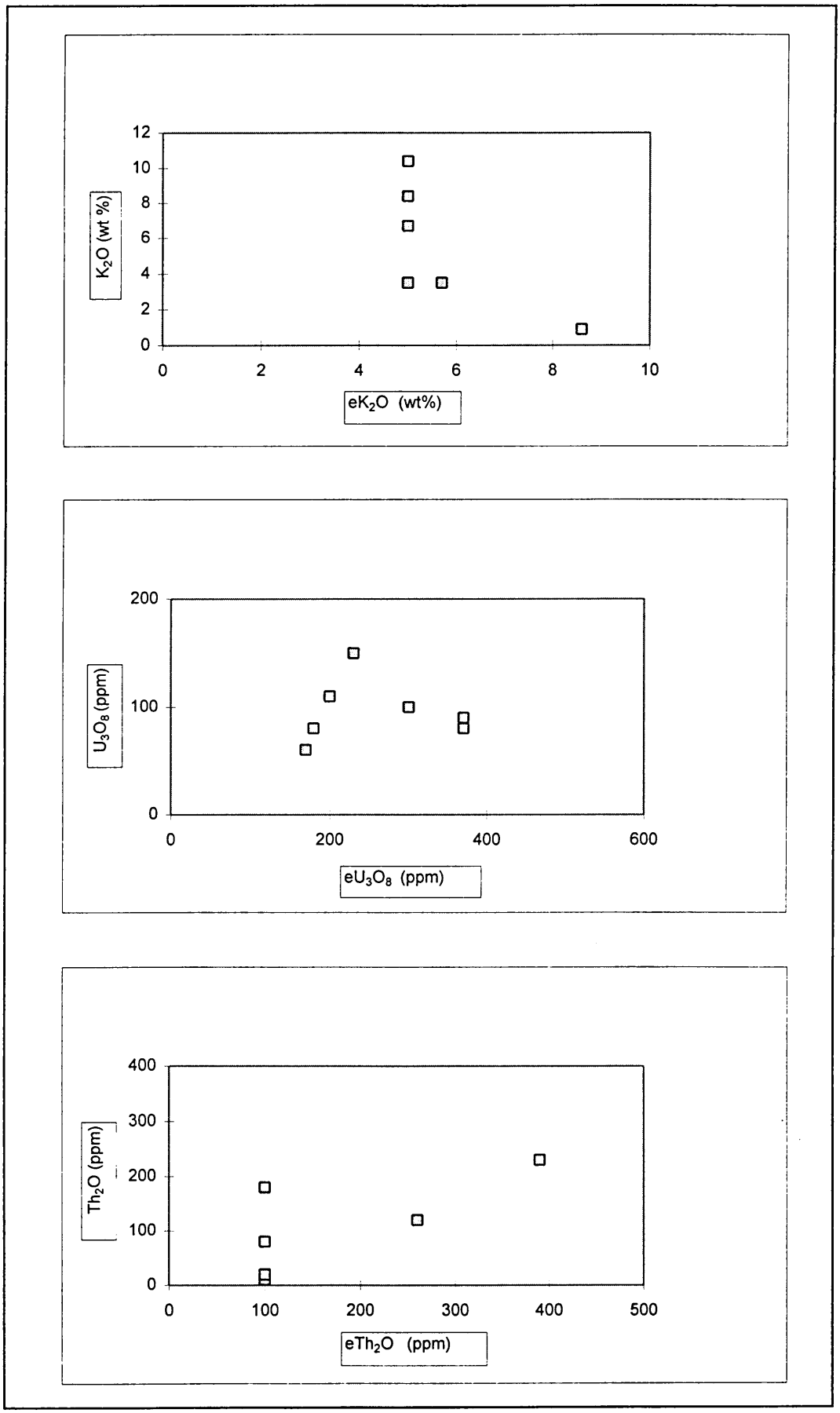

Figure 8.1 Correlation between eK_2O (wt%), $eThO_2$ (ppm) and eU_3O_8 (ppm) (gamma ray spectrometer determination) and K_2O (wt%), ThO_2 and U_3O_8 (ppm) content.

Digitised by the Department of Library Services in support of open access to information, University of Pretoria, 2021

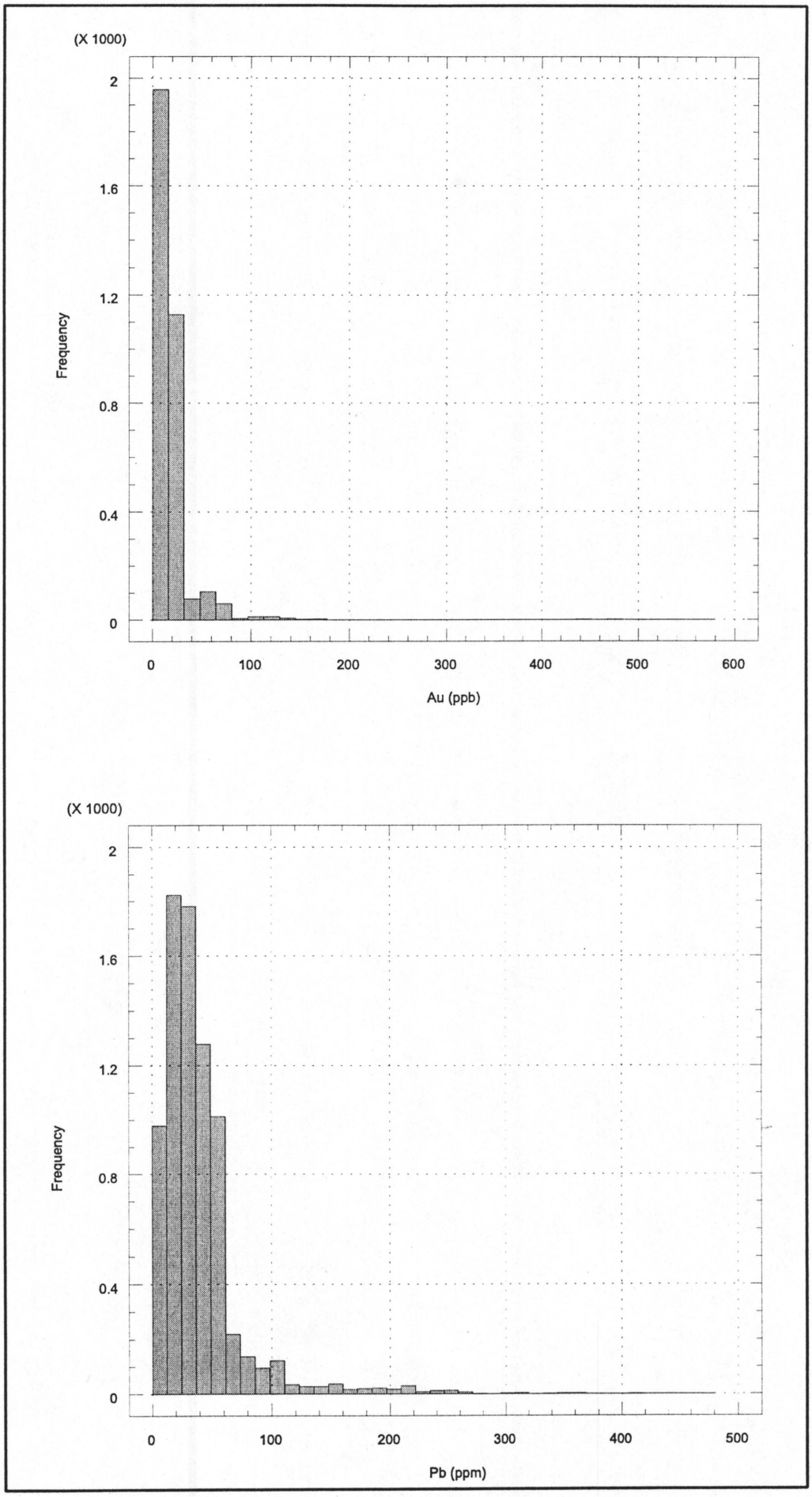

Figure 8.2 Frequency histograms (a) Au (ppb) and (b) Pb (ppm) for the Kruidfontein Complex soil sample set.

Digitised by the Department of Library Services in support of open access to information, University of Pretoria, 2021

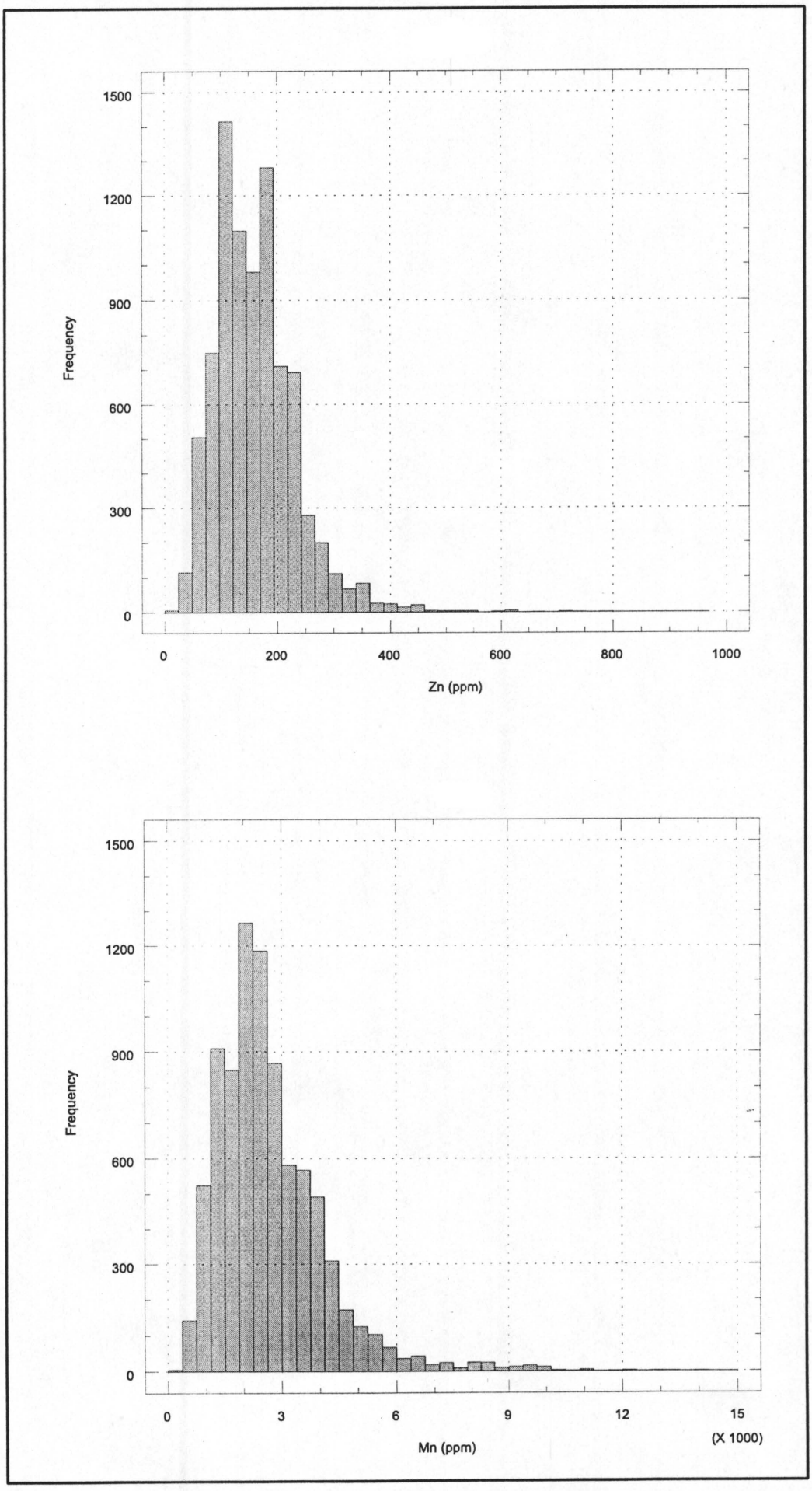

Figure 8.3 Frequency histograms (a) Zn (ppm) and (b) Mn (ppm) for the Kruidfontein Complex soil sample set.

Digitised by the Department of Library Services in support of open access to information, University of Pretoria, 2021

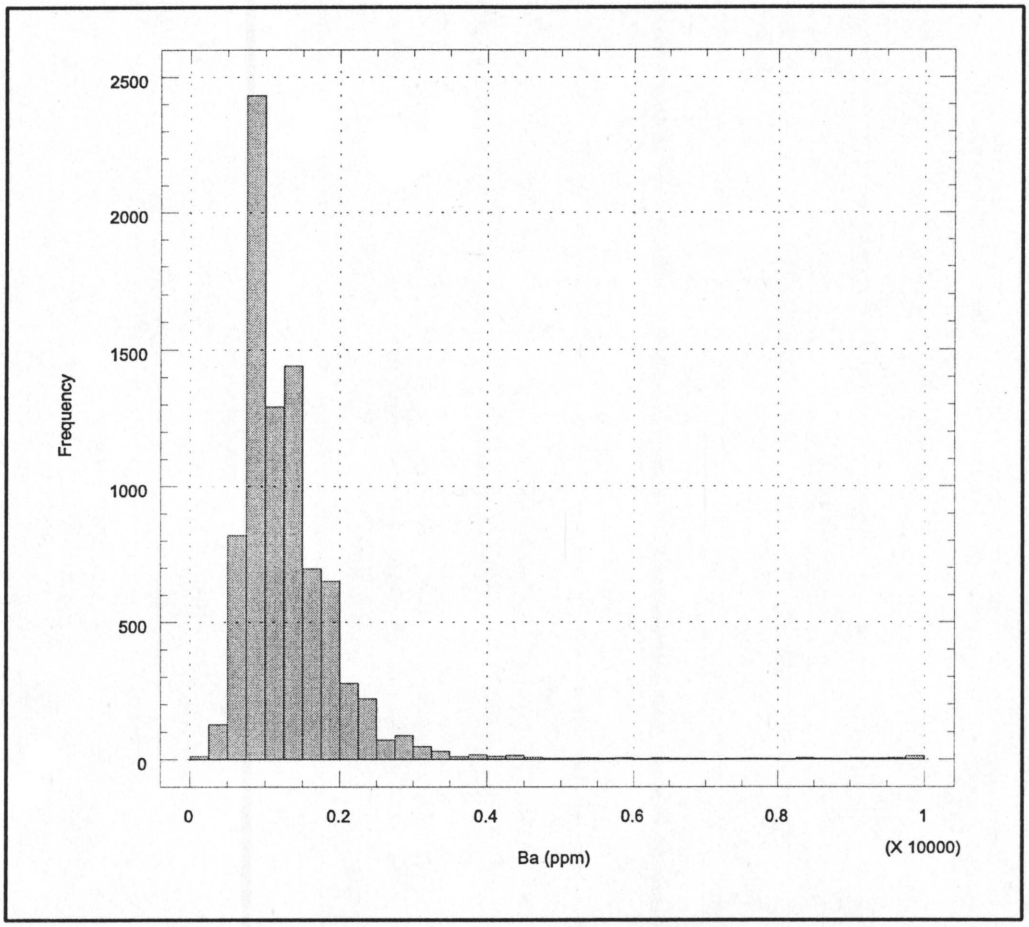

Figure 8.4 Frequency histogram of Ba (ppm) for the Kruidfontein Complex soil sample set.

Digitised by the Department of Library Services in support of open access to information, University of Pretoria, 2021

The threshold values for the elements were taken as the average of the data set plus one standard deviation. The threshold values for Au, Pb, Zn, Mn and Ba are 40 ppb, 75 ppm, 230 ppm, 0.4 % and 0.26 % respectively. The geochemical landscapes of these elements, viz. Au, Pb, Zn, Mn and Ba are shown in Figures 8.5, 8.6, 8.7, 8.8 and 8.9.

8.1 Relative mobility of the elements in the zone of weathering

The mobility of elements during weathering depends to a large extent on the solubility of the compounds formed. In most ore deposits gold occurs as a native element and may be liberated from the enclosing gangue and sulphide minerals during weathering to form isolated grains. Owing to its high density it is commonly enriched in the residual soil. One can therefore expect that gold anomalies will be superimposed with respect to the primary occurrence.

Galena is the most common primary lead ore, and during oxidation it changes to anglesite ($PbSO_4$) which is insoluble. In the presence of complexing agents lead may be soluble (eg. as $PbCl_4^{2-}$), but in a carbonate-rich environment (or due to the carbon dioxide in the atmosphere) it precipitates as cerussite ($PbCO_3$). Consequently lead is rather immobile.

Sphalerite is commonly oxidised to $ZnSO_4$ which is very soluble in an acidic to neutral environment, and consequently mobile. However, at high pH values and in the presence of carbon dioxide or carbonate minerals it would precipitate as smithsonite ($ZnCO_3$). One would therefore expect Zn anomalies to be laterally displaced with respect to primary sphalerite occurrences. Should this not be the case, the environment of weathering favoured the almost immediate formation of an insoluble Zn mineral like smithsonite.

In igneous and pyroclastic rocks manganese is commonly accommodated in Ca-rich and Fe-rich primary minerals, e.g. calcite, ankerite, diopside, etc. The behaviour of manganese during weathering it largely determined by Eh-pH conditions. As manganese becomes progressively more oxidised ($Mn^{2+} \rightarrow Mn^{3+} \rightarrow Mn^{4+}$) it becomes less soluble at a particular pH. Consequently secondary manganese anomalies can be expected to be largely superimposed with respect to the primary concentrations.

In nature barium occurs in a variety of insoluble minerals, the most common being barite ($BaSO_4$) and witherite ($BaCO_3$), but several less common ones are known. The result is that barium is very immobile, and transport of barium is essentially related to that of other clastic mineral phases in soils and sedimentary material. Barium anomalies can therefore be considered to be superimposed with respect to primary occurrences.

Digitised by the Department of Library Services in support of open access to information, University of Pretoria, 2021

During chemical weathering potassium is mobilised as the K^+ ion which is very soluble. However, on account of its large ionic radius it is rapidly adsorbed by hydrolysates (mainly $Al(OH)_3$ and $Si(OH)_4$ also formed during weathering) and ultimately incorporated in the formation of illitic clay minerals. Only under conditions of intense leaching and the formation of kaolinite will potassium be removed entirely. Under the climatic conditions prevailing in the study area potassium will therefore be retained in the soil.

In nature uranium commonly has two predominant oxidation states, viz. U^{4+} and U^{6+}. In igneous rocks uranium is commonly present in the tetravalent state, and U^{4+} is only slightly soluble at low pH values, mostly as fluoride complexes. Under oxidising conditions uranium is readily oxidised to U^{6+} and forms the uranyl radical UO_2^{2+}. It is very soluble under varying pH conditions as uranyl-phosphates, sulphates, fluorides, chlorides: ($UO_2(HPO_4)_2^{2-}$, UO_2SO_4, UO_2F^+, UO_2F_2, $UO_2F_3^-$, $UO_2F_4^{2-}$, UO_2Cl^+) and uranyl carbonate complexes ($UO_2(CO_3)_3^{4-}$, $UO_2(CO_3)_2.2H_2O^{2-}$, (UO_2CO_3). The uranyl ion only precipitates in the presence of suitable cations (K, Ca, Cu, Ba) and/or complex anions (PO_4^{3-}, As_4^{3-},VO_4^{3-}, MoO_4^{2-}). Normally, one would therefore expect that uranium anomalies will be laterally displaced with respect to the primary deposits. Thorium does not have a corresponding six-valent state, and in the zone of weathering it is either transported as a detrital mineral (e.g. thorianite) or as colloidal $Th(OH)_4$. It is therefore relatively immobile.

8.2 Geochemical landscapes

The distribution of gold in the inner and outer zones of the Kruidfontein Carbonatite Complex is recorded in Figure 8.5. Several Au anomalies are defined within the inner zone:

- in the pyroclastic breccia and surrounding lapilli tuff (2F, 2G, 3F and 3G) anomalous values range up to 300 ppb;
- the pyroclastic breccia and possible vent site is also characterised by high values (2E);
- the ferruginous lapilli tuff unit (2H) hosts a major Au anomaly with values ranging up to 480 ppb. It may also be associated with pyroclastic breccia and a north-northwest striking fault zone (Fig. 7.1). However, the high values show an even stronger northeasterly trend (2H, 1H) where the anomaly seems to be related to older pyroclastic breccia of the outer zone. This NE trending anomaly (1H) is assumed to be fault-related;
- anomalies in ash and lapilli tuff (3E and 3F) seem to be aligned along the strike of the carbonatite dykes, but the southward extension of this anomaly along the E/F boundary, does not seem to be related to the lithology;
- a N-NW-trending anomaly also extends into the outer zone (1B to 5C). This pronounced NW trend suggests structural control;

Digitised by the Department of Library Services in support of open access to information, University of Pretoria, 2021

Figure 8.5 Gold distribution in soil samples of the inner and outer zone of the Kruidfontein Carbonatite Complex.

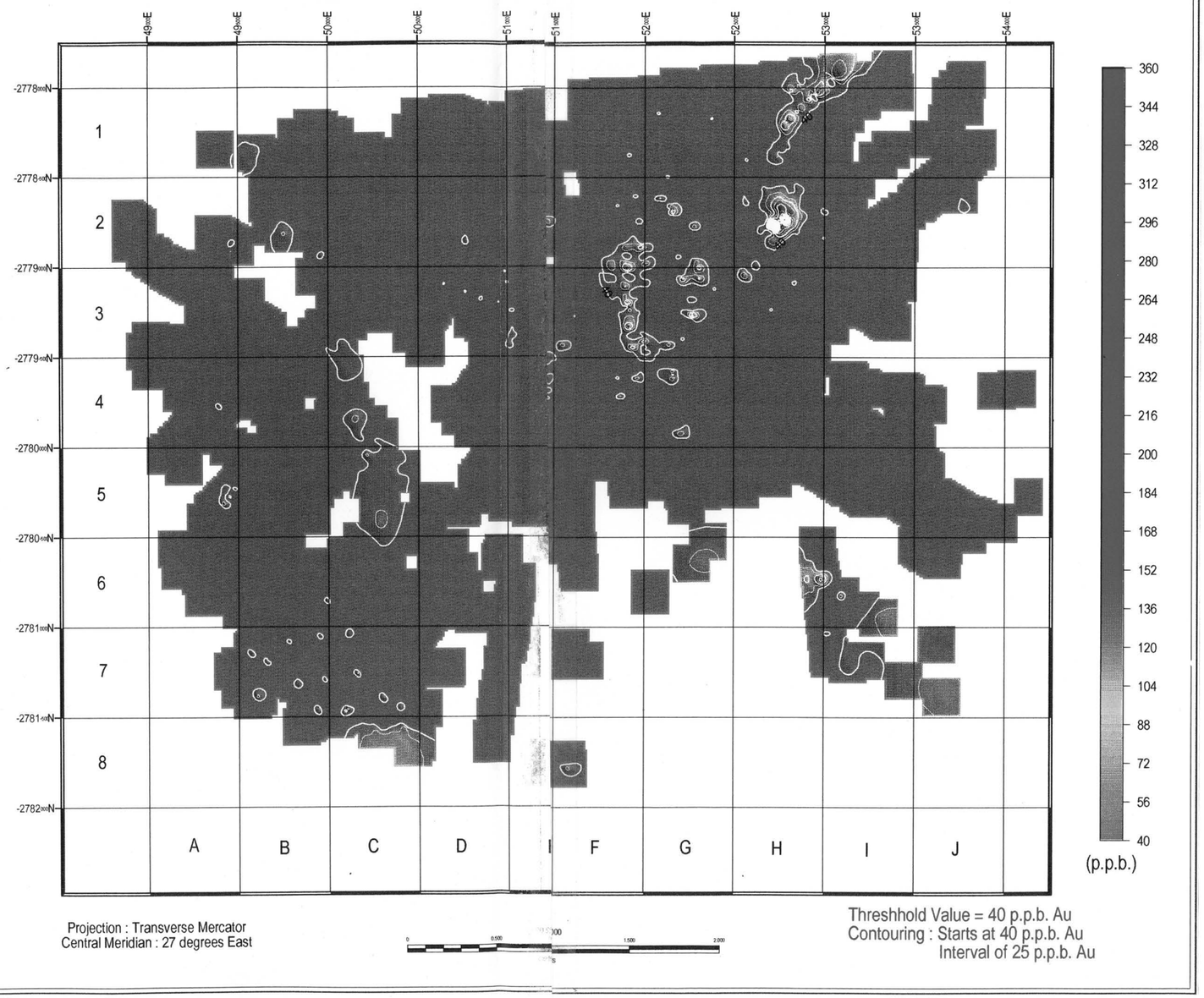

Digitised by the Department of Library Services in support of open access to information, University of Pretoria, 2021

- anomalies with lower Au (up to 60 ppb) values are related to pyroclastic breccia (including possible vent positions) in 4E, and 2D and 3D (Fig. 8.5). The anomalies, however, are slightly displaced with respect to the mapped outcrops, as they reflect soil values, not outcrop values.

Anomalies confined to the outer zone occur in 5G, 6G, 6H, 6I and 7I (Fig. 8.5). Unfortunately they are poorly constrained due to a lack of samples, but they are clearly associated with the younger pyroclastic breccia, ignimbrite and older pyroclastic breccia of the outer zone (Fig. 7.1). Several Au anomalies outside the complex, are situated in blocks 8C, 7I, 7J and 5A.

The highest concentrations of lead occur in the eastern part of the inner zone (Fig. 8.6), mirroring the gold distribution, especially in the case of the northeastern anomaly (2H). Here the anomalous gold concentration of 480 ppb in soil samples is accompanied by anomalous Pb concentrations ranging between 390 and 660 ppm. This pronounced association diminishes to the southwest where gold anomalies are associated with lead levels below 100 ppm. The lead distribution, however, is more extensive in 2E and 1E, and is associated with pyroclastic breccia, mapped as a possible vent site (highest Pb values ranging between 140 to 200 ppm) (Fig. 7.1).

A northwest trending Pb anomaly (highest Pb values of 130 to 410 ppm) (2G and 1F) is closely associated with transported soil along the northeastern flank of the inner zone (Figs. 7.1 and 8.6). The parent material of this soil is assumed to be the pyroclastic breccia present at a higher elevation. The Pb anomaly (highest Pb values 50 to 160 ppm) represented by 3F/G is associated in part with the same pyroclastic breccia. 4/5F depicts an anomaly (approximately 150 ppm) closely associated with intrusive carbonatite dykes.

Zinc, like Pb displays high values within the eastern part of the inner zone (Fig. 8.7). The landscape for Zn mirrors that of Pb and Au, including the anomaly within the sand-covered moat area (6/7F) in the southwestern part of the study area. Detailed blocks 5C, 4C and 3C show a pronounced NW trend of anomalies similar to the geochemical landscapes of Au and Pb, suggesting structural control. The outer zone (especially the southwestern, southern and south-eastern sectors) reflects several pronounced anomalies (values ranging from 200 to 400 ppm), which seem to coincide with the contact zone between the older pyroclastic breccia and the ignimbrite (7D, 7G/H and 4/5J), or with the ignimbrite (5B and 7G/H), and even the older pyroxenite breccia (4/5J).

The manganese distribution depicts the following (Fig. 8.8): (a) the inner zone generally has a higher Mn concentration than the outer zone, and the highest Mn values are found towards the

Digitised by the Department of Library Services in support of open access to information, University of Pretoria, 2021

Figure 8.6 Lead distribution in soil samples of the inner and outer zones Kruidfontein Carbonatite Complex.

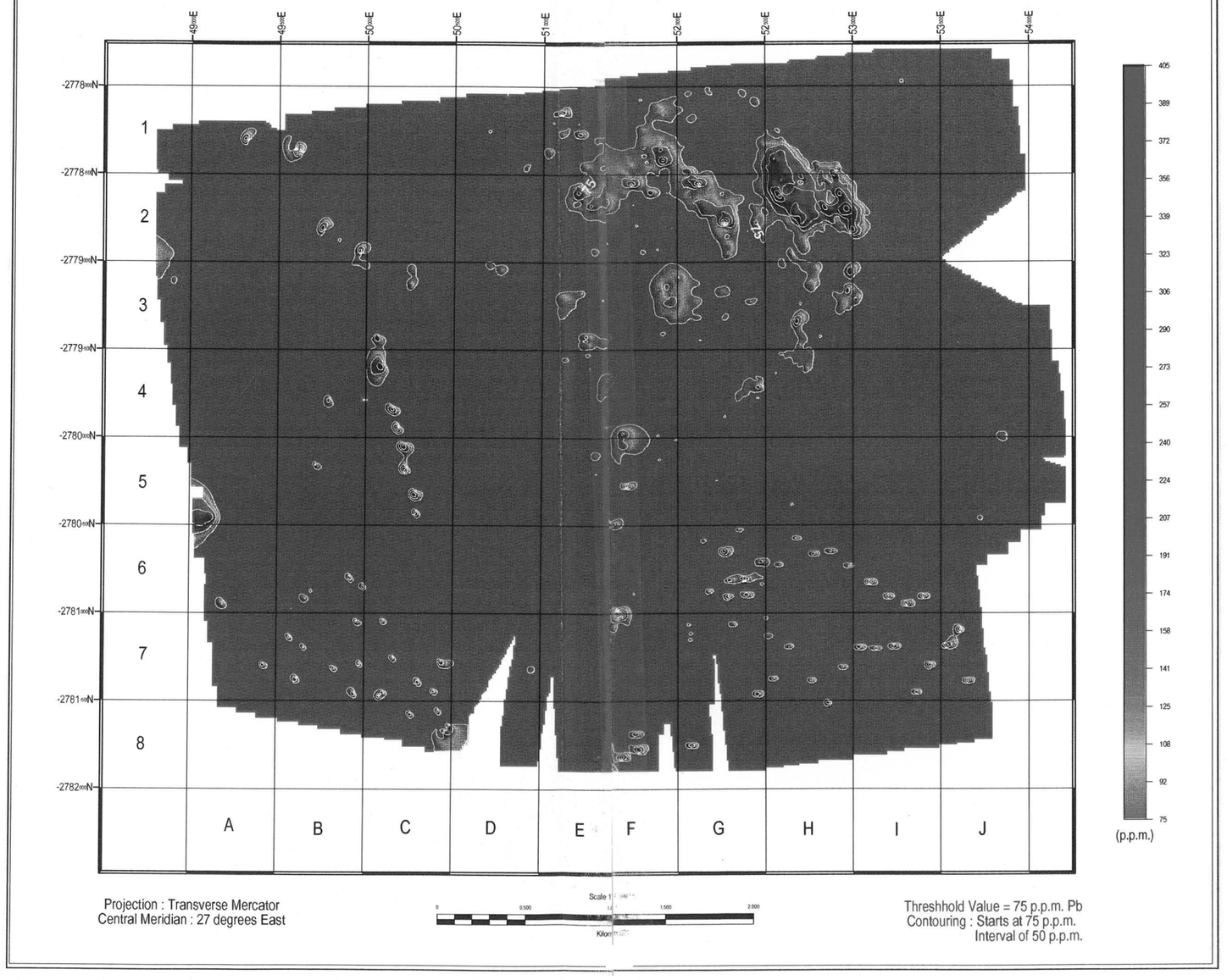

Digitised by the Department of Library Services in support of open access to information, University of Pretoria, 2021

central and eastern part; (b) areas of thick soil cover in the moat area between the inner and outer zones display low Mn values, defining the inner - outer zone boundary clearly (Fig. 7.1), and (c) several northwest and north-northwest striking, linear anomalies are prominent. In general the manganese anomalies in the northeast (1E to 2H to 3/4H to 4/5F to 3E) reflect those of lead and zinc fairly accurately. The association of manganese with gold is less marked. Anomalies in 4E, 3E, 2E and 1E seem to be associated with faulting, although the presence of pyroclastic breccia and the close proximity of possible vent sites may have played a role.

In the northeast the barium anomalies in soil samples (Fig. 8.9) reflect the gold distribution rather well. The linear trend of anomalies in the west (5C to 1B), already identified in the other geochemical maps is once again very pronounced. The anomalies at 5F and 2G coincide with those found for the other elements and suggest a degree of structural control. They may be associated with the fluorite-barite veins (Fig. 7.1).

8.3 Summary

The following conclusions can be made:

- anomalous gold and Ba levels are associated with the pyroclastic breccia, lapilli tuff and ferruginous lapilli tuff;
- a notable increase in Ba correlates with the presence of sövite, alvikite and barite-fluorite veins in 4E, 4F, 1F, 2F, 5F and 3H;
- the Ba and Mn anomalies do not match perfectly, but they do display several similarities, e.g. in 5F and 1E may indicate structure-related mineralisation. In the southeastern and southwestern sectors of the outer zone the match between Ba and Mn anomalies (although of low intensity) is almost perfect. Based on the high values of Mn in the inner zone, the Mn was rapidly oxidised during weathering and soil formation, limiting its movement;
- anomalous levels of Pb, Zn and Au are associated with the vent breccia and the alteration process of ferruginisation (2H and 2E). The latter also caused high Ba and Mn values. Another association is with the sövite and alvikite dykes, and barite-fluorite veins in 4F, 5F, 4E, 3E, 1E and 2E. The similar patterns depicted by Au and Pb in the inner zone indicate that these elements are rather immobile, whereas Zn, while having a similar distribution in the inner zone, displays higher values in the outer zone. This might indicate a change in the pH of the fluids, rendering the Zn mobile.

8.4 High-resolution radiometric survey

8.4.1 Total counts

Low values generally occur in soil-covered areas, such as between the inner and outer

Digitised by the Department of Library Services in support of open access to information, University of Pretoria, 2021

Figure 8.7 Zinc distribution in soil samples of the inner and outer zonene Kruidfontein Carbonatite Complex.

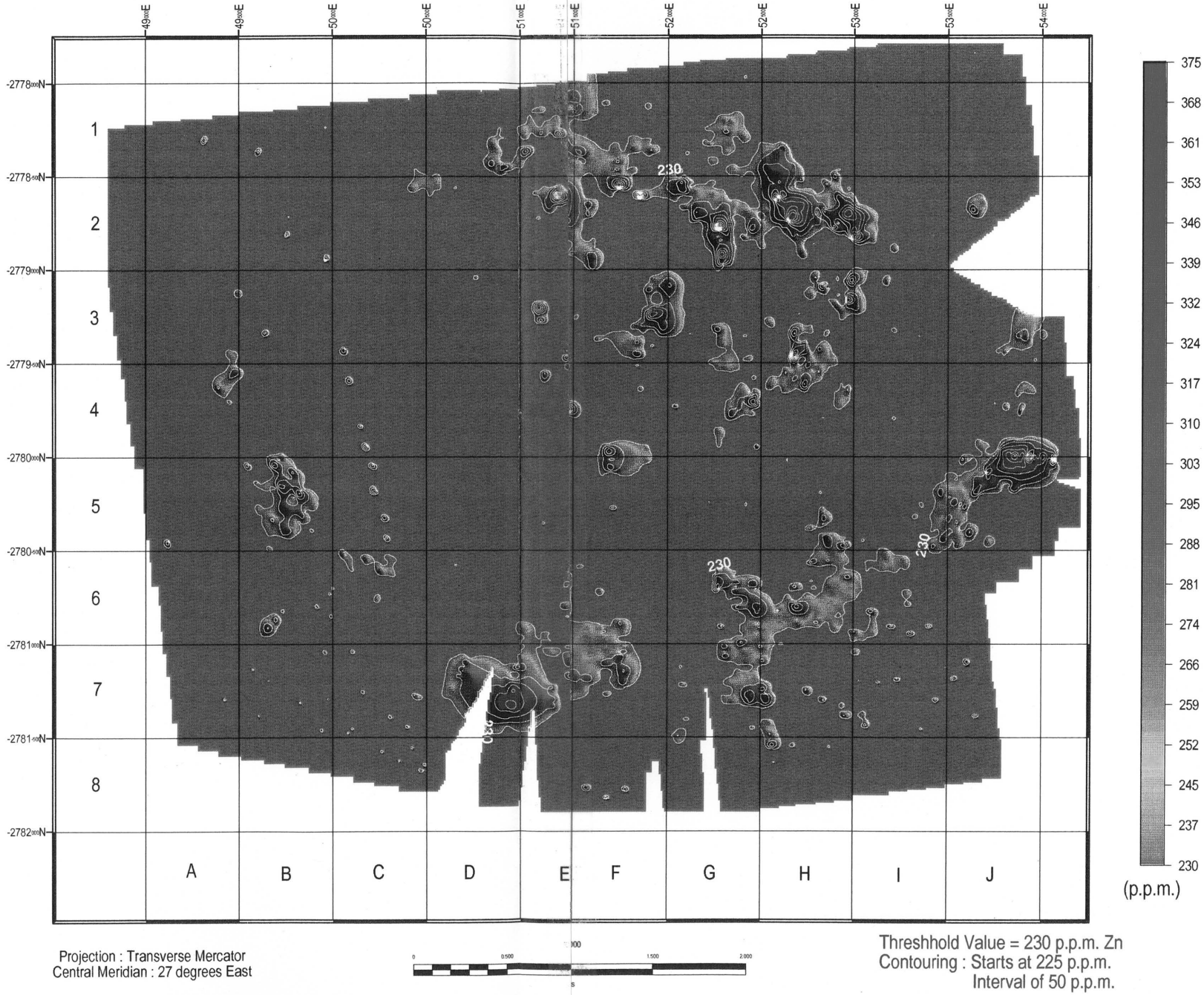

Digitised by the Department of Library Services in support of open access to information, University of Pretoria, 2021

Figure 8.8 Manganese distribution in soil samples of the inner and outnes of the Kruidfontein Carbonatite Complex.

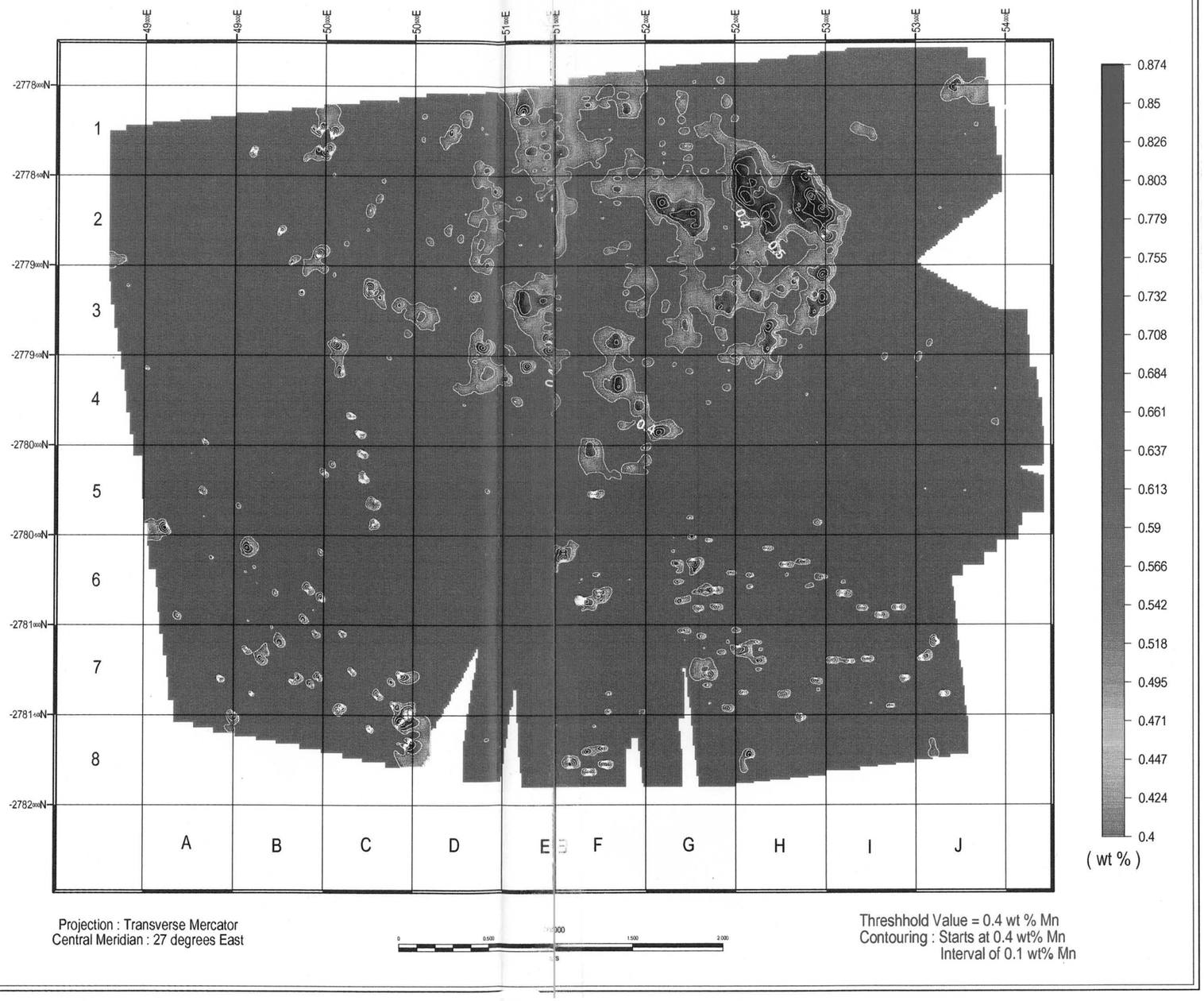

Digitised by the Department of Library Services in support of open access to information, University of Pretoria, 2021

Figure 8.9 Barium distribution in soil samples of the inner and outer zone of the Kruidfontein Complex.

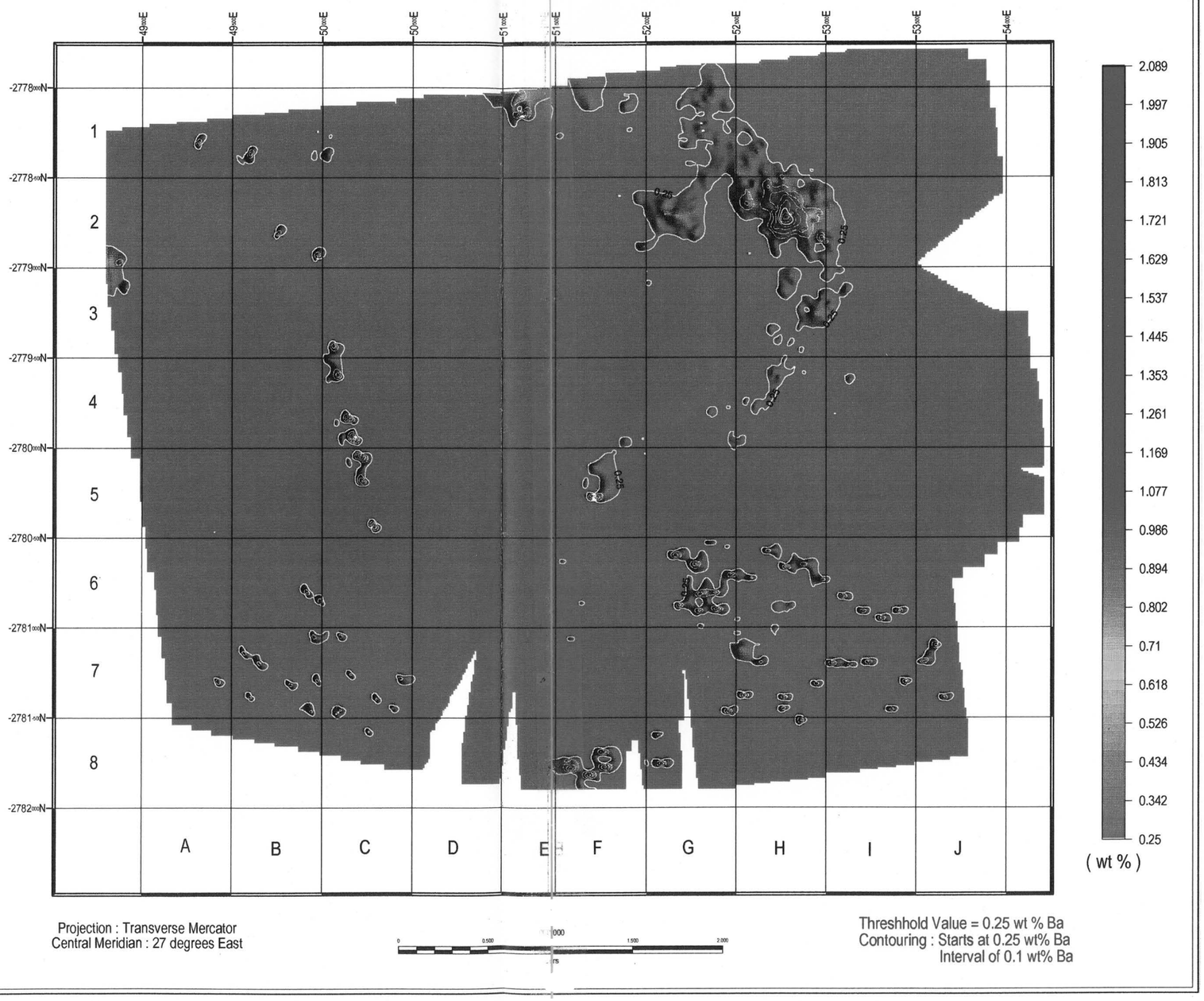

Digitised by the Department of Library Services in support of open access to information, University of Pretoria, 2021

zones (4C, 5D, 5/6F, 5G and 5H), and also in areas of the moat scree and outcrop of banded iron formation such as in 1I and 1J (Fig. 8.10).

Several positive anomalies are present in the inner zone (Figs. 7.1 and 8.10): (a) in the eastern and northeastern part the ferruginous lapilli tuff and associated ash tuff (1H and 2H); (b) in the northern part of the inner zone (3F, 2F, 2E and 1E) associated with pyroclastic breccia and lapilli tuff, carbonatite dykes and plugs, and also with faulting, and (c) towards the southern boundary of the inner zone (3E and 4E), again associated with carbonatite dykes, possible vents and associated breccia and lapilli tuff.

The fenites are located as an arc-like structure on the northeastern, eastern and southeastern sides of the inner zone (Fig. 7.1). The fenite, which consist mainly of K-feldspar, is assumed to have originated from carbonatite-related fluids migrating along a caldera-collapse fault zone in the pre-existing volcaniclastic rocks. The fenite, however, displays low radiometric total counts, which seems to be contradictory to expectations. The low eK_2O values could therefore be due to intense leaching along the fault zone. However, one should keep in mind that the radio-active isotope (^{40}K) is less than 10% of the total potassium and that its contribution to the total counts may be rather small.

The ignimbrite unit is characterised by higher total counts than either the older or the younger pyroclastic breccia units. The locally high values in portions of older pyroclastic breccia unit (e.g. 6E/F), are assumed to be due to transported scree and soil, possibly containing a detrital thorium mineral (e.g. thorianite) or colloidal $Th(OH)_4$.

In the inner zone of the Kruidfontein Carbonatite Complex the correlation between the anomalously high total counts and the geochemical anomalies is surprisingly good. Exceptions in this regard where radiometric anomalies are absent or even negative (e.g. 3G, 4G and 3F) can be attributed to the effective absorption of gamma radiation by the soil. Complete absorption of gamma radiation occurs within 0.5 metres of soil cover.

8.4.2 Thorium channel

The thorium counts mirror the total counts, but obviously at a much lower intensity (Fig. 8.11). However, the quantitative interpretation of the $eThO_2$ distribution is complex due to the relatively large statistical errors associated with these determinations. Nevertheless, the anomaly in 2H is closely associated with the ferruginous lapilli tuff, the associated ash tuff and lapilli tuff units. In 1E, 2E, 2F and 3F anomalous eTh_2O values can be related to vent areas, carbonatite dykes and plugs and as well as pyroclastic

Digitised by the Department of Library Services in support of open access to information, University of Pretoria, 2021

breccia and lapilli tuff.

8.4.3 Summary

- The mapped vents, carbonatite plugs and dykes, pyroclastic breccia, associated lapilli tuff and ferruginous tuff units are closely related to the total radiometric counts. This can be explained by the late-stage carbonatite activity, including dyke intrusion and hydrothermal alteration and/or mineralisation (barite, fluorite, rare-earth minerals in fluorite, K-feldspar in fenite, etc.). Thorium is normally present in minerals like thorianite, monazite, zircon, sphene and anatase, while trace amounts are found in fluorite, apatite, hematite, feldspar and quartz (Boyle, 1982). Substitution of U for Zr (zircon), U for Th (thorianite), U for Ce (monazite), U for Ca (apatite and fluorite) and U for Ba (barite) is common.
- The soil covered moat area between the inner and outer zones is defined by a low count rate, largely due to the absorption of the gamma rays by the soil.

Digitised by the Department of Library Services in support of open access to information, University of Pretoria, 2021

Figure 8.10 Ground radiometric map of the Kruidfontein Carbonatite Cx (total counts).

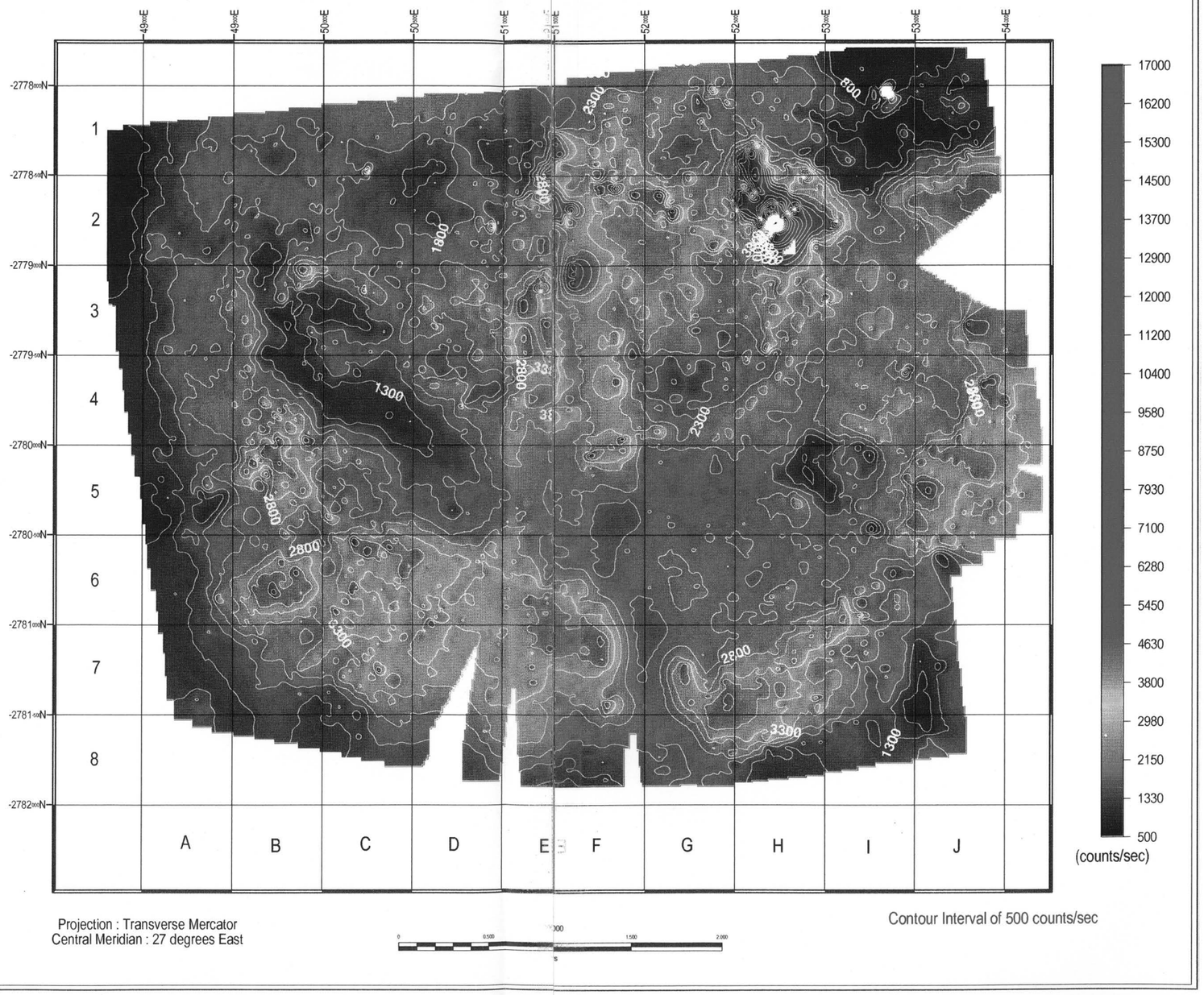

74

Digitised by the Department of Library Services in support of open access to information, University of Pretoria, 2021

Figure 8.11 Ground radiometric map of the Kruidfontein Carbonatite complex (thorium channel).

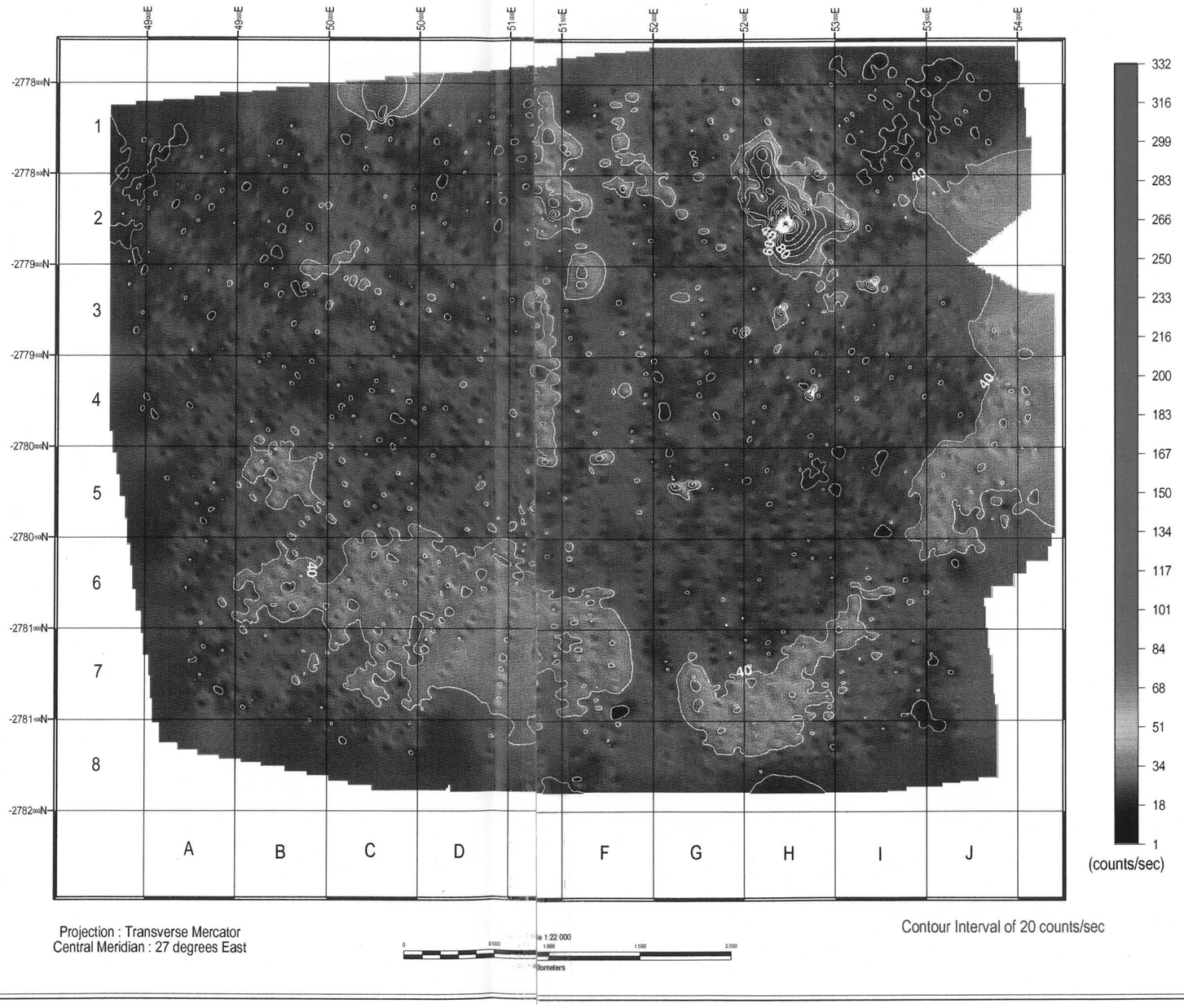

75

Digitised by the Department of Library Services in support of open access to information, University of Pretoria, 2021

9. GEOPHYSICAL APPRAISAL

9.1 Results of the regional gravity and magnetic surveys

On the 1:250 000 aeromagnetic map of Rustenburg the Kruidfontein Carbonatite Complex is characterised by smooth, well spaced contour patterns, indicating the absence of any substantial amount of magnetic material within its confines. This weak magnetic response is manifested by the nearby Nooitgedacht Carbonatite Complex as well. However, on the aeromagnetic map, elongated anomaly trends west of the Kruidfontein Carbonatite Complex are caused by ferruginous rocks belonging to the Penge Formation (banded iron formation). It therefore seems as if the Penge Formation extends as a folded feature towards the northern part of the Kruidfontein Carbonatite Complex. To the east of the Kruidfontein Carbonatite Complex the strong magnetic anomalies caused by the ferruginous parts of the Penge Formation coincide with a strong gravity high, which indicates a considerable thickness of dense ferruginous and dolomitic rocks. In contrast to the Kruidfontein Carbonatite Complex, the aeromagnetic fields over the Tweerivier and Bulhoek Carbonatite Complexes to the south can be modelled as magnetic plug-like structures.

The Bouguer gravity map (Fig. 9.1) does not indicate any characteristic gravitational response by the Kruidfontein Carbonatite Complex. However, it must be noted that, due to the wide spacing of stations, only a few reading were taken on the Complex. This low sampling density is not sufficient to properly model its mass distribution. However, if one could establish the density contrast between the carbonate-rich pyroclastic breccia, lapilli tuff and ash tuff, and the surrounding formations, the volume of the Complex may still be estimated. Density measurements on representative rock specimens from the study area show that pyroclastic breccia, lapilli tuff and ash tuff samples have densities between 2800 and 3000 kg/m^3, which are higher than the mean crustal density (2670 kg/m^3). The presence of large quantities of dense material should therefore give rise to a gravity high. It is possible, however, that the abundance of dolomite and banded iron formation has raised the density of the crust comprising the Crocodile River Fragment so that the density contrast is too low to produce an anomaly. The gravity low (L1) north of the Kruidfontein Carbonatite Complex coincides with the position of the Nooitgedacht Carbonatite Complex. Gravity and magnetic evidence therefore gives no indication of the composition of the Complex in depth. It is, however, possible that the Nooitgedacht Carbonatite Complex could be underlain by a low density pluton.

9.2 High-resolution magnetic survey

Figure 9.2 shows the ground magnetic map with the reference grid superimposed. The intensely "spotty" image may be ascribed either to an abundance of magnetic material lying close to the surface, inconsistency in the measurement, or diurnal variations which were not measured and

Digitised by the Department of Library Services in support of open access to information, University of Pretoria, 2021

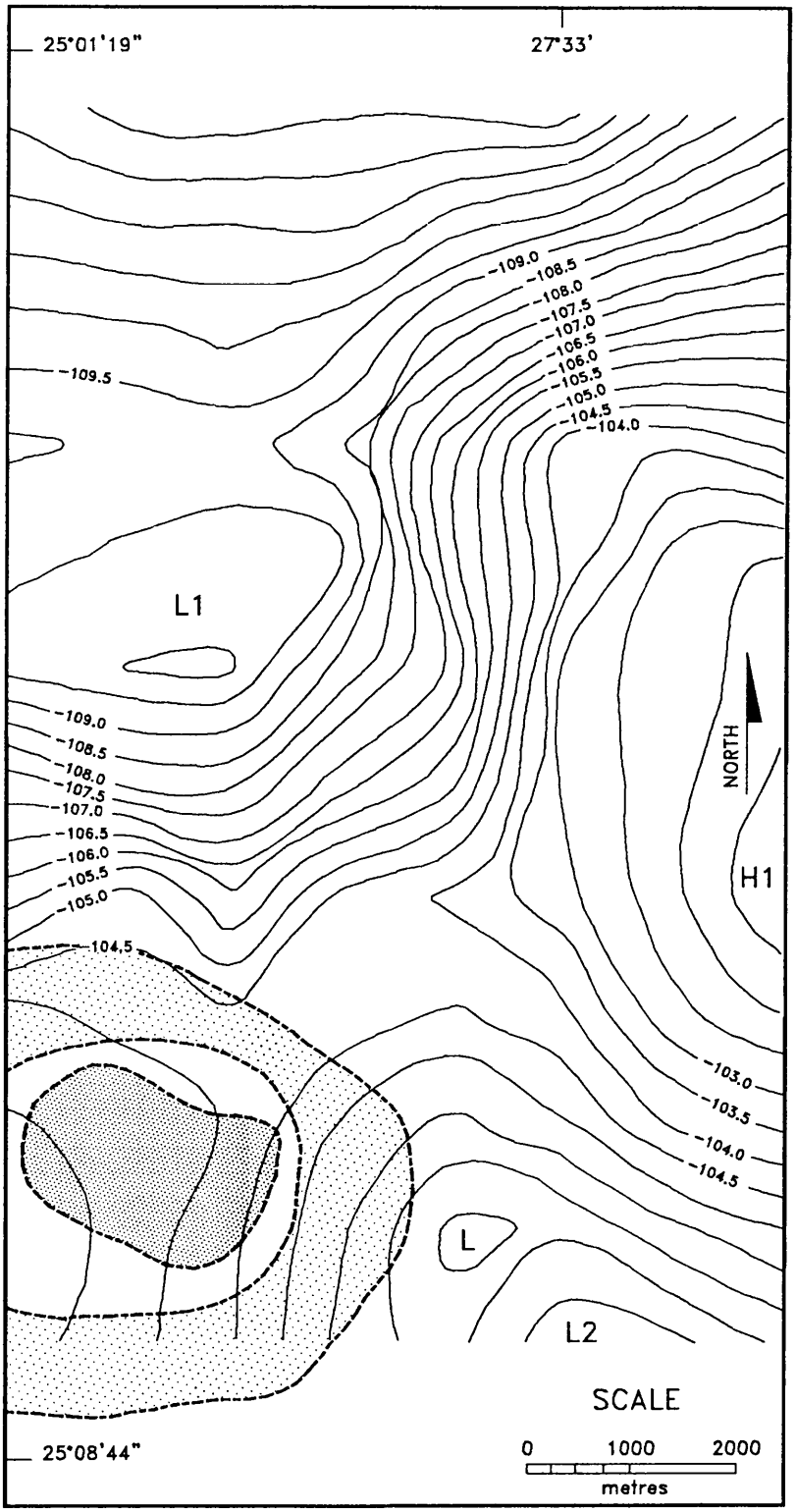

Figure 9.1 The inner (dark shaded) and outer (light shaded) zones of the Kruidfontein Carbonatite Complex superimposed on the Bouguer anomaly map of the area. L1 = Bouguer gravity low; H1 = Bouguer gravity high (Bouguer anomaly values in mgal).

Digitised by the Department of Library Services in support of open access to information, University of Pretoria, 2021

Figure 9.2 Ground magnetic data of the Kruidfontein Carbonatite Cx.

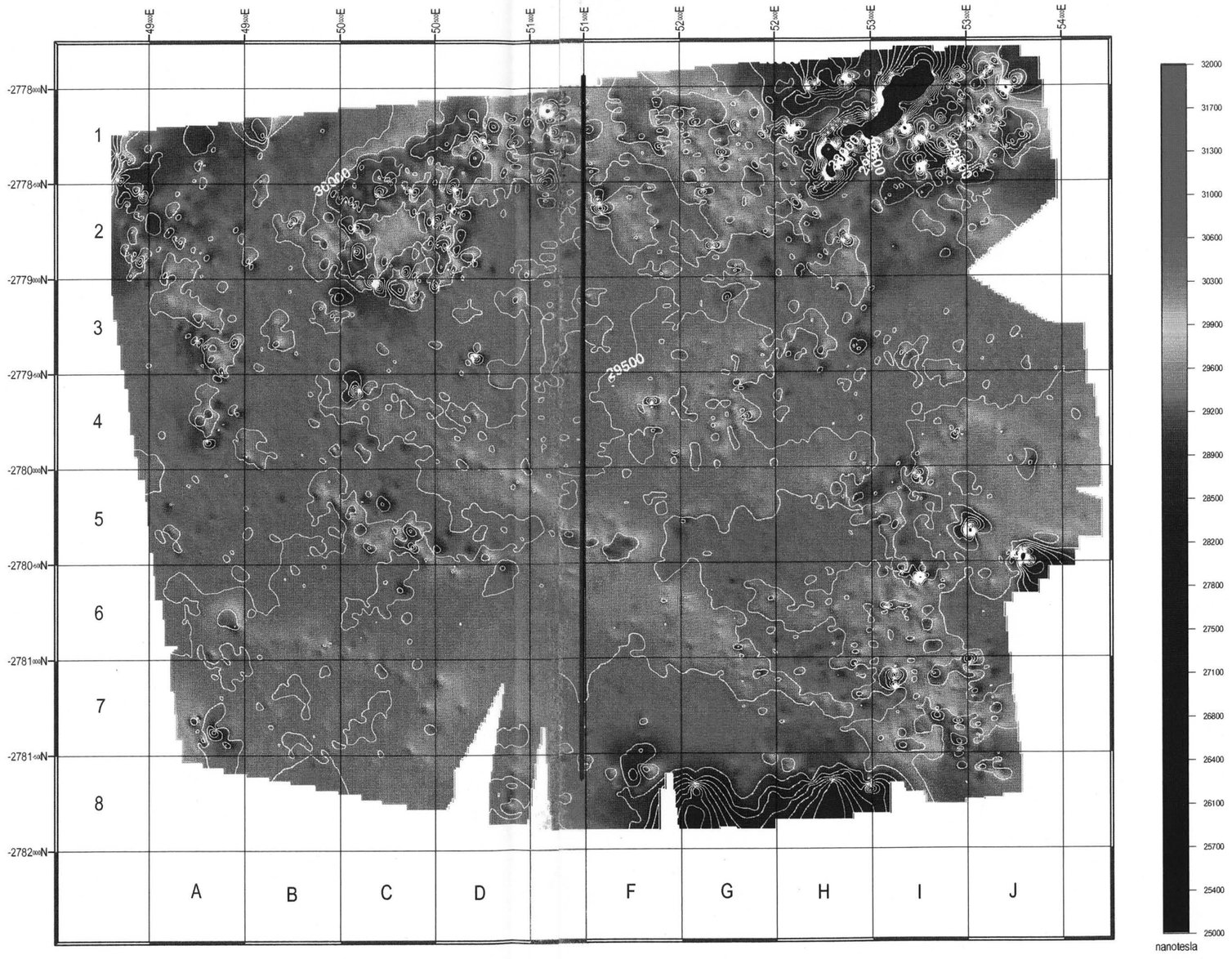

78

Digitised by the Department of Library Services in support of open access to information, University of Pretoria, 2021

hence not corrected for.

A pronounced positive magnetic anomaly is situated along the northern boundary of the inner zone of the Kruidfontein Carbonatite Complex (the northern boundary between the inner and outer zone) (2B, 2C, 1C, 1D, 1E, 1F, 1G and 2G). Several possible causes for this anomaly can be considered, e.g.:

- a thicker volcaniclastic sequence of the inner zone (containing magnetic minerals like magnetite) along the northern boundary compared to the other parts of the Complex;
- an increase in magnetic minerals in the rocks in the above-mentioned area;
- plug-like features or vent positions all along the inner zone - outer zone contact;
- an intrusion of basaltic magma along the inner zone - outer zone contact.
- the presence of hidden protuberances of banded iron formation below and partly within the rocks of the inner zone - the association of magnetic anomalies caused by banded iron formation in 1I/J is a case in point.

Prominent low magnetic values (1H, 1I) are associated with slightly displaced positive Au values (Fig.8.5).

The interpretation of Profile 1 (Figs. 9.2 and 9.3) indicates that the structures in the south comprise gently-dipping, shallow magnetic rocks, whereas in the north, the magnetic rocks are almost vertical.

Carbonatite dykes and plugs occur at several localities in the inner zone (1E, 2E and 4E), and display low magnetic signatures. In the eastern part of the inner zone of the Complex ill-defined concentric magnetic patterns reflect the distribution of the interbedded lapilli and ash tuff, and pyroclastic breccia.

Low magnetic values are present along the southern boundary of the inner zone (4C, 5D, 5G and 5H), in the so-called moat-area. It is in this environment that a large tabular replacement deposit, 2.8 Mt in size, consisting mainly of fluorite (up to 28% CaF_2), has been found (Fig. 5.2).

Three prominent west-northwest trending positive magnetic anomalies traversing the Complex have been picked up (6A, 6B, 7C and 7D; 4A, 5B, 5C and 5/6D; and 3A, 3B, 4C, 4/5D, 5E, 5/6F, 6G and 7H) and are assumed to be deep-seated fracture zones. A linear feature with poorly defined positive anomalies is also present from 4E to 5/6E. A weak N-NW trending lineament (3B/C, 4C, 5C, 6C and 7C) defined by lower magnetic values and positive Au, Pb, Zn, Ba and Mn anomalies, corresponds with the N-NW regional fault on the western side of the Crocodile River

Digitised by the Department of Library Services in support of open access to information, University of Pretoria, 2021

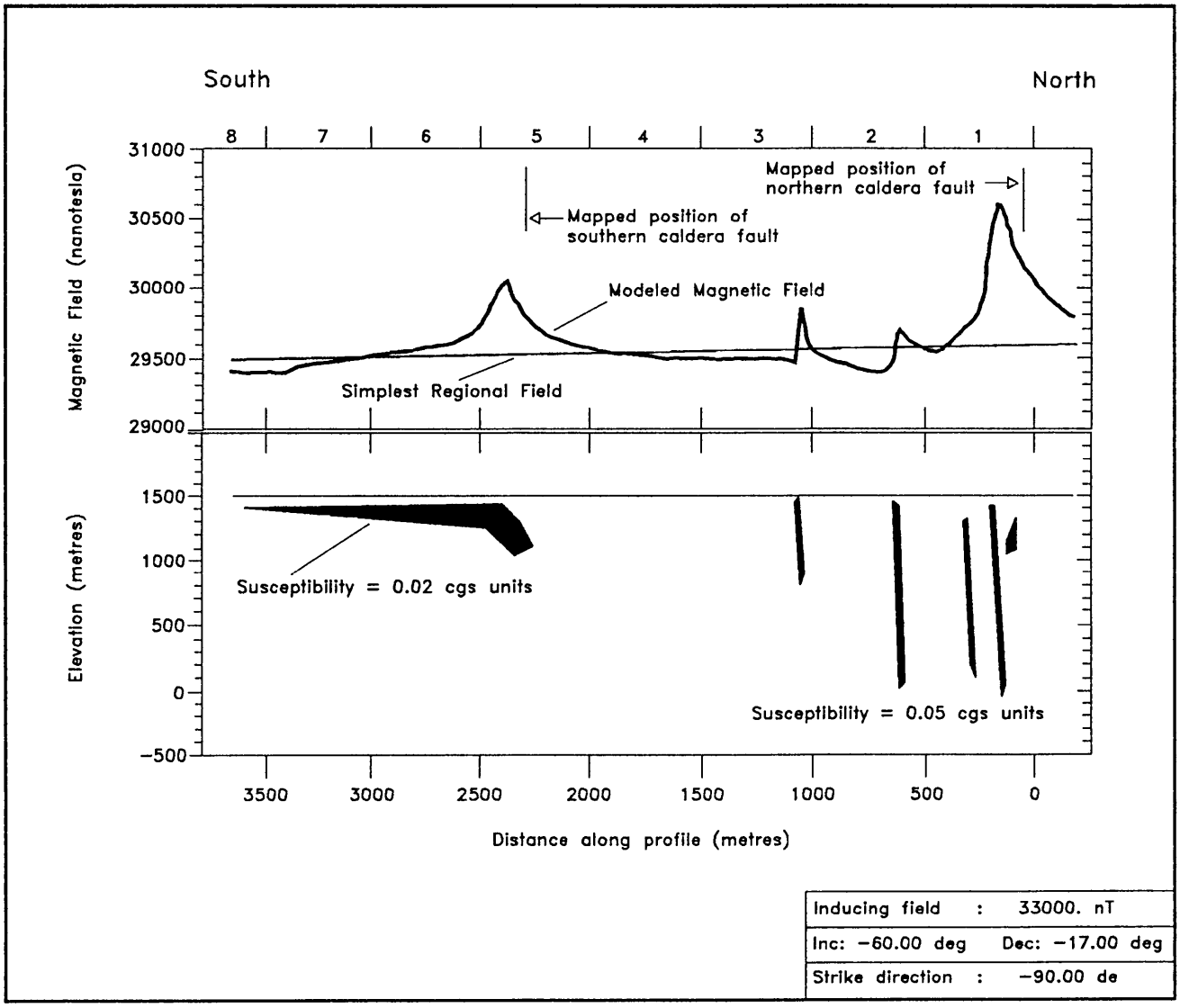

Figure 9.3 North-south magnetic profile 1 across the Kruidfontein Carbonatite Complex (see Figs. 5.2 and 9.2 for the profile locality and orientation).

Digitised by the Department of Library Services in support of open access to information, University of Pretoria, 2021

Fragment.

9.3 Summary

- Gravity and magnetic data indicate that no high-density or strongly magnetic body is present in depth, and it is possible that the Nooitgedacht Carbonatite Complex could be underlain by a low density pluton.
- The interpretation of Profile 1 (Fig. 9.6) indicates that the structures in the south comprise gently-dipping, shallow magnetic rocks, whereas in the north, the magnetic rocks are almost vertical, possibly reflecting the geometry of the feeder routes for hydrothermal fluids.
- The centroclinal dip of the inner zone seems to be variable in the sense that: (a) in the south-southwestern, southern and south-southeastern areas the dip is less that 10° while, (b) in the northern part the dip becomes steeper, as supported by the modelled magnetic Profile 1.
- The carbonatite dykes do not display prominent magnetic signatures.
- The ill-defined magnetic banding in the eastern part of the inner zone (possibly due to the small amount of magnetic material present) could depict the degree of alteration caused by fluids that moved through the volcanic pile. Some layers like the tuff would tend to be more dense (thus inhibiting the migration of fluid or even acting as barriers), while the associated breccias and lapilli tuff could have been more permeable. However, it is not conclusive that the pyroclastic breccia is associated with positive magnetic anomalies.
- Low magnetic values present along the southern boundary of the inner zone (in the so-called moat-area) correspond with the large, tabular replacement deposit of fluorite (Fig. 5.2).
- Three prominent W-NW trending lineaments of positive magnetic anomalies are assumed to be fracture zones, older than the Kruidfontein Carbonatite Complex and Crocodile River Fragment, and that these have provided access for nephelinitic and/or phonolitic and associated carbonatite magma from the mantle. It is further possible that subsequently these zones could have been intruded by magma related to the Pilanesberg Alkaline Province or could have been affected by iron-rich fluids. It can, however, be argued that these zones should then also be present in the "floor" of the Bushveld Complex. However, high resolution aeromagnetic data in support of this hypothesis are not available.

Digitised by the Department of Library Services in support of open access to information, University of Pretoria, 2021

10. DETAILED PETROGRAPHY AND CATHODOLUMINESCENCE

Drilling (boreholes KD01, KD02 and KD03) was confined to the ferruginous ash fall tuff (2H) (Figs. 5.2 and 7.1), as it is characterised by strong geochemical and radiometric anomalies. By applying detailed petrography and cathodoluminescence to the drill core, it was attempted to determine (a) the mineral paragenesis, (b) the degree of mineralisation/alteration, (c) the classification of the different styles of mineralisation and alteration, and (d) the original protolith, and possible primary sources responsible for the mineralisation.

10.1 Mineralogical composition

The volcaniclastic sequence of the inner zone as intersected by the inclined KD01 borehole contains a variety of minerals like calcite, dolomite, ankerite, siderite, fluorite, K-feldspar, hematite, quartz, chlorite, apatite and anatase.

The semi-quantitative mineralogical composition as determined by means of XRD is represented in Figure 10.1 and Table 10.1. The upper ash flow unit mainly consists of the mineral assemblage calcite + dolomite/ ankerite + K-feldspar + quartz (+ minor apatite + anatase + chlorite). The least altered volcaniclastic carbonatite, identified as sample KD016, contains primary volcanic textures (i.e. ash, lapilli and trachytoidal fragments) and consists of calcite + dolomite, and minor anatase, quartz, chlorite, K-feldspar, fluorite and apatite.

The lapilli tuff unit is similar to the upper ash flow unit, except that fluorite becomes more prominent towards the base and that chlorite may increase. The ferruginous lapilli tuff unit is obviously enriched in siderite and hematite, but most of the minerals mentioned earlier are still present, and barite becomes an important minor phase. In the lower ash flow unit dolomite/ankerite becomes more prominent in places, and the barite content seems to increase slightly. The mineralised zones (seen as the final stage of mineralisation)(Fig. 10.1 and Table 10.1) represented by samples KD126, KD130, KD134, KD141, KD142 and KD143, were identified macroscopically and consist mainly of fluorite, with lesser amounts of siderite, apatite, barite, calcite and minor amounts of chlorite + quartz + K-feldspar + dolomite/ankerite. In terms of the semi-quantitative proportions they do not differ significantly from the “unmineralised” equivalent.

10.2 Petrography and cathodoluminescence

The sequence intersected by borehole KD01 consists of extensively altered pyroclastic rocks. Some primary fabrics are preserved and indicate that the sequence was originally a series of bedded ash tuff and lapilli tuff deposits of which the primary phases included both silicate and carbonatite minerals. Samples taken from this sequence represent different rock types (viz. upper ash flow, lapilli tuff, ferruginous lapilli tuff and lower ash flow units) and are thought to represent

Digitised by the Department of Library Services in support of open access to information, University of Pretoria, 2021

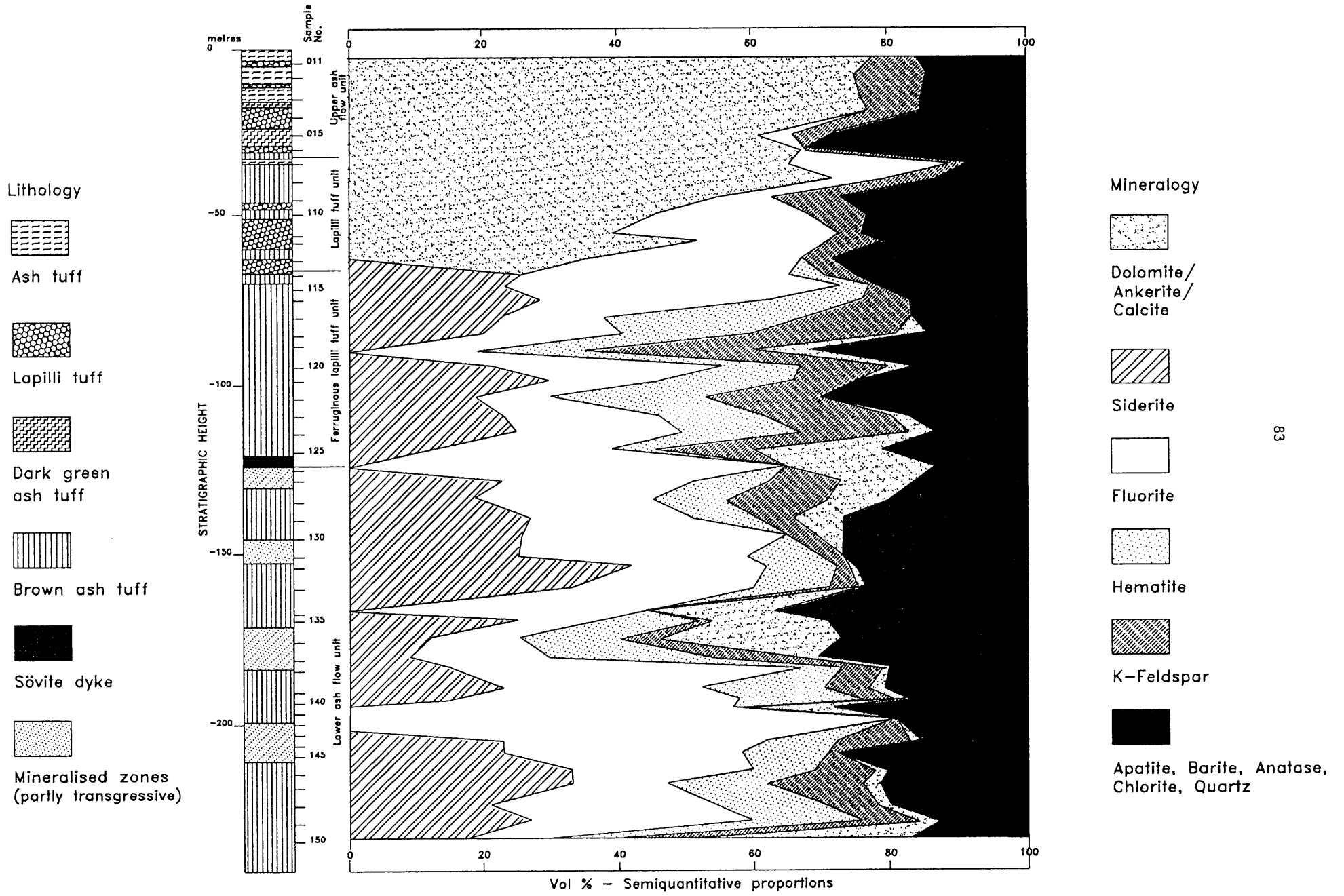

Figure 10.1 Semi-quantitative proportions of the major mineral phases in KD01, as determined by XRD.

Digitised by the Department of Library Services in support of open access to information, University of Pretoria, 2021

Table 10.1 Proportions of minor mineral phases like apatite, barite, anatase, quartz and chlorite (determined by X-ray diffraction) in samples from the KD01 borehole.

SAMPLE	APATITE	BARITE	ANATASE	QUARTZ	CHLORITE
KD011	4			7	2
KD012	4			9	1
KD013	3			9	2
KD014	4		6	6	
KD015	3		12	8	
KD016	3		9	3	17
KD017	2			4	
KD018	3			5	
KD019	3		8	5	10
KD110	2		5	5	11
KD111	3		4	2	16
KD112	4		6	6	4
KD113			4	3	10
KD114			7	3	14
KD115			6	3	12
KD116			6	5	5
KD117	3	6	4	8	
KD118		3	4	7	1
KD119	4	3	8	10	7
KD120		5	3	7	1
KD121	4	2	5	5	13
KD122		4	4	10	12
KD123		4	4	6	3
KD124	3		4	7	1
KD125		5	5	6	
KD126	2	5			2
KD127		1	4	6	1
KD128		6	4	6	4
KD129		7	5	7	8
KD130	2	11	3	4	7
KD131		4	4	8	11
KD132		5	7	4	8
KD133	3	3	2	6	11

SAMPLE	APATITE	BARITE	ANATASE	QUARTZ	CHLORITE
KD134	15	10	3	2	6
KD135	2	5	7	4	10
KD136		4	5	7	9
KD137			3	9	13
KD138	2	4	2	3	2
KD139		2	5	7	2
KD140		2	4	7	2
KD141	12	8	2	1	4
KD142	1	4		5	2
KD143		4	3	3	
KD144		2	3	5	2
KD145		5	6	2	15
KD146		5	4	4	2
KD147		5	5	5	5
KD148		6	3	4	6
KD149		5	3	4	4
KD150		4	4	5	6

Digitised by the Department of Library Services in support of open access to information, University of Pretoria, 2021

all types of alteration and mineralisation in them.

10.2.1 Upper ash flow unit

Three samples were selected at depths of -10.00, -26.40 and -30.10 m, and marked KD012, KD015 and KD016 respectively. General descriptions of these samples are listed in Table 10.2.

Table 10.2 General descriptions of samples from the upper ash flow unit.

SAMPLE	MINERALS IN ORDER OF ABUNDANCE (XRD)	COMPONENTS	PARTICLE DIAMETER	FABRIC	ROCK TYPE
KD012	dolomite/ankerite, K-feldspar, quartz, apatite	ash grains and lapilli	0.2 to 0.5 mm 2 mm to 3 mm	interlayered ash and lapilli	ash and lapilli tuff
KD015	calcite, dolomite/ ankerite, anatase, K-feldspar, quartz, fluorite, apatite	(a) ash grains, (b) phenocrysts, (c) amygdales, (d) microphenocrysts	<1 mm 0.03 to 0.30mm 0.05 to 0.25mm 70-80µm to 15-20µm in length; 10-20µm to 4-5µm wide	massive	ash tuff
KD016	calcite, dolomite/ ankerite, chlorite, anatase, apatite, quartz, K-feldspar	(a) ash grains, (b) phenocrysts, (c) amygdales, (d) microphenocrysts	<1 mm 0.03 to 0.40mm 0.05 to 0.25mm 70-80µm to 15-20µm in length; 10-20µm to 4-5µm wide	massive	ash tuff

Sample KD012 is pale grey and straddles the contact between two ash tuff units, whereas samples KD015 and KD016 consist of green, relatively unaltered ash tuff (Fig. 7.26). These three samples are interbedded with layers of pyroclastic breccia.

10.2.1.1 Sample KD012

The ash matrix is dominated by dolomite/ankerite, but minor amounts of K-feldspar, apatite, fluorite and iron-oxides are also present, as well as some quartz, zircon and a LREE-carbonate. Fine-grained, pale blue-luminescent apatite seems to form an overgrowth on K-feldspar and minor dolomite seems to encapsulate ankerite as well as tiny anatase and pyrite crystals which occur throughout (Figs. 10.2 and 10.3).

The relative abundance and distribution of the ash grains vary markedly between the different ash layers. Ash grains, ovoid to subspherical (maximum aspect ratio of 3:1 in cross-section), are composed mainly of K-feldspar, with lesser ankerite,

Digitised by the Department of Library Services in support of open access to information, University of Pretoria, 2021

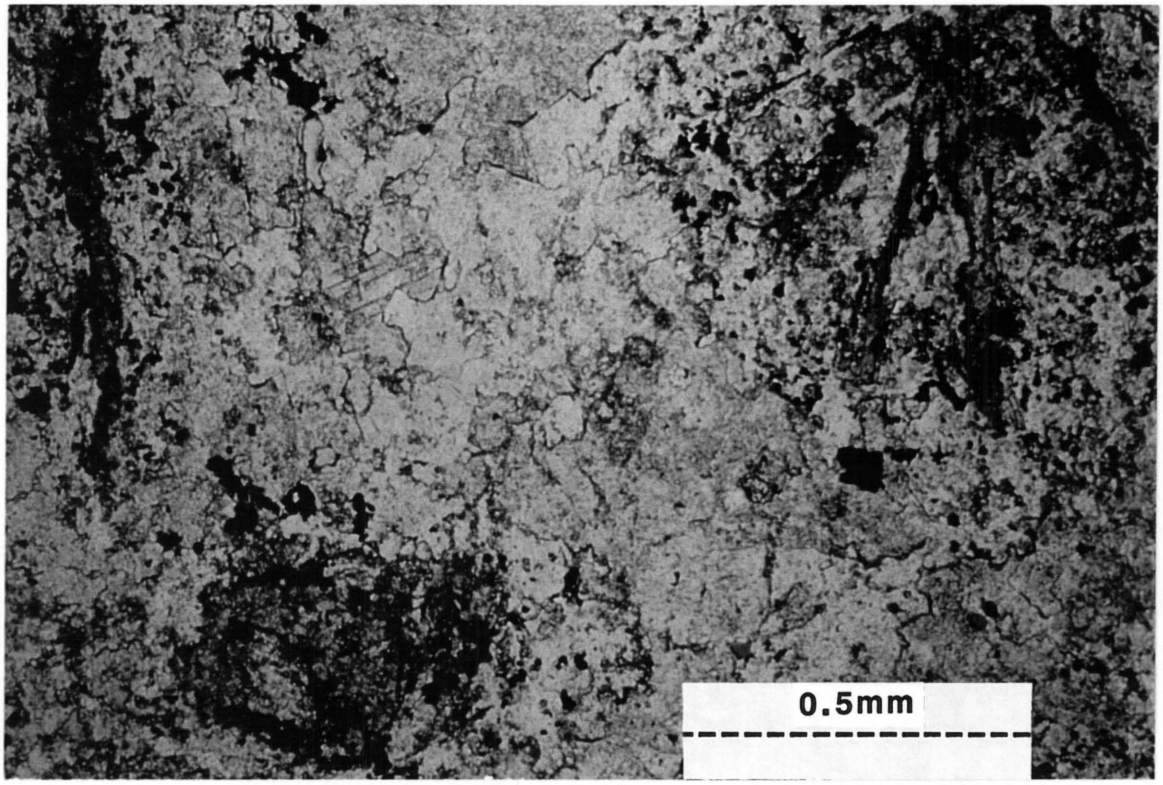

Figure 10.2 Fine-grained tuff with rounded ash grains (500 µm to 1 mm in diameter) (upper left and right and bottom left) in a matrix of volcanic dust (largely replaced by ankerite and fluorite). Dark brown to black material represents pyrite and anatase (Plane polarised light, x50; width of view: 2 mm across; sample KD012, KPPL17-27).

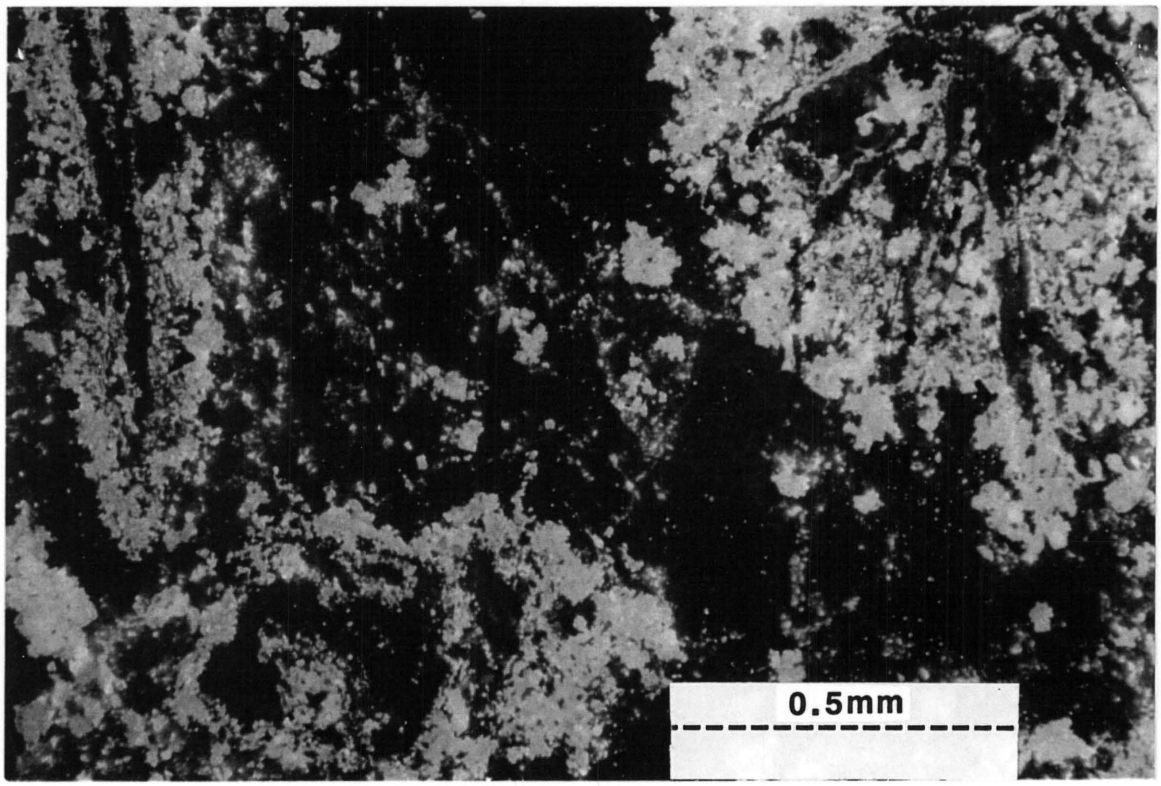

Figure 10.3 Cathodoluminescence image of the field in Figure 10.2. The ash grains consist largely of K-feldspar (green luminescence), ankerite, pyrite, anatase (non-luminescent), and apatite (light-blue luminescence). The non-luminescent volcanic dust in the central portions (the matrix) consists of ankerite and fluorite (dark blue luminescense) (Cathodoluminescence; x50; width of view: 2 mm across; film: 1600 ASA Fuji Provia; exposure time: 2 minute 14 seconds; sample KD012, KCL17-28).

Digitised by the Department of Library Services in support of open access to information, University of Pretoria, 2021

and are relatively rich in iron oxides and apatite. They appear grey in thin section, because the ankerite and K-feldspar are dusted with extremely fine-grained hematite. In many grains, this dusting is concentrated as a thin sinuous band which runs parallel to the long axis of the particles. Euhedral to subhedral pyrite is scattered within the grains, but is concentrated at or near to the rims. Fine-grained, blue-luminescing apatite is concentrated in narrow rims sur-rounding these grains. Many grains also display an ankerite rim, which is itself rimmed by the apatite. Apatite is also seen along the rims of lapilli and replaces elongate non-luminescent phenocrysts within the lapilli.

Fluorite occurs in at least three stages (Fig. 10.4): the first filled in the voids with bright blue fluorite, which later suffered fragmentation so that violet fluorite filled the resulting cracks. In some instances, the violet-luminescing fluorite is itself fragmented and cemented by a third generation of dull, deep blue luminescing fluorite. Pyrite euhedra overgrow early textures. Quartz formed as veins and also as diffuse patches. Calcite occurs as small, irregular patches. Ankerite and dull green-grey K-feldspar-filled veins cut all earlier fabrics and minerals (except probably the quartz).

Interpretation

The two units represented in thin section have been replaced entirely by secondary minerals (Fig. 10.4). The differences between the secondary replacement of the two units indicate significant differences between their primary minerals, especially of the ash grains and lapilli. In particular, the feldspar-rich grains, which also contain appreciable quantities of opaque minerals, suggest that these grains were originally fragments of the silicate rock. The ankerite-dominated grains and lapilli may represent original carbonatite fragments. The original composition of the ash cannot be identified with any certainty. It is plausible that it was originally carbonatitic, and that the original silicate lapilli and grains represent accidental, non-juvenile fragments from the vent entrapped during the carbonatitic eruption.

10.2.1.2 Samples KD015 and KD016

These samples represent relatively unaltered tuff since their composition is dominated by calcite. The fabric of both samples is very similar. Rounded ash grains are composed of phenocrysts and amygdales of calcite in a non-luminescent mesostasis, dominated by chlorite and very fine-grained hematite

Digitised by the Department of Library Services in support of open access to information, University of Pretoria, 2021

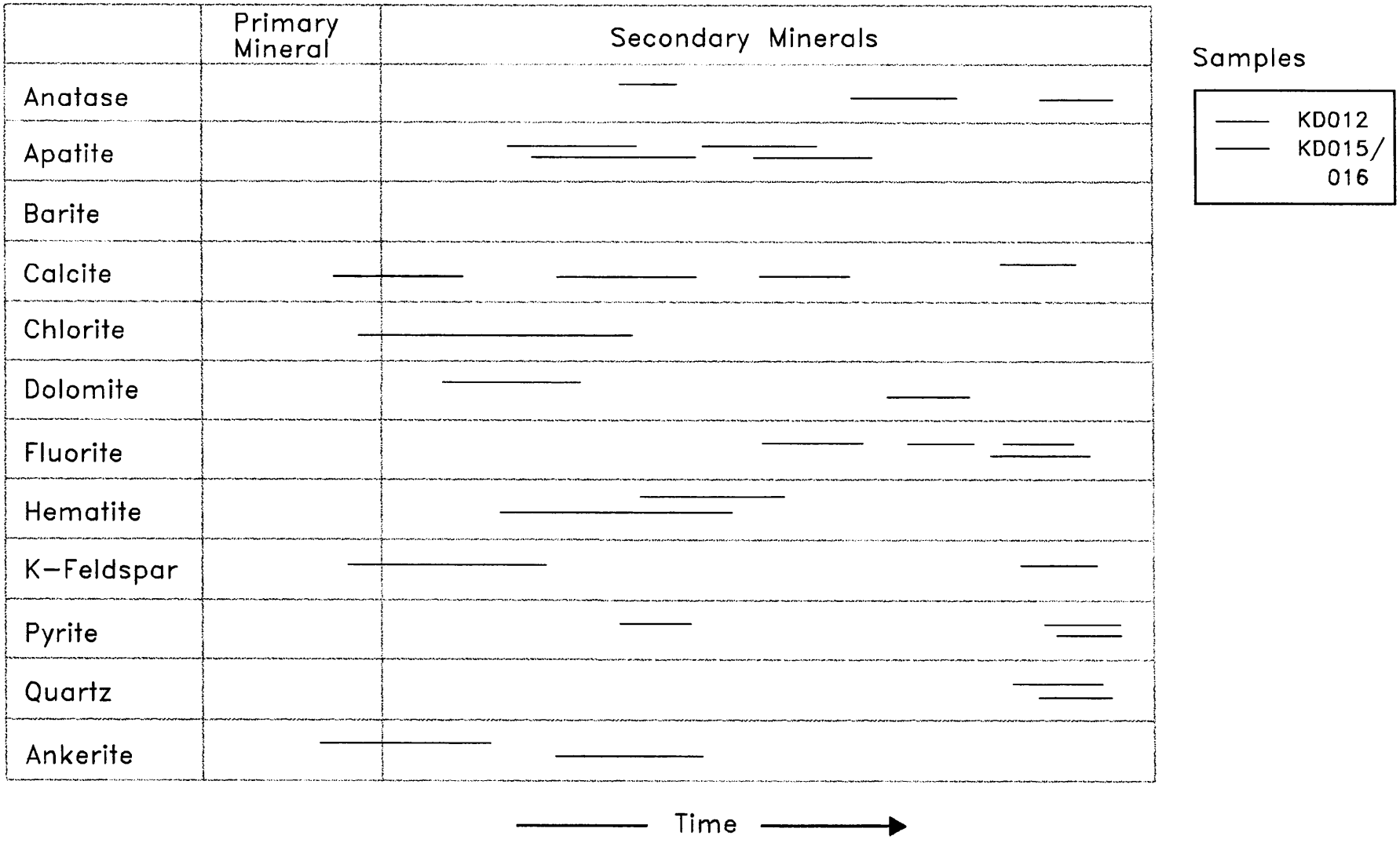

Figure 10.4 Paragenesis of samples KD012, KD015 and KD016.

Digitised by the Department of Library Services in support of open access to information, University of Pretoria, 2021

and anatase. The individual grains are cemented by zoned calcite. Scattered, very fine-grained apatite forms overgrowths on earlier carbonates.

The rounded ash grains are composed of phenocrysts and amygdales (Figs. 10.5 and 10.6). The phenocrysts are pseudomorphosed by calcite. In cross-section they are stubby to quite elongate, square-ended laths (Figs. 10.7 and 10.8). Some resemble skeletal forms and are distributed either singly or in small clusters. Examples are present in which calcite replaces the rims of crystals with pointed terminations, whereas the cores are non-luminescent. Amygdales are subcircular in cross-section and are infilled with either zoned calcite, completely filling the voids, or non-luminescent feldspar. The microphenocrysts can be described as elongate to lath-shaped (Table 10.2 and Fig. 10.9) (Hayward and Schürmann, in prep.). Under cathodoluminescence the calcite is markedly deeper orange than the calcite replacing the phenocrysts or cementing the grains. Rosettes of microphenocrysts (Figs. 10.9 and 10.10) are composed of the same slightly deeper orange calcite. The mesostasis consists mostly of non-luminescent chlorite, but blue-violet luminescent apatite is also present. In some grains the mesostasis is composed of intergrown blue-green-luminescent apatite and non-luminescent chlorite. Small blue-violet luminescent apatite grains overgrow the blue-green luminescent apatite.

Early calcite cement is bright orange and also relatively dully luminescent (Figs. 10.11 and 10.12). Later cement (infilling voids between grains) displays dull luminescence. Fine-scale zonation is seen in parts of the cementing calcite (Hayward and Schürmann, in prep.). Parts of the brightly luminescent cement had been brecciated and was subsequently cemented by a later growth of blue-green apatite. Blue-green-luminescent apatite and K-feldspar form an appreciable proportion of some ash grains. These minerals are intergrown with non-luminescent carbonates, which in turn are overgrown by blue-violet apatite.

Late calcite veins (Fig. 10.13), containing minor fluorite cuts all textures, but is overgrown by the blue-green-luminescing apatite.

Veining by calcite has occurred following lithification of the ash tuff deposit. At least two generations of apatite growth can be distinguished (Fig. 10.4). The earliest is blue-green-luminescent, very fine-grained and replaces parts of the matrix, and of the mesostasis of the grains. This is overgrown by later blue to

Digitised by the Department of Library Services in support of open access to information, University of Pretoria, 2021

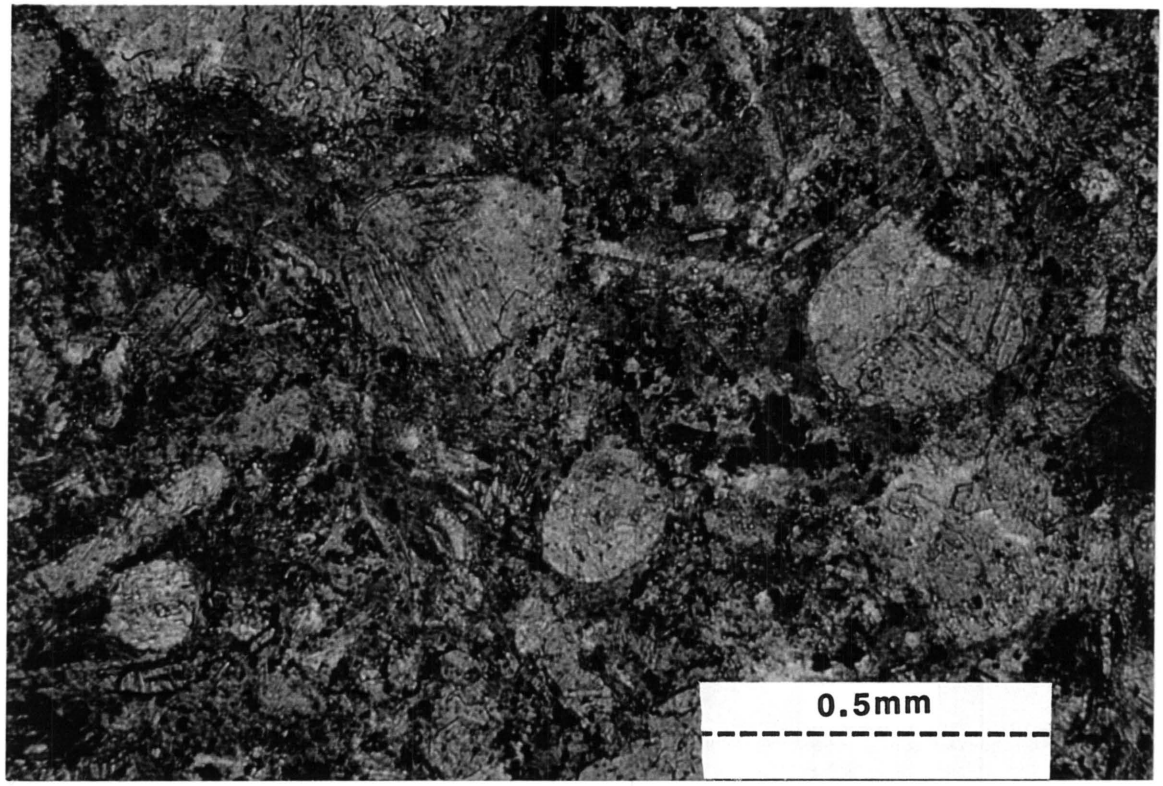

Figure 10.5 The interior of an ash grain with small phenocrysts and amygdales now represented by polycrystalline calcite. The ash grains themselves are embedded in a matrix of volcanic dust, now replaced by calcite, chlorite and K-feldspar (top lefthand corner). The mesostasis of the ash grain is composed of chlorite with subordinate anatase and pyrite (Crossed polarisers, x50; width of view: 2 mm across; sample KD016, KPPL4-17).

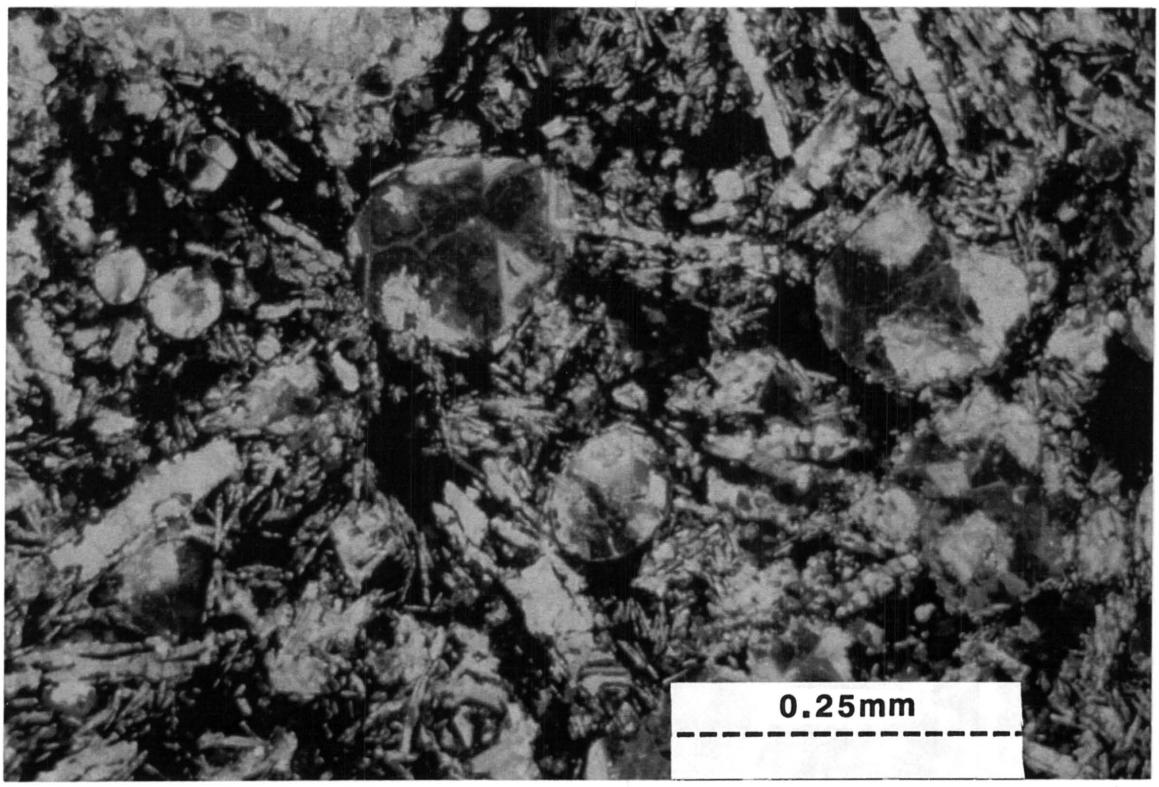

Figure 10.6 Cathodoluminescence image of the field of view shown in Figure 10.5. Note the two-stage infilling of the amygdales. The early, bright luminescent equant grains were followed by dull luminescing calcite which completed the infilling. Phenocrysts, together with smaller phenocrysts are set in a non-luminescent mesostasis consisting of chlorite, anatase and pyrite (Cathodoluminescence; x50; width of view: 2 mm across; film: 1600 ASA Fuji Provia; exposure time: 1 minute 14 seconds; sample KD016, KCL4-19).

Digitised by the Department of Library Services in support of open access to information, University of Pretoria, 2021

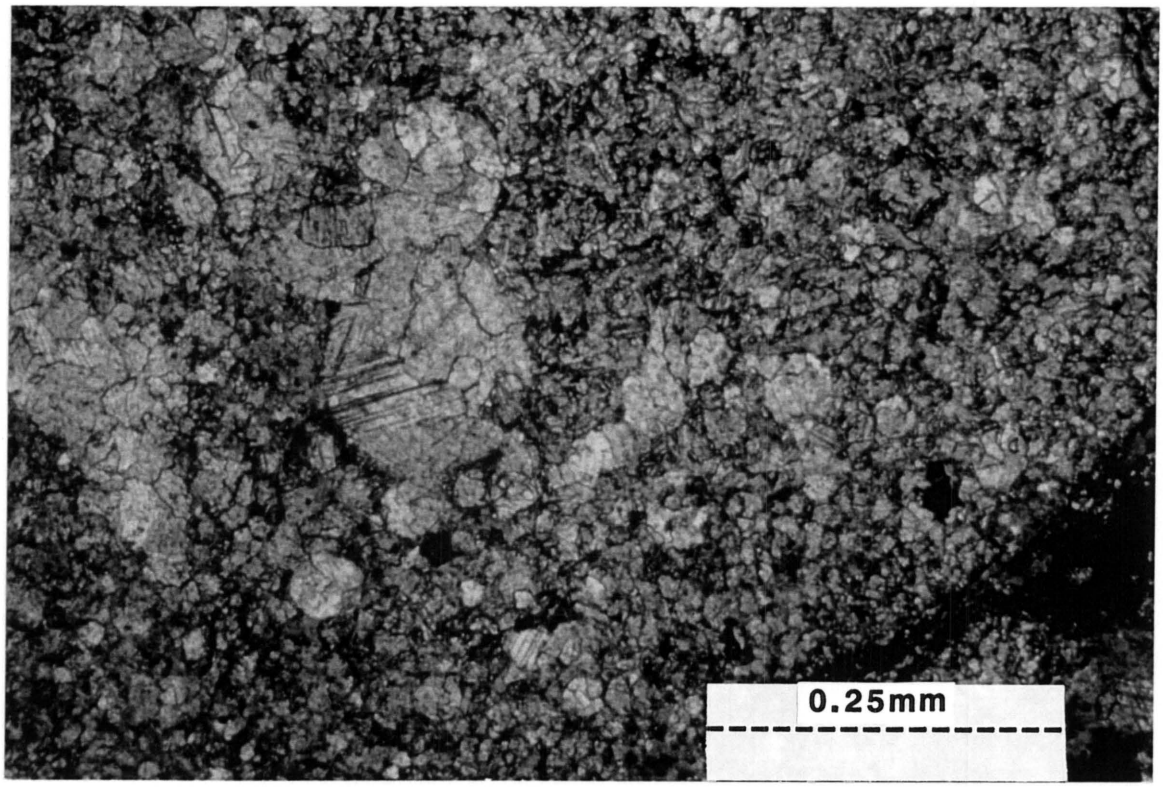

Figure 10.7 A ash grain containing phenocrysts, amygdales and microphenocrysts, replaced by calcite, in a chlorite-rich mesostasis. The boundary of the ash grain with the matrix is sharp (lower right corner) (Crossed polarisers: x100; width of view: 1 mm across; sample KD016, KCL4-15).

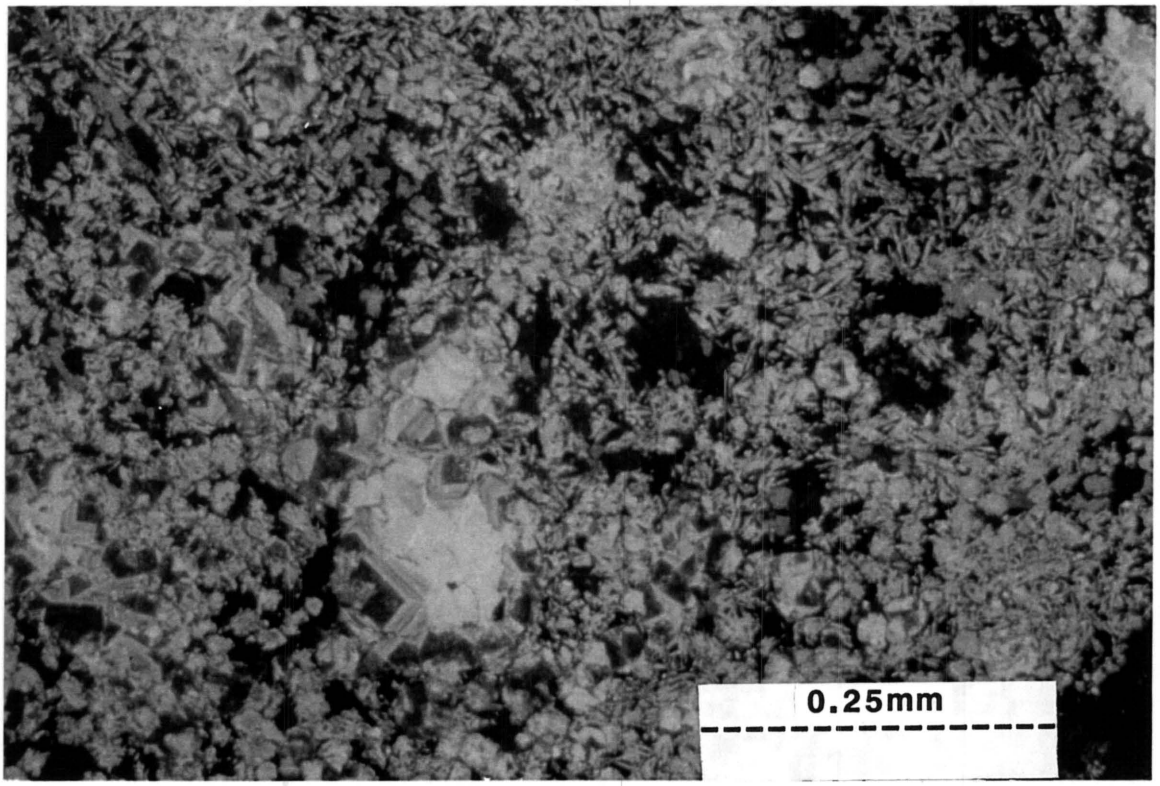

Figure 10.8 Cathodoluminescence image of an ash grain containing microphenocrysts and amygdales largely pseudomorphosed by calcite, in a non-luminescent chlorite mesostasis. The upper righthand part of the image contains acicular phenocrysts arranged in rosettes, while the bottom part displays clusters ("clots") of small acicular microphenocrysts. Note the deeper orange luminescence of the calcite in the microphenocrysts compared to that in the amygdales and cement (top right hand corner) and the zoned nature of the calcite in places (Cathodoluminescence; x100; width of view: 1 mm across; film: 400 ASA Fuji Provia; exposure time: 7 minutes; sample KD016, KCL4-14).

Digitised by the Department of Library Services in support of open access to information, University of Pretoria, 2021

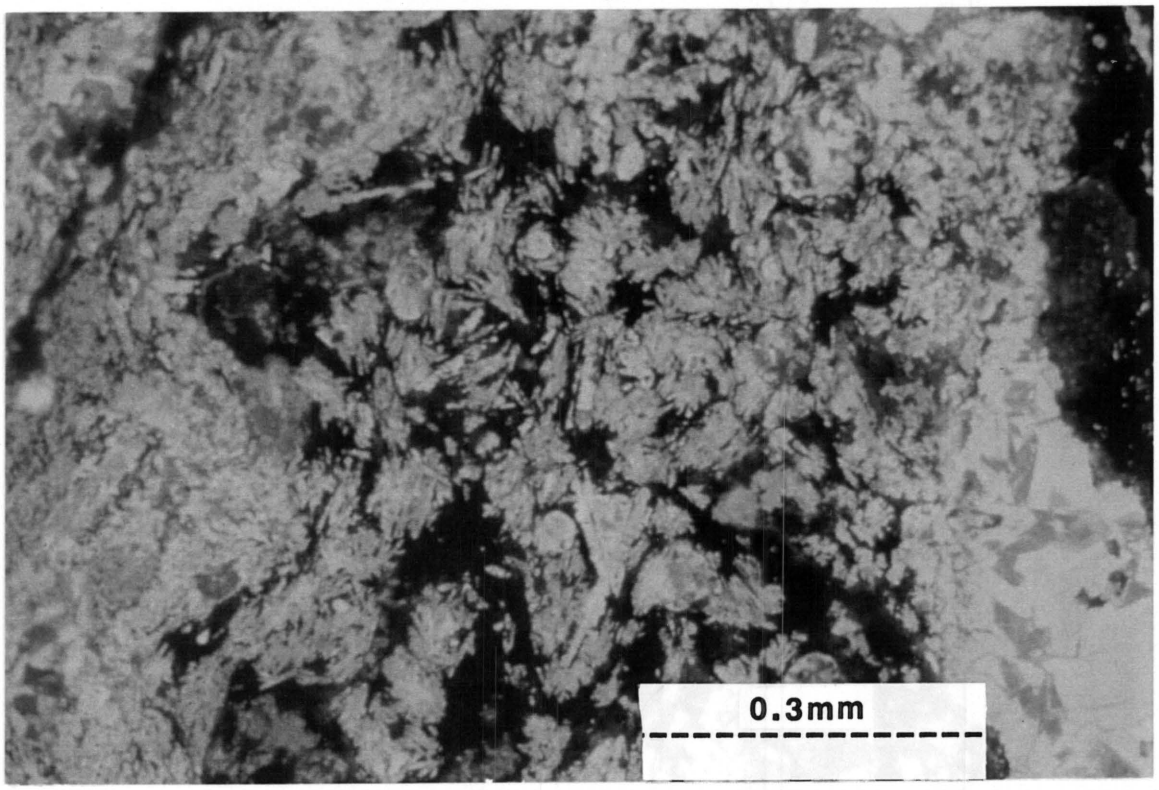

Figure 10.9 Cathodoluminescence image of "clots" of microphenocrysts within an ash grain. Note the zoned calcite cement (left- and righthand sides of the image), and the random orientation of microphenocrysts within "clots". At the bottom edge, towards the right, is an example of an elongate amygdale (Cathodoluminescence; x80; width of view: 1.2 mm across; film: 400 ASA Fuji Provia; exposure time: 1 minutes 20 seconds; sample KD016, KCL4-28).

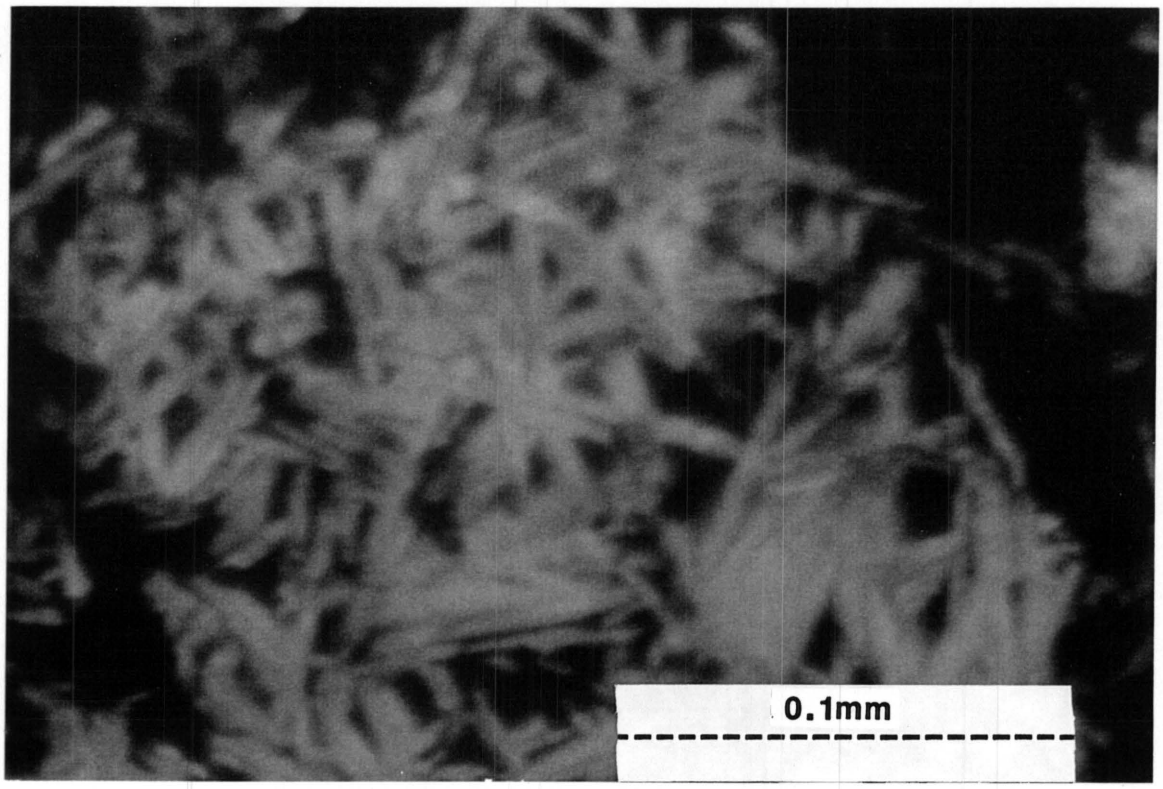

Figure 10.10 High magnification cathodoluminescence image of the microphenocrysts within one "clot", surrounded by chlorite (Cathodoluminescence; x400; width of view: 0.25mm across; film: 1600 ASA Fuji Provia; exposure time: 12 minutes; sample KD016, KCL4-15).

Digitised by the Department of Library Services in support of open access to information, University of Pretoria, 2021

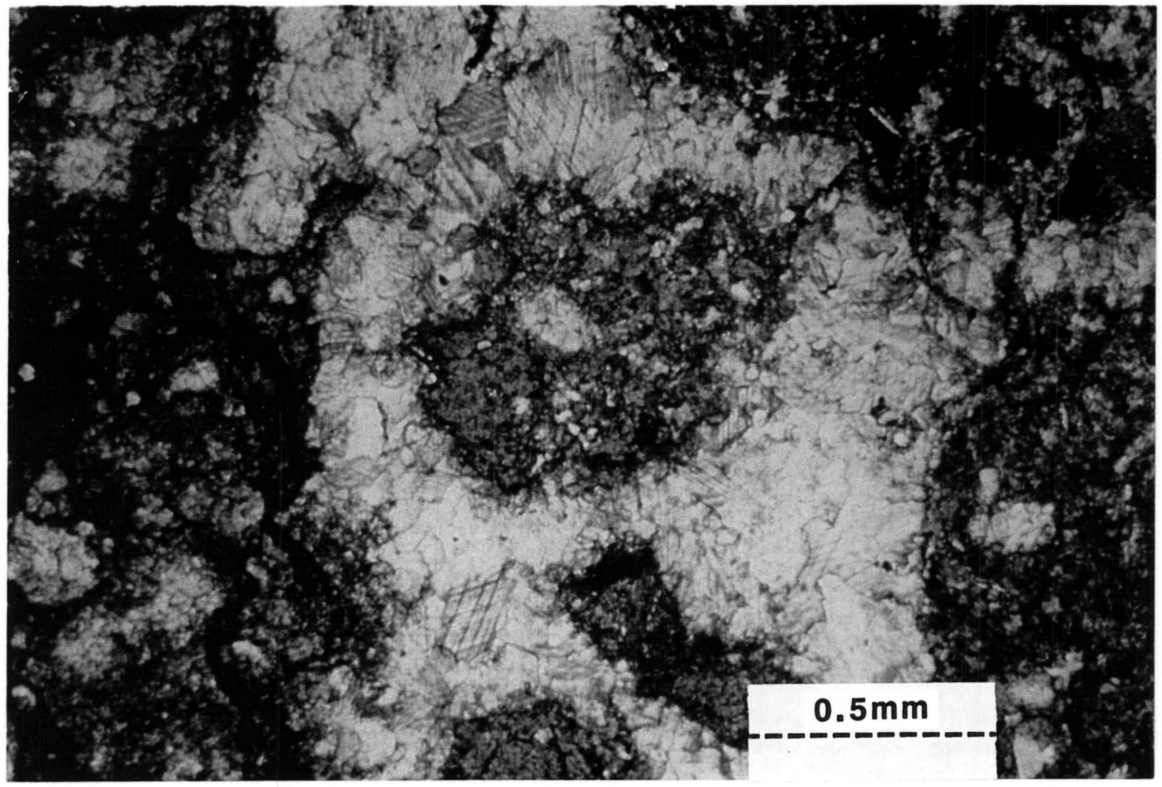

Figure 10.11 Secondary calcite cement surrounding and replacing the matrix. The dark areas (in the centre, and left- and right and corners of the image) are ash grains which consist of calcite, chlorite, apatite, anatase and pyrite (Plane polarised light: x40; width of view: 2.5 mm across; sample KD016, KPPL4-33).

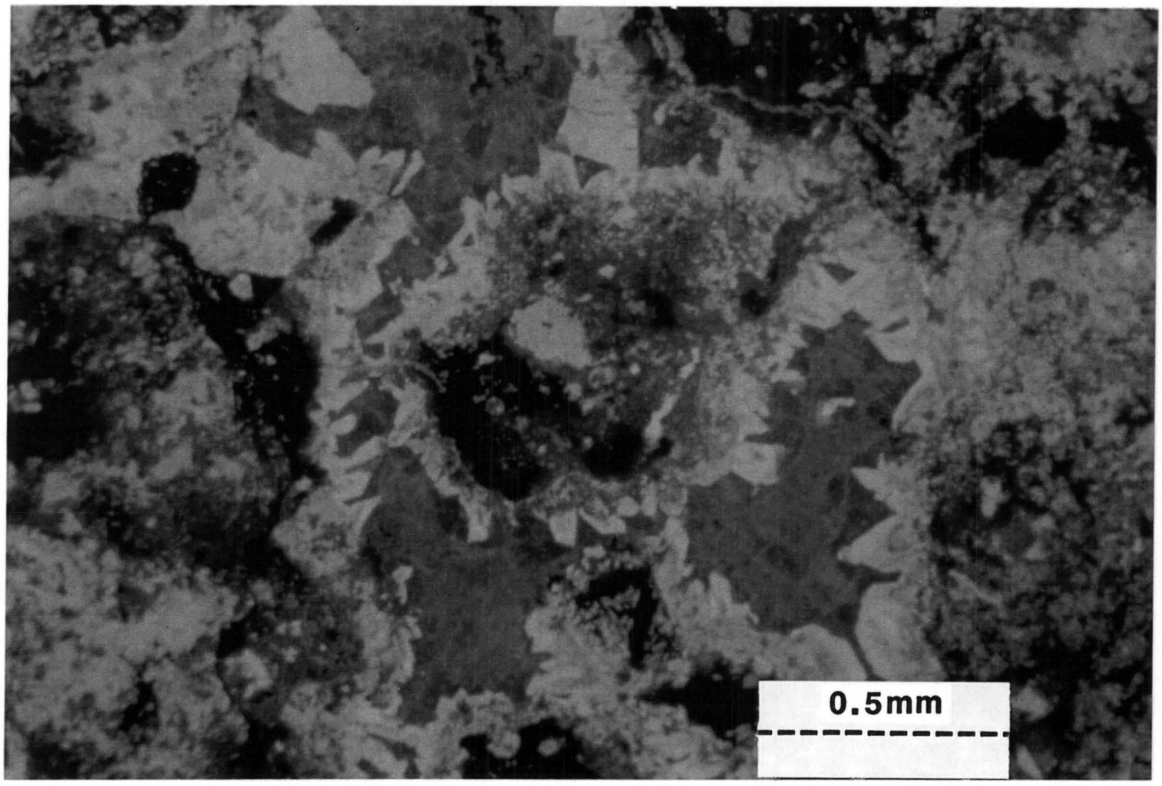

Figure 10.12 Same field as Figure 10.11. The cathodoluminescence image shows inpregnated ash grains partly replaced by bright orange luminescent calcite, forming a crust. Later, dull luminescing calcite followed this, filling in all remaining void space (Cathodoluminescence; x40; width of view: 2.5 mm across; film: 400 ASA Fuji Provia; exposure time: 32 seconds; sample KD016, KCL4-32).

Digitised by the Department of Library Services in support of open access to information, University of Pretoria, 2021

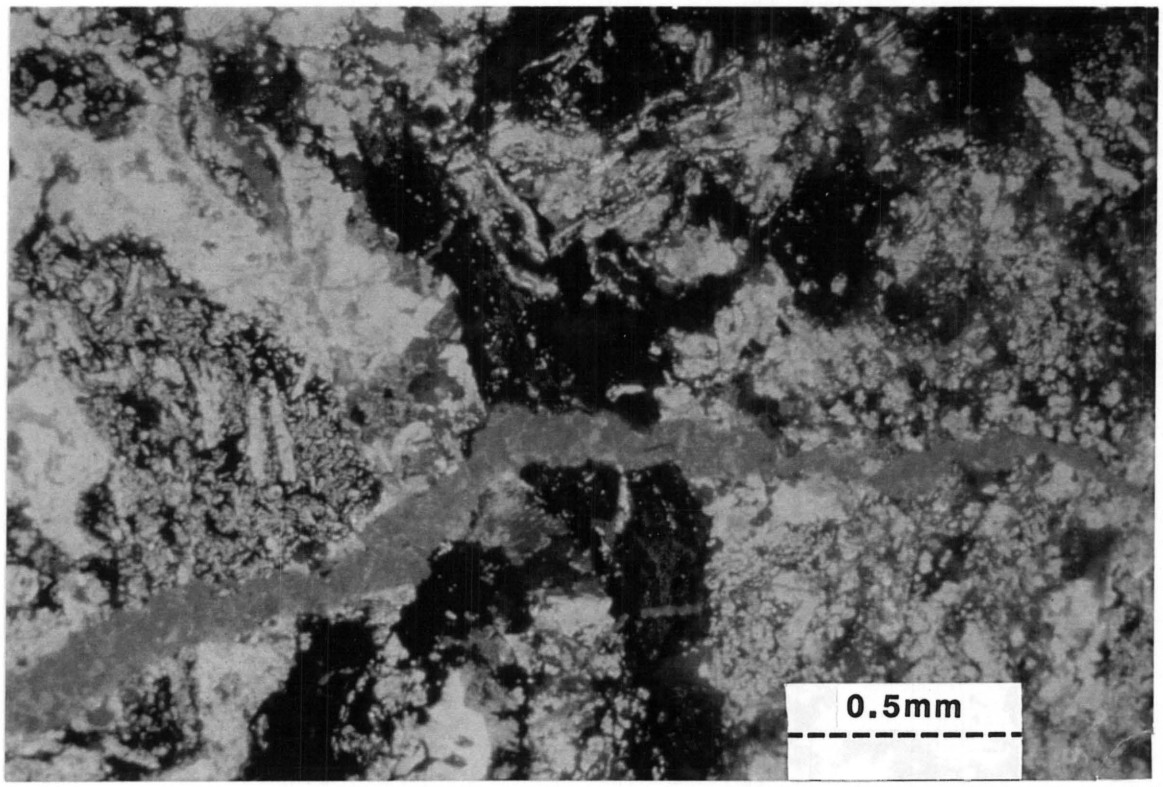

Figure 10.13 An early, dark coloured vein consisting of anatase, chlorite, sulphides (non-luminescing) and fluorite (luminescing dark blue) cut by a younger vein of calcite (dark orange luminescence). The first generation calcite in the matrix luminesces yellow-orange (Cathodoluminescence; x40; width of view: 2.5 mm across; film: 400 ASA Fuji Provia; exposure time: 50 seconds; sample KD016, KCL21-10).

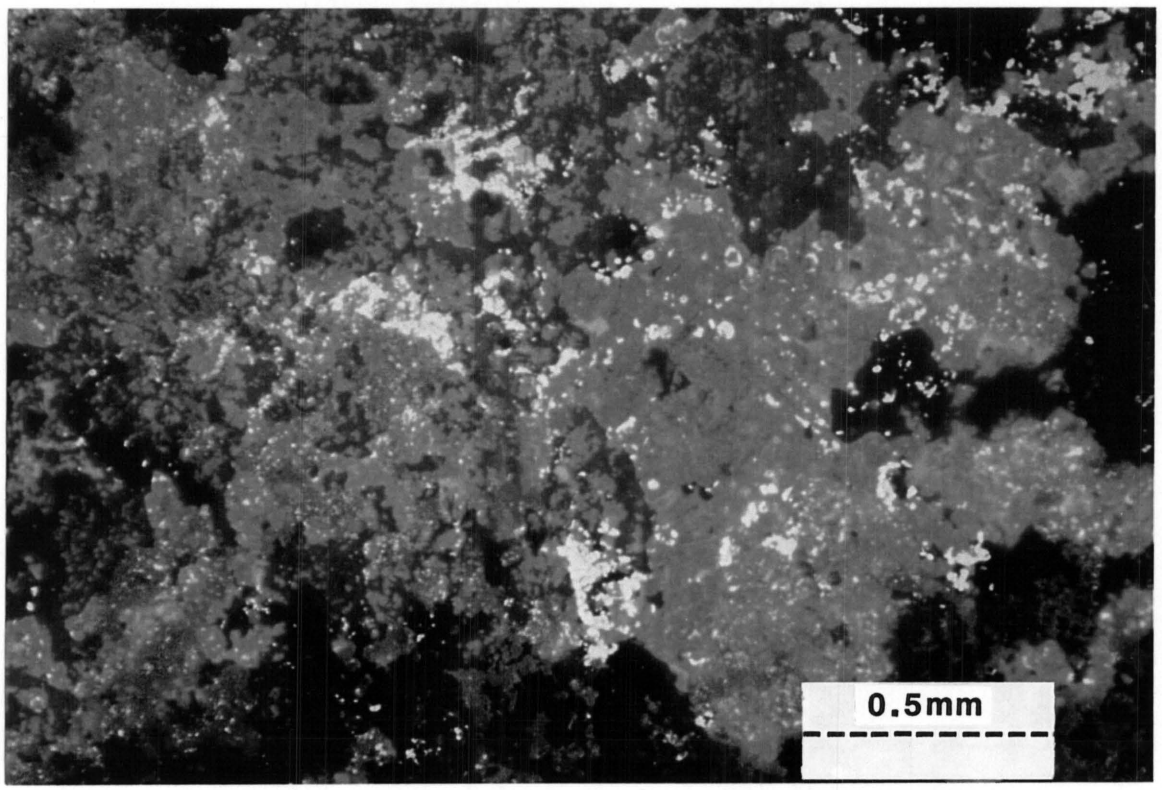

Figure 10.14 Non-luminescing carbonates and feldspar (grey luminescent) being replaced by extremely fine-grained light to deep blue-luminescing fluorite. Note the fine-grained, pale blue to grey-luminescing apatite (Cathodo-luminescence; x40; width of view: 2.5 mm across; film: 400 ASA Fuji Provia; exposure time: 55 seconds; sample KD019, KCL18-24).

Digitised by the Department of Library Services in support of open access to information, University of Pretoria, 2021

violet-luminescent apatite, which also occurs within the mesostasis of the grains. Pyrite euhedra overgrow other textures, while anatase is also present.

Interpretation

The textures and morphology of the ash grains indicate that they had been erupted from a vent as calcium carbonate liquid droplets which cooled whilst still airborne. The needle-like form of the microphenocrysts indicates rapid growth from a quenched melt as do the lack of plastic deformation and agglutination, the elongation of grains, the alignment of their phenocrysts and microphenocrysts, as well as the presence of occasional broken ash grains. Rosettes of tiny needle-like microphenocrysts are interpreted as the result of undercooling. It is therefore not necessary to invoke a thermal boundary between the rosettes and euhedral grains and can thus be ascribed to a delay in nucleation well below the liquidus (for the rosettes) compared with the near-liquidus crystallisation of the euhedral grains (Hayward and Schürmann, in prep.).

10.2.2 Lapilli tuff unit

Three samples, taken at depths of -45.00, -55.00 and -63.30 and marked KD019, KD111 and KD113 respectively, are representative of tuff layers within the lapilli tuff unit. General descriptions of the different samples are summarised in Table 10.3.

The pyroclastic breccia layer consists of a sequence of brown tuff, lapilli tuff and interlayered pyroclastic breccia. Sample KD019 was taken from a fine-grained brown ash tuff layer, whereas sample KD111, which is layered perpendicular to the axis of the borehole, represents a grain-supported tuff and fine ash tuff layers. Sample KD113 was taken from a fine-grained ash tuff interlayered with lapilli tuff layers; it is fine-grained and dark purple in colour. The angle between the core axis and the layering suggests a dip of the layering towards the southwest.

10.2.2.1 Sample KD019

The sample is prominently laminated and consists of ash with a diverse range of grains, e.g. carbonatite lava, feldspar xenocrysts (some veined with magnetite), xenocrysts and other grains of which the original characteristics cannot be determined. Certain of the boundaries between layers represent primary depositional features, whereas others represent the margins of alteration zones. Most layers are themselves finely laminated on a millimetre or even a micrometre scale. Boundaries between adjacent layers may be sharp or

Digitised by the Department of Library Services in support of open access to information, University of Pretoria, 2021

gradational. The sample is mainly composed of dolomite/ ankerite and K-feldspar, but in parts it consists of fine-grained, pale blue- and pink luminescing apatite, and deep-blue to light-blue luminescing fluorite (Fig. 10.14). The sample can be divided roughly into three sections, i.e. an upper, a middle and a lower.

Table 10.3 General descriptions of tuff samples from the lapilli tuff unit.

SAMPLE	MINERALS IN ORDER OF ABUNDANCE (XRD)	COMPONENTS	PARTICLE DIAMETER	FABRIC	ROCK TYPE
KD019	dolomite/ ankerite, K-feldspar, chlorite, fluorite, anatase, apatite	Upper section: (a) ash dolomite/ ankerite grains, (b) inclusion-free rounded K-feldspar, (c) rounded grains composed of feldspar, pyrite and apatite Middle section: (a) K-feldspar grains (b) phenocrysts, (c) amygdales, (d) microphenocrysts, (e) xenocrysts Lower section: (a) ankerite grains	200 to 300 µm 50 to 200 µm 500 to 1000 µm 0.04 to 0.30 mm 0.07 to 0.25 mm 70-80 to 15-20 µm in length 0.8 to 1.8 mm	laminated (1 to 10 mm thick)	ash tuff
KD111	dolomite/ankerite, fluorite, chlorite, anatase, K-feldspar, apatite, quartz	(a) rounded grains	150 to 500 µm	laminated	coarse to fine ash tuff
KD113	dolomite/ ankerite, fluorite, siderite, chlorite, K-feldspar, anatase, quartz	none		massive	fine ash tuff

The **upper section** is dominated by K-feldspar and dolomite/ankerite, with some chlorite overgrowing the K-feldspar. The K-feldspar luminesces mottled dull-brown-grey. Secondary fluorite occurs as patches up to 100 µm across and overgrows dolomite/ankerite and K-feldspar, and it also occurs as void-fillings. Apatite also overgrows dolomite/ankerite and feldspar, and is present as scattered, extremely small grains with intense pink luminescence. The fine ash matrix contains (a) ash dolomite/ankerite grains; (b) inclusion-free rounded K-feldspars with homogeneous brownish to red luminescence; and (c) round grains composed of non-luminescent feldspar, pyrite and apatite (Table 10.3).

Digitised by the Department of Library Services in support of open access to information, University of Pretoria, 2021

Euhedral grains of olive-green luminescent K-feldspar are overgrown by grey-green K-feldspar, which forms small sub- to euhedral grains and also aggregates of small grains in the matrix (Fig. 10.15). Tiny pink-luminescing apatite grains form rims within the grey-green-luminescent K-feldspar growths, but they also occur scattered throughout olive-green K-feldspar. Small brick-red-luminescent areas of K-feldspar are present in many olive-green K-feldspar grains. The transition between these feldspars with differing luminescence is gradual.

The matrix of the **middle section** consists of dolomite/ankerite and dully-luminescing feldspar, but contains a greater abundance of fine-grained apatite, and is darker due to a greater abundance of chlorite and hematite. Except for this, it is similar to the upper section, illustrated in Figure 10.15. The K-feldspar has two prominent luminescent colours: (a) a very dull grey and (b) a relatively brighter, slightly greenish-brown. It contains angular to subrounded inclusions, composed of dusty dolomite/ ankerite and variable amounts of chlorite, either within their interiors or as a discontinuous rim of grains.

Another type of relic grain is very distinctive, and is composed of intensely pink to white-luminescent apatite which forms the matrix of lath-shaped crystals, as well as roundish blebs composed of fine-grained K-feldspar and ankerite. Minor chlorite occurs with the apatite. The apatite and ankerite may rim subangular particles composed of dolomite/ankerite. Hematite and pyrite are scattered within some of these particles, but are absent in others. Dolomite/ ankerite-filled roundish blebs are reminiscent of amygdales or of carbonatite lava ash grains (i.e. samples KD015 and KD016), while the pseudomorphosed phenocrysts resemble calcite phenocrysts from these grains.

Rarer are grains composed of K-feldspar and rimmed by chlorite which is rich in pyrite inclusions. The luminescence of this feldspar is slightly greener than that of the matrix. Also present, within a narrow layer of a few mm, are several grains of K-feldspar of 200 to 300 µm in diameter. These feldspar grains generally show radial extinction under crossed nicols and contain lath-like inclusions of magnetite, as well as peripherally arranged inclusions of hematite, pyrite and apatite. The feldspar has a mottled brownish grey and green luminescence, and in places even a spotty brick-red luminescence. The apatite shows a pinkish luminescence.

Digitised by the Department of Library Services in support of open access to information, University of Pretoria, 2021

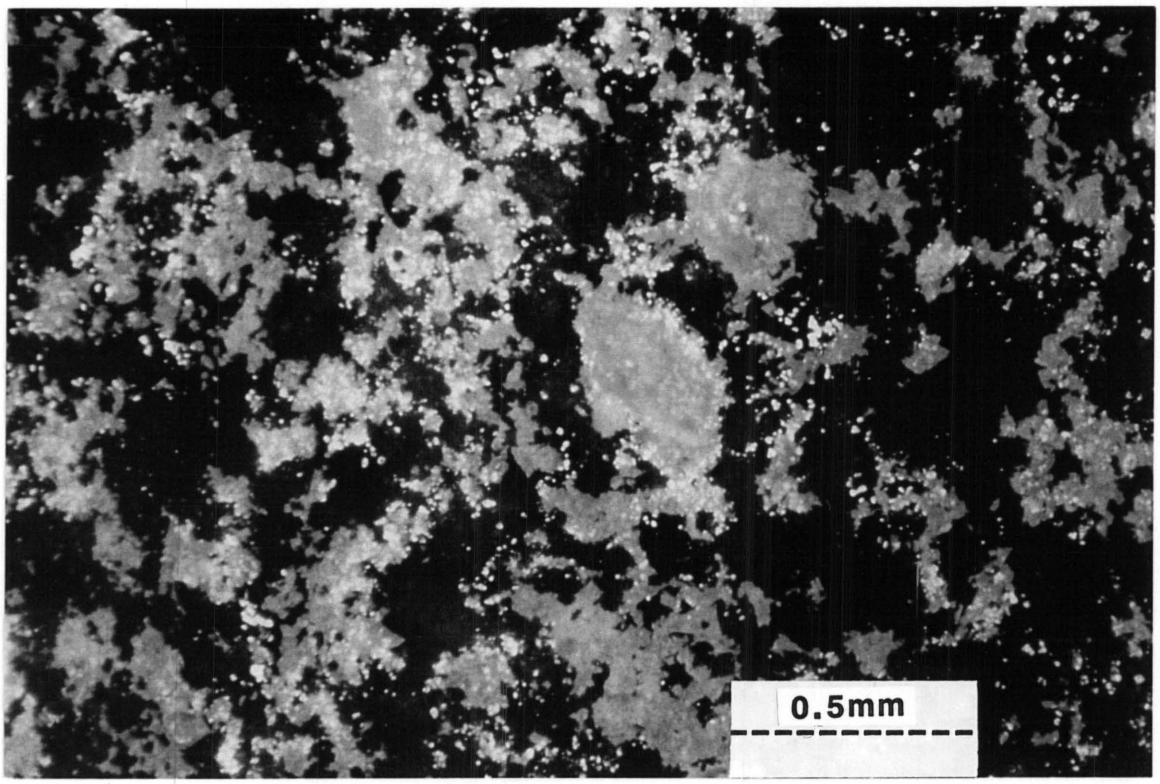

Figure 10.15 A typical cathodoluminescense image of the top section of sample KD019. Bright greenish-yellow to brown and dull-grey-luminescent feldspar grains (some apparently zoned) and light-blue-luminescent apatite associated with a dark, non-luminescent intergrowth of chlorite, opaque and carbonate minerals (Cathodo-luminescence; x40; width of view: 2.5 mm across; film: 400 ASA Fuji Provia; exposure time: 37 seconds; sample KD019, KCL18-20).

Digitised by the Department of Library Services in support of open access to information, University of Pretoria, 2021

The **lower section** resembles the upper section, but it contains less ankerite which occurs as larger grains (Table 10.3). Some of these grains contain minor hematite concentrations within their interiors or along the rims, whereas others are free of opaques. Chlorite, interstitial with respect to dolomite/ankerite grains, is fairly common and becomes increasingly abundant towards the boundary with the middle section.

The euhedral K-feldspar (olive-green to brick-red luminescence) is generally colourless and clear in plane polarised light. The grains often have thin rims and/or irregular patches within their interiors which luminesce pinkish. The grey-green feldspar is fine-grained, colourless and dusty in plane polarised light. Occasionally dolomite/ankerite crystals have sharp points (due to the rhombohedral habit). However, most of the chlorite and ankerite grains are irregular in shape and have corroded rims, with concentrations of opaque mineral grains in their interiors.

Veining by ankerite was followed by fluorite growth (Fig. 10.16). Small pink apatite grains overgrow feldspar, and to a lesser extent also fluorite. Earlier formed fluorite has a bright-blue luminescence and where it has been fragmented the resulting spaces have been filled by fluorite with deeper blue-luminescence. In time fluorite is overgrown by pale-pink-luminescent apatite. Euhedral pyrite and hematite veinlets overprint all other textures, suggesting that they are the youngest in the paragenesis.

Interpretation

The sample represents units of ash tuff, in which the grains are of varied origin, probably representing a mixture of cognate and accidental material. Following the formation of ankerite and olive-green luminescing K-feldspar which replace the primary phenocrysts, mesostasis and xenocrysts, limited chloritisation of the feldspar occurred. Grey-green luminescing feldspar forms an overgrowth on the olive-green luminescing feldspar (Fig. 10.16). This was followed by fluorite growth as scattered grains which occur on olive-green feldspar and dolomite/ ankerite. Fluorite also filled a small number of voids, while apatite grains formed on grey-green feldspar and fluorite.

Digitised by the Department of Library Services in support of open access to information, University of Pretoria, 2021

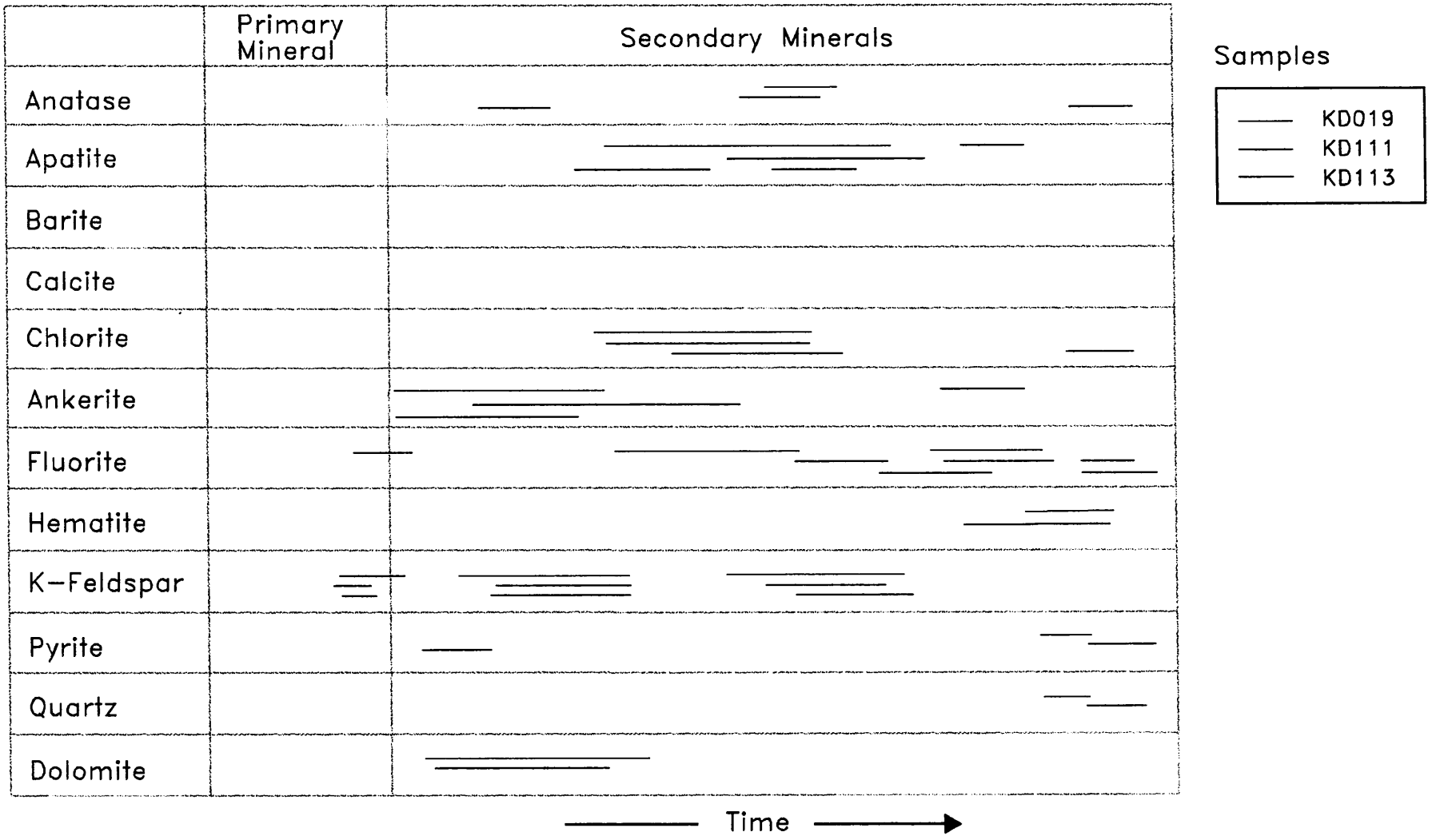

Figure 10.16 Paragenesis of samples KD019, KD111 and KD113.

Digitised by the Department of Library Services in support of open access to information, University of Pretoria, 2021

10.2.2.2 Sample KD111

This coarse to fine ash tuff is composed of non-luminescent dolomite/ankerite, K-feldspar (green-grey and red-brown luminescence), chlorite, anatase and hematite. Fluorite forms an overgrowth on the carbonate, and on less abundant pink-luminescent and very fine-grained apatite.

The grains are rounded, with a circular to slightly ovoid cross-section, and form approximately 70% of this rock unit (Table 10.3). Only the outline of the grains is preserved and provides evidence of some degree of compaction after deposition. Within the layer the grain:matrix ratio is approximately 7 : 3. The rims of the ash grains are preserved by a thin layer of K-feldspar, whereas their interiors are composed of dolomite/ankerite, chlorite, K-feldspar and very small hematite grains (Figs. 10.17 and 10.18). Some of the grains contain appreciable amounts of later, void-filling fluorite, which is zoned (earlier zones have a deep blue and later ones a paler blue luminescence). Fine-grained feldspar forms narrow rims around the grains. The matrix of the grains is composed mostly of dolomite/ankerite and chlorite. Grains of K-feldspar with colourless to brick-red luminescence may contain irregular veins of olive-green-luminescent feldspar, and they are also rimmed by grey-green-luminescent feldspar. In places this in turn is overgrown by fluorite and by pink-luminescent apatite, which also overgrows olive-green luminescing feldspar within the brick-red luminescing feldspar grains. Fluorite also occurs intermixed with the feldspar in the rims and within the cores and commonly has growth zoning. It may occupy a significant proportion of the core, or only small, scattered areas (Fig. 10.19). Very fine-grained pink luminescent apatite is a rare component of the cores.

Some ash grains consist of primary red-brown-luminescing feldspar surrounded by an overgrowth of secondary duller grey-green luminescence K-feldspar (Fig. 10.20).

There is a sharp contact between the grain-supported tuff and the fine ash tuff. The fine ash tuff is dominated by dolomite/ankerite and chlorite, intergrown with extremely fine-grained fluorite, and later apatite (Fig. 10.21). Immediately adjacent to the grain-supported tuff layer there is a thin layer (approximately 2 mm thick) in which dolomite/ankerite is pseudomorphous after some pre-existing crystal. These euhedral, equant pseudomorphs contain patches of chlorite and are densely packed, with little interstitial material. The contact between the grain-

Digitised by the Department of Library Services in support of open access to information, University of Pretoria, 2021

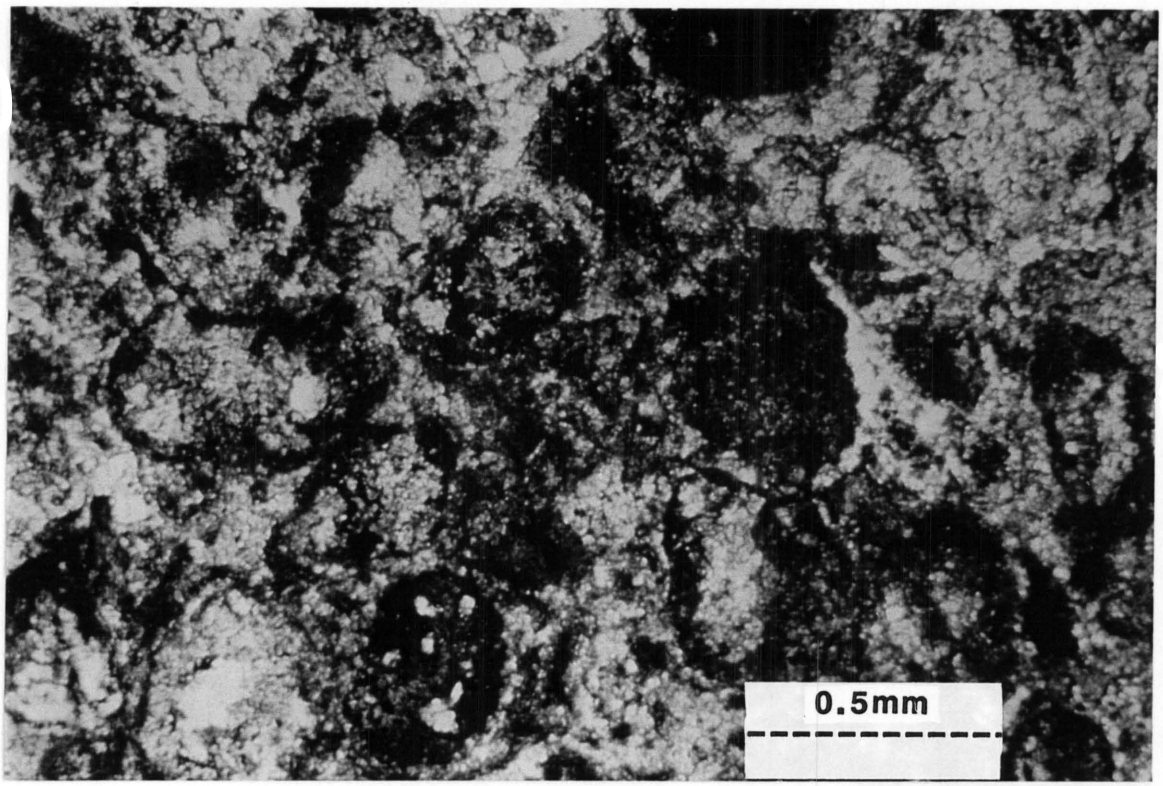

Figure 10.17 Rounded ash grains consisting of K-feldspar, chlorite and opaque minerals (centre of the image), the interior of which has been replaced by ankerite, fluorite and apatite. These minerals have also replaced the original matrix of volcanic dust (Plane polarised light; x40; width of view: 2.5 mm across; sample KD111, KPPL17-33).

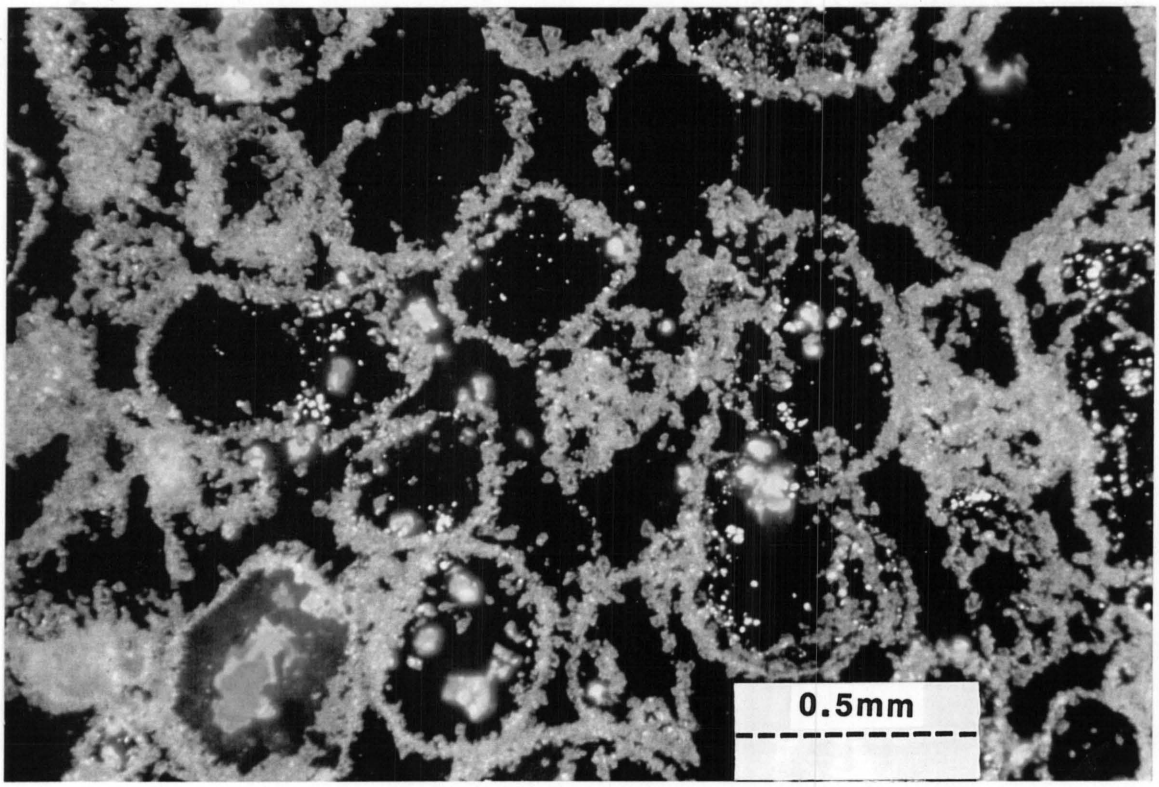

Figure 10.18 Rounded ash grains with rims of feldspar, (greyish green to yellow luminescence), and interiors of ankerite, chlorite, apatite and small opaque minerals (fluorite dark blue, apatite light pink; ankerite and chlorite non-luminescent) (Cathodoluminescence; x40; width of view: 2.5 mm across; film: 400 ASA Fuji Provia; exposure time: 34 seconds; sample KD111, KCL17-34).

Digitised by the Department of Library Services in support of open access to information, University of Pretoria, 2021

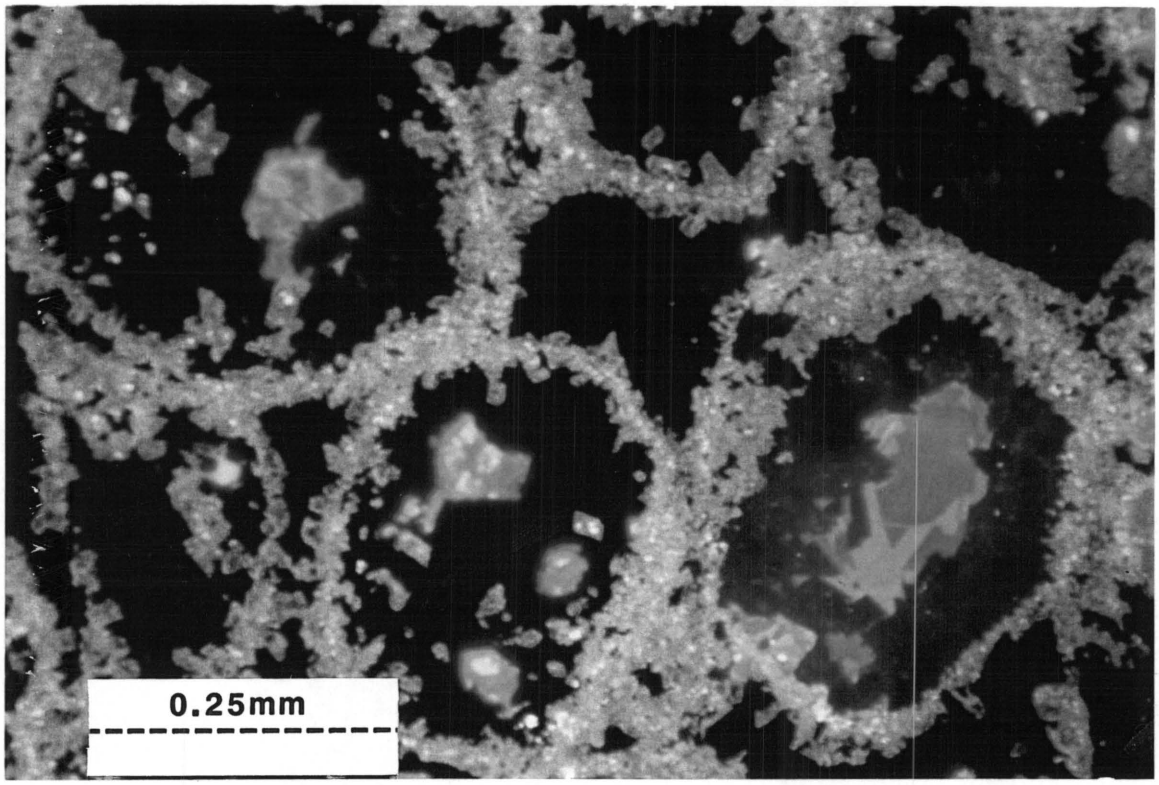

Figure 10.19 Portion of the field shown in Figure 10.18. Feldspar in the rim of the ash grains vary from dull grey-green to brighter yellow-green and even red-brown, while fine-grained apatite displays grey to pink luminescence. Fluorite (light to dark blue) intergrown with the feldspar and also within the cores commonly has growth zoning and may occupy a significant proportion of the core, or be small, scattered areas (Cathodoluminescence; x100; width of view: 1mm across; film: 1600 ASA Fuji Provia; exposure time: 4 minutes 34 seconds; sample KD111, KCL17-2).

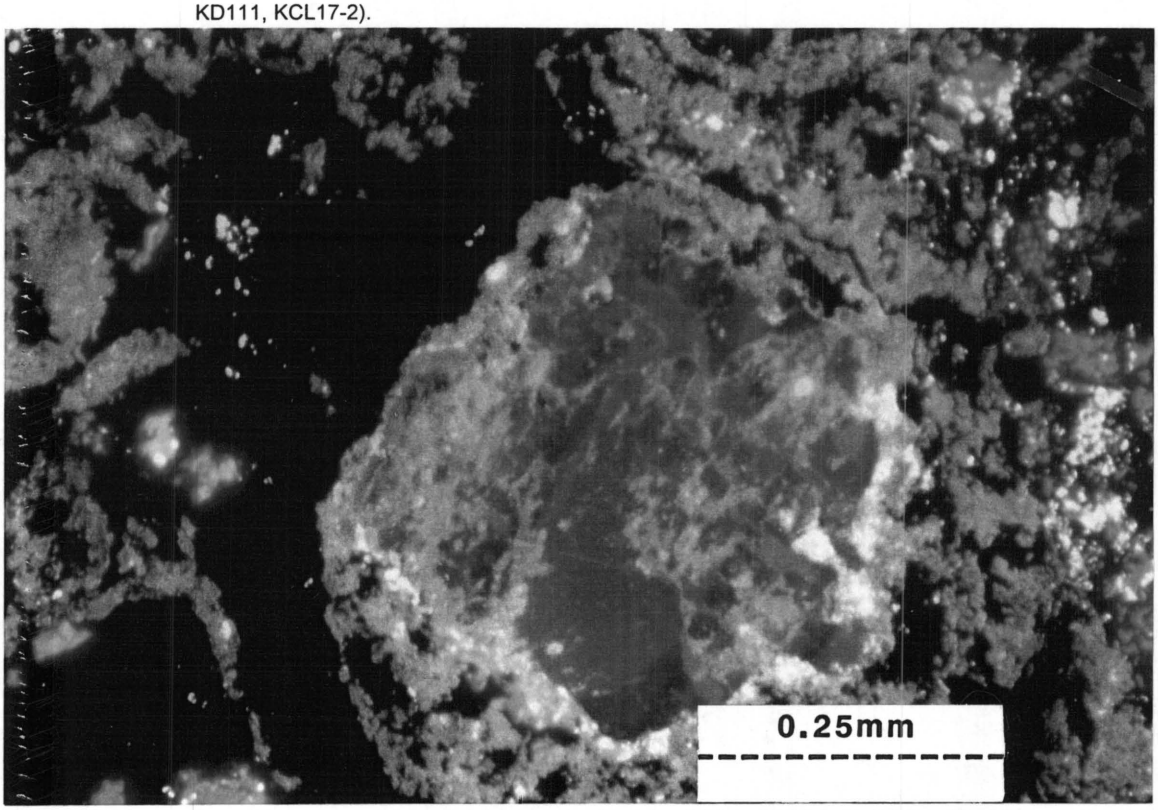

Figure 10.20 An ash grain consisting of red-brown-luminescing feldspar, which contains yellowish-green zones and is rimmed by the duller grey-green luminescent feldspar, set in a matrix of finer-grained feldspar (grey-green luminescence), chlorite and ankerite (non-luminescent), apatite (grey-white to pink luminescence) and fluorite (blue luminescence) (Cathodoluminescence; x100; width of view: 1mm across; film: 1600 ASA Fuji Provia; exposure time: 4 minutes 37 seconds; sample KD111, KCL17-7).

Digitised by the Department of Library Services in support of open access to information, University of Pretoria, 2021

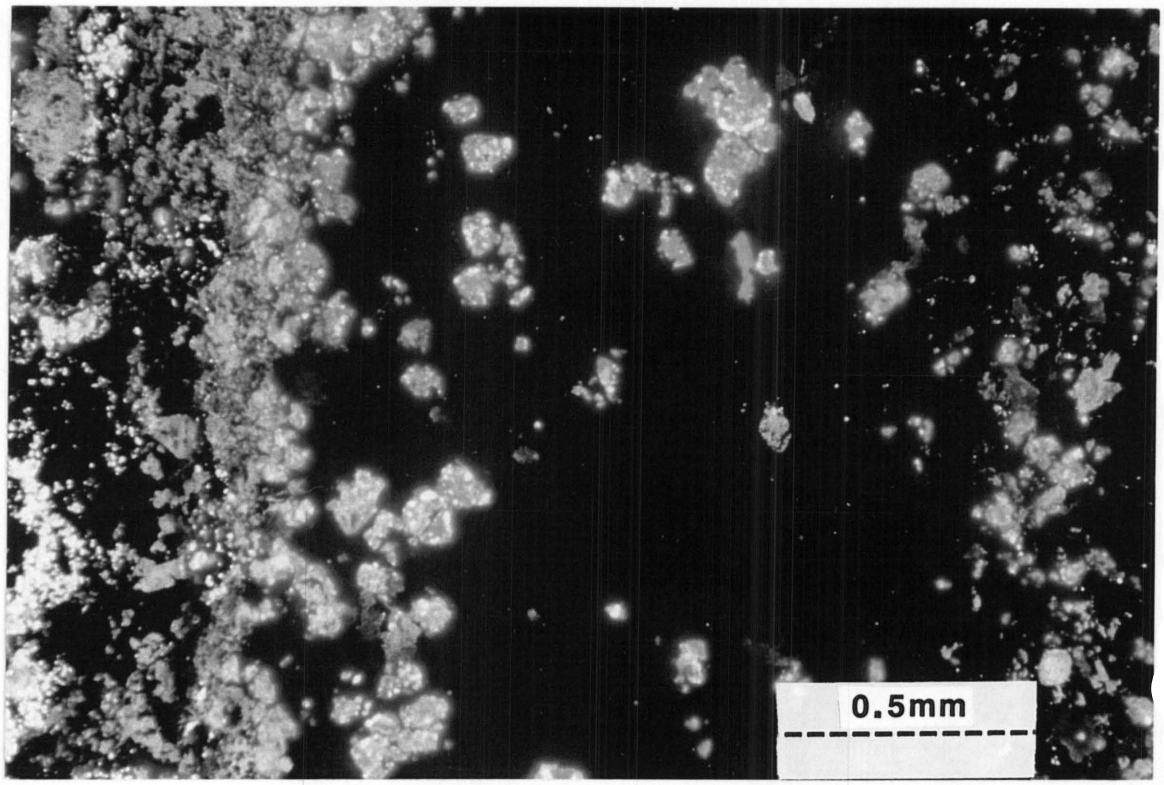

Figure 10.21 Intimately associated non-luminescent chlorite and ankerite in an ash grain-rich layer (vertical orientation). K-feldspar is present as sparsely scattered, greenish to yellow luminescent grains (dark centre and righthand side of image), while the layer on the lefthand side of the image displays an increase in feldspar. Fluorite is present as zoned euhedra, either at the margin of the feldspar-rich layer (left hand side of the image) or scattered throughout the section (Cathodoluminescence; x40; width of view: 2.5 mm across; film: 400 ASA Fuji Provia; exposure time: 37 seconds; sample KD111, KCL17-9).

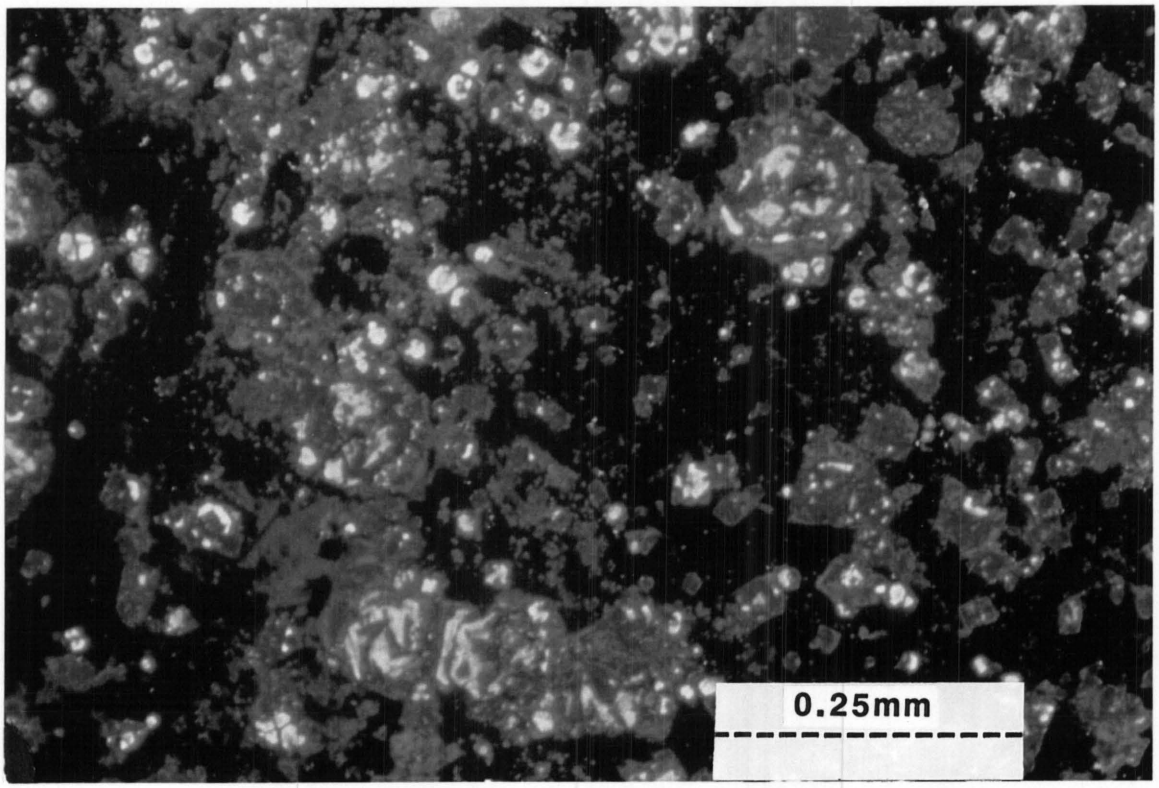

Figure 10.22 A fluorite-rich layer with subhedral to euhedral, zoned fluorite (varying shades of blue luminescence) in a matrix of non-luminescent chlorite and ankerite (Cathodoluminescence; x100; width of view: 1 mm across; film: 1600 ASA Fuji Provia; exposure time: 4 minutes 40 seconds; sample KD111, KCL2-25).

Digitised by the Department of Library Services in support of open access to information, University of Pretoria, 2021

supported tuff and the fine ash tuff is characterised by concentrations of fluorite euhedra, which cut across the depositional layering. Similar euhedra (100 to 200 µm in diameter) also occur within the fine tuff layer, but K-feldspar and apatite are almost absent. The fluorite luminesces medium blue to pale blue in internal concentric and complex zones whereas the rim is even paler blue (Fig. 10.22). Small apatite grains occur in the earlier ankerite, but none is seen to overgrow the fluorite. The fluorite therefore represents a later period of fluorite mineralisation than that in the grain-supported tuff.

10.2.2.3 Sample KD113

In sample KD113 the original mineralogical composition comprised fine-grained intergrown dolomite/ankerite and K-feldspar. The latter is overgrown by minor amounts of chlorite. The feldspar has a mottled appearance with brick-red and olive-green luminescence, and even grey-green luminescence. Fine-grained fluorite mostly replaces only the feldspar, but in places also the ankerite. Corroded, blue-luminescent, concentrically zoned prismatic apatite euhedra are overgrown by thin, concentric rims of bright pink-luminescing apatite. Small grains of similarly luminescing apatite are scattered very sparsely throughout the rest of the section, but do not occur on the fluorite. Chlorite occurs in veins with or without anatase.

The sample was subsequently replaced to an extensive degree by fluorite (Figs. 10.23 and 10.24), with few areas of the earlier mineralogy surviving. Pyrite euhedra are scattered throughout the section.

10.2.3 Ferruginous lapilli tuff unit

Four samples were taken at depths of -71.30, -80.00, -99.40 and -114.90, and marked KD115, KD117, KD121 and KD124 respectively. General descriptions of the different samples are summarised in Table 10.4. These samples were taken of variably mineralised dark brown to red-brown tuff, displaying an ill-defined, welded fabric.

10.2.3.1 Sample KD115

The sample is composed of intergrown K-feldspar (slightly chloritised) and siderite. The chlorite is microgranular and intergrown with anatase and galena grains. The feldspar is being replaced by subhedral to euhedral fluorite, which is associated with the chlorite, pyrite and galena. Pale orange-luminescent, zoned areas of calcite have invaded the sample at a later stage (Fig. 10.25).

Digitised by the Department of Library Services in support of open access to information, University of Pretoria, 2021

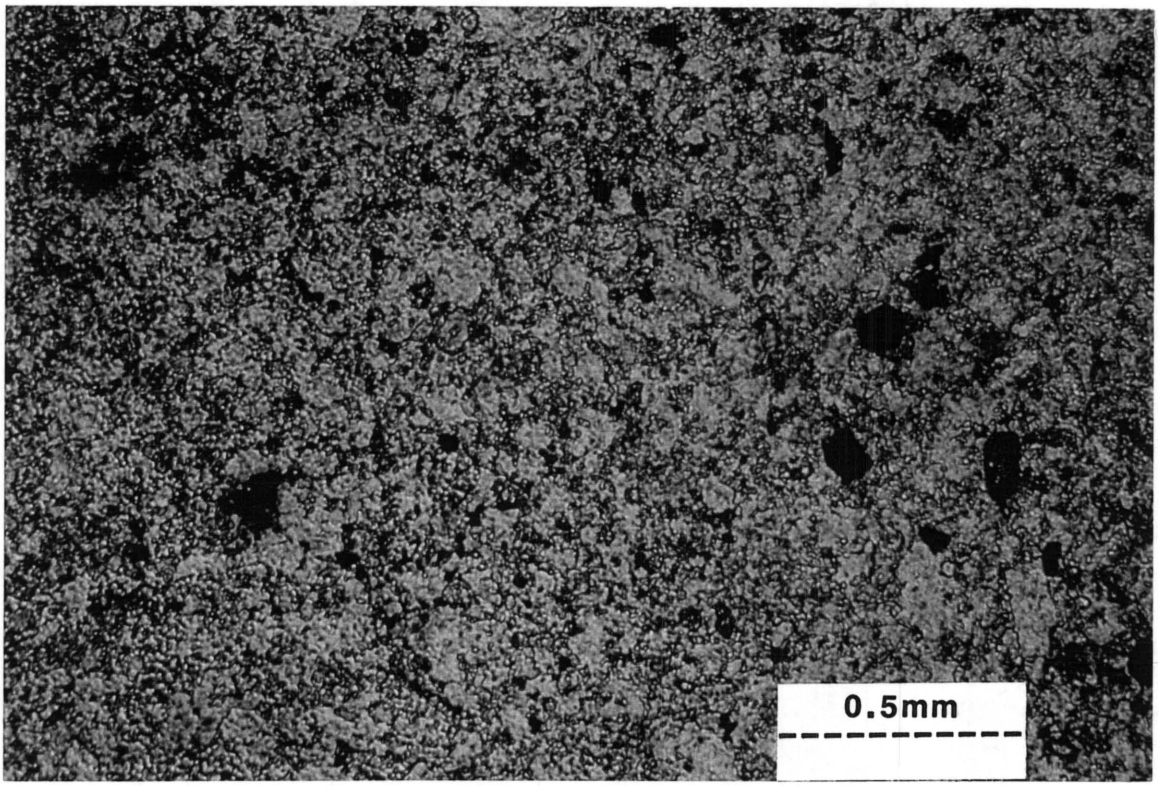

Figure 10.23 The sample consists mainly of fluorite, with minor amounts of carbonate and fine-grained anatase and pyrite (Plane polarised light, x40; width of view: 2.5 mm across; sample KD113, KPPL5-5).

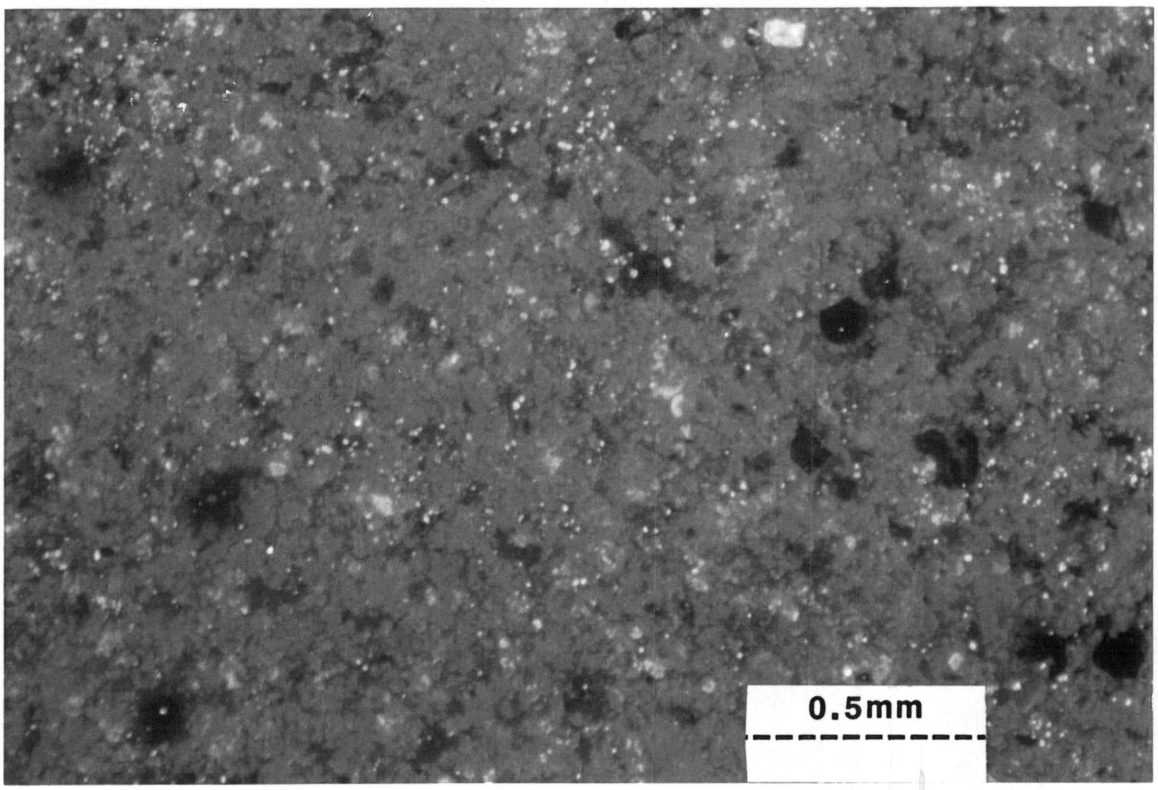

Figure 10.24 Cathodoluminescence image of Figure 10.23. An extensive degree of fluorite (medium blue luminescence) replacement has occurred. Scattered areas (sky-blue areas of zonation) are prominent, while areas of dull to no luminescence represent K-feldspar, ankerite, anatase and pyrite (Cathodoluminescence; x40; width of view: 2.5 mm across; film: 400 ASA Fuji Provia; exposure time: 57 seconds; sample KD113, KCL5-6).

Digitised by the Department of Library Services in support of open access to information, University of Pretoria, 2021

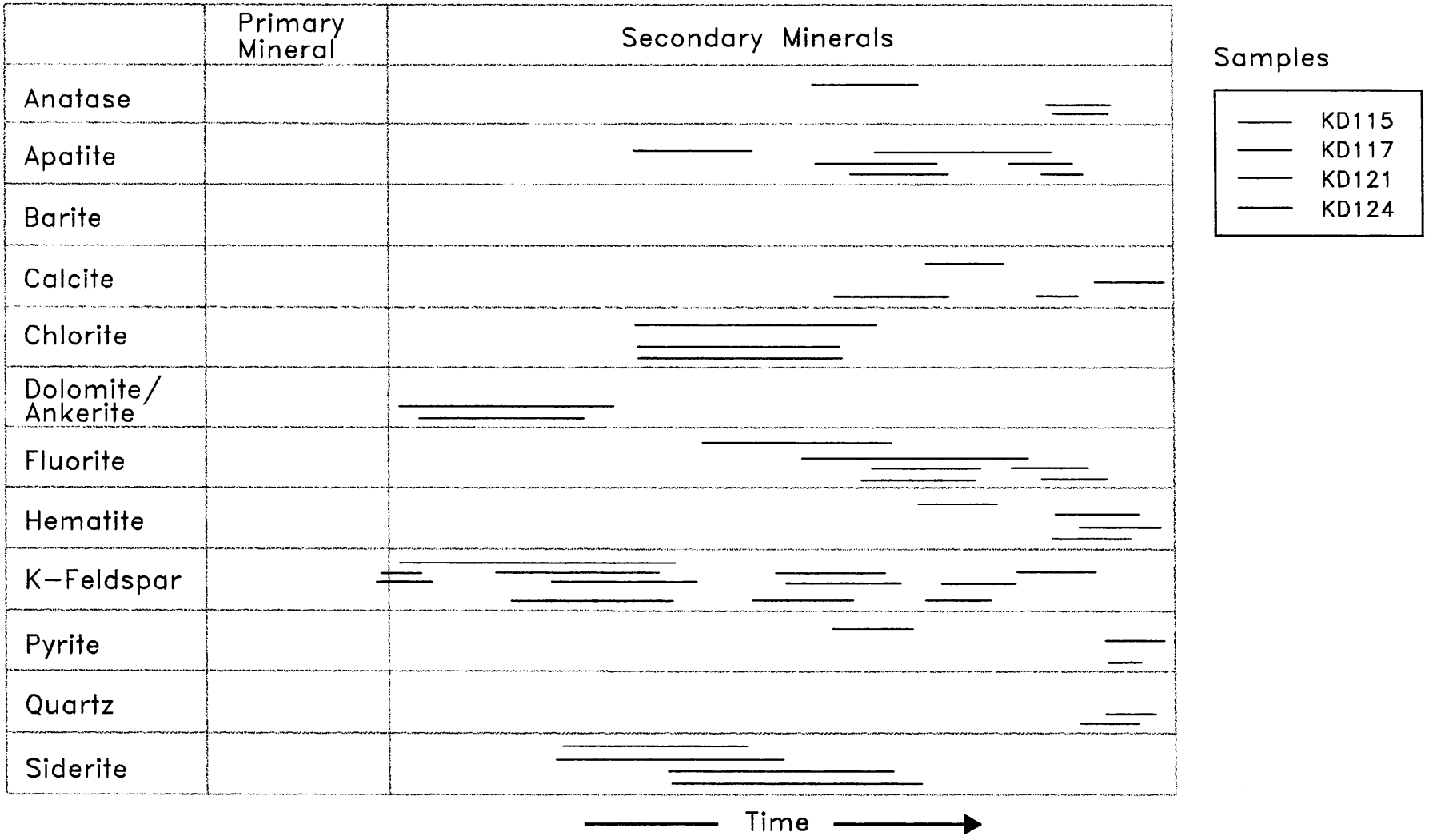

Figure 10.25 Paragenesis of samples KD115, KD117, KD121 and KD124 of the ferruginous lapilli tuff unit.

Digitised by the Department of Library Services in support of open access to information, University of Pretoria, 2021

10.2.3.2 Sample KD117

Sample KD117 is similar to sample KD115, and is macroscopically homogeneous. It contains euhedral to subhedral K-feldspar (Table 10.4) in a matrix of fine-grained K-feldspar, siderite and hematite. Much of the K-feldspar has a very dull luminescence and occurs as (a) well-formed, almost euhedral but partly corroded grains, (b) subhedral grains and (c) anhedral patches. These feldspar grains are free of inclusions and do not have any overgrowths of grey-green luminescent feldspar, fluorite or apatite.

Table 10.4 General descriptions of samples from the ferruginous lapilli tuff unit.

SAMPLE	MINERALS IN ORDER OF ABUNDANCE (XRD)	COMPONENTS	PARTICLE DIAMETER	FABRIC	ROCK TYPE
KD115	fluorite, siderite, chlorite, anatase, hematite, quartz, K-feldspar	fine ash		welded	brown ash tuff
KD117	hematite, siderite, fluorite, K-feldspar, quartz, barite, anatase	(a) K-feldspar grains (b) pseudo-morphosed pyroxene crystals	<100 to 500 µm 400 to 600 µm	massive	brown ash tuff
KD121	siderite, hematite, fluorite, chlorite, K-feldspar, anatase, quartz, barite	(a) ankerite-rich lapilli (b) pseudomorphosed grains	4 to 5 mm 400 to 500 µm	laminated	brown ash tuff
KD124	fluorite, siderite, hematite, K-feldspar, quartz, anatase, dolomite/ ankerite, chlorite	(a) pale grains	0.2 to 1.5 mm	massive	brown ash tuff

There are several types of K-feldspar: (a) the major portion exhibits olive-green luminescence, although the grains contain spots and irregular blebs with brick-red luminescence (commonly near the margins of the grains); (b) less common is K-feldspar with brick-red luminescence, containing blebs and veins with olive-green-luminescence; (c) the least common exhibits pale blue-luminescence, but the grains contain blebs with a pinkish luminescence and lamellae with olive-green luminescence. The third type is probably perthite. All these grains are rimmed by fine-grained grey-green luminescing K-feldspar, which also replaces some of olive-green luminescent feldspar. Brick-red luminescent areas persist in many grains whose luminescence has changed to grey-green. Crystals replaced by the fine-grained grey-green feldspar commonly appear resorbed in outline. Grey-green feldspar dominates the material between the crystals, which contains numerous tiny brick-red spots and patches.

Digitised by the Department of Library Services in support of open access to information, University of Pretoria, 2021

Late-stage fluorite is mid blue-luminescent and restricted to overgrowths on the non-luminescent K-feldspar. Apatite is both pale blue and a second generation (as an overprint) is pale pink, and occurs only as overgrowth on feldspar (Fig. 10.25). Apatite is common and can be locally abundant, post-dating fluorite formation. Pyrite euhedra are scattered throughout the section.

10.2.3.3 Sample KD121

This sample, like KD115 and KD117, appears dark, homogenous and fine-grained. The sample is laminated, and the lamination is defined by variations in the abundance of fluorite. It is composed of intergrown dolomite/ankerite and K-feldspar, with significant overgrows of siderite, hematite, fluorite and minor pink-luminescing apatite (Fig. 10.26). Fluorite is also present as void filling. Orange-luminescent calcite is present as veins and as isolated patches, and represents the last formed mineral. The large feldspar grains have undulose extinction. Ankerite is pseudomorphous after rectangular prismatic grains. The dull-grey-luminescent feldspar occurs in a similar way as observed in sample KD117, and makes up approximately 10 modal percent. The feldspar and fluorite occur in a matrix of very fine-grained hematite.

In one half of the thin section small lapilli are present as faint ovoid patches 4 to 5 mm across. The long axes of these relic lapilli are perpendicular to the axis of the borehole, parallel to the bedding of the rocks. These lapilli consist predominantly of microcrystalline brown ankerite, but feldspar, quartz, possibly apatite and patches of hematite are also present. Some relict, stubby, lath-shaped, rectangular mineral grains have been pseudomorphosed by carbonate. The margins of these pseudomorphs are diffuse and are marked by concentrations of hematite, making it impossible to describe the shapes in any detail.

Dull-grey-luminescent feldspar have a similar distribution as in sample KD117. In addition, the red and olive-green areas of the feldspar euhedra are commonly arranged in transverse zones (as observed in blue-luminescent grains in KD117), indicating exsolution. Brick-red luminescence is commonly seen as rims immediately inside the later grey-green feldspar growth. Some of the large grains

Digitised by the Department of Library Services in support of open access to information, University of Pretoria, 2021

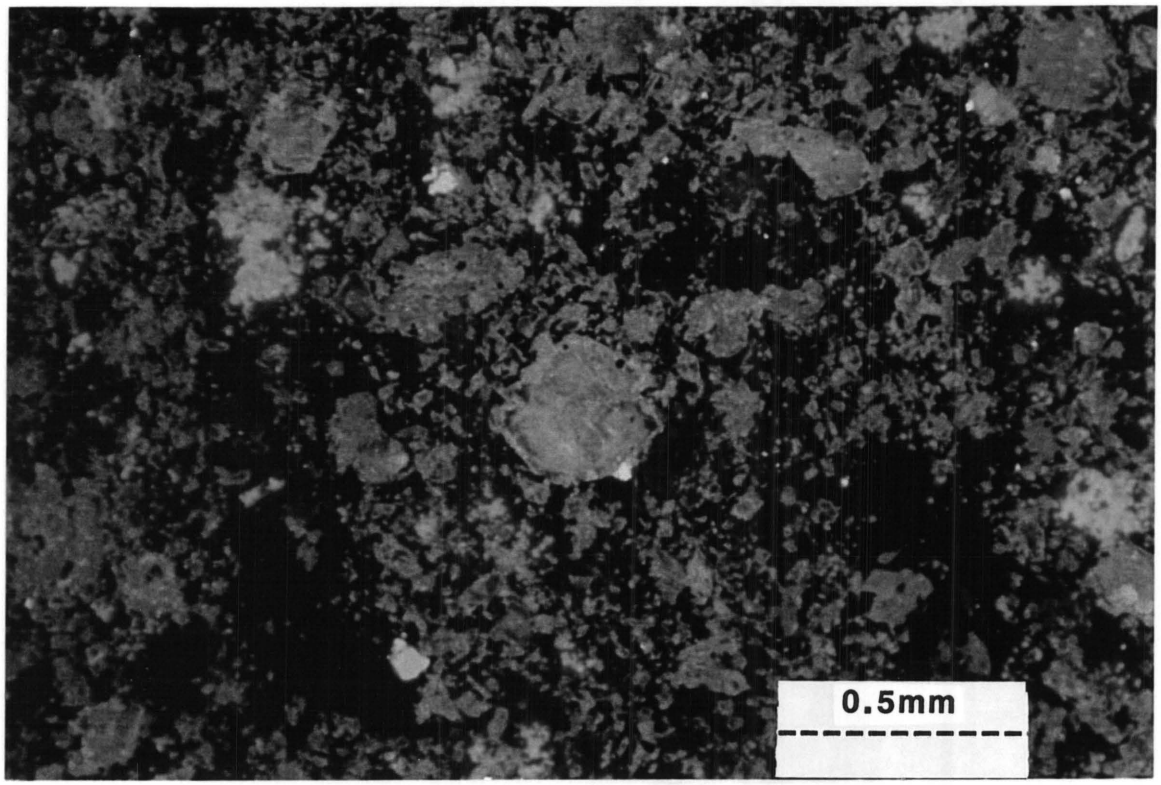

Figure 10.26 Intergrown ankerite (non-luminescent) and K-feldspar (grey-greenish to brown-yellow luminescence), being replaced by irregularly zoned fluorite (blue to pinkish luminescence) and calcite (bright orange luminescence) (Cathodoluminescence; x40; width of view: 2.5 mm across; film: 400 ASA Fuji Provia; exposure time: 38 seconds; sample KD121, KCL19-8).

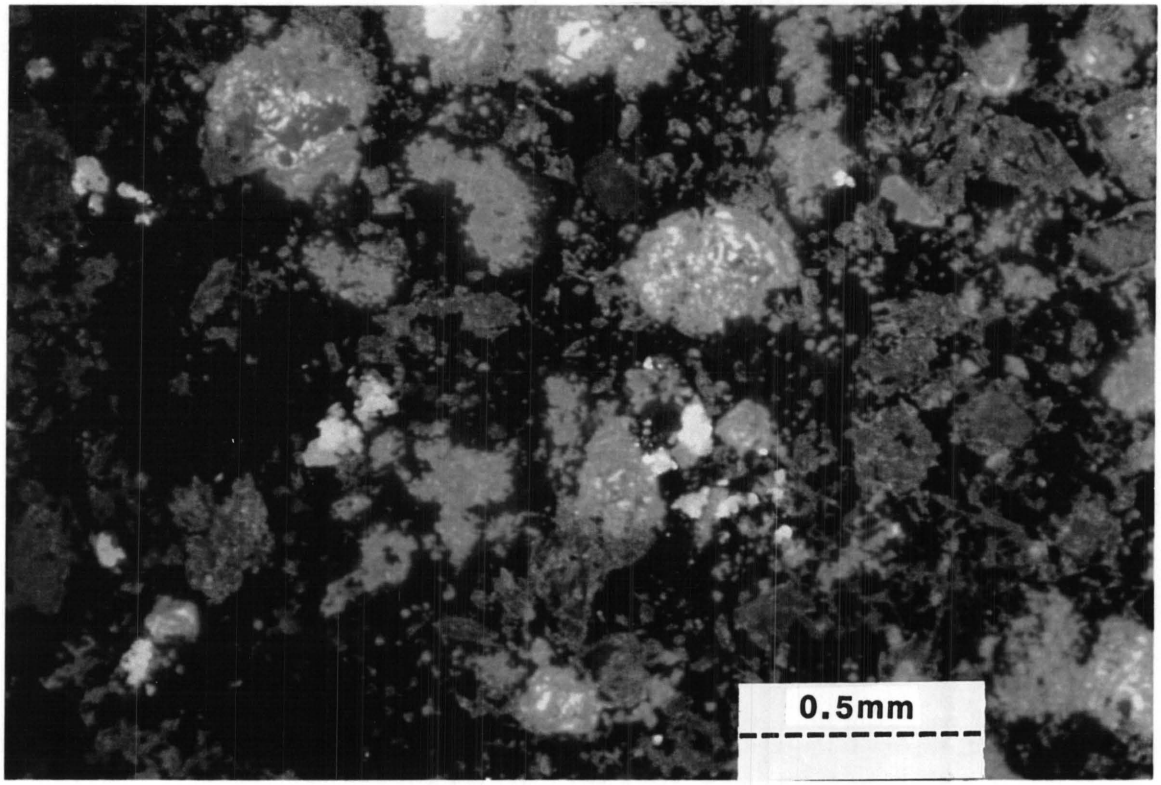

Figure 10.27 Two growth stages of fluorite, the earlier stage as sub- to euhedral (medium blue luninescence) and the second is light blue luminescent and displays concentric zonation. Fluorite is replacing K-feldspar (grey-brown to dark orange luminescence) and non-luminescent ankerite, while apatite (bright pinkish luminescence) is scattered throughout (Cathodoluminescence; x40; width of view: 2.5 mm across; film: 400 ASA Fuji Provia; exposure time: 35 seconds; sample KD121, KCL19-18).

Digitised by the Department of Library Services in support of open access to information, University of Pretoria, 2021

have a corroded appearance, while apatite overgrowth is very uncommon.

Fine-grained fluorite, intimately associated with the grey-green luminescent feldspar predates the large euhedral fluorite. Larger fluorite grains with light-blue luminescence and concentric lighter blue zonation show irregular outlines (Fig. 10.27). A later stage of fluorite is darker blue-luminescent, and occurs as small anhedral grains and aggregates and also as overgrowths on some of the earlier fluorite grains (Fig. 10.28). The darker luminescing fluorite appears mostly within the dolomite/ankerite, the abundance ranging from high to extremely low in different layers of the section. Fluorite also occurs as an infilling of voids (Fig. 10.29). Surrounding the pale feldspar crystals is dark, microcrystalline hematite which is most abundant in the centre of the section where it constitutes the matrix. In other areas this material is present together with brown, microcrystalline carbonate.

Interpretation

The original mineral grains of the described ash tuff have been pseudomorphosed by feldspar. Later, grey-green feldspar growth is possibly accompanied by fine-grained fluorite (Fig. 10.25). The formation of fluorite euhedra was followed by calcite crystallisation along veins and as small pockets. Pyrite euhedra and hematite were formed by the latest mineralisation events.

10.2.3.4 Sample KD124

The sample consists of K-feldspar, ankerite, apatite, siderite, hematite and subordinate pyrite and anatase. The K-feldspar is present as single euhedra and as intergrowths with ankerite. Fluorite and apatite form overgrowths on K-feldspar. This sample is similar to KD121, but contains more K-feldspar and apatite and less ankerite and fluorite (Figs. 10.26 and 10.30).

Thin calcite rims with sharp contacts, and anatase-rich veins with diffuse contacts are also present. The feldspar displays various shades of green luminescence. Cores of grains tend to be relatively bright yellowish-green with irregular rims of duller green. No red-brown areas are observed (in contrast to sample KD121), but areas of some grains have a slight red-brownish tint. The dullest green feldspar is present as small anhedral grains which are scattered

Digitised by the Department of Library Services in support of open access to information, University of Pretoria, 2021

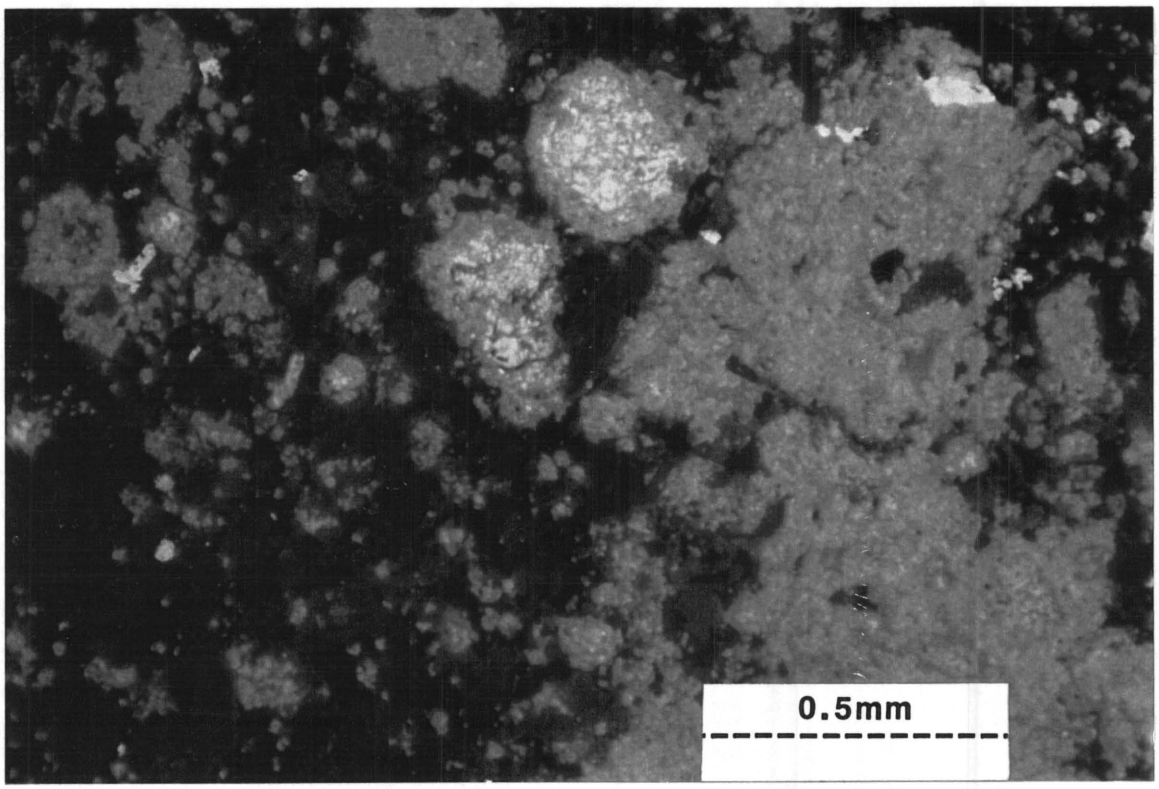

Figure 10.28 A later stage fluorite (darker blue-luminescence) occurs as small anhedral grains and aggregates, and as overgrowths on some of the earlier fluorite grains. The K-feldspar (dark to dull luminescence) and non-luminescent carbonates are being replaced by the fluorite and apatite (pinkish luminescence) (Cathodoluminescence; x50; field of view: 2 mm across; film: 400 ASA Fuji Provia; exposure time: 57 seconds; sample KD121, KCL19-2).

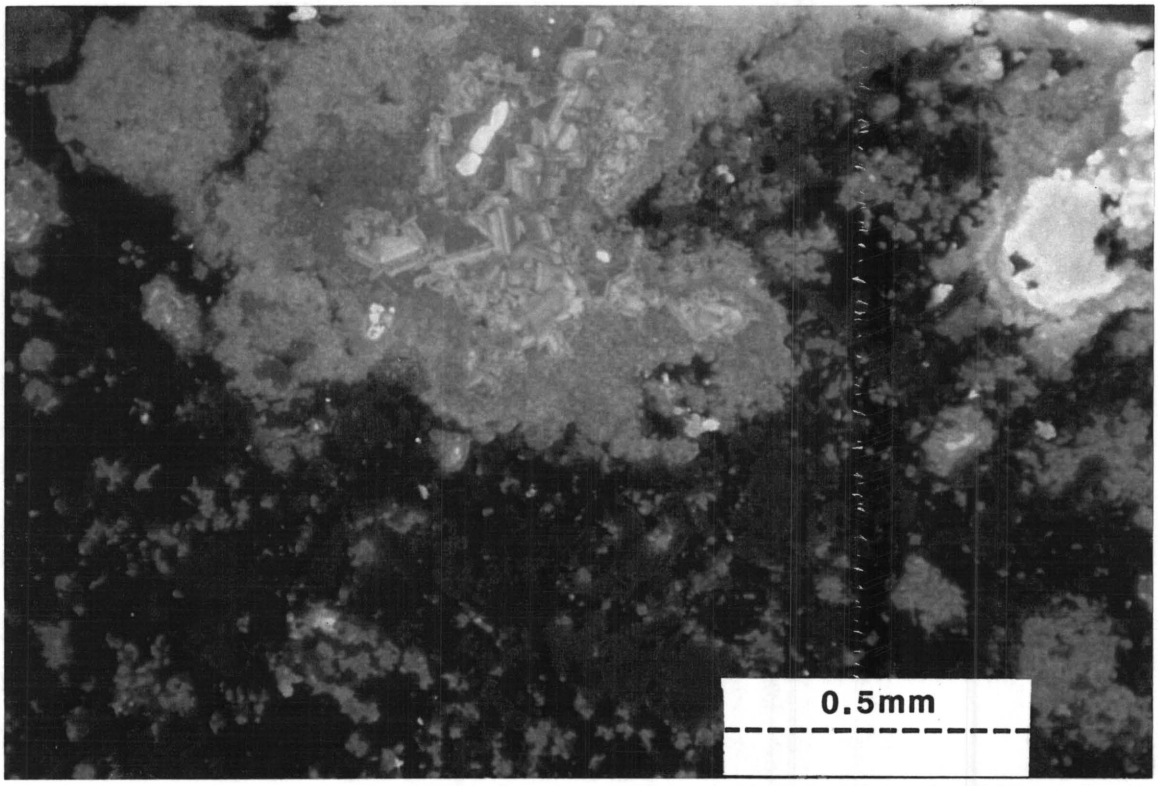

Figure 10.29 Dark blue luminescing fluorite as irregular void filling and as larger irregular patches (light to medium blue, and concentrically zoned). Note the light-blue zoned fluorite, and calcite (yellow luminescence) rimmed by fine-grained pink apatite (right hand top corner) (Cathodoluminescence; x50; width of view: 2 mm across; film: 400 ASA Fuji Provia; exposure time: 60 seconds; sample KD121, KCL19-15).

Digitised by the Department of Library Services in support of open access to information, University of Pretoria, 2021

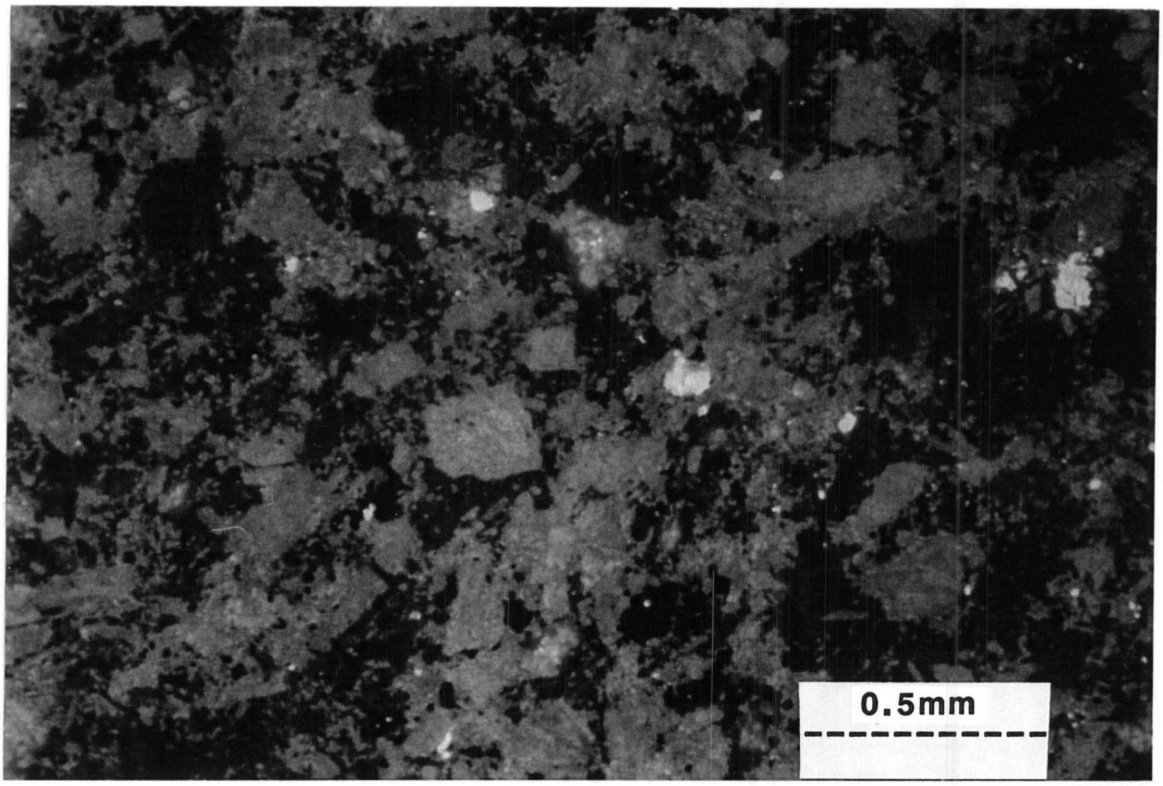

Figure 10.30 Cathodoluminesence image showing K-feldspar euhedra (grey-greenish to red-brown), intergrown K-feldspar and ankerite (dull to non-luminescent), with partial overgrowths of fluorite (blue), apatite (grey-pink luminescence); also scattered pyrite and anatase grains. Note the relatively bright yellowish-green feldspar cores, and irregular rims of dull green luminescent feldspar (Cathodoluminescence; x40; width of view: 2.5 mm across; film: 400 ASA Fuji Provia; exposure time: 32 seconds; sample KD124, KCL19-22).

Digitised by the Department of Library Services in support of open access to information, University of Pretoria, 2021

throughout and overgrow the larger euhedra (Fig. 10.25).

10.2.4 Lower ash flow unit

Five samples were taken at depths of -145.00, -160.00, -167.00, -184.50 and -215.10, and marked KD130, KD133, KD134, KD138 and KD146 respectively. These samples were taken of variably mineralised dark brown to red-brown tuff, displaying an ill-defined laminated to welded fabric (Table 10.5). Sample KD130 displays fine scale layering which represents primary fabric. Sample KD133 is banded at macroscopic scale. Three layers consisting of rounded particles and parallel to the finer scale banding defined by a varying density of iron-oxide grains occur at certain levels. Although sample KD134 contains extensive apatite mineralisation, it is crudely banded because of differing amounts of hematite and pyrite, and carbonate minerals. Sample KD146 is extensively fluoritised and carbonatised.

Table 10.5 General descriptions of samples from the lower ash flow unit.

SAMPLE	MINERALS IN ORDER OF ABUNDANCE (XRD)	COMPONENT	PARTICLE DIAMETER	FABRIC	ROCK TYPE
KD130	siderite, fluorite, hematite, chlorite, dolomite/ankerite, quartz, K-feldspar, anatase	feldspar grains	1 mm	laminated in part	brown ash tuff
KD133	siderite, fluorite, hematite, chlorite, quartz, K-feldspar, calcite, anatase, dolomite/ankerite	(a) pale grains (calcite +fluorite) (b) ovoid grains (calcite-rich)	200 to 400 µm 300 to 500 µm	laminated	brown ash tuff
KD134	fluorite, siderite, apatite, calcite, barite, hematite, chlorite, K-feldspar, anatase	none		massive to crudely banded	brown ash tuff
KD138	fluorite, siderite, calcite, K-feldspar, hematite, barite, quartz, chlorite, anatase, dolomite/ankerite	(a) pale, rounded grains	150 to 450 µm	laminated	brown ash tuff
KD146	siderite, fluorite, hematite, K-feldspar, quartz, calcite, chlorite, dolomite/ankerite	(a) relic grains (fragments) (b) lithic grains (ash and lava)	300 to 700 µm 100 to 300 µm	massive	brown ash tuff

Digitised by the Department of Library Services in support of open access to information, University of Pretoria, 2021

10.2.4.1 Sample KD130

This sample consists of intergrown K-feldspar and dolomite/ankerite, chlorite and hematite with later secondary fluorite, apatite, siderite and calcite. Fluorite, together with later calcite, occurs as bands of varying thickness, parallel to the primary depositional layering.

The feldspar has more irregular forms and shows more varying luminescence colours than the samples from the ferruginous lapilli tuff unit. The crystals have stubby rectangular cross sections, up to 1 mm long, but they are commonly resorbed. The cores of these grains commonly luminesce dull greyish brown, with local spots of olive-green and patches of brick-red. In some grains the green luminescence dominates. Fine-grained grey-green luminescent feldspar forms rims on the feldspar grains first mentioned and may even cement larger, earlier grains. Intergrown with this grey-green luminescent feldspar is relatively dull brick-red luminescing feldspar.

Fluorite is the second most abundant mineral after siderite. In some areas of the section, the fluorite replaces feldspar almost completely. Fluorite also forms veins, which are contemporaneous with the formation of the fine-grained fluorite, replacing dolomite/ankerite. Elsewhere it forms fine-grained aggregates of euhedral to subhedral grains. Fluorite is cut by veins and patches of calcite, so that calcite is late in the paragenesis (Fig. 10.31). Some euhedral grains with hexagonal basal sections and prismatic longitudinal sections (apatite?) are now pseudomorphosed by fluorite.

Fluorite, feldspar and to a lesser extent, ankerite are overgrown by non-luminescent siderite and hematite as well as by fine-grained apatite with luminescence in places showing zonation from pale pink followed by pale blue at the rim. Apatite is distributed very unevenly throughout the section. Calcite occurs as irregular and narrow, cross-cutting veins, or as growths in brecciated areas. In larger veins calcite is accompanied by small pyrite grains.

10.2.4.2 Sample KD133

Original ash grains seem to have been replaced by intergrowths of calcite and fluorite (Table 10.5). The fluorite commonly occurs as small grains within the calcite, which has a luminescence of varying complexity from bright orange to very dull orange (Figs. 10.32, 10.33 and 10.34).

Digitised by the Department of Library Services in support of open access to information, University of Pretoria, 2021

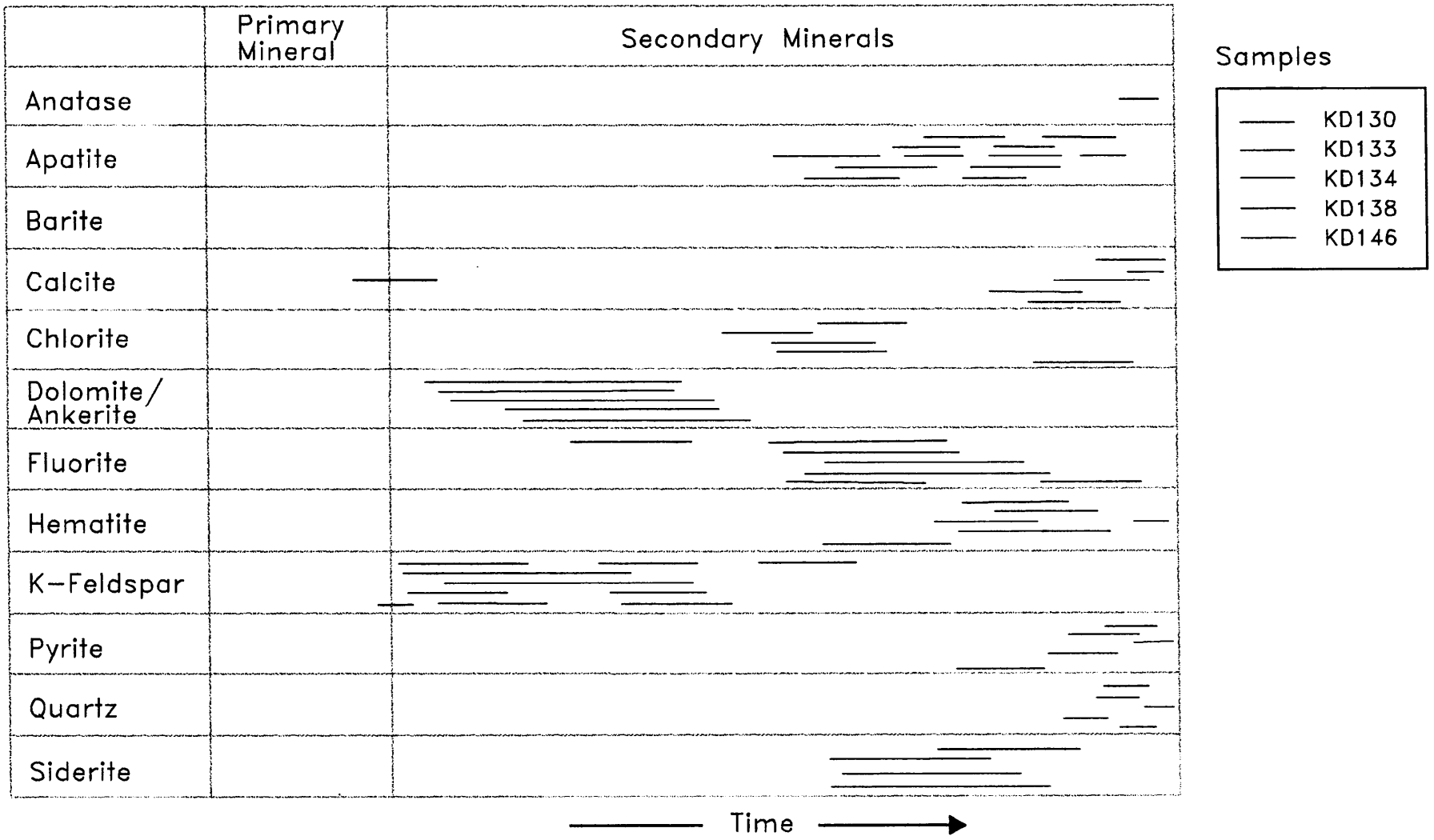

Figure 10.31 Paragenesis of samples KD139, KD133, KD134, KD138 and KD146 of the lower ash flow unit.

Digitised by the Department of Library Services in support of open access to information, University of Pretoria, 2021

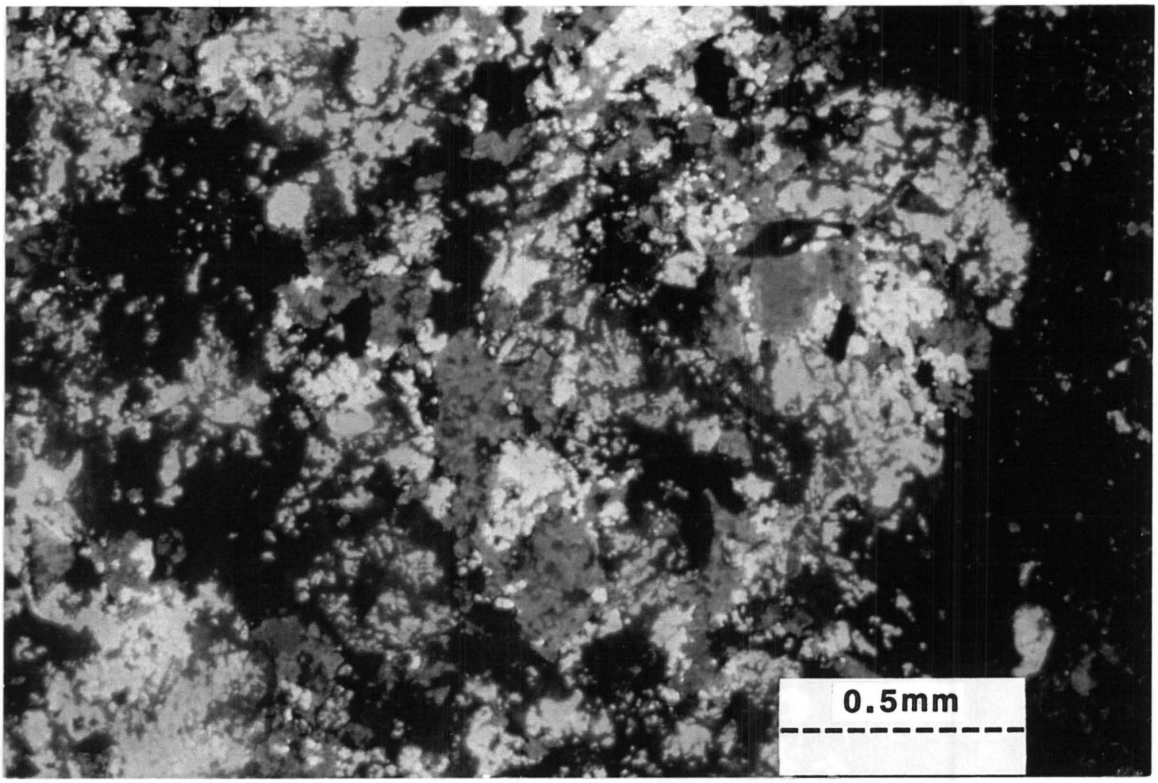

Figure 10.32 A cathodoluminescence image of ovoid ash grains composed of intergrown calcite (bright orange to dull luminescence) and fluorite (blue luminescence). The fluorite occurs as small grains within the calcite. The dark areas along the right hand boundary consist of non-luminescent carbonates and chlorite (Cathodo-luminescence; x40; width of view: 2.5 mm across; film: 400 ASA Fuji Provia; exposure time: 45 seconds; sample KD133, KCL6-31).

Digitised by the Department of Library Services in support of open access to information, University of Pretoria, 2021

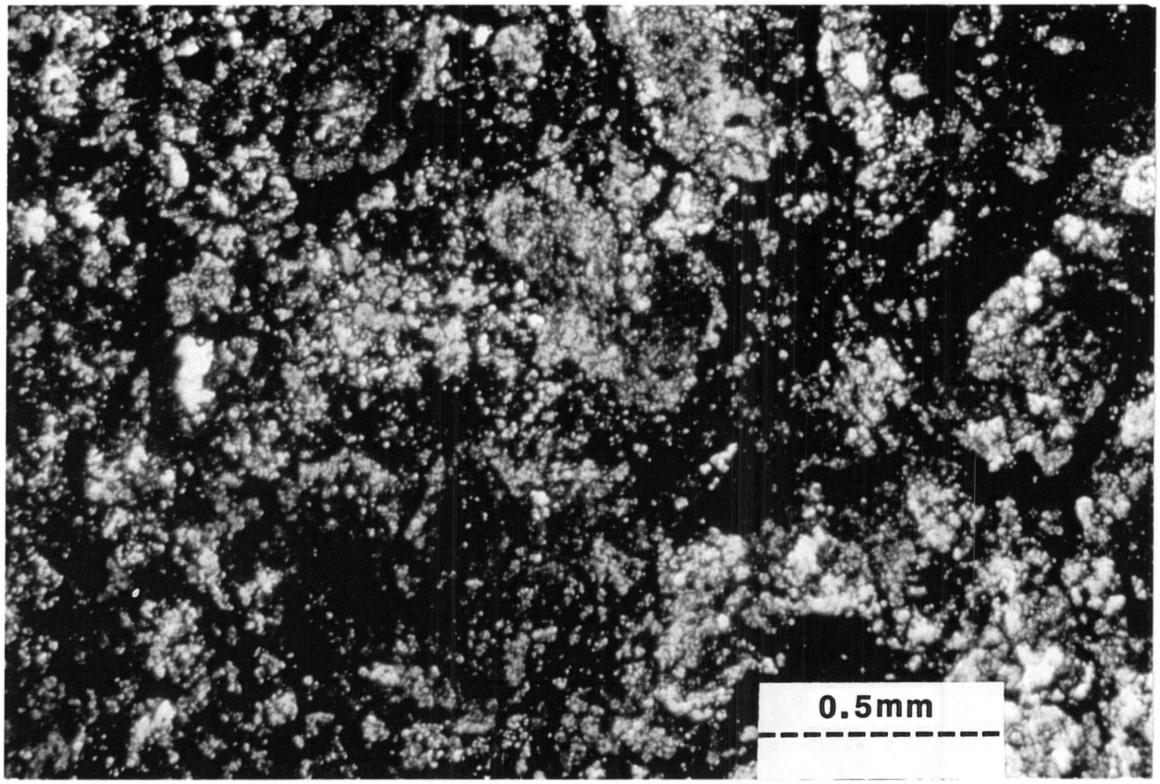

Figure 10.33 The plane polarised light image of ill-defined ovoid ash grains. The dark rims consist of K-feldspar, ankerite, fluorite, apatite and anatase, while the cores are predominantly calcite (Plane polarised light; x40; width of view: 2.5 mm across; film: 400 ASA Fuji Provia; exposure time: 44 seconds; sample KD133, KPPL6-28).

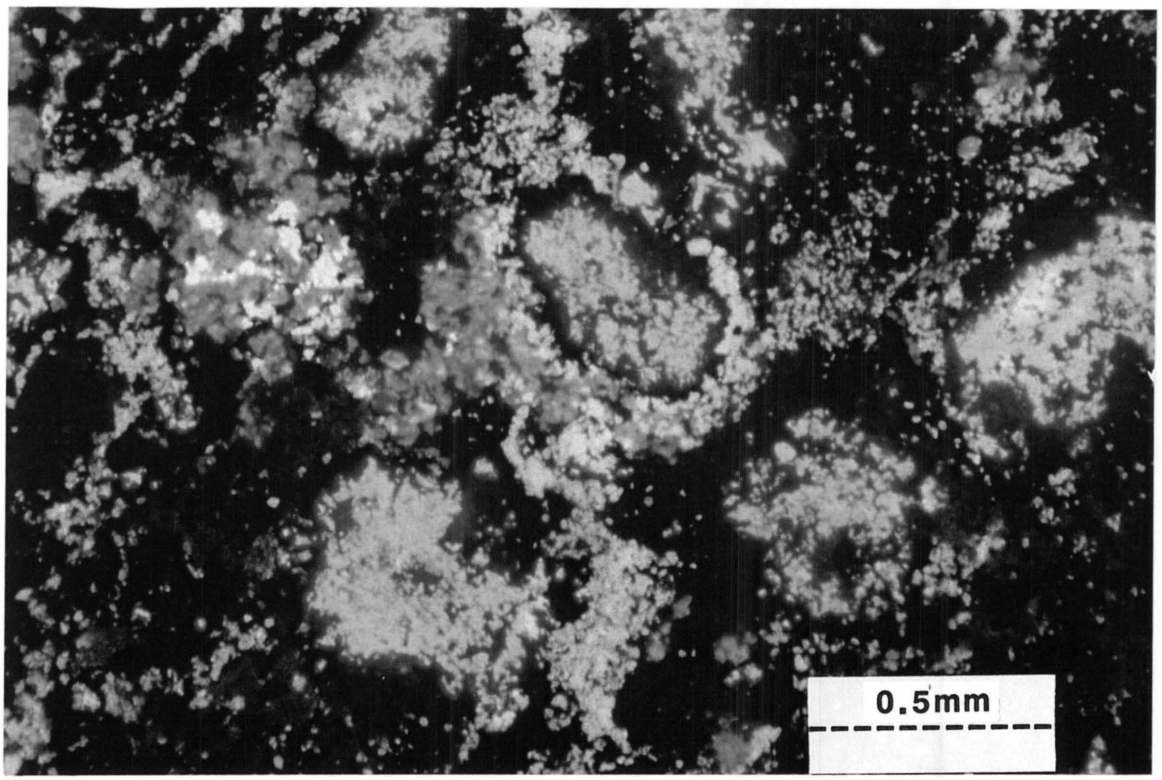

Figure 10.34 A cathodoluminescence image of Figure 10.33. The cores of the relic particles are composed of orange-luminescent calcite and surrounded by rims and matrix of intergrown, non-luminescent K-feldspar, ankerite and chlorite, which is overgrown by fluorite (blue luminescence) and by apatite (white-grey luminescence). (Cathodoluminescence; x40; width of view: 2.5 mm across; film: 400 ASA Fuji Provia; exposure time: 54 seconds; sample KD133, KCL6-29).

Digitised by the Department of Library Services in support of open access to information, University of Pretoria, 2021

Ovoid ash grains composed of orange-luminescent calcite, occur in a matrix of feldspar, dolomite/ankerite, chlorite and siderite, which is overgrown and partially replaced by fluorite and by apatite. These ash grains have obviously been largely replaced by later minerals (Fig. 10.34).

The matrix of the pseudomorphosed ovoid ash grains is dark due to a high concentration of siderite, hematite and pyrite, as a closely-spaced network of veinlets and as fine-grained dusting. It is fine-grained and largely composed of olive to yellow-green and especially grey-green-luminescent K-feldspar. Brick-red-luminescent feldspar is uncommon, and is always surrounded by olive-green feldspar. Some fine-grained aggregates of green-luminescing feldspar seem to be pseudomorphous after a mineral with a rectangular habit (up to 300 μm in length). The feldspar is overgrown by minor chlorite.

Interpretation

Following minor chloritisation, K-feldspar was overgrown by fine-grained fluorite and later by fine-grained apatite as shown in the paragenetic chart (Fig. 10.31). The apatite shows relatively pale pink and blue luminescence. This apatite and fluorite in places form rims surrounding the ovoid calcite grains. Calcite occurs as irregular patches and narrow veinlets, which cut most textures, and appear to post-date the introduction of hematite and pyrite. This calcite has a slightly deeper orange luminescence than that of the grains. The introduction of fine-grained hematite and pyrite into the matrix of the grains and also into veinlets, appears to have occurred in a late stage of mineral formation.

10.2.4.3 Sample KD134

The sample comprises dolomite/ankerite, K-feldspar and apatite. The spheroidal apatite contain radially arranged slivers of dolomite/ankerite, and small inclusions of anatase. Some of the spheroidal apatite have “spongy”, inclusion-rich cores, with turquoise luminescence, and inclusion-free rims with very light turquoise luminescence (Figs. 10.35 and 10.36). The apatite also forms irregular fragments which are cemented by dully-luminescent apatite or calcite (Fig. 10.37), indicating brecciation and cementation of some spherulites. In these brecciated and healed spherulites, there are no radially arranged inclusions. Also present is violet-blue-luminescent apatite, which occurs as fine-grained growths between whole and fragmented spherules in apatite-rich parts of the section.

Digitised by the Department of Library Services in support of open access to information, University of Pretoria, 2021

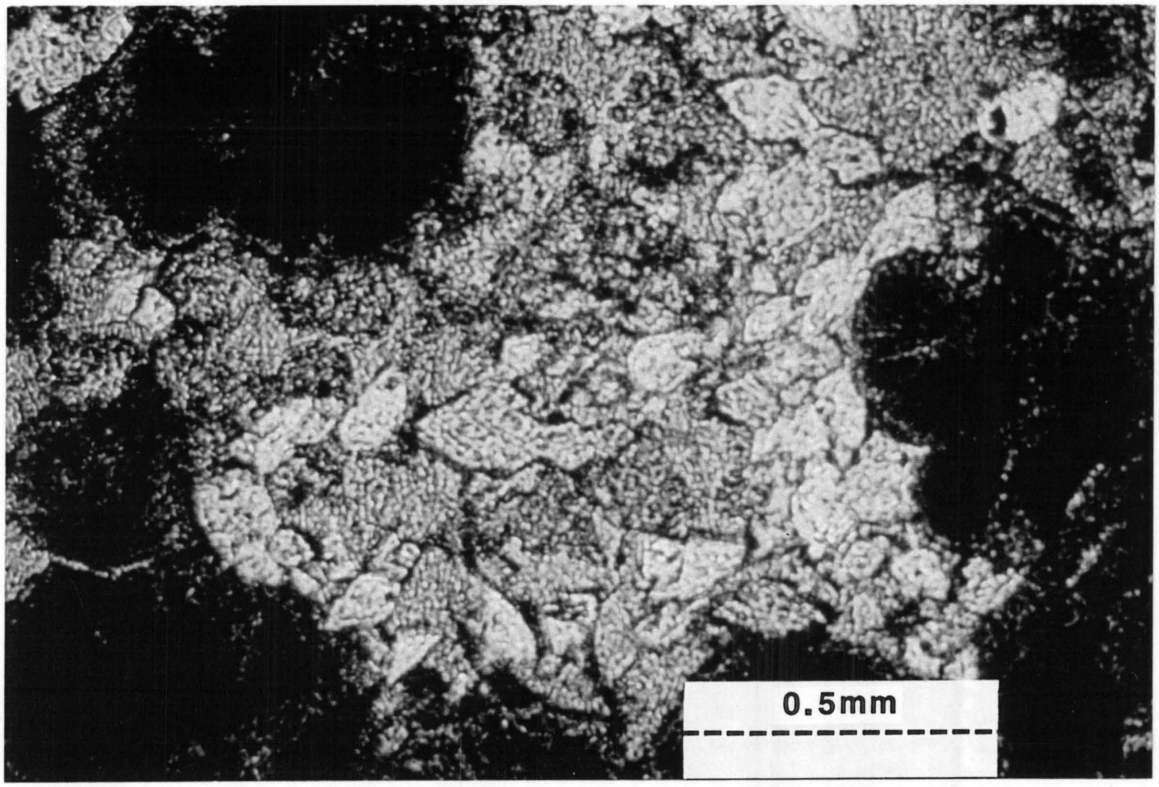

Figure 10.35 The plane polarised light image depicts spheroidal apatite structures (the dark to black round grains).The rims of the structures are well defined, held in a matrix of ankerite (high relief), calcite (lower relief) and fluorite (low relief with a brownish tint) (Plane polarised light; x50; width of view: 2 mm across; sample KD134, KPPL2-2).

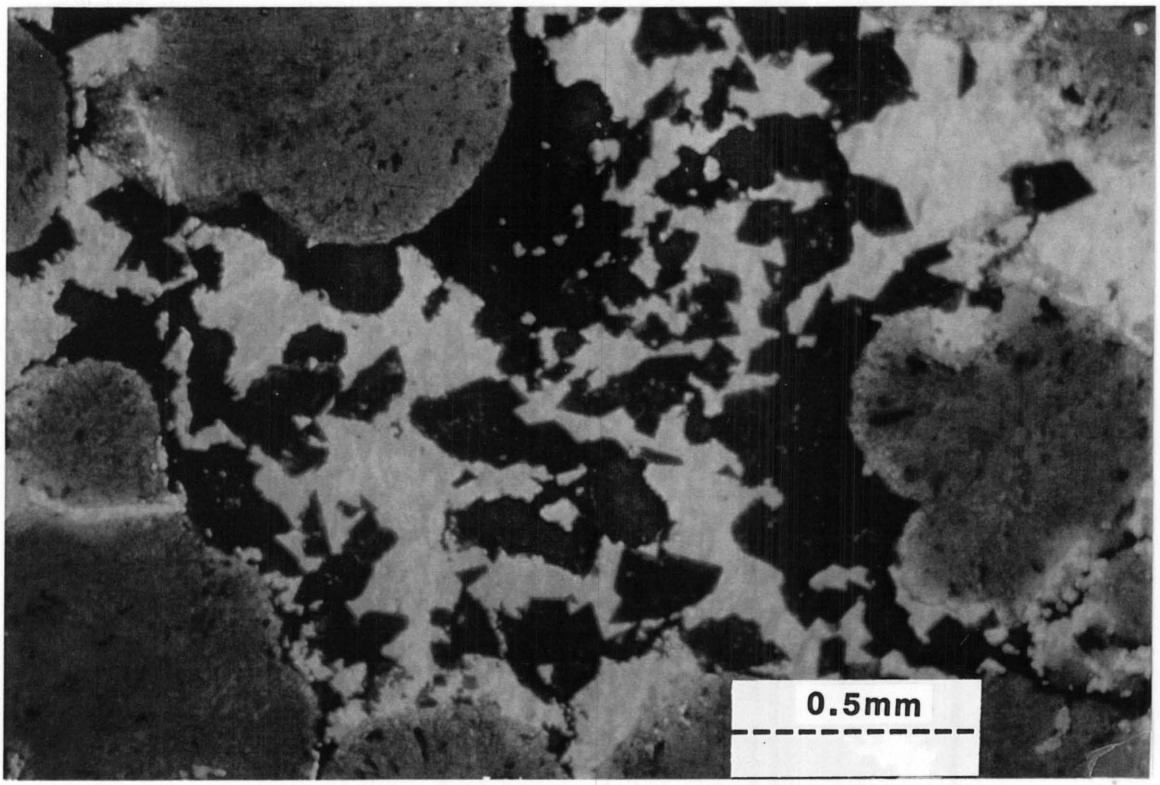

Figure 10.36 Cathodoluminescence image of the field in Figure 10.35. The spheroidal structures are distinctive. The rims have whitish violet-blue luminescence compared to the violet-blue of the bulk. Note the radial orientation of small anatase inclusions within the structures.The matrix consists of calcite (orange luminescence) and fluorite (blue luminescence) replacing non-luminescent ankerite and chlorite (Cathodoluminescence; x40; width of view: 2.5 mm across; film: 400 ASA Fuji Provia; exposure time: 57 seconds; sample KD134, KCL2-6).

Digitised by the Department of Library Services in support of open access to information, University of Pretoria, 2021

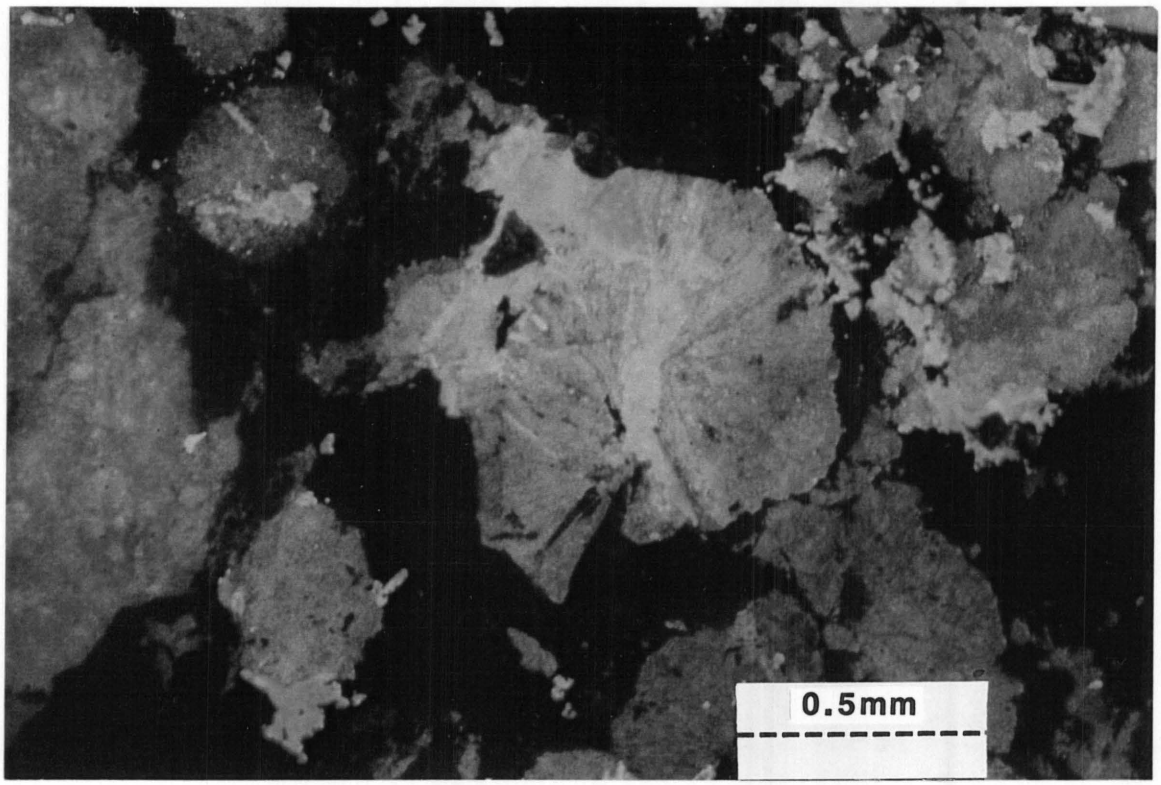

Figure 10.37 Cathodoluminescence image of spheroidal apatite in a matrix of non-luminescent carbonates and chlorite. Several types of apatite are distinct (greenish to pinkish blue luminescence). Calcite (bright orange luminescence) is scattered within and around the apatite grains, and occurs as fracture filling (Cathodoluminescence; x40; width of view: 2.5 mm across; film: 400 ASA Fuji Provia; exposure time: 57 seconds; sample KD134, KCL2-11).

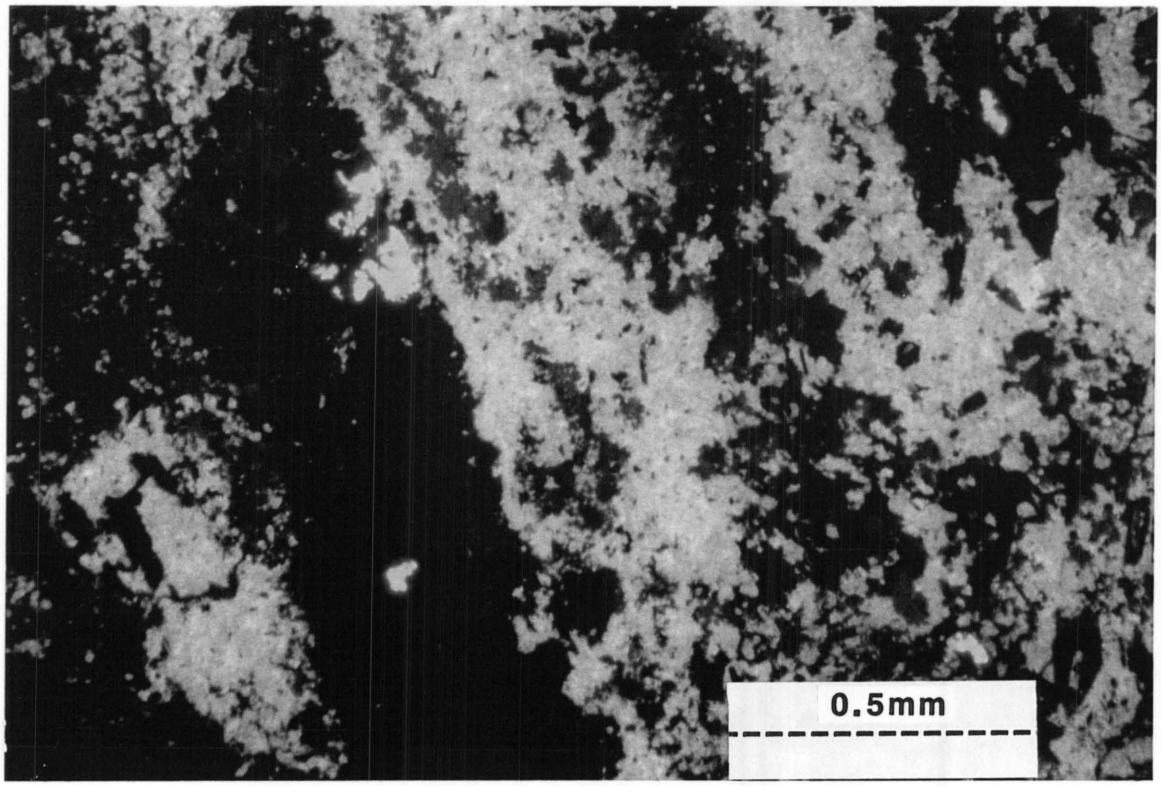

Figure 10.38 Cathodoluminescence image of pink to grey-green luminescent K-feldspar in a non-luminescent, microcrystalline carbonate matrix. Fine-grained fluorite replaces K-feldspar, while calcite (orange luminescence) is found throughout the sample (Cathodoluminescence; x40; width of view: 2.5 mm across; film: 400 ASA Fuji Provia; exposure time: 1 minute 57 seconds; sample KD138, KCL6-19).

Digitised by the Department of Library Services in support of open access to information, University of Pretoria, 2021

Fluorite overgrew the feldspar and also dolomite/ankerite, and commonly occurs between the apatite spherulites, suggesting late-stage formation (Fig. 10.31). It is possible therefore that the introduction of fluorite was accompanied by localised brecciation of the apatite, dolomite/ ankerite and K-feldspar. Calcite formation throughout the sample followed the brecciation, causing the healing of the fractures. There are some veins in which zoned calcite (indicated by variable luminescence) grew from the walls of the cracks and included small fragments of apatite, dolomite/ankerite and fluorite. There is also a later generation of cross-cutting, narrow calcite veins. Some fine-grained hematite and pyrite was introduced prior to the calcite formation, while quartz represents the last mineral to form.

10.2.4.4 Sample KD138

Much of the section is made up of strained, pink to colourless, cloudy K-feldspar in a relatively dark microcrystalline siderite matrix. Replacement of feldspar by dolomite/ankerite and calcite can be seen in many grains. Small patches of chlorite occur in the feldspar.

The feldspar has a grey-green luminescence with subordinate blue luminescing mottles (Fig. 10.38). Fluorite is very common as is apatite. Apatite occurs as very fine-grained aggregates with pink luminescence. Calcite is a late mineral and occurs as isolated grains amongst the other minerals, or as cement in brecciated rock.

The fine-grained pale pink and blue apatite forms irregular patches and bands which cut pre-existing fabrics. It contains inclusions of tiny hematite and pyrite grains, and also fluorite. Hematite and pyrite veinlets form a network through the sample, suggesting their late-stage formation (Fig. 10.31). The veinlets are roughly parallel to banding in the sample, which may represent primary lamination. Calcite occurs in irregular patches and as cement of microbreccias, and cuts all other fabrics.

10.2.4.5 Sample KD146

Despite its extensive fluoritisation and carbonatisation the original textures of the sample can still be recognised. It represents several depositional units of coarse and fine ash tuff (Table 7.1).

Digitised by the Department of Library Services in support of open access to information, University of Pretoria, 2021

The following minerals have been observed microscopically: apatite, calcite, chlorite, dolomite/ankerite, fluorite, hematite, K-feldspar, pyrite and siderite. Feldspar mainly occurs as disseminated, anhedral grains, consisting of brick-red luminescent cores, followed by an olive-green luminescent intermediate zone, largely replaced and overgrown by an irregular rim of dull-brown luminescent, fine-grained feldspar. Euhedral feldspar with green/red luminescence is rare and is invariably overgrown by the brown luminescent feldspar. In some of the disseminated grains the central portion seems to have been replaced by cobalt-blue luminescent fluorite, and the overgrowth of brown luminescent feldspar by chlorite. Fine-grained hematite is also present in these chlorite overgrowths.

The groundmass of subrounded, porphyritic fragments in the coarse tuff has been replaced by fluorite, whereas the scattered prismatic microphenocrysts have been pseudomorphosed by polycrystalline calcite with or without fluorite. Some of these pseudomorphs have thin, incomplete rims of feldspar.

Feldspar and dolomite/ankerite in the matrix of the coarse tuff, and feldspar and fluorite in the ash grains are overgrown by fine-grained apatite with pale pink and blue luminescence and non-luminescent siderite. Pyrite and hematite and also fine-grained fluorite with variable luminescent ("peacock") colours occur as veins that seem to predate veins of apatite and calcite - the latter appears to be the last mineral to crystallise. The textures described suggest a paragenesis as shown in Figure 10.31.

Although the different samples do not seem to have identical paragenetic sequences, it is nevertheless clear that the secondary metasomatic alteration of the rocks was a multistage process, possibly related to different pulses of volcanic activity.

Digitised by the Department of Library Services in support of open access to information, University of Pretoria, 2021

11. MINERAL CHEMISTRY

Thin sections of the different layers and units of the KD01 succession were selected for mineral analyses in such a way that a detailed representation of chemical and mineralogical trends would be obtained (Fig. 7.26). The analytical data for chlorite, carbonates, apatite, fluorite, feldspar and rare-earth minerals are listed in Appendix 1: Mineral analyses.

11.1 Chlorite

Chlorite compositions can be represented by the formula: $[R^{2+}, R^{3+}]^{VI}_{12}[Si_{8-x}R_x^{3+}]^{IV}O_{20}(OH)_{16}$, where R^{2+} = Mg, Fe, Mn, Ni, Zn; and R^{3+} = Al, Fe, Cr, and x is generally is 1 to 3 (Deer et al., 1992).

According to Laird (1988) three problems arise when interpreting chlorite analysis. Firstly, chlorite electron microprobe analyses with appreciable amounts of K_2O, Na_2O or CaO should be treated with caution. This is based on work by Ernst (1983) who showed that K, Na and Ca appear to be covariant. The second problem is that chlorites are sheet silicates and do not polish easily, so that the polishing finish can influence the quality of the analyses. Thirdly, a major problem arises in normalising the data to a structural formula. In this study, chlorite data have been normalised with respect to 28 anhydrous oxygens, as the H_2O^+ content has not been determined.

The chlorite from the different samples displays substantial variations in the concentrations of several chemical components. The largest variation occurs in the contents of FeO (20.9 to 35.7 wt%), and MgO (1.9 to 17.9 wt%) with FeO increasing with an increase in stratigraphic height (the KD01 borehole sequence). Smaller variations are observed in the SiO_2 (20.1 to 39.5 wt%), Al_2O_3 (14.0 to 20.5 wt%) and MnO (0.0 to 2.2 wt%) contents. The contents of TiO_2, K_2O and Na_2O are uniformly low.

The variation of Si against Fe/(Fe+Mg), based on the structural formula, has been used in classification and nomenclature of chlorite (Hey, 1954) (Fig. 11.1a). The chlorites from the different units of the KD01 sequence have Si contents ranging from 4.5 to 7.0, and Fe/(Fe+Mg) ratios from 0.4 to 0.8. Chlorite from the upper part of the KD01 sequence (upper ash flow and lapilli tuff units) agrees in composition to pseudothuringite, iron-rich ripidolite and brunsvigite, while the chlorite from sample KD6E (taken at a depth of 20.5 m in borehole KD02) corresponds to diabantite. The reason for including this sample in this study was to use it as a reference sample, under the assumption that it had not been influenced by secondary processes. Chlorite of the ferruginous lapilli tuff and lower ash flow units and mineralised units of the lower part of the KD01 sequence falls mainly in the brunsvigite field, and in the iron-rich part of the ripidolite field.

In detail, samples KD016, KD019 and KD111 of the upper ash flow and lapilli tuff units display a

Digitised by the Department of Library Services in support of open access to information, University of Pretoria, 2021

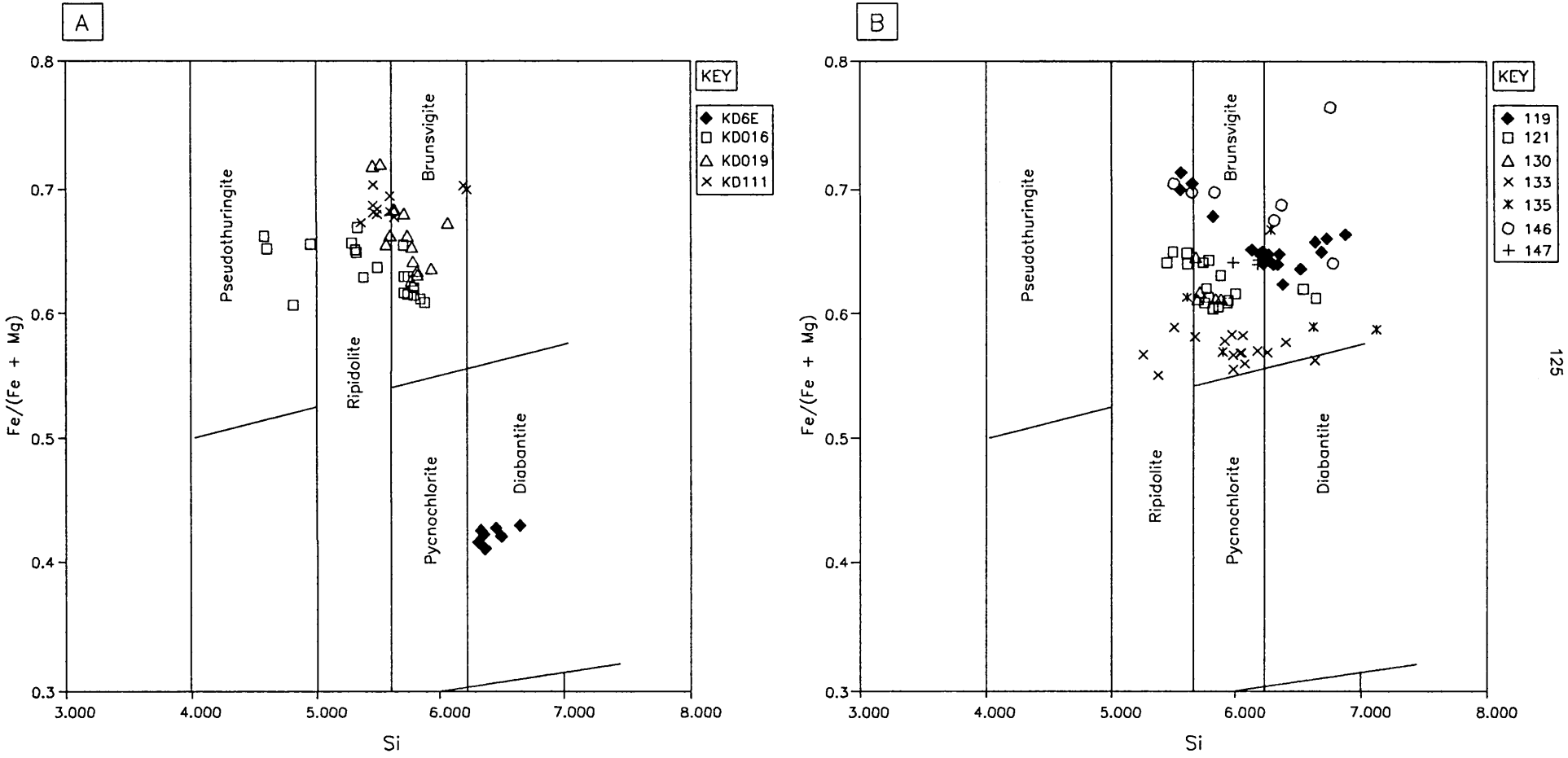

Figure 11.1 Variation of Si against Fe/(Fe+Mg) for (A) the upper ash flow and lapilli tuff units, and (B) the ferruginous lapilli tuff and lower ash flow units, based on the structural formulae of chlorite.

Digitised by the Department of Library Services in support of open access to information, University of Pretoria, 2021

tight grouping. These samples, however, do display a slight shift in Si content (ranges of 4.5 to 5.9, 5.2 to 6.0 and 5.3 to 6.2 respectively). An associated increase in the Fe/(Fe+Mg) ratio is also evident from KD016 to KD019. This can be described as chlorites becoming more Fe-rich with depth. Sample KD6E (taken from borehole KD02), contains chlorite which, when compared to the samples from the KD01 sequence, are Mg-rich. The Mg/(Mg+Fe) ratio varies between 0.56 and 0.58.

For the underlying units (ferruginous lapilli tuff, lower ash flow and mineralised units) the Si content varies between 5.1 and 7.1 (Fig. 11.1b). The Fe/(Fe+Mg) ratio, however, depicts a decreasing trend from sample KD119 to KD135. Samples KD146 and KD147 display similar Si contents, but have scattered Fe/(Fe+Mg) values. These chlorites are similar to the Fe-rich types of the upper part of the pyroclastic breccia unit.

The trends of Mg/(Mg+Fe) and Al/(Al+Mg+Fe) (in atomic proportions) (Fig. 11.2) suggests a negative relationship between Mg/(Mg+Fe) and Al/(Al+Mg+Fe). Both these ratios show a weak negative trend with increasing stratigraphic height (Fig. 11.3).

The $Al^{(iv)}$ varies between 1.62 and 3.58 for chlorite of the KD01 sequence (Fig. 11.4A and B). $Al^{(iv)}$ is inversely proportional to $Al^{(vi)}$. Work done by several other workers (Hey, 1954; Foster, 1962; McLeod and Stanton, 1984) has shown a positive correlation between $Al^{(iv)}$ and Fe/(Fe+Mg) ratio. This they attribute to cation size change and structural adjustments in chlorite: $Al^{(iv)}$ substitution for Si in chlorite increases from 2.3 to 3.01 formula units, based on 8 $Si+Al^{(iv)}$ (Kranidiotis and MacLean, 1987). In the plot of $Al^{(iv)}$ against Fe/(Fe+Mg) ratios for the chlorites of the KD01 sequence (Figs. 11.4A and 11.4B), it is found that for a limited range of $Al^{(iv)}$, the Fe/(Fe+Mg) ratios vary from 0.5 to 0.72. For some samples (KD016 and KD019) a positive correlation is apparent (Fig. 11.4a), while sample KD111 displays a negative correlation. In Figure 11.4B, the different samples display points which range from positive trends (samples KD119, KD121, KD135 and KD146), to no trend at all (KD130, KD133 and KD147). In all cases the correlation coefficients are low.

Based on the critical evaluation by Decaritat et al. (1993) of different chlorite geothermometers the formula of Kranidiotis and MacLean (1987) was used to infer the temperature of formation of the chlorite, viz.:

$$T\ (°C) = 106[Al^{(iv)} + 0.7\ (Fe/(Fe+Mg))] + 18.$$

These temperatures are shown in parenthesis on Figure 11.3. It seems as if the stratigraphically higher chlorite was formed at higher temperatures than the chlorite lower down in the sequence.

Digitised by the Department of Library Services in support of open access to information, University of Pretoria, 2021

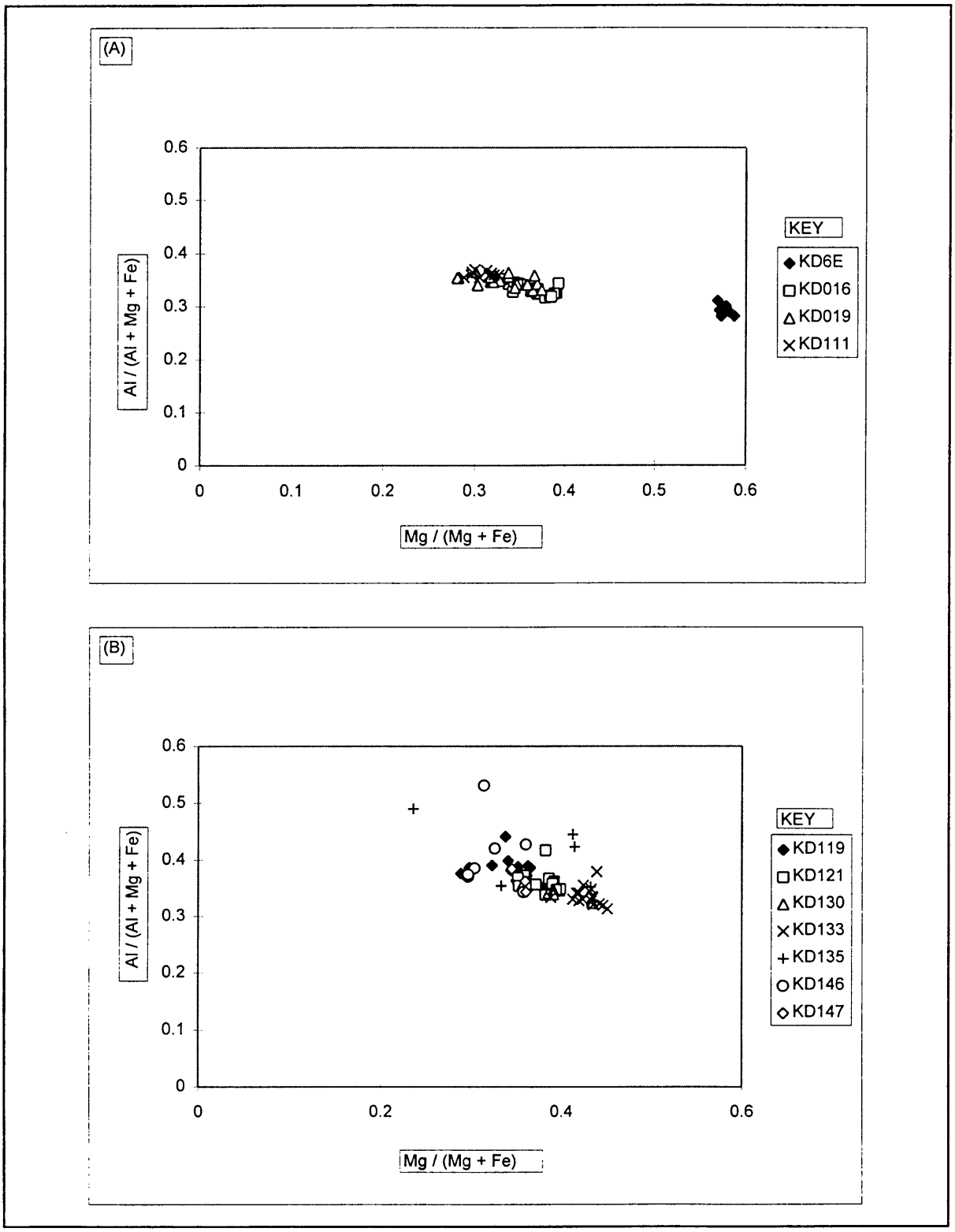

Figure 11.2 Mg/(Mg+Fe) against Al/(Al+Mg+Fe) of chlorite for (A) the upper ash flow and lapilli tuff units, and (B) for the ferruginous lapilli tuff and lower ash flow units, and mineralised zones.

Digitised by the Department of Library Services in support of open access to information, University of Pretoria, 2021

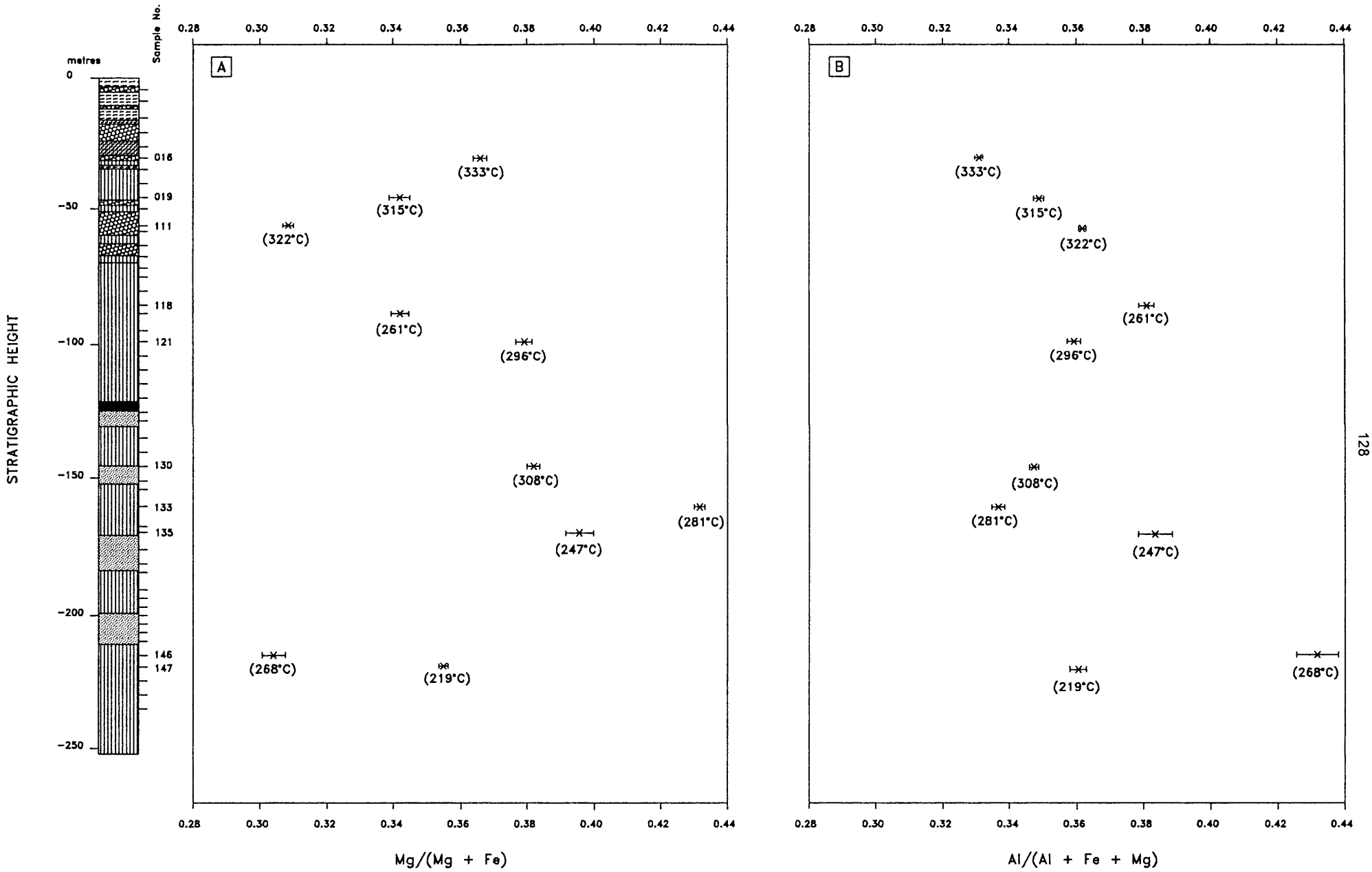

Figure 11.3 Atomic ratios Mg/(Mg+Fe) and Al/(Al+Mg+Fe) of chlorite related to the stratigraphic height for the KD01 sequence. Inferred temperature of formation of the chlorite samples is shown in parenthesis (see Fig. 11.8 for legend).

Digitised by the Department of Library Services in support of open access to information, University of Pretoria, 2021

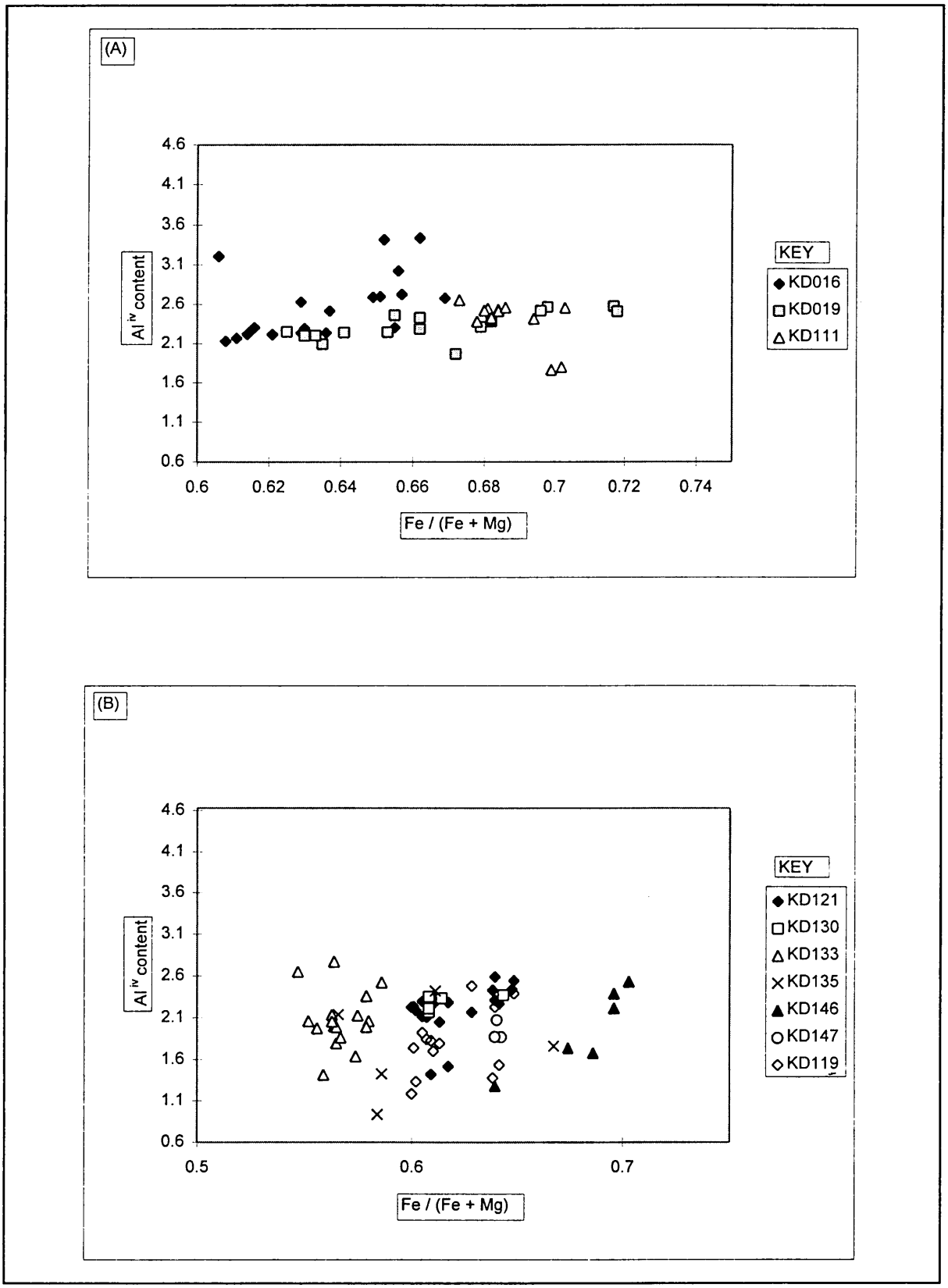

Figure 11.4 Variation in the atomic proportion of aluminium in four-fold coordination ($Al^{(iv)}$) versus Fe/(Fe+Mg) in the structural formulae of chlorite for (A) the upper ash flow and lapilli tuff units, and (B) the ferruginous lapilli tuff and lower ash flow units, and mineralised zones of the KD01 sequence.

Digitised by the Department of Library Services in support of open access to information, University of Pretoria, 2021

This seems to agree with the findings of Zang and Fyfe (1995) that the Mg/(Mg+Fe) ratio of chlorites decreases from distal host rocks (i.e. cooler environment) towards the mineralised zone in the Igarape Bahia gold deposit, Carajas, Brazil. Based on the inclination of borehole KD01 (Fig. 7.27), the samples in the lower portion of the borehole would have been farther away from the vent (and therefore probably in the cooler environment) than the samples higher up in the stratigraphy.

11.2 Carbonates

The carbonate group of minerals, of which calcite ($CaCO_3$), dolomite ($CaMg(CO_3)_2$), ankerite ($Ca(Mg,Fe^{2+},Mn)(CO_3)_2$) and siderite ($FeCO_3$) are the most common, are all present in the KD01 sequence of the inner zone of the Kruidfontein Complex.

In calcite, the Ca can be partially substituted by divalent cations like Mg^{2+}, Mn^{2+}, Fe^{2+} and Sr^{2+} (Deer et al., 1992). The structure of dolomite resembles that of calcite, although the replacement of Mg by Fe^{2+} affects the size of the unit cell. Dolomite containing small amounts of Fe^{2+} (Mg/Fe >4), has a brownish colour in hand-specimen. The replacement of Mg by Fe^{2+} is described by Deer et al. (1992) as continuous, through ankerite ($Ca(Mg,Fe^{2+},Mn)(CO_3)_2$) to $CaFe(CO_3)_2$. The most common substitution in ankerite is that of Fe^{2+} for Mg, but Mn is also found in the (Fe,Mg) position. According to Deer et al. (1992) the term ankerite is used for carbonates with $Mg/Fe \leq 4$. The unit cell parameter of siderite ($FeCO_3$) is smaller than that of calcite, due to the higher percentage covalent bonding in $FeCO_3$, as the ionic radius of Fe^{2+} (0.074 nm) is smaller than that of Ca^{2+}(0.099 nm). Substitution of Fe^{2+} in siderite by Mn and Mg is common, while Ca substitution for Fe^{2+} is limited to between 10 to 15 per cent $CaCO_3$.

Based on petrography, cathodoluminescence and microprobe analyses, the occurrence of the different carbonate minerals in samples from borehole KD01 is summarised in Table 11.1. In order to plot the different carbonate compositions (Appendix 1.2 and 1.3), the compositional fields, expressed in atomic proportions, are defined as follows:

dolomite/ferrodolomite/ankerite: Ca:(Mg+Fe) ≈ 1:1

dolomite: Mg:Fe > 4:1

ankerite: Mg:Fe < 4:1

ferrodolomite: Mg:Fe < 1:3, i.e. ankerite contains less than 75% Fe of the total Mg+Fe.

The boundary between dolomite and ankerite is based on the ideal Ca: (Mg,Fe) ratio being 1:1. Ankerite, however, shows a small deviation with a slight excess of Ca.

From the $CaCO_3$ - $MgCO_3$ - ($FeCO_3$+$MnCO_3$) ternary diagram (Fig. 11.5) it is evident that samples

Digitised by the Department of Library Services in support of open access to information, University of Pretoria, 2021

KD012, KD016, KD019 and KD111 of the upper ash flow and lapilli tuff units contain carbonates which correspond with calcite and/or ankerite (Deer et al., 1966; 1992) (Fig. 11.5). Individual samples may be ankerite or calcite-rich, and texturally they range from matrix replacements to veins. Samples KD115 and KD117 of the upper part of the ferruginous lapilli tuff unit are calcian siderites, and occur as replacement of the matrix (Table 11.1). Sample KD121, also from the ferruginous lapilli tuff unit, contains ferroan calcite which plots close to the $CaCO_3$ apex (Fig. 11.6), and in this regard differs from samples KD115 and KD117. The reason for this is that patches of less altered ferruginous lapilli tuff in the lower part of the unit have been partly altered to calcite, whereas the surrounding brown tuff has been replaced to a larger extent by calcian siderite.

The textures of samples (KD128, KD131 and KD133) from the upper part of the lower ash flow unit, containing calcite, sulphides and K-feldspar, are due to replacement of lapilli and ash grains by calcite and of matrix by ankerite and calcian siderite. Veins and void fillings also occur. These carbonates range from calcite to ferrodolomite to calcian siderite (Fig. 11.6).

Also evident form Figures 11.6 and 11.7 is the variability of carbonates in sample KD134 and KD135, and KD142 respectively. These samples have been taken in close proximity to the mineralised zones. These carbonates occur as replacements of lapilli and ash grains , and also as different generations of matrix replacement. The carbonates comprise calcite, ferroan dolomite, ankerite and calcian siderite. Sample KD147 from the lower part of the lower ash flow unit contains ankerite and calcian siderite, similar to other samples taken of the brown altered tuff (samples KD115, KD117, KD131 and KD133).

The SrO content of the carbonate minerals against stratigraphic height is shown in Figure 11.8. Based on crystal-chemical considerations Sr^{2+} (radius of 0.112 nm) should preferentially proxy for Ca^{2+} (radius of 0.099 nm) in the trigonal carbonates, and not for other cations (Fe^{2+}, radius of 0.074 nm; Mg^{2+}, radius of 0.066 nm; and Mn^{2+}, radius of 0.080 nm).

Manganese, on the other hand, should rather proxy for iron on account of the reasonable agreement in ionic radius and comparable ionicity of the bonds with oxygen. Consequently a linear relationship exists between the MnO content and the normative mole per cent siderite of the carbonates (Fig. 11.9). On a 100 per cent normative siderite basis the MnO content of the siderite-rich samples is reasonably constant (mean of 20.3 %, standard deviation of 3.5%, or 17% relative), compared with SrO content of the calcite-rich samples (mean of 0.84 %, standard deviation of 0.9%, or 107% relative). The MnO content of the carbonate minerals, therefore, does not appear to be suitable for distinguishing different pulses of carbonate formation.

Digitised by the Department of Library Services in support of open access to information, University of Pretoria, 2021

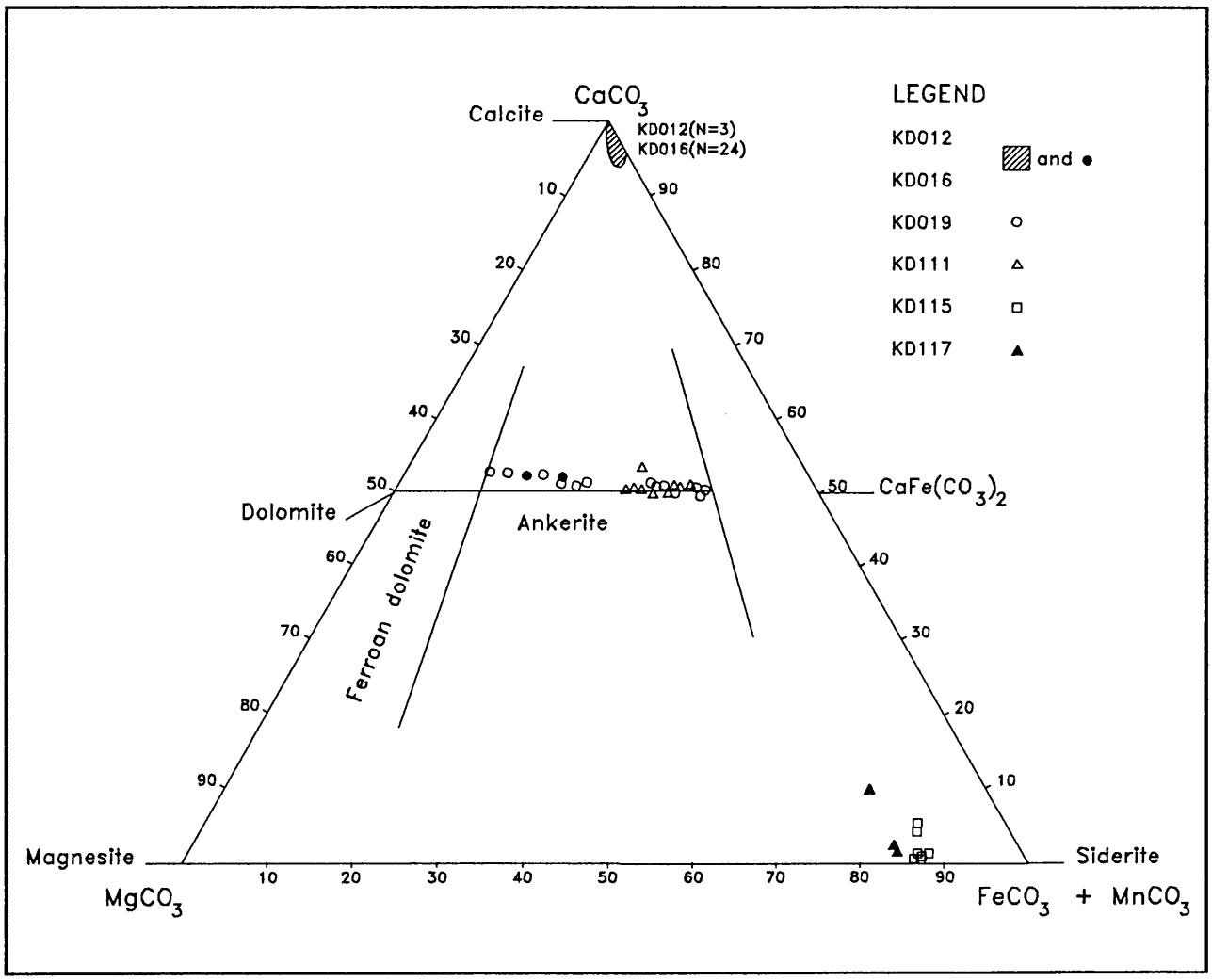

Figure 11.5 Composition (mol%) of carbonates from the upper ash flow, lapilli tuff, and upper part of the ferruginous lapilli tuff units of the KD01 sequence.

Digitised by the Department of Library Services in support of open access to information, University of Pretoria, 2021

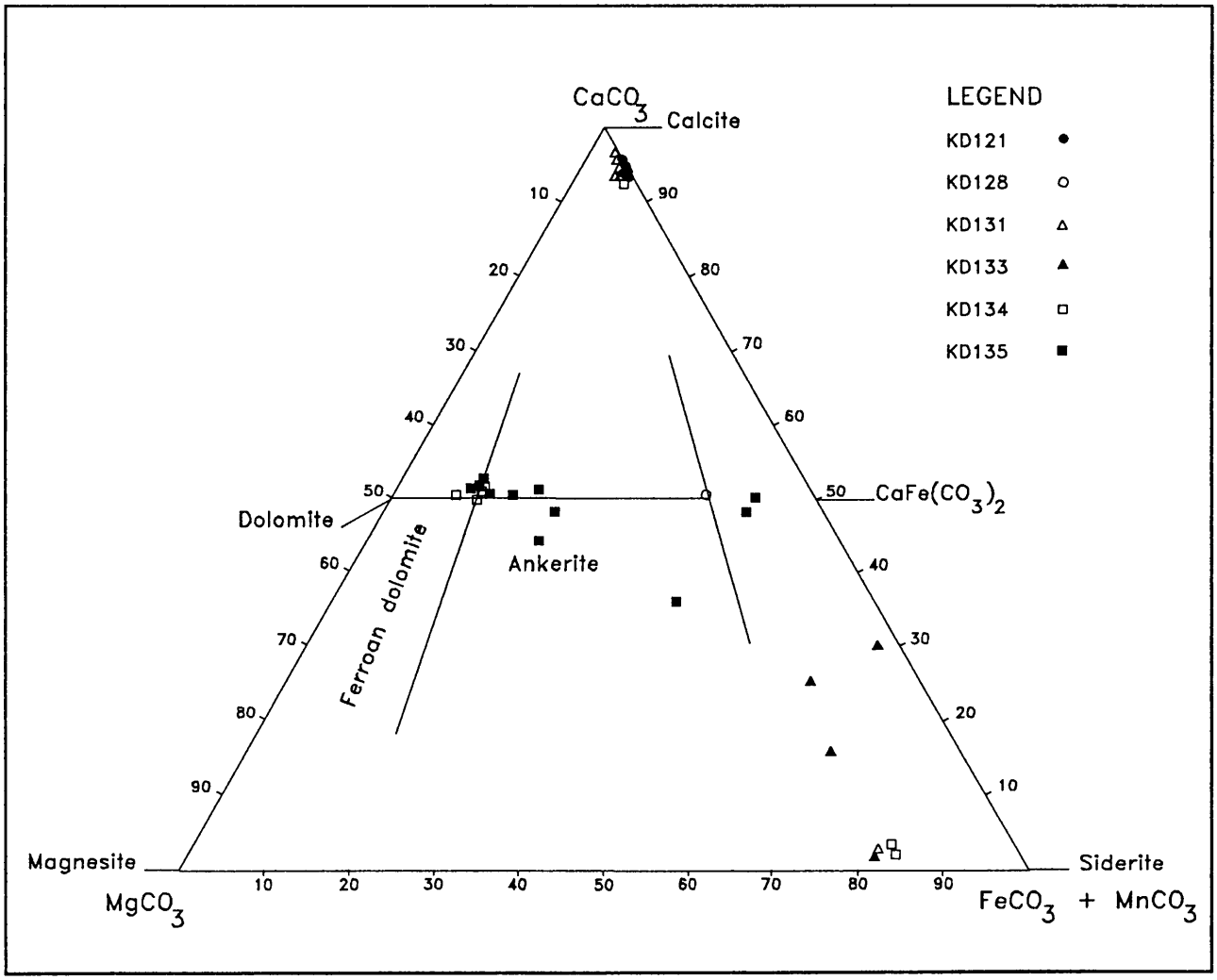

Figure 11.6 Composition (mol%) of carbonates from the ferruginous lapilli tuff and upper part of the lower ash flow units of the KD01 sequence.

Digitised by the Department of Library Services in support of open access to information, University of Pretoria, 2021

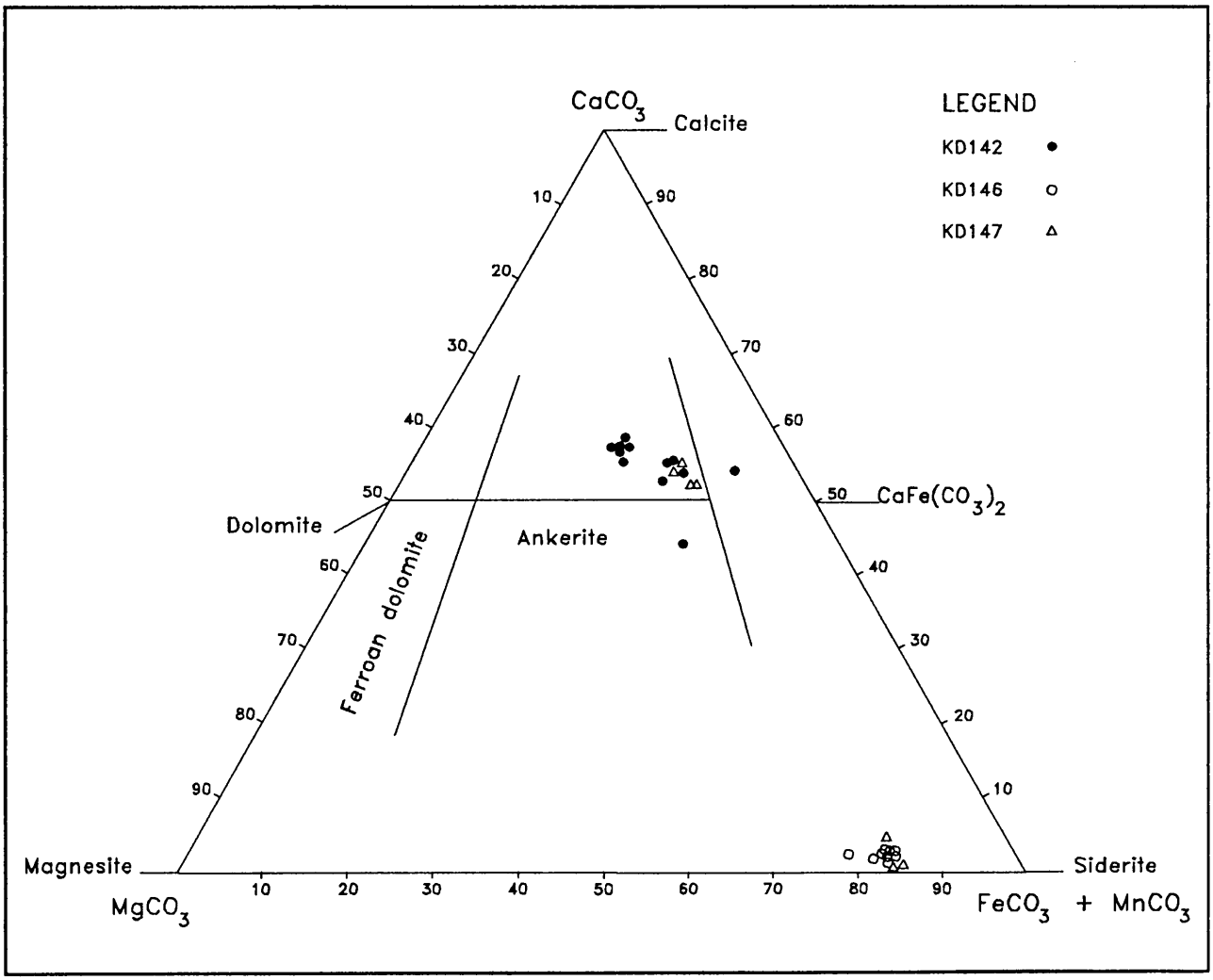

Figure 11.7 Composition (mol%) of carbonates from the lower part of the lower ash flow unit of the KD01 sequence.

Digitised by the Department of Library Services in support of open access to information, University of Pretoria, 2021

Table 11.1 Summary of the mode of occurrence of carbonate minerals in samples from borehole KD01.

SAMPLE	ASSOCIATED MINERALS	TEXTURE TYPE
KD012	ankerite calcite	(a) intergrown with K-feldspar, apatite, chlorite (b) calcite associated with quartz (c) ankerite veins cut through earlier K-feldspar and apatite in the tuff matrix
KD016	calcite	(a) replacement of ash grains and matrix (b) replacements of: phenocrysts, amygdales and microphenocrysts within the tuff matrix
KD019	ankerite ferrodolomite	(a) replacement of ash grains (b) intergrown with K-feldspar in the matrix
KD111	ankerite ferrodolomite	(a) replacement of interiors of ash grains (with chlorite, fluorite and oxides) (b) intergrown with chlorite in the matrix
KD115	ankerite calcian siderite calcite	(a) matrix replacement (ankerite and calcian siderite) (b) late-stage veining (calcite)
KD117	calcian siderite	(a) matrix replacement (ankerite and calcian siderite)
KD121	calcite calcian siderite	(a) replacement of ash grains (b) calcian siderite occurs as rims or as internal replacement of irregular grains (c) microcrystalline replacement with hematite
KD128	ferrodolomite	(a) matrix / intergrown with chlorite
KD131	calcian siderite calcite	(a) matrix replacement (calcian siderite) (b) overgrowths on ankerite and K-feldspar (c) calcite veins and void filling
KD133	calcite calcian siderite	(a) calcite replacement of ash grains, associated with K-feldspar, ankerite and chlorite (b) calcian siderite replacing the matrix
KD134	calcite ferroan dolomite ankerite calcian siderite	(a) several generations of matrix replacement
KD135	calcian siderite calcite	(a) calcian siderite replacement of K-feldspar (b) late-stage veins and breccia filling (calcite)
KD142	ankerite ferro-dolomite	(a) several generations of matrix replacement
KD146	calcian siderite	(a) replacement of phenocrysts in ash grains (b) veining
KD147	ferro-dolomite calcian siderite	(a) replacement of phenocrysts in ash grains (b) veining

11.2.1 Detailed investigation of sample KD016

Petrographic and cathodoluminescence observations of samples from the KD01 sequence reveal several textural types of calcite (Table 11.1). Sample KD016 consists mainly of ash grains (containing phenocrysts, amygdales and microphenocrysts), and

Digitised by the Department of Library Services in support of open access to information, University of Pretoria, 2021

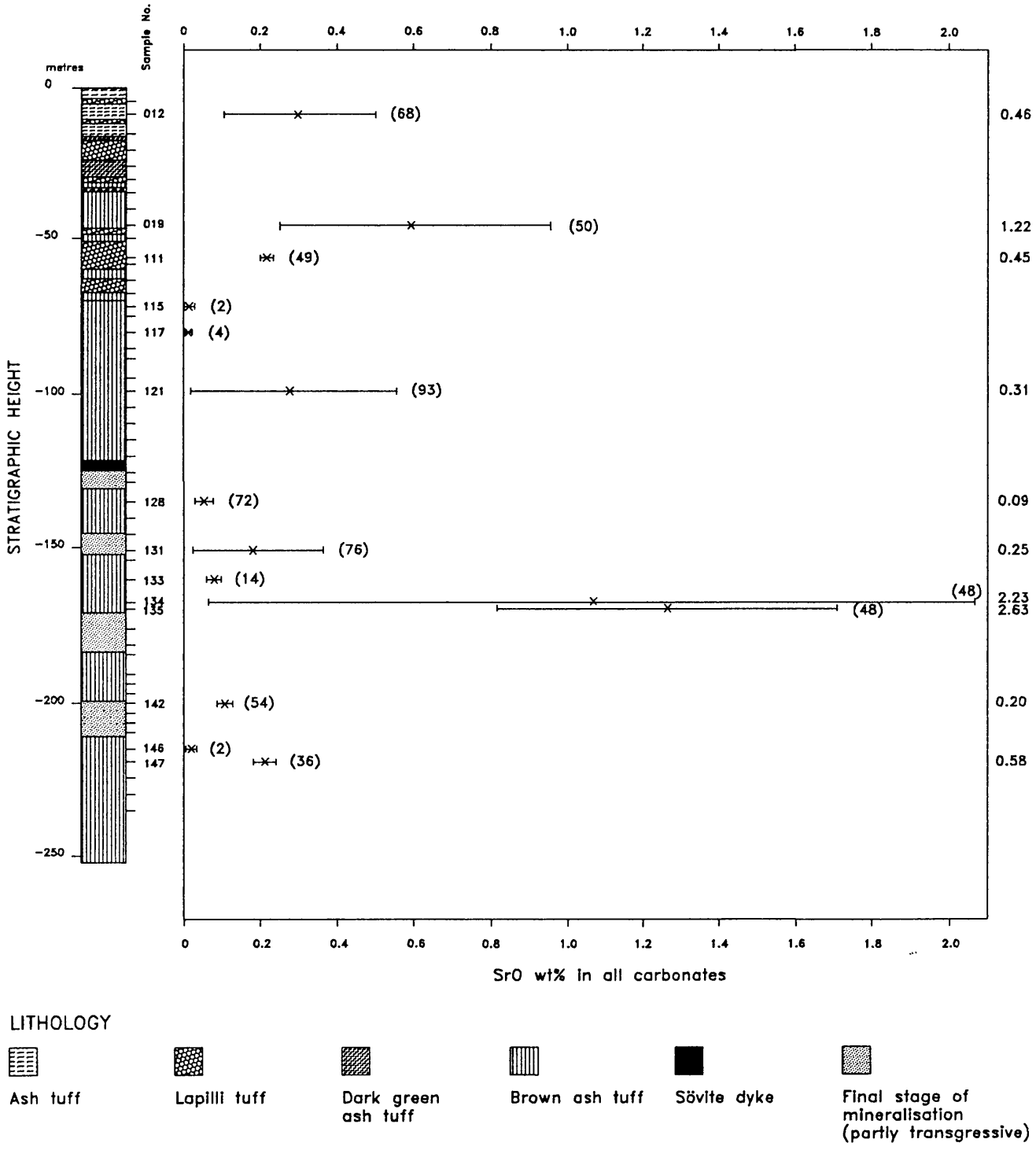

Figure 11.8 SrO content of carbonates against stratigraphic height. Figures in brackets indicate the normative calcite content and those on the right the average SrO content based on 100% normative calcite for relatively calcite-rich samples.

Digitised by the Department of Library Services in support of open access to information, University of Pretoria, 2021

cement composed of polycrystalline strontium-bearing calcite (Appendix 1.2).

Based on their ionic radii and the percentage ionicity of their bonds with oxygen, the affinity of the relevant elements for the calcite structure probably decreases in the order Ce^{3+}, Sr^{2+}, Mn^{2+}, Fe^{2+} and Mg^{2+}. However, the composition of the calcite is also determined by the availability of specific elements. The fact that the calcite composition, as outlined below, does not always agree with that predicted from crystal-chemical considerations, is a further indication of multistage calcite formation.

The calcite of late-stage veins contains the lowest levels of $SrCO_3$ (Fig. 11.10), while some calcite analyses on phenocrysts show normative $Ce_2(CO_3)_3$ contents of up to 0.23 wt%. In the amygdales, the earlier, equant calcite infilling with bright orange luminescence has a $MnCO_3$: $FeCO_3$ ratio of between 0.13 and 29.18 (Fig. 11.10), while the duller luminescent third (and latest) generation of infilling calcite has a lower and more restricted range of $MnCO_3$ and $FeCO_3$ contents. The iron and manganese contents of the dully luminescing second generation amygdale calcite are commonly below the detection limit. $SrCO_3$ values for the early, equant calcite are relatively low, whereas the later calcite has higher values (1.3 to 4.2 wt% $SrCO_3$). The calcite cement has lower $SrCO_3$ contents than the calcite of the amygdales.

The $MnCO_3$: $FeCO_3$ ratios for the calcite veins vary between 0.32 and 5.06, but for the microphenocrysts, it is markedly lower at 0.18 to 11.22. In addition, $MnCO_3$ in microphenocrysts is lower than average for calcite in the sample, being generally below 0.75 wt%. The low ratio and $MnCO_3$ content explain the consistent and relatively dull luminescence of the microphenocrysts.

Discussion

- The textures of the carbonates can be summarised as follows: (a) calcite occurs as replacements of lapilli and ash grains, including delicate textures like phenocrysts, amygdales and microphenocrysts, and also as late stage calcite veins, breccia cement and void fillings; (b) ferrodolomite and ankerite occur mainly as replacements of lapilli and ash grains, as matrix replacements (intergrown with apatite, chlorite and K-feldspar), and as veins; (c) calcian siderite occurs as matrix replacement, associated with K-feldspar, ankerite and fine-grained hematite. It is also evident that the carbonates become progressively more Fe-rich down the KD01 sequence;

Digitised by the Department of Library Services in support of open access to information, University of Pretoria, 2021

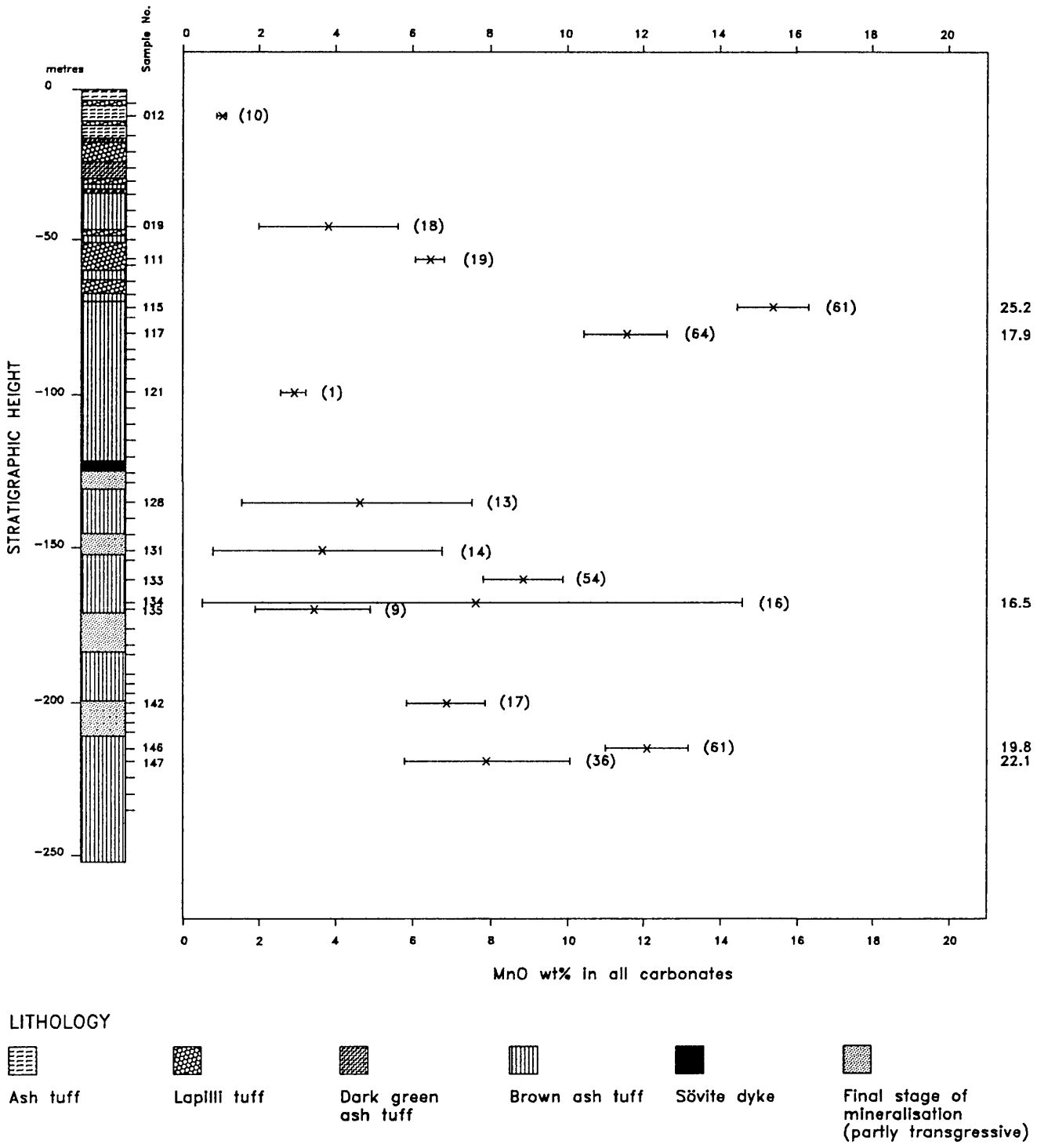

Figure 11.9 MnO content of carbonates against stratigraphic height. Average percentage of normative siderite shown in brackets. Figures on the right are the MnO content based on 100% normative siderite for siderite-rich samples.

Digitised by the Department of Library Services in support of open access to information, University of Pretoria, 2021

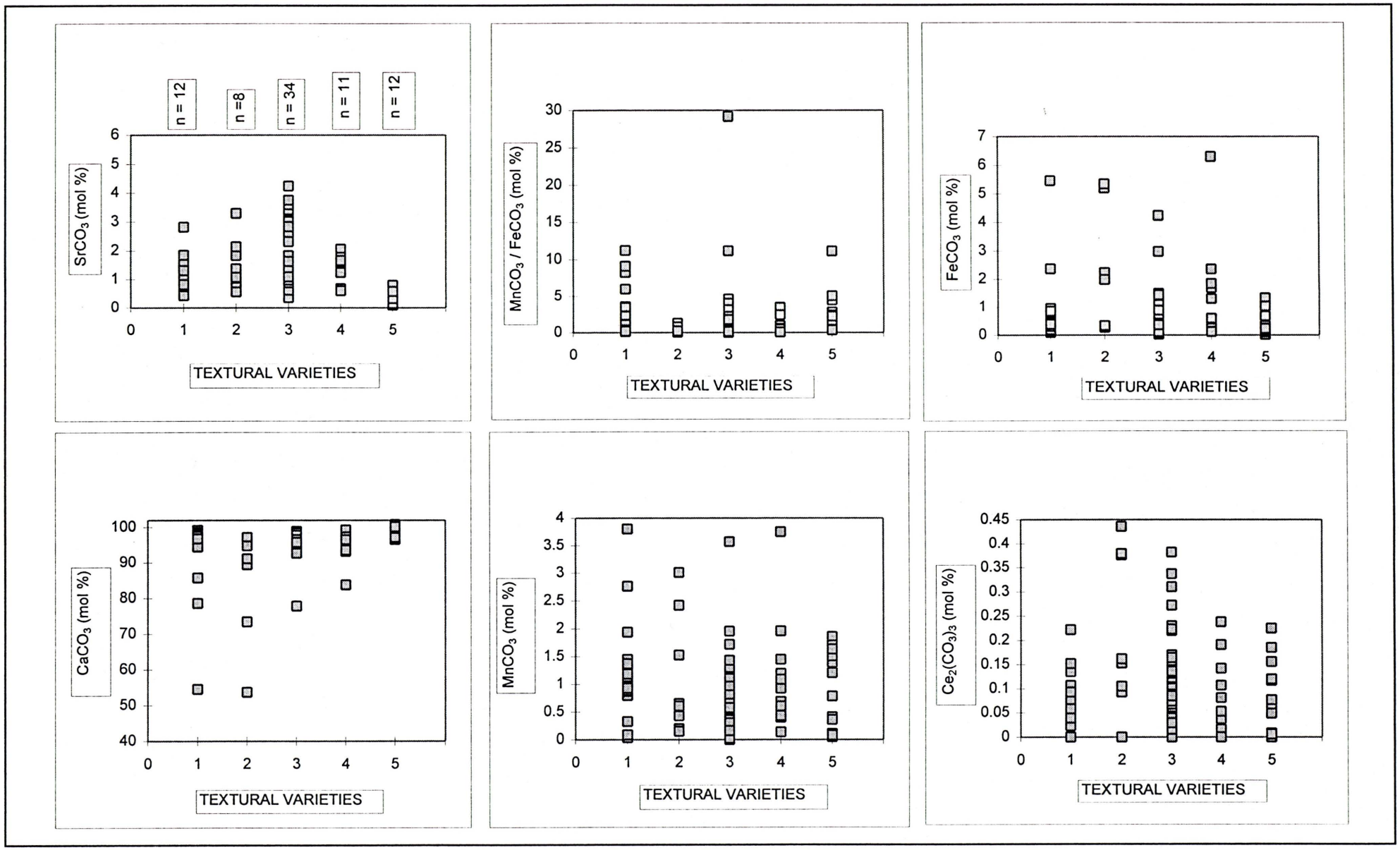

Figure 11.10 $SrCO_3$, $CaCO_3$, $MnCO_3$, $FeCO_3$ and $Ce_2(CO_3)_3$ content and $MnCO_3/FeCO_3$ ratio of different textural varieties of calcite in sample KD016 (1 = phenocrysts; 2 = microphenocrysts; 3 = amygdales; 4 = cement and as 5 = veins). Each square represents one analysis.

Digitised by the Department of Library Services in support of open access to information, University of Pretoria, 2021

- Carbonatite occurs as intrusive, volcanic and hydrothermal bodies (Barker, 1989). Intrusive and volcanic carbonatite complexes are characteristically composed of several episodes of magmatic activity, during which the carbonates display a differentiation from calcium-rich, and to late-stage magnesium- and iron-rich carbonates. The latter types are formed by precipitation from hydrothermal fluids and by replacement of earlier carbonatites and silicate rocks. The manganese content of the carbonatites in this study reflects an increase through the sequence calcite, dolomite, ankerite and siderite, similar to the findings of Quon and Heinrich (1965).
- The erratic behaviour of the SrO contents compared to normative mole per cent calcite (and even on the basis of 100 mole per cent calcite) suggests different pulses of calcite formation. Within one pulse the earlier (i.e. higher temperature) calcite can be expected to have a lower SrO content on account of the larger ionic radius of Sr^{2+}, so that the smaller Ca^{2+} ion would be preferentially accommodated in the structure. This seems to apply to samples KD134 and KD135 where the SrO content varies in accordance with the temperature as inferred from the chlorite composition. Unfortunately too few data points are available to come to a definitive conclusion.

11.3 Apatite

Apatite is one of the most common minerals associated with carbonatites, and occurs as primary and secondary phases. These phases are usually concentrated in (a) intrusive or extrusive carbonatites, and (b) as hydrothermal deposits associated with carbonatitic and alkaline activity.

The unit cell of fluorapatite contains $Ca_{10}P_6O_{24}F_2$. Calcium occupies two distinct positions within the structure: four Ca_i ions are co-ordinated by nine oxygen atoms, and six Ca_{ii} ions are coordinated by six O and one F. Each O is bonded to one P, one Ca_i and then two Ca_{ii} atoms (Hogarth, 1989).

Many substitutions are possible for Ca, P and F in apatite. Calcium is replaced to a limited extent by mainly Sr, rare-earth elements, Fe, Na, and to a lesser extent Mg and Mn. According to Roeder et al. (1987) a common substitute for P is Si, which is coupled with a substitution of Ca by trivalent rare-earth element ions. Smaller amounts of replacement of P by V, As, S and C are possible. F is replaced by Cl and $(OH)^-$.

The rare-earth elements are a cohesive group with similar chemical characteristics. In carbonatites, however, the apatite tends to concentrate light rare-earth elements relative to heavy

Digitised by the Department of Library Services in support of open access to information, University of Pretoria, 2021

rare-earth elements, as the ions of light rare-earth elements ions in oxygen-dominated structures are larger than those of the heavy rare-earth elements. This relative concentration of light rare-earth elements in apatite is further enhanced by the close correspondence in the ionic radii of Ca^{2+} (0.099 nm), Ce^{4+} (0.094 nm) and Eu^{2+} (0.112 nm). The actual rare-earth element concentration in apatite further depends on the apatite structure, and the concentration and chemical characteristics (e.g. complex ions) of the rare-earth elements in the melt or fluid (Roeder et al., 1987).

From the modal distribution of apatite in the KD01 sequence (Table 10.1), it is clear that apatite is mainly concentrated in the upper ash flow and in the upper part of the pyroclastic breccia units. Other samples which contain ≥ 1, but ≤ 5 modal % apatite are KD119 and KD126 of the ferruginous lapilli tuff and lower ash flow units respectively. Details of samples from the upper ash flow and upper part of the lapilli tuff units are given in Table 11.2.

Apatite from carbonatites characteristically has low MnO and high SrO contents. Hogarth (1989) compiled MnO-SrO fields of apatite from skarn, phosphorite, granite pegmatite and carbonatites from localities world-wide. The field for carbonatite is defined by SrO values between 0.5 and 6.0 wt % and MnO values between 0.01 and 0.6 wt %. The apatite analyses of samples KD012 and KD019 overlap partly those of KD134 and largely fall within this defined field (Fig. 11.11).

The apatite from the different samples displays substantial variations in composition. The largest variations occur in SiO_2 (0.0 to 5.7 wt%) and SrO (0.3 to 3.2 wt%), with smaller variations in Na_2O and MgO (Appendix 1.4). Figure 11.12 shows the trends in SrO, Na_2O, MgO, SiO_2 and Ce_2O_3 contents with depth. The Ce_2O_3 and Na_2O contents seem to vary sympathetically and the SrO and MgO contents antipathetically, whereas the mean SiO_2 content shows a peak in the middle of the sequence, which may reflect a positive correlation with Ce_2O_3.

The positive correlations between Ce_2O_3 and Na_2O and between Ce_2O_3 and SiO_2 probably reflect coupled substitutions within the apatite structure:

$$2Ca^{2+} \rightleftharpoons Ce^{3+} + Na^{+}; \text{ and}$$

$$Ca^{2+} + P^{5+} \rightleftharpoons Ce^{3+} + Si^{4+}.$$

The negative correlation between SrO and MgO may be ascribed to the large difference in ionic radii (0.112 nm vs. 0.066 nm), which would make their similtaneous substitution within the apatite structure fairly unlikely.

Digitised by the Department of Library Services in support of open access to information, University of Pretoria, 2021

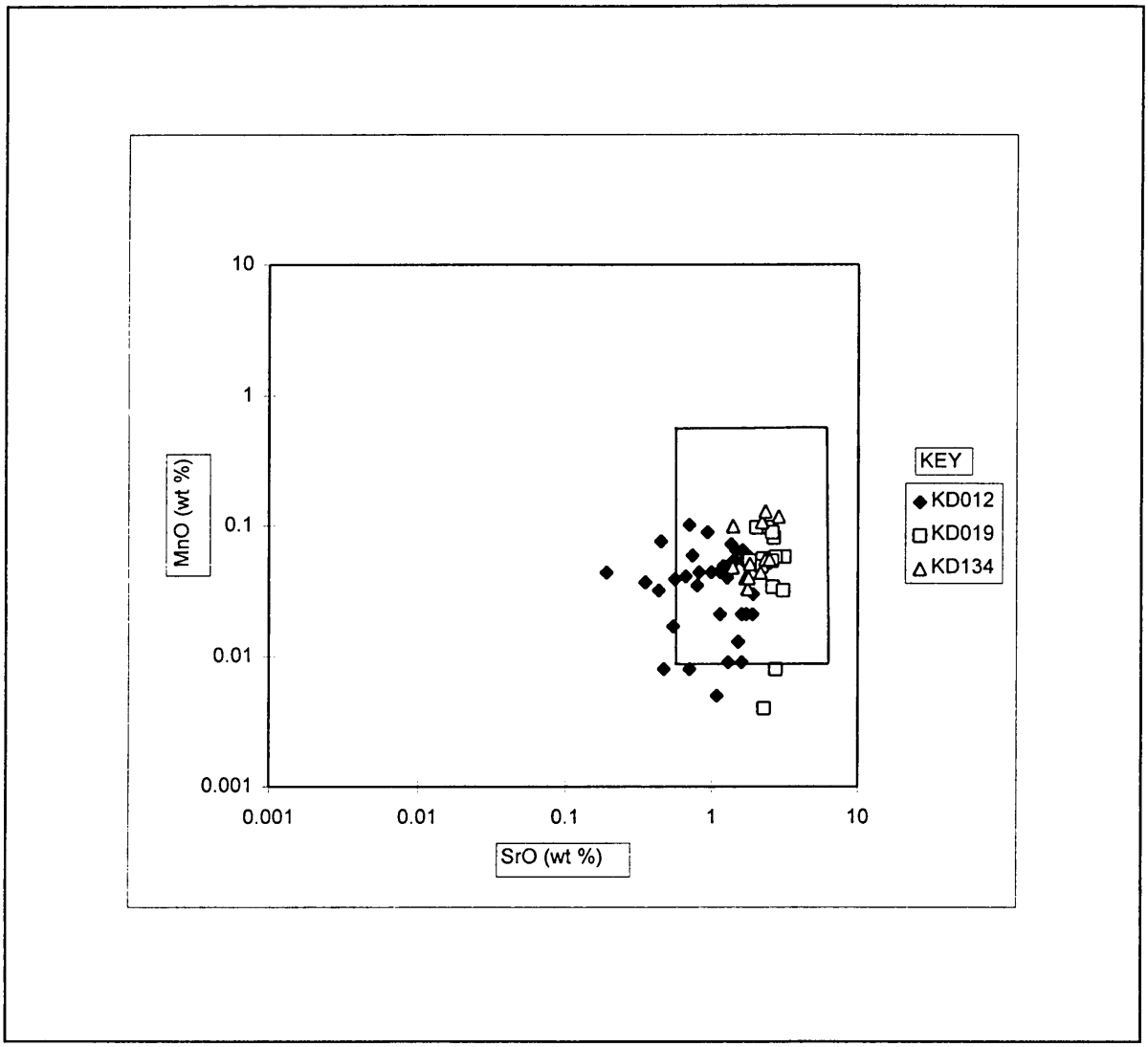

Figure 11.11 SrO against MnO contents of apatite from samples KD012, KD019 and KD134. The MnO-SrO field for carbonatites compiled by Hogarth (1989) is also shown.

Digitised by the Department of Library Services in support of open access to information, University of Pretoria, 2021

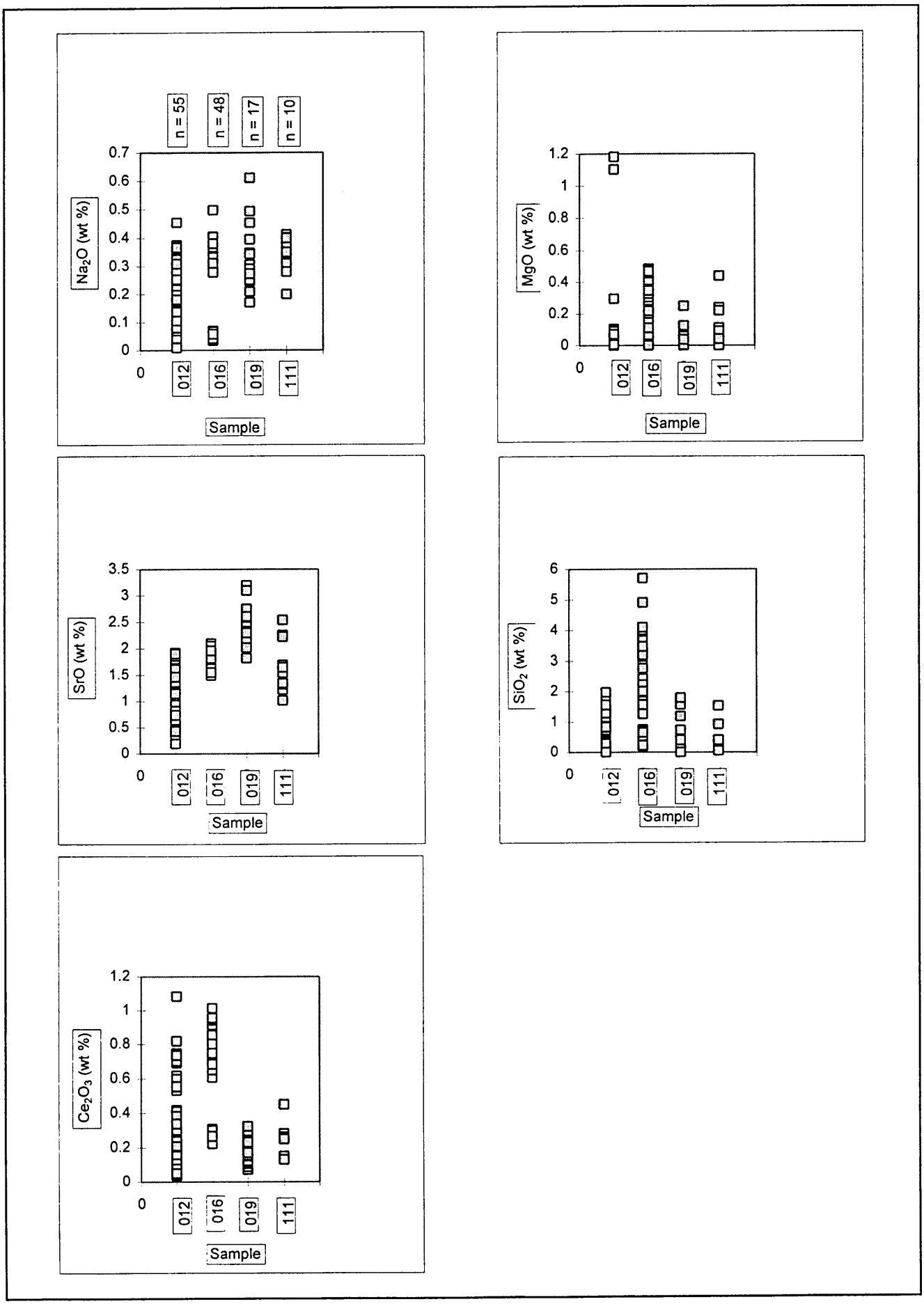

Figure 11.12 Na_2O, MgO, SrO, SiO_2 and Ce_2O_3 contents (wt%) for apatite from samples KD012, KD016, KD019 and KD111, in order of increasing depth.

Digitised by the Department of Library Services in support of open access to information, University of Pretoria, 2021

Table 11.2: Summary of the characteristics of apatite of samples from borehole KD01.

SAMPLE	ASSOCIATED MINERALS	LUMINESCENT COLOURS	APATITE TEXTURE TYPES
KD012	ankerite, calcite, K-feldspar, fluorite, anatase, pyrite	pale blue	(a) euhedral (b) resorbed or replaced (c) fine-grained, resorbed and (d) anhedral grains in rims
KD016	calcite, chlorite, K-feldspar	pale blue to pink	(a) veins (b) euhedral grains in mesostasis (b) fine-grained apatite euhedra in the rims and matrix of ash grains
KD019	ankerite, ferro-dolomite, K-feldspar	pale pink	(a) replacement of relic grains (b) matrix (intergrown with K-feldspar)
KD111	ankerite, ferro-dolomite, K-feldspar, chlorite, anatase		
KD134	calcite, ferroan dolomite, ankerite, calcian siderite, fluorite	orange to violet, blue and turquoise	(a) fine-grained, spherulitic grains

Commonly apatite has rare-earth oxide values ranging between 0.4 and 5 wt%. Apatite concentrates from Phalaborwa contain between 0.4 and 0.9 wt% rare-earth oxide (Russell, 1977; Verwoerd, 1986; Schürmann and Harmer, 1998). According to Mariano (1989b) apatite from the Bond Zone of Oka, Quebec, and Mineville, New York, has averages of 8.6 and 4 wt% rare-earth oxide respectively.

At the Kovdor carbonatite the SrO content in apatite increases from early to later carbonatite. Strontium enters calcite in early carbonatite, while it is concentrated in apatite, strontianite and barite in later stage carbonatites (Hogarth, 1989). Sodium is present in apatite, with a prominent decrease in secondary or hydrothermal apatite. Magnesium and iron appear to substitute for Ca (Hogarth, 1989). The silica concentration can be variable, but is commonly high.

The variation in the composition of apatite from the upper ash flow and upper part of the lapilli tuff units and from sample KD134 from a mineralised zone in the lower ash flow unit is shown in Figures 11.13, 11.14 and 11.15. Samples KD012, KD016, KD019 and KD111 display negative correlations between SiO_2 and P_2O_5. The four textural apatite types in sample KD012 considered as a single population, display a scattered pattern, but except for one rogue value at about 2% SiO_2, the resorbed apatite seems to be the oldest on account of its high P_2O_5 content; similarly the euhedral grains in the rims of ash grains may be intermediate in P_2O_5 content and in paragenetic sequence. In sample KD016 apatite occurring as euhedral grains (oldest generation), veins (intermediate generation) and in the matrix (youngest generation) display a similar trend. The relative age relationships seem to be a reflection of the fact that $(PO_4)^{3-}$ is more stable than

Digitised by the Department of Library Services in support of open access to information, University of Pretoria, 2021

$(SiO_4)^{4-}$ due to the higher charge and smaller radius of the central ion. However, such a deduction does not take the effect of other ionic substitutions into account.

Positive correlations between Ce_2O_3 and Na_2O of apatite from samples KD012, KD016, KD019 and KD111 is evident (Fig. 11.14), probably reflecting a coupled substitution within the apatite structure:

$$2Ca^{2+} \leftrightharpoons Ce^{3+} + Na^{+}.$$

On account of its low electronegativity and its low ionic potential (i.e. ionic charge/ionic radius) sodium forms much weaker bonds with oxygen than calcium. Consequently it can be expected that sodium (and in this case by implication cerium) would be admitted into late formed apatite. Therefore, the apatite in veins (sample KD016) are the youngest, that in the matrix intermediate and the euhedral apatite grains the oldest. Similarly, in sample KD134 the apatite with blue luminescence would be older than the apatite with turquoise luminescence. In samples KD012, KD019 and KD111 no unique deductions are possible due to the degree of overlap.

11.3.1 Detailed mineral chemistry

11.3.1.1 Sample KD012

Four different types of apatite have been recognised in sample KD012 (Table 11.2, and Fig. 11.15). The SiO_2 and SrO content seem to vary apathetically, probably due to the admission of the large Sr^{2+} (radius of 0.112 nm) in the calcium positions of phosphorus-rich apatite. The Ce_2O_3 and SrO contents seem to vary sympathetically, probably due to the admission of Na^{+} (together with Sr^{2+}) in the calcium positions of apatite, and therefore requiring the simultaneous substitution of a Ca^{2+} by Ce^{3+} to maintain electrical neutrality.

11.3.1.2 Sample KD016

Several generations of apatite occur within the sample (Table 11.2) and representative analyses are shown in Figure 11.16. The positive correlations between Na_2O and Ce_2O_3, SrO and SiO_2 and SrO and MgO and negative one between CaO and SiO_2 reflect possible coupled substitutions within the apatite structure:

$$2Ca^{2+} \leftrightharpoons Ce^{3+} + Na^{+};$$

$$10Ca^{2+} + 6P^{5+} \leftrightharpoons 7Ce^{3+} + 2Sr^{2+} + Na^{+} + 6Si^{4+}; \text{ and}$$

$$2Ca^{2+} \leftrightharpoons Sr^{2+} + Mg^{2+}$$

Digitised by the Department of Library Services in support of open access to information, University of Pretoria, 2021

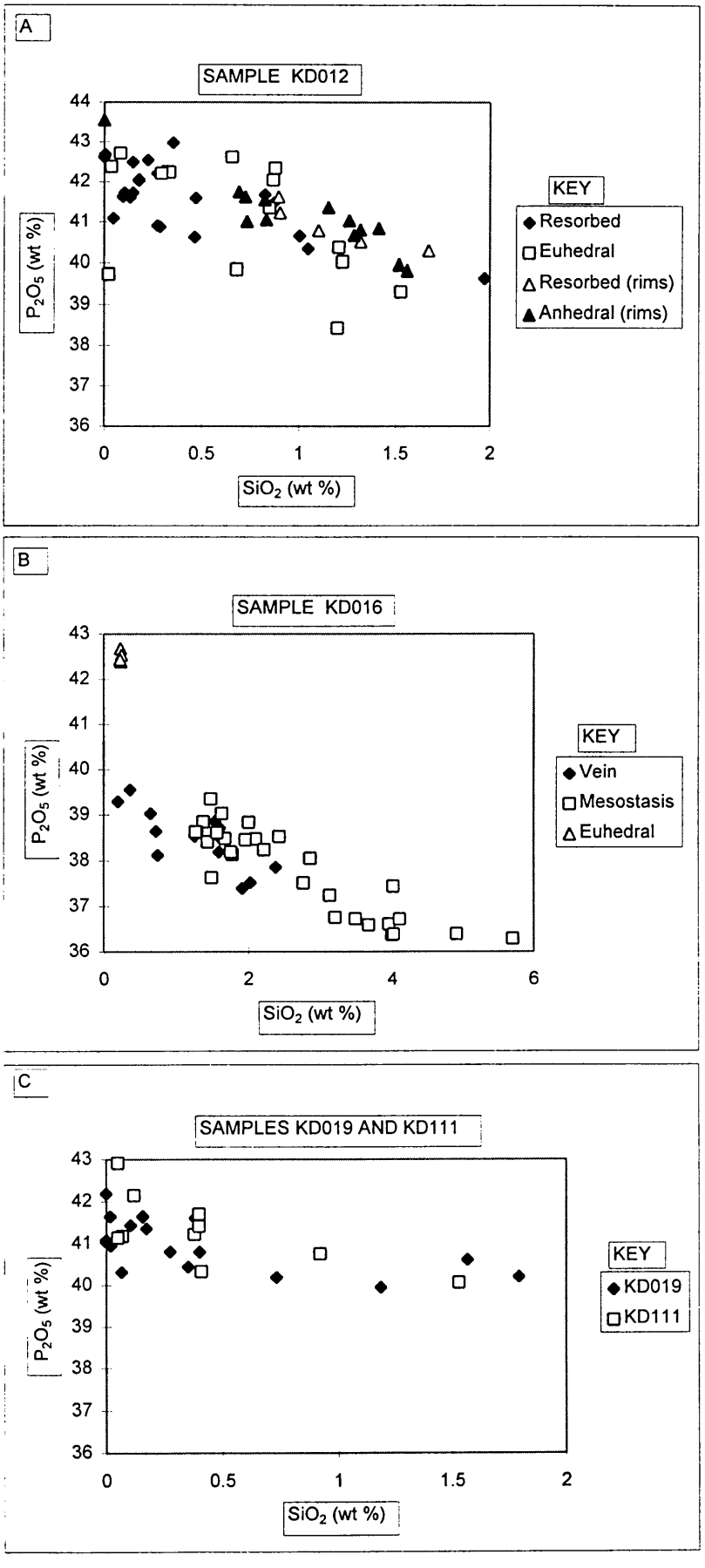

Figure 11.13 SiO_2 against P_2O_5 (wt%) of apatite for samples (A) KD012, (B) KD016, (C) KD019 and KD111.

Digitised by the Department of Library Services in support of open access to information, University of Pretoria, 2021

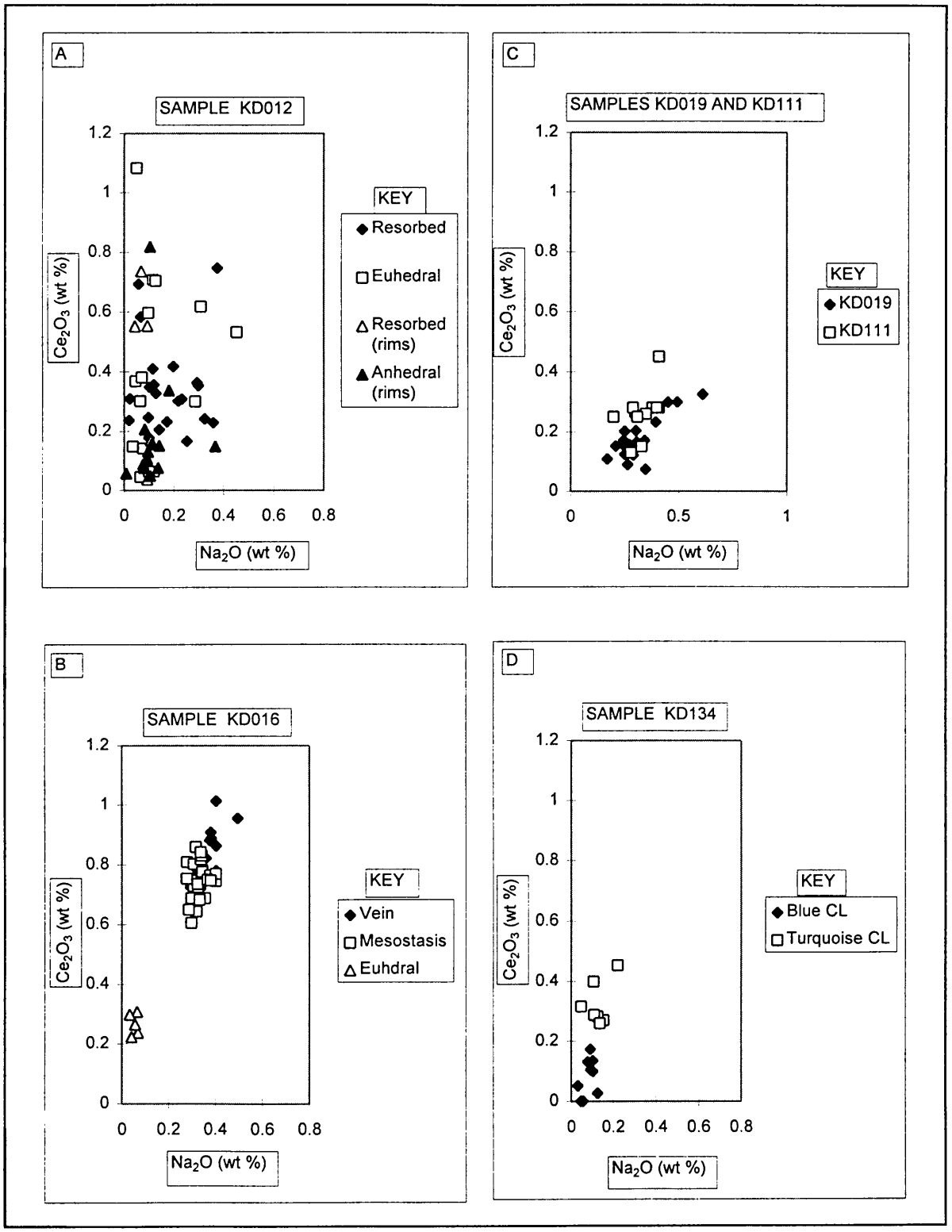

Figure 11.14 Na_2O against Ce_2O_3 (wt%) of apatite for samples (A) KD012, (B) KD016, (C) KD019 and KD111, and (D) KD134.

Digitised by the Department of Library Services in support of open access to information, University of Pretoria, 2021

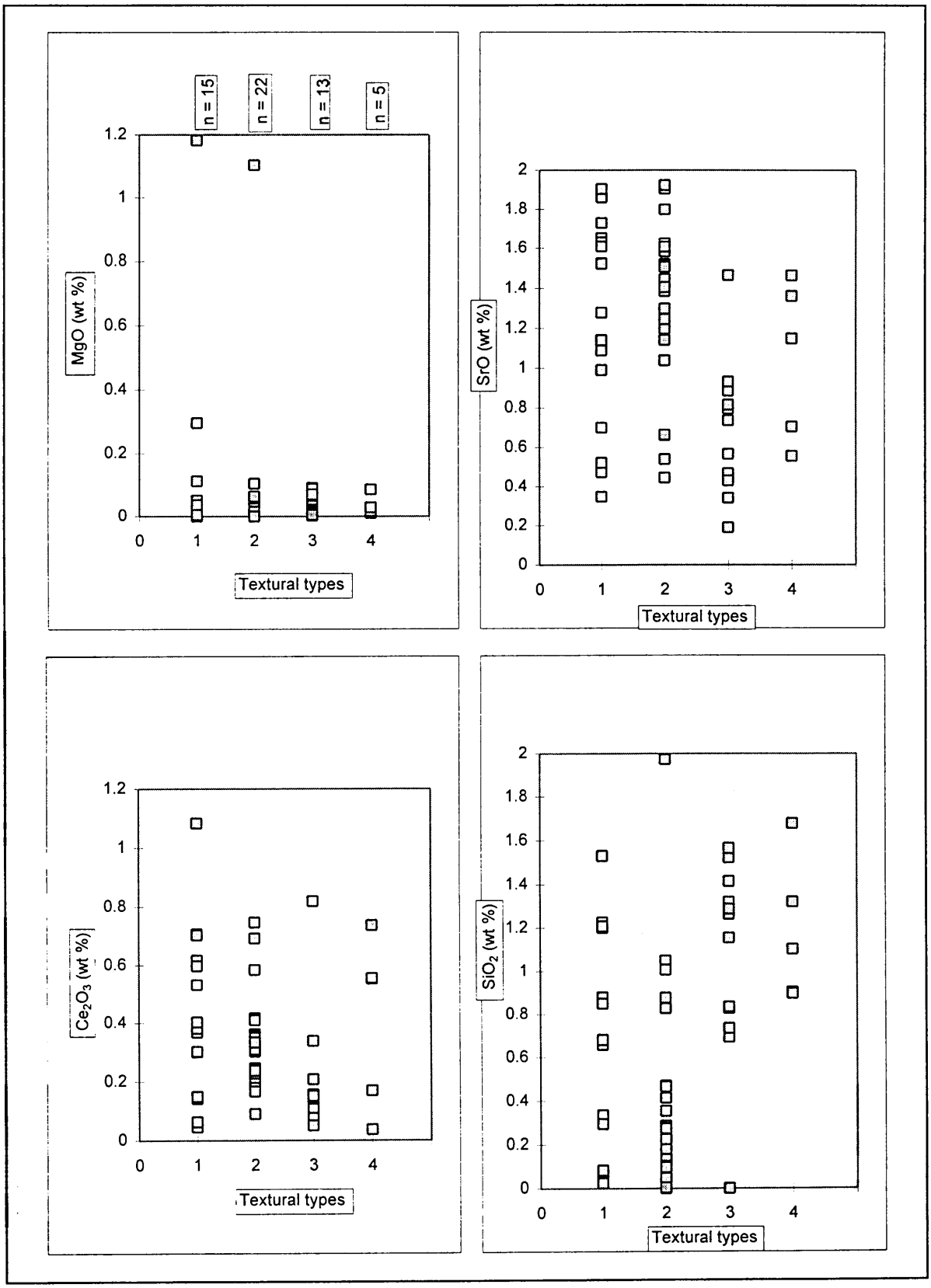

Figure 11.15 MgO, SrO, Ce_2O_3 and SiO_2 (wt%) contents of different textural types of apatite in sample KD012 (1 = euhedral; 2 = resorbed; 3 and 4 = apatite on grain rims).

Digitised by the Department of Library Services in support of open access to information, University of Pretoria, 2021

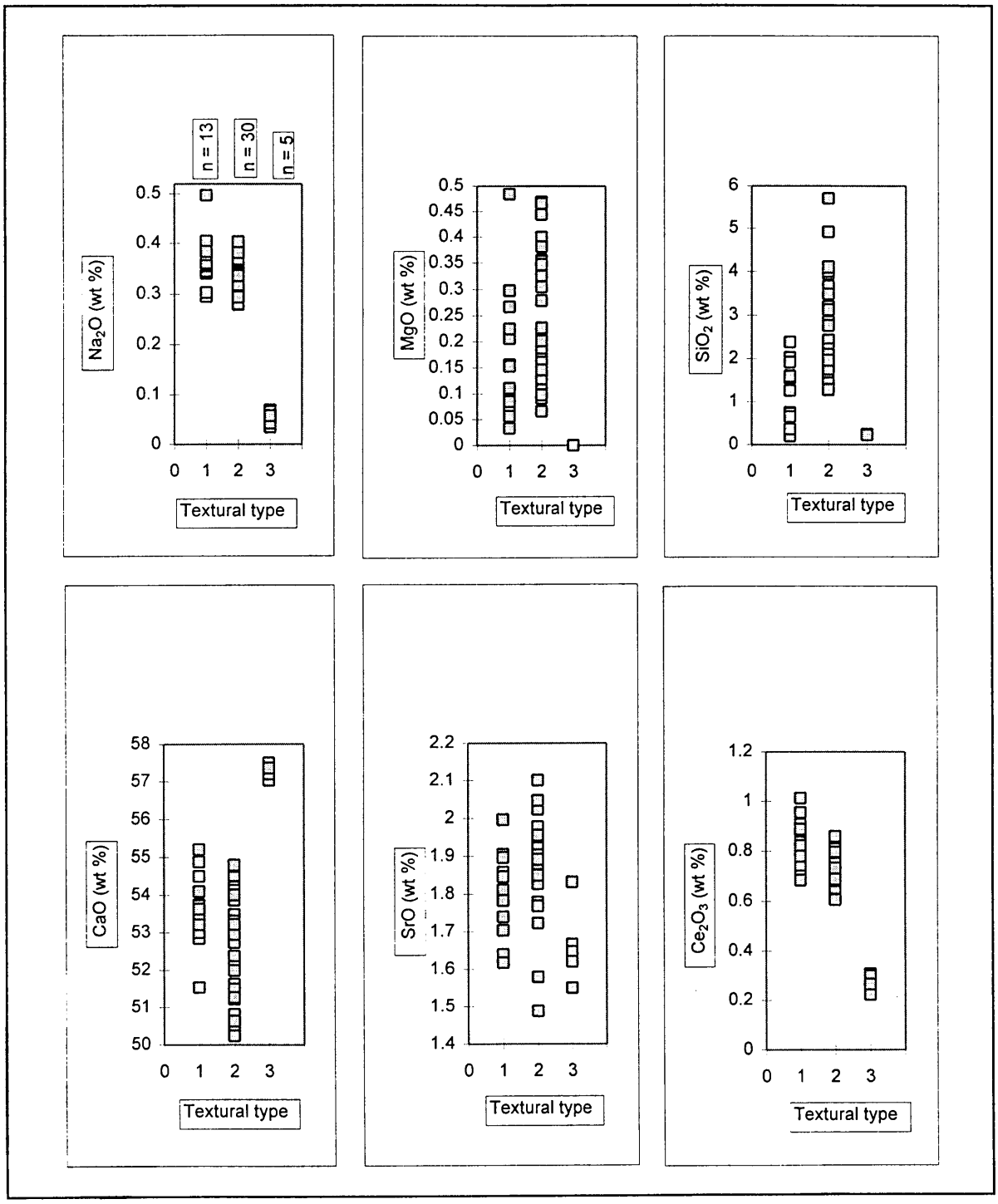

Figure 11.16 Na_2O, MgO, SiO_2, CaO, SrO and Ce_2O_3 (wt%) contents of different apatite textural types in sample KD016 (1 = vein; 2 = ash grain mesostasis; 3 = apatite euhedra).

Digitised by the Department of Library Services in support of open access to information, University of Pretoria, 2021

11.3.1.3 Sample KD134

Apatite from sample KD134 display several types (Table 11.2) based on the luminescence: orange, violet, blue and turquoise. Representative chemical analyses of (a) blue and (b) turquoise luminescent apatite are presented in Figure 11.17. The turquoise luminescent apatite contains a low percentage FeO (0.0 to 0.2 wt%) and a high percentage Ce_2O_3 (0.25 to 0.47 wt%), whereas the blue luminescent type displays the opposite (FeO 0.1 to 1.7 wt% and Ce_2O_3 0.0 to 0.16 wt%). This negative correlation may be ascribed to the large difference in ionic radii (0.074 nm for Fe^{2+} vs. 0.112 nm for Ce^{3+}), which would make their similtaneous substitution within the apatite structure unlikely.

11.3.2 Discussion

A study by Roeder et al. (1987) shows that there is a positive relationship between cathodoluminescence of apatite and the content of rare-earth elements. Of the fourteen samples investigated by them, four were compared with examples of this study: (a) supergene apatite from Australia, which occurs as botryoidal masses in laterite overlying carbonatite; (b) apatite associated with quartz, augite, microcline, sodic plagioclase, calcite, allanite and trace amounts of thorite, hematite, rutile and fluorite, from a granite pegmatite, north of Timmins, Ontario, Canada; (c) apatite from Llallagua, Bolivia, which occurs as transparent to translucent crystals in the Contacto vein, XX Mine; and (d) apatite from pyroxenite of the Tapira Carbonatite Complex, Minas Gerais, Brazil.

Natural apatite shows luminescence due to the presence of elements that function as activators or coactivators. Generally, principal activators are Mn^{2+}, Sm^{3+}, Dy^{3+}, Tb^{3+}, Eu^{2+} and Eu^{3+} (Mariano and Ring, 1975), of which Mn^{2+} in apatite produces a broad band in the yellow-green part of the visible spectrum. Eu^{2+}, which is sensitive to structural changes within a host crystal (Roeder et al., 1987), produces a strong blue component of the spectrum.

The apatite in the lateritic sample from Australia, has an excellent resolution of the luminescence of Sm^{3+} and Dy^{3+} due to the absence of the broad Mn^{2+} band. The apatite from Timmins, Ontario produces major Sm^{3+} (595 nm) and Dy^{3+} (568 nm) peaks which seem to coalesce due to a broad Mn^{2+} peak. The Tapira apatite presents a major Tb^{3+} peak, although Tb is usually present in only trace amounts. Most of the peaks described fall in the yellow-orange (560 to 600 nm) part of the spectrum, due to the dominant activators Sm^{3+}, Dy^{3+} and Mn^{2+}. The Llallagua apatite has been shown by Roeder et al. (1987) to have a less prominent Mn^{2+} and four Eu^{3+} peaks (585, 613, 645 and 690 nm),

Digitised by the Department of Library Services in support of open access to information, University of Pretoria, 2021

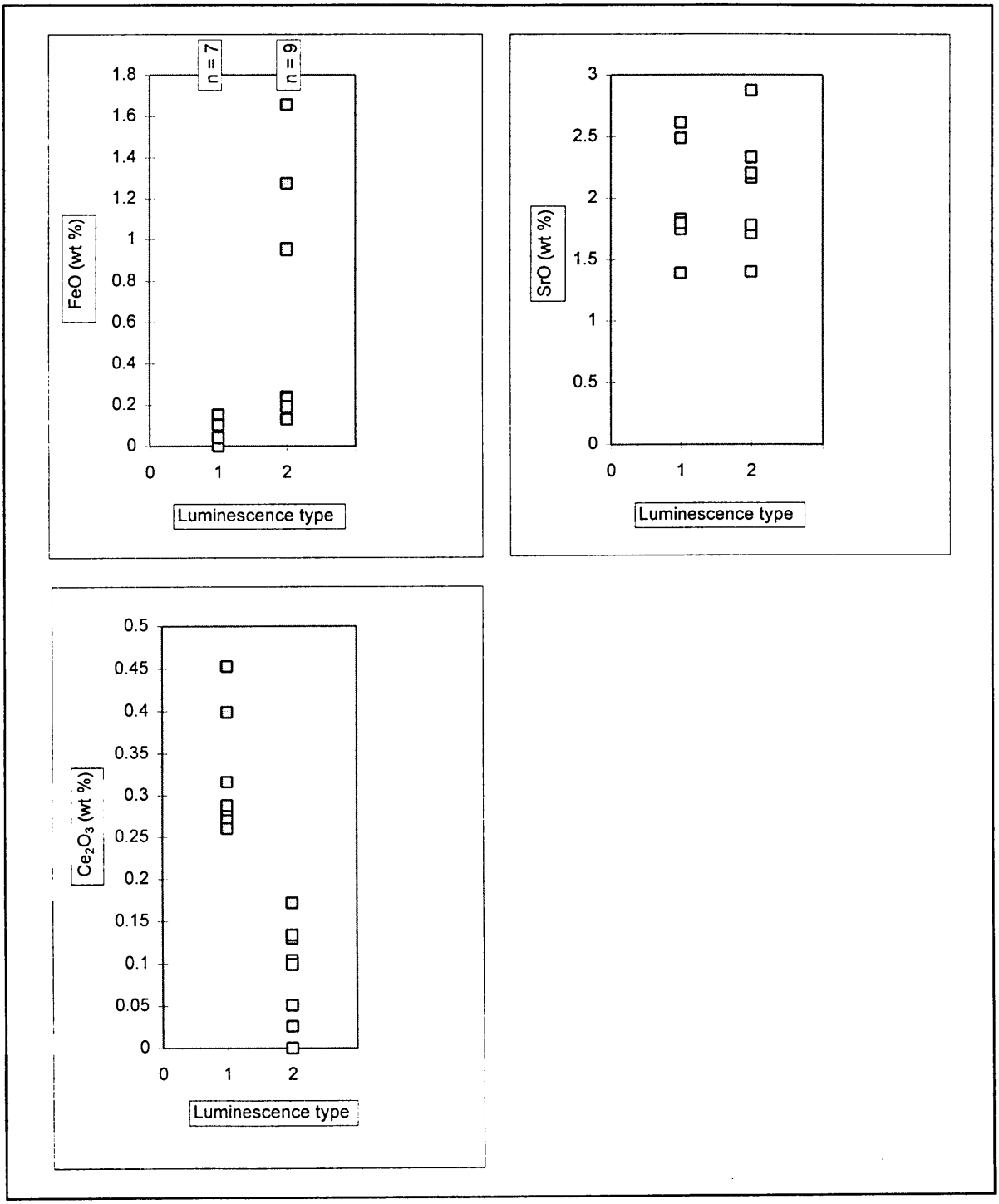

Figure 11.17 FeO, SrO and Ce_2O_3 (wt%) contents of different luminescence types seen in apatite in sample KD134 (1= turquoise luminescence; 2 = blue luminescence).

Digitised by the Department of Library Services in support of open access to information, University of Pretoria, 2021

thus producing yellow to orange to red luminescence colours. A peak at 450 nm is also identified due to the presence of Eu^{2+}, producing a strong blue luminescence.

The luminescence of the apatite in the KD01 sequence is turquoise, pale to violet blue to pink. Colours may vary from blue to violet, depending on the rare-earth element activators Eu^{2+}, Sm^{3+} and Dy^{3+}. Blue luminescence in sample KD134 is indicative of primary apatite, and is largely due to Eu^{2+} activation. The hydrothermal apatite (KD134) possibly displays dominant Mn^{2+} activation, with weaker line spectra from Sm^{3+} and Dy^{3+}. Dysprosium emission is seen to be stronger than that of Sm^{3+}, reflecting a heavy rare-earth element dominance (Marshall, 1978).

11.4 Fluorite

Fluorite (CaF_2) is a very common accessory mineral in carbonatites and associated alkaline rocks, often occurring in economical concentrations. In fluorite the Ca ions are arranged on a cubic face-centred lattice. Each Ca is coordinated by eight F ions and each F is surrounded by four Ca ions arranged at the corners of a regular tetrahedron (Deer et al., 1992). Fluorite consists mainly of Ca and F. Calcium can be replaced by mainly Sr, Y and Ce.

The largest carbonatite-related fluorite deposits are confined to late-carbonatite or hydrothermal activity (Mariano, 1989b). Carbonatite-derived fluids, with low crystallisation temperatures (100 to 150 °C) as revealed by fluid inclusions, deposit fluorite in overlying pyroclastic sediments and lavas. In the inner zone of the Kruidfontein Complex fluorite, associated with calcite, ankerite, quartz and barite, is an important constituent of the calcite-carbonatite and calcite-fluorite-carbonatite dykes. These dykes contain an average of 10% CaF_2, but in some occurrences fluorite becomes a major constituent with concentrations varying between 15 and 50% CaF_2 (Crocker et al., 1988). The fluorite is interstitial with respect to the calcite grains, and vug fillings and veinlets are also common. Two replacement textures can be observed (Clarke, 1989): (a) ankerite-calcite replacement, in fluorite-poor portions of the mineralised carbonatite dykes, consists of fine-grained ankerite partly replacing calcite; and (b) fluorite-calcite replacements in fluorite-rich portions, consist of purple fluorite selectively replacing calcite, resulting in a rock composed of ankerite and fluorite.

Sporadic high Sr, Fe and Ce contents are characteristic of the fluorite sampled in the KD01 sequence (samples KD111, KD121 and KD130) (Appendix 1.5) (Fig. 11.18). A negative trend between Sr and Ce contents seems to exist (Fig. 11.18). From crystal-chemical considerations the fluorite from sample KD130 appears to have formed before that from KD121, which in turn appears to predate that from KD111. Different ages are also suggested by Table 11.3.

Digitised by the Department of Library Services in support of open access to information, University of Pretoria, 2021

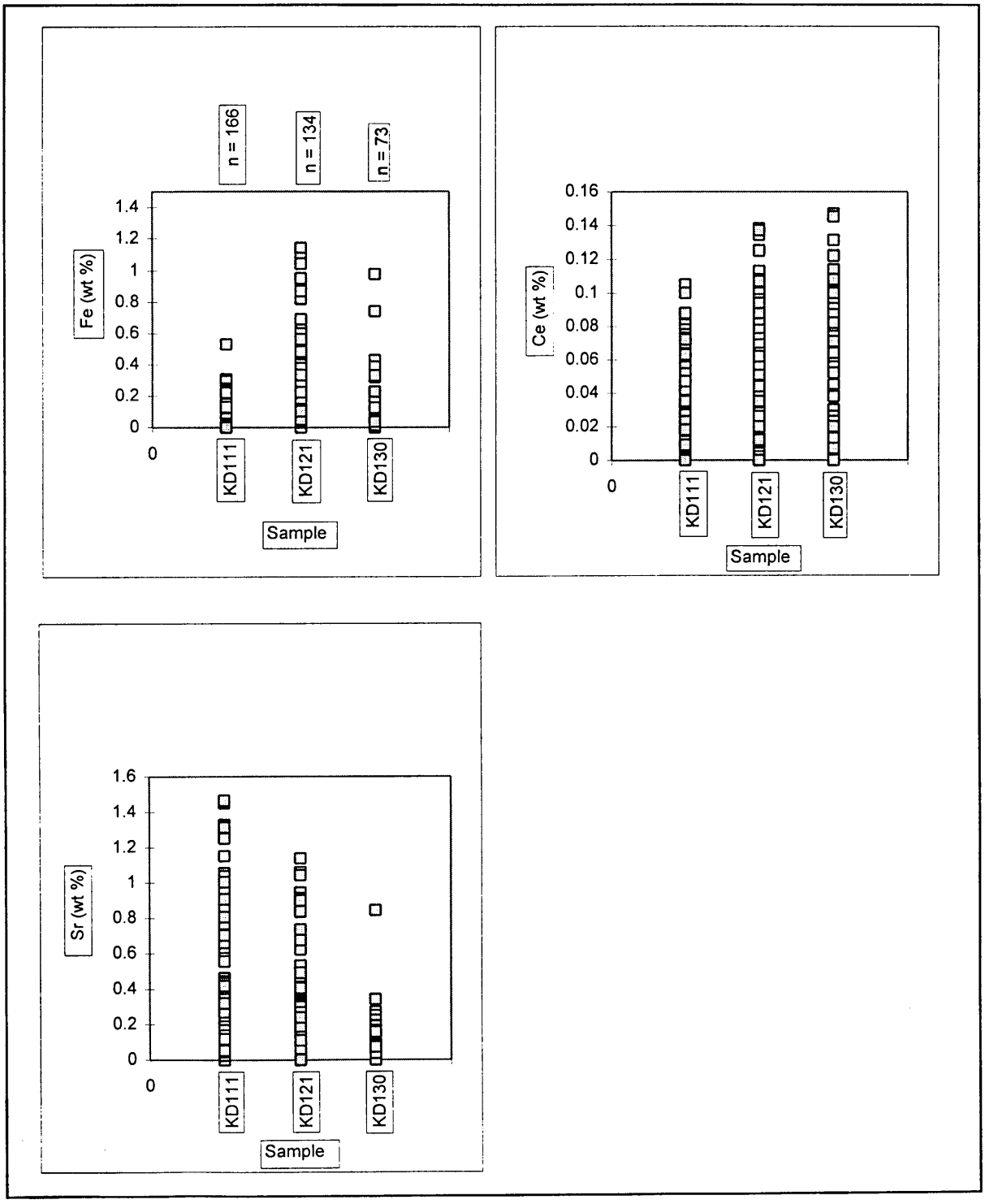

Figure 11.18 Fe, Ce and Sr contents (wt%) for fluorite from samples KD111, KD121 and KD130 taken from the KD01 sequence.

Digitised by the Department of Library Services in support of open access to information, University of Pretoria, 2021

Figure 11.18 shows an increase in Ce and a decrease in Sr content in fluorite with an increase in depth. The Fe content tends to be high in sample KD121, and then decreases to samples KD130 and KD111. No trend between Fe and Sr is apparent.

The fluorite generations identified by means of texture (Table 11.3) are responsible for the trends seen in Figure 11.19A, B and C. Sample KD111 displays a strong negative correlation between Ca and Sr. A clustering of data points towards lower Sr contents is prominent, and is assumed to represent early-formed fluorite (as euhedral grains), compared to the wider spread of data points representing later replacement fluorite (Fig. 11.19A). The data from sample KD121 (Fig. 11.19B) depict a similar negative correlation. The low Sr contents characterise older, euhedral fluorite grains, while the anhedral and aggregated fluorite replacements have higher Sr contents. The small fluorite euhedra in sample KD130 display a low Sr content and a narrow range in Ca content (Fig. 11.19C) suggesting early formation.

Table 11.3: Summary of the mode of occurrence of fluorite of samples from borehole KD01.

SAMPLE	ASSOCIATED MINERALS	LUMINESCENT COLOURS	FLUORITE TEXTURE TYPES
KD111	ankerite, ferro-dolomite, K-feldspar, chlorite, anatase	(a) mid blue (b) pale blue (c) pale blue	(a) euhdral (b) replacements along rim (c) internal, concentric zonation
KD121	calcite, calcian siderite, chlorite, K-feldspar	(a) pale blue (b) dark blue	(a) euhedral grains with concentric zoning (b) anhedral to aggregated small grains and overgrowths on some earlier euhedra
KD130	calcite, calcian siderite, ankerite, chlorite, K-feldspar, opaques	(a) pale blue to dark blue	(a) small, zoned euhedra (b) fine-grained aggregates, replacements and veins

Backscatter electron images show that the fluorite is zoned (Figs. 11.20a, b - photo 510051 and 510054). The brighter irregular areas represent zones which are enriched in elements with high atomic numbers (e.g. Fe, Sr, Y and Ce). A small amount of Fe is present in the fluorite, but this does not correlate with the bright and dark zones.

11.5 Feldspar

The general formula of alkali feldspar is $X[YZ_3O_8]$, where the Si occupies the tetrahedral Z site, Al occupies the Y position, and the large ions K and Na fill the X positions. If more Si is replaced by Al, the formula becomes $X[Y_2Z_2O_8]$, in which X is divalent, e.g. Ca^{2+}, Sr^{2+} and Ba^{2+}. Other elements may enter the feldspar structure e.g. Fe^{3+}, Fe^{2+}, Mg, Ti and Mn (Deer et al., 1992), but on account of the generally large differences in electronegativity and ionic radii of the corresponding major-elements, the amounts are low. Iron as Fe^{3+} should replace Al, while Ca may be replaced

Digitised by the Department of Library Services in support of open access to information, University of Pretoria, 2021

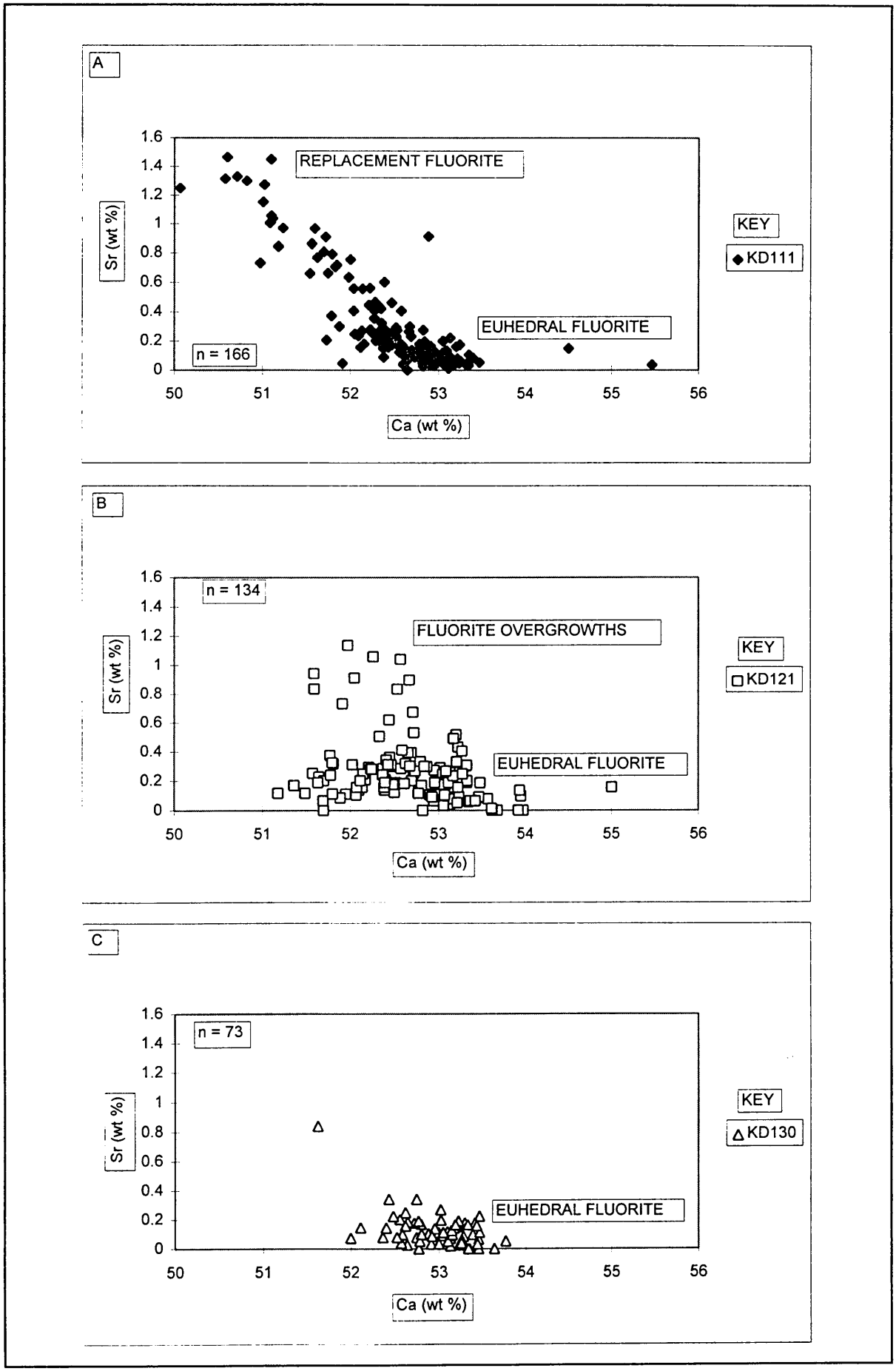

Figure 11.19 Ca against Sr (wt%) for fluorite for samples (A) KD111, (B) KD121 and (C) KD130, taken from the KD01 sequence.

Digitised by the Department of Library Services in support of open access to information, University of Pretoria, 2021

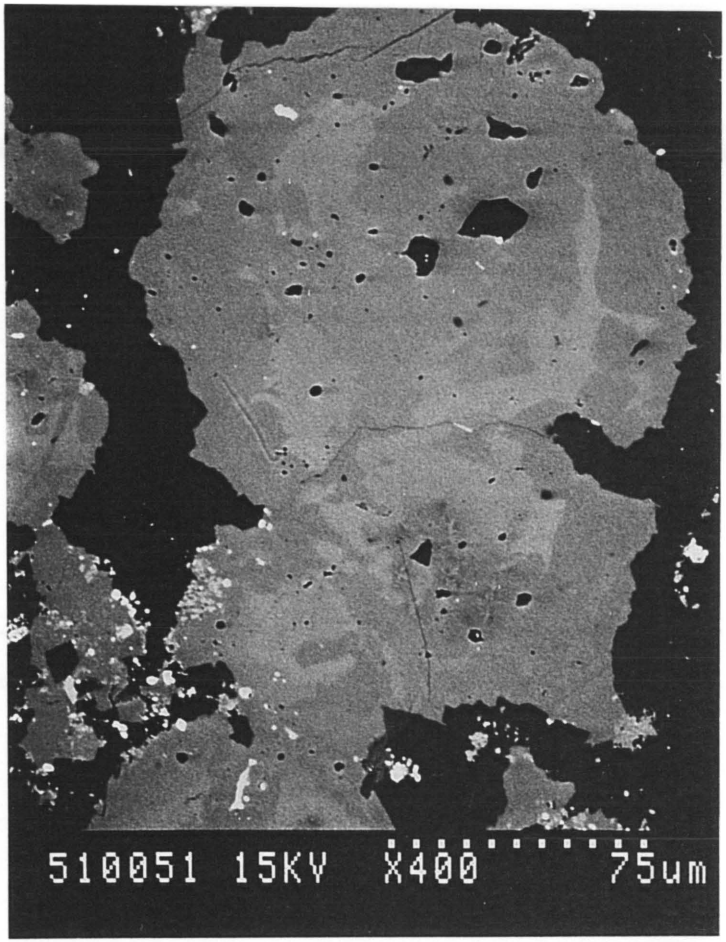

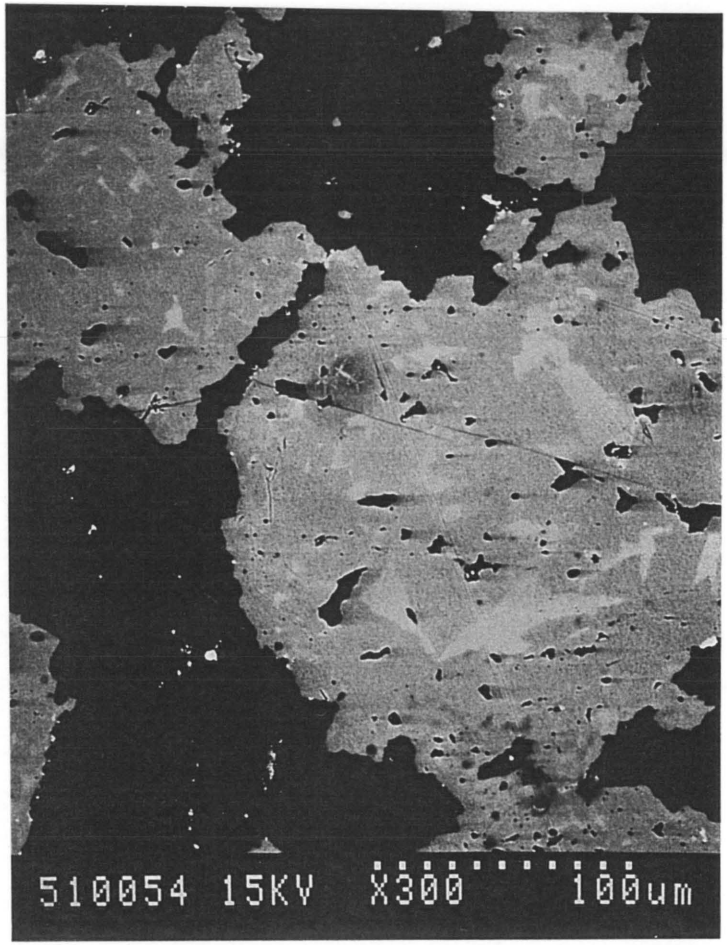

Figure 11.20 Anhedral fluorite (back-scatter images 510051 and 510054) displaying zoning, set within a dark matrix of carbonate and chlorite. The irregular, brighter zones possibly correspond to higher Sr, Fe and Ce contents (sample KD111).

Digitised by the Department of Library Services in support of open access to information, University of Pretoria, 2021

by Fe^{2+}, Mn and Mg. The TiO_2 content is generally low, and Ti is found to replace Al.

Elecromicroprobe analyses of the feldspars from the KD01 sequence are presented in Appendix 1.6. The analyses have been recalculated in terms of cations per 32 oxygens. The largest variations are shown by FeO (0.00 to 2.95 wt%) and SiO_2 (59.46 to 67.76 wt%). The FeO contents and its degree of variation increase with a decrease in stratigraphic height (Fig. 11.21). Smaller variations are observed for Al_2O_3 (17.74 to 19.50 wt%), K_2O (14.88 to 17.12 wt%) and TiO_2 (0.00 to 1.53 wt%). The feldspar is moderately Ba-rich (upto 2.74 wt% BaO).

The composition in weight per cent of the three major feldspar end members is as follows:

- orthoclase: K_2O 16.9%, Al_2O_3 18.4%, SiO_2 64.7%
- albite: Na_2O 11.8%, Al_2O_3 19.5%, SiO_2 68.7%
- anorthite: CaO 20.1%, Al_2O_3 36.7%, SiO_2 43.2%

In samples KD016 and KD019 the relationship between weight per cent K_2O and SiO_2 is linear, so that the orthoclase contents (weight per cent) of the feldspar vary from about 90 to 95 and 88 to 94 respectively (Fig. 11.22). Lower down in the sequence the correlation between K_2O and SiO_2 is weak, probably because larger percentages of Na_2O and CaO are present in the feldspar. Howerver, the orthclase content in the feldspar of a single sample may be up to 100% e.g. from 93 to 100 (KD111), 95 to 100 (KD117), 95 to 98 (KD119) and 92 to 100 (KD124)(Fig. 11.22). This suggests that some of these samples have been subjected to more intense potassium metasomatism. The feldspar compositions in terms of mole per cent of the end members is shown in Figure 11.23.

As summarised in Table 11.4, the feldspar in these samples displays different, and complex luminescence colours. Besides the dull green to grey to bright green colours (present as replacements and overgrowths), grains with red to red-brown and brown luminescent cores and patches are present. Samples KD012, KD016 and KD019 taken from the upper part of the KD01 sequence display fine-grained feldspar replacing structures (lapilli, ash grains and dust) and occurring in veins. All the feldspar present in these samples display bright to dull green luminescent colours. Samples KD124, KD133, KD138 and KD146 are located in close proximity of mineralised zones. They, like the upper part of the KD01 sequence, do not display red to red-brown luminescent colours, but green to yellowish green.

Discussion

- The feldspars studied in the sequence are potassium-rich with significant iron-substitu-

Digitised by the Department of Library Services in support of open access to information, University of Pretoria, 2021

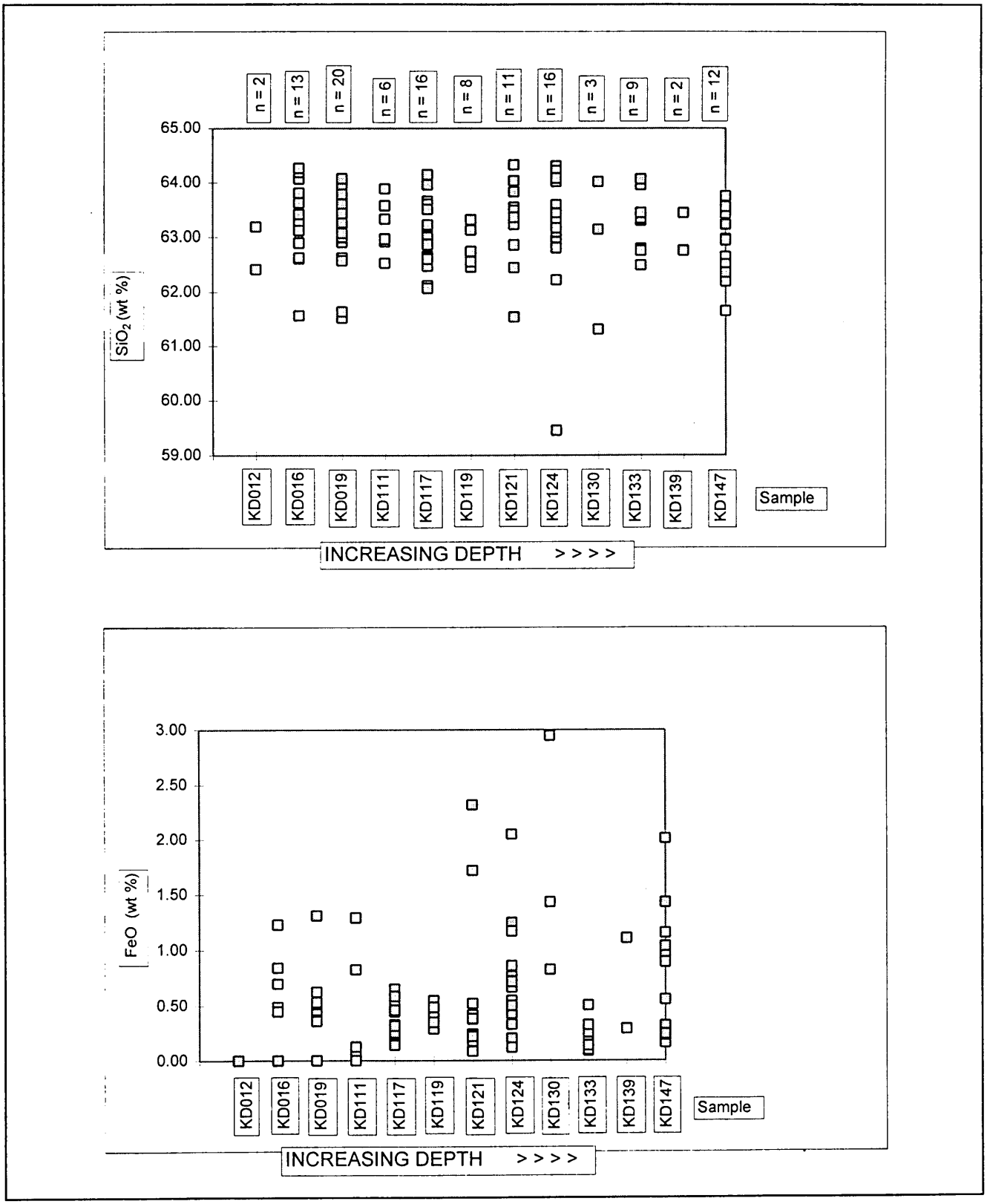

Figure 11.21 SiO_2 and FeO (wt%) contents for feldspars studied in the KD01 sequence.

Digitised by the Department of Library Services in support of open access to information, University of Pretoria, 2021

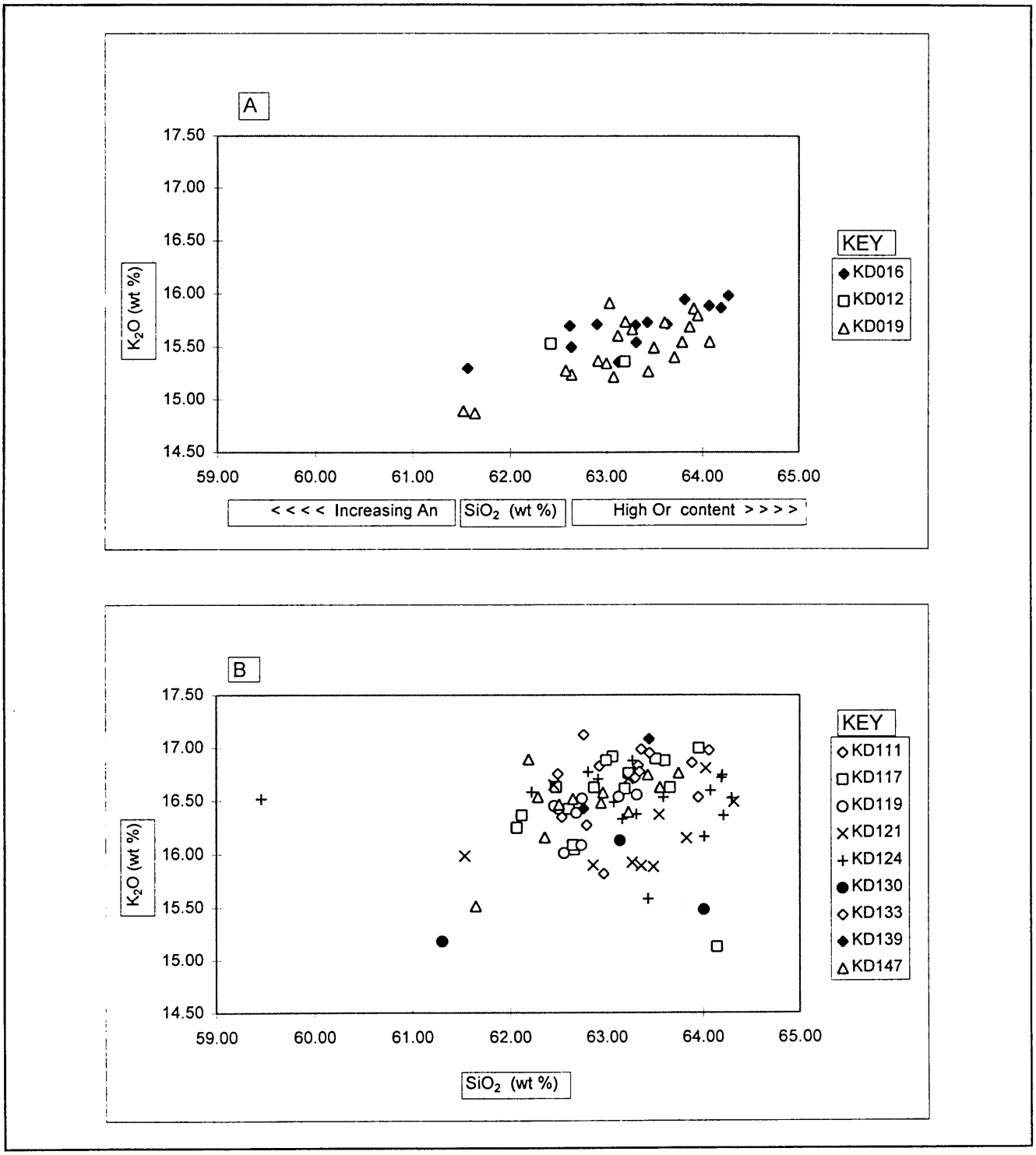

Figure 11.22 SiO_2 against K_2O (wt%) content for (a) samples KD012, KD016 and KD019 of the upper ash flow and pyroclastic breccia units, and (b) samples KD111, KD117, KD119, KD121, KD124, KD130, KD133, KD139 and KD147 of the ferruginous lapilli tuff and lower ash flow units of the KD01 sequence.

Digitised by the Department of Library Services in support of open access to information, University of Pretoria, 2021

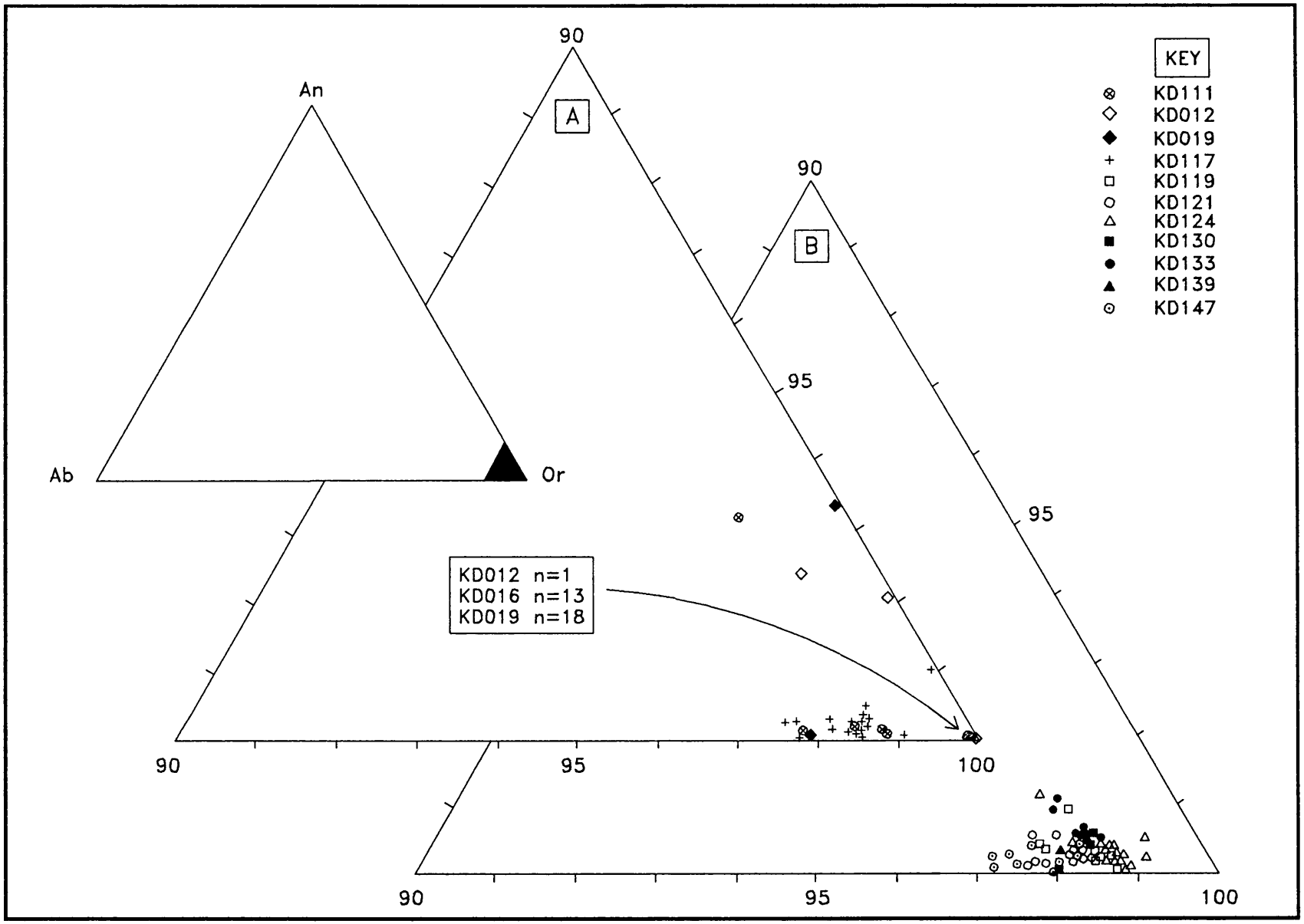

Figure 11.23 Plot of composition (mol %) of feldspars from samples (a) KD012, KD016, KD019, KD111, KD117 and (b) KD119, KD121, KD124, KD130, KD133, KD139 and KD147 taken from the KD01 sequence.

Digitised by the Department of Library Services in support of open access to information, University of Pretoria, 2021

tion. The iron content of feldspar depends on the iron content of the parent magma or the hydrothermal fluid, the temperature of crystallisation and the oxidation state of the iron. Iron substitution can be reflected by a deficiency of Al. Very high Fe_2O_3 contents (in excess of 0.5 wt% for normal feldspars) (Deer et al., 1992) is unusual and can be assumed to be due to inclusions of ferromagnesian minerals as impurities or to an iron mineral which exsolved on cooling.

- Based on the cathodoluminescence investigation, feldspar with red luminescent cores (samples KD019, KD111, KD113, KD115 and KD121) (Table 11.4) are regarded as clasts affected by an earlier fenitisation episode, and which have been incorporated in the present rock where they underwent Fe^{3+} activation.

11.6 Rare-earth minerals

Of all the rare-earth minerals associated with carbonatites, the bastnaesite-group REE-carbonates like synchysite, bastnaesite, parisite and röntgenite are important (Taylor and Pollard, 1995). Mariano (1989b) described hydrothermal mineralisation in the form of ancylite, monazite, or bastnaesite-type minerals as replacements in carbonatites, where they are associated with minerals like fluorite, barite, quartz and strontianite. Wyllie et al. (1995) also stated that rare-earth element mineralisation in most carbonatites is due to hydrothermal action. Late-stage, low temperature carbonatites containing hematite, barite and fluorite are likely to be enriched in rare-earth elements and in U and Th.

The REE-fluorocarbonates include bastnaesite ($(Ce,La)(CO_3)F$), parisite ($(Ce,La)_2Ca(CO_3)_3F_2$), röntgenite ($(Ce,La)Ca_2(CO_3)_3F$) and synchysite ($(Ce,La)Ca(CO_3)_2F$). Bastnaesite has a sheet structure with Ce in irregular coordination with eight O and three F. This bastnaesite-like sheet is interlayered with $CaCO_3$ sheets in patterns BBCBBC... for parisite, BBCBCBBCBC... for röntgenite and BCBC... for synchysite (where B indicates a bastnaesite-like sheet and C a $CaCO_3$ sheet) (Burt, 1989). In ancylite ($SrCe(CO_3)_2OH.H_2O$) Sr can be replaced by Ca, and the Sr/REE ratio varies. Monazite ($(Ce,La)PO_4$), a rare-earth phosphate, dominated by the Ce-group (i.e. light REE).

The geochemical behaviour of rare-earth elements in magmatic systems is mainly controlled by their ionic radii. In fluorite rare-earth elements and Th are held in solid solution, as they proxy for Ca in eight-fold coordination. According to Burt (1989) Ce^{3+} and Th^{4+} substitution for Ca requires a coupled substitution involving Na^+, forming two unit vectors $NaCeCa_{-2}$ (horizontal) and Na_2ThCa_{-3} (vertical). In apatite [$Ca_5(PO_4)_3F$], the Ca or A sites are not all equivalent, two are co-ordinated by 9 and three by 7 to 8 anions. The rare-earth elements, however appear to be able to occupy both sites. Trivalent Ce can substitute for divalent Ca with a coupled substitution by Na

Digitised by the Department of Library Services in support of open access to information, University of Pretoria, 2021

(i.e. 2Ca ⇆ Ce Na), or by a coupled substitution involving the tetrahedral site (e.g. Ca P ⇆ Ce Si).

Table 11.4 Summary of the mode of occurrence of feldspar of samples taken from KD01.

SAMPLE	TYPE (K-feldspar)	LUMINESCENCE	ASSOCIATED MINERALS
KD012	fine-grained replacement of (a) lapilli and grains; (b) vein fillings	bright to dull-green	calcite, ankerite, apatite
KD016	fine-grained replacement of lapilli rims	green	calcite, chlorite, apatite
KD019	fine-grained replacement of (a) matrix and (b) grains	dull-grey to green, yellow and brown-red	ankerite, ferro-dolomite, chlorite, apatite
KD111	fine-grained replacement of (a) lapilli tuff and (b) grains (rims and cores)	dull-green, grey-green to bright yellow, red to brown	ankerite, ferro-dolomite, chlorite, apatite
KD113	fine-grained replacement of (a) matrix and (b) grains	dull olive to grey-green (rims) to brown to red (cores)	chlorite, calcian siderite, ankerite, apatite
KD115	fine-grained replacement of (a) matrix and (b) grains	dull olive to grey-green (rims) to red to brown (cores)	chlorite, ankerite, calcian siderite, calcite, apatite
KD121	replacement of (a) matrix and (b) grains	dull olive to grey-green (rims), red to brown (cores)	chlorite, calcite, calcian siderite, apatite
KD124	fine-grained replacement	yellow-green to red-brown tint (cores) and dull-green (rims)	calcian siderite, ankerite, chlorite
KD130	fine-grained replacement of (a) matrix and (b) grains	greenish to red-brown cores, bright yellow and green rims	calcian siderite, ankerite, calcite, chlorite, opaques
KD133	fine-grained replacement of (a) matrix and (b) lapilli and grains	dull green	calcian siderite, chlorite, calcite, opaques
KD138	fine-grained replacement of matrix	grey-green to bluish	calcian siderite, chlorite, calcite, opaques
KD146	fine-grained replacement of (a) lapilli and (b) matrix	grey-green to greenish yellow	calcian siderite, chlorite, opaques

In aqueous (i.e. hydrothermal) systems rare-earth elements are mobile, as is shown by investigations on seawater (Humphris and Thompson, 1978), groundwater (Martin et al., 1976) and fluid inclusions. Concentrations of rare-earth elements are also enhanced in metasomatised rocks and their distribution also changes as a result of weathering (Henderson, 1995). The mobility of the rare-earth elements is dependent on factors like pH, Eh, temperature, the availability of potential ligands, rock-fluid ratios, constituent minerals and reaction kinetics. Conditions for the complexing of rare-earth elements in aqueous systems are ideal at neutral to alkaline pH, and much less ideal at low pH, where rare-earth element ions tend to be stable. The

Digitised by the Department of Library Services in support of open access to information, University of Pretoria, 2021

halides form some of the more important complexing groups, as seen in the association of fluoride-bearing minerals with rare-earth element enrichment. The trivalent rare-earth elements form strong complexes with fluoride ions of which the strength increases from La to Lu (Henderson, 1995).

Two samples of the KD01 sequence were studied in detail for the presence of rare-earth minerals and their possible mode of occurrence (Table 11.5 and Appendix 1.7). The energy-dispersive analyses of the rare-earth minerals have been normalised according to Wakita et al. (1971). The rare-earth mineral (Figs. 11.24a and b: back-scatter images 510056 and 510055) (sample KD111) contains inclusions of K-feldspar and has a variable brightness on the back-scatter electron image, suggesting that it consists of two rare-earth element phases which are intergrown. This is common for rare-earth fluorcarbonates such as bastnaesite, parisite and synchysite. Analyses FW29 and FW31 of sample KD111(Fig. 11.25) match best with parisite-(Ce) [$Ca(Ce,La)(CO_3)_3F_2$]. Analysis FW30 (Fig. 11.25) does not match so well, probably due to intergrown chlorite and carbonate The analysis does not contain detectable Y, but it contains higher Ca contents but not enough for synchysite. Fe is a common impurity in REE fluorcarbonates, but it is not certain whether it substitutes into the structure. The chondrite normalised values are enriched in light rare-earth elements (Fig. 11.25).

Table 11.5 Summary of the mode of occurrence of the rare-earth minerals of samples taken from KD01.

SAMPLE	FLUOROCARBONATES	TEXTURE	ASSOCIATED MINERALS
KD111	synchysite, parisite	intergrown laths, with inclusions of K-feldspar	ankerite, ferro-dolomite, chlorite, K-feldspar, apatite
KD141	synchysite, bastnaesite	intergrown laths, with inclusions of quartz and barite	ankerite, ferrodolomite, fluorite, quartz, barite

Sample KD141 contains rare-earth minerals at the edge of a fluorite grain and in cavities in fluorite, often intergrown with barite and quartz. A back-scatter electron image (Fig. 11.26: image 510069) shows two intergrown phases. The Ca:REE ratio is higher than in KD111 and analyses FW70 matches well with synchysite-(Ce) [$Ca,Ce,La)(CO_3)_2F$. However, it has a flat rare-earth element pattern with a particularly low La content (Fig. 11.27). Analyses FW71 has an unusual ratio of 1:3 for Ca:total REE. It could be an analysis of impure, intergrown bastnaesite. Its chondrite-normalised pattern is in marked contrast to that of FW70 in that it has a much higher La content (Fig. 11.27).

Digitised by the Department of Library Services in support of open access to information, University of Pretoria, 2021

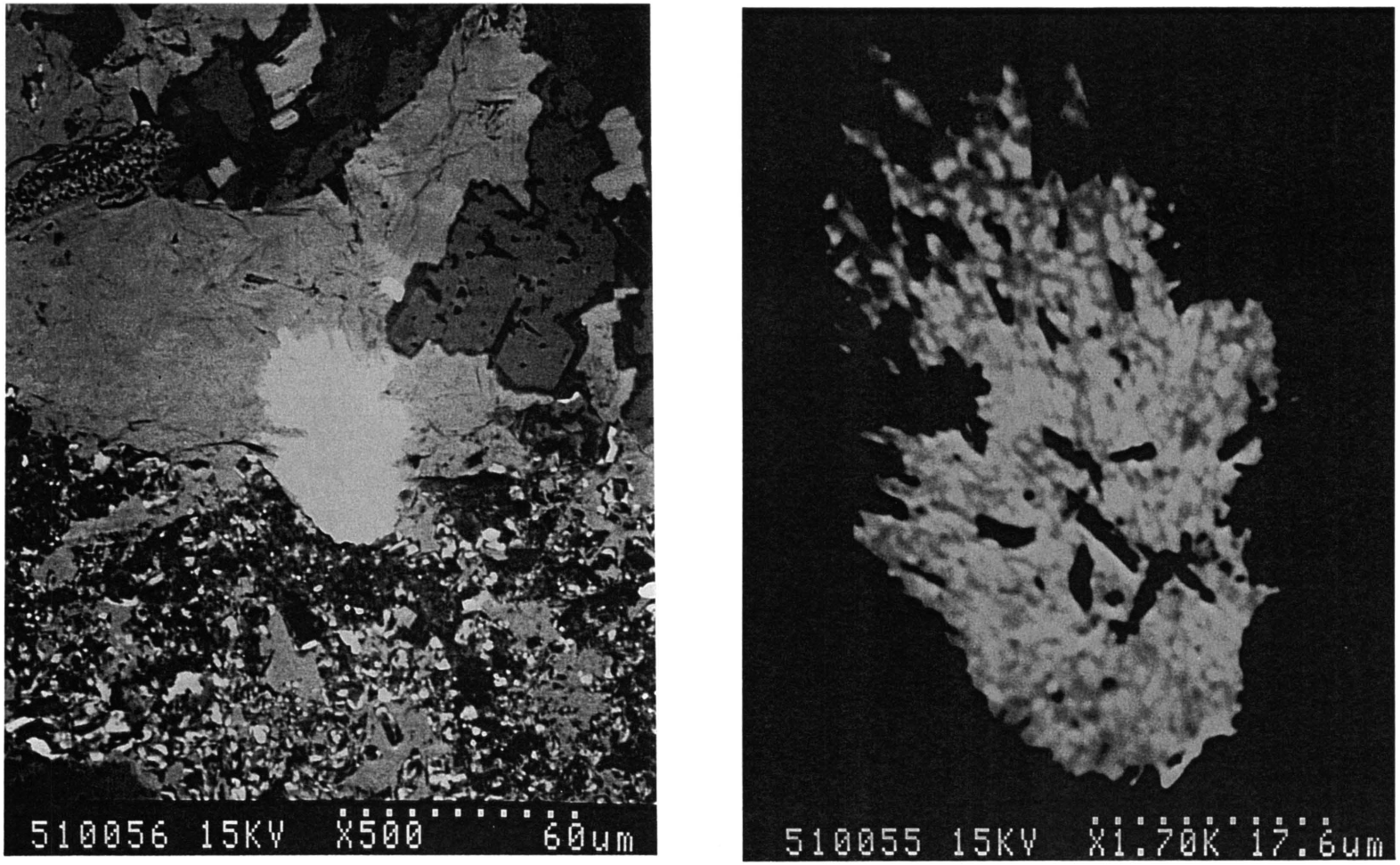

Figure 11.24 A rare-earth mineral (bright white) (back-scatter image 510056) is set in a large patch of chlorite (light grey), surrounded by zoned carbonate (darker to dark colours). The lower half of the back-scatter image displays smaller, rare-earth mineral grains. Back-scatter image (510055) is a magnification of the bright rare-earth mineral grain. The black sparry-like grains set in the rare-earth mineral grain are K-feldspar inclusions (sample KD111).

Digitised by the Department of Library Services in support of open access to information, University of Pretoria, 2021

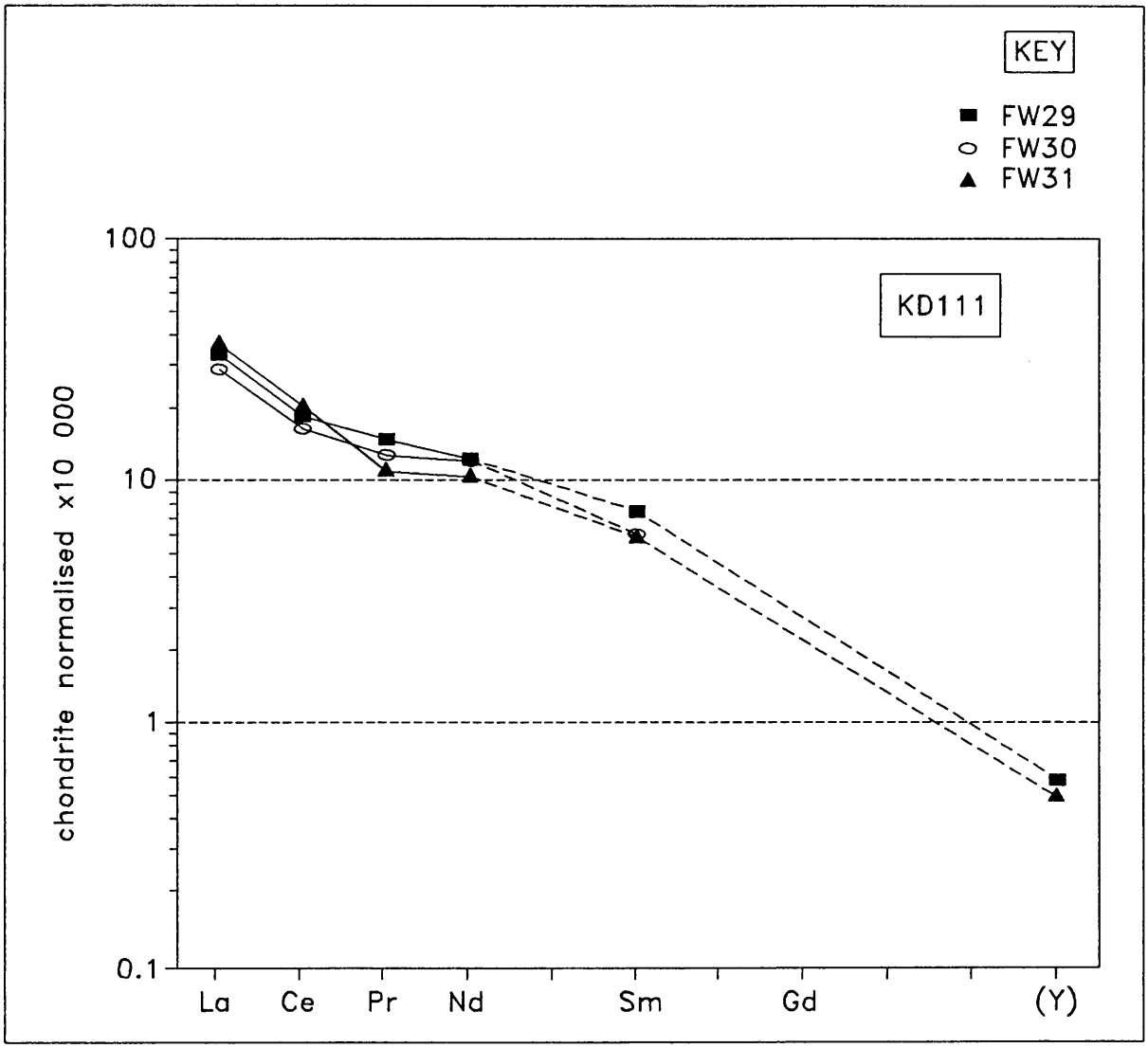

Figure 11.25 Energy-dispersive analyses of rare earth minerals from sample KD111. The values have been normalised according to Wakita et al., 1971). The trends match best with parisite-(Ce), showing a light rare-earth element enrichment.

Digitised by the Department of Library Services in support of open access to information, University of Pretoria, 2021

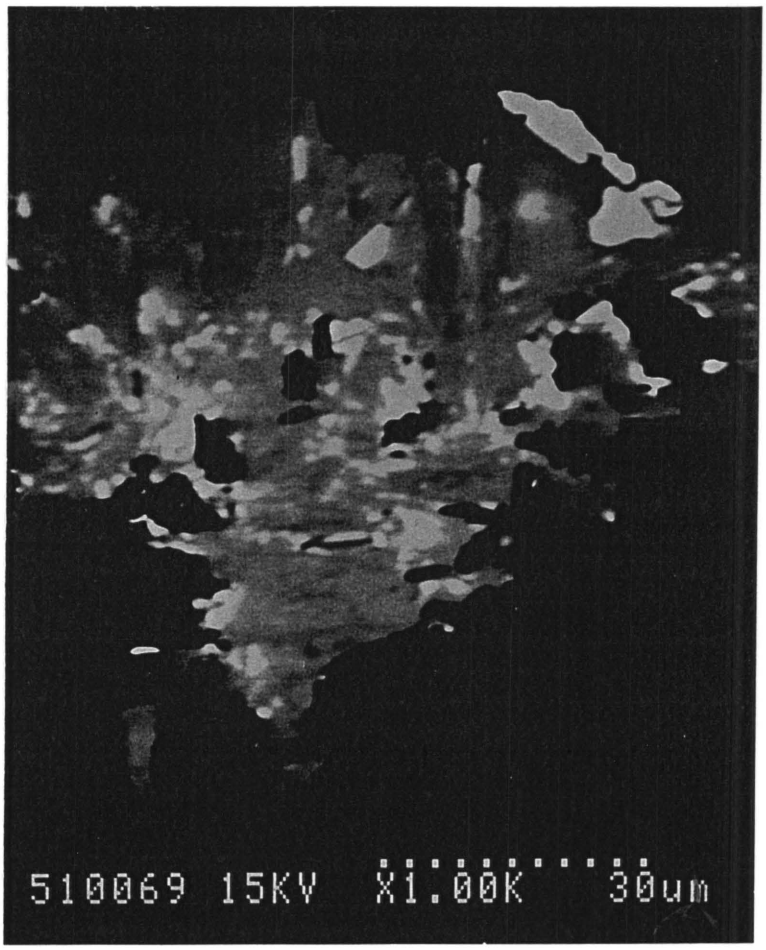

Figure 11.26 Rare-earth minerals in cavities in fluorite. Two intergrown phases are present (bright white and light grey). The large white grains in the top right corner are irregular grains of barite, while the isolated black spots in the rare-earth minerals are quartz (sample KD141).

Digitised by the Department of Library Services in support of open access to information, University of Pretoria, 2021

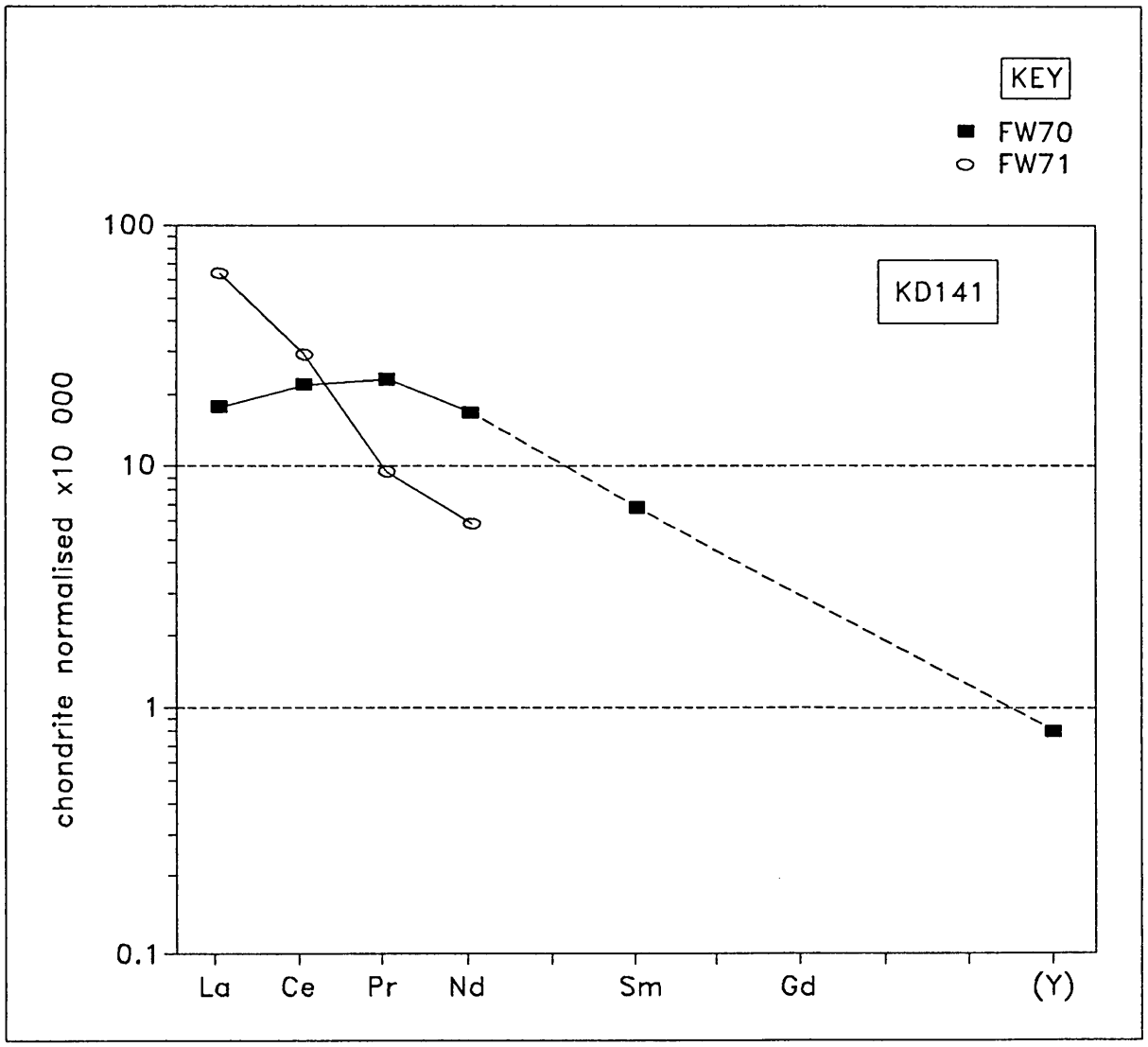

Figure 11.27 Energy-dispersive analyses of rare-earth minerals (sample KD141). The trend of analysis FW70 matches well with synchysite-(Ce), but is unusual due to a flatter pattern and low La content. The FW71 analysis represents intergrown bastnaesite.

Digitised by the Department of Library Services in support of open access to information, University of Pretoria, 2021

11.7 Discussion

Microscopical examination by means of cathodoluminescence of the borehole core from the inner zone of the Complex revealed that the metasomatic alteration of the volcaniclastic rocks was a multistage process. Consequently more than one generation of the major minerals (or mineral groups), each characterised by a specific chemical composition and/or cathodoluminescent colours, can be distinguished (Fig.11.28). In some cases (e.g. chlorite) these chemical characteristics seem to be related to the temperature of formation of the relevant mineral.

Red cored feldspars are considered to be clasts transported from an earlier fenitisation episode, and which have undergone Fe^{3+} activation. According to Marshall (1988) red luminescence in feldspars is indicative of crystallisation under conditions of high alkalinity and moderate to high temperature, or during fenitisation due to the introduction of Na and K ions. Fe^{3+} activation causing red luminescence could have occurred prior to deposition of the clasts, or the activation could have occurred in situ. The green to blue luminescence of the rims of these clasts is indicative of a sudden change in condition.

The presence of parisite and synchysite in KD019 and KD111 suggests that leaching of apatite by carbonated water led to the formation of REE-fluorocarbonates according to reactions of the type:

REE-fluorapatite + CO_2 → REE-free fluorapatite + REE-fluorocarbonates

(Hogarth et al., 1985).

Synchysite and parisite, and synchysite and bastnaesite display complex fine-grained intergrowths. In sample KD141 the synchysite and bastnaesite are enclosed by fluorite and quartz; barite seems to have crystallised before the crystallisation of synchysite had stopped. A suggested crystallisation sequence is quartz, synchysite, bastnaesite and barite. The contrast between samples FW70 and FW71 after normalisation with respect to chondrite (Fig. 11.27) seems to have been produced by crystal chemical fractionation between bastnaesite and synchysite (although the difference between the two patterns is too pronounced), or by different phases of mineralisation. In this regard hydrochemical mineralisation (low temperature) is known to produce similar patterns (Andersen, 1986; Wall and Mariano, 1996).

Suggestions have been made that synchysite and parisite might be syntaxially intergrown (Donnay and Donnay, 1953). Mariano (1989b), however, argued that syntaxy among fluorocarbonates is relatively uncommon, and that the described textures seem to suggest that parisite originates from alteration of synchysite. Based on the model for rare-earth mineralisation (Ngwenya, 1994) the following aspects should be considered in any attempt to explain the fluoro-

Digitised by the Department of Library Services in support of open access to information, University of Pretoria, 2021

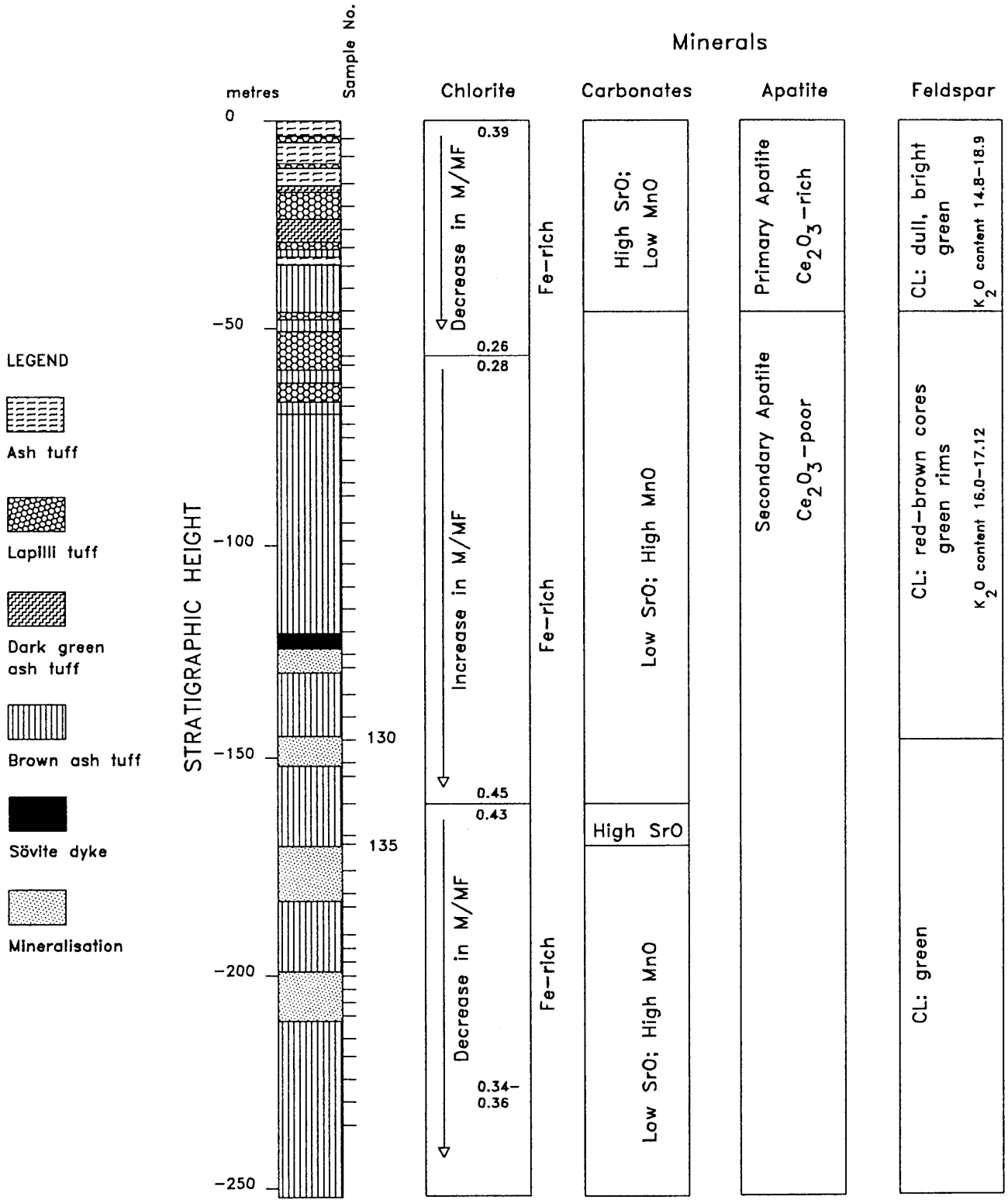

Figure 11.28 Summary of the mineral chemistry trends for chlorite, carbonates, apatite and K-feldspar (M/MF = atomic ratio Mg/(Mg+Fe) of chlorite).

Digitised by the Department of Library Services in support of open access to information, University of Pretoria, 2021

carbonate mineralisation in the KD01 sequence of the inner zone of the Kruidfontein Carbonatite Complex: (a) the hydrothermal mineral assemblage is dependent on the type of wallrock or host mineral assemblage (sample KD111 contains synchysite, parisite, carbonates, chlorite and K-feldspar, whereas sample KD141 contains bastnaesite, synchysite, fluorite, quartz and barite); (b) based on work by Donnay and Donnay (1953) and Ngwenya (1994) on the Tundulu Complex, the crystallisation sequence synchysite → parisite → bastnaesite represents a progressive depletion in Ca^{2+} and CO_3^{2-} from the parental fluid; (c) invoking wallrock as a source for Ca^{2+} and CO_3^{2-} requires an acidic hydrothermal fluid. In this regard, the following reactions between the REE-enriched fluid and the host rock can be used to explain the fluorocarbonate minerals in samples KD111 and KD141, assuming that the rare-earth elements (REE) are in the form of $REECO_3F$ or $REEF^{2+}$ complexes (Wood, 1990).

Firstly calcite and ankerite dissolve according to reactions (1) and (2) respectively:

$$3CaCO_{3\,(s)} + 3H^+_{(aq)} \rightarrow 3Ca^{2+}_{(aq)} + 3HCO_3^-{}_{(aq)} \quad \text{..... (1), and}$$

$$CaMgFe(CO_3)_{3\,(s)} + 3H^+_{(aq)} \rightarrow Fe^{2+}_{(aq)} + Mg^{2+}_{(aq)} + Ca^{2+}_{(aq)} + 3HCO_3^-{}_{(aq)} \text{ .... (2).}$$

For the sample with synchysite and parisite intergrowths, the $REECO_3F$ complex reacts with calcite to form synchysite:

$$CaCO_{3\,(s)} + REECO_3F_{(aq)} \rightarrow REECa(CO_3)_2F_{(s)} \text{ ..... (3).}$$

Should $CaCO_3$ start crystallising during later stages of the development of the hydrothermal fluid, synchysite will become unstable, and parisite will start to precipitate. Parisite can also be formed by the breakdown of synchysite (reaction 4).

$$2REECa(CO_3)_2F_{(s)} \rightarrow REE_2Ca(CO_3)_3F_{2\,(s)} + CaCO_{3\,(s)} \text{ ..... (4).}$$

Ngwenya (1994) describes a further reaction whereby parisite can precipitate directly from the fluids:

$$CaCO_{3\,(s)} + 2REECO_3F_{(aq)} \rightarrow REE_2Ca(CO_3)_3F_{2\,(s)} \text{ ..... (5).}$$

For sample KD141, which contains intergrown synchysite and bastnaesite, a similar reaction is envisaged. The difference, however, is that prior to the crystallisation of synchysite (reaction 3), all the CO_3^{2-} produced by reaction (1) or (2) is consumed. According to Ngwenya (1994),

Digitised by the Department of Library Services in support of open access to information, University of Pretoria, 2021

bastnaesite can crystallise according to:

$$REEF^{2+}_{(aq)} + HCO_3^-{}_{(aq)} \rightarrow REECO_3F_{(aq)} + H^+{}_{(aq)} \quad \text{..... (6),}$$

when the dissolution of ankerite begins to limit the Ca^{2+} supply.

Digitised by the Department of Library Services in support of open access to information, University of Pretoria, 2021

12. GEOCHEMISTRY

Fifty samples from the KD01 borehole were analysed for major-, trace- and rare-earth elements (Appendix 2). The Spearman rank coefficient of correlation was applied to the data (Appendix 2.3A, B and C).

12.1 Major-elements

The chemical classification of carbonatites (Woolley, 1982; Woolley and Kempe, 1989) is based on the chemical composition of the rock, using wt% CaO, MgO, and ($FeO+Fe_2O_3+MnO$) (Fig.12.1). The sum of these is calculated to 100% and each of the components is plotted on a triangle, by means of which the following fields are defined:

- ❑ sövite or calcite-carbonatite: $CaO/(CaO+MgO+FeO+Fe_2O_3+MnO) > 0.8$;
- ❑ beforsite or dolomite-carbonatite: $CaO/(CaO+MgO+FeO+Fe_2O_3+MnO) < 0.8$ and $MgO>FeO+Fe_2O_3+MnO$;
- ❑ ferrocarbonatite: $CaO/(CaO+MgO+FeO+Fe_2O_3+MnO) < 0.8$ and $MgO<FeO+Fe_2O_3+MnO$.

The chemical composition of the hypabyssal and volcaniclastic rocks is compared on the CaO-MgO-(FeO_{Total}+MnO) diagram. In the present study the analyses have been corrected by subtracting a portion of the CaO, corresponding to the stoichiometric amount of fluorine, to account for the fluorite in the samples. No attempt was made to correct the data for the presence of iron-oxides in the form of overgrowths and staining (Harmer and Gittins,1997).

The fluorite-free calcite-carbonatite or sövite group is obviously rich in CaO (Fig. 12.1), whereas the fluorite-calcite-carbonatite group tends to contain less CaO (after correction), reflecting its more ferroan or a more fractionated composition. The analyses of samples from the upper ash flow and lapilli tuff units plot within the ferrocarbonatite field, while those from the ferruginous lapilli tuff and lower ash flow units plot very close to the (FeO_{Total} + MnO) apex. Analyses of samples of the mineralised zones (KD126, KD130, KD134, KD138, KD141, KD142 and KD143) plot in the ferrocarbonatite field, with KD126 and KD142 the closest to the CaO apex.

The general sequence of intrusive carbonatites is calcite-carbonatite ➡ fluorite-calcite-carbonatite ➡ ferrocarbonatite ➡ late-stage carbonatitic fluids (Le Bas, 1989). Similar trends (calcite-carbonatite ➡ more Mg- or Fe-rich carbonatite) are described by Woolley (1982) and Mian (1987). The enrichment of iron in either carbonate or oxide phases is due to the prevailing oxygen fugacity: iron will partition into ankerite rather than magnetite at a low Fe^{3+} : Fe^{2+} ratio, whereas magnetite and hematite will form at progressively higher Fe^{3+} : Fe^{2+} ratios together with Mg-rich carbonate minerals (Le Bas, 1989). In the Kruidfontein Complex the MnO content varies from 0.54 to 1.85 wt% and from 2.21 to 4.27 wt% for intrusive rocks and mineralised zones res-

Digitised by the Department of Library Services in support of open access to information, University of Pretoria, 2021

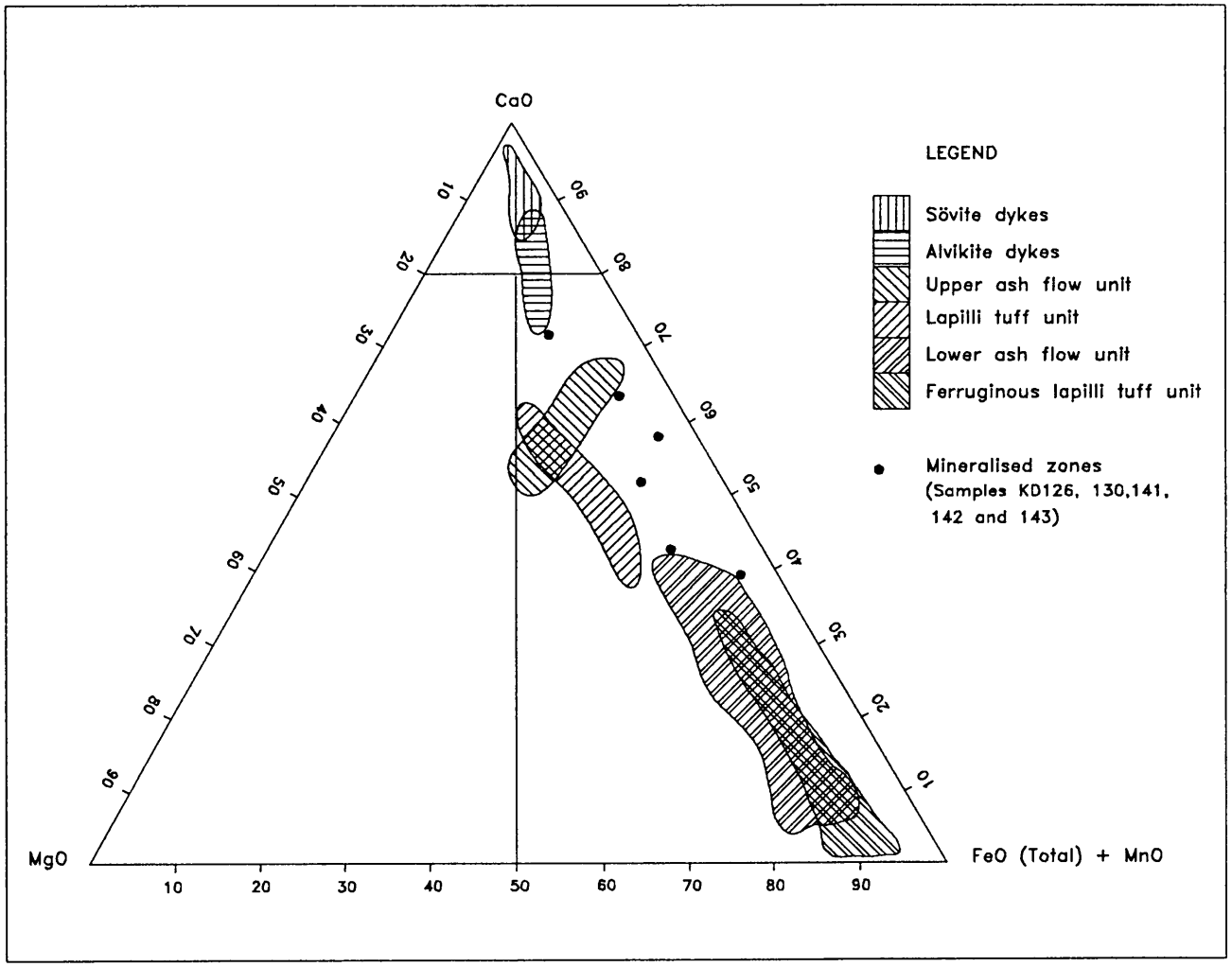

Figure 12.1 The chemistry of the intrusive dykes and volcaniclastic rocks in terms of CaO - MgO - (FeO_{Total} + MnO).

Digitised by the Department of Library Services in support of open access to information, University of Pretoria, 2021

pectively. Although there is a no correlation between FeO_{Total} and MnO for the sample suite as a whole (Appendix 2.3A), a good correlation exists for the intrusive rocks and mineralised zones (Fig. 12.2).

SiO_2 is positvely correlated with Al_2O_3, Fe_2O_3 and K_2O (Appendix 2.3A) and negatively with MgO, CaO, SrO and P_2O_5. The positive correlation can be ascribed to the presence of especially K-feldspar and chlorite. Al_2O_3 correlates with K_2O and Fe_2O_3 due to the presence of chlorite and K-feldspar, while MnO correlates with ZnO. Mn^{2+} and Zn^{2+} (ion radii of 0.080 and 0.074 nm respectively) are both held in chlorite in the R^{2+} site of the formula $[R^{2+},R^{3+}]_{12}[Si_{8-x}R_x^{3+}]_4O_{20}(OH)_{16}$. CaO correlates positively with P_2O_5 and SrO due to the presence of apatite. Negative correlations between SiO_2, MgO, CaO, SrO and P_2O_5 are ascribed to the inverse relationship between carbonate and phosphate minerals on the one hand and silicates on the other.

The SiO_2 content of the volcaniclastic (upper ash flow, lapilli tuff, ferruginous lapilli tuff and lower ash flow units) and intrusive rocks varies from 12.46 to 46.00 wt% and from 0.1 to 3.55 wt% respectively, and in the mineralised samples, SiO_2 varies from 3.89 to 33.19 wt%. The relatively high SiO_2 contents can be ascribed to the presence of especially K-feldspar and chlorite, but quartz has been identified in most of the rocks as a secondary phase, mainly in thin veinlets or along grain boundaries.

The TiO_2 content of the mineralised samples varies between 0.12 and 3.69 wt%. This is higher than the TiO_2 contents of the sövite and alvikite (values between 0.01 and 3.31 wt% TiO_2). The correlation between TiO_2 and FeO (Fig. 12.3) is weak (0.35), the reason for this being that FeO is held by several minerals (e.g. chlorite, carbonates and ilmenite, etc.). The only noteworthy positive correlation is in the FLT and LAF units, which is probably due to the presence of a limited amount of ilmenite or ilmenomagnetite (Tillmans and Correns, 1978).

12.2 Trace-elements

Rare-earth and trace-element data for the samples from borehole KD01 and the carbonatite dykes are tabulated in Appendix 2.1 and 2.2. The Spearman rank coefficient of correlation was applied to the data and summarised in Apendix 2.3B.

Sulphur correlates positively with Ba, probably due to the presence of $BaSO_4$. Small amounts of S are present as pyrite, sphalerite and galena. The positive correlation between Zn and Pb is due to the fact that sphalerite and galena are both low-temperature minerals, and are commonly associated in low-temperature sulphide deposits.

Digitised by the Department of Library Services in support of open access to information, University of Pretoria, 2021

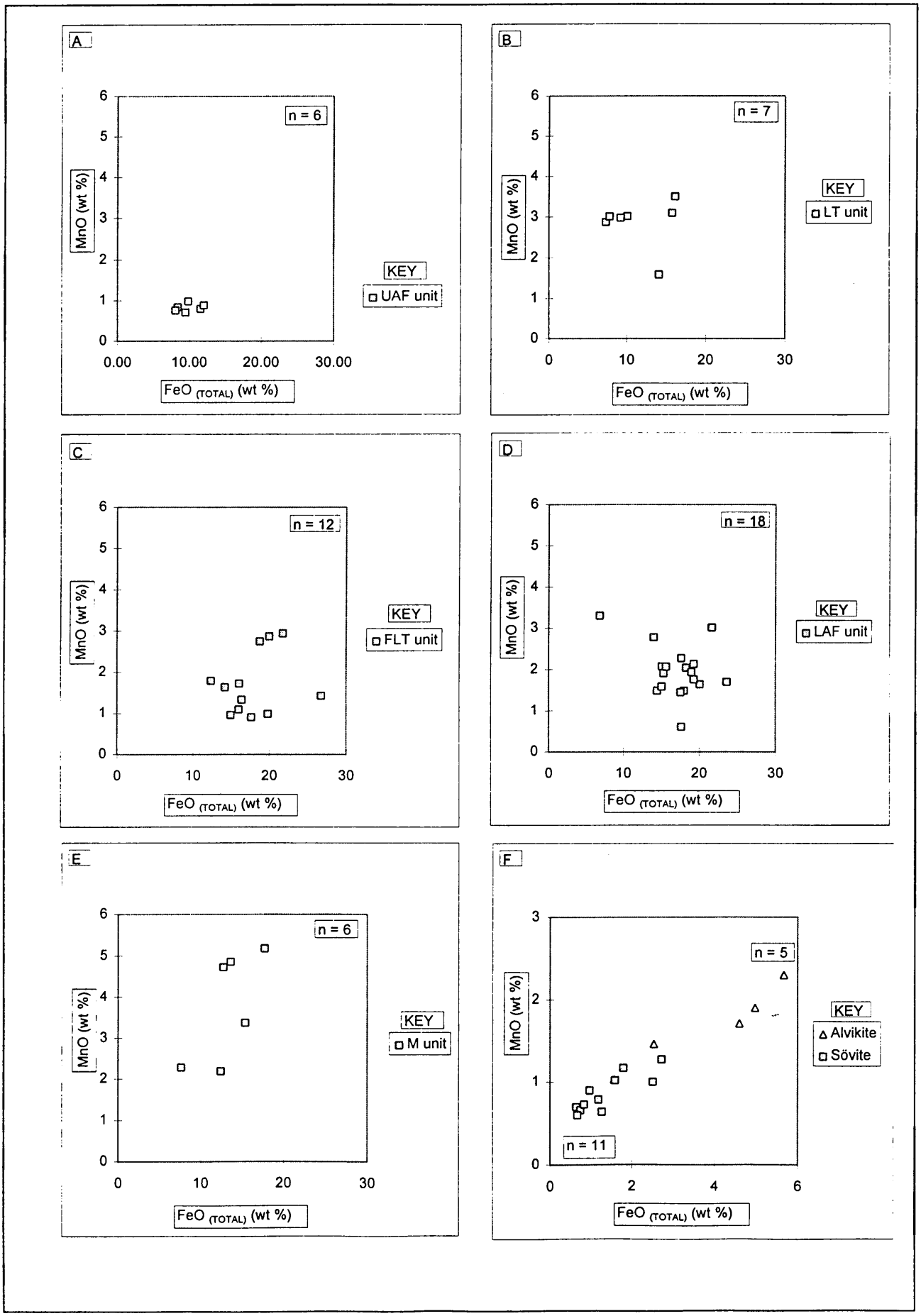

Figure 12.2 Correlation of MnO (wt%) with FeO_{Total} (wt%) concentrations of all the volcaniclastic samples (UAF = upper ash flow unit; LT = lapilli tuff unit; FLT = ferruginous lapilli tuff unit; LAF = lower ash flow unit)(A to D); the mineralised zones (M unit) (E); and the sövite and alvikite dykes (F).

Digitised by the Department of Library Services in support of open access to information, University of Pretoria, 2021

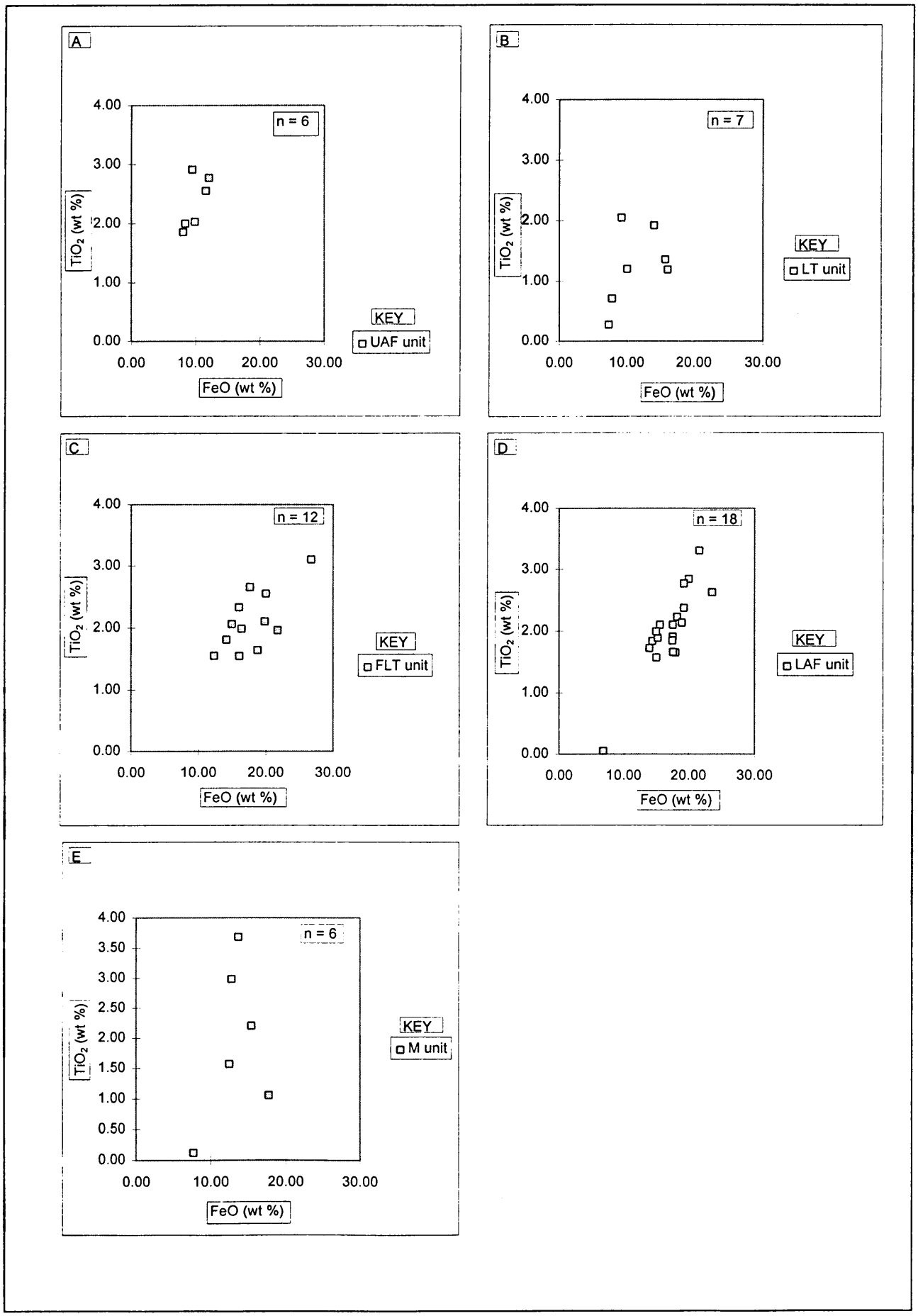

Figure 12.3 Correlation between TiO_2 (wt%) and FeO_{Total} (wt%) concentrations of all the volcaniclastic samples (UAF = upper ash flow unit; LT = lapilli tuff unit; FLT = ferruginous lapilli tuff unit; LAF = lower ash flow unit)(A to D) and the mineralised zones (M unit) (E).

Digitised by the Department of Library Services in support of open access to information, University of Pretoria, 2021

Chrome correlates positively with TiO_2, Al_2O_3 and Fe_2O_3, and negatively with MnO and CaO. Cr^{3+} closely resembles Al^{3+} and Fe^{3+} in its chemical properties and ionic size (Cr^{3+} = 0.063 nm; Al^{3+} = 0.051 nm; Fe^{3+} = 0.064 nm; Fe^{2+} = 0.074 nm; Mg^{2+} = 0.066 and Ti^{4+} = 0.068 nm)(Battey, 1972), and fill the R^{3+} site in chlorite (the being formula $[R^{2+},R^{3+}]_{12}[Si_{8-x}R_x^{3+}]_4O_{20}(OH)_{16}$). The negative correlation between Cr_2O_3, MnO and CaO is probably due to the inverse relationship between carbonate minerals and silicates.

Positive correlations are reasonably strong between Nb and Zr, TiO_2, FeO and ZnO, while Y correlates positively with Pb, F, Nb and Th. The presence of zirconium in titanium minerals (rutile, brookite, ilmenite, sphene and anatase) is well known (Vlasov, 1966). Further, the presence of Ti in zirconium minerals indicates that isovalent diadochy occurs between the two elements. The ionic substitution of Nb and Ta by Zr (accompanied by the simultaneous substitution of other cations and anions into a crystal lattice for purposes of valency compensation) has been reported for columbite, tantalite and pyrochlore (Flörke at.al., 1978). Furthermore, heterovalent substitution is pronounced between Y and Ca, Zr, U, Pb, Mn, Fe and other crystal-chemically similar elements (Vlasov, 1966):

$Y^{3+} + S^{2-} \rightarrow Pb^{2+}$ (galena);

$Y^{3+} + B^{3+} \rightarrow Ca^{2+} + C^{4+}$ (calcite);

$Y^{3+} + O^{2-} \rightarrow Ca^{2+} + F^{-}$ (fluorite);

$Y^{3+} + Ti^{4+} \rightarrow Ca^{2+} + Nb^{5+}$.

Fergusonite $(Y,Ca,U,Th)(Ti,Nb)O_4$ or pyrochlore $(Na,Ca)_2(Nb,Ta)_2O_6(O,F)$, in which Y may proxy for Ca and Th for Nb/Ta, can possibly be responsible for the positive correlation between Y, F, Nb and Th. Scandium displays a positive correlation with U. Sc is one of the elements with an intermediate ionic potential of 35.9 (radius of Sc^{3+} = 0.084 nm), (i.e. it is an element forming comparatively stable hydroxides) (Frondel, 1978) similar to U^{4+}, Fe^{3+}, Th^{4+}, Y^{3+}, Mn^{3+}, Zr^{4+}, Al^{3+}.

12.3 Geochemistry of lithologic units

The rare-earth element distribution patterns of the mineralised samples display a strong enrichment in light rare-earth elements with respect to chondrite. This corresponds with distribution patterns found by Möller et al. (1980) who also provide an explanation for this trend. It is due to polarisation of CO_3^{2-}, O^{2-} and OH^- complexes which form with the rare-earth elements. The polarising effect decreases from the light rare-earth elements to the heavy rare-earth elements. The rare-earth element trend displays a concave curve, with relative enrichment of the heavy rare-earth elements compared with the middle rare-earth elements. According to Hodgson (1985) and Clarke (1989) the presence of apatite will produce an convex curve due to the increased content of middle rare-earth elements relative to the heavy rare-earth elements. They

Digitised by the Department of Library Services in support of open access to information, University of Pretoria, 2021

therefore explain a convex trend to early fractionation of all apatite prior to the intrusion.

The variation in Ce, La and Nd concentrations of the mineralised samples, and of the sövite and alvikite dykes (Fig. 12.4) is similar to the values given by Clarke (1989). The sövite samples have lower La, Ce and Nd concentrations (120 to 610 ppm) than the alvikite dykes (180 and 1390 ppm). The mineralised samples are the most enriched in REE, with La, Ce and Nd concentrations between 1181 and 9073 ppm. A possible explanation for this is that the fluorite content increases from sövite through alvikite to the mineralised zones. Hetrovalent diadochy is pronounced between REE^{3+} and Ca:

$$REE^{3+}\ O^{2-} \rightarrow Ca^{2+}\ F^{-}.$$

The relation between La and P_2O_5 is inconsistent. In the UAF and LT units the correlation seems to be negative, in the FLT and LAF units and for the alvikite dykes it is weakly positive, and there seems to be no correlation in the sövite and the mineralised zones (Fig. 12.5). The relation between Ce and P_2O_5 is essentially a reflection of that between La and P_2O_5, except that the Ce contents are higher (Fig. 12.6). The variable relation of REE and P_2O_5 suggests that the rare-earth elements are not always concentrated in apatite. Clarke (1989) found that up to 1 wt% La_2O_3 is contained in fluorite, with average values ranging between 0.06 and 0.21 wt% La_2O_3.

The Sr concentration in the sövite and alvikite dykes, and the mineralised zones (Fig. 12.7) seems to be apathetic with respect to the rare-earth elements, especially in the sövite and alvikite (Fig. 12.4). The Sr content of the sövite is higher than the values of the associated alvikite. In the mineralised zones no relationship between the two groupings of elements (i.e. REE and Sr) exists. This is also substantiated by the data in Figure 12.8.

The ratio Sr/Ba for the sövite, alvikite and mineralised zones is compared (Fig. 12.7). The alvikite and especially the mineralised samples are strongly enriched in Ba, whereas the sövite samples are generally impoverished in Ba (or enriched in Sr). Based on this one can assume that (a) the alvikite dykes have undergone a higher degree of mineralisation than the sövite; (b) that the mineralised samples have undergone an extreme degree of mineralisation; or (c) that the alvikite dykes and the mineralised zones are more differentiated fractions of the magma source. The association of Ba (in the form of barite) with late-stage mineralisation is supported by Le Bas (1989).

Microprobe analyses show that Sr is present in calcite and fluorite at values of up to 2.54 wt% and 1.47 wt% respectively when it substitutes for Ca. However, Sr is weakly correlated with CaO in the upper ash flow unit. A strong positive correlation is apparent for the FLT unit only. In all the

Digitised by the Department of Library Services in support of open access to information, University of Pretoria, 2021

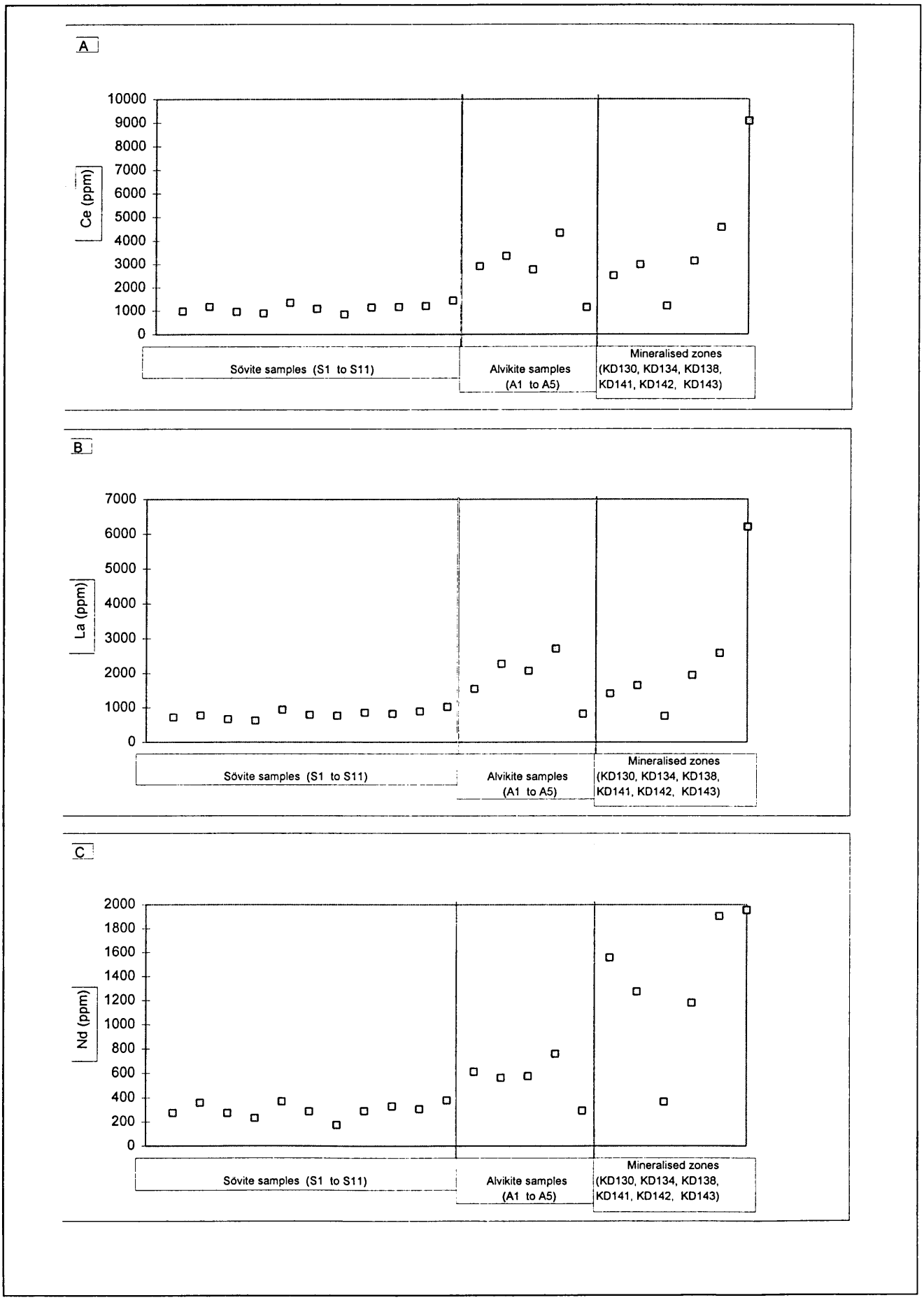

Figure 12.4 The variation of Ce, La and Nd concentrations (ppm) of sövite (samples S1 to S11), alvikite (samples A1 to A5) dykes and the mineralised zones (samples KD126, KD130, KD134, KD141, KD142, KD143).

Digitised by the Department of Library Services in support of open access to information, University of Pretoria, 2021

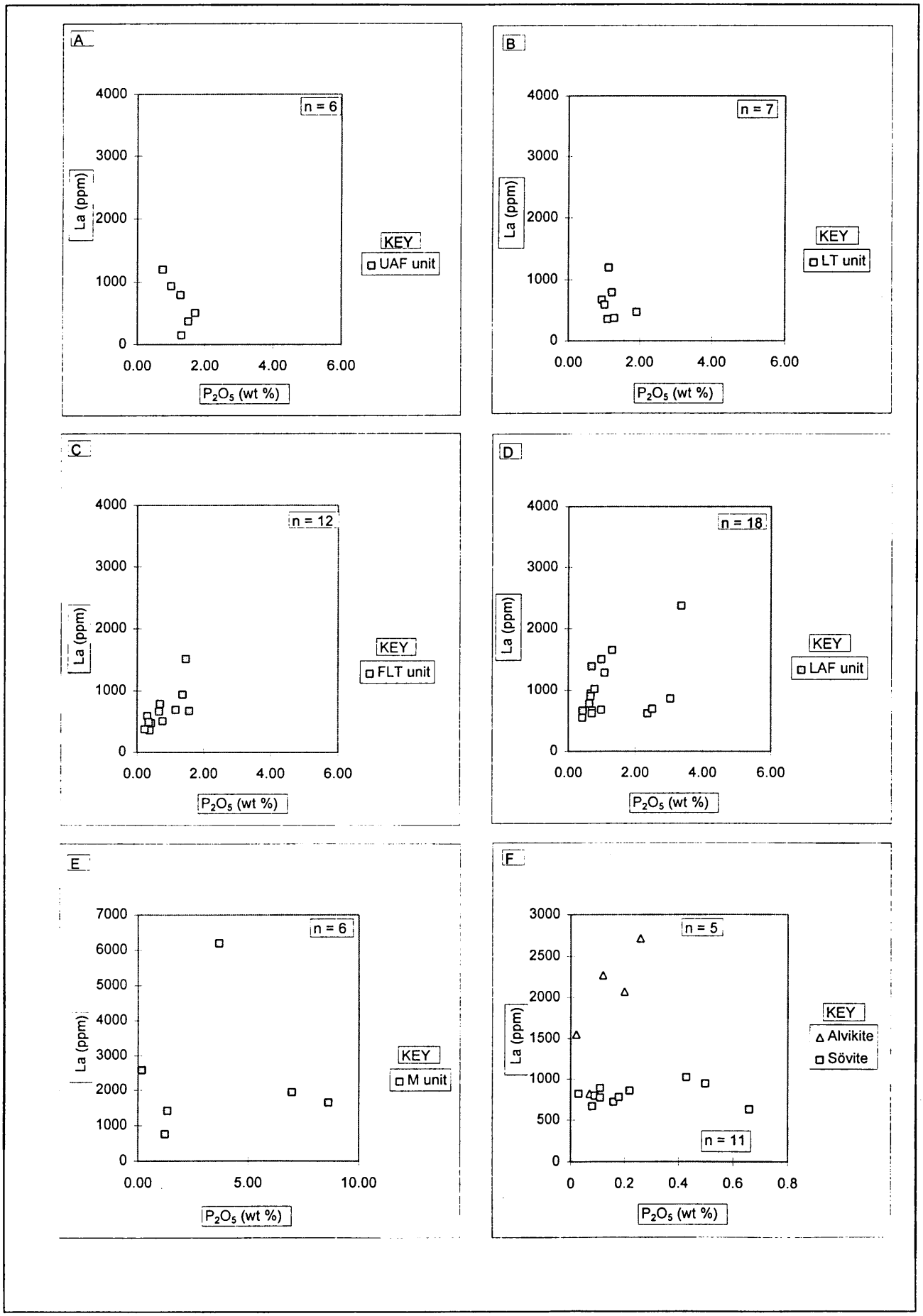

Figure 12.5 Correlation between La (ppm) and P_2O_5 (wt %) concentrations of all the volcaniclastic samples (UAF = upper ash flow unit; LT = lapilli tuff unit; FLT = ferruginous lapilli tuff unit; LAF = lower ash flow unit)(A to D); the mineralised zones (M unit) (E); and the sövite and alvikite dykes (F).

Digitised by the Department of Library Services in support of open access to information, University of Pretoria, 2021

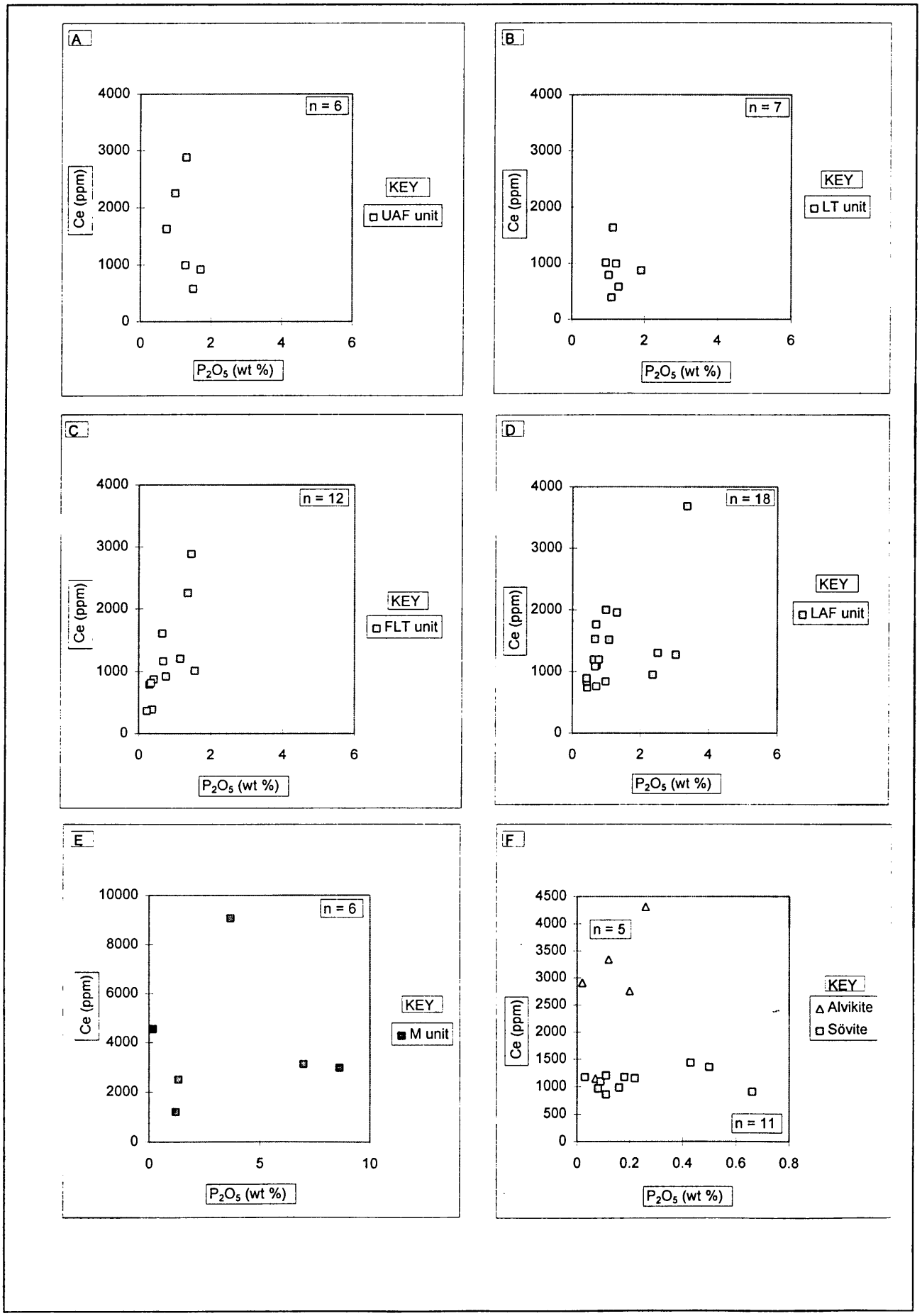

Figure 12.6 Correlation between Ce (ppm) and P_2O_5 (wt %) concentrations of all the volcaniclastic samples (UAF = upper ash flow unit; LT = lapilli tuff unit; FLT = ferruginous lapilli tuff unit; LAF = lower ash flow unit)(A to D); the mineralised zones (M unit) (E); and the sövite and alvikite dykes (F).

Digitised by the Department of Library Services in support of open access to information, University of Pretoria, 2021

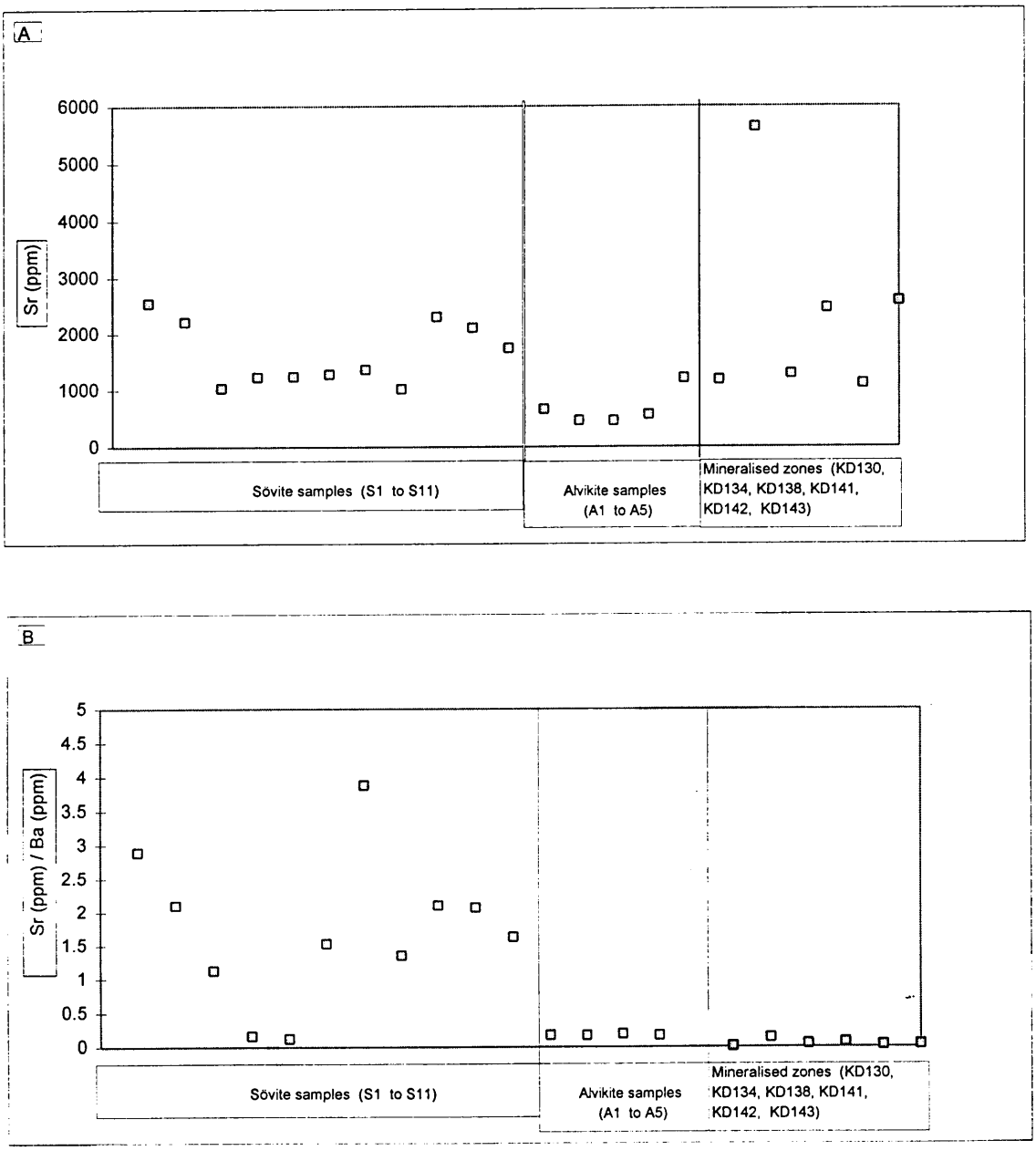

Figure 12.7 The variation of (A) Sr concentrations (ppm) and (B) Sr/Ba ratio of the sövite (samples S1 to S11), and alvikite dykes (samples A1 to A5), and the mineralised zones (samples KD126, KD130, KD134, KD141, KD142 and KD143).

Digitised by the Department of Library Services in support of open access to information, University of Pretoria, 2021

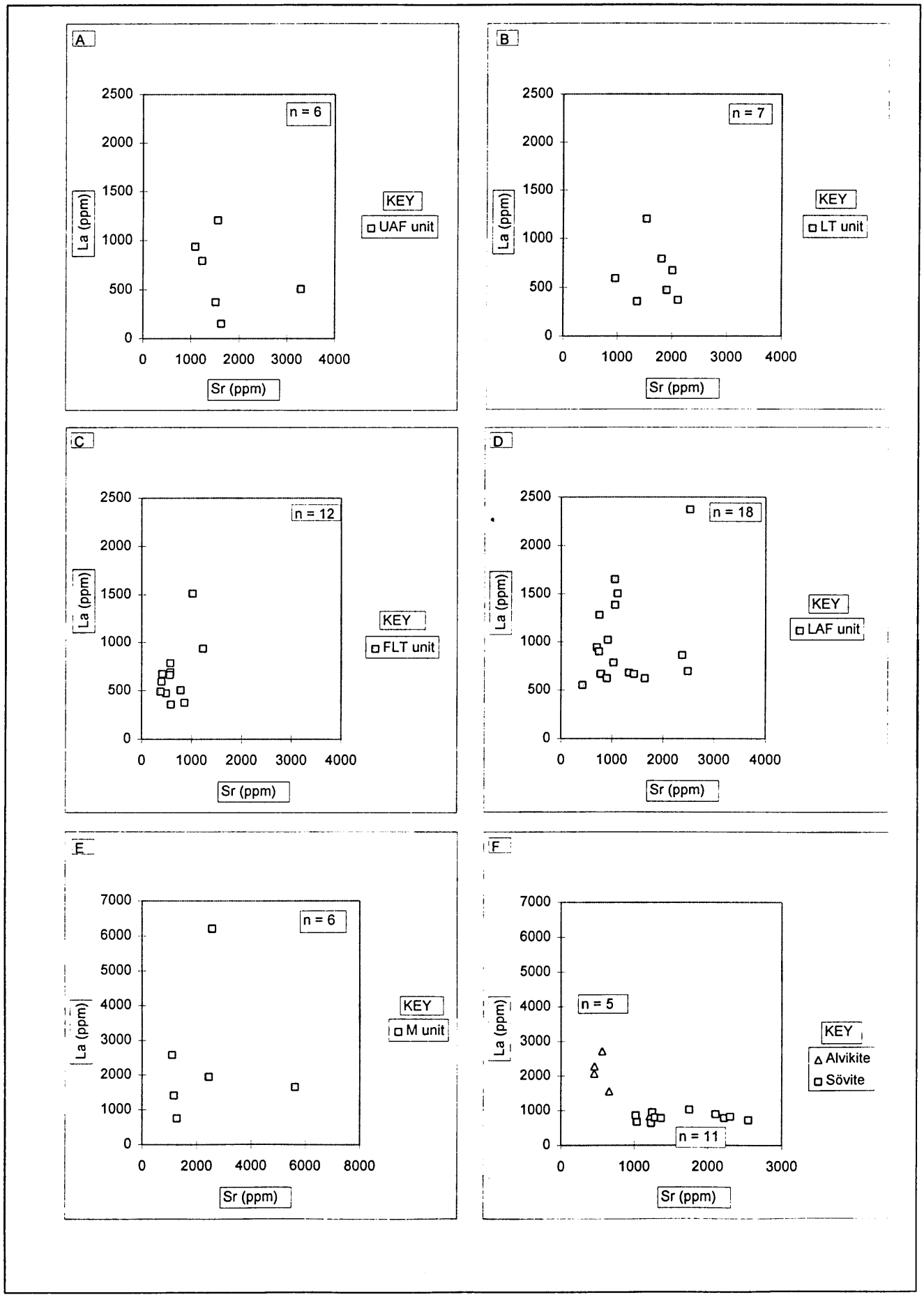

Figure 12.8 Correlation between La (ppm) and Sr (ppm) concentrations of all the volcaniclastic samples (UAF = upper ash flow unit; LT = lapilli tuff unit; FLT = ferruginous lapilli tuff unit; LAF = lower ash flow unit)(A to D); the mineralised zones (M unit) (E); and the sövite and alvikite dykes (F).

Digitised by the Department of Library Services in support of open access to information, University of Pretoria, 2021

other cases there is no correlation (Fig. 12.9). An explanation for the poor correlation is that Sr not only replaces Ca in apatite and calcite, but that it can also be contained in feldspar (up to 30-40 %)(Vlasov, 1966). Another possible explanation for the poor correlation is that the Sr occurs as ancylite or even goyazite ($(SrAl_3(PO_4)(PO_3OH)(OH)_6)$.

No correlation between Sr and F (Fig. 12.10) is evident, except for the sövite and alvikite samples, which display a weak negative correlation between the two. It suggests that Sr is largely accommodated in carbonates (and feldspar?) whereas F is accommodated in fluorite. The volcaniclastic rocks and mineralised zones display a reasonably strong positive correlation between Sr and P_2O_5 (Fig. 12.11), but a weak negative correlation in the sövite and alvikite. This indicates that the P_2O_5 content is probably controlled by the presence of apatite, especially in the alvikite and sövite, and goyazite ($SrAl_3(PO_4)(PO_3OH)(OH)_6$) in most of the other units.

The chrome content of the mineralised zones varies from below the detection limit to 247 ppm. For the sövite and alvikite dykes the Cr concentrations are below the detection limit. High chrome values seem to be associated with high FeO, Fe_2O_3 and Al_2O_3 values, so that one may conclude that it is mainly housed in magnetite and chlorite. The vanadium content displays a positive correlation with FeO_{Total} (Fig. 12.12), so that it seems reasonable to assume that it is mainly contained in magnetite.

The zirconium content of carbonatites is usually low (average of 127 ppm for ferrocarbonatite) (Woolley and Kempe, 1989). Zr correlates positively with Nb for the ferruginous lapilli tuff unit, the lower ash flow unit and mineralised zones. No clear correlations exist for the upper ash flow and lapilli tuff units, sövite and alvikite (Fig. 12.13). The positive correlation may be due to the isomorphism of Zr^{4+} (0.079 nm) with Nb^{4+} and Ta^{5+} reported for pyrochlore, tantalite and columbite. Furthermore, zircon can contain Nb^{4+} (0.074 nm), especially in naegite.

Negative correlations between SiO_2 and Nb are recorded for the ferruginous lapilli tuff, lower ash flow tuff units and mineralised zones, and positive ones for the lapilli tuff unit and the sövite and alvikite (Fig. 12.14). The positive correlation between Nb and P_2O_5 for all the rock units, except the upper ash flow unit and the carbonatite dykes (Fig. 12.15) indicates that apatite or a P_2O_5-rich mineral could possibly control the Nb values in these cases. Otherwise Nb may be held by minerals like columbite, tantalite, pyrochlore, or naegite (a zircon variety). Although no pyrochlore has been identified, the presence of a small amount (approximately 0.025 wt%) could be responsible for ±100 ppm Nb.

The lead content of the mineralised zones varies between 54 and 7000 ppm. From Figures 12.16

Digitised by the Department of Library Services in support of open access to information, University of Pretoria, 2021

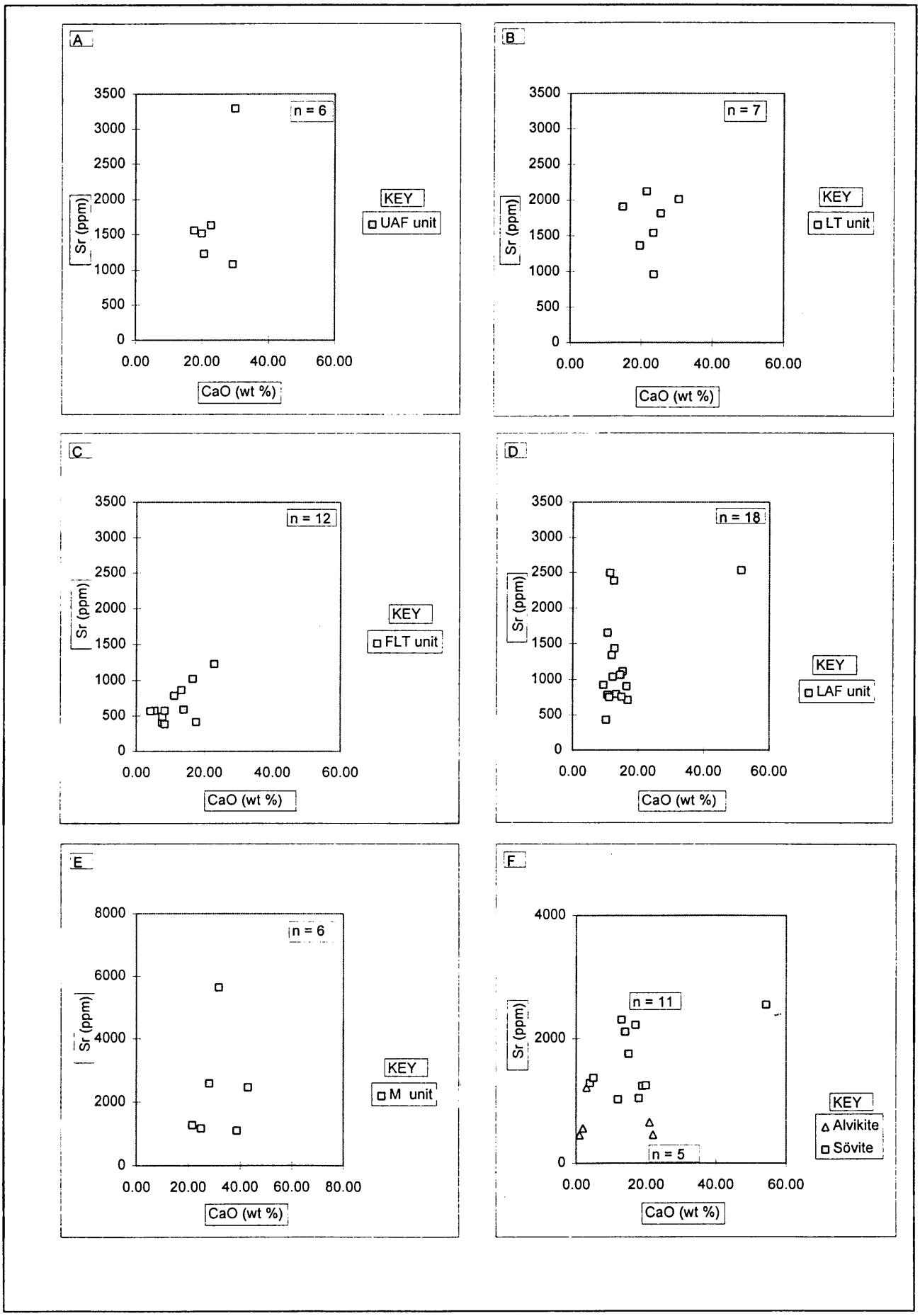

Figure 12.9 Correlation between Sr (ppm) and CaO (wt%) concentrations of all the volcaniclastic samples (UAF = upper ash flow unit; LT = lapilli tuff unit; FLT = ferruginous lapilli tuff unit; LAF = lower ash flow unit)(A to D); the mineralised zones (M unit) (E); and the sövite and alvikite dykes (F).

Digitised by the Department of Library Services in support of open access to information, University of Pretoria, 2021

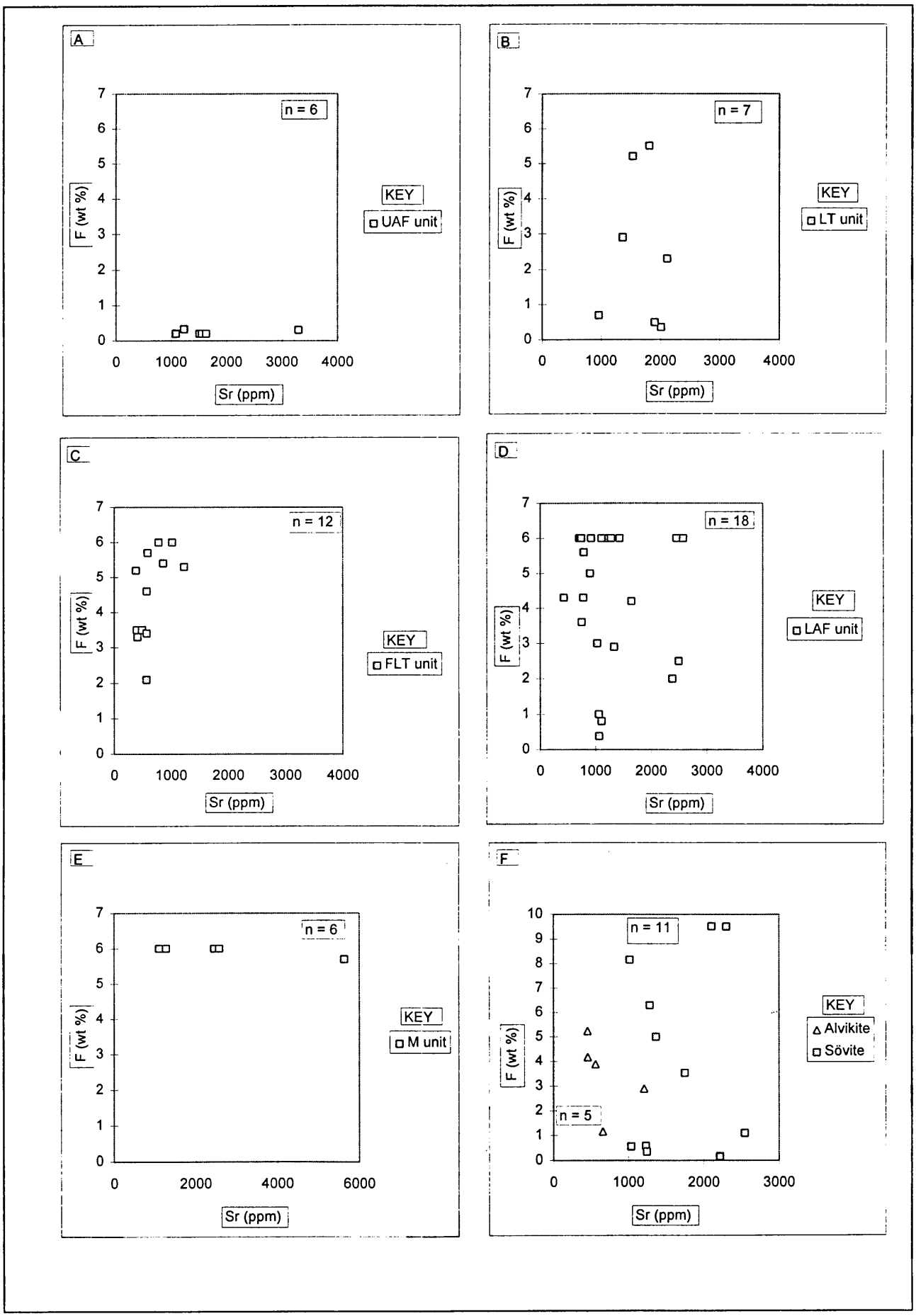

Figure 12.10 Correlation between F (wt%) and Sr (ppm) concentrations of all the volcaniclastic samples (UAF = upper ash flow unit; LT = lapilli tuff unit; FLT = ferruginous lapilli tuff unit; LAF = lower ash flow unit)(A to D); the mineralised zones (M unit) (E); and the sövite and alvikite dykes (F).

Digitised by the Department of Library Services in support of open access to information, University of Pretoria, 2021

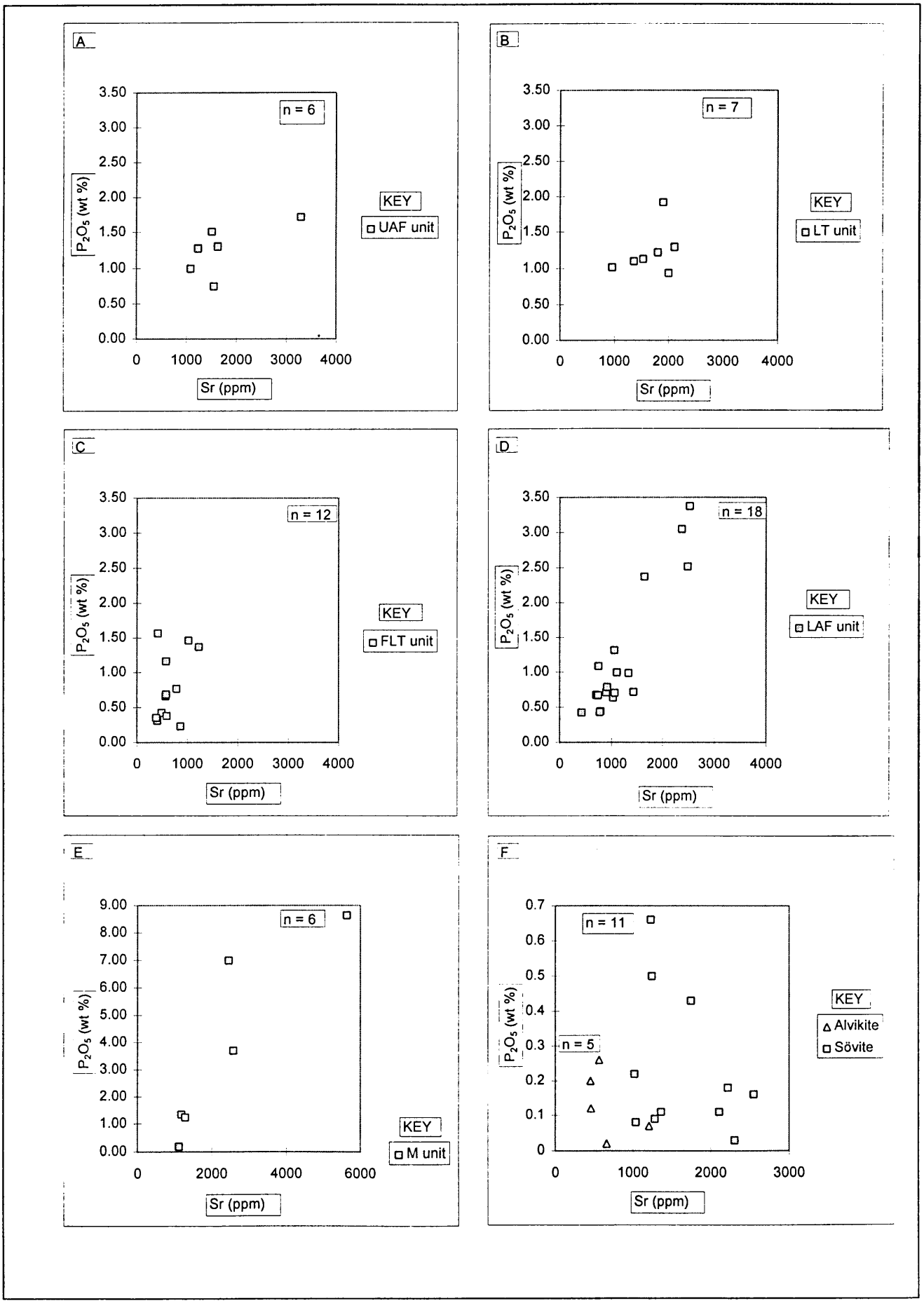

Figure 12.11 Correlation between P_2O_5 (wt%) and Sr (ppm) concentrations of all the volcaniclastic samples (UAF = upper ash flow unit; LT = lapilli tuff unit; FLT = ferruginous lapilli tuff unit; LAF = lower ash flow unit)(A to D); the mineralised zones (M unit) (E); and the sövite and alvikite dykes (F).

Digitised by the Department of Library Services in support of open access to information, University of Pretoria, 2021

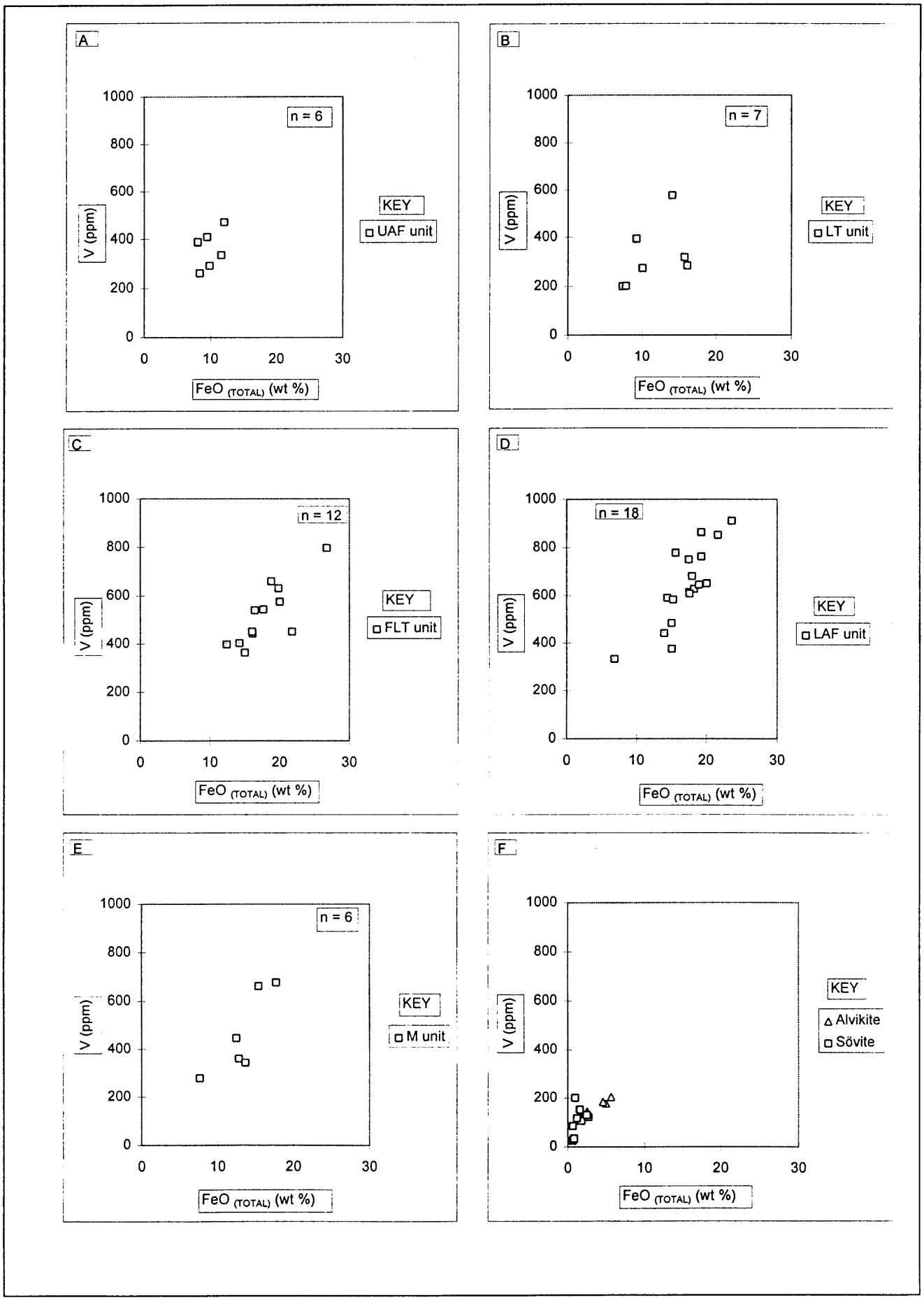

Figure 12.12 Correlation between V (ppm) and FeO_{Total} (wt%) concentrations of all the volcaniclastic samples (UAF = upper ash flow unit; LT = lapilli tuff unit; FLT = ferruginous lapilli tuff unit; LAF = lower ash flow unit)(A to D); the mineralised zones (M unit) (E); and the sövite and alvikite dykes (F).

Digitised by the Department of Library Services in support of open access to information, University of Pretoria, 2021

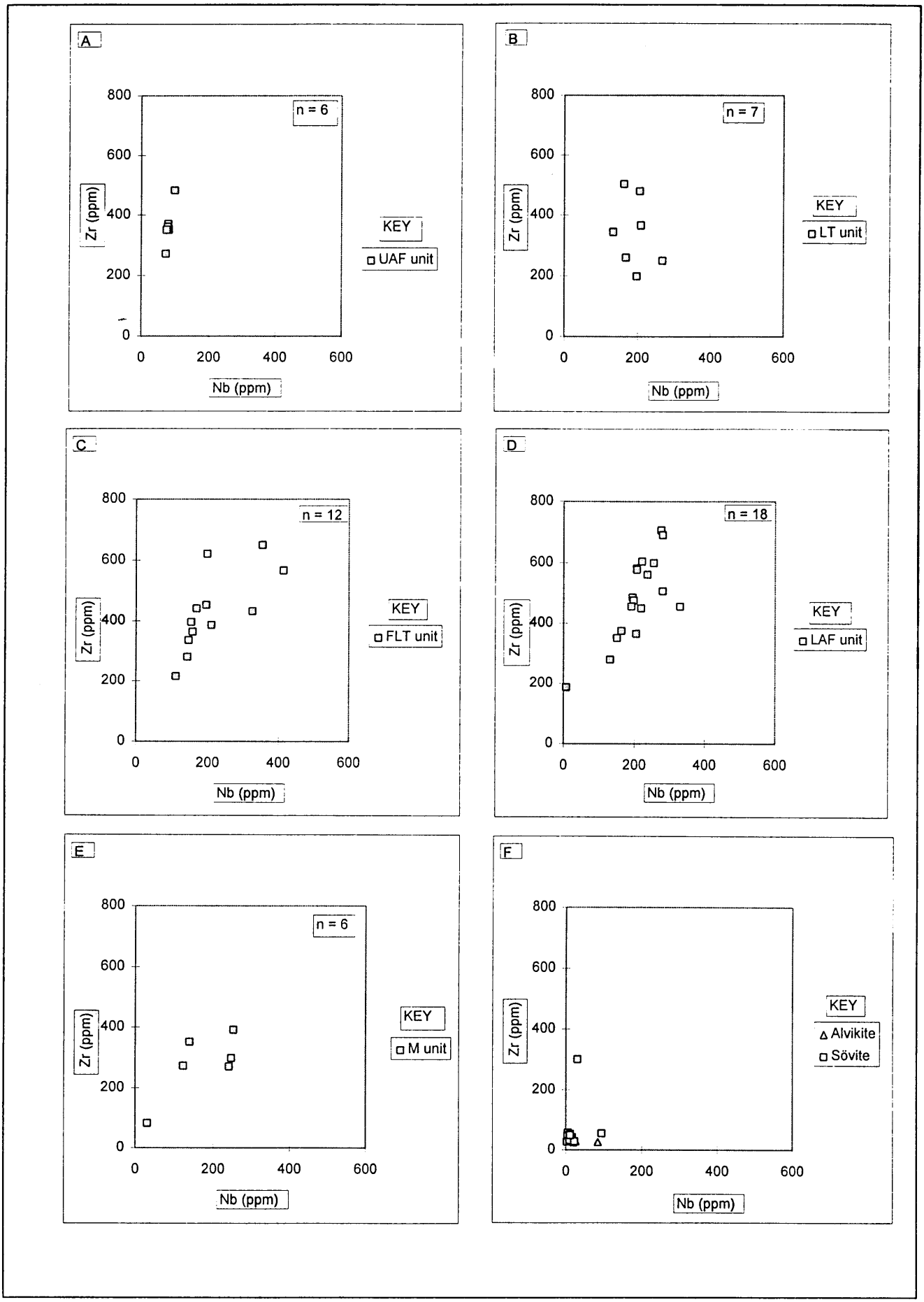

Figure 12.13 Correlation between Zr (ppm) and Nb (ppm) concentrations of all the volcaniclastic samples (UAF = upper ash flow unit; LT = lapilli tuff unit; FLT = ferruginous lapilli tuff unit; LAF = lower ash flow unit)(A to D); the mineralised zones (M unit) (E); and the sövite and alvikite dykes (F).

Digitised by the Department of Library Services in support of open access to information, University of Pretoria, 2021

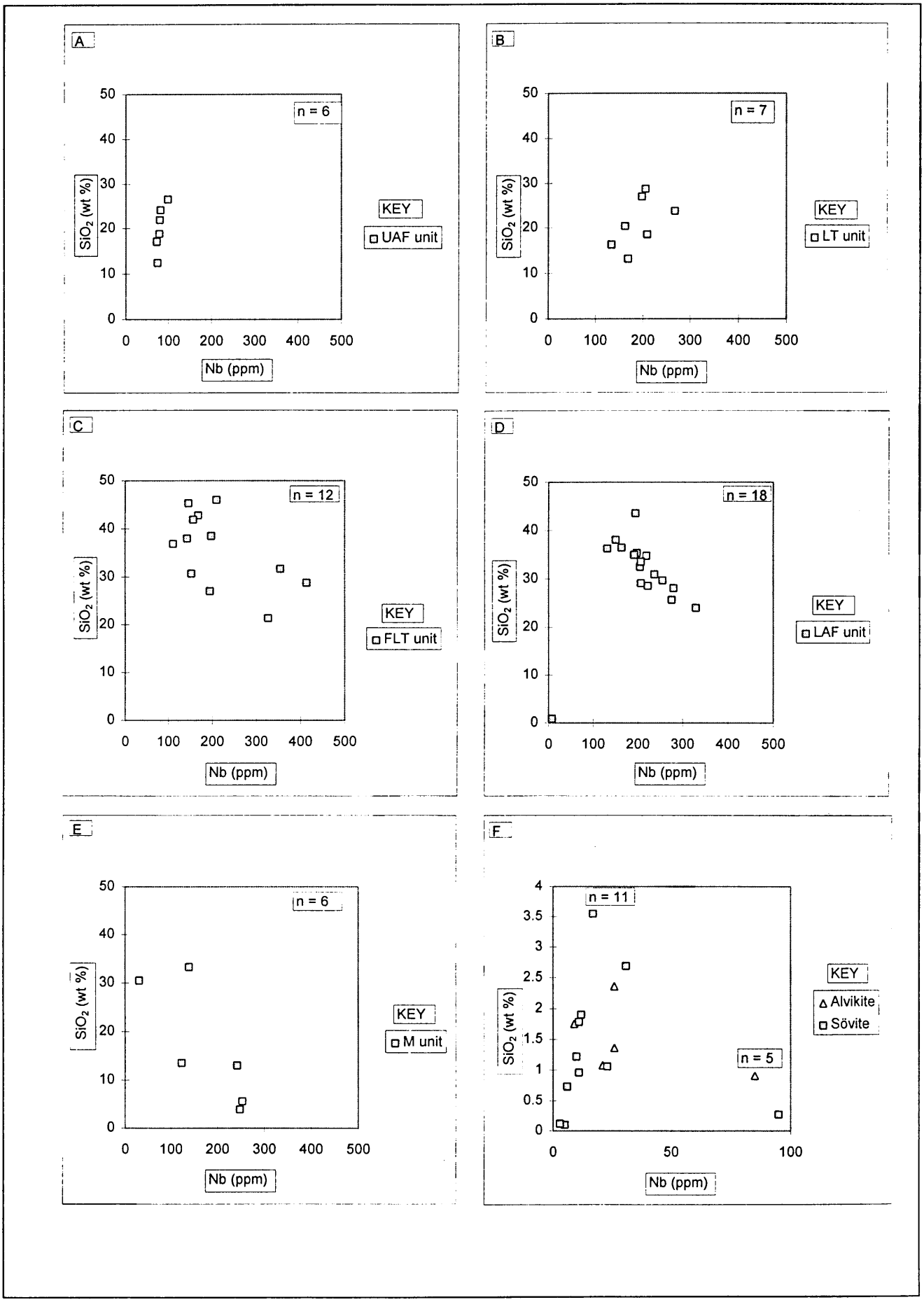

Figure 12.14 Correlation between SiO_2 (wt%) and Nb (ppm) concentrations of all the volcaniclastic samples (UAF = upper ash flow unit; LT = lapilli tuff unit; FLT = ferruginous lapilli tuff unit; LAF = lower ash flow unit)(A to D); the mineralised zones (M unit) (E); and the sövite and alvikite dykes (F).

Digitised by the Department of Library Services in support of open access to information, University of Pretoria, 2021

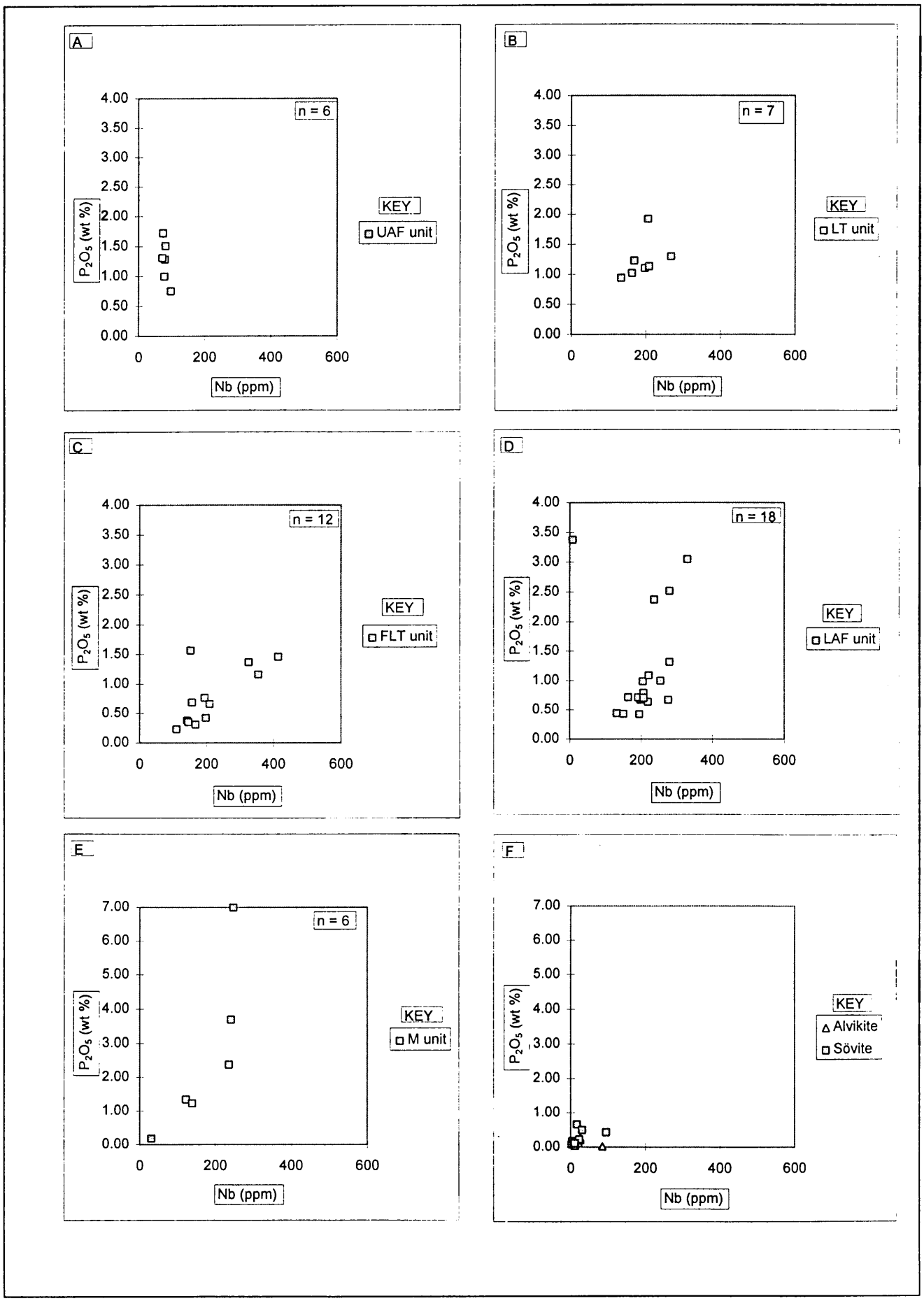

Figure 12.15 Correlation between P_2O_5 (wt%) and Nb (ppm) concentrations of all the volcaniclastic samples (UAF = upper ash flow unit; LT = lapilli tuff unit; FLT = ferruginous lapilli tuff unit; LAF = lower ash flow unit)(A to D); the mineralised zones (M unit)(E); and the sövite and alvikite dykes (F).

Digitised by the Department of Library Services in support of open access to information, University of Pretoria, 2021

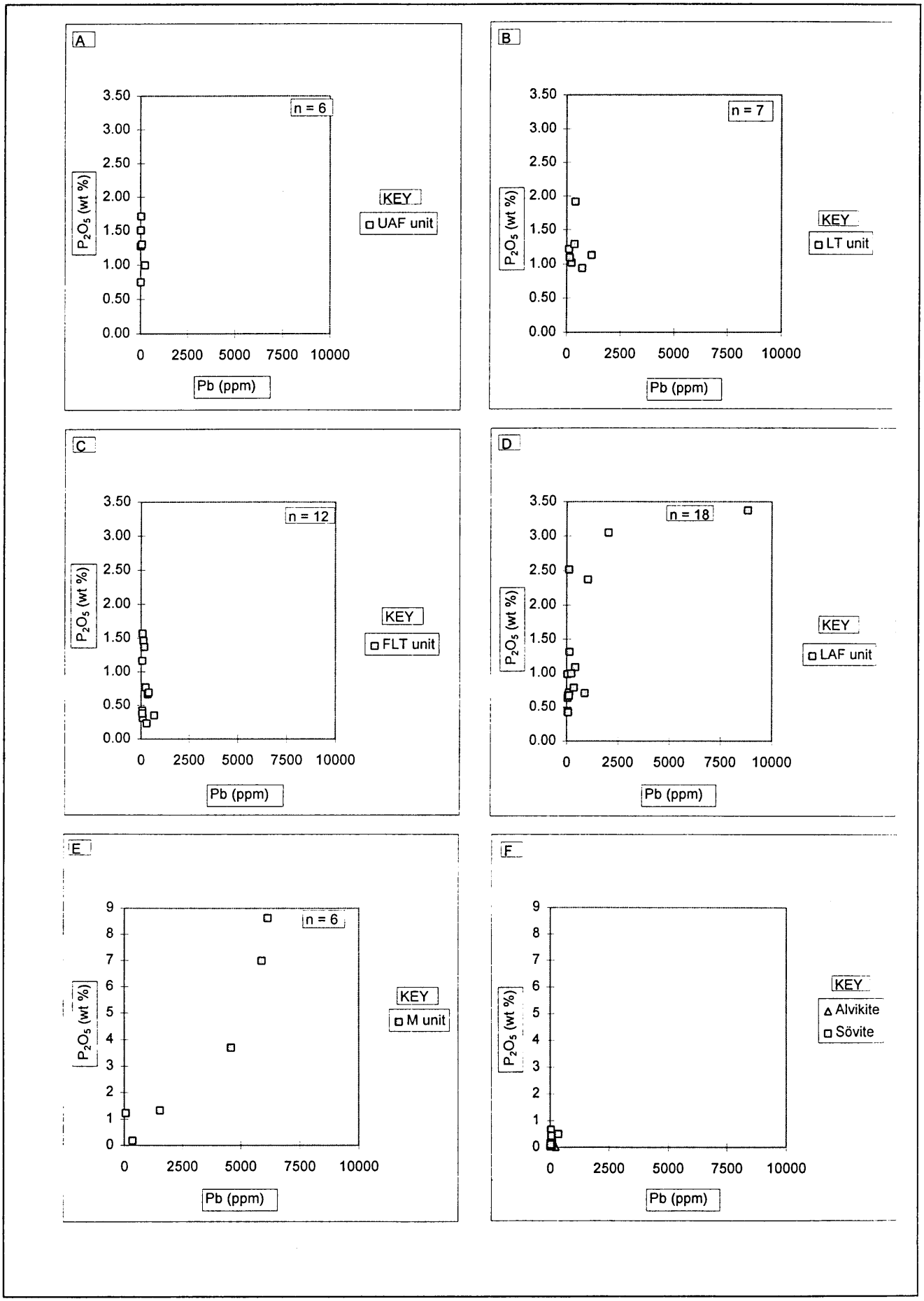

Figure 12.16 Correlation between P_2O_5 (wt%) and Pb (ppm) concentrations of all the volcaniclastic samples (UAF = upper ash flow unit; LT = lapilli tuff unit; FLT = ferruginous lapilli tuff unit; LAF = lower ash flow unit)(A to D); the mineralised zones (M unit)(E); and the sövite and alvikite dykes (F).

Digitised by the Department of Library Services in support of open access to information, University of Pretoria, 2021

and 12.17 it is evident that Pb correlates with P_2O_5, and to some degree with S in the mineralised zones, but not in the other rock units. Lead is evidently present as galena, but plumbogummite has also been identified by means of XRD.

12.4 Statistical method

A summary of the major-element analyses of the samples from borehole KD01 is plotted as histograms of mass gains and losses (measured in weight per cent) calculated relative to the least altered volcaniclastic carbonatite (LAVC) (Figs. 12.18, 12.19 and 12.20). Sample KD016 of the upper ash flow unit in borehole KD01 was identified as the least altered, based on the presence of primary textures and calcite.

For the statistical study, Ga was identified as an element which does not display any systematic variation within the sample suite and as such, it is a suitable reference element for statistically testing of the data. Since the abundance of Ga is regarded to be unchanged in all data sets, use of the variable obtained permits absolute changes between data sets to be calculated; if Ga had been mobile, changes reported would be relative.

All tests reported here follow the methodology outlined by Woronow (1990) and Woronow and Love (1990). The system of equations presented allows the calculation of chemical variations and shifts between data sets, and the computation of an f-value that maps each respective suite onto the reference suite. Results are presented of one run, in which a parametric t-test was used to provide 90% confidence levels for estimates of the variation in mean abundances of elements between data suites (Table 12.1).

The results indicate that the titanium contents and modal anatase contents in the upper ash flow unit are significantly lower in the lapilli tuff, ferruginous lapilli tuff and lower ash flow units. P_2O_5 is significantly lower in the ferruginous lapilli tuff and lower ash flow units. There is an apparent decrease in P_2O_5 from the upper ash flow to the pyroclastic breccia unit, but this cannot be verified statistically; consequently one must accept that there is no real difference in the mean P_2O_5 values, between the upper ash flow and lapilli tuff units. The lapilli tuff, ferruginous lapilli tuff and lower ash flow units are significantly enriched in Nb, Y, F, La and Er, with respect to the upper ash flow unit. This supports an earlier interpretation that the rare-earth elements are most probably associated with fluorite. It also appears as if rare-earth element abundances are not correlated with P_2O_5, TiO_2 or Nb abundances, which suggests that rare-earth element abundances are not solely dependent on apatite or TiO_2- or Nb-rich phases like pyrochlore.

Digitised by the Department of Library Services in support of open access to information, University of Pretoria, 2021

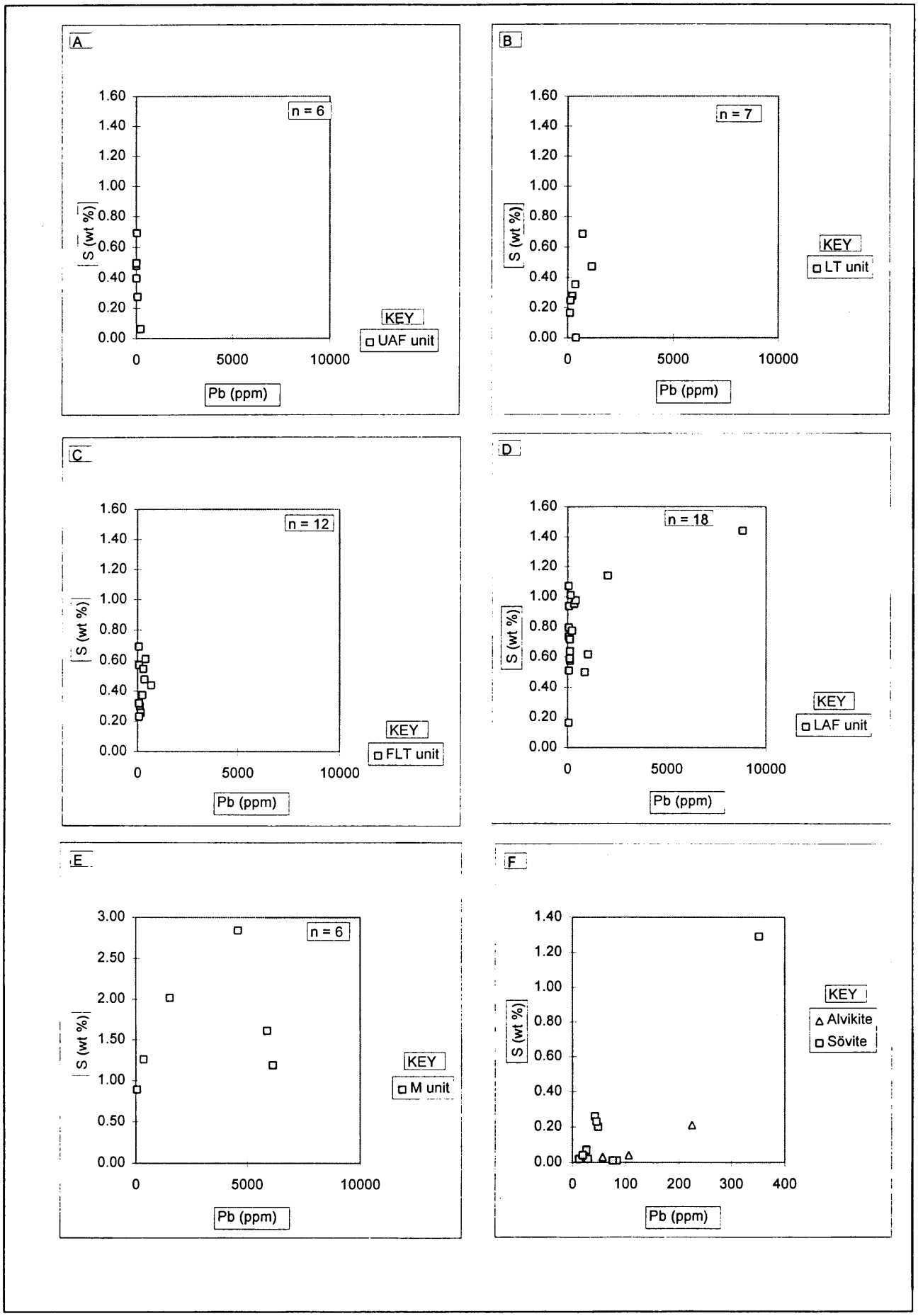

Figure 12.17 Correlation between S (wt%) and Pb (ppm) concentrations of all the volcaniclastic samples (UAF = upper ash flow unit; LT = lapilli tuff unit; FLT = ferruginous lapilli tuff unit; LAF = lower ash flow unit)(A to D); the mineralised zones (M unit) (E); and the sövite and alvikite dykes (F).

Digitised by the Department of Library Services in support of open access to information, University of Pretoria, 2021

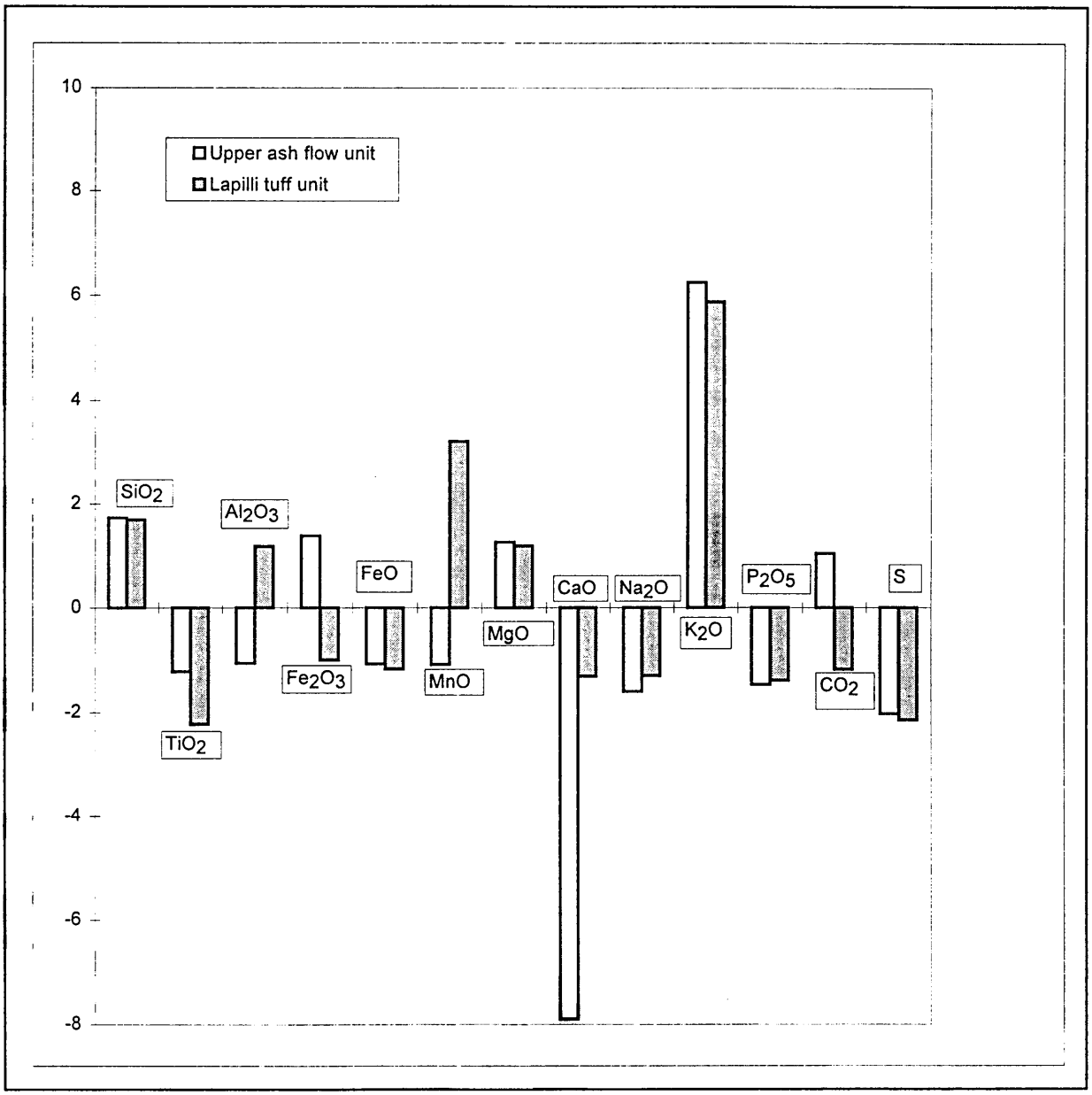

Figure 12.18 Major element analyses of the upper ash flow and lapilli tuff units plotted as histograms of mass gains and losses (measured in wt%). The measured changes are relative to the least altered volcaniclastic carbonatite (LAVC).

Digitised by the Department of Library Services in support of open access to information, University of Pretoria, 2021

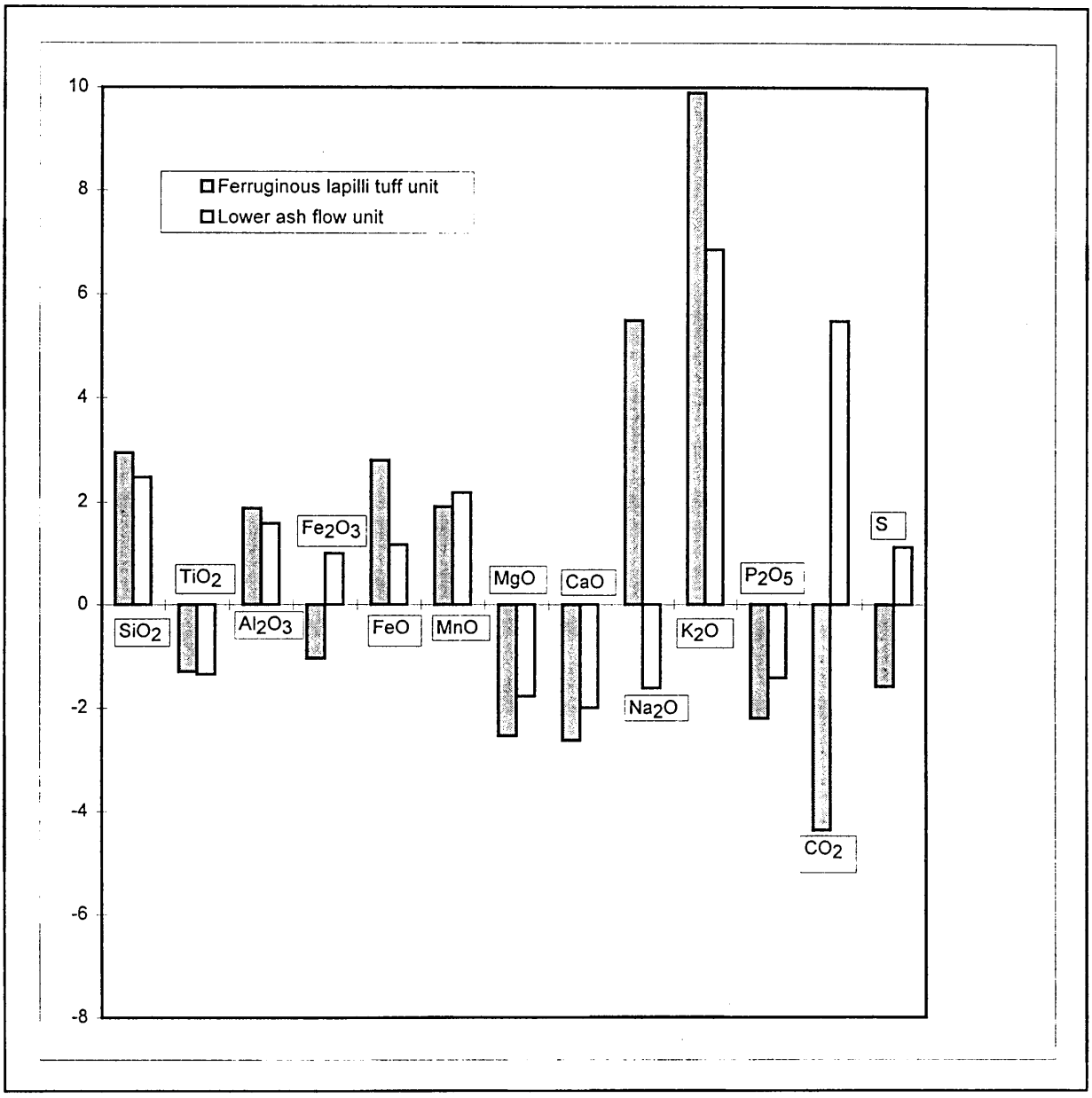

Figure 12.19 Major element analyses of the ferruginous lapilli tuff and lower ash flow units plotted as histograms of mass gains and losses (measured in wt%). The measured changes are relative to the least altered volcaniclastic carbonatite (LAVC).

Digitised by the Department of Library Services in support of open access to information, University of Pretoria, 2021

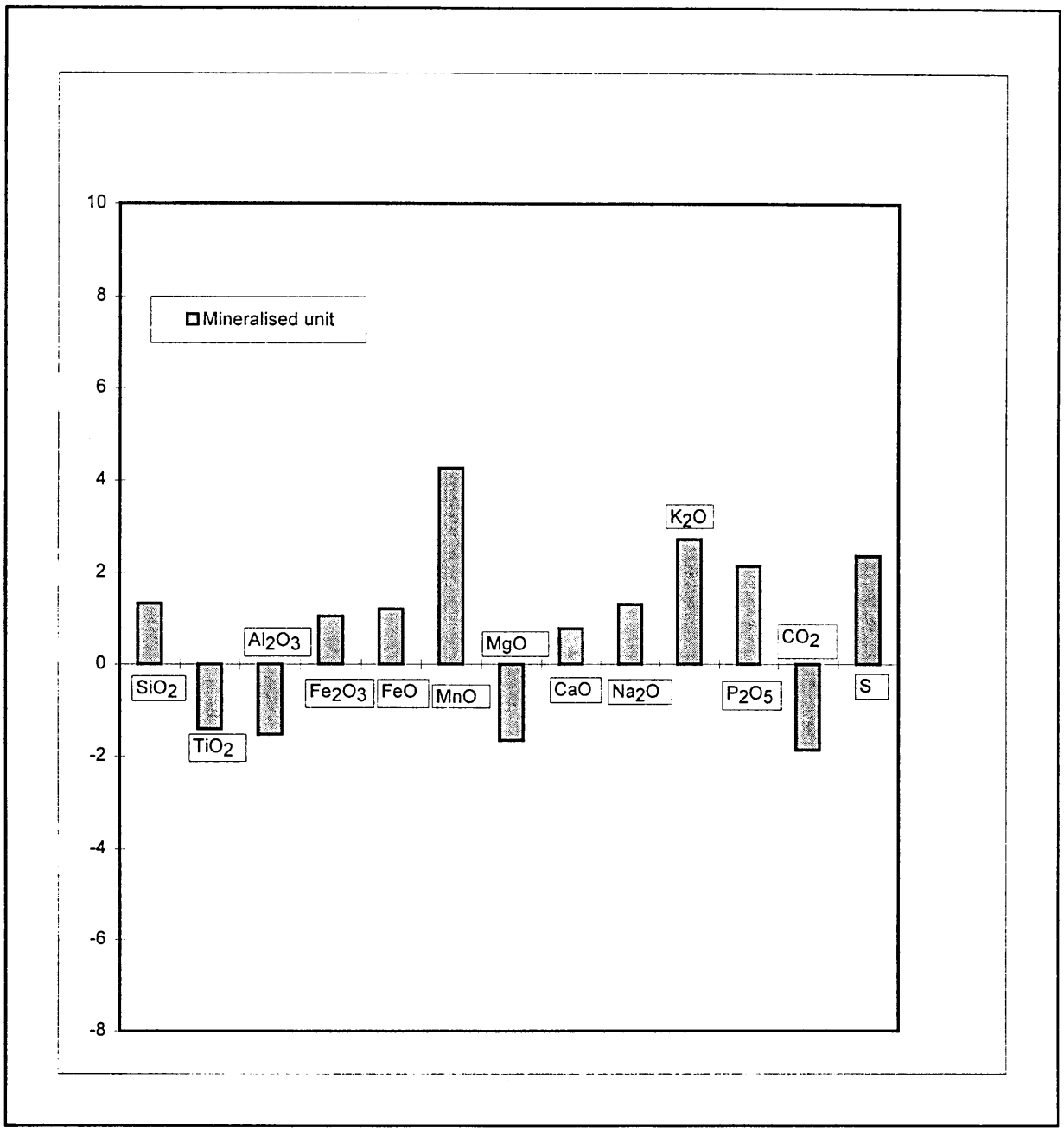

Figure 12.20 Major element analyses of the mineralised zones plotted as histograms of mass gains and losses (measured in wt%). The measured changes are relative to the least altered volcaniclastic carbonatite (LAVC).

Digitised by the Department of Library Services in support of open access to information, University of Pretoria, 2021

Table 12.1 Results of the parametric (t-test) option of geochemical data from borehole KD01.

VBL	CLASS	DELTA %	LOG (*f*)	C.I.	SIG. LEVEL	S.L.
TiO_2	2	-58.321	-0.38009	0.16483	0.00082	— — —
TiO_2	3	-21.718	-0.10634	0.09076	0.02878	— —
TiO_2	4	-19.622	-0.09486	0.08791	0.03861	— —
TiO_2	5	-68.598	-0.50304	0.46582	0.03936	— —
P_2O_5	2	-17.355	-0.08278	0.12381	0.12747	— — —
P_2O_5	3	-63.213	-0.43431	0.21978	0.00164	— —
P_2O_5	4	-36.295	-0.19583	0.18812	0.04377	
P_2O_5	5	58.321	0.19954	0.28431	0.11602	
Nb	2	117.006	0.33647	0.10460	0.00006	+ + +
Nb	3	102.479	0.30638	0.15425	0.00158	+ + +
Nb	4	106.385	0.31468	0.09221	0.00000	+ + +
Nb	5	-18.318	-0.08787	0.55366	0.38971	
U	2	35.228	0.13107	0.30374	0.22730	
U	3	-63.473	-0.43739	0.18798	0.00045	— — —
U	4	-36.160	-0.19491	0.16302	0.02599	— —
U	5	172.536	0.43542	0.35028	0.02394	+ +
Y	2	481.404	0.76448	0.09501	0.00000	+ + +
Y	3	182.231	0.45060	0.17173	0.00015	+ + +
Y	4	117.557	0.33757	0.08613	0.00000	+ + +
Y	5	419.603	0.71567	0.39210	0.00395	+ + +
Zr	2	-20.110	-0.09751	0.21486	0.21613	
Zr	3	-2.126	0.00933	0.11916	0.44645	
Zr	4	16.665	0.06694	0.09491	0.11944	
Zr	5	-62.631	-0.42749	0.21035	0.00211	— — —
K_2O	2	-6.767	-0.03043	0.42751	0.45028	
K_2O	3	80.693	0.25694	0.36125	0.11605	
K_2O	4	-9.542	-0.04355	0.25536	0.38631	
K_2O	5	-95.676	-1.36416	0.82497	0.00710	— — —
Fluorite	2	459.014	0.74742	0.42083	0.00599	+ + +
Fluorite	3	556.112	0.81698	0.40252	0.00176	+ + +
Fluorite	4	666.869	0.88472	0.27624	0.00001	+ + +
Fluorite	5	1787.797	1.27596	0.52736	0.00166	+ + +
Anatase	2	-55.422	-0.35088	0.21294	0.00927	— — —

Digitised by the Department of Library Services in support of open access to information, University of Pretoria, 2021

VBL	CLASS	DELTA %	LOG (f)	C.I.	SIG.LEVEL	S.L.
Anatase	3	-54.720	-0.34410	0.17091	0.00172	— — —
Anatase	4	-62.273	-0.42335	0.19830	0.00074	— — —
Anatase	5	-58.706	-0.38411		0.50000	
F	2	496.299	0.77546	0.31032	0.00046	+ + +
F	3	1437.954	1.18694	0.19734	0.00000	+ + +
F	4	1137.312	1.09248	0.28468	0.00000	+ + +
F	5	2690.797	1.44573	0.36883	0.00002	+ + +
La	2	124.688	0.35158	0.26576	0.01837	+ +
La	3	109.312	0.32079	0.17593	0.00288	+ + +
La	4	198.218	0.47453	0.11877	0.00000	+ + +
La	5	796.485	0.95254	0.33546	0.00022	+ + +
Er	2	420.902	0.71676	0.17034	0.00001	+ + +
Er	3	188.240	0.45975	0.16007	0.00006	+ + +
Er	4	157.945	0.41153	0.11561	0.00000	+ + +
Er	5	386.395	0.68699	0.32250	0.00158	+ + +

(**VBL** = name of the compositional variable being evaluated; **CLASS** = class or target data (unit) being evaluated - **(1)** upper ash flow unit, **(2)** lapilli tuff unit, **(3)** ferruginous lapilli tuff unit, **(4)** lower ash flow unit, **(5)** mineralised zones; **DELTA %** = difference in the numerical abundance of the given target variable between the reference data suite and the target data suite; **LOG(f)** = mean difference in log(f) between the reference and target data suites for the given target variable; **C.I.** = the 90% confidence interval about the mean difference in log(f); **SIG. LEVEL** = the significance level of a 1-tail t-test of log(f) for the hypothesis H_0: [log(f) = log(f_p); **S.L.** = summary of the results in the significance level: **"+"** indicates that log(f) is significantly greater than zero at the 10% level, **"++"** that log(f) is significantly greater than zero at the 5% level, **"+++"** indicates that log(f) is significantly greater than zero at the 1% level. Minus signs indicate values significantly less than zero and a blank indicates that none of these conditions exists.

Detailed scattergrams showing La versus F and Er versus F indicate that these REE are not directly related to the F content (Fig. 12.21). A plot of La versus Er seems to suggest that there are two sample suites present: the LAF and FLT units display separate positive correlations, while the UAF and LT units are more enriched in Er relative to La than the LAF sample set. The mineralised zones represent no trend. La/Er ratios are not coupled to F or Nb contents. On the other hand, Er and Y correlate well except in the UAF unit, as can be seen from the respective delta % values (Table 12.1) and the plot of Er versus Y.

12.5 Chondrite-normalised rare-earth elements

The rare-earth element pattern of the least altered volcaniclastic carbonatite sample (sample KD016 from borehole KD01) is characterised by a moderately steep slope [mean $(La/Yb)_{cn}$ = 47.50; cn = chondrite-normalised; normalising factors from Evensen et al., 1978)] (Fig. 12.22).

Digitised by the Department of Library Services in support of open access to information, University of Pretoria, 2021

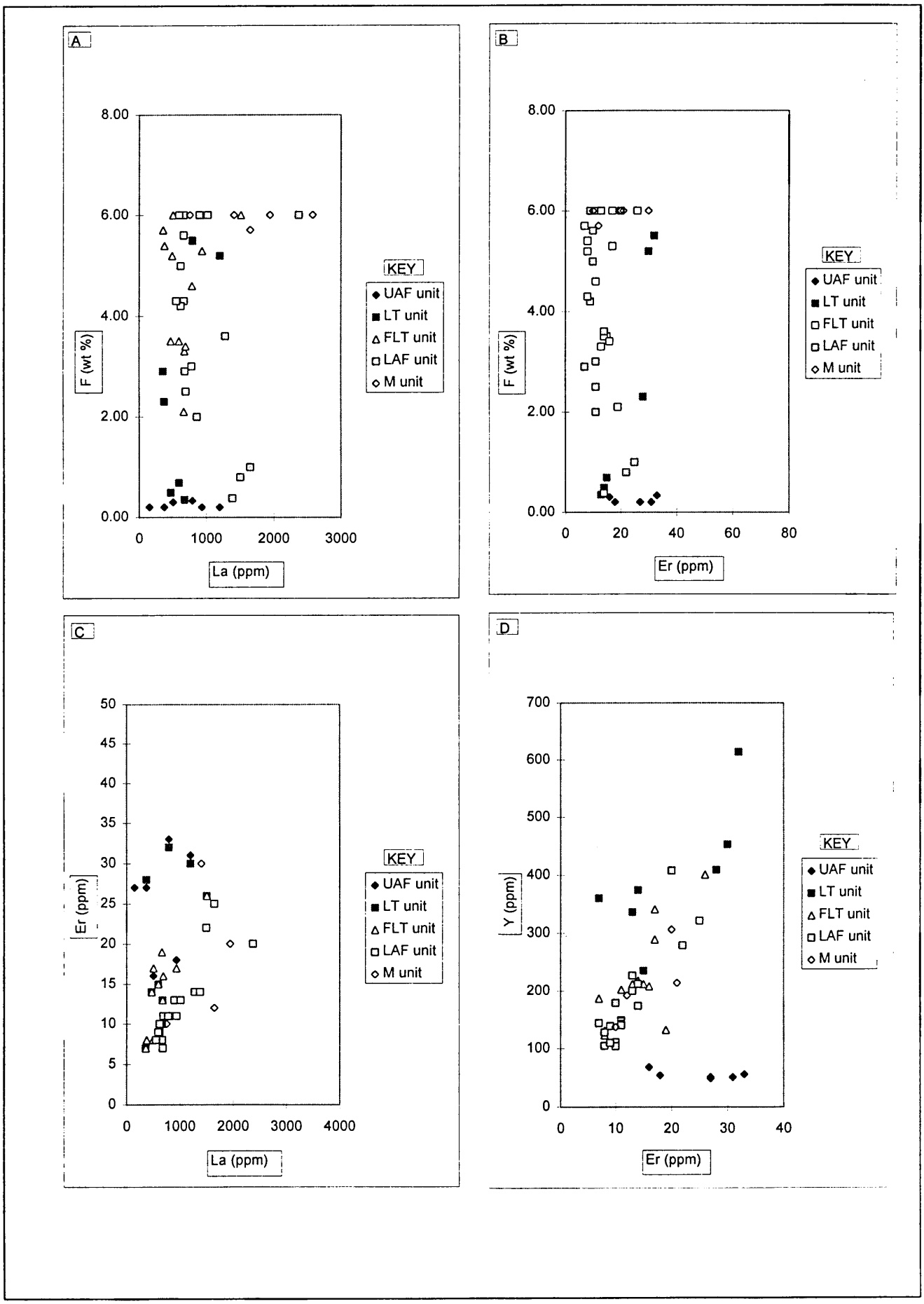

Figure 12.21 Scattergrams (A) La (ppm) versus F (wt%); (B) Er (ppm) versus F (wt%); (c) La (ppm) versus Er (ppm); and (D) Er (ppm) versus Y (ppm) for the volcaniclastic samples (UAF = upper ash flow unit; LT = lapilli tuff unit; FLT = ferruginous lapilli tuff unit; LAF = lower ash flow unit) and mineralised zones (M unit).

Digitised by the Department of Library Services in support of open access to information, University of Pretoria, 2021

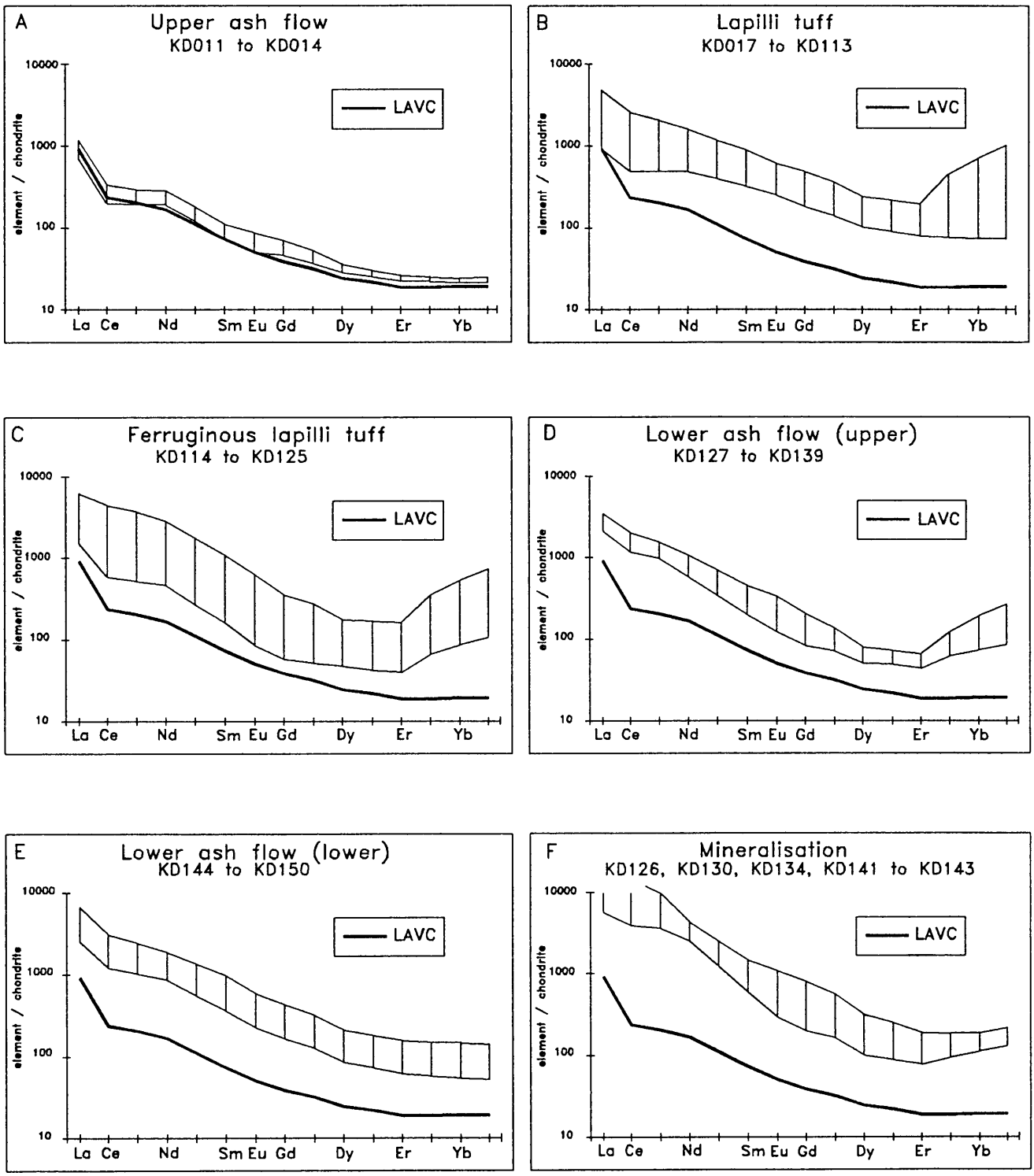

Figure 12.22 Chondrite-normalised (normalising factors from Eversen et al., 1978) rare-earth element trends for samples of the upper ash flow, lapilli tuff, ferruginous lapilli tuff, lower ash flow units and mineralised zones, compared to the least altered volcaniclastic carbonatite (LAVC).

Digitised by the Department of Library Services in support of open access to information, University of Pretoria, 2021

Typically, the light rare-earth elements (LREE) are more strongly fractionated than the heavy rare-earth elements (HREE) [$(La/Sm)_{cn}$ = 11.67; $(Dy/Yb)_{cn}$ = 1.38].

Based on the rare-earth element trends, three broad groups are identified (Fig. 12.22). In general, the more intensely altered rocks have rare-earth element patterns which differ most remarkably from that of the LAVC (least altered volcaniclastic carbonatite). GROUP 1 constitutes weakly altered rocks, such as the upper ash flow unit, which display rare-earth element patterns very similar to that of LAVC. GROUP 2 (lapilli tuff, ferruginous lapilli tuff, and the upper part of the lower ash flow units) is characterised by concave curves with depleted middle rare-earth elements, and enriched light- and heavy rare-earth elements. This group displays quite different rare-earth element ratios, when compared with LAVC, in particular the heavy rare-earth elements are much more strongly fractionated. The increase in fractionation is accompanied by a decrease in the $(Dy/Yb)_{cn}$ ratio from 0.79 (for the pyroclastic breccia unit) to 0.48 (for the upper part of the lower ash flow unit). The increase in heavy rare-earth element fractionation corresponds with an increase in the overall fractionation trend, based on the $(La/Yb)_{cn}$ ratio down the sequence (14.28 for the lapilli tuff unit to 20.55 for the upper part of the lower ash flow unit).

The lower part of the lower ash flow unit and the mineralised zones, constitute GROUP 3 which generally has subparallel to bow-like trends. The light rare-earth elements are highly enriched, while the heavy rare-earth elements are more depleted when compared with those in the overlying GROUP 2.

There is a prominent depletion in rare-earth elements, from the lapilli tuff unit to the ferruginous lapilli tuff unit, and an enrichment from the ferruginous lapilli tuff unit to the mineralised zones. This effect is probably due to the increase in the modal amount of fluorite or any other rare-earth element-enriched phase, with depth. This is accompanied by a coincidental increase in the $(La/Yb)_{cn}$ ratio (seen as an increase in fractionation) from 14.28 (lapilli tuff unit) and 14.06 (ferruginous lapilli tuff unit) to 20.55 (upper part of the lower ash flow unit), 55.38 (lower part of the lower ash flow unit) and 75.48 (mineralised zones).

The rare-earth element trends suggest the involvement of two mineralising phases: (a) a process responsible for rare-earth element trends characterised by a decrease and an increase in heavy rare-earth element fractionation with depth (lapilli tuff, ferruginous lapilli tuff and upper part of the lower ash flow units); and (b) a second process with a prominent enrichment in HREE, an increase in $(La/Dy)_{cn}$ ratio and a decrease in heavy rare-earth element fractionation with depth (lower part of the lower ash flow unit and mineralised zones). The upper ash flow unit was influenced the least by the hydrothermal fluid.

Digitised by the Department of Library Services in support of open access to information, University of Pretoria, 2021

13. STABLE CARBON AND OXYGEN ISOTOPES

Stable isotope analysis provides an important tool to either determine the extent of the rock alteration, or to obtain information about the source of the ore-forming fluids and conditions of the ore deposition. The technique can possibly be used to characterise the fluids involved in the ore-forming processes within the inner zone of the Kruidfontein Carbonatite Complex. Such circulating fluids can cause extensive alteration and leach ore metals from the rock and transport them to other crustal levels where they can be concentrated into ore bodies.

The results of the carbon and oxygen isotope ratio determinations are given in Table 13.1. The whole-rock carbonate oxygen isotope composition varies between $\delta^{18}O$ = 11.5 and 17.7‰, whereas the carbon isotope ratios cover a much smaller range from $\delta^{13}C$ = -3.0 to -1.6‰. No sample plots in the primary igneous carbonatite field (Fig. 13.1), as defined by Taylor et al. (1967); thus a primary magmatic stable isotopic composition was not retained.

The dykes show a linear increase in $\delta^{18}O$ due to oxygen isotope fractionation from sövite to alvikite without a significant change in their $\delta^{13}C$ (Fig. 13.1), as has already been observed by Clarke et al. (1991). Three samples (with >50% carbonate content) from the upper ash flow and lapilli tuff units also follow this trend, but a carbonatitic ash tuff sample (DC in Fig. 13.1) from the upper ash flow unit, has an exceptionally low $\delta^{13}C$ value (-2.9‰). No obvious trend exists for the samples from all other units, which, however, are not strictly carbonatites (with <50% carbonate). The ferruginous lapilli tuff and lower ash flow units show somewhat lower $\delta^{18}O$ values (average 12.2 to 12.8‰) than the upper ash flow and pyroclastic breccia units, and the mineralised zones (averages 14.7 to 14.8 ‰).

The variation in $\delta^{13}C$ for the dolomite- and siderite-dominated ash flow, ash fall, lapilli tuff and mineralised units is relatively small (from -3.0 to -2.0‰) (Fig. 13.1), and no particular trend in the $\delta^{13}C$ values of these units exists. However, $\delta^{18}O$ vs. $\delta^{13}C$ trends for calcite (obtained by sequentially reacting the minerals) differ for calcite-carbonatite dykes (trend **A**) and for calcite in siderite bearing samples (trend **B**) (Fig. 13.2).

The carbon and oxygen isotope pattern of the inner zone of the Complex is the result of several, at least partly, overlapping processes. Deines and Gold (1973) ascribed the higher $\delta^{18}O$ values of the volcanic-subvolcanic carbonatites with decreasing depth to (a) a loss of isotopically light water during pressure release at the time of emplacement; (b) an equilibration of some carbonates with magmatic carbonatite waters at low temperatures; and (c) an influx of meteoric water.

Digitised by the Department of Library Services in support of open access to information, University of Pretoria, 2021

Table 13.1 Carbon and oxygen isotope data of samples from KD01 borehole.

				WHOLE CARBONATE				CALCITE		DOLOMITE CALCITE		SIDERITE	
				ANALYSED		CALCULATED							
Unit	Rock	Sample	Carbonate	$\delta^{18}O$	$\delta^{13}C$	$\delta^{18}O$	$\delta^{13}C$	$\delta^{18}O$	$\delta^{13}C$	$\delta^{18}O$	$\delta^{13}C$	$\delta^{18}O$	$\delta^{13}C$
Dyke	sövite	S2	calcite	12.1	-2.0								
	sövite	S3	calcite	13.4	-2.0								
	alvikite	A1	calcite	14.0	-2.1								
	alvikite	A2	calcite dolomite	17.7	-1.6	17.2	-1.8	15.8	-2.1	21.9	-1.1		
UAF	tuff	KD013	dolomite	15.7	-2.0								
	tuff	KD016	dolomite calcite	13.6	-2.9								
LT	tuff	KD019	dolomite	13.7	-1.9								
	tuff	KD111	dolomite	15.1	-2.2								
	tuff	KD113	dolomite siderite	15.5	-2.0								
FLT	tuff	KD116	siderite	11.8	-2.5								
	tuff	KD118	dolomite siderite	12.8	-2.4								
	tuff	KD121	siderite	11.5	-2.4								
	tuff	KD124	dolomite siderite	12.7	-2.2								
LAF	tuff	KD133	ankerite calcite, siderite	12.5	-2.3	12.0	-2.3	14.1	-2.6	13.2	-2.1	11.6	-2.3
	tuff	KD138	ankerite calcite, siderite	13.4	-2.6	13.0	-2.5	14.2	-3.0	13.4	-2.8	12.6	-2.4
	tuff	KD146	calcite ankerite siderite	14.7	-2.0	14.6	-2.0	14.2	-2.5	15.0	-2.1	14.6	-2.0
	tuff	KD147	calcite ankerite, siderite	14.1	-2.2	13.5	-2.3	15.0	-2.7	14.3	-2.6	13.3	-2.2
M	tuff	KD130	calcite siderite	11.8	-2.7	11.8	-2.8	13.7	-2.2			11.5	-2.8
	tuff	KD134	dolomite calcite, siderite	13.7	-2.1	12.8	-2.4	14.2	-2.5	14.5	-2.1	11.3	-2.5
	tuff	KD141	calcite siderite	13.9	-1.8								
	tuff	KD142	siderite calcite	15.9	-3.0	15.7	-3.2	16.1	-3.2			15.3	-3.2

UAF = upper ash flow unit, LT = lapilli tuff unit; FLT = ferruginous lapilli tuff unit; LAF = lower ash flow unit

Digitised by the Department of Library Services in support of open access to information, University of Pretoria, 2021

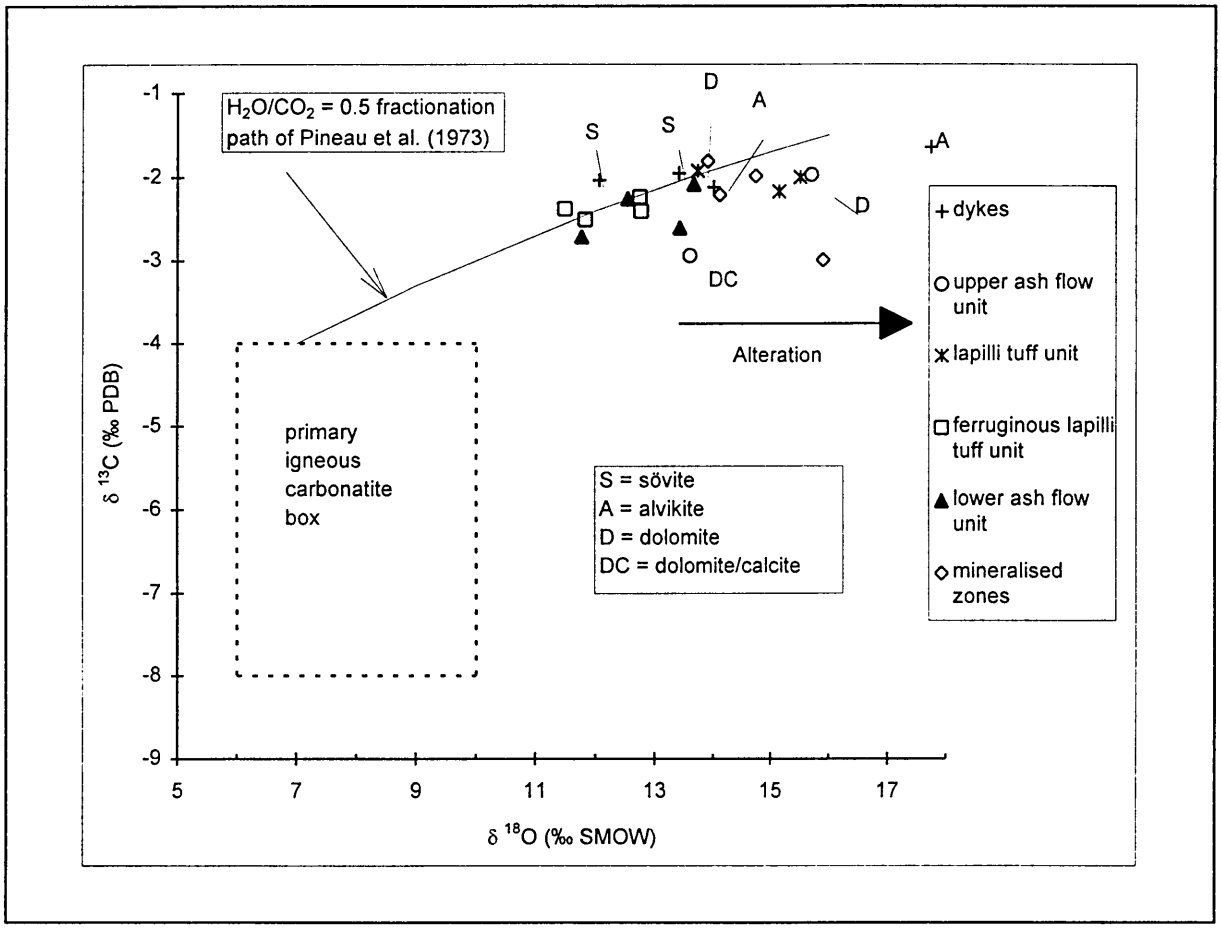

Figure 13.1 C and O isotope distribution pattern of carbonates from the Kruidfontein Carbonatite Complex compared with the fractionation path after Pineau et al. (1973). Letters mark samples from carbonatite dykes and carbonatitic ash flow tuffs with >50% carbonates.

Digitised by the Department of Library Services in support of open access to information, University of Pretoria, 2021

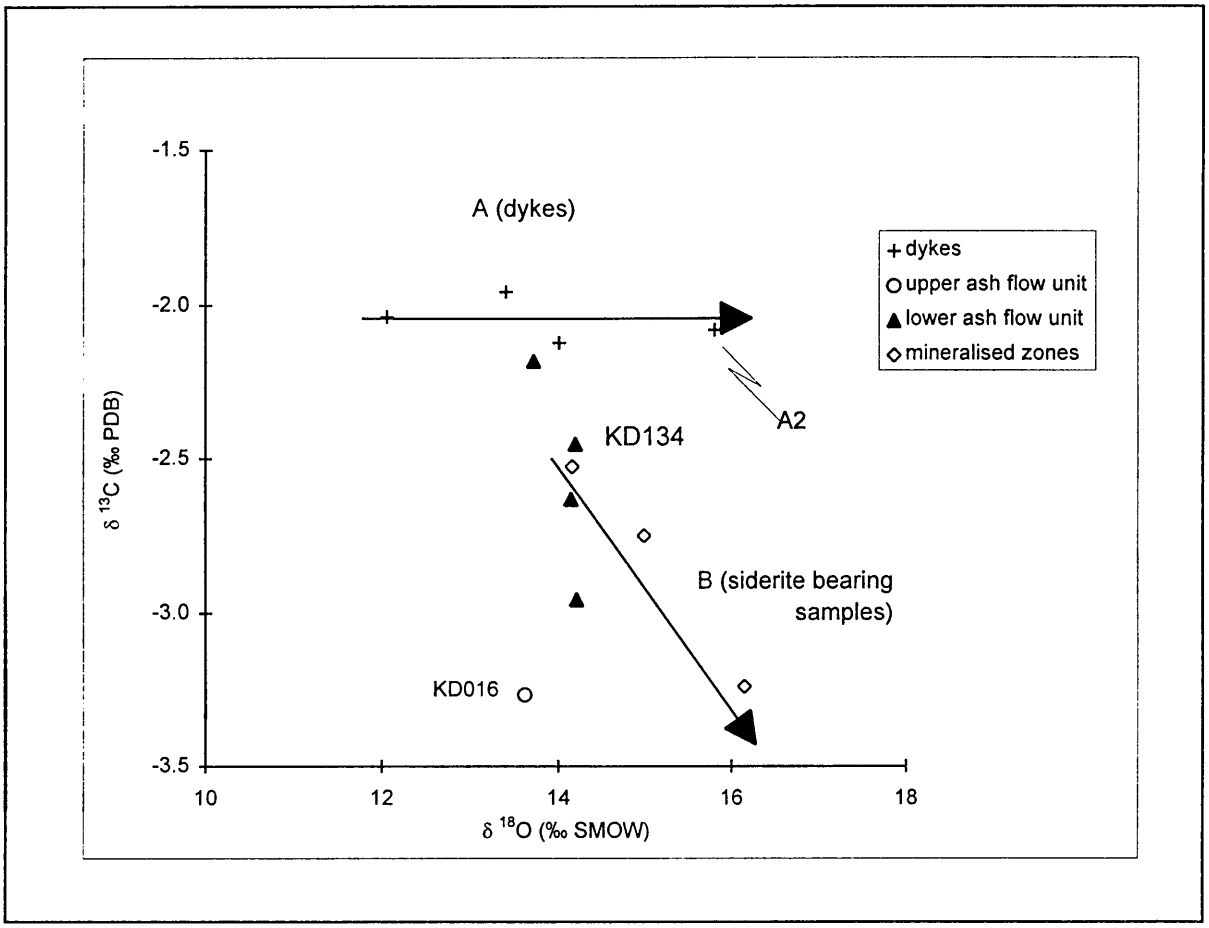

Figure 13.2 $\delta^{18}O$ and $\delta^{13}C$ of calcite (data from sequential reactions in cases where two or more carbonate minerals are present). Trend **A** characterises intrusive carbonatite dykes, trend **B** belongs to siderite-bearing samples.

Digitised by the Department of Library Services in support of open access to information, University of Pretoria, 2021

13.1 Rayleigh fractionation

Secondary alteration and mineralisation which relate to explanations (b) and (c) of Deines and Gold (1973), surely contributed to the carbon and oxygen isotope distribution observed at Kruidfontein. The $\delta^{18}O$/ $\delta^{13}C$ pattern (Fig. 13.1) suggests a slight, positive correlation between $\delta^{18}O$ and $\delta^{13}C$, especially for the carbonatitic lower ash flow tuff. Such a trend seems to be common among carbonatites (Deines, 1989) and cannot be explained simply by a loss of isotopically light water. Pineau et al. (1973) suggested that the increase in $\delta^{18}O$ and $\delta^{13}C$ values in volcanic carbonatite complexes could be the result of Rayleigh fractionation of the carbon and oxygen isotopes during the differentiation of the carbonatite from an alkaline silicate magma at magmatic temperatures. In the course of this differentiation process a CO_2-rich fluid phase with high $\delta^{13}C$ values is separated. This fluid interacts with the surrounding rock and becomes enriched in rare-earth elements and volatiles, further enhancing $\delta^{13}C$ and $\delta^{18}O$. Upon re-entering the carbonatite, this fluid is re-incorporated resulting in the observed increase in $\delta^{13}C$ and $\delta^{18}O$ values. The enrichment of heavy carbon and oxygen isotopes therefore appears to be a late-magmatic/metasomatic process rather than a direct magmatic fractionation of carbonates, which precipitate from a magma with a coexisting vapour phase under closed-system conditions.

Pineau et al. (1973) calculated Rayleigh fractionations between calcite and a coexisting vapour phase at 700°C in a closed system with different H_2O/CO_2 ratios. When less than 30% of the oxygen present is in the form of water and silicates, a ^{13}C- and ^{18}O-enriched fluid is formed. The slope of the $\delta^{18}O/\delta^{13}C$ evolution curves is dependent on the H_2O/CO_2 ratio and decreases with decreasing temperature, in some cases reaching negative values at temperatures below 400°C.

The oxygen and carbon isotope fractionation path of Pineau et al. (1973), which refers to a reservoir with a H_2O/CO_2 molar ratio of 0.5, is shown on Figure 13.1. It appears to agree closely with the data of this study. This has also been observed by Clarke et al. (1991). Samples that lie below the fractionation path must have been affected by other isotopic exchange processes. This implies that the suggested Rayleigh fractionation path could also be represented by curves through the maximum $\delta^{13}C$ values of calcite from magmatic sequences (Nielsen and Buchardt, 1985). Accordingly, the H_2O/CO_2 curve shown could possibly be moved to a starting composition of lower $\delta^{18}O$ and higher $\delta^{13}C$ values, without affecting its slope (Fig. 13.1). However, an exact calculation of the fractionation path cannot be made because fractionation temperatures and the composition of the coexisting vapour phase are unknown.

The Rayleigh fractionation model of Pineau et al. (1973) has been applied in a similar manner by Clarke et al. (1991) to the Kruidfontein Carbonatite Complex, by Nielsen and Buchardt (1985) to the Tertiary Gardiner Complex in east Greenland and by Reid and Cooper (1992) to the Tertiary

Digitised by the Department of Library Services in support of open access to information, University of Pretoria, 2021

Dicker Willem Carbonatite Complex in Namibia. The process of carbon and oxygen isotope fractionation seems to be common to the evolution of relatively high-level intrusive, volcanic to subvolcanic carbonatite complexes, from the mid-Proterozoic to the Tertiary. In contrast, deep-seated intrusions like the Qaqarssuk Carbonatite Complex, southwest Greenland, (Knudsen and Buchardt, 1991) do not adhere to the model of Pineau et al. (1973). Knudsen and Buchardt (1991) describe a depletion in heavy carbon from the main-stage carbonatites to the late-stage calcite-carbonatite, which they explain as a loss of heavy carbon to a gas phase. Rare-earth element-carbonatites, as well as ferrocarbonatites at Qaqarssuk, however, have elevated $\delta^{18}O$ and $\delta^{13}C$ values which, after Knudsen and Buchardt (1991), are most likely caused by Rayleigh fractionation. Therefore the site of intrusion and the stage of evolution of a carbonatite complex seem to determine the applicability of the Rayleigh fractionation model of Pineau et al. (1973).

The Kruidfontein carbonatite dykes intruded at the highest possible level and affected their own pyroclastic cover. The carbon and oxygen isotope distribution pattern could, therefore, well have originated from a Rayleigh fractionation at an early stage of carbonatite evolution, as discussed above. The high level of intrusion, however, allowed fluids such as meteoric ground water, to enter and leave the carbonatite magma, especially in the later stages of the carbonatite evolution. It can thus be concluded that the primary carbon and oxygen isotope pattern of the carbonatite originated from fractionation of carbon and oxygen isotopes between the carbonatite and an H_2O-CO_2 vapour phase, and that of the stable isotope distribution was later changed by subsolidus, secondary alteration, to the present pattern.

13.2 Carbon and oxygen stable isotopes and temperature estimation

Three samples (A2, KD016 and KD134) contained reasonable quantities of coexisting dolomite and calcite and were suitable for sequential CO_2-extraction. The oxygen isotope fractionation between dolomite and calcite of these samples, however, yielded unreasonable $\Delta^{18}O_{dol/cal}$ values (6, -0.1 and 0.3 respectively), so that meaningful temperatures could not be obtained from the oxygen isotope data. By contrast, the calculated carbon isotope fractionation of A2 and KD016 is $\Delta^{13} C_{dol/cal}$ = 1.0 and 1.3 respectively, leading to temperatures of 192°C and 126°C respectively, according to the isotope thermometer of Sheppard and Schwarcz (1970) (in Friedman and O'Neil, 1977). Sample KD134 showed a very low $\Delta^{13}C_{dol/cal}$ of 0.4 which implies an unrealistically high temperature of more than 600°C.

The carbon isotope temperatures of samples A2 and KD016 may therefore be considered to indicate the temperature at which alteration in the Kruidfontein Carbonatite Complex took place. The difference in carbon isotope fractionation between these two samples and KD134 can be explained by their provenance and mineralogical composition. Samples A2 and KD016 are from

Digitised by the Department of Library Services in support of open access to information, University of Pretoria, 2021

a dyke and a carbonatitic ash flow respectively, with their carbonates comprising only dolomite and calcite, whereas KD134 was taken from a mineralised zone within the lower ash flow unit and it contained three carbonate species: dolomite, calcite and siderite. Siderite mineralisation facilitates isotopic exchange between the carbonate species, and this is thought to be the most likely cause of the extremely small carbon-isotope fractionation of KD134. This interpretation is supported by Figure 13.2, where the siderite-bearing KD134 lies in a trend of increasing $\delta^{18}O$ and decreasing $\delta^{13}C$ values. By contrast A2 forms part of a trend of consistent $\delta^{13}C$, and KD016 is on its own on the $\delta^{18}O$/ $\delta^{13}C$ diagram. This observation points to a difference in evolution of the dykes and carbonatitic ash flows consisting of dolomite and calcite, on one hand, and the siderite + (dolomite + ankerite + calcite)-bearing ash flow tuff units on the other.

Wall et al. (1994) interpreted a trend like **A** on Figure 13.2 as re-equilibration of Fe-bearing carbonates with a carbonatite-derived fluid as the intrusion cooled, and a trend like **B** as a response to low temperature interaction with ground water in the course of deep weathering.

The mean temperature of samples A2 and KD016, derived from the carbon isotope ratios, is 159°C. In the following discussion the temperature of the fluids involved in the secondary alteration of the dykes and ash flows at Kruidfontein will be assumed to be 150°C. This is well in agreement with the suggestion of Clarke et al. (1991), namely from 100°C to 200°C for the hydrothermal alteration of the Kruidfontein Carbonatite Complex, partly due to equilibration of the hydrothermal fluid with ground water at low temperatures. It should be mentioned, however, that Knudsen and Buchardt (1991) found that the dolomite/calcite isotope thermometer of Sheppard and Schwarcz (1970) could not be applied directly to the Qaqarssuk Carbonatite Complex, as originally it had been calibrated on metamorphosed dolomitic limestones.

13.3 Characteristics of secondary alteration fluid

13.3.1 Calcite/dolomite

This estimated temperature of 150°C can be used to determine the isotopic characteristics of the fluid which caused the secondary alteration of the dykes and carbonatitic ash flows in the Kruidfontein Carbonatite Complex. Equilibration of the hydrothermal fluids with meteoric waters was very likely (Clarke et al., 1991) and this implies that the isotopic exchange had to occur below 200°C to 250°C, in order to increase the $\delta^{18}O$ value of the carbonates (Deines, 1989). In this fluid, H_2O was the predominant oxygen carrier and hence the fractionation between calcite and H_2O can be calculated, i.e. $\Delta^{18}O_{cal/H_2O}$ at 150°C equals 12.6‰ (Friedman and O'Neil, 1977). The average $\delta^{18}O_{cal}$ of the dykes and carbonatitic ash flows (Table 13.1) is 13.8‰ which

Digitised by the Department of Library Services in support of open access to information, University of Pretoria, 2021

results in a fluid isotopic value of $\delta^{18}O_{H_2O}$ = 1.2‰. This value is considerably higher than that of meteoric waters (-6 to -10‰), and this increase can only be explained by isotopic exchange with country rocks. Such a country rock is the surrounding Malmani dolomite with a strong positive $\delta^{18}O$ of 20±1‰ (Schiffries and Rye, 1989; Horstmann and Verwoerd, 1997), and these values (-6 ‰ for meteoric water and 20 ‰ for dolomite) would imply roughly a 77% contribution from the meteoric water and a 23% contribution from the dolomite. Such an influx of ground water from the Malmani dolomite, leading to high $\delta^{18}O$ values, was suggested by Clarke et al. (1991). They also assumed that vadose water from a caldera lake overlying the Kruidfontein Carbonatite Complex might have played a role.

The $\delta^{13}C$ value of the alteration fluid can be calculated by using the $\delta^{13}C$ value of the carbonate mineral involved (calcite) and the fractionation between the mineral and H_2CO_3. At a temperature of 150°C the amount of HCO_3^- is negligible when compared to H_2CO_3 (Ohmoto, 1986). Based on the approximation by Ohmoto (1972) the C-isotope fractionation between H_2CO_3 and CO_2 (gas) is:

$$\delta^{13}C_{H_2CO_3} \approx \delta^{13}C_{CO_2}.$$

The ^{13}C value of a fluid can be calculated as:

$$\delta^{13}C_{CO_2} = \delta^{13}C_{calcite} - \Delta^{13}C_{calcite/CO_2}.$$

$\Delta^{13}C_{calcite/CO_2}$ at 150°C equals 1.5 (Friedman and O'Neil, 1977) which yields a value of $\delta^{13}C_{CO_2}$ = -3.8‰ for a CO_2/H_2CO_3 bearing fluid, and taking $\delta^{13}C$ = -2.3‰ as the average of the dykes and carbonatitic ash flows. The above evidence indicates that the fluids have remained at temperatures below 250°C, i.e. the temperature required for equilibration between CO_2 and CH_4 (low-temperature non-equilibrium system, Ohmoto, 1986). Therefore, following Ohmoto (1986), the $\delta^{13}C_{CO_2}$ values most probably directly indicate the source of carbonate carbon. The value of $\delta^{13}C_{CO_2}$ = -3.8‰ lies within the range of geothermal fluids Hoefs (1987) and deep-seated carbon (Deines and Gold, 1973).

This corresponds to the recrystallisation described by Clarke and Le Bas (1990), and most probably includes the formation of dolomite (and possibly ankerite) in the carbonatites (dolomitisation after Verwoerd, 1967). A separate ankeritisation process which would be characterised by a somewhat higher $\delta^{13}C$ value, as outlined by Clarke and Le Bas (1990), cannot be deduced from the present stable isotope data, as ankerite

Digitised by the Department of Library Services in support of open access to information, University of Pretoria, 2021

was only observed sporadically, and in small quantities (2 to 5%; Table 13.1) in the siderite-bearing ash flow tuff units. The Malmani dolomite could have been a source of the Mg, and possibly the Fe, required for the formation of dolomite (and possibly ankerite). Ground waters emanating from these rocks would carry leached Mg (and Fe) and enrich the above mentioned alteration fluid in these elements, facilitating dolomitisation (ankeritisation).

13.3.2 Siderite

Siderite mineralisation has not been described previously from the Kruidfontein Carbonatite Complex. Isotopically, the siderite and siderite-bearing samples can be distinguished from calcite and calcite / dolomite / ankerite samples by an average 1-2‰ lower $\delta^{18}O$ values. δ^{8} O of whole-carbonate analyses and the modal percentage of siderite show a strong negative correlation (Fig. 13.3) when two samples from the mineralised units are excluded. Figure 13.4 displays a reasonably strong positive correlation between $\delta^{18}O$ and δ^{13} C of siderite (sequentially reacted in case of multi-carbonate samples), when one mineralised sample (KD142) and a siderite-rich sample of the lower ash flow tuff (KD130) are excluded.

The carbon and oxygen isotope fractionation of siderite has been experimentally investigated in the temperature range between 33°C and 197°C by Carothers et al. (1988). An estimation of the siderite mineralisation temperature, however, is much more difficult than in the case of dolomite/calcite, as no siderite thermometer exists. Furthermore, the isotopic ratio of the only dolomite/calcite pair in a siderite-bearing sample (KD134) was disturbed by the formation of siderite. An attempt was therefore made to relate the formation of siderite to the alteration temperature based on the isotopic ratio of dolomite/calcite in the dykes and carbonatitic ash flows. Replacements of other carbonates by siderite suggests that siderite is younger than the other carbonates and hence it can be assumed that it formed at lower temperatures during cooling of the Kruidfontein Carbonatite Complex, probably at or below 150°C. Assuming further that water was the major source of oxygen, the oxygen isotope fractionation of siderite/water can be inferred to be $\Delta^{18}O_{sid/H_2O}$= +14‰ at 150°C, based on data from Carothers et al. (1988). Based on an average of $\delta^{18}O$ = 12.6‰ for the siderite samples, this value leads to a $\delta^{18}O_{H_2O}$ of -1.4‰ for the siderite precipitating fluid. Carbon isotope fractionation between siderite and CO_2 can be determined in a similar way. According to Carothers et al. (1988) $\Delta^{13}C_{sid/CO_2}$ = 5.63‰ at 150°C and with an average $\delta^{13}C$ of -2.4‰ of the siderite analysed, the mineralising fluid causing the precipitation of siderite had a $\delta^{13}C_{CO_2}$ of -8.0 ‰. The siderite in the Kruidfontein Carbonatite Complex is thus likely to

Digitised by the Department of Library Services in support of open access to information, University of Pretoria, 2021

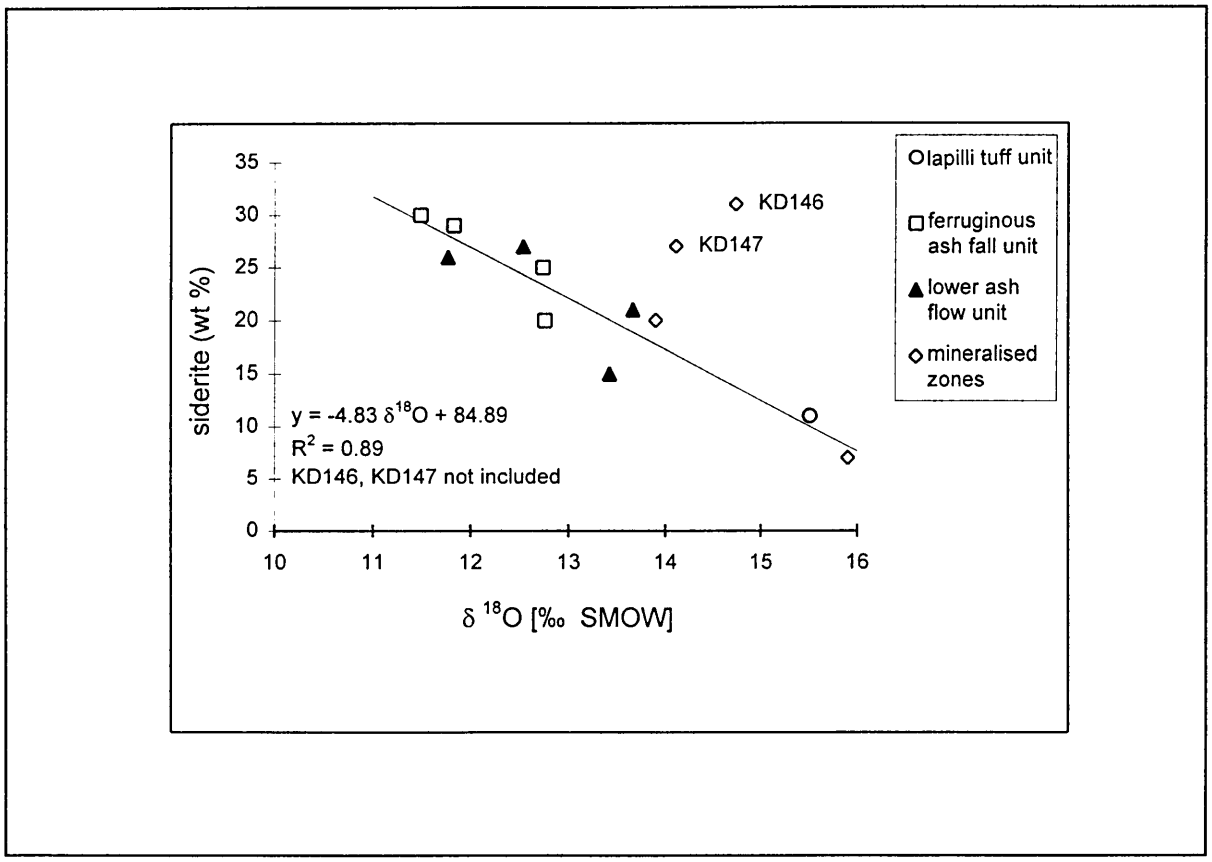

Figure 13.3 Whole rock carbonate $\delta^{18}O$ ratio versus modal siderite content.

Digitised by the Department of Library Services in support of open access to information, University of Pretoria, 2021

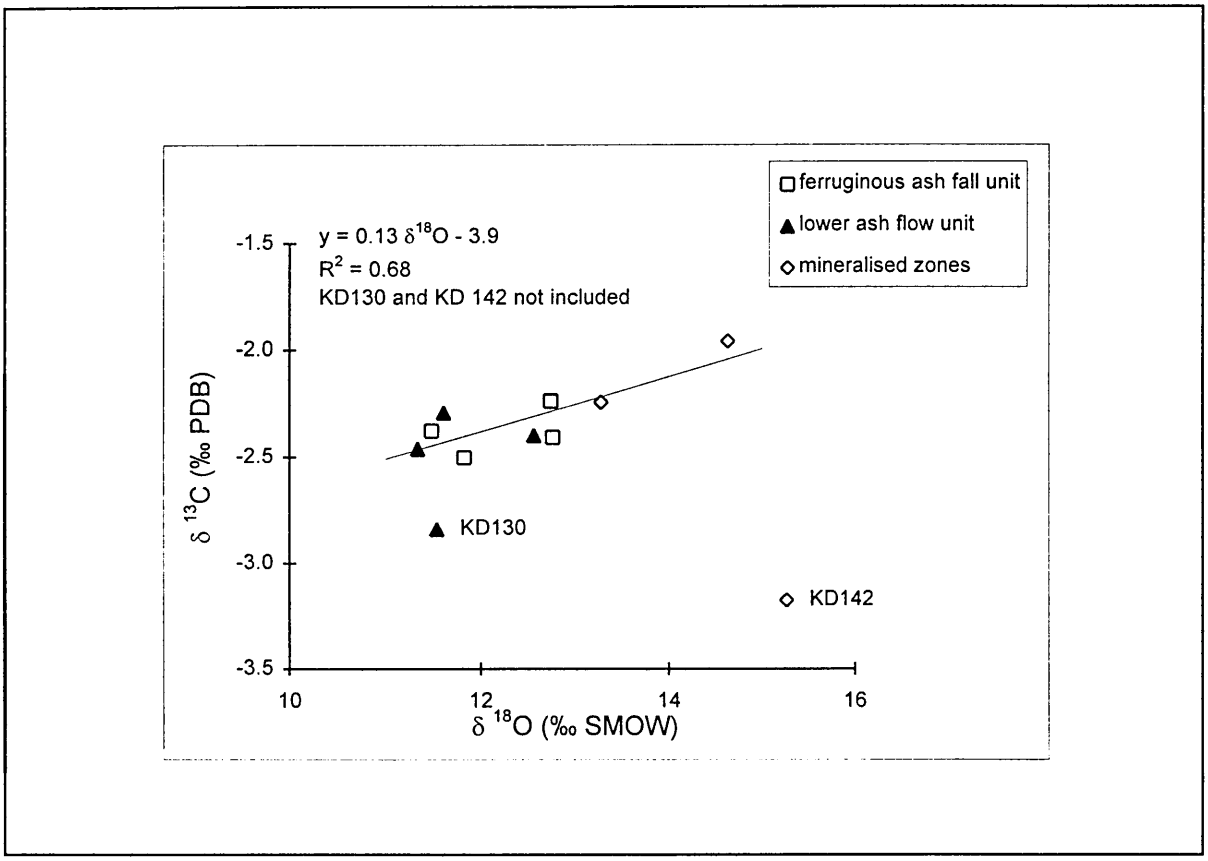

Figure 13.4 $\delta^{18}O$ versus $\delta^{13}C$ of siderite in monocarbonates and sequentially reacted siderite from multicarbonates.

Digitised by the Department of Library Services in support of open access to information, University of Pretoria, 2021

have been precipitated from by a late-stage Fe-bearing hydrothermal fluid, depleted in ^{18}O and ^{13}C.

This deduced depletion in ^{18}O and ^{13}C for the siderite precipitating fluids suggests that the negative correlation between the whole carbonate $\delta^{18}O$ values and the modal siderite content points to an overprint of the siderite fluids on the whole carbonate ^{18}O contents (Fig. 13.3), causing lower $\delta^{18}O$ values with increasing precipitation of siderite. This underlines the secondary nature of the siderite mineralisation with respect to the alteration of dykes and the carbonatitic ash flow. Another line of evidence for secondary siderite mineralisation comes from ^{18}O and ^{13}C enrichments in calcite relative to the associated siderite. This is the opposite of what one would expect when applying the appropriate fractionation factors from Friedman and O'Neil (1977), and Carothers et al. (1988) to cogenetic minerals precipitated during a single stage from one fluid. Figure 13.4 supports the assumption that siderite formed during progressive cooling of the Kruidfontein Carbonatite Complex, so that during cooling, lower temperatures led to higher $\delta^{18}O$ and $\delta^{13}C$ values of siderite, as reflected by the positive correlation between $\delta^{18}O$ and $\delta^{13}C$. The fact that two samples (KD130 and KD142) do not fall on the trend line is probably the result of variations in temperature and/or the ^{18}O content of the fluid.

The strongly negative $\delta^{13}C$ values deduced for the siderite precipitating fluid, point to a source of deep-seated carbon. Siderite is thus thought to have been formed by hydrothermal fluids containing carbon from a deep-seated source whereas the Fe could have been leached from the country rocks through which the fluid passed. A similar process was also noted by Cortecci and Frizzo (1993), who found stratiform siderite metasomatically replacing calcite in host carbonate rocks.

13.4 Ankeritisation

In trying to explain the ankeritisation of carbonatitic tuffs at Kruidfontein, Clarke and Le Bas (1990) could not identify the source of the Fe, but suggested that it was related to the earliest metasomatic process. This would agree with the normal sequence of late-stage activity at carbonatitic centres, as recognised by Le Bas (1987), with iron-mineralisation followed by rare-earth-element mineralisation, and finally fluorite and barite precipitation. In the case of Kruidfontein, processes like iron-mineralisation followed by fluorite mineralisation postdate the dykes and carbonatitic ash flow alteration, although a partial overlap in time cannot be excluded. Verwoerd (1967) described carbonatisation of the tuffaceous deposits at Kruidfontein that had apparently taken place in two stages, leading to the initial formation of metasövite and later of

Digitised by the Department of Library Services in support of open access to information, University of Pretoria, 2021

metabeforsite. The results of this work suggest that the metasövite formation of Verwoerd (1967) could be related to the alteration of the dykes and the carbonatitic ash flow tuffs, or to the recrystallization proposed by Clarke and Le Bas (1990). The metabeforsite stage can be considered to be an equivalent of the siderite mineralisation, although Verwoerd (1967) did not record any siderite, but found only ankerite as Fe-carbonate in the metabeforsites. Hydrothermal activity manifested itself in all the carbonate rocks at Kruidfontein by the presence of fluorite, barite, apatite and anatase, and Verwoerd (1967) also suggested that it was also responsible for the carbonatisation.

13.5 Relationship between $\delta^{18}O$ and fluorite

No relationship exists between $\delta^{18}O$ of the carbonates as a whole and the fluorite content of the rocks (Fig. 13.5) in contrast the relationship between $\delta^{18}O$ and siderite (Fig. 13.3). Neither does the carbon isotope composition change systematically with the fluorite content. In some units (e.g. the mineralised zones) there may be a rough trend of higher $\delta^{18}O$ values with increasing fluorite content. Within the dykes, the sample with the lowest fluorite content is a calcite-carbonatite with a $\delta^{18}O$ value of 13.30‰; the two others with higher fluorite contents are fluorite-calcite-carbonatite and have higher $\delta^{18}O$ values. This is much more poorly constrained in the present data set than in that described by Clarke and Le Bas (1990). From the scatter in the oxygen isotope composition and the $\delta^{18}O$ values it is suggested that the fluorite mineralisation was probably a late-stage event, initiated by F-bearing hydrothermal solutions which mixed with vadose water at temperatures of between 100°C and 200°C. Le Bas (1987) and Clarke et al. (1991) reached similar conclusions.

Digitised by the Department of Library Services in support of open access to information, University of Pretoria, 2021

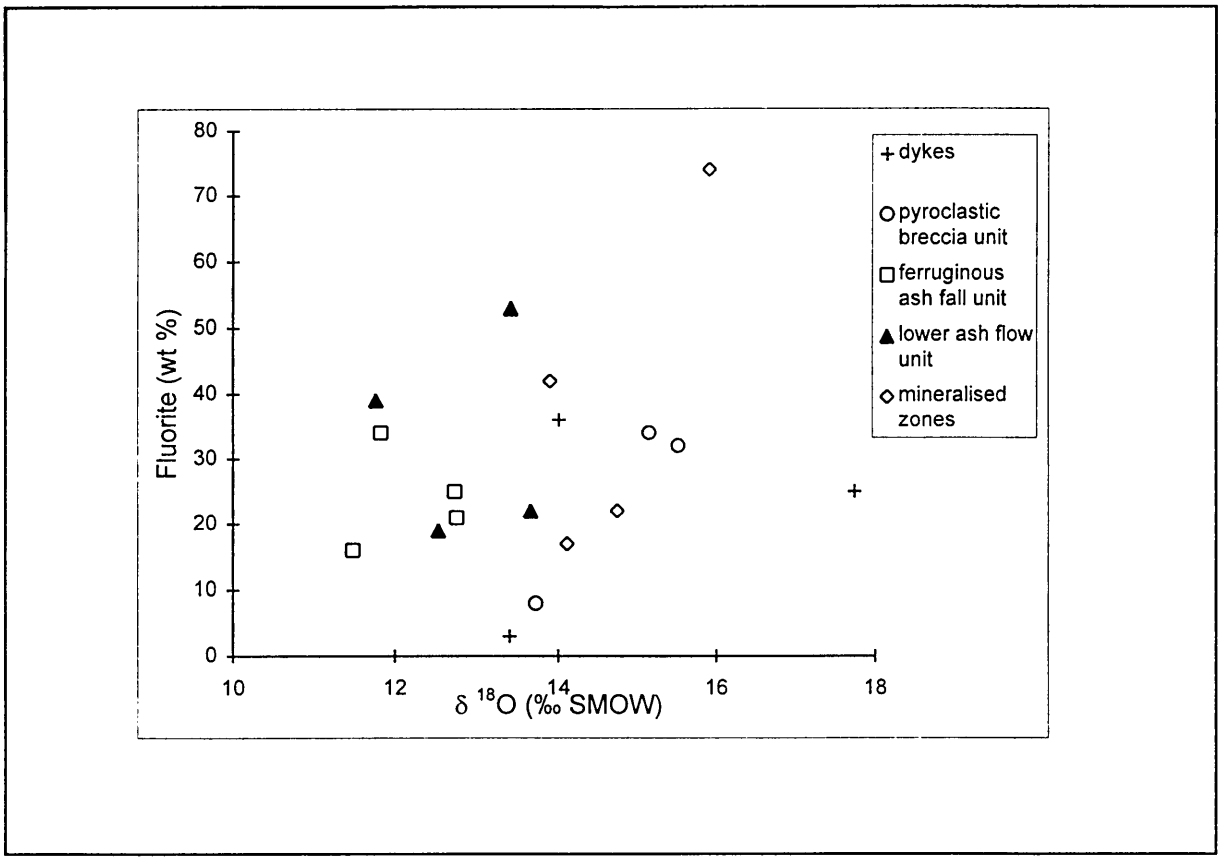

Figure 13.5 Whole rock carbonate $\delta^{18}O$ ratio versus modal fluorite content.

Digitised by the Department of Library Services in support of open access to information, University of Pretoria, 2021

14. TOWARDS A MODEL FOR THE KRUIDFONTEIN CARBONATITE COMPLEX

14.1 Properties of carbonatite magma and its relation to alkaline magmatism

Eruptive styles of carbonatite volcanism are closely linked to the chemical and physical properties of the carbonatite magma. Barker (1996) showed that carbonatite liquid has lower a density and viscosity, and higher heat capacity and thermal expansion than most silicate liquids. Fluid inclusions in calcite from Fort Portal, Uganda yield homogenisation temperatures of 630 to 650°C, while temperatures for fluid inclusions in apatite from carbonatite were estimated at 690 to 710°C (Romanchef and Sokolov, 1980). Other properties of carbonate liquid are summarised in Table 14.1.

Table 14.1 Physical properties of calcium carbonate liquid.

PROPERTY	CARBONATE LIQUID	REFERENCE
Enthalpy of fusion, J g^{-1}	315	Treimann, 1995
Volume change on fusion, cm^{-3} g^{-1}	0.025	Treimann, 1995
Density, kg m^{-3}	2200 - 2400	Wolff, 1994
Viscosity, Pa s	0.08	Wolff, 1994
Surface tension, N m^{-1}	0.25	Wolff, 1994
Heat capacity at constant pressure, J K^{-1} g^{-1}	1.65	Genge et al., 1995b
Isobaric thermal expansion, 10^{-4} m K^{-1}	1.457	Genge et al., 1995b
Isothermal compressibility, 10^{-3} kb^{-1}	6.7	Genge et al., 1995b

It is important to note that carbonatites seldom occur in isolation without associated silica-undersaturated rocks of the same age and related genesis. Two suites of silicate rocks have been identified in the Gregory Rift, East Africa (Williams, 1969; Le Bas, 1979; 1987; Barker, 1996). The first suite is nephelinite - basanite - phonolitic tephrite - tephritic phonolite - phonolite, and the second is alkali basalt - hawaiite - mugearite - benmoreite - trachyte - phonolite. According to Le Bas (1987) the first association originates from olivine-poor, but clinopyroxene-rich nephelinite (<10% MgO) and is associated with carbonatites. On account the low olivine content these magmas can be expected to have a higher viscosity, and hence to be more prone to pyroclastic eruptions than corresponding members of the second suite. The second association is thought to originate from olivine-rich nephelinites and melilitites (≥10% MgO), and is not associated with carbonatite. Examples of silica-undersaturated magmas are the following: the Miocene Yatta phonolite, Kenya; Mount Suswa, Kenya and phonolite lava domes, Le Velay, France (Barker, 1987, 1996; Mergoil et al., 1993).

Digitised by the Department of Library Services in support of open access to information, University of Pretoria, 2021

14.2 Properties of pyroclastic deposits

Several types of deposits, based on three mechanisms of transport and deposition have been defined (Barker, 1996). Air-fall deposits display moderate to good size sorting and stratification, and their basal contacts usually are depositional and not erosional (Barker, 1996). Pyroclastic surge deposits are formed by rapidly moving, low-concentration gravity flows, showing variable stratification, an erosional basal contact, and abrupt changes in sorting and grain size. Pyroclastic flow deposits are formed by rapidly moving, turbulent to laminar, high-concentration gravity flows. These deposits are poorly sorted and may be welded, containing flattened clasts and fragments.

According to Barker (1996), two styles of volcanism can be distinguished, based on the persistence of eruption through a vent. A monogenetic volcano will erupt for a brief time span from a specific vent, thus displaying a narrow compositional range, building scoria cones, tuff rings, tuff cones or maars. A new conduit may be formed, starting a new vent. Examples of monogenetic volcanic fields, consisting of tens or hundreds of small volcanoes are found around Auckland, New Zealand (Johnson et al., 1989) Honolulu, Hawaii (Clague, 1987) and in the East African rift valley (Le Bas, 1987).

Volcanoes which display a wide variation in magma composition, of which the Kruidfontein Complex, may be an example, are built over a span of thousands of years of activity and are classified as polygenetic. They can be found in the form of shields, stratovolcanoes, caldera systems and flood lavas (Barker, 1996). Stratovolcanoes are built by eruptions in which pyroclastic deposits dominate. Reworked debris is also a significant component, and according to Cas and Wright, (1987) and Barker, (1996) reworking is promoted by long repose times, high elevations and steep slopes. Barker (1996) also reports that calderas in silica-undersaturated magma systems are relatively small and fairly uncommon.

Although in terms of volume, carbonatite magma batches are small, both in monogenetic and polygenetic volcanism (Barker, 1996), their eruptive style is similar to that of silica-undersaturated volcanism. It includes air-fall and surge deposits, pyroclastic breccias and debris flows. Examples of carbonatitic lapilli tuff are known from Kaiserstuhl (Keller, 1981; 1989), Fort Portal, Uganda (Barker and Nixon, 1989) and the Island of Brava, Cape Verdes (Lorenz, 1986).

14.3 Volcanic interpretation of the Kruidfontein Carbonatite Complex

14.3.1 Outer zone

Although the outer zone has been subdivided into the younger pyroclastic breccia, ignimbrite and older pyroclastic breccia (Verwoerd, 1967) it will be discussed as a unit (Fig. 7.1). Although Clarke (1989) inferred shallow dips towards the centre of the

Digitised by the Department of Library Services in support of open access to information, University of Pretoria, 2021

Complex, present field evidence suggests the centroclinal dip in the southern, southeastern and eastern sides of the outer zone to be about 15°, whereas it increases considerably in the western part. The northwestern, northern and northeastern sides display dips of about 40°.

The pyroclastic breccias are thought to be the proximal facies of larger flows of which the fine-grained, distal portions have been eroded. However, it is possible that several irregular pockets of distal volcaniclastic rocks may be preserved north of the Kruidfontein Complex on the farms Boschkop 138JQ and Elandsfontein 23JQ. The presence of deformed vesicular material (indicating the extrusion of hot material), the wide lateral extent of the breccias of the outer zone and the close association of ignimbrite flows and the breccias indicate that these breccias were formed by the sedimentation of coarse-grained, dense, juvenile pyroclastic flows. On account of their proximal nature, their coarseness and thickness, Clarke (1989) postulated that these breccias could be lag deposits, formed in a turbulent near-vent region. The variation in clast size, together with the varying composition of clasts and matrix, points to different stages of volcanic activity from different vents. The ignimbrite unit is seen as a sequence of pyroclastic flows, showing incipient welding and a well developed flow banding (i.e. eutaxitic texture), emphasising hot and rapid eruption.

14.3.2 Inner zone

Based on their fabric, the volcaniclastic rocks of the inner zone can be classified as ash and lapilli tuffs and pyroclastic breccias, according to the recommendations of the IUGS Subcommission on the Systematics of Igneous Rocks (Schmid, 1981). The lapilli tuff is generally matrix-supported and together with the ash tuff (well-rounded clasts between 20 and 40 mm in diameter) are regarded as distal deposits, whereas the pyroclastic breccia and coarser lapilli tuff (lapilli diameter >40 mm) with angular clasts are regarded as proximal deposits, and even vent breccias.

The lapilli tuff units are unwelded, and display a crude stratification in terms of clast and grain size. Trains of clasts probably indicate emplacement as high-concentration laminated flows. The fine-grained tuff units are commonly bedded, and are associated with pyroclastic flow units. They are similar to surge deposits. Individual thinly bedded units represent laminated to planar bedded facies, and can perhaps be interpreted as ash-cloud surge deposits, which normally cannot be distinguished from bedded ash fall deposits. The following characteristics, however, favour the interpretation as ash fall deposits:

Digitised by the Department of Library Services in support of open access to information, University of Pretoria, 2021

- ❒ the presence of fine-grained ash layers of uniform thickness, regarded to be due to ash settling after the formation of pyroclastic flows;
- ❒ the presence of accretionary lapilli and cored lapilli are common in ash fall deposits, but these lapilli are also found in surge deposits;
- ❒ ballistic blocks or volcanic bombs (>64 mm in diameter) are indicative of ash fall deposits;
- ❒ the composition of the ash fall deposits is similar to that of the associated pyroclastic flow deposits.

Pyroclastic breccias are considered to be vent breccias. This interpretation is supported by the fact that fenite is developed around and within the breccia.

Load-and-flame structures and intraformational folds in bedded tuffs are the result of failure due to liquification of the underlying water saturated layers and of subaqueous slumping. These structures are interpreted to have been caused by earthquakes (Scott and Price, 1988) as seismic events related to volcanic activity and cauldron subsidence are quite common.

14.4 Original volcanic material of the inner zone

The ash tuff (samples KD015 and KD016) is composed predominately of approximately spherical to ovoid ash grains (<0.5 mm to approximately 3.5 mm in diameter) set in a recrystallised matrix. It is clast- or grain-supported and there is no orientation of the long axes of the ovoid lapilli and ash grains. The tuff contains three types of clast: carbonate grains interpreted as quenched calcite-carbonatite lava droplets, altered fragments of possible silicate lava and rare elongate and irregular lapilli which were plastic when they landed and may represent semi-consolidated spatter (Schürmann, 1992a). There is no evidence of compaction or plastic deformation or agglutination of the grains, and occasional broken grains with clean fracture surfaces indicate that they were solid upon landing.

Carbonatite pyroclastic deposits have a relatively low preservation potential, being susceptible to dissolution by rain water or to alteration by circulating groundwater. Consequently it can be concluded that cementation of the Kruidfontein ash must have occurred very soon after eruption, as the tuff shows no evidence of compaction or dissolution. It retained its rather open, grain-supported fabric, with relatively large voids between the grains and lapilli. The euhedral, early cement crystals indicate growth in open space and it seems as if very little dust-sized material was incorporated into the ash deposit.

Digitised by the Department of Library Services in support of open access to information, University of Pretoria, 2021

The early, equant cement grains resemble the crystal morphology of calcite. According to Moore (1989) this implies cementation in the meteoric-diagenetic environment at low Mg^{2+} concentrations, probably soon after the deposition of the ash, by the action of meteoric water or even steam. The later calcite, which completed the infilling of void space, crystallised from fluids with a lower Mn:Fe ratio and also a lower Mn content. As the early, brightly luminescent calcite within amygdales contains up to 2.5 wt% more $SrCO_3$ than the cementing calcite, it appears that some of the vesicle infilling have not taken place at the same time as cementation.

The textures of the lava grains and their spherical to subspherical form suggest that they had erupted from a vent as calcium carbonate liquid droplets which were quenched whilst airborne. The needle-like form of the microphenocrysts within the grains indicates rapid growth in a quenching melt. Rapid quenching of grain- to lapilli-sized alkali carbonatite lava droplets has been observed during eruptions of Oldoinyo Lengai during late September 1995. These droplets had flight times of 4-8 seconds, under conditions of low wind velocity, and upon landing were solid, consisting of phenocrysts and a quenched groundmass. The Kruidfontein droplets would have had similar flight times, in similarly light winds. The shapes of the microphenocrysts match very closely those observed in the Kaiserstuhl calciocarbonatite liquid droplet lapilli (Keller, 1981; 1989).

The "clots" of tiny needle-like microphenocrysts are interpreted as being the result of higher rates of cooling and consequently higher nucleation rates than growth rates, compared to those which gave rise to the formation of the discrete microphenocrysts (Hayward and Schürmann, in prep.). A thermal boundary is therefore likely to be responsible for the transition observed between "clots" and discrete microphenocrysts. If this view is correct, it would imply that the droplets were thermally heterogeneous immediately following their eruption. The gradation in certain ash grains between discrete microphenocrysts and clots means that the two forms cannot be ascribed to two different minerals.

The considerable variation in the abundance of microphenocrysts, amygdales and phenocrysts in different grains suggests that the lava body from which they were erupted was heterogeneous. The paucity of phenocrysts indicates either that the lava may have been essentially non-porphyritic, or that formed phenocrysts were removed by efficient crystal settling. The implication of efficient crystal settling in lava with a viscosity as low as that of carbonatites, is that there is little turbulence in the lava. However it is difficult to visualise an eruption mechanism for the ash grains, other than propulsion of lava droplets from a vent by vigorous gas emission, or by violent upwelling of relatively hot magma. Both of these mechanisms would tend to cause turbulence. The low abundance and small size of vesicles in the grains suggest that the lava from which they

Digitised by the Department of Library Services in support of open access to information, University of Pretoria, 2021

formed contained relatively little dissolved gas at the time of eruption (which is quite likely in view of the low viscosity of carbonatite liquid which would promote the liberation of gas), unless the droplets solidified too rapidly to permit significant exsolution of dissolved gas. The evidence suggests that the ash grains were blown from a vent by sudden and violent rises in the lava level, possibly caused by upwellings of gas or relatively hot magma from depth. Between these surges, the lava may have been relatively quiet within the vent, which would permit crystal settling and passive gas emission. When the lava was surging up within the vent, some overspill of lava as small flows or as spattering could have taken place. The absence of lava flows from the KD01 borehole may be the result of a fairly great distance to the vent(s). Rare larger lapilli may be the result of spatter. Carbonatite lapilli formed from liquid droplets from Kaiserstuhl (Keller, 1981; 1989) have similarly low abundances of phenocrysts and amygdales, although they do contain some small apatite and magnetite phenocrysts. A similar mechanism of eruption may have operated at both these localities.

The phenocrysts and microphenocrysts at Kruidfontein have been replaced by polygranular Sr-bearing calcite. Their morphology closely resembles that of Miocene quench microphenocrysts from Kaiserstuhl, which undoubtedly have a calcite-dominated primary mineralogy (Keller, 1981; 1989) with calcite forming >90 modal %. It is highly unlikely that either an alkaline carbonate (e.g. nyerereite: $Na_2Ca(CO_3)_2$ or $(Na,Ca)_2(Mg,Al)(Si,Al)_2O_7$), a silicate phase like melilite) could have been the original mineral in these clasts because of the excellent state of preservation of very delicate primary textures. The volume reduction which would take place when nyerereite or melilite is replaced by calcite (42% and 44% respectively) would result in the destruction of the original textures. The liquid from which the crystals formed must therefore have been composed of calcium carbonate (Hayward and Schürmann, in prep.). From experimental evidence, calcium carbonate glass is very unlikely to form (e.g. Genge et al., 1995b). It is therefore most likely that the matrix, immediately after formation of the ash grains, was composed of microcrystalline or cryptocrystalline calcium carbonate. Replacement of this matrix probably took place at a relatively early stage, soon after infilling of the vesicles and cementation, since the micro-crystalline carbonate would have been the most unstable component of the ash in the weathering environment because of its very fine grain size and resulting high chemical reactivity.

The calcite of which the ash grain phenocrysts and microphenocrysts presently consist contains between 0.8 wt% and 3.5 wt% $SrCO_3$. It is chemically indistinguishable from much of the calcite which infilled primary voids within and between the ash grains. The primary composition of the phenocrysts or microphenocrysts is not known, nor the composition of the original lava. High strontium levels in carbonatitic calcite is considered to be a primary characteristic. However, the strontium content of the calcite at the Kruidfontein Carbonatite Complex merely suggests that

Digitised by the Department of Library Services in support of open access to information, University of Pretoria, 2021

there was a significant amount of strontium in the fluids which caused the metasomatism of the original rocks.

14.5 Structural interpretation of caldera formation

Models for the structural and volcanic evolution of ash-flow calderas are given by Smith and Bailey (1968), Christiansen et al. (1977), Rytuba (1981; 1994), Lipman (1984; 1992), Drewes et al. (1988) and Rytuba et al. (1990). The summary that follows relates to major structural features, several stages of volcanism, the associated cauldron subsidence, resurgent volcanic and intrusive magmatism and to late hydrothermal activity and mineralisation.

The accumulation of magma in a shallow magma chamber will eventually lead to several stages of volcanism, or an initial voluminous eruption. The accumulation of magma will cause updoming resulting in radial and ring structures. The cycle begins with the eruption of lava and pyroclastic material, building a volcanic cone (or several cones or vents). According to Christiansen (1977), the pre-caldera magmatic stage commonly consists of magma of a different composition to that of the ash-flow and ash-fall tuffs and pyroclastic breccias following the post-cauldron stage.

The final climax of the pre-caldera cycle is characterised by a rapid and voluminous eruption (in this case the outer zone of the Kruidfontein Carbonatite Complex) which empties the shallow magma chamber. Due to the lack of support, the roof and the associated surface features will collapse, forming single or composite ring faults (Lipman, 1992) that dip vertically or steeply inward. Scalloped topographic walls are formed due to secondary gravitational slumping during subsidence.

Post-collapse volcanism will take place from new vents within the caldera. According to Lipman (1992) ring-vent eruptions are common in resurgent calderas - reflecting a renewed magma supply, and in the case of Kruidfontein, a change in magma composition. During long intervals between volcanic cycles a new vertical compositional zonation and consolidation of the magma (if any magma is left in the chamber) will occur, so that successive eruptions would tend to become smaller, probably forming smaller calderas, mostly within the earlier caldera. Examples of this are recorded from the Thirsty Canyon Tuff and the Black Mountain caldera and by the first two cycles of the Yellow Stone Plateau volcanic field (Christiansen, 1977). In these examples large extrusions, related to the resurgence, are exposed within the caldera. Within large calderas (>10 km in diameter) resurgence yields symmetrical domes which are accompanied by faulting and geometrical uplift structures. In the case of Kruidfontein (<5 km in diameter), however, faulting and the intrusion of carbonatite dykes without doming are prominent.

Digitised by the Department of Library Services in support of open access to information, University of Pretoria, 2021

The caldera cycle may be repeated at different intervals, leading to a complex relation between intrusive and extrusive units and different calderas. Repeated voluminous eruptions produce multiple cooling units.

14.6 Carbonatite-related fluids

In general, carbonatite complexes show a sequence from extrusive nephelinite or intrusive ijolite to carbonatite. The origin of the carbonatite is commonly ascribed to exsolution as carbonatite forms an immiscible liquid with a phonolitic-nephelinitic melt, or to fractional crystallisation (Wyllie et al., 1995). Different types of carbonatite, commonly of varying composition, have been recognized (Kapustin, 1986). The first type forms plugs or nested cone sheets and is usually calcitic. A second type is represented by cone sheets, and dykes along shear zones and consist of calcite and dolomite. Type three consists of dykes and veins of ankerite or dolomite, or thin hydrothermal veins, stockworks and replacement bodies of calcite, dolomite or ankerite respectively. This type is characterised also by accessory minerals like barite, fluorite, chlorite hematite, pyrite and quartz (Barker, 1989). Carbonatite of types one and two (consisting of magmatic calcite and dolomite) will tend to react with carbonatite-related fluids (i.e. so-called carbothermal fluids) at lower temperatures, producing replacement bodies (carbonatite types three and four), with the alteration assemblage dolomite or ankerite, quartz, zeololites, fluorite, chlorite, anatase and hematite.

Carbonatite-related fluids are responsible for fenitisation of host and country rock, late-stage iron enrichment and dolomitisation of earlier calcitic carbonatite (Gittins, 1989) as well as mineralisation by fluorite. In early experimental investigations Wyllie and Tuttle (1960) chose these fluids to be H_2O and CO_2 in different ratios, and showed that calcite could melt at petrologically acceptable temperatures and pressures in the presence of fluids. This led to the concept that carbothermal fluids of variable CO_2/H_2O ratios occur in nature. According to Gittins (1989) this view changed when Treiman and Essene (1984) deduced that the fluid in equilibrium with the Oka Carbonatite consisted of H_2O and CO_2 with $X(H_2O)+X(CO_2) > 0.99$ and $X(CO_2) = 0.1$.

According to Gittins (1989), the deduction made by Treiman and Essene (1984) that the carbonatite was an eutectic assemblage, was incorrect. Jago (1990) showed that the carbonatite rock did not melt in the presence of excess H_2O (even at 950°C and 1 Kb). In the presence of both F and Na_2CO_3, however, carbonatite melts over a considerable temperature range. The gas phase present at deeper crustal to mantle levels was assumed to consist of CO_2, H_2O and CH_4 (Wyllie, 1989). Compositions of fluids can also be estimated from fluid inclusions and the mineralogy of fenite. These fluids consist principally of CO_2, H_2O, F and Cl.

Digitised by the Department of Library Services in support of open access to information, University of Pretoria, 2021

Gittins (1989) further states that Cl present in a carbonatite magma will partition strongly into the associated aqueous fluid, while the F will remain in the carbonatite magma. He concludes that in the normal evolution of carbonatite, the aqueous fluid will separate from a water-saturated magma, and become a supercritical brine, capable of removing alkalies, Ca, Fe and Mg from the carbonatite as chlorides. It will therefore be enriched in Ca, Fe^{3+}, Mg and Na.

The metasomatism whereby Mg^{2+} substitutes for Ca^{2+}, and $CaCO_3$ becomes $CaMg(CO_3)_2$, is known as dolomitisation. From the mineralisation point of view, it is important to note that this reaction involves a loss in volume of up to 15% (Morrow, 1982). This can enhance the porosity of the rock, so that it becomes more receptive to mineralising carbothermal fluids.

At Kruidfontein carbothermal alteration and mineralisation, however, evolved into a low-temperature (epithermal) hydrothermal process, producing replacement and vein-type mineralisation along fractures. These veins can be an important depository, although rarely, of Cu, Pb, Zn, Mo, Cu and Au.

Fluorite mineralisation linked to carbonatites in the Kruidfontein Carbonatite Complex are associated with the most fractionated dykes and plugs along the southern and northern boundaries of the inner zone; similar, and higher grade replacement deposits are also present in the moat-like closed basin between the inner zone and the outer zone on the southwestern side.

Fluorite is also concentrated in mineralised zones (Fig. 14.1) that are localized within the lower ash flow unit (fault-controlled channels), and it is present throughout the altered inner zone sequence (especially in the lapilli tuff, ferruginous lapilli tuff and lower ash flow units).

Based on the KD02-KD01-KD03 section across the ferruginous lapilli tuff unit in the northeastern part of the inner zone (Fig.14.1) the sequence of events in the formation of the Kruidfontein Carbonatite Complex is summarised as follows:

① Phase 1 eruption of the nephlinitic pyroclastic breccia and ignimbrite, producing the outer zone;

② Phase 2 cauldron subsidence (stage 2);

③ Phase 3 extrusion of the carbonatitic lapilli and ash tuff, pyroclastic flows and breccia, producing the inner zone;

④ Phase 4 cauldron subsidence (stage 4), forming a nested caldera;

Digitised by the Department of Library Services in support of open access to information, University of Pretoria, 2021

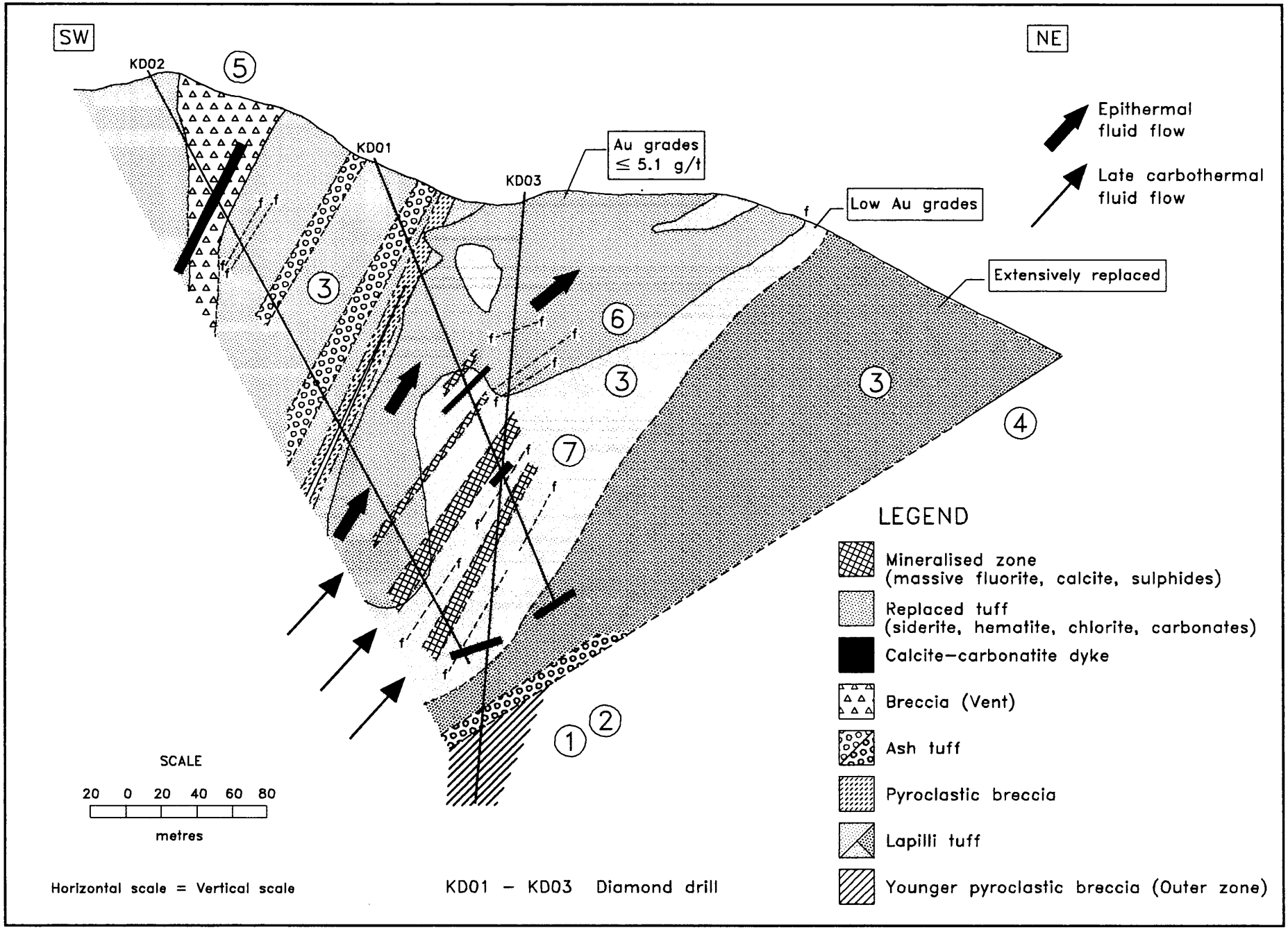

Figure 14.1 KD02-KD01-KD03 section across the ferruginous ash fall unit in the northeastern part of the inner zone (see Fig. 5.2 for the borehole localities). The numbers indicate the envisaged seven different stages of formation and associated mineralisation.

Digitised by the Department of Library Services in support of open access to information, University of Pretoria, 2021

⑤	Phase 5	re-activation and subsequent deposition of pyroclastic breccia and associated flows in the inner zone;
⑥	Phase 6	hydrothermal (epithermal) mineralisation;
⑦	Phase 7	intrusion of carbonatite dykes, associated with carbonatite-related hydrothermal fluids (i.e. carbothermal fluids).

14.7 Mineralisation in the surrounding area related to the Kruidfontein Carbonatite Complex

The mineralisation in the Kruidfontein Carbonatite Complex was controlled by structures developed during caldera formation and by regional faults which intersected and reactivated caldera-related structures. Mineralisation in the country rocks may also in part be related to these structures. Zinc and lead anomalies are present in the dolomite of the Malmani Subgroup, banded iron formation of the Penge Formation, in clastic sediments of the Pretoria Group and in the outer zone of the Kruidfontein Carbonatite Complex. However, according to Hinder (1993) the Frisco Formation of the Malmani Subgroup hosts most of the potential targets.

Geochemical anomalies have been encountered in the Eccles and Frisco Formations of the Malmani Subgroup. On Langrand 143JQ, Brosdoornhoek 433KQ and Buffelsdraai 151JQ, several faults are present in the above mentioned formations, and could have aided fluid movement and concomitant Zn and Pb mineralisation (Fig. 14.2). The coarse-grained nature of the middle part of Frisco Formation could have led to an increase in porosity and permeability, thus aiding mineralisation whereas the presence of an impermeable chert layer on the contact between the Eccles and Frisco Formations could have acted as a barrier to the fluids, thus confining the mineralisation to the dolomite. The impermeability of the overlying Penge Formation could have had a similar effect on migrating fluids.

The enrichment in lead and zinc within the Penge Formation, the overlying Pretoria Group, and in the outer zone of the Kruidfontein Carbonatite Complex, is either fault controlled, or has taken place as a result of the presence of impermeable horizons like quartzite or banded iron formation (e.g. Elandsfontein 23JQ, north of the Kruidfontein Carbonatite Complex), Ramakokskraal 25JQ and Geluk 26JQ west of the Kruidfontein Carbonatite Complex, and Buffelspoort 149JQ to the east of the Kruidfontein Carbonatite Complex.

All these examples of mineralisation are uneconomical under present conditions. Hinder (1993) ascribes this to the fact that the dolomite was not exposed to weathering, so that no karst development could take place. It is also possible that an insufficient amount of mineralising fluids

Digitised by the Department of Library Services in support of open access to information, University of Pretoria, 2021

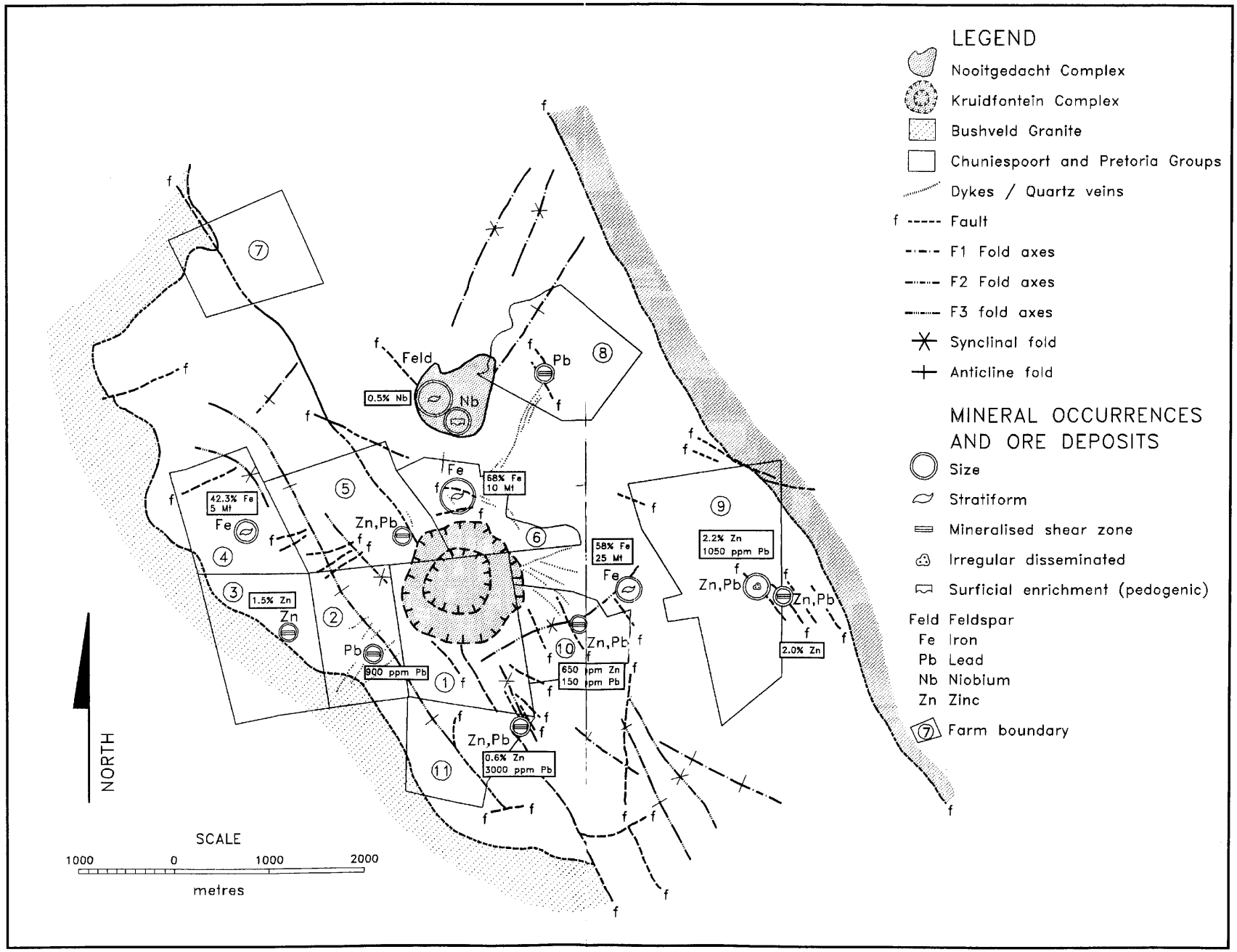

Figure 14.2 Generalised geology and structure of the Crocodile River Fragment (modified afte Hartzer, 1994). The farm boundaries are shown to facilitate the discussion of the different mineral occurrences and potential deposits (KEY: 1 = Kruidfontein 139JQ; 2 = Geluk 24JQ; 3 = Ramaokskraal 25JQ; 4 = Pylkop 26JQ; 5 = Elandsfontein 23JQ; 6 = Boschkop 138JQ; 7 = Brosdoorhoek 433KQ; 8 = Karoobult 144JQ; 9 = Buffelspoort 149JQ; 10 = Doornkloof 141JQ; 11 = Lanrand 143JQ).

Digitised by the Department of Library Services in support of open access to information, University of Pretoria, 2021

emanated from the Kruidfontein Carbonatite Complex, or that these fluids did not contain high enough concentrations of the heavy metals.

14.8 A model for the formation of the Kruidfontein Carbonatite Complex

The Kruidfontein Carbonatite Complex is an example of an intra-continental caldera related to carbonatite activity and associated mineralisation. The structure and associated extrusions and intrusions (dykes and plugs) of the Complex have been preserved remarkably well due to at least two subsidence episodes. Despite its age (1243±117 Ma according to Harmer, 1992) its geological history can be reconstructed with reasonable confidence. Studies of diverse earth science disciplines provide a frame work for evaluating the interaction between magma processes, caldera formation, rock alteration and mineralisation.

Prior to the eruption of the volcanic rocks of the Kruidfontein Complex its country rocks belonging to the Transvaal Supergroup were folded and faulted (Fig. 14.3: Stage 1). The volcanism associated with the outer and inner zones was initiated along the western regional fault which was intermittently active before and after the caldera cycles. The outer zone is characterised by (a) varying centroclinal dips of 15 to 90°; (b) an original nephelinitic magma composition (Clarke, 1989); (c) an eruption mechanism, which produced pyroclastic breccias and ignimbrites; and (d) the development of the first caldera by collapse faulting (Figs. 14.4: Stages 2 and 3).

After the first cauldron subsidence, resurgent extrusion resumed, extruding compositionally distinct carbonatitic magma in the form of pyroclastic breccia, lapilli and ash tuff (Fig. 14.5: Stage 3). This extrusive activity occurred on the floor of the first formed caldera, and had a substantially smaller volume than that of the nephelinitic outer zone.

The second cycle of caldera formation occurred after carbonatite extrusion had resumed, resulting in a deep caldera filled with steeply dipping volcaniclastic layers and units like carbonatitic tuffs and agglomerates (Fig. 14.5: Stages 4 and 5). Due to the subsidence, the primary units and layers were remobilised, forming proximal and distal debris flows, together with breccias and massive and bedded tuffs. The Kruidfontein Carbonatite Complex can thus be described as a cluster of two calderas, the inner one hosting the carbonatitic volcaniclastic rocks and closely associated dykes, plugs and mineralisation.

Digitised by the Department of Library Services in support of open access to information, University of Pretoria, 2021

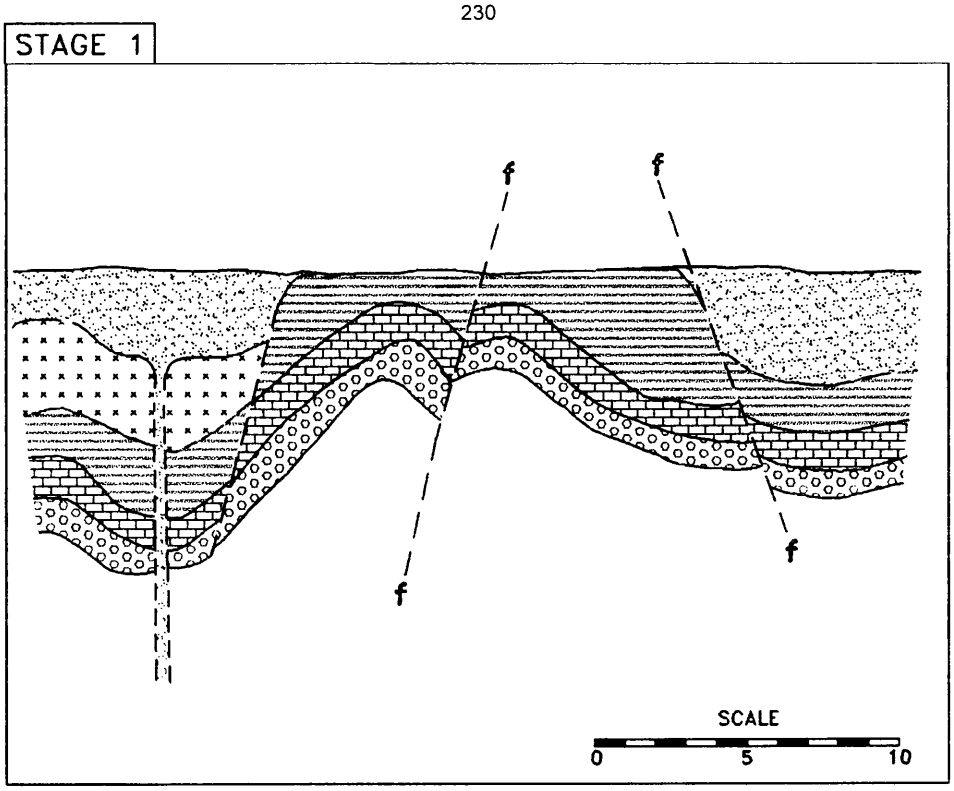

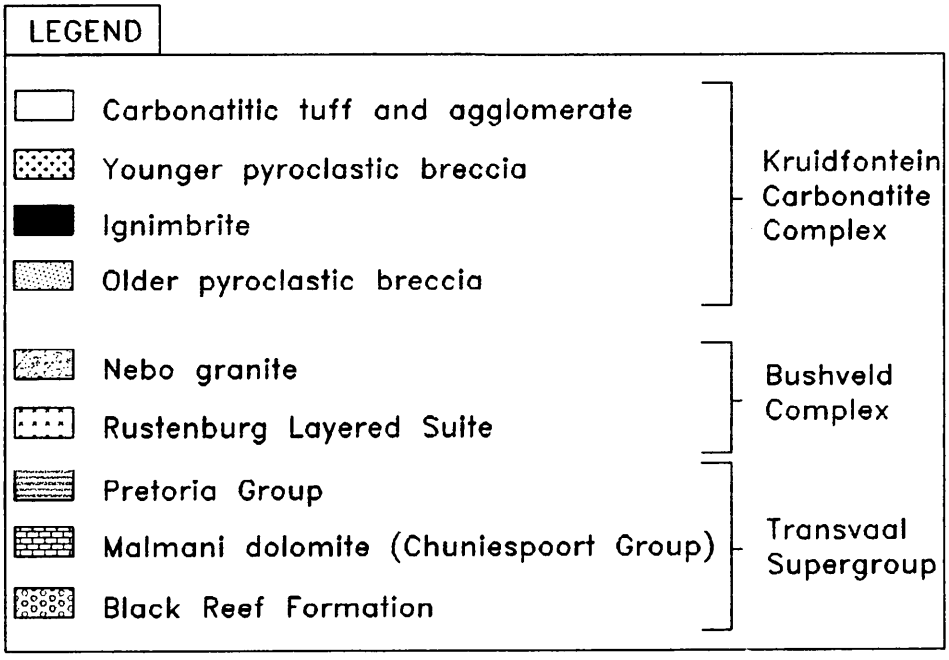

Figure 14.3 Schematic model depicting the evolution of the Kruidfontein Carbonatite Complex: Stage 1.

Digitised by the Department of Library Services in support of open access to information, University of Pretoria, 2021

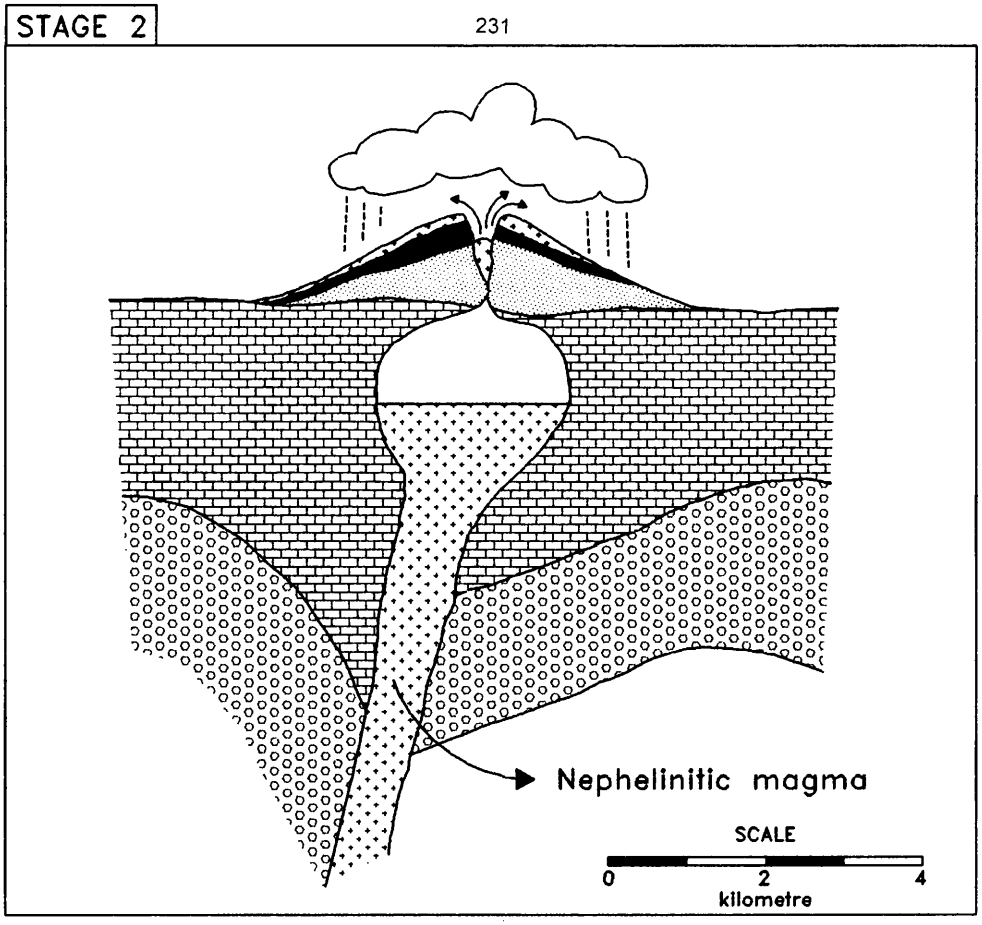

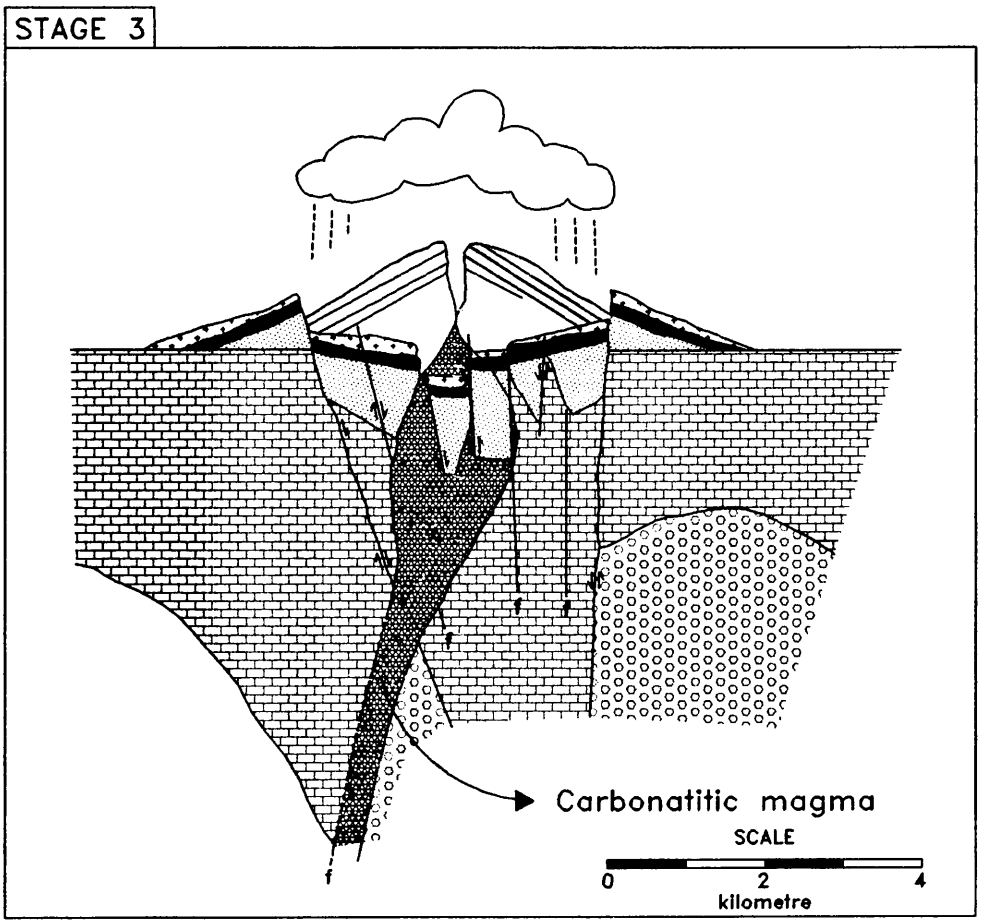

Figure 14.4 Schematic model depicting the evolution of the Kruidfontein Carbonatite Complex: Stages 2 and 3.

Digitised by the Department of Library Services in support of open access to information, University of Pretoria, 2021

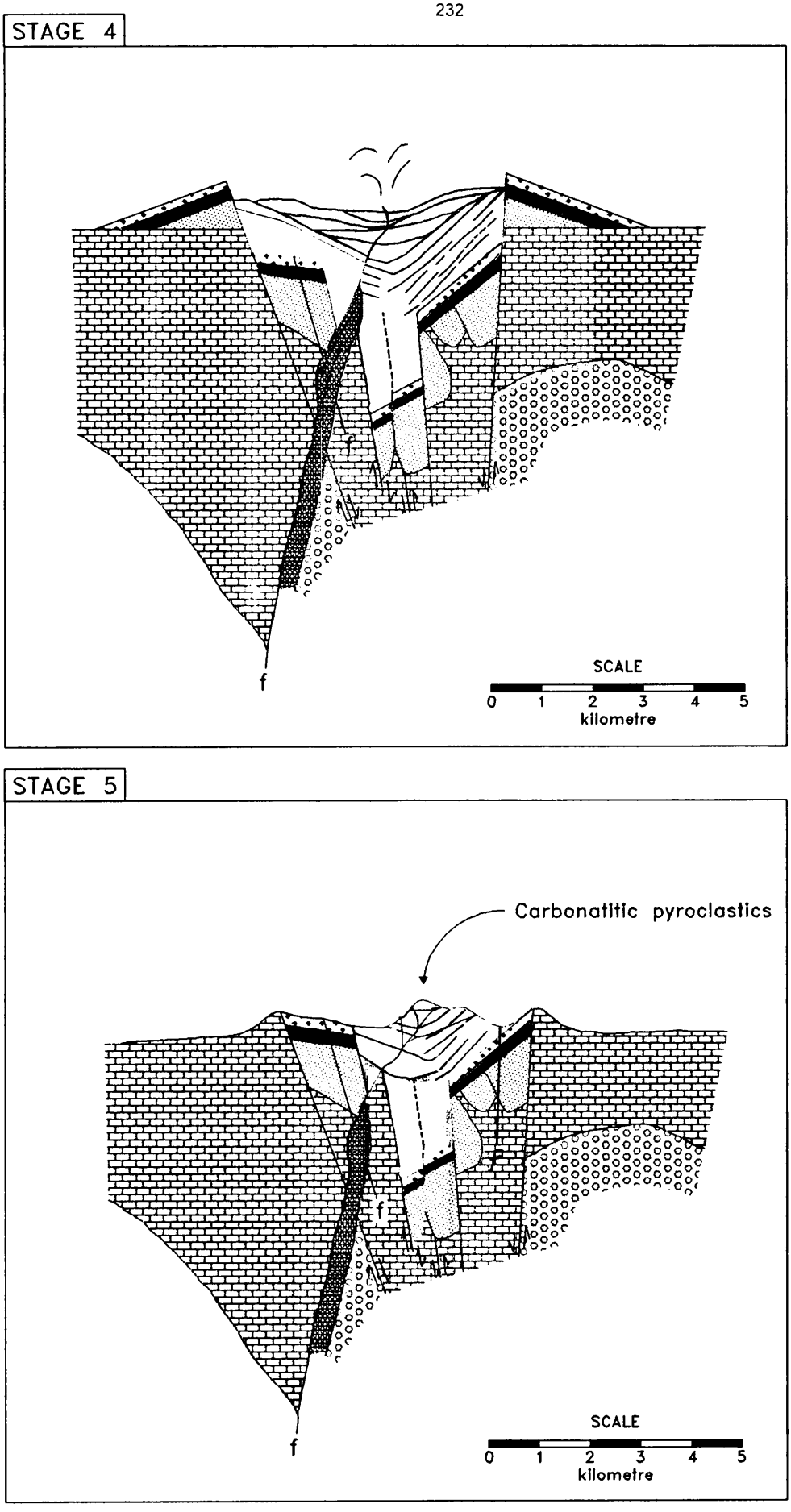

Figure 14.5 Schematic model depicting the evolution of the Kruidfontein Carbonatite Complex: Stages 4 and 5.

Digitised by the Department of Library Services in support of open access to information, University of Pretoria, 2021

15. SUMMARY AND CONCLUSIONS

The Kruidfontein volcano (1243 Ma ± 171 Ma) had a two-stage history, beginning with a cone-building period of predominantly nephelinitic pyroclastics followed by cauldron subsidence, and a second stage of carbonatitic volcanism also followed by cauldron subsidence. Today, the eroded volcano comprises an approximately circular carbonatitic inner zone, surrounded by an outer zone, of the silicate pyroclastics. The cauldron subsidence contributed to the preservation of the inner zone carbonatite sequence dominated by tuff. This carbonatite sequence is of great significance as it represents one of the oldest and best-preserved recognised carbonatite extrusives. Core recovered from a 250 m borehole, drilled in the NE area of the inner zone, has revealed great detail about the carbonatitic volcaniclastic sequence.

The carbonatite sequence encountered in the borehole consists mainly of ash fall and ash flow tuffs. With the exception of a unit 32 m below the collar of the borehole, most of the others have been replaced by a fine-grained intergrowth of potassium feldspar, ankerite and chlorite.

In certain units, the original depositional fabric, including grains, lapilli, crystals and volcanic blocks are preserved. However, a later period of veins, consisting of intimately intergrown, very fine grained chlorite, apatite, anatase and pyrite affected the primary fabric. The feldspar-ankerite-chlorite assemblage has been overprinted by apatite, followed by fluorite. Both these minerals occur either as euhedra or as very fine, scattered grains. The latest alteration to affect the rock was some fine-scale brecciation and the introduction of calcite which replaced parts of the existing assemblage. Cathodoluminescence reveals complex details in the growth and overgrowth of the silicate and later minerals and permits a good understanding of the alteration history.

Soil geochemistry led to the recognition of several anomalies throughout the inner and outer zones of the Complex. The anomalous Au, Pb and Zn levels are mainly associated with vent breccia and secondary ferruginisation. High Ba values are associated with zones of fenitisation and also show a degree of structural control. Also notable is the correlation between an increase in Ba and the presence of calcite-carbonatite, fluorite-calcite-carbonatite dykes and barite-fluorite veins.

The results of the geophysical appraisal are the following: (a) according to the Bouguer gravity map no gravitational response is visible in the area occupied by the Complex, suggesting that no buried pluton of high density is present; and (b) that the high-resolution radiometric survey depict several positive anomalies. These are on the ferruginous lapilli tuff unit in the eastern and northeastern part of the inner zone; in the northern part of the inner zone associated with vents, vent breccia, proximal debris flow deposits, carbonatite dykes and plugs as well as faulting, and along the southern boundary of the inner zone, once again associated with dykes, vents, vent breccia and debris flow deposits.

Digitised by the Department of Library Services in support of open access to information, University of Pretoria, 2021

The structure of the Complex is clearly delineated by the high-resolution ground magnetic survey. A pronounced magnetic anomaly is situated along the northern boundary of the inner zone, the extent of which is limited to the assumed position of the caldera-collapse fault. In addition a north-south magnetic profile over the Complex indicates a gently-dipping units in the south, whereas in the north the magnetic zone is almost vertical. Concerning the volcaniclastic rocks of the inner zone, concentric magnetic patterns similar to the circular distribution of the interbedded tuffs and breccias are prominent. Four prominent W-NW trending positive anomalies have been defined and are assumed to be deep-seated fracture zones.

Structures closely associated with the caldera formation are radial and ring faults outside the Kruidfontein Complex, along which several occurrences and potential economic deposits have been described. The banded iron formation on the farms Boschkop 138JQ, Pylkop 26JQ, Doornkloof 141JQ and Buffelspoort 149JQ have locally been enriched to form high-grade hematite ore. Lead and zinc mineralisation has been reported on Langrand 143JQ, Buffelspoort 149JQ, Buffeldraai 151JQ, Elandsfontein 23JQ, Doornkloof 141JQ, Ramakokskraal 25JQ, Geluk 26JQ and Karoobult 22JQ. The anomalies mentioned above are present in the dolomite of the Malmani Subgroup, the banded iron formation of the Penge Formation and in the clastic rocks of the Pretoria Group, and are fault-related or occur within the dolomite as disseminated mineralisation.

Mineralogically three distinct chlorite groups were defined according to Mg/(Mg+Fe) ratio. This grouping compares with the SrO and MnO contents of the carbonates, the Ce_2O_3 content of apatite and the cathodo-luminescence characteristics of the feldspar. The upper ash flow and upper part of the pyroclastic breccia units contain chlorite with decreasing Mg/(Mg+Fe) ratios, carbonates with high SrO and low MnO contents, Ce_2O_3-rich primary apatite, and K-feldspar with dull to bright green luminescence. The lower part of the pyroclastic breccia, the ferruginous lapilli tuff and the upper part of the lower ash flow unit are defined by more intense alteration (an increase in Mg/(Mg+Fe) ratios of the chlorite, lower SrO and higher MnO contents for the carbonates, secondary apatite (Ce_2O_3-poor) and K-feldspar displaying red-brown luminescent cores and green rims). The lower part of the lower ash flow and mineralised zones contain chlorite with increasing Mg/(Mg+Fe) ratios, carbonates with higher SrO and lower MnO contents and K-feldspar with green luminescence; the apatite is secondary, Ce_2O_3-poor.

Siderite, ankerite, fluorite, K-feldspar, hematite, quartz, apatite, calcite and chlorite are alteration minerals. Different generations of fluorite have been distinguished on account of rare-earth element content and LREE to HREE ratios. Some of these phases correlate positively with the rare-earth minerals, whilst others show a negative correlation.

Altered carbonatitic lapilli tuffs have been recovered from the 250 m borehole already mentioned. Some of these lapilli have exceptionally well-preserved primary textures, including quench microphenocrysts,

Digitised by the Department of Library Services in support of open access to information, University of Pretoria, 2021

and less abundant vesicles and phenocrysts. There are also groups, or "clots" of tiny microphenocrysts, which have not previously been observed in carbonatite lavas. Optical cathodo-luminescence has been used as many features of the lapilli are not visible in transmitted light. It is concluded that the lapilli have been erupted as droplets of calcite-carbonatite lava, which formed an unconsolidated lapilli deposit, also containing some altered silicate lava fragments. Their primary mineralogy has been completely replaced by Sr-bearing calcite, chlorite and apatite. Late stage mineralisation by anatase, apatite, chlorite and pyrite has occurred. No evidence has been found to suggest that the deposit represents replacement of a natrocarbonatite or alkali silicate precursor.

Carbon and oxygen isotope patterns point to three major stages of development of the inner zone of the Complex. Stage one involves carbonatite magma which originated from fractionation, and which contained a H_2O-CO_2 vapour phase, at 700°C in a closed system with a H_2O/CO_2 molar ratio of 0.5. The second stage of the development is recorded in the intrusive carbonatitic dykes, and at least in part in the carbonatitic ash flow tuffs, by a shift to higher $\delta^{18}O$ values without major changes in the $\delta^{13}C$ values. This is a consequence of a secondary alteration for which a temperature of approximately 150°C has been estimated. The isotopic characteristic of the alteration fluid could be determined as $\delta^{18}O_{H_2O}$ = 1.2‰ and $\delta^{13}C_{CO_2}$ = -3.8‰; a possible source being a hydrothermal fluid which introduced isotopically light C from a deep subvolcanic area, mixed with high $\delta^{18}O$ ground water that had equilibrated at about 150°C. The third stage is characterised by siderite mineralisation, with a concomitant precipitation of fluorite. Siderite appears to have formed later than the other carbonates and can thus be assumed to have formed at temperatures at or below 150°C. The secondary nature of the siderite is re-inforced by a negative correlation between the whole-rock carbonate $\delta^{18}O$ values and the modal siderite content. By applying the siderite/water and siderite/CO_2 fractionation factors, the C and O isotope composition of the siderite precipitating fluid was found to be approximated as $\delta^{13}C_{CO_2}$ = -8.0‰ and $\delta^{18}O_{H2O}$ = -1.4‰. From these findings it is concluded that the siderite in the Kruidfontein Carbonatite Complex is likely to have been precipitated by a late-stage Fe-bearing hydrothermal fluid, depleted in ^{18}O and ^{13}C. C was provided by a deep-seated source within the subvolcanic region and Fe was leached from rocks that the hydrothermal fluid passed through. The siderite mineralisation and concomitant fluorite formation most probably took place during progressive cooling of the Kruidfontein Complex, as can be deduced from the positive correlation between the $\delta^{18}O$ and $\delta^{13}C$ values of siderite.

Digitised by the Department of Library Services in support of open access to information, University of Pretoria, 2021

16. REFERENCES

Al-Aasm, I.S., Taylor, B.E. and South, B. 1990. Stable isotope analysis of multiple carbonate samples using selective acid extraction. Chemical Geology, 80, 119-125.

Andersen, T. 1986. Compositional variation of some rare earth minerals from the Fen complex (Telemark, SE Norway): implications for the mobility of rare earths in a carbonatite system. Mineralogical Magazine, 50, 503-509.

Bailey, D.K. 1993. Carbonate magmas. Journal of the Geological Society of London, 150, 637-651.

Barker, D.S. 1987. Tertiary alkaline magmatism in Trans-Pecos Texas. In: J.G. Fitton and B.G.J. Upton (Eds.) Alkaline Rocks. Geological Society of London, Special publication, 30, 415-431.

Barker, D.S. 1989. Field relations of carbonatites. In K. Bell (Ed.) Carbonatites: Genesis and evolution. Unwin Hyman, London, 15-34.

Barker, D.S. 1996. Carbonatite volcanism. In: R.H. Mitchell (Ed.) Undersaturated Alkaline Rocks: Mineralogy, Petrogenesis, and Economic Potential. Mineralogical Association of Canada, Short Course, 24, 45-61.

Barker, D.S. and Nixon, P.H. 1989. High-Ca, low-alkali carbonatite volcanism at Fort Portal, Uganda. Contributions to Mineralogy and petrology, 103, 166-177.

Basson, J.K., 1979. Basic physics of natural radioactivity. In: Training course on radiometric prospecting techniques. Presented by the Atomic Energy Board in collaboration with the South African Geophysical Association and the Geological Society of South Africa, 15 p.

Battey, M.H. 1972. Mineralogy for students. Department of Geology, University of Newcastle upon Tyne. Longman, 323 p.

Boyle, R.W. 1982. Geochemical prospecting for thorium and uranium deposits. Developments in Economic Geology, 16, Elsevier Scientific Publishing Company, Amsterdam, 498 p.

Burt, D.M. 1989. Compositional and phase relations among rare earth element minerals. In B.R. Lipin and G.A. McKay (Eds.) Geochemistry and Mineralogy of Rare Earth Elements. Reviews in Mineralogy, 21, Mineralogical Society of America, 259-302.

Carothers, W.W., Adami, L.H. and Rosenbauer, R.J. 1988. Experimental oxygen isotope fractionation between siderite-water and phosphoric acid liberated CO_2-siderite. Geochimica et Cosmochimica Acta, 52, 2445-2450

Cas, R.A.F. and Wright, J.V. 1987. Volcanic successions: Modern and Ancient. George Allen and Unwin, London, 528 p.

Christiansen, R.L. 1979. Cooling units and composite sheets in relation to caldera structure. In: Chapin, C.E. and Elston, W.E. (Eds.) Ash-flow tuffs: Special Paper, Geological Society of America, 180, 29-42.

Christiansen, R.L., Lipman, P.W., Carr, W.J., Byers, F.M., Orkild, P.P. and Sargent, K.A. 1977. Timber Mountain-Oasis Valley caldera complex of southern Nevada. Geological Society of America, Bulletin, 88, 943-959.

Church, A.A. and Woolley, A.R. 1995. Extrusive carbonatites of the world. Geological Society of Africa, 10th Conference, Nairobi. Abstracts, 127.

Digitised by the Department of Library Services in support of open access to information, University of Pretoria, 2021

Clague, D.A. 1987. Hawaiian alkaline volcanism. In: J.G. Fitton and B.G.J. Upton (Eds.) Alkaline Igneous Rocks. Geological Society of London, Special Publication, 30, 227-252.

Clarke, L.B. 1989. The geology of the Kruidfontein volcanic Complex, Transvaal, South Africa. Unpublished Ph.D. Thesis, University of Leicester, England, 208 p.

Clarke, L.B. and Le Bas, M.J. 1990. Magma mixing and metasomatic reaction in silicate-carbonate liquids at the Kruidfontein carbonatitic volcanic complex, Transvaal. Mineralogical Magazine, 54, 45-56.

Clarke, L.B., Le Bas, M.J. and Spiro, B. 1991. Rare earth, trace element and stable isotope fractionation of carbonatites at Kruidfontein, Transvaal, South Africa. Proceedings of the 5th International Kimberlite Conference. Brazil, 225-241.

Cortecci, G. and Frizzo, P. 1993. Origin of siderite deposits from the Lombardy Valleys, northern Italy: a carbon, oxygen and strontium isotope study. Chemical Geology (Isotope Geoscience Section), 105, 293-303.

Crocker, I.T., Martini, J.E.J. and Söhnge, A.P.G. 1988. The fluorspar deposits of the Republics of South Africa and Bophuthatswana. Handbook of the Geological Survey of South Africa, 11, 172 p.

Decatitat, P., Hutchson, I. and Walsche, J.L. 1993. Chlorite geothermometry - a review. Clays and Clay Minerals, 41, 119-239.

Deer, W.A., Howie, R.A. and Zussman, J. 1966. An introduction to the rock-forming minerals. Longman, London, 528 p.

Deer, W.A., Howie, R.A. and Zussman, J. 1992. An introduction to the rock-forming minerals. John Wiley and Sons, New York, 696 p.

Deines, P. 1989. Stable isotope variations in carbonatites. In: K. Bell, (Ed.) Carbonatites: Genesis and evolution. George Allen and Unwin, London, 301-359.

Deines, P. and Gold, D.P. 1973. The isotopic composition of carbonatite and kimberlite carbonates and their bearing on the isotopic composition of deep-seated carbon. Geochimica et Cosmochimica Acta, 37, 1709-1733.

Donnay, G. and Donnay, J.D.H. 1953. The crystallography of bastnäesite, parisite, roentgenite, and synchysite. American Mineralogist, 38, 932-963.

Drewes, H., klein, D.P., and Birmingham, S.D., 1988. Volcanic and structural controls of mineralization in the Dos Cabezas Mountains of southeastern Arizona: United States Geological Survey Bulletin, 1676, 45 p.

Ernst, W.G. 1983. Mineral paragenesis in metamorphic rocks exposed along Tailuko Gorge, Central Mountain Range, Taiwan. Journal of Metamorphic Geology, 1, 305-329.

Evensen, N.M., Hamilton, P.J. and O'Nions, R.K. 1978. Rare-earth abundances in chondritic meteorites. Geochimica et Cosmochimica Acta, 42, 1199-1212.

Flörke, O.W., Gerbert, W. and Heinrich, E.W. 1978. Niobium. In: K.H. Wedepohl (Ed.) Handbook of Geochemistry, Volume II/41. Springer-Verlag, Berlin.

Fockema, R.A.P. 1949. An occurrence of alkaline and acid lavas and volcanic breccias on the farm Kruidfontein 147, Rustenburg District. Transactions of the Geological Society of South Africa, 52, 226-229.

Digitised by the Department of Library Services in support of open access to information, University of Pretoria, 2021

Foster, M.D. 1962. Interpretation of the composition and a classification of the chlorites. United States Geological Survey Professional Paper, 414-A, A1-A33.

Friedman, I. and O'Neil, J.R. 1977. Compilation of stable isotope fractionation factors of geochemical interest. In: M. Fleischer (Ed.) Data of Geochemistry - Sixth Edition, Chapter KK, Geological Survey Professional Papers, 440-KK, 1-117.

Frondel, L. 1978. Scandium. In: K.H. Wedepohl (Ed.) Handbook of Geochemistry, Volume II/21. Springer-Verlag, Berlin.

Genge, M.J., Jones, A.P. and Price, G.D., 1995a. An infrared and Raman study of carbonate glasses: Implications for the structure of carbonatite magmas. Geochimica et Cosmochimica Acta, 59, 927-937.

Genge, M.J., Price, G.D. and Jones, A.P., 1995b. Molecular dynamics simulations of $CaCO_3$ melts to mantle pressures and temperatures: implications for carbonatite magmas. Earth and Planetary Science Letters, 131, 225-238.

Gies, H. 1976. Zur Beziehung zwischen Photolumineszenze und Chemismus natürlicher karbonate. Neues Jahrbuch für Mineralogie, Abhandlungen, 127, 1-46.

Gittins, J. 1989. The origin and evolution of carbonatite magmas. In: K. Bell (Ed.) Carbonatites: Genesis and Evolution. Unwin Hyman, London, 580-599.

Gold, D.P. 1963. Average chemical composition of carbonatites. Economic Geology, 58, 988-991.

Gold, D.P. 1966. The average and typical chemical composition of carbonatites. International Mineralogical Association, papers, 4th General meeting, Mineralogical Society of India, 83-91.

Groeneveld, D. 1948. The geology of the area north-west of the confluence of the Crocodile and Pienaars Rivers. Unpublished M.Sc. thesis, University of Pretoria.

Hall, A.L. 1932. The Bushveld Igneous Complex of the central Transvaal. Memoir of the Geological Survey of South Africa, 28 p.

Harmer, R.E., 1992. The geochemistry of Spitskop and related Alkaline Complexes. Unpublished Ph.D thesis, University of Cape Town, 287 p.

Hartzer, F.J. 1989. Stratigraphy, structure and tectonic evolution of the Crocodile River Fragment. South African Journal of Geology, 92, 110-124.

Hartzer, F.J. 1994. Geology of Transvaal inliers in the Bushveld Complex. Unpublished Ph.D thesis, Rand Afrikaans University, 363 p.

Hayward. C.L. and Schürmann, L.W. (in prep.). Calcite-carbonatite lava droplets erupted from the Proterozoic Kruidfontein volcano, South Africa.

Heinrich, E.W. 1966. The geology of carbonatites. Chicago, Rand McNally.

Henderson, P. 1995. The rare earth elements: introduction and review. In: A.P. Jones, F. Wall and C.T. Williams (Eds.) Rare Earth Minerals: Chemistry, origin and ore deposits. Mineralogical Society Series, 7, Chapman and Hall, London, 1-19.

Hey, M.H. 1954. A new review of the chlorites. Mineralogical Magazine, 30, 277-292.

Hinder, G. 1993. Crocodile River Fragment: Review of prospecting activities, 1991 - February 1993: Unpublished report of Iscor, 17.

Digitised by the Department of Library Services in support of open access to information, University of Pretoria, 2021

Hoefs, J. 1987. Stable isotope geochemistry. Springer-Verlag, Berlin, 241 p.

Hodgson, N.A. 1985. Carbonatites and associated rocks from the Cape Verde Islands. Unpublished Ph.D thesis, University of Leicester.

Horstmann, U.E. and Verwoerd, W.J. 1997. Carbon and oxygen isotope variations in southern African carbonatites. Journal of African Earth Sciences, 25, 115-136.

Hogarth, D.D., Hartree, R. and Loop, J. 1985. Rare-earth element minerals in four carbonatites near Gatineau, Quebec. American Mineralogist, 70, 1135-1142.

Hogarth, D.D. 1989. Pyrochlore, apatite and amphibole: Distinctive minerals in carbonatites. In: K. Bell (Ed.) Carbonatites: Genesis and Evolution. Unwin Hyman, London, 105-148.

Humphrey, W.A. 1909. On a portion of the Bushveld bordering the Crocodile River and including the Rooiberg tin-field. Annual Report of the Geological Survey, Transvaal, 103-122.

Humphris, S.E. and Thompson, G. 1978. Hydrothermal alteration of oceanic basalts by seawater. Geochimica et Cosmochimica Acta, 42, 107-125.

International Centre for Diffraction Data 1992. Powder Diffraction File 1992, PDF-2 Database Sets 1 - 42, CD Rom Disc, Swarthmore, USA.

Jago, B.C. 1990. The role of fluorine in the evolution of alkali-bearing carbonatite magmas and the formation of carbonatite-hosted apatite and pyrochlore deposits. Unpublished Ph.D thesis, University of Toronto, Toronto.

Jago, B.C. and Gittins, J. 1991.The role of fluorine in carbonatite magma evolution. Nature, 349, 56-58.

Johnson, R.W., Knutson, J. and Taylor, S.R. 1989. Intraplate volcanism in Eastern Australia and New Zealand. Cambridge University Press, Cambridge, England, 408 p.

Jones, A.P., Wall, F. and Williams, C.T. 1996. Rare earth minerals: Chemistry, origin and ore deposits. Mineralogical Society Series, 7, Chapman and Hall, 372 p.

Kapustin, Yu.L. 1986. The origin of early calcitic carbonatites. International Geology Review, 28, 1031-1044.

Keller, J. 1981. Carbonatite volcanism in the Kaiserstuhl alkaline complex: evidence for highly fluid carbonatitic melts at the earth's surface. Journal of Volcanic and Geothermal Research, 9, 423-431.

Keller, J. 1989. Extrusive carbonatites and their significance. In: K. Bell (Ed.) Carbonatites: Genesis and Evolution. Unwin Hyman, London, 70-88.

Knudsen, C. and Buchardt, B. 1991. Carbon and oxygen isotope composition of carbonates from the Qaqarssuk Carbonatite Complex, south west Greenland. Chemical Geology, 86, 263-274.

Kranidiotis. P. and MacLean, W.H. 1987. Systematics of chlorite alteration at the Phelps Dodge massive sulphide deposit, Matagami, Quebec. Economic Geology, 82, 1898-1911.

Laird, J. 1988. Chlorites: Metamorphic Petrology. In: S.W. Bailey (Ed.) Hydrous Phyllosilicates (exclusive of micas), Reviews in Mineralogy, 19, 405-453.

Digitised by the Department of Library Services in support of open access to information, University of Pretoria, 2021

Le Bas, M.J. 1979. (Ed.) Carbonatite-Nephelinite Volcanism. An African Case History. Wiley, London, United Kingdom, 347 p.

Le Bas, M.J. 1987. Nephelinites and carbonatites. In: J.G Fitton and B.G.J. Upton (Eds.) Alkaline Igneous Rocks. Special Publication of the Geological Society of London, 53-83.

Le Bas, M.J. 1989. Diversification of carbonatite. In K. Bell (Ed.) Carbonatites: Genesis and evolution. Unwin Hyman, London, 428-445.

Le Roux, A.P. and Watkins, R.T. 1990. Analysis of rare-earth elements in geological samples by gradient ion chromatography. Chemical Geology, 88, 151-162.

Lipman, P.W. 1984. The roots of ash flow calderas in western North America: Windows into the top of granitic batholiths: Journal of Geophysical Research, 89, 8801-8841.

Lipman, P.W. 1992. Ash-flow calderas as structural controls of ore deposits - recent work and future problems: United States Geological Survey Bulletin, 2012, L1-L12.

Lorenz, V. 1986. On the growth of maars and diatremes and its relevance of the formation of tuff rings. Bulletin of Volcanology, 48, 265-274.

Machel, H.G. 1985. Cathodoluminescence in calcite and dolomite and its chemical interpretation. Geoscience Canada, 12, 139-147.

Marfunin, A.S. 1979. Spectroscopy, luminescence and radiation centres in minerals. Springer-Verlag, Berlin, 352 p.

Mariano, A.N. 1978. The application of cathodoluminescence for carbonatite exploration and characterization. In: C.J. Braga (Ed.) Proceedings of the International Symposium on Carbonatites, 1st, Pocos de Caldas, Minas Gerais, Brazil, 39-57.

Mariano, A.N. 1989a. Nature of economic mineralization in carbonatites and related rocks . In: K. Bell (Ed.) Carbonatites. Genesis and Evolution. Unwin Hyman, London, 149-176.

Mariano, A.N. 1989b. Economic geology of the rare earth elements. In: B.R. Lipin and G.A. McKay (Eds.) Geochemistry and Mineralogy of the rare earth elements. Reviews in Mineralogy, 21, 309-337.

Mariano, A.N., Ito, J. and Ring, P.J. 1973. Cathodoluminescence of plagioclase feldspars. Abstracts with Program, 5, Boulder, Co: Geological Society of America, 726.

Mariano, A.N. and Ring, P.J. 1975. Europium-activated cathodoluminescence in minerals. Geochimica et Cosmochimica Acta, 39, 649-660.

Marshall, D.J. 1978. Suggested standards for the reporting of cathodoluminescence results. Journal of Sedimentary Petrology, 48, 651-653.

Marshall, D.J. 1988. Cathodoluminescence of Geological Materials. Unwin and Allen Inc. Oxford, 146 p.

Martin, J.-M., Hogdahl, O.T. and Phillippot, J.C. 1976. Rare earth element supply to the ocean. Journal of Geophysical Research, 81, 3119-3124.

McCrea, J.M. 1950. On the isotope chemistry of carbonates and a paleotemperature scale. Journal of Chemistry and Physics, 18, 849-857.

McLeod, R.L. and Stanton, R.L. 1984. Phyllosilicates and associated minerals in some Paleozoic stratiform sulphide deposits of southeastern Australia. Economic Geology, 79, 1-22.

Digitised by the Department of Library Services in support of open access to information, University of Pretoria, 2021

Mergoil, J. and Boivin, P., Bles, J-L., Cantagrel, J-M. and Turland, M. 1993. Le Velay. Son volcanisme et les formations associées. Notice de le carte à 1/100 000. Geologie de la France, 3, Editions BRGM, 3-96.

Meyers, W.J. 1974. Carbonate cements: their regional distribution and interpretation in Mississippian limestones of southwestern New Mexico. Sedimentology, 25, 371-399.

Mian, I. 1987. Mineralogy and petrology of the carbonatites, syenites and fenites of the North West Frontier Province, Pakistan. Unpublished Ph.D. thesis, University of Leicester.

Möller, P., Morteani, G. and Schley, F. 1980. Discussion of REE distribution patterns of carbonatites and alkaline rocks. Lithos, 13, 171-179.

Moore,C.H. 1989. Developments in Sedimentology 46: Carbonate Diagenesis and Porosity. Elsevier, Oxford.

Morrow, D.W. 1982. Diagenesis 1. Dolomite - Part 1: The chemistry of dolomitisation and dolomite precipitation. Geoscience Canada, 9, 5-13.

Ngwenya, B.T. 1994. Hydrothermal rare earth mineralisation in carbonatites of the Tundulu complex, Malawi: Processes at the fluid/rock interface. Geochimica et Cosmochimica Acta, 9, 2061-2072.

Nickel, E.1978. The present status of cathodoluminescence as a tool in sedimentology. Minerals Science and Engineering, 10, 73-100.

Nielsen, T.F.D. and Buchardt, B. 1985. Sr-C-O isotopes in nephelinitic rocks and carbonatites, Gardiner Complex, Tertiary of East Greenland. Chemical Geology, 53, 207-217.

Ohmoto, H. 1972. Systematics of sulphur and carbon isotopes in hydrothermal ore deposits. Economic Geology, 67, 551-579.

Ohmoto, H. 1986. Stable isotope geochemistry of ore deposits. In: J.W. Valley, H.P. Taylor and J.R. O'Neil (Eds.) Stable isotopes in high temperature processes. Reviews in Mineralogy. Mineralogical Society of America, 16, 491-559.

Pineau, F., Javoy, M. and Allegre, C.J. 1973. Etude systematique des isotopes de l'oxygène, du carbon et du strontium dans les carbonatites. Geochimica et Cosmochimica Acta, 37, 2363-2377.

Pirajno, F., Butt, C.R.M. and Winter, E. (1995). Gold enrichment in weathered carbonatite pyroclastics of the Kruidfontein Volcanic Complex, South Africa. South African Journal of Geology, 98, 319-325.

Quon, S.H. and Heinrich, E.W. 1965. Abundance and significance of some minor elements in carbonatitic calcites and dolomites. International Mineralogical Association, papers, 4th General meeting, Mineralogical Society of India, 29-36.

Reading, H.G. 1978. Sedimentary environments and facies. ISBN 0-632-00435-5. Whitefriars Press Ltd, London and Tonbridge, 569 p.

Reid, D.L. and Cooper, A.F. 1992. Oxygen and carbon isotope patterns in the Dicker Willem Carbonatite Complex, southern Namibia. Chemical Geology, 94, 293-305.

Reischmann, T. 1995. Precise U/Pb age determination with baddeleyite (ZrO_2), a case study from the Phalaborwa Igneous Complex, South Africa. South African Journal of Geology, 98, 1-4.

Digitised by the Department of Library Services in support of open access to information, University of Pretoria, 2021

Richter, D.K. and Zinkernagel, U. 1981. Zur Anwendung der Kathodenlumineszenze in der Karbonatpetrographie. Geologische Rundschau, 70, 1276-1302.

Roeder, P.L., MacArthur, D., Ma, X-P., Palmer, G.R and Mariano, A.N. 1987. Cathodoluminescence and microprobe study of rare-earth elements in apatite. American Mineralogist, 27, 801-811.

Romanchev, B.P. and Sokolov, S.V. 1980. Liquation in the production and geochemistry of the rocks in carbonatite complexes. Geochemistry International, 16, 125-135.

Rosenbaum, J. and Sheppard, S.M.F. 1986. An isotopic study of siderites, dolomites and ankerites at high temperatures. Geochimica et Cosmochimica Acta, 50, 1147-1150.

Russell, B.G. 1977. A study of the possible recovery of rare earth elements from the Foskor concentrate during phosphoric acid manufacture. Unpublished report of the National Institute for Metallurgy.

Rytuba, J.J. 1981. Relation of calderas to ore deposits in the western United States. Arizona Geological Society Digest, 14, 227-236.

Rytuba, J.J. 1994. Evolution of volcanic and tectonic features in caldera settings and their importance in the localization of ore deposits. Economic Geology, 89, 1687-1696.

Rytuba, J.J., Arribas Jr., A., Cunningham, C.G., McKee, E.H., Podwysocki, M.H., Smith, L.G., Kelly, W.C., and Arribas, A. 1990. Mineralized and unmineralized calderas in Spain; Part II, evolution of the Rodalquilar caldera complex and associated gold-alunaite deposits. Mineralium Deposita, 25, S29-S35.

Schmid, R. 1981. Descriptive nomenclature and classification of pyroclastic deposits and fragments: Recommendations of the IUGS Subcommission on the Systematic of Igneous Rocks. Geology, 9, 41-43.

Schiffries, C.M. and Rye, D.M. 1989. Stable isotope systematics of the Bushveld Complex: I. Constraints of magmatic processes in layered intrusions. American Journal of Science, 289, 841-873.

Schürmann, L.W. 1992a. Description of borehole KD01: The results of borehole KD01 drilled on Kruidfontein 139JQ, northwest of Brits. Report of the Geological Survey of South Africa, 1992-0006.

Schürmann, L.W. 1992b. Description of borehole KD02: The results of borehole KD02 drilled on Kruidfontein 139JQ, northwest of Brits. Report of the Geological Survey of South Africa, 1992-0007.

Schürmann, L.W. 1992c. Description of borehole KD03: The results of borehole KD03 drilled on Kruidfontein 139JQ, northwest of Brits. Report of the Geological Survey of South Africa, 1992-0008.

Schürmann, L.W. 1993. Raw materials for advanced technologies IV - Rare earths. In: Annual Technical Report of the Geological Survey of South Africa, 1993, 117-119.

Schürmann, L.W. and Harmer, R.E. 1998. Rare-earth elements. In: M. Wilson (Ed.) Mineral Resources of South Africa, Handbook 6, Council for Geoscience, 569-574.

Scott, B. and Price, S. 1988. Earthquake-induced structures in young sediments. Tectonophysics, 147, 165-170.

Sharma, T. and Clayton, R.N. 1965. Measurement of O^{18}/O^{16} ratios of total oxygen of carbonates. Geochimica et Cosmochimica Acta, 29, 1347-1353.

Sheppard, S.M.F. and Schwarcz, H.P. 1970. Fractionation of carbon and oxygen isotopes and magnesium between coexisting metamorphic calcite and dolomite. Contributions to Petrology, 26, 161-198.

Sippel, R.F. and Glover, E.D. 1965. Structures in carbonate rocks made visible by luminescence petrography. Science, 150, 1283-1287.

Digitised by the Department of Library Services in support of open access to information, University of Pretoria, 2021

Smith, R.L and Bailey, R.A. 1968. Resurgent cauldrons: Geological Society of America Memoir, 116, 613-662.

Streckeisen, A. 1979. Classification and nomenclature of volcanic rocks, lamprophyres, carbonatites and melilitic rocks: Recommendations and suggestions of the IUGS Subcommission of the Systematics of Igneous rocks. Geology, 7, 331-335.

Taylor, H.P.Jr., Frechen, J. and Degens, E.T. 1967. Oxygen and carbon isotope studies of carbonatites from the Laacher See District, West Germany, and the Alnö District, Sweden. Geochimica et Cosmochimica Acta, 31, 407-430.

Taylor, R.P. and Pollard, P.J. 1995. Rare earth element mineralization in peralkaline systems: the T-Zone REE-Y-Be deposit, Thor Lake, Northwest Territories, Canada. In: A.P. Jones, F. Wall and C.T. Williams (Eds.) Rare Earth Minerals: Chemistry, origin and ore deposits. Mineralogical Society Series 7, Chapman and Hall, London, 167-192.

Tao, G.Y., Pella, P.A. and Rousseau, R.M. 1985. NBSGSC- A FORTRAN Program for Quantitative X-ray Fluorescence Analysis. National Bureau of Standards. Technical note, 1213, 119.

Tillmans, E. and Corens, C.W. 1978. Titanium. In: K.H. Wedepohl (Ed.) Handbook of Geochemistry, Volume II/22. Springer-Verlag, Berlin.

Treiman, A.H. 1995. Ca-rich carbonate melts: A regular-solution model, with applications to carbonatite magma + vapor equilibria and carbonate lavas on Venus. American Mineralogist, 80, 115-130.

Treiman, A.H. and Essene, E.J. 1984. A periclase-dolomite-calcite carbonatite from the Oka complex, Quebec, and its calculated volatile composition. Contributions to Mineralogy and Petrology, 85, 149-157.

Truter, F.C. 1949. Discussion on a paper by R.A.P. Fockema - An occurrence of alkaline and acid lavas and volcanic breccias on the farm Kruidfontein 147, Rustenburg District. Transactions of the Geological Society of South Africa, 52, 226-229.

Tuttle, O.F. and Gittins, J. 1966. Carbonatites. New York: John Wiley, 591 p.

Verwoerd, W.J. 1956. Report on the radioactivity of Kruidfontein Diatreme, Kruidfontein 147, Rustenburg District, Transvaal. Report of the Atomic Energy Board, 5 p.

Verwoerd, W.J. 1963. Die geologiese struktuur van die Krokodilrivier fragment. Transactions of the Geological Society of South Africa, 66, 49-66.

Verwoerd, W.J. 1964. South African carbonatites and their probable mode of origin. Annals, University of Stellenbosch, Series A41, 115-233.

Verwoerd, W.J. 1967. The carbonatites of South Africa and South West Africa. Handbook of the Geological Survey of South Africa, 6, 452.

Verwoerd, W.J. 1986. Mineral deposits associated with carbonatites and alkaline rocks. In: C.R Anhaeusser and S. Maske (Eds.) Mineral deposits of southern Africa, Vol. I and II, Geological Society of South Africa, Johannesburg, 2173-2191.

Vlasov, K.A. 1966. Geochemistry and Mineralogy of Rare Elements and Genetic Types of Their Deposits: Geochemistry of Rare Elements. Volume 1. Academy of Sciences of the USSR. State Geological Committee of the USSR, Institute of Mineralogy, Geochemistry and Crystal Chemistry of Rare elements, 204 p.

Digitised by the Department of Library Services in support of open access to information, University of Pretoria, 2021

Wakita, H., Rey, P. and Schmitt, R.A. 1971. Abundances of the 14 rare-earth elements and 12 other trace elements in Apollo 12 samples: five igneous and one breccia rocks and four soils. Proceeding of the 2nd Lunar Science Conference, Pergamon Press, Oxford, 1319-1329.

Wall, F., Barreiro, B.A. and Spiro, B. 1994. Isotopic evidence for late-stage processes in carbonatites: rare earth mineralization in carbonatites and quartz rocks at Kangankunde, Malawi. Mineralogical Magazine, 58A, 951-952.

Wall, F. and Mariano, A.N. 1996. Rare earth minerals in carbonatites: a discussion centred on the Kangankunde Carbonatite, Malawi. In: A.P. Jones, F. Wall and C.T. Williams (Eds.) Rare earth minerals: chemistry, origin and ore deposits. Mineralogical Society Series, 7, Chapman and Hall, 193-222.

Williams, L.A.J. 1969. Volcanic associations in the Gregory Rift Valley, East Africa. Nature, 224, 61-64.

Willis, J.P. 1989. Compton scatter and matrix correction for trace element analysis of geological materials. In: S.T. Ahmedali (Ed.) X-Ray Fluorescence Analysis in the Geological Sciences. Advances in methodology. Geological Association of Canada. Short Course, 7.

Wolff, J.A. 1994. Physical properties of carbonatite magmas inferred from molten salt data, and application to extraction patterns from carbonatite-silicate magma chambers. Geological Magazine, 131, 145-153.

Wood, S.A. 1990. The aqueous geochemistry of rare-earth elements and yttrium 2. Theoretical predictions of speciation in hydrothermal solutions to 350°C at saturation water vapour pressure. Chemical Geology, 34, 229-259.

Woolley, A.R. 1982. A discussion of carbonatite evolution and nomenclature, and the generation of sodic and potassic fenites. Mineralogical Magazine, 46, 13-17.

Woolley, A.R. and Kempe, R.C. 1989. Carbonatites: Nomenclature, average chemical compositions, and element distribution. In K. Bell (Ed.) Carbonatites: Genesis and evolution. Unwin Hyman, London, 1-14.

Woronow, A. 1990. Methods for quantifying, statistically testing, and graphically displaying shifts in compositional abundances across data suites. Computers and Geosciences, 16, 1209-1233.

Woronow, A. and Love, K.M. 1990. Quantifying and testing differences among means of compositional data suites. Journal of Mathematical Geology, 22, 837-852.

Wyllie, P.J. 1989. Origin of carbonatites: evidence from phase equilibrium studies. In K. Bell (Ed.) Carbonatites: Genesis and evolution. Unwin Hyman, London, 500-545.

Wyllie, P.J. and Tuttle, O.F. 1960. The system $CaO-CO_2-H_2O$ and the origin of carbonatites. Journal of Petrology, 1, 1-46.

Wyllie, P.J., Jones, A.P. and Deng, J. 1995. Rare earth elements in carbonate-rich melts from the mantle to crust. In: A.P. Jones, F. Wall and C.T. Williams (Eds.) Rare Earth Minerals: Chemistry, origin and ore deposits. Mineralogical Society Series 7, Chapman and Hall, UK, 77-103.

Zang, W. and Fyfe, W.S. 1995. Chloritization of the hydrothermally altered bedrock at the Igarape Bahia gold deposit, Carajas, Brazil. Mineralium Deposita, 30, 30-38.

Digitised by the Department of Library Services in support of open access to information, University of Pretoria, 2021

APPENDIX 1: MINERAL CHEMISTRY

Digitised by the Department of Library Services in support of open access to information, University of Pretoria, 2021

CHLORITE ANALYSES: KD01 SEQUENCE

Sample KD6E (borehole KD02)
Samples KD016 and KD019 (borehole KD01)

Code of textural varieties and sample number (CODE): FP = in silicate clasts; LP = in ash grains; V = veins; CH = undifferentiated analysis

APPENDIX 1.1

												Structural formula, based on 28 oxygen atoms									
SAMPLE	CODE	SiO_2	TiO_2	Al_2O_3	FeO	MnO	MgO	CaO	Na_2O	K_2O	TOTAL	Si	Ti	Al	Fe^{2+}	Mn	Mg	Ca	Na	K	SUM
KD6E	FP1	29.07	0.17	14.80	21.65	0.19	16.53	0.27	0.29	0.30	83.27	6.348	0.028	3.810	3.954	0.035	5.379	0.063	0.123	0.084	19.823
KD6E	FP2	29.73	0.09	14.90	21.68	0.00	16.25	0.47	0.23	0.58	83.93	6.434	0.015	3.801	3.924	0.000	5.241	0.109	0.097	0.160	19.780
KD6E	FP3	30.44	0.19	15.20	22.41	0.00	17.92	0.39	0.08	0.14	86.77	6.357	0.030	3.742	3.914	0.000	5.577	0.087	0.032	0.037	19.777
KD6E	FP4	29.51	0.20	14.84	22.65	0.00	17.08	0.30	0.30	0.22	85.10	6.321	0.032	3.748	4.058	0.000	5.453	0.069	0.125	0.060	19.865
KD6E	FP5	31.64	0.21	15.55	20.88	0.00	15.48	1.03	0.22	1.00	86.01	6.632	0.033	3.843	3.660	0.000	4.836	0.231	0.090	0.267	19.592
KD6E	FP6	30.26	0.08	15.60	22.59	0.00	17.68	0.57	0.23	0.28	87.29	6.300	0.013	3.829	3.934	0.000	5.486	0.127	0.093	0.074	19.856
KD6E	FP7	31.27	0.34	15.74	21.65	0.17	16.65	0.37	0.14	0.82	87.15	6.485	0.053	3.849	3.755	0.030	5.146	0.082	0.056	0.217	19.674
AVERAGE		30.27	0.18	15.23	21.93	0.05	16.80	0.49	0.21	0.48	85.65	6.411	0.029	3.803	3.886	0.009	5.303	0.110	0.088	0.128	19.767
KD016	LP1	25.67	0.25	17.80	31.51	0.09	10.40	0.49	0.44	0.11	86.76	5.698	0.042	4.658	5.849	0.017	3.440	0.117	0.190	0.031	20.042
KD016	LP2	26.23	0.13	16.98	30.09	0.13	10.86	0.61	0.20	0.19	85.42	5.870	0.022	4.480	5.632	0.025	3.622	0.146	0.087	0.054	19.938
KD016	LP3	25.26	0.33	16.31	30.22	0.15	10.61	1.64	0.36	0.11	84.99	5.739	0.056	4.368	5.742	0.029	3.592	0.399	0.159	0.032	20.116
KD016	LP4	25.52	0.00	17.15	30.65	0.00	10.14	1.54	0.11	0.13	85.24	5.765	0.000	4.567	5.790	0.000	3.414	0.373	0.048	0.037	19.994
KD016	LP5	25.52	0.19	16.63	30.94	0.23	10.56	0.63	0.23	0.21	85.14	5.782	0.032	4.442	5.863	0.044	3.566	0.153	0.101	0.061	20.045
KD016	LP6	25.46	0.14	17.21	31.84	0.00	10.48	0.61	0.44	0.05	86.23	5.706	0.024	4.548	5.968	0.000	3.501	0.146	0.192	0.014	20.099
KD016	LP7	22.94	0.16	15.52	28.18	0.15	9.29	7.56	0.16	0.38	84.34	5.370	0.028	4.283	5.517	0.030	3.241	1.896	0.073	0.113	20.553
KD016	LP8	25.36	0.28	16.90	31.10	0.15	10.24	0.80	0.12	0.05	85.00	5.753	0.048	4.520	5.900	0.029	3.462	0.194	0.053	0.014	19.973
KD016	LP9	25.69	0.20	17.13	31.50	0.21	10.38	1.05	0.23	0.11	86.50	5.737	0.034	4.510	5.883	0.040	3.455	0.251	0.100	0.031	20.040
KD016	LP10	26.13	0.48	16.94	31.89	0.17	10.88	0.30	0.17	0.00	86.96	5.786	0.080	4.422	5.905	0.032	3.590	0.071	0.073	0.000	19.960
KD016	LP11	23.76	3.32	18.02	31.47	0.11	9.45	0.33	0.22	0.00	86.68	5.303	0.557	4.742	5.875	0.021	3.144	0.079	0.095	0.000	19.816
KD016	V12	20.09	14.60	14.83	26.53	0.12	7.58	0.84	0.35	0.05	84.99	4.565	2.495	3.973	5.042	0.023	2.567	0.205	0.154	0.014	19.038
KD016	V13	24.29	4.73	17.76	31.23	0.11	9.47	0.39	0.19	0.00	88.17	5.312	0.778	4.579	5.712	0.020	3.087	0.091	0.081	0.000	19.661
KD016	V14	22.32	8.32	16.92	29.48	0.00	8.66	0.53	0.30	0.00	86.53	4.980	1.396	4.451	5.501	0.000	2.880	0.127	0.130	0.000	19.464
KD016	V15	21.57	12.33	15.60	25.43	0.00	9.26	1.18	0.30	0.00	85.67	4.797	2.062	4.090	4.730	0.000	3.069	0.281	0.130	0.000	19.160
KD016	V16	21.19	1.54	14.73	27.93	0.19	8.16	5.52	0.07	0.09	79.42	5.276	0.288	4.323	5.815	0.040	3.028	1.473	0.034	0.029	20.306
KD016	V17	22.99	2.15	17.76	30.83	0.41	8.55	1.15	0.17	0.08	84.09	5.323	0.374	4.847	5.969	0.080	2.950	0.285	0.076	0.024	19.929
KD016	V18	26.44	0.58	17.27	30.79	0.11	10.97	0.11	0.25	0.06	86.58	5.835	0.096	4.493	5.682	0.021	3.608	0.026	0.107	0.017	19.885
KD016	V19	20.49	14.34	15.11	26.84	0.09	8.03	0.97	0.28	0.00	86.15	4.587	2.414	3.988	5.025	0.017	2.679	0.233	0.122	0.000	19.065
KD016	V20	24.70	0.06	16.04	29.43	0.00	10.27	2.98	0.36	0.09	83.93	5.698	0.010	4.362	5.678	0.000	3.531	0.737	0.161	0.026	20.204
KD016	V21	22.73	0.00	14.90	27.24	0.00	8.69	7.41	0.33	0.35	81.65	5.485	0.000	4.239	5.498	0.000	3.125	1.916	0.155	0.108	20.526
KD016	V22	25.60	0.16	16.42	30.31	0.21	10.67	1.62	0.18	0.21	85.38	5.783	0.027	4.373	5.726	0.040	3.592	0.392	0.079	0.061	20.073
KD016	V23	24.81	0.00	16.61	29.65	0.27	9.49	1.82	0.17	0.37	83.19	5.764	0.000	4.550	5.761	0.053	3.286	0.453	0.077	0.110	20.054
AVERAGE		24.12	2.80	16.55	29.79	0.13	9.70	1.74	0.24	0.11	85.17	5.475	0.472	4.426	5.655	0.024	3.280	0.437	0.108	0.034	19.910
KD019	CH108	25.26	0.00	18.82	31.55	0.00	9.01	0.00	0.00	0.28	84.92	5.713	0.000	5.018	5.968	0.000	3.037	0.000	0.000	0.081	19.818
KD019	CH109	24.32	0.61	19.80	33.90	0.00	8.19	0.00	0.00	0.27	87.09	5.435	0.103	5.216	6.335	0.000	2.728	0.000	0.000	0.077	19.893
KD019	CH110	24.34	0.00	18.19	32.90	0.00	8.59	0.00	0.00	0.39	84.41	5.613	0.000	4.946	6.345	0.000	2.952	0.000	0.000	0.115	19.971
KD019	CH117	26.53	0.00	17.52	31.58	0.00	10.18	0.00	0.00	0.20	86.01	5.907	0.000	4.599	5.881	0.000	3.378	0.000	0.000	0.057	19.822

Digitised by the Department of Library Services in support of open access to information, University of Pretoria, 2021

CHLORITE ANALYSES: KD01 SEQUENCE

Samples KD019 (continued), KD111 and KD119

Code of textural varieties and sample number (CODE): CH = undifferentiated analysis

APPENDIX 1.1

												Structural formula, based on 28 oxygen atoms									
SAMPLE	CODE	SiO_2	TiO_2	Al_2O_3	FeO	MnO	MgO	CaO	Na_2O	K_2O	TOTAL	Si	Ti	Al	Fe^{2+}	Mn	Mg	Ca	Na	K	SUM
KD019	CH118	26.14	0.00	18.60	32.76	0.00	9.74	0.00	0.00	0.19	87.43	5.754	0.000	4.827	6.031	0.000	3.195	0.000	0.000	0.053	19.860
KD019	CH130	23.92	0.00	19.19	35.15	0.37	7.78	0.33	0.00	0.00	86.74	5.426	0.000	5.132	6.668	0.071	2.630	0.080	0.000	0.000	20.008
KD019	CH131	24.75	0.00	19.39	35.74	0.39	7.84	0.48	0.00	0.00	88.59	5.491	0.000	5.071	6.631	0.073	2.592	0.114	0.000	0.000	19.973
KD019	CH135	27.20	0.00	17.85	31.52	0.00	8.63	0.00	0.46	0.96	86.62	6.033	0.000	4.667	5.847	0.000	2.853	0.000	0.198	0.272	19.869
KD019	CH137	25.70	0.00	18.72	33.74	0.45	8.92	0.00	0.00	0.18	87.71	5.688	0.000	4.885	6.245	0.084	2.942	0.000	0.000	0.051	19.895
KD019	CH179	26.16	0.00	18.43	31.95	0.00	10.04	0.00	0.45	0.31	87.34	5.757	0.000	4.782	5.881	0.000	3.293	0.000	0.192	0.087	19.992
KD019	CH180	26.66	0.00	18.67	31.78	0.00	10.45	0.00	0.00	0.41	87.97	5.798	0.000	4.787	5.780	0.000	3.387	0.000	0.000	0.114	19.866
KD019	CH190	24.68	0.00	19.29	31.41	0.39	8.98	0.20	0.40	0.00	85.35	5.570	0.000	5.133	5.929	0.075	3.021	0.048	0.175	0.000	19.951
KD019	CH191	24.46	0.00	18.79	32.58	0.42	8.51	0.00	0.00	0.00	84.76	5.594	0.000	5.066	6.231	0.081	2.900	0.000	0.000	0.000	19.873
KD019	CH211	26.86	0.00	19.43	30.92	0.37	10.05	0.41	0.00	0.17	88.21	5.795	0.000	4.942	5.579	0.068	3.232	0.095	0.000	0.047	19.757
KD019	CH235	24.49	0.00	18.71	35.34	0.00	8.66	0.53	0.00	0.00	87.73	5.482	0.000	4.937	6.615	0.000	2.889	0.127	0.000	0.000	20.050
KD019	CH241	24.31	1.19	17.71	32.28	0.00	9.50	0.00	0.00	0.00	84.99	5.539	0.204	4.757	6.151	0.000	3.226	0.000	0.000	0.000	19.878
KD019	CH247	26.51	0.00	18.33	32.41	0.00	10.90	0.32	0.00	0.00	88.47	5.748	0.000	4.686	5.878	0.000	3.522	0.074	0.000	0.000	19.909
AVERAGE		25.43	0.11	18.67	32.79	0.14	9.17	0.13	0.08	0.20	86.73	5.667	0.018	4.909	6.117	0.027	3.046	0.032	0.033	0.056	19.905
KD111	CH1	23.97	0.06	19.22	32.99	0.21	8.54	0.13	0.10	0.06	85.28	5.466	0.010	5.167	6.292	0.041	2.902	0.032	0.044	0.017	19.971
KD111	CH2	24.29	0.00	19.75	33.24	0.27	8.70	0.13	0.06	0.05	86.49	5.453	0.000	5.227	6.241	0.051	2.911	0.031	0.026	0.014	19.954
KD111	CH3	24.04	0.00	19.05	33.10	0.22	8.73	0.11	0.06	0.09	85.40	5.478	0.000	5.117	6.308	0.042	2.965	0.027	0.027	0.026	19.990
KD111	CH4	23.88	0.00	19.09	32.82	0.17	8.47	0.08	0.06	0.00	84.57	5.486	0.000	5.170	6.306	0.033	2.900	0.020	0.027	0.000	19.942
KD111	CH5	28.39	0.00	18.64	31.25	0.24	7.53	0.10	0.07	0.00	86.22	6.236	0.000	4.827	5.740	0.045	2.465	0.024	0.030	0.000	19.366
KD111	CH6	28.51	0.00	18.66	32.13	0.33	7.62	0.12	0.07	0.06	87.50	6.200	0.000	4.784	5.843	0.061	2.470	0.028	0.030	0.017	19.431
KD111	CH10	23.51	0.05	19.02	33.47	0.23	7.92	0.09	0.07	0.06	84.42	5.444	0.009	5.192	6.482	0.045	2.733	0.022	0.031	0.018	19.976
KD111	CH11	25.19	0.00	19.37	32.87	0.23	8.73	0.13	0.06	0.00	86.58	5.619	0.000	5.094	6.132	0.043	2.902	0.031	0.026	0.000	19.847
KD111	CH12	24.61	0.00	18.92	33.55	0.19	8.28	0.06	0.07	0.00	85.68	5.585	0.000	5.062	6.368	0.037	2.801	0.015	0.031	0.000	19.899
KD111	CH13	24.47	0.00	19.11	32.59	0.18	8.49	0.09	0.07	0.05	85.05	5.571	0.000	5.129	6.205	0.035	2.881	0.022	0.031	0.015	19.887
KD111	CH14	23.43	0.00	18.52	31.19	0.22	8.49	3.85	0.00	0.08	85.78	5.346	0.000	4.982	5.952	0.043	2.887	0.941	0.000	0.023	20.174
KD111	CH15	23.94	0.08	19.73	32.71	0.25	8.39	0.12	0.07	0.05	85.34	5.441	0.014	5.287	6.218	0.048	2.842	0.029	0.031	0.014	19.924
AVERAGE		24.85	0.02	19.09	32.66	0.23	8.32	0.42	0.06	0.04	85.69	5.610	0.003	5.087	6.174	0.044	2.805	0.102	0.028	0.012	19.863
KD119	CH16	27.63	0.10	18.24	29.33	0.34	8.85	0.80	0.18	0.94	86.41	6.077	0.017	4.730	5.395	0.063	2.901	0.189	0.077	0.264	19.712
KD119	CH17	28.64	0.10	18.50	27.67	0.31	8.50	0.23	0.13	1.20	85.28	6.297	0.017	4.795	5.088	0.058	2.785	0.054	0.056	0.337	19.485
KD119	CH18	30.78	0.00	18.23	25.61	0.16	7.42	1.25	0.16	2.21	85.82	6.665	0.000	4.654	4.638	0.029	2.394	0.290	0.067	0.610	19.347
KD119	CH19	27.95	0.11	18.45	27.85	0.27	8.60	0.24	0.21	1.01	84.69	6.204	0.018	4.828	5.170	0.051	2.845	0.057	0.091	0.286	19.551
KD119	CH20	28.11	0.05	18.73	28.71	0.35	8.85	0.12	0.15	1.00	86.07	6.157	0.008	4.837	5.260	0.065	2.889	0.028	0.064	0.279	19.588
KD119	CH21	28.69	0.06	19.26	27.11	0.27	8.64	0.21	0.14	1.11	85.49	6.258	0.010	4.952	4.945	0.050	2.808	0.049	0.059	0.309	19.441
KD119	CH22	28.28	0.06	18.77	28.50	0.29	9.05	0.18	0.13	0.94	86.20	6.170	0.010	4.828	5.201	0.054	2.943	0.042	0.055	0.262	19.564
KD119	CH23	30.51	0.10	18.27	26.26	0.22	7.99	0.15	0.16	1.83	85.49	6.621	0.016	4.674	4.766	0.040	2.584	0.035	0.067	0.507	19.312
KD119	CH24	29.79	0.00	18.56	26.38	0.35	8.53	0.60	0.15	1.21	85.57	6.464	0.000	4.748	4.787	0.064	2.759	0.140	0.063	0.335	19.361

Digitised by the Department of Library Services in support of open access to information, University of Pretoria, 2021

CHLORITE ANALYSIS: KD01 SEQUENCE

Samples KD119 (continued), KD121, KD130 and KD133

Code of textural varieties and sample number (CODE): CH = undifferentiated analysis

APPENDIX 1.1

												Structural formula, based on 28 oxygen atoms									
SAMPLE	CODE	SiO_2	TiO_2	Al_2O_3	FeO	MnO	MgO	CaO	Na_2O	K_2O	TOTAL	Si	Ti	Al	Fe^{2+}	Mn	Mg	Ca	Na	K	SUM
KD119	CH25	24.71	0.40	20.33	32.24	0.31	7.82	0.31	0.06	0.21	86.39	5.518	0.067	5.353	6.022	0.059	2.603	0.074	0.026	0.060	19.781
KD119	CH26	26.30	4.71	18.43	27.47	0.31	7.35	0.44	0.00	1.06	86.07	5.771	0.777	4.767	5.041	0.058	2.403	0.103	0.000	0.297	19.217
KD119	CH27	24.85	0.09	19.64	30.85	0.31	7.34	2.10	0.00	0.29	85.47	5.611	0.015	5.228	5.826	0.059	2.470	0.508	0.000	0.084	19.801
KD119	CH28	32.82	0.08	20.50	24.25	0.23	6.93	0.31	0.08	2.56	87.76	6.814	0.012	5.018	4.211	0.040	2.144	0.069	0.032	0.678	19.020
KD119	CH33	24.42	0.00	19.95	33.18	0.32	7.56	0.22	0.06	0.11	85.82	5.524	0.000	5.321	6.278	0.061	2.549	0.053	0.026	0.032	19.844
KD119	CH34	27.81	0.05	17.82	29.38	0.35	8.94	0.21	0.19	0.80	85.55	6.164	0.008	4.657	5.446	0.066	2.953	0.050	0.082	0.226	19.653
KD119	CH35	28.37	0.00	18.01	28.29	0.21	9.00	0.21	0.20	0.89	85.18	6.263	0.000	4.688	5.223	0.039	2.961	0.050	0.086	0.251	19.561
KD119	CH36	30.11	0.06	18.07	27.09	0.33	7.95	0.22	0.19	1.24	85.26	6.573	0.010	4.651	4.946	0.061	2.587	0.051	0.081	0.345	19.305
KD119	CH37	28.54	0.00	17.28	27.96	0.25	9.56	0.21	0.10	0.75	84.65	6.328	0.000	4.517	5.185	0.047	3.159	0.050	0.043	0.212	19.541
AVERAGE		28.11	0.35	18.75	28.35	0.29	8.29	0.46	0.13	1.03	85.75	6.168	0.057	4.857	5.215	0.054	2.715	0.109	0.053	0.286	19.516
KD121	CH38	25.78	0.00	18.58	30.02	0.27	10.96	0.35	0.08	0.05	86.09	5.703	0.000	4.846	5.554	0.051	3.613	0.083	0.034	0.014	19.898
KD121	CH39	25.68	0.06	18.37	29.96	0.23	10.72	0.12	0.09	0.10	85.33	5.732	0.010	4.834	5.593	0.043	3.566	0.029	0.039	0.028	19.875
KD121	CH40	26.51	0.00	18.64	29.65	0.29	10.97	0.17	0.07	0.18	86.48	5.811	0.000	4.817	5.435	0.054	3.584	0.040	0.030	0.050	19.821
KD121	CH41	27.36	0.00	19.28	28.73	0.25	10.15	0.17	0.05	0.54	86.53	5.950	0.000	4.943	5.225	0.046	3.290	0.040	0.021	0.150	19.664
KD121	CH42	26.98	0.00	18.54	27.93	0.29	10.12	2.21	0.00	0.61	86.68	5.893	0.000	4.774	5.102	0.054	3.294	0.517	0.000	0.170	19.805
KD121	CH43	26.24	0.05	18.63	29.87	0.29	11.11	0.05	0.05	0.00	86.29	5.768	0.008	4.828	5.491	0.054	3.639	0.012	0.021	0.000	19.821
KD121	CH44	31.18	0.00	17.89	27.56	0.27	9.89	0.33	0.10	0.34	87.56	6.580	0.000	4.451	4.864	0.048	3.110	0.075	0.041	0.092	19.261
KD121	CH45	25.24	0.00	19.28	31.71	0.27	10.09	0.06	0.46	0.00	87.11	5.570	0.000	5.016	5.853	0.050	3.319	0.014	0.197	0.000	20.020
KD121	CH46	26.14	0.00	19.94	30.43	0.26	9.54	0.05	0.08	0.26	86.70	5.730	0.000	5.153	5.579	0.048	3.117	0.012	0.034	0.073	19.746
KD121	CH47	26.28	0.00	18.67	29.82	0.26	9.91	0.28	0.07	0.43	85.72	5.833	0.000	4.886	5.536	0.049	3.278	0.067	0.030	0.122	19.800
KD121	CH48	24.29	0.05	19.70	31.55	0.32	9.98	0.60	0.00	0.00	86.49	5.412	0.008	5.175	5.879	0.060	3.314	0.143	0.000	0.000	19.992
KD121	CH49	24.31	0.00	19.84	31.10	0.28	9.47	0.50	0.08	0.10	85.68	5.457	0.000	5.250	5.838	0.053	3.168	0.120	0.035	0.029	19.950
KD121	CH50	26.18	0.07	18.64	29.55	0.23	11.01	0.10	0.06	0.14	85.98	5.772	0.012	4.845	5.449	0.043	3.618	0.024	0.026	0.039	19.826
KD121	CH51	27.20	0.07	18.62	29.80	0.28	10.91	0.22	0.06	0.37	87.53	5.886	0.011	4.751	5.394	0.051	3.519	0.051	0.025	0.102	19.791
KD121	CH52	25.88	0.06	18.24	31.06	0.33	10.81	0.16	0.06	0.11	86.71	5.716	0.010	4.749	5.737	0.062	3.558	0.038	0.026	0.031	19.928
KD121	CH53	24.47	0.00	18.89	31.36	0.30	9.57	0.00	0.06	0.06	84.71	5.562	0.000	5.062	5.961	0.058	3.242	0.000	0.026	0.017	19.929
KD121	CH54	25.29	0.00	18.59	30.83	0.32	9.77	0.19	0.09	0.17	85.25	5.689	0.000	4.930	5.800	0.061	3.275	0.046	0.039	0.049	19.890
KD121	CH55	31.09	0.50	20.46	24.81	0.22	8.62	0.11	0.00	1.98	87.79	6.483	0.078	5.030	4.327	0.039	2.679	0.025	0.000	0.527	19.187
AVERAGE		26.45	0.05	18.93	29.76	0.28	10.20	0.32	0.08	0.30	86.37	5.808	0.008	4.908	5.479	0.051	3.344	0.074	0.035	0.083	19.789
KD130	CH56	25.09	0.00	18.12	30.29	0.24	10.67	0.19	0.13	0.10	84.83	5.663	0.000	4.822	5.718	0.046	3.589	0.046	0.057	0.029	19.969
KD130	CH57	24.72	0.00	18.71	30.68	0.30	9.52	0.18	0.06	0.20	84.37	5.627	0.000	5.021	5.841	0.058	3.230	0.044	0.027	0.058	19.905
KD130	CH58	26.50	0.00	18.47	29.68	0.22	10.73	0.14	0.10	0.52	86.36	5.831	0.000	4.792	5.462	0.041	3.519	0.033	0.043	0.146	19.867
KD130	CH59	26.36	0.40	18.41	29.84	0.26	10.79	0.09	0.06	0.34	86.55	5.789	0.066	4.766	5.480	0.048	3.531	0.021	0.026	0.095	19.823
KD130	CH60	25.04	0.40	17.95	29.95	0.24	10.82	0.15	0.13	0.11	84.79	5.647	0.068	4.772	5.649	0.046	3.637	0.036	0.057	0.032	19.943
AVERAGE		25.54	0.16	18.33	30.09	0.25	10.51	0.15	0.10	0.25	85.38	5.711	0.027	4.835	5.630	0.048	3.501	0.036	0.042	0.072	19.901
KD133	CH61	22.45	0.00	14.02	23.30	0.24	10.08	14.51	0.05	0.28	84.93	5.230	0.000	3.851	4.540	0.047	3.500	3.622	0.023	0.083	20.897

Digitised by the Department of Library Services in support of open access to information, University of Pretoria, 2021

CHLORITE ANALYSES: KD01 SEQUENCE

Samples KD133 (continued), KD135, KD146 and KD147

Code of textural varieties and sample number (CODE): CH = undifferentiated analysis

APPENDIX 1.1

												Structural formula, based on 28 oxygen atoms									
SAMPLE	NUM	SiO_2	TiO_2	Al_2O_3	FeO	MnO	MgO	CaO	Na_2O	K_2O	TOTAL	Si	Ti	Al	Fe^{2+}	Mn	Mg	Ca	Na	K	SUM
KD133	CH62	29.37	0.50	18.18	27.15	0.16	11.70	0.13	0.00	0.71	87.90	6.206	0.079	4.529	4.798	0.029	3.684	0.029	0.000	0.191	19.546
KD133	CH63	24.91	0.12	16.37	27.50	0.19	11.21	4.43	0.08	0.08	84.89	5.639	0.020	4.369	5.206	0.036	3.782	1.075	0.035	0.023	20.185
KD133	CH64	27.80	0.05	17.50	27.51	0.23	11.93	1.67	0.05	0.44	87.18	6.001	0.008	4.453	4.966	0.042	3.838	0.386	0.021	0.121	19.836
KD133	CH65	28.07	0.12	17.65	28.85	0.19	12.42	0.22	0.00	0.34	87.86	6.010	0.019	4.455	5.166	0.034	3.963	0.050	0.000	0.093	19.790
KD133	CH66	27.89	0.00	17.25	28.35	0.17	12.70	0.20	0.11	0.33	87.00	6.026	0.000	4.394	5.123	0.031	4.089	0.046	0.046	0.091	19.846
KD133	CH67	26.95	0.06	17.37	29.21	0.26	12.68	0.20	0.08	0.14	86.95	5.866	0.010	4.457	5.317	0.048	4.113	0.047	0.034	0.039	19.932
KD133	CH68	27.23	0.24	16.75	27.81	0.25	12.65	1.28	0.07	0.18	86.46	5.942	0.039	4.309	5.075	0.046	4.114	0.299	0.030	0.050	19.904
KD133	CH80	23.09	0.00	14.29	24.14	0.19	11.20	11.34	0.08	0.24	84.57	5.349	0.000	3.903	4.677	0.037	3.867	2.815	0.036	0.071	20.753
KD133	CH81	28.21	0.06	17.75	27.09	0.18	11.57	0.24	0.12	0.71	85.93	6.134	0.010	4.550	4.926	0.033	3.749	0.056	0.051	0.197	19.705
KD133	CH82	27.32	0.15	18.13	28.73	0.18	11.58	0.14	0.08	0.36	86.67	5.938	0.025	4.646	5.223	0.033	3.751	0.033	0.034	0.100	19.781
KD133	CH83	26.99	0.22	17.67	29.03	0.30	12.04	0.39	0.12	0.22	86.98	5.872	0.036	4.532	5.282	0.055	3.904	0.091	0.051	0.061	19.882
KD133	CH84	30.13	0.16	18.14	26.62	0.12	11.07	0.18	0.11	1.40	87.93	6.361	0.025	4.515	4.700	0.021	3.483	0.041	0.045	0.377	19.568
KD133	CH85	27.75	0.06	18.08	28.45	0.23	11.59	0.15	0.06	0.43	86.80	6.008	0.010	4.615	5.152	0.042	3.740	0.035	0.025	0.119	19.746
KD133	CH86	24.33	0.00	16.35	27.33	0.11	10.82	6.32	0.90	0.13	86.29	5.477	0.000	4.339	5.146	0.021	3.630	1.525	0.393	0.037	20.569
KD133	CH87	27.48	0.00	17.88	28.41	0.22	12.37	0.24	0.05	0.22	86.87	5.946	0.000	4.561	5.141	0.040	3.989	0.056	0.021	0.061	19.814
KD133	CH88	31.66	0.13	18.78	24.23	0.19	10.72	0.21	0.10	1.87	87.89	6.584	0.020	4.604	4.214	0.033	3.322	0.047	0.040	0.496	19.362
AVERAGE		27.15	0.11	17.19	27.28	0.20	11.67	2.46	0.12	0.48	86.65	5.917	0.018	4.417	4.980	0.037	3.795	0.603	0.052	0.130	19.948
KD135	CH89	24.69	0.53	17.70	30.48	0.29	10.88	0.26	0.09	0.17	85.09	5.579	0.090	4.716	5.761	0.056	3.664	0.063	0.039	0.049	20.017
KD135	CH90	26.50	0.16	18.56	27.17	0.24	11.67	0.08	0.05	0.11	84.54	5.862	0.027	4.840	5.026	0.045	3.847	0.019	0.021	0.031	19.718
KD135	CH91	27.92	0.74	16.76	28.73	0.18	8.04	1.12	0.09	2.00	85.58	6.238	0.124	4.415	5.369	0.034	2.677	0.268	0.039	0.570	19.735
KD135	CH92	34.29	0.10	19.16	21.49	0.19	8.59	0.26	0.09	3.08	87.25	7.066	0.015	4.655	3.704	0.033	2.638	0.057	0.036	0.810	19.014
KD135	CH93	30.86	0.06	19.07	19.65	0.14	7.77	5.83	0.06	2.29	85.73	6.574	0.010	4.790	3.501	0.025	2.467	1.331	0.025	0.622	19.345
AVERAGE		28.85	0.32	18.25	25.50	0.21	9.39	1.51	0.08	1.53	85.64	6.264	0.053	4.683	4.672	0.039	3.059	0.348	0.032	0.416	19.566
KD146	CH94	31.01	0.88	19.60	21.87	0.16	3.80	4.02	0.16	4.86	86.36	6.697	0.143	4.990	3.950	0.029	1.223	0.930	0.067	1.339	19.368
KD146	CH95	32.08	0.80	19.71	23.82	0.14	7.54	0.38	0.18	2.57	87.22	6.717	0.126	4.866	4.171	0.025	2.353	0.085	0.073	0.687	19.104
KD146	CH96	28.76	0.11	20.71	25.76	0.16	6.60	0.09	0.00	2.39	84.58	6.319	0.018	5.364	4.733	0.030	2.161	0.021	0.000	0.670	19.316
KD146	CH97	25.95	0.05	19.95	31.19	0.21	7.64	0.09	0.08	0.79	85.95	5.786	0.008	5.244	5.816	0.040	2.539	0.022	0.035	0.225	19.713
KD146	CH98	28.44	0.22	20.16	26.38	0.15	7.13	0.13	0.06	2.13	84.80	6.259	0.036	5.230	4.855	0.028	2.338	0.031	0.026	0.598	19.401
KD146	CH99	23.63	0.05	19.14	32.25	0.26	7.62	1.09	0.05	0.13	84.22	5.467	0.009	5.220	6.240	0.051	2.627	0.270	0.022	0.038	19.945
KD146	CH100	24.84	0.07	19.67	32.26	0.19	7.88	0.14	0.10	0.45	85.60	5.610	0.012	5.237	6.093	0.036	2.652	0.034	0.044	0.130	19.847
AVERAGE		27.82	0.31	19.85	27.65	0.18	6.89	0.85	0.09	1.90	85.53	6.122	0.050	5.164	5.123	0.034	2.270	0.199	0.038	0.527	19.528
KD147	CH101	26.73	0.11	16.17	28.06	2.21	8.75	0.31	0.17	1.60	84.11	6.129	0.019	4.371	5.381	0.429	2.990	0.076	0.076	0.468	19.939
KD147	CH102	27.08	0.13	16.60	28.62	1.60	9.07	0.25	0.12	1.38	84.85	6.126	0.022	4.427	5.414	0.307	3.058	0.061	0.053	0.398	19.864
KD147	CH103	39.52	0.05	15.47	22.88	0.59	6.75	0.51	0.33	1.48	87.58	8.020	0.008	3.701	3.883	0.101	2.041	0.111	0.130	0.383	18.379
KD147	CH104	27.40	1.20	18.61	29.50	0.72	9.29	0.15	0.10	0.81	87.78	5.928	0.195	4.747	5.338	0.132	2.995	0.035	0.042	0.224	19.636
AVERAGE		30.18	0.37	16.71	27.27	1.28	8.47	0.31	0.18	1.32	86.08	6.551	0.061	4.312	5.004	0.242	2.771	0.071	0.075	0.368	19.455

Digitised by the Department of Library Services in support of open access to information, University of Pretoria, 2021

CHLORITE ANALYSES: KD01 SEQUENCE

Sample KD6E (borehole KD02)
Samples KD016 and KD019 (borehole KD01)

APPENDIX 1.1

SAMPLE	CODE	Al^{4+}	Al^{6+}	F/FM	T = 106 (Al^{4+} + 0.7[Fe/(Fe+Mg)]) + 18 degrees Celsius
KD6E	FP1	1.65	2.16	0.42	
KD6E	FP2	1.56	2.24	0.43	
KD6E	FP3	1.64	2.10	0.41	
KD6E	FP4	1.68	2.07	0.43	
KD6E	FP5	1.37	2.48	0.43	
KD6E	FP6	1.70	2.13	0.42	
KD6E	FP7	1.52	2.33	0.42	
AVERAGE		1.59	2.22	0.42	
TEMPERATURE					218
KD016	LP1	2.30	2.36	0.66	
KD016	LP2	2.13	2.35	0.61	
KD016	LP3	2.26	2.11	0.62	
KD016	LP4	2.24	2.33	0.63	
KD016	LP5	2.22	2.22	0.62	
KD016	LP6	2.29	2.25	0.63	
KD016	LP7	2.63	1.65	0.63	
KD016	LP8	2.25	2.27	0.63	
KD016	LP9	2.26	2.25	0.63	
KD016	LP10	2.21	2.21	0.62	
KD016	LP11	2.70	2.05	0.65	
KD016	V12	3.44	0.54	0.66	
KD016	V13	2.69	1.89	0.65	
KD016	V14	3.02	1.43	0.66	
KD016	V15	3.20	0.89	0.61	
KD016	V16	2.72	1.60	0.66	
KD016	V17	2.68	2.17	0.67	
KD016	V18	2.17	2.33	0.61	
KD016	V19	3.41	0.58	0.65	
KD016	V20	2.30	2.06	0.62	
KD016	V21	2.52	1.72	0.64	
KD016	V22	2.22	2.16	0.61	
KD016	V23	2.24	2.31	0.64	
AVERAGE		2.50	1.90	0.63	
TEMPERATURE					333
KD019	CH108	2.29	2.73	0.66	
KD019	CH109	2.57	2.65	0.70	
KD019	CH110	2.38	2.56	0.68	
KD019	CH117	2.09	2.51	0.64	
KD019	CH118	2.25	2.58	0.65	
KD019	CH130	2.57	2.56	0.72	
KD019	CH131	2.51	2.56	0.72	
KD019	CH135	1.97	2.70	0.67	
KD019	CH137	2.31	2.57	0.68	
KD019	CH179	2.24	2.54	0.64	
KD019	CH180	2.20	2.59	0.63	
KD019	CH190	2.43	2.70	0.66	
KD019	CH191	2.41	2.66	0.68	
KD019	CH211	2.21	2.74	0.63	
KD019	CH235	2.52	2.42	0.70	
KD019	CH241	2.46	2.30	0.66	
KD019	CH247	2.25	2.43	0.63	
AVERAGE		2.35	2.55	0.65	
TEMPERATURE					315

Digitised by the Department of Library Services in support of open access to information, University of Pretoria, 2021

CHLORITE ANALYSES: KD01 SEQUENCE

Samples KD111, KD119 and KD121

APPENDIX 1.1

SAMPLE	CODE	Al^{4+}	Al^{6+}	F/FM	T = 106 (Al^{4+} + 0.7[Fe/(Fe+Mg)]) + 18 degrees Celsius
KD111	CH1	2.53	2.63	0.68	
KD111	CH2	2.55	2.68	0.68	
KD111	CH3	2.52	2.60	0.68	
KD111	CH4	2.51	2.66	0.68	
KD111	CH5	1.76	3.06	0.70	
KD111	CH6	1.80	2.98	0.70	
KD111	CH10	2.56	2.64	0.70	
KD111	CH11	2.38	2.71	0.68	
KD111	CH12	2.42	2.65	0.69	
KD111	CH13	2.43	2.70	0.68	
KD111	CH14	2.65	2.33	0.67	
KD111	CH15	2.56	2.73	0.69	
AVERAGE		2.40	2.68	0.69	
TEMPERATURE					322
KD119	CH16	1.92	2.81	0.65	
KD119	CH17	1.70	3.09	0.65	
KD119	CH18	1.34	3.32	0.66	
KD119	CH19	1.80	3.03	0.65	
KD119	CH20	1.84	2.99	0.65	
KD119	CH21	1.74	3.21	0.64	
KD119	CH22	1.83	3.00	0.64	
KD119	CH23	1.38	3.30	0.65	
KD119	CH24	1.54	3.21	0.63	
KD119	CH25	2.48	2.87	0.70	
KD119	CH26	2.23	2.54	0.68	
KD119	CH27	2.39	2.84	0.70	
KD119	CH28	1.19	3.83	0.66	
KD119	CH33	1.72	2.97	0.71	
KD119	CH34	1.84	2.82	0.65	
KD119	CH35	1.74	2.95	0.64	
KD119	CH36	1.43	3.22	0.66	
KD119	CH37	1.67	2.85	0.62	
AVERAGE		1.71	3.07	0.66	
TEMPERATURE					261
KD121	CH38	2.30	2.55	0.61	
KD121	CH39	2.27	2.57	0.61	
KD121	CH40	2.19	2.63	0.60	
KD121	CH41	2.05	2.89	0.61	
KD121	CH42	2.11	2.67	0.61	
KD121	CH43	2.23	2.60	0.60	
KD121	CH44	1.42	3.03	0.61	
KD121	CH45	2.43	2.59	0.64	
KD121	CH46	2.27	2.88	0.64	
KD121	CH47	2.17	2.72	0.63	
KD121	CH48	2.59	2.59	0.64	
KD121	CH49	2.54	2.71	0.65	
KD121	CH50	2.23	2.62	0.60	
KD121	CH51	2.11	2.64	0.61	
KD121	CH52	2.28	2.47	0.62	
KD121	CH53	2.44	2.62	0.65	
KD121	CH54	2.31	2.62	0.64	
KD121	CH55	1.52	3.51	0.62	
AVERAGE		2.21	2.74	0.62	
TEMPERATURE					296

Digitised by the Department of Library Services in support of open access to information, University of Pretoria, 2021

CHLORITE ANALYSES: KD01 SEQUENCE

Samples KD130, KD133, KD135, KD146 and KD147

APPENDIX 1.1

SAMPLE	CODE	Al^{4+}	Al^{6+}	F/FM	T = 106 (Al^{4+} + 0.7[Fe/(Fe+Mg)]) + 18 degrees Celsius
KD130	CH56	2.34	2.49	0.61	
KD130	CH57	2.37	2.65	0.64	
KD130	CH58	2.17	2.62	0.61	
KD130	CH59	2.21	2.56	0.61	
KD130	CH60	2.35	2.42	0.61	
AVERAGE		2.29	2.55	0.62	
TEMPERATURE					308
KD133	CH61	2.77	1.08	0.56	
KD133	CH62	1.79	2.74	0.57	
KD133	CH63	2.36	2.01	0.58	
KD133	CH64	2.00	2.45	0.56	
KD133	CH65	1.99	2.47	0.57	
KD133	CH66	1.97	2.42	0.56	
KD133	CH67	2.13	2.32	0.56	
KD133	CH68	2.06	2.25	0.55	
KD133	CH80	2.65	1.25	0.55	
KD133	CH81	1.87	2.68	0.57	
KD133	CH82	2.06	2.58	0.58	
KD133	CH83	2.13	2.40	0.58	
KD133	CH84	1.64	2.88	0.57	
KD133	CH85	1.99	2.62	0.58	
KD133	CH86	2.52	1.82	0.59	
KD133	CH87	2.05	2.51	0.56	
KD133	CH88	1.42	3.19	0.56	
AVERAGE		1.97	2.57	0.57	
TEMPERATURE					281
KD135	CH89	2.42	2.30	0.61	
KD135	CH90	2.14	2.70	0.57	
KD135	CH91	1.76	2.65	0.67	
KD135	CH92	0.93	3.72	0.58	
KD135	CH93	1.43	3.36	0.59	
AVERAGE		1.78	2.88	0.60	
TEMPERATURE					247
KD146	CH94	1.30	3.69	0.76	
KD146	CH95	1.28	3.58	0.64	
KD146	CH96	1.68	3.68	0.69	
KD146	CH97	2.21	3.03	0.70	
KD146	CH98	1.74	3.49	0.67	
KD146	CH99	2.53	2.69	0.70	
KD146	CH100	2.39	2.85	0.70	
AVERAGE		1.88	3.29	0.69	
TEMPERATURE					268
KD147	CH101	1.87	2.50	0.64	
KD147	CH102	1.87	2.55	0.64	
KD147	CH103	0.00	3.70	0.66	
KD147	CH104	2.07	2.68	0.64	
AVERAGE		1.68	2.93	0.66	
TEMPERATURE					219

Digitised by the Department of Library Services in support of open access to information, University of Pretoria, 2021

CARBONATE ANALYSIS: KD01 SEQUENCE

Sample KD016

APPENDIX 1.2

Code of textural varieties (TYPE): 3 = amygdales; 4 = cement; 5 = veins

SAMPLE	TYPE	$Ce_2(CO_3)_3$	$MgCO_3$	$CaCO_3$	$MnCO_3$	$FeCO_3$	$SrCO_3$	Na_2CO_3	K_2CO_3	TOTAL	$MnCO_3/FeCO_3$
KD016	5	0.12	0.04	100.18	0.11	0.3	0.71	0.00	0.01	101.50	0.32
KD016	5	0.06	0.02	99.07	0.78	0.2	0.57	0.02	0.02	100.71	4.43
KD016	5	0.12	0.47	98.20	1.39	1.1	0.09	0.00	0.02	101.40	1.25
KD016	5	0.05	0.34	98.37	1.51	1.0	0.11	0.03	0.03	101.47	1.45
KD016	5	0.23	0.00	100.60	0.41	0.1	0.23	0.00	0.00	101.54	5.06
KD016	5	0.00	0.00	100.80	0.05	0.0	0.56	0.04	0.02	101.48	2.82
KD016	5	0.00	0.05	99.02	1.20	0.1	0.58	0.06	0.00	101.02	11.13
KD016	5	0.08	0.58	96.51	1.85	1.3	0.37	0.03	0.03	100.78	1.39
KD016	5	0.16	0.41	97.55	1.70	1.0	0.15	0.00	0.00	101.00	1.64
KD016	5	0.19	0.41	97.18	1.63	0.7	0.33	0.04	0.05	100.50	2.39
KD016	5	0.01	0.01	99.71	0.36	0.2	0.80	0.04	0.00	101.08	2.25
KD016	5	0.01	0.00	100.13	0.08	0.2	0.58	0.04	0.01	101.07	0.33
AVERAGE		0.08	0.19	98.94	0.92	0.53	0.42	0.02	0.02	101.13	2.87
KD016	4	0.00	0.13	97.30	0.40	0.4	2.05	0.04	0.00	100.34	0.96
KD016	4	0.11	1.77	94.91	0.92	1.7	1.35	0.06	0.00	100.80	0.54
KD016	4	0.19	0.19	97.10	0.68	0.2	1.77	0.03	0.03	100.19	3.48
KD016	4	0.24	0.15	98.37	0.60	0.2	1.24	0.09	0.02	100.95	2.49
KD016	4	0.08	5.90	83.76	1.19	6.3	1.45	0.02	0.06	98.76	0.19
KD016	4	0.14	2.41	93.18	1.09	2.4	1.33	0.06	0.03	100.59	0.46
KD016	4	0.04	0.13	99.24	0.43	0.1	1.63	0.07	0.02	101.68	3.49
KD016	4	0.02	0.94	93.54	3.75	1.3	0.68	0.01	0.02	100.24	2.89
KD016	4	0.00	0.29	97.30	0.14	1.8	1.24	0.02	0.00	100.83	0.07
KD016	4	0.04	0.20	96.29	1.96	0.6	0.60	0.02	0.00	99.67	3.45
KD016	4	0.05	0.76	96.48	1.45	0.6	1.66	0.00	0.04	101.03	2.41
AVERAGE		0.08	1.17	95.22	1.15	1.42	1.36	0.04	0.02	100.46	1.86
KD016	3	0.17	0.20	98.31	0.36	0.4	1.09	0.01	0.05	100.58	0.94
KD016	3	0.11	0.09	95.84	3.57	0.3	0.45	0.00	0.01	100.39	11.16
KD016	3	0.15	0.23	97.41	1.10	0.5	0.87	0.02	0.00	100.25	2.42
KD016	3	0.04	0.35	96.98	1.95	1.1	0.50	0.04	0.00	100.94	1.80
KD016	3	0.11	0.29	98.63	0.45	1.4	0.53	0.05	0.00	101.50	0.31
KD016	3	0.05	0.21	97.37	0.18	0.8	1.20	0.06	0.02	99.89	0.22
KD016	3	0.22	0.06	97.81	0.26	0.1	1.83	0.00	0.00	100.28	2.56
KD016	3	0.04	0.61	96.49	0.38	1.5	0.88	0.00	0.00	99.88	0.25
KD016	3	0.13	0.49	97.34	1.72	0.4	0.86	0.04	0.03	100.97	4.64
KD016	3	0.23	0.01	97.33	0.13	0.3	3.03	0.04	0.06	101.11	0.47
KD016	3	0.12	0.32	97.52	0.35	1.3	0.62	0.00	0.02	100.22	0.28
KD016	3	0.14	8.16	77.83	0.82	11.9	1.12	0.07	0.00	100.08	0.07
KD016	3	0.16	0.78	95.70	0.96	1.4	0.71	0.08	0.00	99.82	0.67
KD016	3	0.06	0.09	96.99	0.65	0.4	1.32	0.05	0.00	99.55	1.67

Digitised by the Department of Library Services in support of open access to information, University of Pretoria, 2021

CARBONATE ANALYSIS: KD01 SEQUENCE

Sample KD016

APPENDIX 1.2

Code of textural varieties (TYPE): 2 = microphenocrysts; 3 = amygdales

SAMPLE	TYPE	$Ce_2(CO_3)_3$	$MgCO_3$	$CaCO_3$	$MnCO_3$	$FeCO_3$	$SrCO_3$	Na_2CO_3	K_2CO_3	TOTAL	$MnCO_3/FeCO_3$
KD016	3	0.03	0.00	97.96	0.04	0.0	2.60	0.06	0.00	100.72	1.46
KD016	3	0.13	0.00	97.54	0.09	0.0	3.17	0.05	0.06	101.06	4.00
KD016	3	0.16	0.00	97.67	0.00	0.04	3.03	0.02	0.00	100.93	0.00
KD016	3	0.14	0.22	97.42	0.12	0.15	3.01	0.01	0.00	101.05	0.77
KD016	3	0.00	0.16	97.75	1.42	0.50	0.50	0.00	0.00	100.34	2.87
KD016	3	0.09	0.16	98.59	1.27	0.66	0.36	0.00	0.00	101.12	1.91
KD016	3	0.07	0.15	97.98	1.30	0.42	0.62	0.00	0.15	100.68	3.13
KD016	3	0.02	0.32	98.88	0.57	0.32	0.88	0.00	0.03	101.03	1.82
KD016	3	0.08	0.16	96.67	1.43	1.08	0.98	0.00	0.00	100.40	1.32
KD016	3	0.22	0.10	97.71	0.64	0.02	1.20	0.00	0.00	99.90	29.18
KD016	3	0.10	0.05	97.10	0.14	0.19	2.84	0.10	0.02	100.52	0.73
KD016	3	0.03	0.29	98.39	0.30	0.88	1.34	0.02	0.01	101.27	0.34
KD016	3	0.10	0.00	97.22	0.12	0.06	3.71	0.02	0.01	101.25	2.20
KD016	3	0.31	0.03	96.76	0.00	0.26	3.42	0.13	0.02	100.91	0.00
KD016	3	0.09	0.00	96.62	0.07	0.11	4.24	0.00	0.01	101.14	0.66
KD016	3	0.07	0.00	97.72	0.02	0.07	3.59	0.00	0.08	101.55	0.34
KD016	3	0.34	0.00	96.51	0.16	0.12	3.75	0.11	0.03	101.00	1.34
KD016	3	0.09	1.45	94.24	0.80	2.98	1.09	0.02	0.00	100.66	0.27
KD016	3	0.27	0.24	95.76	0.65	0.36	2.32	0.30	0.01	99.91	1.79
KD016	3	0.38	1.55	92.63	0.57	4.24	1.62	0.11	0.05	101.16	0.13
AVERAGE		0.11	0.45	96.78	0.68	0.88	1.68	0.03	0.02	100.64	2.61
KD016	2	0.15	1.31	95.94	0.65	2.23	0.86	0.03	0.07	101.24	0.29
KD016	2	0.38	2.36	89.43	0.20	5.21	1.83	0.12	0.12	99.64	0.04
KD016	2	0.09	0.03	95.67	0.15	0.26	3.29	0.00	0.02	99.51	0.56
KD016	2	0.38	0.29	97.15	0.43	0.34	2.14	0.16	0.00	100.88	1.27
KD016	2	0.11	19.95	53.72	3.01	21.56	0.56	0.03	0.10	99.02	0.14
KD016	2	0.44	1.80	91.13	0.60	5.34	1.38	0.06	0.06	100.81	0.11
KD016	2	0.00	0.64	94.72	1.52	1.98	1.04	0.02	0.84	100.75	0.77
KD016	2	0.16	11.57	73.41	2.42	11.06	1.07	0.13	0.01	99.83	0.22
AVERAGE		0.21	4.75	86.39	1.12	6.00	1.52	0.07	0.15	100.21	0.43

Digitised by the Department of Library Services in support of open access to information, University of Pretoria, 2021

CARBONATE ANALYSIS: KD01 SEQUENCE

Sample KD016

APPENDIX 1.2

Code of textural varieties (TYPE): 1 = phenocrysts

SAMPLE	TYPE	$Ce_2(CO_3)_3$	$MgCO_3$	$CaCO_3$	$MnCO_3$	$FeCO_3$	$SrCO_3$	Na_2CO_3	K_2CO_3	TOTAL	$MnCO_3/FeCO_3$
KD016	1	0.00	0.32	99.17	0.32	0.09	0.43	0.01	0.02	100.37	3.60
KD016	1	0.14	1.94	96.84	0.88	0.11	1.35	0.06	0.01	101.31	8.24
KD016	1	0.04	0.45	98.54	0.80	0.23	0.72	0.03	0.01	100.81	3.46
KD016	1	0.11	0.80	96.88	1.24	0.21	1.47	0.00	0.00	100.70	5.96
KD016	1	0.00	0.82	96.19	1.45	0.13	1.08	0.05	0.07	99.78	11.22
KD016	1	0.15	0.61	96.78	0.87	0.96	1.13	0.04	0.04	100.57	0.91
KD016	1	0.05	0.03	98.02	0.04	0.19	1.56	0.09	0.02	99.99	0.18
KD016	1	0.00	0.14	97.00	1.10	0.50	1.85	0.07	0.00	100.66	2.20
KD016	1	0.00	1.52	94.43	1.37	2.37	0.66	0.11	0.00	100.45	0.58
KD016	1	0.02	0.61	97.69	0.97	0.43	0.94	0.02	0.06	100.74	2.26
KD016	1	0.05	0.04	97.02	2.76	0.30	0.69	0.03	0.00	100.88	9.12
KD016	1	0.07	0.62	97.73	0.89	0.79	1.05	0.00	0.00	101.15	1.12
AVERAGE		0.05	0.66	97.19	1.06	0.52	1.08	0.04	0.02	100.62	4.07

Digitised by the Department of Library Services in support of open access to information, University of Pretoria, 2021

APPENDIX 1.3

CARBONATE ANALYSIS: KD01 SEQUENCE

Samples KD012, KD019, KD111 and KD115

Code of textural varieties and sample number (CODE): CH = undifferentiated analysis

										End-member composition (mol per cent)					
SAMPLE	CODE	MgO	Al_2O_3	SiO_2	CaO	MnO	FeO	SrO	CO_2	$CaCO_3$	$MnCO_3$	$FeCO_3$	$MgCO_3$	$SrCO_3$	TOTAL
KD012	CH5	0.00	0.00	0.00	55.61	0.00	0.00	0.93	42.67	99.26	0.00	0.00	0.00	1.32	100.58
KD012	CH250	15.70	0.00	0.00	29.75	1.92	7.20	0.00	45.06	53.09	3.11	11.61	32.84	0.00	100.65
KD012	CH251	13.58	0.00	0.00	28.40	1.09	10.63	0.00	46.30	50.69	1.76	17.13	28.40	0.00	97.99
AVE.		9.76	0.00	0.00	37.92	1.00	5.94	0.31	44.68	67.68	1.62	9.58	20.41	0.44	99.74
KD019	CH193	8.76	0.00	0.00	27.55	3.76	14.81	0.51	44.52	49.17	6.09	23.87	18.33	0.73	98.20
KD019	CH195	8.93	0.00	0.00	27.56	3.18	15.21	0.45	44.34	49.19	5.15	24.52	18.69	0.64	98.19
KD019	CH196	14.92	0.00	0.00	28.73	2.95	6.66	0.90	45.49	51.28	4.77	10.74	31.21	1.28	99.29
KD019	CH200	16.92	0.00	0.00	28.38	1.13	5.31	1.41	46.19	50.65	1.83	8.56	35.40	2.01	98.45
KD019	CH201	13.19	0.00	0.00	27.84	5.80	7.30	0.00	45.92	49.70	9.40	11.77	27.60	0.00	98.46
KD019	CH202	8.35	0.00	0.00	27.14	4.80	14.96	0.42	43.40	48.44	7.78	24.12	17.47	0.60	98.42
KD019	CH203	8.74	0.00	0.00	27.06	4.58	14.98	0.59	43.74	48.30	7.43	24.15	18.29	0.83	99.00
KD019	CH213	8.97	0.00	0.00	27.11	4.26	14.74	0.46	45.46	48.38	6.90	23.76	18.76	0.66	98.45
KD019	CH214	12.77	0.00	0.00	28.69	5.66	8.20	0.55	43.72	51.21	9.17	13.22	26.71	0.78	101.09
KD019	CH237	16.39	0.00	0.00	28.43	1.40	6.29	1.08	46.69	50.75	2.27	10.15	34.29	1.54	99.00
KD019	CH245	8.29	0.00	0.00	27.29	3.42	16.14	0.61	44.42	48.71	5.55	26.03	17.33	0.87	98.50
KD019	CH246	13.97	0.00	0.00	28.72	3.93	8.06	0.37	44.24	51.25	6.36	13.00	29.23	0.52	100.36
AVE.		11.68	0.00	0.00	27.88	3.74	11.05	0.61	44.84	49.75	6.06	17.82	24.44	0.87	98.95
KD111	CH247	9.05	0.00	0.04	27.38	6.68	12.63	0.16	44.05	48.87	10.82	20.37	18.93	0.23	99.22
KD111	CH248	9.83	0.03	0.00	28.96	5.65	10.71	0.31	44.49	51.69	9.15	17.27	20.56	0.44	99.12
KD111	CH249	10.88	0.00	0.02	27.24	6.13	10.87	0.22	44.64	48.62	9.93	17.53	22.76	0.31	99.15
KD111	CH250	7.93	0.04	0.18	27.21	6.86	13.48	0.19	44.11	48.56	11.12	21.74	16.59	0.27	98.28
KD111	CH251	9.70	0.02	0.02	27.41	6.84	11.37	0.21	44.44	48.92	11.08	18.33	20.29	0.30	98.93
KD111	CH252	8.81	0.02	0.03	27.28	6.78	12.77	0.21	44.09	48.69	10.99	20.59	18.43	0.30	99.00
KD111	CH253	10.73	0.05	0.02	27.56	6.51	9.95	0.17	44.99	49.19	10.55	16.04	22.45	0.24	98.47
KD111	CH254	10.55	0.03	0.00	27.43	5.81	11.13	0.31	44.73	48.96	9.41	17.95	22.07	0.44	98.83
KD111	CH255	8.69	0.01	0.03	27.22	6.36	13.09	0.23	44.37	48.58	10.31	21.11	18.18	0.33	98.50
KD111	CH256	7.65	0.00	0.00	26.86	6.68	14.55	0.21	44.03	47.94	10.82	23.46	16.00	0.30	98.53
AVE.		9.38	0.02	0.03	27.46	6.43	12.06	0.22	44.39	49.00	10.42	19.44	19.63	0.32	98.80
KD115	CH257	5.44	0.00	0.06	0.66	15.14	38.01	0.00	40.69	1.19	24.54	61.30	11.37	0.00	98.39
KD115	CH258	4.90	0.00	0.06	2.99	15.58	35.65	0.00	40.82	5.34	25.24	57.48	10.26	0.00	98.32
KD115	CH259	5.25	0.12	0.17	2.50	15.69	37.08	0.00	39.18	4.47	25.42	59.80	10.99	0.00	100.68
KD115	CH260	5.89	0.00	0.00	0.72	15.77	37.76	0.00	39.86	1.28	25.55	60.89	12.32	0.00	100.05
KD115	CH261	5.65	0.10	0.11	0.72	16.32	38.26	0.02	38.82	1.29	26.45	61.69	11.81	0.04	101.27
KD115	CH262	5.71	0.00	0.01	0.64	15.74	38.57	0.00	39.34	1.14	25.50	62.19	11.95	0.00	100.78
KD115	CH263	6.31	0.02	0.00	0.68	15.18	38.64	0.07	39.09	1.22	24.60	62.31	13.20	0.10	101.42
KD115	CH264	6.65	0.74	0.81	0.66	13.43	38.40	0.00	39.33	1.17	21.75	61.91	13.92	0.00	98.76
AVE.		5.67	0.12	0.15	1.34	15.39	37.72	0.01	39.59	2.40	24.94	60.82	11.87	0.02	100.04

Digitised by the Department of Library Services in support of open access to information, University of Pretoria, 2021

CARBONATE ANALYSIS: KD01 SEQUENCE

Samples KD117, KD121, KD128, KD131, KD133, KD134 and KD135

APPENDIX 1.3

Code of textural varieties and sample number (CODE): CH = undifferentiated analysis

										End-member composition (mol per cent)					
SAMPLE	NUM	MgO	Al_2O_3	SiO_2	CaO	MnO	FeO	SrO	CO_2	$CaCO_3$	$MnCO_3$	$FeCO_3$	$MgCO_3$	$SrCO_3$	TOTAL
KD117	CH265	7.00	0.03	0.11	0.62	10.76	41.07	0.00	40.41	1.10	17.44	66.22	14.65	0.00	99.41
KD117	CH266	7.05	0.00	0.01	5.33	13.06	34.93	0.07	39.55	9.51	21.16	56.33	14.74	0.10	101.84
KD117	CH267	6.95	0.00	0.06	1.32	11.58	40.26	0.00	39.83	2.35	18.76	64.92	14.53	0.00	100.57
KD117	CH268	7.11	0.04	0.09	0.62	10.48	42.30	0.00	39.37	1.11	16.98	68.20	14.87	0.00	101.16
AVE.		7.03	0.02	0.07	1.97	11.47	39.64	0.02	39.79	3.52	18.58	63.92	14.70	0.03	100.75
KD121	CH269	0.09	0.02	1.22	51.60	2.78	0.46	0.49	43.78	92.10	4.50	0.73	0.18	0.69	98.21
KD121	CH270	0.13	0.05	0.27	52.01	3.21	0.67	0.00	43.66	92.83	5.21	1.08	0.27	0.00	99.39
KD121	CH271	0.05	0.03	0.00	53.03	2.67	0.25	0.02	43.94	94.65	4.33	0.41	0.11	0.03	99.53
KD121	CH272	0.15	0.00	0.03	52.91	3.20	0.50	0.14	43.07	94.43	5.19	0.81	0.31	0.20	100.95
KD121	CH273	0.36	0.00	0.01	51.98	2.56	0.55	0.82	43.73	92.77	4.15	0.88	0.75	1.17	99.71
AVE.		0.15	0.02	0.31	52.31	2.89	0.49	0.29	43.63	93.35	4.68	0.78	0.32	0.42	99.56
KD128	CH274	0.18	0.06	0.07	53.21	2.23	0.52	0.01	43.71	94.97	3.61	0.84	0.38	0.02	99.82
KD128	CH275	6.42	0.39	0.36	27.77	6.86	15.85	0.12	42.22	49.56	11.12	25.56	13.43	0.17	99.83
AVE.		3.30	0.23	0.22	40.49	4.55	8.19	0.07	42.97	72.27	7.36	13.20	6.90	0.09	99.83
KD131	CH277	0.09	0.02	0.03	52.77	2.95	0.46	0.07	43.63	94.18	4.78	0.73	0.18	0.09	99.96
KD131	CH278	0.32	0.01	0.05	53.34	2.20	0.53	0.59	42.97	95.20	3.56	0.86	0.66	0.84	101.12
KD131	CH279	0.06	0.01	0.04	53.15	2.19	0.41	0.32	43.83	94.86	3.55	0.66	0.13	0.45	99.65
KD131	CH280	7.61	0.01	0.05	1.40	9.28	40.81	0.00	40.84	2.51	15.04	65.80	15.91	0.00	99.27
KD131	CH281	0.29	0.09	2.12	51.74	2.20	1.62	0.00	41.94	92.35	3.57	2.61	0.60	0.00	99.13
AVE.		1.67	0.03	0.46	42.48	3.76	8.76	0.19	42.64	75.82	6.10	14.13	3.50	0.28	99.83
KD133	CH282	7.95	0.02	0.07	7.96	9.40	32.65	0.11	41.85	14.20	15.24	52.64	16.63	0.15	98.87
KD133	CH283	8.32	0.02	0.09	0.72	8.14	41.41	0.03	41.27	1.29	13.19	66.77	17.40	0.04	98.69
KD133	CH284	6.07	0.04	0.16	13.81	8.08	29.45	0.15	42.24	24.64	13.09	47.48	12.70	0.22	98.14
KD133	CH285	8.23	0.06	0.39	8.75	10.03	31.13	0.05	41.36	15.62	16.25	50.19	17.21	0.07	99.34
AVE.		7.64	0.04	0.18	7.81	8.91	33.66	0.08	41.68	13.94	14.44	54.27	15.99	0.12	98.76
KD134	CH288	7.40	0.02	0.01	0.86	19.45	31.09	0.03	41.15	1.54	31.51	50.13	15.48	0.04	98.70
KD134	CH289	18.99	0.00	0.01	26.82	2.48	2.18	2.27	47.26	47.86	4.02	3.51	39.72	3.23	98.35
KD134	CH290	7.27	0.00	0.00	1.50	19.47	30.71	0.00	41.05	2.67	31.55	49.53	15.20	0.00	98.95
KD134	CH291	18.13	0.04	0.05	27.08	3.02	2.84	1.93	46.91	48.33	4.90	4.58	37.93	2.75	98.49
KD134	CH292	18.86	0.02	0.01	26.45	2.89	2.82	2.54	46.42	47.20	4.68	4.54	39.45	3.62	99.49
KD134	CH293	0.22	0.00	0.04	52.96	3.09	0.61	0.25	42.84	94.51	5.00	0.99	0.45	0.35	101.32
KD134	CH294	0.11	0.00	0.00	52.77	2.62	0.53	0.47	43.49	94.18	4.24	0.86	0.23	0.68	100.19
AVE.		10.14	0.01	0.02	26.92	7.57	10.11	1.07	44.16	48.04	12.27	16.31	21.21	1.52	99.35
KD135	CH297	20.51	0.01	0.18	27.19	2.11	2.70	1.70	45.58	48.53	3.42	4.35	42.91	2.43	101.65
KD135	CH298	15.88	0.01	0.38	26.80	3.73	8.31	0.99	43.91	47.84	6.04	13.39	33.22	1.40	101.89
KD135	CH299	16.45	0.04	0.09	27.10	3.34	5.30	1.38	46.32	48.36	5.42	8.54	34.41	1.96	98.69
KD135	CH300	11.24	0.00	0.01	19.94	7.18	18.12	0.45	43.06	35.59	11.64	29.21	23.51	0.65	100.59

Digitised by the Department of Library Services in support of open access to information, University of Pretoria, 2021

CARBONATE ANALYSIS: KD01 SEQUENCE

Samples KD135 (continued), KD142, KD146 and KD147

APPENDIX 1.3

Code of textural varieties and sample number (CODE): CH = undifferentiated analysis

										End-member composition (mol per cent)					
SAMPLE	NUM	MgO	Al_2O_3	SiO_2	CaO	MnO	FeO	SrO	CO_2	$CaCO_3$	$MnCO_3$	$FeCO_3$	$MgCO_3$	$SrCO_3$	TOTAL
KD135	CH311	20.00	0.03	0.00	27.81	2.13	2.04	1.51	46.49	49.63	3.45	3.29	41.84	2.15	100.35
KD135	CH312	16.96	0.03	0.13	24.32	3.13	8.80	1.28	45.35	43.41	5.06	14.19	35.48	1.83	99.98
KD135	CH313	18.00	0.00	0.02	27.69	2.13	4.04	1.62	46.50	49.41	3.45	6.51	37.66	2.30	99.34
KD135	CH314	19.82	0.02	0.01	28.21	2.44	2.80	1.18	45.52	50.34	3.96	4.52	41.46	1.68	101.96
KD135	CH315	18.22	0.00	0.03	28.03	2.53	3.02	1.70	46.48	50.03	4.09	4.87	38.11	2.42	99.52
KD135	CH316	15.29	0.01	0.02	28.00	5.28	5.17	0.48	45.76	49.97	8.56	8.33	31.99	0.68	99.52
KD135	CH317	17.84	0.00	0.00	27.69	2.98	3.39	1.59	46.53	49.43	4.83	5.46	37.32	2.27	99.30
AVE.		17.29	0.01	0.08	26.62	3.36	5.79	1.26	45.59	47.50	5.45	9.33	36.17	1.80	100.25
KD142	CH318	6.81	0.00	0.00	30.37	5.79	12.53	0.29	44.20	54.21	9.39	20.21	14.24	0.41	98.47
KD142	CH319	7.69	0.01	0.04	29.85	6.35	12.53	0.26	43.27	53.27	10.29	20.21	16.09	0.37	100.23
KD142	CH320	7.46	0.00	0.00	30.76	5.79	12.44	0.24	43.30	54.91	9.38	20.06	15.61	0.35	100.31
KD142	CH321	6.48	0.00	0.02	29.91	6.77	12.90	0.16	43.76	53.39	10.97	20.80	13.57	0.23	98.96
KD142	CH322	5.03	0.00	0.00	29.51	6.99	14.71	0.31	43.17	52.67	11.32	23.73	10.52	0.44	98.68
KD142	CH323	9.67	0.01	0.01	31.26	6.78	7.28	0.00	44.98	55.79	10.99	11.73	20.24	0.00	98.76
KD142	CH324	9.38	0.00	0.01	30.10	7.23	8.03	0.00	45.25	53.72	11.71	12.94	19.63	0.00	98.00
KD142	CH325	8.55	0.00	0.01	24.46	9.39	14.28	0.00	43.31	43.66	15.21	23.03	17.88	0.00	99.77
KD142	CH326	9.24	0.01	0.03	31.13	7.69	6.81	0.05	45.04	55.56	12.46	10.98	19.34	0.07	98.41
KD142	CH327	10.24	0.00	0.01	31.34	6.47	6.83	0.00	45.12	55.94	10.48	11.01	21.41	0.00	98.84
KD142	CH328	9.96	0.00	0.03	31.79	6.30	7.31	0.00	44.60	56.75	10.21	11.79	20.84	0.00	99.59
KD142	CH329	9.63	0.00	0.01	30.93	6.71	7.62	0.01	45.08	55.20	10.88	12.28	20.15	0.01	98.53
AVE.		8.35	0.00	0.01	30.12	6.86	10.27	0.11	44.26	53.76	11.11	16.56	17.46	0.16	99.05
KD146	CH330	7.47	0.86	0.40	0.83	11.65	38.66	0.04	40.09	1.49	18.87	62.34	15.62	0.05	98.38
KD146	CH331	9.45	0.96	0.85	0.90	10.85	36.74	0.00	40.25	1.60	17.59	59.24	19.76	0.00	98.19
KD146	CH332	7.13	0.05	0.03	0.94	13.74	37.47	0.00	40.63	1.68	22.27	60.43	14.92	0.00	99.30
KD146	CH333	8.26	0.66	0.23	0.86	11.88	37.45	0.02	40.64	1.53	19.25	60.39	17.27	0.03	98.47
KD146	CH334	7.33	0.25	0.16	0.98	13.14	37.98	0.02	40.14	1.75	21.29	61.24	15.33	0.03	99.64
KD146	CH335	7.30	1.15	0.96	0.89	12.85	37.64	0.03	39.18	1.58	20.82	60.69	15.28	0.05	98.42
KD146	CH336	7.84	0.50	0.26	0.85	10.52	39.10	0.04	40.89	1.51	17.05	63.05	16.40	0.05	98.06
AVE.		7.82	0.63	0.41	0.89	12.09	37.86	0.02	40.26	1.59	19.59	61.05	16.37	0.03	98.64
KD147	CH337	6.39	0.10	0.25	0.56	12.13	39.86	0.00	40.70	0.99	19.66	64.28	13.36	0.00	98.30
KD147	CH338	7.09	0.02	0.04	2.11	9.18	41.03	0.08	40.46	3.76	14.88	66.16	14.83	0.11	99.73
KD147	CH339	6.79	0.03	0.44	29.10	6.88	14.56	0.24	42.36	51.93	11.15	23.47	14.21	0.34	101.10
KD147	CH340	6.64	0.12	0.08	30.23	6.19	13.45	0.37	42.93	53.95	10.03	21.70	13.89	0.52	100.08
KD147	CH341	6.89	0.01	0.03	28.76	6.63	14.22	0.29	43.17	51.33	10.74	22.93	14.42	0.41	99.83
KD147	CH342	6.38	0.00	0.00	30.54	6.63	12.49	0.32	43.64	54.50	10.74	20.14	13.35	0.45	99.20
AVE		6.70	0.05	0.14	20.21	7.94	22.60	0.21	42.21	36.08	12.87	36.45	14.01	0.31	99.71

Digitised by the Department of Library Services in support of open access to information, University of Pretoria, 2021

APATITE ANALYSES: KD01 SEQUENCE

APPENDIX 1.4

Sample KD012

Code of textural varieties (TYPE): KD012 apatite types: 1 = euhdral; 2 = "ragged"; 3 = rim (euhdral); 4 = rim ("ragged");
Code and sample number (CODE): CH = undifferentiated analysis

SAMPLE	CODE	TYPE	F	Na_2O	MgO	SiO_2	P_2O_5	Cl	CaO	MnO	FeO	SrO	Ce_2O_3	TOTAL
KD012	CH13	1	1.69	0.29	0.02	0.68	39.84	0.01	56.63	0.02	1.10	1.73	0.30	101.19
KD012	CH22	1	1.50	0.05	0.00	1.23	40.03	0.00	56.03	0.00	0.05	1.86	1.08	101.78
KD012	CH25	1	1.43	0.08	0.01	0.08	42.72	0.00	56.12	0.01	0.15	1.09	0.14	101.67
KD012	CH33	1	1.51	0.12	0.30	1.20	38.42	0.00	54.53	0.05	0.52	1.65	0.71	98.43
KD012	CH34	1	1.50	0.45	0.00	0.33	42.26	0.01	54.86	0.00	0.06	1.90	0.53	101.84
KD012	CH35	1	1.67	0.31	0.01	0.04	42.38	0.00	55.72	0.05	0.15	1.14	0.62	101.89
KD012	CH36	1	1.37	0.04	1.18	0.02	39.73	0.01	55.86	0.10	0.73	0.70	0.15	99.06
KD012	CH37	1	1.40	0.07	0.01	0.34	42.24	0.00	56.05	0.01	0.22	1.52	0.30	101.93
KD012	CH38	1	1.37	0.05	0.00	0.30	42.22	0.00	55.66	0.00	0.12	1.63	0.37	101.58
KD012	CH39	1	1.50	0.13	0.03	1.53	39.31	0.01	56.38	0.02	0.14	1.61	0.70	101.19
KD012	CH40	1	1.38	0.07	0.02	0.66	42.62	0.00	56.88	0.04	0.11	0.99	0.38	103.00
KD012	CH41	1	1.38	0.10	0.01	1.21	40.37	0.01	56.05	0.04	0.24	1.28	0.60	101.01
KD012	CH43	1	1.17	0.07	0.05	0.87	42.05	0.01	57.03	0.00	0.12	0.47	0.05	101.76
KD012	CH44	1	1.06	0.12	0.04	0.88	42.35	0.01	56.34	0.00	0.11	0.52	0.06	101.38
KD012	CH45	1	1.31	0.10	0.01	0.85	41.35	0.01	57.68	0.04	0.10	0.35	0.06	101.72
AVE.			1.42	0.13	0.11	0.68	41.19	0.00	56.12	0.03	0.26	1.23	0.40	101.29
KD012	CH11	2	1.71	0.14	0.00	0.11	41.73	0.01	56.73	0.01	0.05	1.52	0.21	102.14
KD012	CH12	2	1.58	0.23	0.00	0.15	41.73	0.01	56.12	0.00	0.07	1.58	0.31	101.71
KD012	CH14	2	1.43	0.12	0.02	1.05	40.33	0.00	57.28	0.05	0.04	1.20	0.75	102.18
KD012	CH15	2	1.49	0.13	0.01	0.18	42.03	0.00	56.56	0.00	0.05	1.25	0.33	101.97
KD012	CH16	2	1.55	0.17	0.05	0.47	41.59	0.01	56.52	0.02	0.13	1.14	0.23	101.73
KD012	CH17	2	1.42	0.33	0.00	0.27	40.91	0.02	56.70	0.02	0.28	1.90	0.24	101.79
KD012	CH18	2	1.71	0.36	0.00	0.13	41.61	0.01	56.61	0.00	0.10	1.04	0.23	101.70
KD012	CH19	2	1.61	0.06	0.00	1.01	40.65	0.00	55.95	0.00	0.07	1.51	0.69	101.48
KD012	CH20	2	1.63	0.10	0.10	0.05	41.09	0.01	57.83	0.02	0.76	0.54	0.18	101.53
KD012	CH21	2	1.20	0.10	1.10	1.97	39.62	0.00	53.43	0.04	2.96	0.66	0.25	98.33
KD012	CH23	2	1.40	0.22	0.04	0.29	40.88	0.01	57.13	0.03	0.81	1.92	0.30	102.19
KD012	CH24	2	1.53	0.25	0.00	0.10	41.63	0.01	56.63	0.07	0.15	1.63	0.17	101.93
KD012	CH26	2	1.57	0.29	0.00	0.47	40.63	0.01	56.23	0.05	0.17	1.92	0.36	101.47
KD012	CH27	2	1.49	0.20	0.00	0.15	42.49	0.00	56.09	0.00	0.12	1.30	0.42	102.13
KD012	CH28	2	1.57	0.12	0.00	0.18	42.06	0.00	55.65	0.01	0.71	1.61	0.36	101.53
KD012	CH29	2	1.42	0.07	0.00	0.88	41.49	0.00	55.76	0.05	0.06	1.45	0.58	101.65
KD012	CH30	2	1.42	0.02	0.00	0.23	42.54	0.00	55.77	0.06	0.04	1.80	0.24	102.01
KD012	CH31	2	1.55	0.02	0.00	0.36	42.98	0.00	55.54	0.00	0.06	1.41	0.31	102.17
KD012	CH32	2	1.55	0.12	0.00	0.27	42.21	0.00	56.16	0.01	0.04	1.30	0.41	102.02
KD012	CH42	2	0.93	0.09	0.06	0.83	41.68	0.01	56.37	0.08	0.15	0.45	0.09	100.50
KD012	CH46	2	1.33	0.10	0.02	0.00	42.68	0.00	58.47	0.00	0.19	0.66	0.35	103.62
KD012	CH47	2	1.45	0.30	0.00	0.00	42.62	0.01	55.99	0.05	0.15	1.39	0.35	102.11
AVE.			1.48	0.16	0.06	0.41	41.60	0.01	56.34	0.03	0.32	1.32	0.33	101.72
KD012	CH49	3	1.18	0.08	0.04	0.73	41.63	0.01	57.22	0.00	0.15	0.34	0.21	101.43
KD012	CH50	3	1.41	0.18	0.04	1.52	39.96	0.00	56.08	0.00	0.19	0.89	0.34	100.41
KD012	CH55	3	1.10	0.10	0.05	1.26	41.04	0.01	57.39	0.00	0.14	0.44	0.13	101.52
KD012	CH56	3	1.34	0.11	0.07	1.32	40.81	0.02	56.87	0.00	0.16	0.57	0.16	101.26
KD012	CH57	3	1.10	0.08	0.01	0.69	41.76	0.00	56.19	0.04	0.04	0.80	0.09	100.71
KD012	CH58	3	1.26	0.37	0.00	0.73	41.02	0.01	57.68	0.09	0.04	0.93	0.15	102.15
KD012	CH59	3	1.24	0.14	0.02	0.83	41.56	0.01	55.64	0.04	0.07	0.82	0.15	100.40
KD012	CH60	3	1.07	0.09	0.01	0.83	41.06	0.00	56.06	0.06	0.09	0.74	0.11	99.98
KD012	CH61	3	1.38	0.01	0.00	0.00	43.55	0.01	58.21	0.00	0.08	0.45	0.06	103.67
KD012	CH62	3	0.77	0.14	0.09	1.41	40.85	0.01	56.81	0.04	0.25	0.19	0.08	100.34
KD012	CH63	3	0.74	0.08	0.09	1.15	41.36	0.01	57.19	0.01	0.09	0.47	0.08	101.16
KD012	CH64	3	1.24	0.11	0.07	1.29	40.67	0.01	57.21	0.03	0.10	0.43	0.05	101.07
KD012	CH65	3	1.56	0.11	0.01	1.56	39.82	0.00	54.94	0.07	0.07	1.47	0.82	100.27
AVE.			1.18	0.12	0.04	1.03	41.16	0.01	56.73	0.03	0.11	0.65	0.19	101.10
KD012	CH48	4	1.47	0.04	0.01	0.90	41.23	0.00	56.40	0.00	0.17	1.47	0.55	102.07
KD012	CH51	4	1.43	0.07	0.01	1.68	40.30	0.00	56.01	0.07	0.07	1.36	0.74	101.58
KD012	CH52	4	1.51	0.09	0.02	1.10	40.79	0.00	56.26	0.04	0.18	1.15	0.55	101.48
KD012	CH53	4	1.31	0.11	0.03	0.90	41.63	0.01	57.30	0.01	0.23	0.70	0.17	102.15

Digitised by the Department of Library Services in support of open access to information, University of Pretoria, 2021

APATITE ANALYSES: KD01 SEQUENCE

APPENDIX 1.4

Sample KD012 (continued) and KD016

Code of textural varieties (TYPE): KD012 apatite types: 1 = euhdral; 2 = "ragged"; 3 = rim (euhdral); 4 = rim ("ragged");
KD016 apatite types: 1 = vein; 2 = lapillus matrix; 3 = euhedral;
Code and sample number (CODE): CH = undifferentiated analysis; n = not analysed

SAMPLE	CODE	TYPE	F	Na_2O	MgO	SiO_2	P_2O_5	Cl	CaO	MnO	FeO	SrO	Ce_2O_3	TOTAL
KD012	CH54	4	0.94	0.09	0.09	1.32	40.51	0.10	57.45	0.04	0.25	0.56	0.04	101.10
AVE.			1.33	0.08	0.03	1.18	40.89	0.02	56.68	0.03	0.18	1.05	0.41	101.68
KD016	CH66	1	1.62	0.34	0.03	0.20	39.29	0.01	54.88	0.00	n	1.86	0.83	99.06
KD016	CH67	1	1.47	0.40	0.09	0.75	38.12	0.01	53.74	0.00	n	1.90	0.86	97.34
KD016	CH68	1	1.71	0.30	0.21	2.03	37.52	0.01	53.44	0.00	n	1.91	0.73	97.83
KD016	CH69	1	1.72	0.35	0.16	1.54	38.85	0.01	53.00	0.00	n	1.64	0.80	98.05
KD016	CH70	1	1.71	0.36	0.23	1.60	38.50	0.01	53.72	0.00	n	1.85	0.75	98.71
KD016	CH71	1	1.67	0.38	0.07	0.73	38.63	0.01	54.10	0.00	n	1.79	0.91	98.28
KD016	CH72	1	1.55	0.36	0.30	1.92	37.39	0.01	52.84	0.00	n	1.90	0.82	97.09
KD016	CH73	1	1.62	0.38	0.15	1.60	38.71	0.01	53.01	0.00	n	1.70	0.88	98.06
KD016	CH74	1	1.44	0.50	0.11	1.59	38.19	0.01	53.21	0.00	n	2.00	0.96	98.00
KD016	CH75	1	1.69	0.40	0.06	0.65	39.02	0.01	54.50	0.00	n	1.81	1.01	99.16
KD016	CH76	1	1.57	0.40	0.09	0.36	39.54	0.01	55.20	0.00	n	1.74	0.78	99.69
KD016	CH77	1	1.79	0.38	0.27	1.26	38.53	0.01	53.63	0.00	n	1.78	0.89	98.53
KD016	CH78	1	1.75	0.30	0.48	2.38	37.85	0.01	51.53	0.00	n	1.62	0.69	96.61
AVE.			1.64	0.37	0.17	1.28	38.47	0.01	53.60	0.00	n	1.81	0.84	98.18
KD016	CH79	2	1.49	0.32	0.31	4.91	36.39	0.00	50.50	0.00	n	1.85	0.65	96.41
KD016	CH80	2	1.52	0.30	0.31	4.01	37.44	0.01	51.22	0.00	n	1.49	0.61	96.89
KD016	CH81	2	1.62	0.31	0.44	3.99	36.38	0.01	50.24	0.00	n	1.97	0.80	95.76
KD016	CH82	2	1.60	0.35	0.10	1.63	39.03	0.01	54.52	0.00	n	1.58	0.78	99.58
KD016	CH83	2	1.73	0.29	0.40	3.95	36.61	0.01	50.81	0.00	n	1.84	0.65	96.28
KD016	CH84	2	1.74	0.30	0.09	1.48	39.35	0.01	53.35	0.00	n	2.10	0.75	99.16
KD016	CH85	2	1.65	0.38	0.18	2.85	38.05	0.01	54.19	0.00	n	1.77	0.77	99.84
KD016	CH86	2	1.82	0.31	0.33	5.71	36.29	0.01	50.64	0.00	n	1.93	0.73	97.74
KD016	CH87	2	1.45	0.33	0.36	4.02	36.39	0.01	52.14	0.00	n	1.78	0.73	97.20
KD016	CH88	2	1.73	0.28	0.35	4.10	36.72	0.01	51.63	0.00	n	1.77	0.75	97.34
KD016	CH89	2	1.73	0.28	0.35	4.10	36.72	0.01	51.63	0.00	n	1.77	0.75	97.34
KD016	CH90	2	1.44	0.36	0.21	3.20	36.76	0.01	52.38	0.00	n	1.86	0.69	96.89
KD016	CH91	2	1.87	0.34	0.11	1.68	38.48	0.01	53.49	0.00	n	2.02	0.82	98.82
KD016	CH92	2	1.68	0.34	0.07	1.27	38.62	0.01	54.22	0.00	n	1.90	0.83	98.94
KD016	CH93	2	1.63	0.33	0.15	2.42	38.52	0.01	52.10	0.00	n	1.93	0.73	97.82
KD016	CH94	2	1.99	0.33	0.22	2.76	37.51	0.01	52.74	0.00	n	1.97	0.74	98.26
KD016	CH95	2	1.42	0.40	0.35	1.49	37.63	0.01	53.18	0.00	n	1.92	0.75	97.14
KD016	CH96	2	1.73	0.40	0.17	2.22	38.24	0.01	53.31	0.00	n	2.05	0.77	98.89
KD016	CH97	2	1.58	0.34	0.47	3.67	36.59	0.01	51.50	0.00	n	1.83	0.84	96.82
KD016	CH98	2	1.66	0.37	0.15	2.01	38.83	0.00	53.87	0.00	n	1.90	0.75	99.54
KD016	CH99	2	1.62	0.38	0.22	3.48	36.73	0.01	51.99	0.00	n	1.77	0.75	96.94
KD016	CH100	2	1.80	0.33	0.20	1.57	38.61	0.01	53.87	0.00	n	1.90	0.68	98.97
KD016	CH106	2	1.97	0.28	0.13	1.38	38.84	0.01	54.04	0.00	n	1.85	0.81	99.30
KD016	CH107	2	1.64	0.33	0.38	3.13	37.24	0.01	51.27	0.00	n	1.88	0.80	96.66
KD016	CH108	2	1.80	0.31	0.16	1.44	38.41	0.00	54.13	0.00	n	1.88	0.75	98.87
KD016	CH109	2	1.57	0.30	0.15	2.10	38.47	0.00	54.01	0.00	n	1.98	0.69	99.26
KD016	CH110	2	1.42	0.32	0.10	1.78	38.13	0.01	54.76	0.00	n	1.72	0.86	99.09
KD016	CH111	2	1.80	0.30	0.47	1.76	38.19	0.01	52.96	0.00	n	1.89	0.75	98.12
KD016	CH112	2	1.67	0.29	0.28	1.96	38.45	0.00	53.22	0.00	n	1.96	0.75	98.58
KD016	CH113	2	1.96	0.34	0.23	1.29	38.62	0.00	54.80	0.00	n	1.85	0.73	99.81
AVE.			1.68	0.33	0.25	2.71	37.74	0.01	52.76	0.00	n	1.86	0.75	98.07
KD016	CH101	3	1.28	0.07	0.00	0.23	42.68	0.00	57.03	0.00	n	1.67	0.24	103.20
KD016	CH102	3	1.53	0.07	0.00	0.24	42.54	0.00	57.40	0.00	n	1.65	0.31	103.73
KD016	CH103	3	1.29	0.03	0.00	0.23	42.41	0.00	57.20	0.00	n	1.62	0.30	103.08
KD016	CH104	3	1.42	0.04	0.00	0.24	42.39	0.01	57.50	0.00	n	1.55	0.22	103.37
KD016	CH105	3	1.54	0.06	0.00	0.23	42.44	0.00	57.36	0.00	n	1.83	0.27	103.71
AVE.			1.41	0.05	0.00	0.23	42.49	0.00	57.30	0.00	n	1.66	0.27	103.42
KD016	CH114	u	1.54	0.33	0.11	0.66	38.89	0.01	55.76	0.04	0.50	1.82	0.85	99.98
KD016	CH115	u	1.75	0.31	0.22	1.26	39.23	0.01	54.71	0.01	0.80	1.96	0.80	100.25
AVE.			1.64	0.32	0.17	0.96	39.06	0.01	55.24	0.02	0.65	1.89	0.83	100.11

Digitised by the Department of Library Services in support of open access to information, University of Pretoria, 2021

APATITE ANALYSES: KD01 SEQUENCE

APPENDIX 1.4

Sample KD019, KD111 and KD134

Code of textural varieties (TYPE): KD019 and KD111 apatite types: u = undifferentiated analysis; KD0134 apatite types: 1 = turquoise CL; 2 = blue CL
Code and sample number (CODE): CH = undifferentiated analysis

SAMPLE	CODE	TYPE	F	Na_2O	MgO	SiO_2	P_2O_5	Cl	CaO	MnO	FeO	SrO	Ce_2O_3	TOTAL
KD019	CH116	u	1.35	0.25	0.25	1.57	40.61	0.01	53.79	0.10	1.18	2.44	0.20	100.46
KD019	CH117	u	1.38	0.26	0.11	1.80	40.19	0.00	53.91	0.05	0.87	2.33	0.15	100.12
KD019	CH118	u	1.50	0.30	0.01	0.00	42.18	0.01	55.68	0.10	0.52	2.16	0.25	102.10
KD019	CH119	u	1.56	0.25	0.04	0.16	41.64	0.00	54.97	0.06	0.48	3.16	0.17	101.93
KD019	CH120	u	1.50	0.30	0.03	0.16	41.66	0.00	55.84	0.06	0.41	2.24	0.20	101.92
KD019	CH121	u	1.63	0.35	0.02	0.35	40.44	0.00	55.38	0.08	0.44	2.67	0.07	100.91
KD019	CH122	u	1.67	0.27	0.00	0.02	40.95	0.01	55.78	0.05	0.30	2.19	0.09	100.98
KD019	CH123	u	1.24	0.31	0.02	0.28	40.80	0.01	55.52	0.03	0.35	2.63	0.17	100.95
KD019	CH124	u	1.47	0.17	0.02	0.00	41.07	0.00	56.55	0.06	0.32	2.74	0.11	102.13
KD019	CH125	u	1.56	0.29	0.03	0.38	41.60	0.00	55.10	0.01	0.31	2.75	0.12	101.84
KD019	CH126	u	1.50	0.25	0.08	0.17	41.35	0.00	56.00	0.05	0.52	1.82	0.12	101.30
KD019	CH127	u	1.66	0.21	0.02	0.40	40.79	0.00	54.49	0.00	0.55	3.19	0.15	100.92
KD019	CH128	u	1.51	0.34	0.05	0.73	40.18	0.00	54.00	0.03	0.83	3.10	0.17	100.08
KD019	CH129	u	1.35	0.49	0.10	0.07	40.31	0.01	54.76	0.09	0.55	2.60	0.30	99.98
KD019	CH130	u	1.46	0.40	0.12	0.11	41.43	0.01	56.03	0.10	0.38	2.02	0.23	101.81
KD019	CH131	u	1.40	0.45	0.06	1.19	39.94	0.00	54.04	0.00	0.34	2.61	0.30	99.97
KD019	CH132	u	1.54	0.61	0.04	0.00	41.03	0.01	54.68	0.00	0.32	2.30	0.32	100.52
AVE.			1.49	0.32	0.06	0.43	40.95	0.00	55.09	0.05	0.51	2.53	0.18	101.05
KD111	CH133	u	1.55	0.41	0.44	1.53	40.06	0.00	50.94	0.00	2.13	2.25	0.45	97.63
KD111	CH134	u	1.57	0.20	0.24	0.12	42.15	0.00	54.12	0.00	0.62	1.69	0.25	100.34
KD111	CH135	u	1.44	0.41	0.04	0.07	41.18	0.00	52.79	0.00	0.42	2.22	0.28	98.43
KD111	CH136	u	1.58	0.38	0.01	0.40	41.70	0.00	54.01	0.00	0.38	2.54	0.28	100.91
KD111	CH137	u	1.69	0.40	0.02	0.05	41.14	0.00	54.74	0.00	0.29	1.22	0.28	99.54
KD111	CH138	u	1.69	0.29	0.22	0.92	40.75	0.01	53.26	0.00	1.28	1.32	0.28	98.74
KD111	CH139	u	1.49	0.33	0.00	0.05	42.91	0.00	54.37	0.00	0.26	1.34	0.15	100.65
KD111	CH140	u	1.73	0.35	0.11	0.38	41.22	0.00	53.93	0.00	0.92	1.54	0.26	99.53
KD111	CH141	u	1.59	0.31	0.09	0.41	40.33	0.00	54.18	0.00	0.77	1.64	0.25	98.80
KD111	CH142	u	1.48	0.28	0.04	0.40	41.41	0.01	55.10	0.00	0.49	1.01	0.13	99.86
AVE.			1.58	0.34	0.12	0.43	41.29	0.00	53.74	0.00	0.76	1.68	0.26	99.44
KD134	CH1	2	2.01	0.05	0.02	0.21	41.06	0.00	54.78	0.04	0.24	1.71	0.00	100.12
KD134	CH2	2	2.82	0.05	0.00	0.31	42.15	0.00	52.10	0.06	0.11	1.80	0.07	99.47
KD134	CH3	2	2.02	0.13	0.00	0.30	41.00	0.00	55.01	0.00	0.96	2.18	0.03	101.63
KD134	CH4	2	2.52	0.08	0.01	0.29	45.10	0.00	51.01	0.04	0.20	2.17	0.13	101.55
KD134	CH5	2	2.23	0.03	0.02	0.22	42.12	0.00	54.67	0.10	0.23	1.40	0.05	101.07
KD134	CH6	2	2.05	0.09	0.00	0.25	42.35	0.00	53.71	0.00	0.13	1.78	0.17	100.53
KD134	CH7	2	2.65	0.10	0.01	0.32	40.12	0.00	54.38	0.11	1.28	2.21	0.13	101.31
KD134	CH8	2	2.38	0.09	0.02	0.36	41.98	0.00	50.99	0.12	0.19	2.88	0.10	99.11
KD134	CH9	2	2.64	0.10	0.00	0.24	41.20	0.00	52.10	0.06	1.66	2.33	0.10	100.43
KD134	CH10	2	2.49	0.06	0.00	0.58	40.21	0.00	53.65	0.10	0.12	2.16	0.08	99.45
KD134	CH11	2	1.81	0.14	0.00	0.16	39.86	0.00	56.62	0.09	0.82	2.32	0.09	101.91
KD134	CH12	2	2.69	0.06	0.01	0.35	41.58	0.00	52.26	0.13	0.95	2.33	0.00	100.36
KD134	CH13	2	2.77	0.06	0.02	0.38	42.87	0.00	52.70	0.07	0.09	2.01	0.08	101.05
KD134	CH17	2	2.66	0.11	0.00	0.78	41.98	0.00	54.66	0.07	0.13	1.20	0.11	101.70
AVE.			2.41	0.08	0.01	0.34	41.68	0.00	53.47	0.07	0.51	2.03	0.08	100.69
KD134	CH14	1	2.19	0.11	0.00	0.15	42.01	0.00	53.09	0.00	0.00	2.62	0.40	100.57
KD134	CH15	1	1.89	0.05	0.00	0.25	41.56	0.00	53.12	0.05	0.01	1.83	0.32	99.08
KD134	CH16	1	2.26	0.22	0.00	0.22	41.20	0.00	52.75	0.03	0.00	1.76	0.45	98.89
KD134	CH18	1	2.08	0.15	0.01	0.17	41.01	0.00	56.38	0.05	0.11	1.39	0.27	101.62
KD134	CH19	1	2.84	0.13	0.00	0.69	40.68	0.00	56.36	0.06	0.17	2.49	0.28	100.70
KD134	CH20	1	2.70	0.11	0.00	0.32	40.37	0.00	53.24	0.03	0.10	2.06	0.25	99.18
KD134	CH21	1	2.34	0.11	0.00	0.24	39.58	0.00	54.94	0.00	0.04	1.74	0.29	99.28
KD134	CH22	1	2.44	0.14	0.00	0.22	41.29	0.00	53.47	0.04	0.10	1.80	0.26	99.76
AVE.			2.34	0.13	0.00	0.28	40.96	0.00	54.17	0.03	0.07	1.96	0.32	99.89

Digitised by the Department of Library Services in support of open access to information, University of Pretoria, 2021

FLUORITE ANALYSIS: KD01 SEQUENCE

Sample KD111

CODE: CF = sample number

APPENDIX 1.5

SAMPLE	NUM	Na	F	Mg	Si	Cl	Ca	Ti	Mn	Fe	Sr	Y	Ce	TOTAL
KD111	CF1	0.00	49.89	0.02	0.00	0.03	53.05	0.00	0.05	0.03	0.04	0.02	0.09	103.21
KD111	CF2	0.00	49.64	0.01	0.00	0.02	53.35	0.00	0.05	0.15	0.11	0.00	0.04	103.36
KD111	CF3	0.00	49.66	0.00	0.00	0.03	51.59	0.00	0.08	0.16	0.97	0.05	0.00	102.54
KD111	CF4	0.00	49.68	0.01	0.00	0.01	53.16	0.00	0.11	0.20	0.03	0.00	0.00	103.20
KD111	CF5	0.00	48.37	0.00	0.00	0.01	52.88	0.00	0.06	0.14	0.91	0.01	0.11	102.47
KD111	CF6	0.00	47.00	0.00	0.00	0.00	55.47	0.00	0.04	0.17	0.04	0.01	0.06	102.79
KD111	CF7	0.00	49.80	0.01	0.00	0.01	53.14	0.00	0.05	0.11	0.03	0.02	0.06	103.24
KD111	CF8	0.00	49.51	0.00	0.00	0.02	50.82	0.00	0.02	0.20	1.30	0.07	0.00	101.93
KD111	CF9	0.00	49.87	0.00	0.00	0.01	53.09	0.00	0.00	0.08	0.13	0.00	0.04	103.23
KD111	CF10	0.00	49.12	0.04	0.00	0.03	50.97	0.00	0.02	0.53	0.73	0.07	0.05	101.57
KD111	CF11	0.00	49.62	0.01	0.00	0.03	52.57	0.00	0.00	0.15	0.18	0.05	0.02	102.65
KD111	CF12	0.00	49.84	0.00	0.00	0.00	52.82	0.00	0.03	0.10	0.13	0.04	0.07	103.03
KD111	CF13	0.00	47.55	0.01	0.00	0.00	54.51	0.00	0.04	0.12	0.15	0.07	0.06	102.49
KD111	CF14	0.00	49.96	0.00	0.00	0.01	53.22	0.00	0.02	0.07	0.08	0.00	0.04	103.38
KD111	CF15	0.00	49.91	0.01	0.00	0.00	52.24	0.00	0.01	0.03	0.28	0.07	0.00	102.55
KD111	CF16	0.00	49.72	0.00	0.00	0.01	52.23	0.00	0.01	0.02	0.56	0.01	0.07	102.62
KD111	CF17	0.00	47.52	0.04	0.00	0.02	51.46	0.00	0.00	0.09	0.30	0.06	0.03	99.50
KD111	CF18	0.00	49.51	0.00	0.00	0.01	51.79	0.00	0.02	0.07	0.37	0.05	0.00	101.81
KD111	CF19	0.00	49.55	0.00	0.00	0.00	52.35	0.00	0.01	0.05	0.25	0.00	0.08	102.29
KD111	CF20	0.00	49.38	0.01	0.00	0.12	51.02	0.00	0.01	0.04	1.27	0.00	0.06	101.92
KD111	CF21	0.00	49.66	0.00	0.00	0.00	52.93	0.00	0.02	0.04	0.08	0.00	0.06	102.79
KD111	CF22	0.00	49.63	0.01	0.00	0.01	52.57	0.00	0.02	0.02	0.15	0.01	0.06	102.47
KD111	CF23	0.00	49.41	0.02	0.00	0.00	51.88	0.00	0.04	0.23	0.30	0.02	0.03	101.91
KD111	CF24	0.00	49.60	0.02	0.00	0.00	52.61	0.00	0.02	0.03	0.05	0.01	0.04	102.37
KD111	CF25	0.00	49.68	0.14	0.00	0.00	52.88	0.00	0.03	0.11	0.07	0.00	0.04	102.95
KD111	CF26	0.00	49.82	0.00	0.00	0.00	52.94	0.00	0.07	0.13	0.04	0.00	0.03	103.03
KD111	CF27	0.00	49.83	0.00	0.00	0.01	52.90	0.00	0.05	0.08	0.04	0.00	0.06	102.96
KD111	CF28	0.00	49.05	0.02	0.00	0.00	52.82	0.00	0.09	0.31	0.03	0.00	0.06	102.38
KD111	CF29	0.00	49.87	0.00	0.00	0.01	52.96	0.00	0.06	0.06	0.08	0.00	0.06	103.10
KD111	CF30	0.00	49.69	0.00	0.00	0.01	52.39	0.00	0.00	0.02	0.60	0.03	0.08	102.81
KD111	CF31	0.00	49.87	0.00	0.00	0.01	52.95	0.00	0.01	0.07	0.06	0.00	0.07	103.03
KD111	CF32	0.00	49.93	0.00	0.00	0.02	52.60	0.00	0.05	0.08	0.04	0.00	0.02	102.74
KD111	CF33	0.00	49.28	0.01	0.00	0.12	51.73	0.00	0.00	0.04	0.21	0.05	0.00	101.42
KD111	CF34	0.00	49.72	0.00	0.00	0.00	52.04	0.00	0.04	0.06	0.40	0.07	0.07	102.41
KD111	CF35	0.00	49.79	0.00	0.00	0.01	52.84	0.00	0.09	0.16	0.06	0.00	0.04	102.99
KD111	CF36	0.00	49.95	0.00	0.00	0.01	52.00	0.00	0.01	0.00	0.75	0.05	0.02	102.80
KD111	CF37	0.00	49.32	0.01	0.00	0.00	52.38	0.00	0.02	0.09	0.15	0.06	0.10	102.12
KD111	CF38	0.00	49.21	0.00	0.00	0.02	52.33	0.00	0.01	0.06	0.26	0.04	0.05	101.98
KD111	CF39	0.00	49.68	0.00	0.00	0.00	52.56	0.00	0.01	0.06	0.12	0.03	0.02	102.48
KD111	CF40	0.00	49.73	0.02	0.00	0.01	52.65	0.00	0.05	0.09	0.11	0.04	0.03	102.71
KD111	CF41	0.00	49.64	0.00	0.00	0.00	52.64	0.00	0.05	0.08	0.06	0.00	0.00	102.47
KD111	CF42	0.00	49.52	0.00	0.00	0.00	51.10	0.00	0.04	0.02	1.06	0.11	0.05	101.91
KD111	CF43	0.00	49.82	0.02	0.00	0.01	52.44	0.00	0.00	0.03	0.22	0.09	0.01	102.63
KD111	CF44	0.00	49.82	0.00	0.00	0.00	51.18	0.00	0.00	0.00	0.84	0.09	0.05	101.98
KD111	CF45	0.00	50.00	0.00	0.00	0.01	53.07	0.00	0.02	0.06	0.11	0.00	0.00	103.28
KD111	CF46	0.00	49.32	0.02	0.00	0.00	50.07	0.00	0.01	0.21	1.25	0.00	0.02	100.89
KD111	CF47	0.00	49.74	0.00	0.00	0.03	50.71	0.00	0.00	0.00	1.33	0.06	0.02	101.89
KD111	CF48	0.00	49.87	0.00	0.00	0.00	53.10	0.00	0.04	0.05	0.04	0.00	0.02	103.11
KD111	CF49	0.00	49.81	0.00	0.00	0.00	51.75	0.00	0.00	0.04	0.66	0.06	0.00	102.32
KD111	CF50	0.00	49.08	0.01	0.00	0.01	52.44	0.00	0.00	0.08	0.16	0.02	0.00	101.79
KD111	CF51	0.00	49.75	0.00	0.00	0.00	53.32	0.00	0.00	0.00	0.04	0.00	0.03	103.14
KD111	CF52	0.00	49.79	0.00	0.00	0.03	52.90	0.00	0.03	0.06	0.07	0.04	0.01	102.93
KD111	CF53	0.00	49.79	0.01	0.00	0.03	53.01	0.00	0.09	0.13	0.07	0.03	0.01	103.16
KD111	CF54	0.00	49.67	0.01	0.00	0.02	51.99	0.00	0.03	0.15	0.63	0.05	0.05	102.59
KD111	CF55	0.00	49.68	0.00	0.00	0.02	52.28	0.00	0.01	0.05	0.35	0.00	0.04	102.44
KD111	CF56	0.00	49.72	0.02	0.00	0.01	53.05	0.00	0.02	0.05	0.20	0.07	0.02	103.15
KD111	CF57	0.00	49.86	0.00	0.00	0.00	52.47	0.00	0.01	0.05	0.46	0.04	0.04	102.95
KD111	CF58	0.00	49.62	0.02	0.00	0.00	52.82	0.00	0.06	0.07	0.10	0.00	0.00	102.69
KD111	CF59	0.00	49.79	0.00	0.00	0.00	52.92	0.00	0.01	0.04	0.12	0.04	0.02	102.93
KD111	CF60	0.00	49.62	0.00	0.00	0.01	52.67	0.00	0.00	0.00	0.30	0.00	0.03	102.62

Digitised by the Department of Library Services in support of open access to information, University of Pretoria, 2021

FLUORITE ANALYSIS: KD01 SEQUENCE

Sample KD111 (continued)

CODE: CF = sample number

APPENDIX 1.5

SAMPLE	NUM	Na	F	Mg	Si	Cl	Ca	Ti	Mn	Fe	Sr	Y	Ce	TOTAL
KD111	CF65	0.00	49.64	0.00	0.00	0.00	53.12	0.00	0.07	0.08	0.01	0.00	0.03	102.95
KD111	CF66	0.00	49.48	0.00	0.00	0.05	52.89	0.00	0.00	0.01	0.11	0.00	0.02	102.56
KD111	CF67	0.00	49.91	0.01	0.00	0.02	53.25	0.00	0.00	0.06	0.06	0.00	0.00	103.32
KD111	CF68	0.00	49.97	0.00	0.00	0.02	53.20	0.00	0.02	0.07	0.16	0.01	0.03	103.49
KD111	CF69	0.00	49.77	0.02	0.00	0.02	52.04	0.00	0.03	0.11	0.56	0.03	0.06	102.64
KD111	CF70	0.00	49.52	0.00	0.00	0.00	52.38	0.00	0.05	0.15	0.09	0.01	0.00	102.19
KD111	CF71	0.00	49.76	0.00	0.00	0.00	53.13	0.00	0.04	0.17	0.06	0.00	0.00	103.15
KD111	CF72	0.00	49.63	0.01	0.00	0.01	53.03	0.00	0.02	0.08	0.09	0.02	0.07	102.94
KD111	CF73	0.00	49.79	0.01	0.00	0.04	53.39	0.00	0.06	0.03	0.09	0.11	0.04	103.55
KD111	CF74	0.00	49.83	0.01	0.00	0.00	52.38	0.00	0.03	0.04	0.17	0.05	0.01	102.52
KD111	CF75	0.00	49.53	0.01	0.00	0.02	52.43	0.00	0.00	0.10	0.25	0.09	0.07	102.49
KD111	CF76	0.00	49.67	0.00	0.00	0.00	52.38	0.00	0.02	0.08	0.28	0.07	0.00	102.50
KD111	CF77	0.00	49.46	0.00	0.00	0.00	53.14	0.00	0.06	0.08	0.22	0.02	0.03	103.00
KD111	CF78	0.00	48.08	0.02	0.00	0.02	51.23	0.00	0.03	0.51	0.13	0.07	0.06	100.16
KD111	CF79	0.00	49.68	0.00	0.00	0.02	53.07	0.00	0.03	0.01	0.08	0.00	0.02	102.90
KD111	CF80	0.00	49.76	0.01	0.00	0.01	53.34	0.00	0.00	0.03	0.03	0.00	0.03	103.22
KD111	CF81	0.00	49.60	0.00	0.00	0.03	51.56	0.00	0.00	0.06	0.86	0.02	0.04	102.18
KD111	CF82	0.00	49.78	0.02	0.00	0.03	53.18	0.00	0.00	0.02	0.04	0.02	0.00	103.09
KD111	CF83	0.00	49.53	0.00	0.00	0.03	52.28	0.00	0.05	0.08	0.46	0.09	0.07	102.59
KD111	CF84	0.00	49.66	0.00	0.00	0.02	53.15	0.00	0.00	0.04	0.05	0.00	0.06	102.99
KD111	CF85	0.00	49.57	0.01	0.00	0.00	52.34	0.00	0.08	0.16	0.20	0.03	0.00	102.38
KD111	CF86	0.00	49.25	0.02	0.00	0.02	51.54	0.00	0.15	0.29	0.66	0.10	0.03	102.06
KD111	CF87	0.00	49.47	0.00	0.00	0.00	52.79	0.00	0.03	0.13	0.13	0.00	0.07	102.62
KD111	CF88	0.00	49.45	0.01	0.00	0.00	52.91	0.00	0.10	0.19	0.10	0.00	0.00	102.77
KD111	CF89	0.00	49.56	0.02	0.00	0.00	52.69	0.00	0.01	0.12	0.23	0.00	0.09	102.71
KD111	CF90	0.00	49.28	0.00	0.00	0.04	51.09	0.00	0.05	0.15	1.01	0.09	0.01	101.71
KD111	CF91	0.00	49.65	0.01	0.00	0.01	51.10	0.00	0.06	0.00	1.45	0.00	0.01	102.28
KD111	CF92	0.00	49.61	0.00	0.00	0.01	51.23	0.00	0.00	0.01	0.97	0.04	0.00	101.87
KD111	CF93	0.00	49.80	0.01	0.00	0.02	51.72	0.00	0.00	0.08	0.91	0.03	0.00	102.58
KD111	CF94	0.00	50.01	0.01	0.00	0.00	52.43	0.00	0.00	0.01	0.22	0.01	0.00	102.69
KD111	CF95	0.00	49.73	0.00	0.00	0.00	52.77	0.00	0.00	0.06	0.14	0.03	0.00	102.73
KD111	CF96	0.00	49.25	0.00	0.00	0.00	52.23	0.00	0.02	0.07	0.27	0.00	0.00	101.84
KD111	CF97	0.00	49.76	0.00	0.00	0.00	53.24	0.00	0.02	0.05	0.05	0.00	0.00	103.11
KD111	CF98	0.00	49.92	0.00	0.00	0.00	53.18	0.00	0.00	0.00	0.05	0.02	0.03	103.19
KD111	CF99	0.00	49.90	0.01	0.00	0.00	52.88	0.00	0.02	0.00	0.11	0.01	0.06	103.00
KD111	CF100	0.00	49.54	0.01	0.00	0.00	51.11	0.00	0.00	0.01	1.04	0.05	0.04	101.80
KD111	CF101	0.00	49.82	0.01	0.00	0.00	51.79	0.00	0.07	0.02	0.79	0.06	0.07	102.62
KD111	CF102	0.00	49.72	0.01	0.00	0.00	51.85	0.00	0.04	0.04	0.72	0.01	0.00	102.39
KD111	CF103	0.00	49.59	0.00	0.00	0.00	51.09	0.00	0.01	0.00	1.00	0.10	0.00	101.78
KD111	CF104	0.00	49.84	0.00	0.00	0.02	53.47	0.00	0.02	0.03	0.05	0.00	0.07	103.49
KD111	CF105	0.00	49.75	0.00	0.00	0.03	53.24	0.00	0.02	0.02	0.17	0.02	0.07	103.32
KD111	CF106	0.00	49.91	0.00	0.00	0.02	52.97	0.00	0.00	0.00	0.06	0.00	0.03	102.98
KD111	CF107	0.00	49.69	0.00	0.00	0.01	52.79	0.00	0.02	0.06	0.18	0.00	0.03	102.77
KD111	CF108	0.00	49.30	0.12	0.00	0.00	51.91	0.00	0.18	0.25	0.05	0.04	0.00	101.85
KD111	CF109	0.00	48.78	0.00	0.00	0.02	52.16	0.00	0.01	0.24	0.18	0.10	0.03	101.53
KD111	CF110	0.00	49.73	0.00	0.00	0.00	52.14	0.00	0.04	0.08	0.56	0.03	0.00	102.59
KD111	CF111	0.00	48.39	0.02	0.00	0.03	51.62	0.00	0.05	0.17	0.04	0.00	0.04	100.37
KD111	CF112	0.00	49.63	0.00	0.00	0.01	52.28	0.00	0.11	0.22	0.41	0.07	0.03	102.75
KD111	CF113	0.00	49.55	0.00	0.00	0.04	52.84	0.00	0.03	0.22	0.15	0.03	0.07	102.91
KD111	CF114	0.00	49.45	0.01	0.00	0.03	52.76	0.00	0.08	0.20	0.09	0.00	0.02	102.64
KD111	CF115	0.00	49.47	0.00	0.00	0.01	52.22	0.00	0.08	0.17	0.44	0.02	0.08	102.48
KD111	CF116	0.00	49.69	0.03	0.00	0.02	52.70	0.00	0.06	0.15	0.14	0.00	0.00	102.79
KD111	CF117	0.00	50.00	0.01	0.00	0.00	52.52	0.00	0.06	0.06	0.23	0.04	0.02	102.95
KD111	CF118	0.00	49.81	0.00	0.00	0.02	53.09	0.00	0.05	0.02	0.11	0.00	0.04	103.15
KD111	CF119	0.00	49.75	0.00	0.00	0.00	52.80	0.00	0.00	0.12	0.08	0.00	0.00	102.75
KD111	CF120	0.00	49.68	0.00	0.00	0.02	52.95	0.00	0.01	0.08	0.13	0.02	0.05	102.94
KD111	CF121	0.00	49.52	0.01	0.00	0.01	52.62	0.00	0.07	0.17	0.10	0.02	0.06	102.56
KD111	CF122	0.00	49.64	0.01	0.00	0.00	51.63	0.00	0.05	0.05	0.77	0.03	0.02	102.18
KD111	CF123	0.00	49.38	0.02	0.00	0.00	52.12	0.00	0.00	0.06	0.16	0.06	0.01	101.80
KD111	CF124	0.00	49.71	0.00	0.00	0.02	52.29	0.00	0.01	0.09	0.20	0.10	0.01	102.43

Digitised by the Department of Library Services in support of open access to information, University of Pretoria, 2021

FLUORITE ANALYSIS: KD01 SEQUENCE

Samples KD111 (continued) and KD121

CODE: CF = sample number

APPENDIX 1.5

SAMPLE	NUM	Na	F	Mg	Si	Cl	Ca	Ti	Mn	Fe	Sr	Y	Ce	TOTAL
KD111	CF125	0.00	49.64	0.00	0.00	0.04	52.53	0.00	0.07	0.13	0.23	0.04	0.06	102.74
KD111	CF126	0.00	49.74	0.00	0.00	0.01	52.10	0.00	0.00	0.05	0.23	0.08	0.04	102.25
KD111	CF127	0.00	49.64	0.00	0.00	0.00	52.91	0.00	0.05	0.09	0.16	0.00	0.00	102.86
KD111	CF128	0.00	49.60	0.00	0.00	0.01	52.47	0.00	0.03	0.04	0.17	0.00	0.04	102.36
KD111	CF129	0.00	49.83	0.00	0.00	0.02	53.36	0.00	0.00	0.06	0.07	0.00	0.04	103.36
KD111	CF130	0.00	49.81	0.01	0.00	0.03	53.18	0.00	0.01	0.08	0.05	0.00	0.01	103.17
KD111	CF131	0.00	49.68	0.01	0.00	0.00	52.73	0.00	0.04	0.03	0.09	0.01	0.04	102.62
KD111	CF132	0.00	49.34	0.01	0.00	0.02	52.14	0.00	0.02	0.16	0.27	0.00	0.01	101.95
KD111	CF133	0.00	49.66	0.03	0.00	0.02	52.71	0.00	0.05	0.04	0.10	0.02	0.00	102.63
KD111	CF134	0.00	49.63	0.00	0.00	0.00	52.33	0.00	0.00	0.12	0.43	0.03	0.04	102.57
KD111	CF135	0.00	46.98	0.00	0.00	0.00	50.55	0.00	0.00	0.15	0.38	0.12	0.11	98.29
KD111	CF136	0.00	49.57	0.00	0.00	0.00	52.62	0.00	0.01	0.11	0.10	0.02	0.02	102.45
KD111	CF137	0.00	49.24	0.02	0.00	0.01	52.06	0.00	0.05	0.08	0.25	0.00	0.01	101.71
KD111	CF138	0.00	49.03	0.01	0.00	0.00	50.60	0.00	0.03	0.16	1.47	0.01	0.00	101.31
KD111	CF139	0.00	49.54	0.00	0.00	0.02	52.58	0.00	0.02	0.07	0.40	0.01	0.07	102.71
KD111	CF140	0.00	49.62	0.01	0.00	0.03	51.83	0.00	0.00	0.09	0.70	0.03	0.00	102.31
KD111	CF141	0.00	49.04	0.01	0.00	0.01	51.01	0.00	0.05	0.20	1.15	0.03	0.02	101.52
KD111	CF142	0.00	49.61	0.00	0.00	0.00	52.82	0.00	0.03	0.14	0.05	0.00	0.00	102.65
KD111	CF143	0.00	49.66	0.00	0.00	0.01	52.52	0.00	0.05	0.05	0.29	0.00	0.00	102.59
KD111	CF144	0.00	49.44	0.00	0.00	0.01	50.58	0.00	0.00	0.02	1.31	0.07	0.00	101.43
KD111	CF145	0.00	49.36	0.01	0.00	0.00	52.65	0.00	0.04	0.09	0.00	0.00	0.04	102.20
KD111	CF146	0.00	49.72	0.00	0.00	0.03	52.25	0.00	0.05	0.04	0.25	0.05	0.00	102.40
KD111	CF147	0.00	49.72	0.02	0.00	0.01	52.84	0.00	0.04	0.13	0.20	0.00	0.02	102.98
KD111	CF148	0.00	49.34	0.00	0.00	0.00	52.75	0.00	0.06	0.13	0.11	0.02	0.06	102.48
KD111	CF149	0.00	49.80	0.01	0.00	0.00	52.90	0.00	0.09	0.10	0.11	0.00	0.02	103.02
KD111	CF150	0.00	49.81	0.01	0.00	0.00	52.59	0.00	0.00	0.10	0.17	0.00	0.00	102.69
KD111	CF151	0.00	49.65	0.00	0.00	0.03	52.95	0.00	0.03	0.06	0.03	0.00	0.00	102.75
KD111	CF152	0.00	49.55	0.01	0.00	0.02	51.96	0.00	0.00	0.04	0.20	0.10	0.05	101.92
KD111	CF153	0.00	46.93	0.35	0.00	0.00	49.09	0.00	0.04	1.59	0.17	0.00	0.00	98.17
KD111	CF154	0.00	49.71	0.00	0.00	0.02	53.13	0.00	0.00	0.22	0.05	0.00	0.05	103.16
KD111	CF155	0.00	49.69	0.00	0.00	0.00	52.64	0.00	0.10	0.10	0.13	0.06	0.06	102.78
KD111	CF156	0.00	49.66	0.00	0.00	0.01	52.83	0.00	0.00	0.10	0.27	0.00	0.01	102.88
KD111	CF157	0.00	49.76	0.00	0.00	0.02	52.67	0.00	0.03	0.02	0.26	0.02	0.05	102.83
KD111	CF158	0.00	49.32	0.02	0.00	0.02	53.14	0.00	0.02	0.02	0.09	0.03	0.04	102.70
KD111	CF159	0.00	49.60	0.00	0.00	0.00	52.46	0.00	0.01	0.02	0.25	0.04	0.07	102.44
KD111	CF160	0.00	49.70	0.00	0.00	0.02	52.53	0.00	0.00	0.13	0.27	0.01	0.01	102.67
KD111	CF161	0.00	49.58	0.00	0.00	0.02	52.59	0.00	0.04	0.06	0.14	0.06	0.01	102.49
KD111	CF162	0.00	49.83	0.00	0.00	0.04	53.05	0.00	0.05	0.02	0.12	0.01	0.00	103.12
KD111	CF163	0.00	49.79	0.01	0.00	0.01	53.13	0.00	0.05	0.01	0.03	0.00	0.05	103.06
KD111	CF164	0.00	49.91	0.00	0.00	0.02	51.70	0.00	0.01	0.00	0.81	0.00	0.10	102.55
KD111	CF165	0.00	49.65	0.00	0.00	0.01	52.35	0.00	0.02	0.00	0.42	0.00	0.02	102.48
KD111	CF166	0.00	49.44	0.00	0.00	0.01	52.90	0.00	0.00	0.15	0.05	0.00	0.02	102.56
KD111	CF167	0.00	48.17	0.00	0.00	0.00	50.92	0.00	0.08	0.23	0.73	0.21	0.08	100.42
KD111	CF168	0.00	48.57	0.08	0.00	0.03	50.08	0.00	0.01	0.52	0.98	0.10	0.00	100.37
KD111	CF169	0.00	49.47	0.00	0.00	0.03	52.91	0.00	0.00	0.13	0.06	0.00	0.07	102.67
KD111	CF170	0.00	49.71	0.00	0.00	0.01	52.36	0.00	0.06	0.13	0.32	0.03	0.01	102.62
AVE.		0.00	49.52	0.01	0.00	0.01	52.42	0.00	0.03	0.10	0.31	0.03	0.03	102.47
KD121	CF172	0.05	48.97	0.00	0.01	0.01	52.38	0.00	0.00	0.26	0.28	0.00	0.05	102.01
KD121	CF173	0.02	49.10	0.02	0.02	0.02	53.02	0.00	0.00	0.20	0.29	0.00	0.07	102.74
KD121	CF174	0.04	49.03	0.01	0.00	0.00	53.68	0.03	0.00	0.11	0.00	0.00	0.02	102.91
KD121	CF175	0.04	49.03	0.00	0.01	0.02	53.28	0.01	0.00	0.11	0.30	0.00	0.01	102.81
KD121	CF176	0.00	49.11	0.00	0.02	0.00	53.56	0.00	0.00	0.00	0.08	0.00	0.02	102.80
KD121	CF177	0.06	48.80	0.00	0.06	0.02	53.62	0.01	0.00	0.14	0.00	0.00	0.00	102.71
KD121	CF178	0.00	49.01	0.00	0.03	0.02	53.95	0.02	0.00	0.04	0.10	0.00	0.00	103.17
KD121	CF179	0.07	48.98	0.01	0.07	0.02	53.28	0.02	0.00	0.44	0.29	0.00	0.00	103.18
KD121	CF181	0.08	48.88	0.02	0.07	0.01	52.78	0.00	0.00	0.32	0.14	0.00	0.00	102.28
KD121	CF182	0.04	48.85	0.02	0.03	0.00	52.44	0.01	0.00	0.16	0.62	0.00	0.04	102.22
KD121	CF183	0.05	49.12	0.00	0.01	0.01	52.95	0.00	0.00	0.14	0.27	0.00	0.09	102.65
KD121	CF185	0.01	48.71	0.04	0.12	0.02	53.13	0.03	0.00	0.27	0.04	0.00	0.00	102.35
KD121	CF184	0.07	48.39	0.01	0.12	0.01	52.45	0.17	0.00	0.34	0.36	0.00	0.04	101.97

Digitised by the Department of Library Services in support of open access to information, University of Pretoria, 2021

FLUORITE ANALYSIS: KD01 SEQUENCE

Samples KD121 (continued)

CODE: CF = sample number

APPENDIX 1.5

SAMPLE	NUM	Na	F	Mg	Si	Cl	Ca	Ti	Mn	Fe	Sr	Y	Ce	TOTAL
KD121	CF191	0.05	48.92	0.00	0.03	0.02	53.20	0.01	0.00	0.03	0.52	0.00	0.14	102.91
KD121	CF192	0.06	48.72	0.00	0.00	0.00	52.54	0.00	0.00	0.13	0.83	0.00	0.02	102.31
KD121	CF193	0.05	47.83	0.09	0.06	0.01	51.77	0.00	0.00	0.84	0.38	0.00	0.01	101.03
KD121	CF194	0.08	48.51	0.00	0.05	0.01	52.26	0.02	0.00	0.17	1.06	0.00	0.07	102.23
KD121	CF195	0.05	48.85	0.01	0.04	0.03	53.23	0.04	0.00	0.04	0.43	0.00	0.05	102.75
KD121	CF196	0.14	48.57	0.01	0.02	0.00	51.97	0.00	0.00	0.15	1.14	0.00	0.00	102.00
KD121	CF197	0.02	48.76	0.00	0.01	0.03	53.24	0.00	0.00	0.09	0.09	0.00	0.00	102.24
KD121	CF198	0.03	48.98	0.00	0.03	0.00	52.90	0.02	0.00	0.10	0.11	0.00	0.08	102.25
KD121	CF199	0.02	49.14	0.01	0.00	0.03	53.98	0.01	0.00	0.06	0.00	0.00	0.07	103.31
KD121	CF200	0.04	48.86	0.03	0.05	0.00	53.31	0.05	0.00	0.14	0.30	0.00	0.10	102.89
KD121	CF201	0.04	48.73	0.00	0.01	0.02	53.17	0.00	0.00	0.11	0.26	0.00	0.01	102.34
KD121	CF202	0.08	48.65	0.00	0.03	0.00	52.57	0.00	0.00	0.13	1.04	0.00	0.04	102.55
KD121	CF203	0.07	48.23	0.00	0.02	0.11	51.59	0.82	0.00	0.08	0.94	0.00	0.02	101.87
KD121	CF204	0.16	48.19	0.00	0.26	0.00	52.80	0.05	0.00	0.45	0.30	0.00	0.02	102.23
KD121	CF205	0.00	49.02	0.00	0.06	0.00	53.34	0.00	0.00	0.08	0.06	0.00	0.03	102.59
KD121	CF206	0.05	48.54	0.02	0.01	0.03	52.72	0.02	0.00	0.25	0.29	0.00	0.00	101.91
KD121	CF207	0.04	48.08	0.08	0.11	0.03	51.81	0.02	0.00	0.90	0.32	0.00	0.05	101.42
KD121	CF208	0.00	48.80	0.00	0.02	0.01	52.50	0.02	0.00	0.40	0.12	0.00	0.03	101.91
KD121	CF209	0.08	48.34	0.03	0.07	0.01	52.69	0.01	0.00	0.54	0.40	0.00	0.09	102.25
KD121	CF210	0.03	48.98	0.00	0.02	0.04	53.17	0.00	0.00	0.20	0.16	0.00	0.06	102.65
KD121	CF211	0.19	48.72	0.00	0.15	0.01	52.05	0.00	0.00	0.21	0.91	0.00	0.00	102.24
KD121	CF212	0.10	48.93	0.00	0.13	0.02	52.71	0.00	0.00	0.12	0.67	0.00	0.02	102.71
KD121	CF213	0.03	48.84	0.00	0.03	0.03	52.46	0.01	0.00	0.14	0.30	0.00	0.00	101.84
KD121	CF214	0.00	48.26	0.07	0.02	0.02	52.03	0.01	0.00	0.88	0.31	0.00	0.07	101.68
KD121	CF215	0.05	48.65	0.01	0.01	0.00	53.05	0.01	0.00	0.23	0.25	0.00	0.10	102.35
KD121	CF216	0.07	48.39	0.02	0.01	0.05	52.33	0.01	0.00	0.44	0.51	0.00	0.13	101.95
KD121	CF217	0.02	48.87	0.01	0.02	0.03	52.66	0.01	0.00	0.17	0.40	0.00	0.07	102.24
KD121	CF218	0.20	47.53	0.01	0.33	0.01	51.57	0.08	0.00	0.89	0.25	0.00	0.07	100.93
KD121	CF219	0.03	48.67	0.00	0.05	0.03	52.38	0.00	0.00	0.18	0.29	0.00	0.01	101.64
KD121	CF220	0.06	48.38	0.03	0.02	0.06	52.41	0.02	0.00	0.49	0.34	0.00	0.00	101.80
KD121	CF221	0.05	48.78	0.00	0.02	0.03	53.24	0.00	0.00	0.28	0.26	0.00	0.06	102.72
KD121	CF222	0.04	48.51	0.02	0.08	0.02	53.08	0.02	0.00	0.43	0.18	0.00	0.04	102.41
KD121	CF223	0.06	48.70	0.01	0.02	0.03	52.47	0.00	0.00	0.22	0.31	0.00	0.04	101.86
KD121	CF224	0.07	48.83	0.03	0.08	0.00	52.72	0.18	0.00	0.34	0.53	0.00	0.07	102.84
KD121	CF225	0.15	48.53	0.02	0.28	0.03	52.72	0.01	0.00	0.29	0.25	0.00	0.04	102.31
KD121	CF226	0.04	48.26	0.10	0.02	0.02	52.58	0.01	0.00	0.82	0.29	0.00	0.06	102.18
KD121	CF227	0.10	48.55	0.00	0.33	0.00	51.80	0.16	0.00	0.29	0.32	0.00	0.00	101.56
KD121	CF228	0.01	49.08	0.01	0.08	0.01	53.92	0.03	0.00	0.06	0.00	0.00	0.09	103.29
KD121	CF229	0.11	48.57	0.01	0.09	0.01	51.59	0.05	0.00	0.14	0.84	0.00	0.08	101.48
KD121	CF230	0.04	49.39	0.00	0.05	0.00	53.61	0.01	0.00	0.04	0.01	0.00	0.02	103.17
KD121	CF231	0.00	49.16	0.01	0.08	0.01	53.36	0.07	0.00	0.10	0.07	0.00	0.01	102.86
KD121	CF232	0.02	49.12	0.00	0.01	0.00	53.94	0.00	0.00	0.06	0.14	0.00	0.02	103.30
KD121	CF233	0.04	49.00	0.00	0.10	0.02	53.17	0.01	0.00	0.16	0.49	0.00	0.02	103.01
KD121	CF234	0.00	48.26	0.01	0.14	0.02	53.03	0.00	0.00	0.29	0.14	0.00	0.00	101.88
KD121	CF235	0.02	48.44	0.00	0.02	0.00	53.21	0.00	0.00	0.19	0.33	0.00	0.01	102.21
KD121	CF236	0.00	48.61	0.02	0.05	0.00	53.11	0.00	0.00	0.39	0.04	0.00	0.00	102.21
KD121	CF237	0.02	48.25	0.01	0.01	0.02	52.81	0.03	0.00	0.48	0.17	0.00	0.02	101.81
KD121	CF238	0.02	48.55	0.02	0.09	0.00	52.82	0.00	0.00	0.43	0.00	0.00	0.01	101.93
KD121	CF239	0.04	47.57	0.08	0.12	0.03	52.04	0.01	0.00	0.52	0.40	0.00	0.02	100.81
KD121	CF240	0.00	47.29	0.14	0.11	0.01	52.06	0.02	0.00	0.89	0.16	0.00	0.06	100.74
KD121	CF241	0.04	47.96	0.11	0.07	0.01	52.29	0.04	0.00	0.63	0.05	0.00	0.01	101.21
KD121	CF243	0.01	48.21	0.04	0.05	0.01	53.02	0.02	0.00	0.26	0.14	0.00	0.05	101.81
KD121	CF244	0.03	48.04	0.04	0.12	0.00	52.87	0.03	0.00	0.26	0.30	0.00	0.04	101.73
KD121	CF245	0.05	48.37	0.00	0.08	0.04	53.47	0.01	0.00	0.38	0.09	0.00	0.00	102.48
KD121	CF246	0.05	48.43	0.01	0.02	0.00	53.12	0.00	0.00	0.25	0.08	0.00	0.01	101.96
KD121	CF247	0.03	47.74	0.10	0.12	0.02	52.05	0.03	0.00	0.66	0.15	0.00	0.00	100.89
KD121	CF248	0.02	48.70	0.00	0.00	0.02	53.48	0.02	0.00	0.31	0.19	0.00	0.00	102.74
KD121	CF250	0.04	48.62	0.01	0.03	0.01	53.06	0.04	0.00	0.25	0.07	0.00	0.00	102.12
KD121	CF251	0.05	48.08	0.05	0.12	0.00	52.10	0.01	0.00	0.58	0.14	0.00	0.08	101.19
KD121	CF249	0.00	48.10	0.09	0.07	0.01	52.13	0.01	0.00	0.52	0.12	0.00	0.00	101.06

Digitised by the Department of Library Services in support of open access to information, University of Pretoria, 2021

FLUORITE ANALYSIS: KD01 SEQUENCE

Samples KD121 (continued)

CODE: CF = sample number

APPENDIX 1.5

SAMPLE	NUM	Na	F	Mg	Si	Cl	Ca	Ti	Mn	Fe	Sr	Y	Ce	TOTAL
KD121	CF252	0.02	47.77	0.09	0.06	0.05	52.14	0.00	0.00	0.82	0.16	0.00	0.02	101.12
KD121	CF253	0.04	48.34	0.02	0.06	0.00	52.51	0.00	0.00	0.21	0.19	0.00	0.03	101.40
KD121	CF254	0.03	48.56	0.07	0.10	0.02	52.70	0.03	0.00	0.33	0.20	0.00	0.00	102.04
KD121	CF255	0.02	47.48	0.12	0.14	0.04	51.89	0.02	0.00	0.65	0.19	0.00	0.00	100.54
KD121	CF256	0.05	47.28	0.00	0.81	0.05	51.34	0.01	0.00	0.60	0.02	0.00	0.00	100.17
KD121	CF257	0.03	47.90	0.03	0.49	0.01	52.18	0.02	0.00	0.39	0.21	0.00	0.00	101.25
KD121	CF258	0.10	47.80	0.12	0.55	0.00	52.07	0.01	0.00	0.40	0.10	0.00	0.01	101.17
KD121	CF259	0.06	48.25	0.04	0.20	0.01	52.49	0.03	0.00	0.42	0.18	0.00	0.00	101.66
KD121	CF260	0.03	48.09	0.03	0.15	0.04	52.21	0.04	0.00	0.42	0.29	0.00	0.00	101.30
KD121	CF261	0.07	48.07	0.03	0.20	0.03	52.43	0.02	0.00	0.48	0.31	0.00	0.03	101.66
KD121	CF262	0.06	48.01	0.04	0.10	0.03	52.40	0.04	0.00	0.51	0.21	0.00	0.08	101.47
KD121	CF263	0.03	47.90	0.07	0.09	0.00	52.15	0.02	0.00	0.61	0.25	0.00	0.04	101.16
KD121	CF264	0.04	48.40	0.04	0.10	0.03	53.08	0.03	0.00	0.29	0.25	0.00	0.02	102.28
KD121	CF265	0.03	48.63	0.02	0.07	0.00	52.91	0.02	0.00	0.20	0.10	0.00	0.11	102.10
KD121	CF266	0.00	48.77	0.05	0.04	0.04	52.80	0.00	0.00	0.27	0.33	0.00	0.03	102.32
KD121	CF267	0.04	48.64	0.03	0.10	0.01	53.06	0.01	0.00	0.20	0.03	0.00	0.03	102.16
KD121	CF268	0.04	48.80	0.00	0.05	0.00	53.32	0.02	0.00	0.12	0.19	0.00	0.04	102.58
KD121	CF269	0.15	48.07	0.03	0.33	0.04	52.37	0.03	0.00	0.51	0.24	0.00	0.11	101.86
KD121	CF270	0.03	48.87	0.00	0.03	0.03	53.22	0.01	0.00	0.09	0.05	0.00	0.02	102.35
KD121	CF271	0.09	48.09	0.03	0.16	0.05	51.64	0.02	0.00	0.66	0.23	0.00	0.09	101.05
KD121	CF272	0.04	48.52	0.01	0.05	0.00	52.62	0.00	0.00	0.13	0.18	0.00	0.00	101.55
KD121	CF273	0.00	48.60	0.06	0.10	0.04	52.63	0.01	0.00	0.20	0.32	0.00	0.03	101.98
KD121	CF274	0.03	48.58	0.01	0.01	0.00	52.67	0.01	0.00	0.04	0.90	0.00	0.06	102.31
KD121	CF275	0.12	48.56	0.04	0.18	0.06	51.69	0.03	0.00	0.41	0.07	0.00	0.07	101.23
KD121	CF276	0.03	48.19	0.04	0.13	0.03	53.33	0.03	0.00	0.48	0.20	0.00	0.07	102.53
KD121	CF277	0.06	46.80	0.01	0.09	0.04	55.01	0.01	0.00	0.37	0.16	0.00	0.10	102.64
KD121	CF278	0.04	48.75	0.01	0.06	0.02	52.95	0.01	0.00	0.25	0.07	0.00	0.00	102.14
KD121	CF279	0.10	47.55	0.05	0.60	0.00	51.18	0.03	0.00	0.58	0.12	0.00	0.07	100.28
KD121	CF280	0.07	48.06	0.02	0.26	0.02	52.24	0.02	0.00	0.47	0.28	0.00	0.01	101.45
KD121	CF281	0.05	48.54	0.04	0.04	0.00	52.74	0.03	0.00	0.17	0.27	0.00	0.10	101.97
KD121	CF282	0.04	47.27	0.10	0.29	0.04	51.70	0.02	0.00	0.60	0.20	0.00	0.13	100.39
KD121	CF283	0.06	48.18	0.04	0.10	0.02	52.59	0.01	0.00	0.32	0.41	0.00	0.09	101.82
KD121	CF284	0.00	48.33	0.05	0.00	0.00	53.03	0.01	0.00	0.46	0.18	0.00	0.05	102.11
KD121	CF285	0.03	48.31	0.00	0.06	0.03	53.11	0.00	0.00	0.31	0.19	0.00	0.08	102.12
KD121	CF286	0.02	48.43	0.01	0.03	0.00	52.84	0.00	0.00	0.21	0.30	0.00	0.05	101.89
KD121	CF287	0.15	46.76	0.12	0.38	0.03	51.48	0.02	0.00	0.95	0.12	0.00	0.02	100.03
KD121	CF288	0.01	48.46	0.03	0.15	0.00	53.22	0.01	0.00	0.25	0.16	0.00	0.07	102.35
KD121	CF289	0.09	48.47	0.03	0.15	0.02	52.39	0.00	0.00	0.29	0.14	0.00	0.11	101.69
KD121	CF290	0.01	47.86	0.17	0.15	0.03	52.08	0.03	0.00	0.40	0.16	0.00	0.02	100.91
KD121	CF291	0.05	48.00	0.07	0.20	0.04	52.25	0.00	0.00	0.38	0.28	0.00	0.08	101.34
KD121	CF292	0.06	47.91	0.05	0.35	0.02	51.95	0.00	0.00	0.52	0.11	0.00	0.14	101.11
KD121	CF293	0.08	47.83	0.12	0.22	0.01	52.12	0.01	0.00	0.87	0.20	0.00	0.04	101.50
KD121	CF294	0.02	49.05	0.00	0.03	0.00	53.32	0.01	0.00	0.13	0.31	0.00	0.05	102.92
KD121	CF295	0.05	49.02	0.00	0.04	0.03	52.93	0.01	0.00	0.19	0.09	0.00	0.11	102.47
KD121	CF296	0.03	48.82	0.01	0.05	0.05	53.17	0.01	0.00	0.29	0.24	0.00	0.01	102.66
KD121	CF297	0.03	48.92	0.02	0.02	0.05	53.28	0.00	0.00	0.15	0.25	0.00	0.03	102.73
KD121	CF298	0.03	48.91	0.02	0.04	0.00	53.07	0.01	0.00	0.18	0.11	0.00	0.00	102.37
KD121	CF299	0.05	48.83	0.03	0.03	0.04	52.77	0.00	0.00	0.34	0.12	0.00	0.00	102.20
KD121	CF300	0.03	48.75	0.04	0.06	0.01	53.42	0.00	0.00	0.56	0.07	0.00	0.07	103.00
KD121	CF301	0.02	49.13	0.01	0.04	0.03	53.27	0.00	0.00	0.23	0.41	0.00	0.11	103.24
KD121	CF302	0.12	48.47	0.02	0.24	0.01	52.39	0.02	0.00	0.47	0.16	0.00	0.06	101.95
KD121	CF303	0.11	47.87	0.11	0.13	0.00	51.80	0.04	0.00	1.05	0.11	0.00	0.00	101.22
KD121	CF304	0.16	48.25	0.01	0.24	0.04	52.40	0.05	0.00	0.48	0.19	0.00	0.02	101.82
KD121	CF305	0.13	48.51	0.03	0.26	0.00	51.63	0.04	0.00	0.48	0.19	0.00	0.09	101.38
KD121	CF306	0.03	49.03	0.01	0.04	0.02	52.96	0.00	0.00	0.09	0.19	0.00	0.06	102.42
KD121	CF307	0.03	49.30	0.00	0.02	0.00	52.68	0.04	0.00	0.12	0.30	0.00	0.00	102.48
KD121	CF308	0.06	49.47	0.00	0.05	0.03	53.09	0.02	0.00	0.05	0.27	0.00	0.00	103.02
KD121	CF310	0.04	47.75	0.15	0.01	0.04	51.42	0.00	0.00	0.87	0.31	0.00	0.00	100.59
KD121	CF311	0.05	47.96	0.14	0.21	0.00	51.78	0.01	0.00	0.69	0.20	0.00	0.00	101.03
KD121	CF309	0.11	48.99	0.02	0.02	0.00	51.91	0.00	0.00	0.10	0.73	0.00	0.06	101.95

Digitised by the Department of Library Services in support of open access to information, University of Pretoria, 2021

FLUORITE ANALYSIS: KD01 SEQUENCE

Samples KD121 (continued) and KD130

CODE: CF = sample number

APPENDIX 1.5

SAMPLE	NUM	Na	F	Mg	Si	Cl	Ca	Ti	Mn	Fe	Sr	Y	Ce	TOTAL
KD121	CF312	0.06	47.62	0.09	0.20	0.01	51.14	0.00	0.00	0.82	0.26	0.00	0.08	100.29
AVE.		0.06	48.11	0.02	0.10	0.02	51.89	0.02	0.00	0.34	0.26	0.00	0.03	101.20
KD130	CF314	0.15	48.77	0.04	0.06	0.02	53.30	0.03	0.00	0.20	0.18	0.00	0.00	102.74
KD130	CF315	0.00	48.77	0.00	0.01	0.01	53.45	0.00	0.00	0.05	0.07	0.00	0.11	102.47
KD130	CF316	0.03	48.75	0.00	0.00	0.00	53.02	0.03	0.00	0.04	0.27	0.00	0.00	102.14
KD130	CF317	0.03	48.63	0.00	0.00	0.00	52.43	0.01	0.00	0.07	0.34	0.00	0.04	101.56
KD130	CF318	0.01	48.69	0.00	0.02	0.03	52.74	0.00	0.00	0.04	0.08	0.00	0.00	101.61
KD130	CF319	0.04	48.99	0.00	0.01	0.00	52.64	0.00	0.00	0.07	0.03	0.00	0.03	101.80
KD130	CF320	0.03	48.70	0.00	0.03	0.00	52.79	0.03	0.00	0.00	0.17	0.00	0.15	101.91
KD130	CF321	0.03	48.55	0.00	0.02	0.01	52.88	0.00	0.00	0.08	0.11	0.00	0.03	101.69
KD130	CF322	0.02	48.96	0.00	0.02	0.00	52.62	0.00	0.00	0.00	0.25	0.00	0.01	101.87
KD130	CF323	0.03	48.46	0.00	0.00	0.02	53.02	0.00	0.00	0.00	0.09	0.00	0.06	101.67
KD130	CF324	0.00	48.68	0.00	0.00	0.04	52.72	0.00	0.00	0.00	0.18	0.00	0.10	101.71
KD130	CF325	0.00	47.72	0.12	0.00	0.01	51.33	0.00	0.00	0.62	0.22	0.00	0.05	100.07
KD130	CF326	0.03	49.06	0.01	0.01	0.01	53.39	0.00	0.00	0.04	0.10	0.00	0.00	102.64
KD130	CF327	0.00	48.93	0.01	0.01	0.03	53.13	0.00	0.00	0.10	0.07	0.00	0.09	102.36
KD130	CF328	0.00	48.25	0.11	0.01	0.00	51.22	0.01	0.00	0.70	0.00	0.00	0.00	100.31
KD130	CF329	0.00	48.92	0.00	0.01	0.03	53.03	0.00	0.00	0.02	0.09	0.00	0.00	102.10
KD130	CF330	0.02	48.92	0.00	0.01	0.03	52.80	0.01	0.00	0.01	0.10	0.00	0.05	101.94
KD130	CF331	0.03	49.05	0.00	0.02	0.04	52.77	0.02	0.00	0.04	0.00	0.00	0.10	102.06
KD130	CF332	0.05	48.82	0.00	0.00	0.02	52.75	0.04	0.00	0.00	0.34	0.00	0.01	102.03
KD130	CF333	0.05	48.50	0.00	0.00	0.01	53.13	0.02	0.00	0.04	0.02	0.00	0.11	101.88
KD130	CF334	0.11	47.33	0.13	0.01	0.01	51.36	0.01	0.00	0.58	0.12	0.00	0.00	99.65
KD130	CF335	0.00	48.92	0.01	0.00	0.02	53.46	0.00	0.00	0.02	0.22	0.00	0.07	102.72
KD130	CF336	0.02	48.48	0.03	0.00	0.03	52.64	0.00	0.00	0.17	0.18	0.00	0.03	101.58
KD130	CF337	0.01	48.82	0.00	0.01	0.01	53.14	0.00	0.00	0.10	0.09	0.00	0.00	102.17
KD130	CF338	0.01	48.81	0.00	0.01	0.02	52.56	0.02	0.00	0.04	0.20	0.00	0.00	101.66
KD130	CF339	0.03	48.58	0.01	0.02	0.03	52.62	0.01	0.00	0.03	0.16	0.00	0.08	101.56
KD130	CF340	0.01	48.96	0.01	0.03	0.01	53.19	0.00	0.00	0.10	0.16	0.00	0.00	102.45
KD130	CF341	0.00	48.02	0.07	0.00	0.00	52.58	0.01	0.00	0.32	0.10	0.00	0.01	101.11
KD130	CF342	0.01	48.73	0.00	0.00	0.03	53.21	0.00	0.00	0.14	0.15	0.00	0.08	102.36
KD130	CF343	0.02	47.94	0.05	0.03	0.02	52.37	0.00	0.00	0.43	0.08	0.00	0.12	101.05
KD130	CF344	0.02	48.69	0.02	0.01	0.02	52.91	0.01	0.00	0.14	0.03	0.00	0.00	101.86
KD130	CF345	0.00	48.69	0.00	0.00	0.01	53.28	0.00	0.00	0.09	0.09	0.00	0.06	102.21
KD130	CF346	0.00	49.19	0.01	0.00	0.02	53.64	0.01	0.00	0.02	0.00	0.00	0.05	102.94
KD130	CF347	0.01	48.93	0.00	0.01	0.03	53.77	0.02	0.00	0.05	0.05	0.00	0.00	102.86
KD130	CF348	0.02	48.77	0.00	0.00	0.05	53.24	0.01	0.00	0.00	0.03	0.00	0.03	102.14
KD130	CF349	0.02	48.82	0.00	0.02	0.05	52.78	0.04	0.00	0.01	0.05	0.00	0.07	101.87
KD130	CF350	0.03	49.00	0.00	0.00	0.00	52.57	0.02	0.00	0.03	0.04	0.00	0.07	101.76
KD130	CF351	0.00	48.12	0.10	0.01	0.04	53.02	0.00	0.00	0.35	0.20	0.00	0.07	101.91
KD130	CF352	0.00	47.83	0.12	0.01	0.00	51.64	0.02	0.00	0.61	0.02	0.00	0.00	100.24
KD130	CF353	0.00	48.88	0.00	0.02	0.03	52.58	0.00	0.00	0.05	0.10	0.00	0.00	101.67
KD130	CF354	0.00	49.02	0.01	0.01	0.02	53.10	0.02	0.00	0.00	0.05	0.00	0.00	102.24
KD130	CF355	0.00	47.20	0.09	0.00	0.04	51.40	0.00	0.00	1.04	0.05	0.00	0.00	99.82
KD130	CF356	0.00	48.85	0.00	0.01	0.01	52.99	0.01	0.00	0.03	0.11	0.00	0.00	102.02
KD130	CF357	0.00	48.93	0.01	0.02	0.01	53.17	0.01	0.00	0.03	0.14	0.00	0.00	102.33
KD130	CF358	0.04	49.02	0.01	0.01	0.03	52.40	0.01	0.00	0.03	0.14	0.00	0.01	101.72
KD130	CF359	0.06	49.08	0.00	0.01	0.02	53.09	0.01	0.00	0.06	0.12	0.00	0.01	102.45
KD130	CF360	0.04	48.97	0.01	0.01	0.02	53.15	0.00	0.00	0.02	0.10	0.00	0.00	102.33
KD130	CF361	0.02	48.37	0.08	0.02	0.02	53.00	0.00	0.00	0.32	0.03	0.00	0.02	101.89
KD130	CF362	0.02	48.97	0.00	0.01	0.02	53.25	0.00	0.00	0.05	0.05	0.00	0.00	102.37
KD130	CF363	0.00	48.57	0.02	0.01	0.01	53.14	0.15	0.00	0.07	0.13	0.00	0.04	102.14
KD130	CF364	0.03	48.65	0.02	0.03	0.00	52.77	0.01	0.00	0.17	0.19	0.00	0.13	101.98
KD130	CF365	0.01	48.77	0.01	0.01	0.04	52.95	0.02	0.00	0.04	0.14	0.00	0.04	102.02
KD130	CF366	0.01	47.88	0.11	0.00	0.00	52.11	0.00	0.00	0.74	0.15	0.00	0.00	101.01
KD130	CF367	0.02	48.97	0.00	0.01	0.00	52.48	0.00	0.00	0.06	0.22	0.00	0.07	101.83
KD130	CF368	0.02	49.01	0.00	0.02	0.00	53.41	0.00	0.00	0.00	0.18	0.00	0.07	102.70
KD130	CF370	0.02	48.92	0.03	0.02	0.03	52.80	0.00	0.00	0.23	0.10	0.00	0.00	102.14
KD130	CF371	0.02	48.98	0.00	0.01	0.00	53.46	0.00	0.00	0.05	0.11	0.00	0.08	102.72
KD130	CF369	0.02	49.01	0.01	0.02	0.02	53.33	0.03	0.00	0.11	0.16	0.00	0.10	102.80

Digitised by the Department of Library Services in support of open access to information, University of Pretoria, 2021

FLUORITE ANALYSIS: KD01 SEQUENCE

Sample KD130 (continued)

APPENDIX 1.5

CODE: CF = sample number

SAMPLE	NUM	Na	F	Mg	Si	Cl	Ca	Ti	Mn	Fe	Sr	Y	Ce	TOTAL
KD130	CF372	0.03	48.99	0.00	0.02	0.01	53.23	0.03	0.00	0.03	0.03	0.00	0.00	102.36
KD130	CF373	0.00	48.93	0.00	0.00	0.03	53.04	0.00	0.00	0.07	0.11	0.00	0.00	102.19
KD130	CF374	0.00	49.21	0.00	0.01	0.00	53.22	0.00	0.00	0.00	0.19	0.00	0.02	102.65
KD130	CF375	0.02	49.05	0.01	0.02	0.00	53.35	0.00	0.00	0.03	0.00	0.00	0.00	102.49
KD130	CF376	0.02	48.97	0.01	0.00	0.01	53.45	0.01	0.00	0.00	0.00	0.00	0.07	102.55
KD130	CF377	0.03	48.89	0.00	0.00	0.00	53.19	0.03	0.00	0.00	0.17	0.00	0.09	102.38
KD130	CF378	0.00	48.78	0.00	0.01	0.00	53.44	0.02	0.00	0.12	0.03	0.00	0.06	102.46
KD130	CF379	0.00	49.30	0.00	0.01	0.00	53.26	0.00	0.00	0.02	0.06	0.00	0.07	102.72
KD130	CF380	0.04	49.35	0.00	0.00	0.04	53.43	0.03	0.00	0.04	0.16	0.00	0.08	103.17
KD130	CF381	0.01	48.68	0.03	0.01	0.01	53.34	0.01	0.00	0.38	0.00	0.00	0.04	102.51
KD130	CF382	0.01	49.05	0.00	0.03	0.03	53.25	0.00	0.00	0.12	0.04	0.00	0.00	102.53
KD130	CF383	0.01	48.34	0.01	0.01	0.01	52.52	0.01	0.00	0.39	0.08	0.00	0.01	101.39
KD130	CF384	0.02	49.01	0.01	0.00	0.03	52.92	0.01	0.00	0.33	0.09	0.00	0.04	102.44
KD130	CF385	0.02	47.70	0.14	0.16	0.00	52.00	0.17	0.00	0.98	0.07	0.00	0.15	101.39
KD130	CF386	0.10	48.04	0.00	0.27	0.05	51.62	0.02	0.00	0.33	0.84	0.00	0.06	101.34
AVE.		0.02	48.70	0.02	0.02	0.02	52.86	0.01	0.00	0.15	0.12	0.00	0.04	101.96

Digitised by the Department of Library Services in support of open access to information, University of Pretoria, 2021

FELDSPAR ANALYSES: KD01 SEQUENCE

Samples KD012, KD016 and KD019

CODE: CFE = sample number; n = not analysed

APPENDIX 1.6

												Structural formula, based on 32 oxygen atoms								
Sample	CODE	Na_2O	MgO	Al_2O_3	SiO_2	K_2O	CaO	TiO_2	FeO	BaO	TOTAL	Si	Ti	Al	Fe^{2+}	Mg	Ca	Na	K	Ba
KD012	CFE270	0.00	0.00	18.23	62.42	15.53	0.34	0.00	0.00	0.00	98.01	11.93	0.00	4.11	4.11	0.00	0.07	0.00	3.79	0.00
KD012	CFE271	0.00	0.00	18.55	63.19	15.37	0.00	0.00	0.00	0.00	98.60	11.96	0.00	4.14	4.14	0.00	0.00	0.00	3.71	0.00
AVE.		0.00	0.00	18.39	62.80	15.45	0.17	0.00	0.00	0.00	98.30	11.95	0.00	4.13	4.13	0.00	0.04	0.00	3.75	0.00
KD016	CFE273	0.00	0.00	18.23	61.56	15.30	0.00	0.00	0.49	0.00	98.63	11.90	0.00	4.16	0.08	0.00	0.00	0.00	3.77	0.00
KD016	CFE274	0.00	0.00	18.29	63.31	15.54	0.00	0.00	0.70	0.00	99.06	11.96	0.00	4.07	0.11	0.00	0.00	0.00	3.75	0.00
KD016	CFE275	0.00	0.00	18.19	62.90	15.71	0.00	0.00	0.00	0.86	98.54	11.96	0.00	4.08	0.00	0.00	0.00	0.00	3.81	0.06
KD016	CFE276	0.00	0.00	18.52	63.63	15.71	0.00	0.00	0.45	0.80	98.78	11.93	0.00	4.09	0.07	0.00	0.00	0.00	3.75	0.06
KD016	CFE277	0.00	0.00	18.03	62.61	15.70	0.00	0.00	0.84	0.00	98.32	11.94	0.00	4.05	0.13	0.00	0.00	0.00	3.92	0.00
KD016	CFE278	0.00	0.00	18.49	62.63	15.50	0.00	0.00	1.23	1.08	99.82	11.84	0.00	4.12	0.19	0.00	0.00	0.00	3.74	0.08
KD016	CFE279	0.00	0.00	18.76	63.12	15.36	0.00	0.00	0.00	1.49	98.78	11.88	0.00	4.17	0.00	0.00	0.00	0.00	3.70	0.11
KD016	CFE280	0.00	0.00	18.71	63.81	15.95	0.00	0.00	0.00	0.00	98.98	11.95	0.00	4.13	0.00	0.00	0.00	0.00	3.81	0.00
KD016	CFE281	0.00	0.00	18.93	64.07	15.88	0.00	0.00	0.00	0.73	99.83	11.92	0.00	4.15	0.00	0.00	0.00	0.00	3.77	0.05
KD016	CFE282	0.00	0.00	18.70	64.19	15.87	0.00	0.00	0.00	1.00	100.22	11.95	0.00	4.01	0.00	0.00	0.00	0.00	3.77	0.07
KD016	CFE283	0.00	0.00	18.60	63.30	15.70	0.00	0.00	0.00	0.80	99.00	11.93	0.00	4.13	0.00	0.00	0.00	0.00	3.77	0.06
KD016	CFE284	0.00	0.00	18.89	64.27	15.98	0.00	0.00	0.00	0.00	99.28	11.95	0.00	4.14	0.00	0.00	0.00	0.00	3.79	0.00
KD016	CFE285	0.00	0.00	18.63	63.42	15.73	0.00	0.00	0.00	0.65	98.04	11.93	0.00	4.13	0.00	0.00	0.00	0.00	3.77	0.04
AVE.		0.00	0.00	18.54	63.29	15.69	0.00	0.00	0.28	0.57	99.02	11.93	0.00	4.11	0.04	0.00	0.00	0.00	3.78	0.04
KD019	CFE286	0.00	0.00	19.06	63.71	15.41	0.00	0.00	0.00	1.25	101.41	11.89	0.00	4.19	0.00	0.00	0.00	0.00	3.67	0.09
KD019	CFE287	0.00	0.00	18.33	63.03	15.91	0.00	0.00	0.00	0.00	98.10	11.96	0.00	4.10	0.00	0.00	0.00	0.00	3.85	0.00
KD019	CFE288	0.00	0.00	18.64	63.20	15.74	0.00	0.00	0.00	0.72	99.33	11.92	0.00	4.14	0.00	0.00	0.00	0.00	3.78	0.05
KD019	CFE289	0.00	0.00	18.65	63.49	15.50	0.00	0.00	0.00	0.92	99.74	11.93	0.00	4.13	0.00	0.00	0.00	0.00	3.71	0.06
KD019	CFE290	0.34	0.00	18.75	63.12	15.61	0.00	0.00	0.37	1.76	99.33	11.83	0.00	4.14	0.05	0.00	0.00	0.12	3.73	0.12
KD019	CFE291	0.00	0.00	19.16	63.91	15.86	0.00	0.00	0.45	1.31	100.73	11.84	0.00	4.18	0.07	0.00	0.00	0.00	3.75	0.09
KD019	CFE292	0.00	0.00	18.75	61.52	14.90	0.00	0.59	0.00	2.74	98.94	11.74	0.08	4.21	0.00	0.00	0.00	0.00	3.62	0.20
KD019	CFE293	0.00	0.00	19.15	63.87	15.69	0.00	0.00	0.00	1.29	101.66	11.87	0.00	4.19	0.00	0.00	0.00	0.00	3.72	0.09
KD019	CFE294	0.00	0.00	18.59	63.27	15.67	0.00	0.00	1.31	1.07	100.09	11.84	0.00	4.10	0.20	0.00	0.00	0.00	3.74	0.07
KD019	CFE295	0.00	0.00	18.85	63.95	15.80	0.00	0.00	0.42	1.44	101.72	11.88	0.00	4.12	0.06	0.00	0.00	0.00	3.74	0.10
KD019	CFE296	0.00	0.00	18.92	63.79	15.55	0.00	0.00	0.00	1.62	100.21	11.89	0.00	4.15	0.00	0.00	0.00	0.00	3.70	0.11
KD019	CFE297	0.00	0.00	18.55	62.63	15.24	0.00	0.00	0.37	1.76	98.74	11.87	0.00	4.14	0.05	0.00	0.00	0.00	3.68	0.13
KD019	CFE298	0.00	0.00	18.56	62.91	15.37	0.00	0.00	0.00	1.21	98.30	11.91	0.00	4.14	0.00	0.00	0.00	0.00	3.71	0.09
KD019	CFE299	0.00	0.00	18.55	64.07	15.55	0.00	0.00	0.00	1.04	99.68	11.97	0.00	4.08	0.00	0.00	0.00	0.00	3.70	0.07
KD019	CFE300	0.00	0.30	18.72	62.57	15.28	0.55	0.00	0.36	0.90	99.28	11.80	0.00	4.16	0.05	0.08	0.11	0.00	3.67	0.06
KD019	CFE301	0.00	0.00	18.84	63.60	15.73	0.00	0.00	0.62	0.00	99.97	11.89	0.00	4.15	0.09	0.00	0.00	0.00	3.75	0.00
KD019	CFE302	0.00	0.00	18.95	61.64	14.88	0.00	0.00	0.00	2.25	98.43	11.80	0.00	4.27	0.00	0.00	0.00	0.00	3.63	0.16
KD019	CFE303	0.00	0.00	18.81	63.00	15.35	0.00	0.00	0.00	1.49	98.71	11.88	0.00	4.18	0.00	0.00	0.00	0.00	3.69	0.11
KD019	CFE304	0.00	0.00	19.50	63.07	15.22	0.00	0.00	0.53	1.94	100.36	11.76	0.00	4.28	0.08	0.00	0.00	0.00	3.62	0.14
KD019	CFE305	0.00	0.00	19.16	63.44	15.27	0.00	0.70	0.00	1.64	101.27	11.78	0.09	4.19	0.00	0.00	0.00	0.00	3.62	0.11

Digitised by the Department of Library Services in support of open access to information, University of Pretoria, 2021

FELDSPAR ANALYSES: KD01 SEQUENCE

Samples KD019 (continued), KD111, KD117, KD119 and KD121

CODE: CFE = sample number; n = not analysed

APPENDIX 1.6

												Structural formula, based on 32 oxygen atoms								
Sample	NUM	Na_2O	MgO	Al_2O_3	SiO_2	K_2O	CaO	TiO_2	FeO	BaO	TOTAL	Si	Ti	Al	Fe^{2+}	Mg	Ca	Na	K	Ba
AVE.		0.02	0.02	18.82	63.19	15.48	0.03	0.06	0.22	1.32	99.80	11.86	0.01	4.16	0.03	0.00	0.01	0.01	3.70	0.09
KD111	CFE306	0.18	0.16	18.83	62.53	16.35	0.00	0.05	0.82	n	98.96	11.77	0.01	4.17	0.13	0.04	0.00	0.06	3.92	0.00
KD111	CFE307	0.39	0.16	18.43	62.92	16.82	0.00	0.02	0.06	n	98.84	11.85	0.00	4.09	0.00	0.04	0.00	0.14	4.04	0.00
KD111	CFE308	0.74	0.16	17.94	62.97	15.82	0.00	0.04	1.29	n	99.01	11.86	0.00	3.98	0.20	0.04	0.00	0.27	3.80	0.00
KD111	CFE309	0.22	0.16	18.05	63.89	16.86	0.00	0.03	0.05	n	99.32	11.96	0.00	3.98	0.00	0.04	0.00	0.08	4.02	0.00
KD111	CFE310	0.21	0.16	18.49	63.58	16.87	0.00	0.00	0.13	n	99.48	11.88	0.00	4.07	0.02	0.04	0.00	0.07	4.02	0.00
KD111	CFE311	0.16	0.16	18.58	63.33	16.83	0.00	0.00	0.00	n	99.12	11.87	0.00	4.10	0.00	0.04	0.00	0.05	4.02	0.00
AVE.		0.31	0.16	18.39	63.20	16.59	0.00	0.02	0.39	n	99.12	11.87	0.00	4.07	0.06	0.04	0.00	0.11	3.97	0.00
KD117	CFE312	0.28	0.17	18.57	63.06	16.91	0.02	0.03	0.65	0.00	99.69	11.81	0.00	4.10	0.10	0.04	0.00	0.10	4.04	0.00
KD117	CFE313	0.28	0.16	18.89	63.96	17.00	0.00	0.02	0.27	0.00	100.56	11.84	0.00	4.12	0.04	0.04	0.00	0.10	4.01	0.00
KD117	CFE314	0.27	0.16	18.77	63.66	16.62	0.00	0.00	0.23	0.00	99.72	11.85	0.00	4.12	0.03	0.04	0.00	0.10	3.95	0.00
KD117	CFE315	0.37	0.16	18.97	63.19	16.61	0.02	0.01	0.33	0.00	99.66	11.79	0.00	4.17	0.05	0.04	0.00	0.13	3.95	0.00
KD117	CFE316	0.25	0.16	18.97	62.99	16.88	0.00	0.00	0.26	0.00	99.52	11.78	0.00	4.18	0.04	0.04	0.00	0.09	4.03	0.00
KD117	CFE317	0.24	0.16	19.15	62.12	16.36	0.00	0.02	0.49	0.00	98.54	11.73	0.00	4.26	0.07	0.04	0.00	0.08	3.94	0.00
KD117	CFE318	0.28	0.16	18.94	62.47	16.63	0.01	0.01	0.31	0.00	98.82	11.77	0.00	4.20	0.04	0.04	0.00	0.10	3.99	0.00
KD117	CFE319	0.26	0.16	19.04	62.87	16.62	0.03	0.05	0.44	0.00	99.48	11.77	0.00	4.20	0.06	0.04	0.00	0.09	3.97	0.00
KD117	CFE320	0.30	0.16	19.28	62.66	16.04	0.02	0.06	0.16	0.00	98.69	11.76	0.01	4.26	0.03	0.04	0.00	0.11	3.84	0.00
KD117	CFE321	0.37	0.17	18.95	62.65	16.08	0.00	0.06	0.50	0.00	98.78	11.78	0.01	4.19	0.07	0.04	0.00	0.13	3.85	0.00
KD117	CFE322	0.26	0.17	18.81	62.07	16.25	0.01	0.10	0.58	0.00	98.24	11.76	0.01	4.20	0.09	0.04	0.00	0.09	3.92	0.00
KD117	CFE323	0.37	0.16	18.97	62.60	16.42	0.02	0.02	0.32	0.00	98.89	11.77	0.00	4.20	0.05	0.04	0.00	0.13	3.94	0.00
KD117	CFE324	0.21	0.16	16.85	64.15	15.13	0.03	0.02	0.46	0.00	100.62	12.17	0.00	3.76	0.07	0.04	0.00	0.07	3.66	0.00
KD117	CFE325	0.27	0.16	19.10	63.60	16.88	0.00	0.02	0.14	0.00	100.71	11.80	0.00	4.18	0.02	0.04	0.00	0.09	3.99	0.00
KD117	CFE326	0.23	0.16	18.82	63.51	16.89	0.01	0.01	0.25	0.00	99.99	11.83	0.00	4.13	0.03	0.04	0.00	0.08	4.01	0.00
KD117	CFE327	0.32	0.16	18.94	63.23	16.76	0.01	0.02	0.32	0.00	100.03	11.80	0.00	4.17	0.05	0.04	0.00	0.11	3.99	0.00
AVE.		0.29	0.16	18.81	63.05	16.51	0.01	0.03	0.36	0.00	99.50	11.81	0.00	4.15	0.05	0.04	0.00	0.10	3.94	0.00
KD119	CFE328	0.27	0.16	18.13	62.49	16.42	0.00	0.04	0.51	0.00	98.78	11.87	0.00	4.05	0.08	0.05	0.00	0.10	3.98	0.00
KD119	CFE329	0.21	0.16	18.82	62.68	16.38	0.16	0.03	0.31	0.00	98.57	11.80	0.00	4.17	0.04	0.05	0.03	0.07	3.93	0.00
KD119	CFE330	0.28	0.16	18.69	62.46	16.45	0.01	0.10	0.49	0.00	98.86	11.79	0.01	4.15	0.08	0.05	0.00	0.10	3.96	0.00
KD119	CFE331	0.32	0.16	18.83	62.56	16.01	0.03	0.12	0.55	0.00	98.47	11.78	0.01	4.18	0.08	0.05	0.00	0.11	3.84	0.00
KD119	CFE332	0.34	0.16	18.89	62.74	16.08	0.02	0.05	0.39	0.00	98.49	11.80	0.00	4.18	0.06	0.05	0.00	0.12	3.86	0.00
KD119	CFE333	0.25	0.16	18.48	63.13	16.54	0.03	0.03	0.49	0.00	98.71	11.85	0.00	4.09	0.08	0.05	0.00	0.09	3.96	0.00
KD119	CFE334	0.24	0.16	18.52	63.32	16.55	0.00	0.46	0.29	0.00	98.94	11.82	0.06	4.08	0.05	0.05	0.00	0.08	3.94	0.00
KD119	CFE335	0.23	0.16	18.39	62.74	16.52	0.00	0.01	0.35	0.00	98.98	11.85	0.00	4.09	0.06	0.05	0.00	0.08	3.98	0.00
AVE.		0.27	0.16	18.59	62.76	16.37	0.03	0.11	0.42	0.00	98.73	11.82	0.01	4.12	0.06	0.05	0.00	0.09	3.93	0.00
KD121	CFE336	0.24	0.16	19.02	61.54	15.98	0.02	0.07	0.24	0.00	98.49	11.74	0.01	4.28	0.03	0.04	0.00	0.08	3.89	0.00

Digitised by the Department of Library Services in support of open access to information, University of Pretoria, 2021

FELDSPAR ANALYSES: KD01 SEQUENCE

Samples KD121 (continued), KD124, KD130 and KD133

CODE: CFE = sample number; n = not analysed

APPENDIX 1.6

												Structural formula, based on 32 oxygen atoms								
Sample	NUM	Na_2O	MgO	Al_2O_3	SiO_2	K_2O	CaO	TiO_2	FeO	BaO	TOTAL	Si	Ti	Al	Fe^{2+}	Mg	Ca	Na	K	Ba
KD121	CFE337	0.34	0.17	18.82	62.86	15.90	0.01	0.08	1.72	0.00	98.57	11.74	0.01	4.14	0.26	0.04	0.00	0.08	3.78	0.00
KD121	CFE338	0.38	0.17	18.40	63.27	15.92	0.00	0.14	2.32	0.00	100.18	11.77	0.02	4.03	0.36	0.04	0.00	0.12	3.77	0.00
KD121	CFE339	0.36	0.16	19.20	63.55	16.37	0.03	0.03	0.38	0.00	99.79	11.79	0.00	4.20	0.05	0.04	0.00	0.13	3.87	0.00
KD121	CFE340	0.27	0.16	19.00	63.49	15.88	0.02	0.04	0.52	0.00	99.44	11.83	0.00	4.17	0.08	0.04	0.00	0.13	3.77	0.00
KD121	CFE341	0.29	0.16	19.13	64.32	16.49	0.04	0.04	0.18	0.00	99.80	11.85	0.00	4.15	0.02	0.04	0.00	0.09	3.87	0.00
KD121	CFE342	0.26	0.16	19.20	63.22	16.70	0.07	0.03	0.18	0.00	100.92	11.77	0.00	4.21	0.02	0.04	0.01	0.10	3.97	0.00
KD121	CFE343	0.34	0.16	18.73	63.83	16.15	0.04	0.06	0.22	0.00	98.92	11.88	0.00	4.11	0.03	0.04	0.00	0.09	3.83	0.00
KD121	CFE344	0.29	0.16	19.41	64.03	16.81	0.02	0.01	0.08	0.00	100.61	11.80	0.00	4.21	0.00	0.04	0.00	0.12	3.95	0.00
KD121	CFE345	0.29	0.16	19.10	62.45	16.65	0.10	0.06	0.42	0.00	100.80	11.73	0.00	4.22	0.06	0.04	0.02	0.10	3.98	0.00
KD121	CFE346	0.29	0.16	19.13	63.36	15.89	0.02	0.11	0.38	0.00	98.44	11.80	0.01	4.20	0.05	0.04	0.00	0.10	3.77	0.00
AVE.		0.30	0.17	19.01	63.26	16.25	0.03	0.06	0.60	0.00	99.63	11.79	0.00	4.17	0.09	0.04	0.00	0.10	3.86	0.00
KD124	CFE347	0.19	0.17	18.94	63.31	16.37	0.03	0.01	0.66	0.00	99.73	11.81	0.00	4.16	0.10	0.04	0.00	0.06	3.89	0.00
KD124	CFE348	0.22	0.17	18.93	62.22	16.58	0.03	0.19	0.54	0.00	99.96	11.73	0.02	4.20	0.08	0.04	0.00	0.08	3.98	0.00
KD124	CFE349	0.30	0.17	18.61	63.59	16.53	0.03	0.04	0.72	0.00	98.62	11.84	0.00	4.08	0.11	0.04	0.00	0.10	3.92	0.00
KD124	CFE350	0.24	0.17	18.64	63.07	16.49	0.02	0.06	0.76	0.00	99.97	11.81	0.00	4.11	0.11	0.04	0.00	0.08	3.94	0.00
KD124	CFE351	0.21	0.17	17.74	63.43	15.58	0.00	0.04	1.24	0.00	100.53	11.96	0.00	3.94	0.19	0.04	0.00	0.07	3.74	0.00
KD124	CFE352	0.23	0.16	18.64	63.27	16.88	0.01	0.04	0.33	0.00	99.38	11.84	0.00	4.11	0.05	0.04	0.00	0.08	4.03	0.00
KD124	CFE353	0.22	0.17	18.91	64.30	16.52	0.02	0.08	0.55	0.00	99.90	11.85	0.01	4.11	0.08	0.04	0.00	0.07	3.88	0.00
KD124	CFE354	0.18	0.17	19.15	64.01	16.16	0.00	0.05	1.17	0.00	100.15	11.79	0.00	4.16	0.18	0.04	0.00	0.06	3.79	0.00
KD124	CFE355	0.26	0.16	19.18	62.91	16.70	0.00	0.06	0.20	0.00	100.86	11.76	0.00	4.22	0.03	0.04	0.00	0.09	3.98	0.00
KD124	CFE356	0.20	0.16	18.96	64.20	16.74	0.00	0.03	0.43	0.00	100.54	11.84	0.00	4.12	0.06	0.04	0.00	0.70	3.94	0.00
KD124	CFE357	0.21	0.17	18.89	63.16	16.33	0.00	1.53	0.86	0.00	100.89	11.64	0.21	4.10	0.13	0.04	0.00	0.07	3.84	0.00
KD124	CFE358	0.19	0.16	18.74	64.19	16.72	0.01	0.01	0.50	0.00	100.53	11.87	0.00	4.08	0.07	0.04	0.00	0.06	3.94	0.00
KD124	CFE359	0.23	0.17	18.79	64.21	16.36	0.02	0.10	2.05	0.00	100.89	11.78	0.01	4.06	0.31	0.04	0.00	0.08	3.82	0.00
KD124	CFE360	0.28	0.17	18.86	64.08	16.59	0.21	0.06	0.72	0.00	100.89	11.81	0.00	4.10	0.11	0.04	0.04	0.10	3.90	0.00
KD124	CFE361	0.14	0.17	19.12	59.46	16.52	0.02	0.04	0.72	0.00	100.94	11.58	0.00	4.39	0.11	0.04	0.00	0.05	4.10	0.00
KD124	CFE362	0.23	0.16	19.24	62.81	16.77	0.01	0.02	0.12	0.00	100.62	11.76	0.00	4.24	0.01	0.04	0.00	0.08	4.00	0.00
AVE.		0.22	0.17	18.83	63.26	16.49	0.03	0.15	0.72	0.00	100.27	11.79	0.02	4.14	0.11	0.04	0.00	0.11	3.92	0.00
KD130	CFE363	0.19	0.16	18.23	61.31	15.18	0.06	4.55	1.43	0.00	99.26	11.33	0.63	3.97	0.22	0.04	0.01	0.06	3.58	0.00
KD130	CFE364	0.25	0.16	18.70	63.14	16.13	0.00	0.28	0.82	0.00	99.15	11.80	0.03	4.11	0.12	0.04	0.00	0.09	3.84	0.00
KD130	CFE365	0.31	0.16	18.19	64.01	15.48	0.00	0.67	2.95	0.00	99.07	11.76	0.09	3.94	0.45	0.04	0.00	0.11	3.63	0.00
AVE.		0.25	0.16	18.37	62.82	15.60	0.02	1.83	1.73	0.00	99.16	11.63	0.25	4.01	0.26	0.04	0.00	0.09	3.68	0.00
KD133	CFE366	0.24	0.16	18.89	63.36	16.98	0.17	0.00	0.09	0.00	100.55	11.81	0.00	4.15	0.01	0.04	0.03	0.08	4.03	0.00
KD133	CFE367	0.26	0.16	19.16	63.95	16.53	0.04	0.12	0.14	0.00	99.03	11.82	0.01	4.17	0.02	0.04	0.00	0.09	3.89	0.00
KD133	CFE368	0.25	0.16	18.99	63.30	16.71	0.08	0.09	0.50	0.00	100.15	11.82	0.01	4.16	0.07	0.04	0.01	0.09	3.96	0.00
KD133	CFE369	0.28	0.16	18.91	62.49	16.75	0.06	0.08	0.29	0.00	100.48	11.77	0.01	4.19	0.04	0.04	0.01	0.10	4.02	0.00

Digitised by the Department of Library Services in support of open access to information, University of Pretoria, 2021

FELDSPAR ANALYSES: KD01 SEQUENCE

Samples KD133 (continued), KD139 and KD147

CODE: CFE = sample number; n = not analysed

APPENDIX 1.6

												Structural formula, based on 32 oxygen atoms								
Sample	NUM	Na_2O	MgO	Al_2O_3	SiO_2	K_2O	CaO	TiO_2	FeO	BaO	TOTAL	Si	Ti	Al	Fe^{2+}	Mg	Ca	Na	K	Ba
KD133	CFE370	0.24	0.16	18.90	64.06	16.97	0.06	0.04	0.20	0.00	99.88	11.76	0.00	4.11	0.03	0.04	0.01	0.08	4.00	0.00
KD133	CFE371	0.25	0.16	18.92	62.79	16.27	0.06	0.14	0.26	0.00	98.55	11.84	0.02	4.18	0.04	0.04	0.01	0.09	3.89	0.00
KD133	CFE372	0.26	0.16	18.62	63.34	16.77	0.17	0.05	0.10	0.00	100.20	11.79	0.01	4.10	0.01	0.04	0.03	0.09	4.00	0.00
KD133	CFE373	0.22	0.16	18.66	62.76	17.12	0.11	0.03	0.32	0.00	99.42	11.84	0.00	4.13	0.05	0.04	0.02	0.08	4.10	0.00
KD133	CFE374	0.27	0.16	18.77	63.44	16.95	0.04	0.01	0.14	0.00	99.67	11.79	0.00	4.12	0.02	0.04	0.00	0.09	4.03	0.00
AVE.		0.25	0.16	18.87	63.28	16.78	0.09	0.06	0.23	0.00	99.77	11.80	0.01	4.15	0.03	0.04	0.01	0.09	3.99	0.00
KD139	CFE375	0.20	0.16	18.54	62.76	16.42	0.00	0.08	1.10	0.00	99.26	11.79	0.01	4.10	0.17	0.04	0.00	0.07	3.93	0.00
KD139	CFE376	0.33	0.16	18.54	63.44	17.08	0.03	0.03	0.29	0.00	99.90	11.84	0.00	4.08	0.04	0.04	0.00	0.12	4.06	0.00
AVE.		0.27	0.16	18.54	63.10	16.75	0.02	0.05	0.70	0.00	99.58	11.82	0.01	4.09	0.11	0.04	0.00	0.10	4.00	0.00
KD147	CFE377	0.34	0.16	18.08	62.64	16.52	0.00	0.03	0.97	0.00	98.74	11.85	0.00	4.03	0.15	0.04	0.00	0.12	3.98	0.00
KD147	CFE378	0.32	0.16	18.13	62.29	16.53	0.03	0.18	1.15	0.00	98.76	11.79	0.02	4.04	0.18	0.04	0.00	0.11	3.99	0.00
KD147	CFE379	0.29	0.16	19.14	62.50	16.46	0.05	0.04	0.21	0.00	98.84	11.76	0.00	4.24	0.03	0.04	0.01	0.10	3.95	0.00
KD147	CFE380	0.43	0.16	18.77	62.96	16.58	0.06	0.09	0.16	0.00	99.22	11.80	0.01	4.14	0.02	0.04	0.01	0.15	3.96	0.00
KD147	CFE381	0.30	0.16	18.64	63.75	16.76	0.02	0.06	0.55	0.00	100.24	11.84	0.01	4.08	0.08	0.04	0.00	0.10	3.97	0.00
KD147	CFE382	0.30	0.16	18.61	63.43	16.74	0.00	0.01	0.32	0.00	99.57	11.85	0.00	4.10	0.05	0.04	0.00	0.10	3.99	0.00
KD147	CFE383	0.32	0.16	18.12	62.19	16.89	0.00	0.01	1.03	0.00	98.71	11.80	0.00	4.05	0.16	0.04	0.00	0.11	4.09	0.00
KD147	CFE384	0.28	0.16	18.35	63.55	16.62	0.00	0.05	0.89	0.00	99.41	11.86	0.00	4.03	0.13	0.04	0.00	0.10	3.95	0.00
KD147	CFE385	0.32	0.16	17.81	61.65	15.51	0.05	0.19	2.01	0.00	97.70	11.79	0.02	4.01	0.32	0.04	0.01	0.11	3.78	0.00
KD147	CFE386	0.42	0.16	18.56	62.35	16.16	0.00	0.11	1.43	0.00	99.19	11.74	0.01	4.12	0.22	0.04	0.00	0.15	3.88	0.00
KD147	CFE387	0.45	0.16	18.65	63.23	16.39	0.05	0.02	0.23	0.00	99.18	11.84	0.00	4.11	0.03	0.04	0.01	0.16	3.91	0.00
KD147	CFE388	0.48	0.16	18.80	62.94	16.48	0.01	0.05	0.24	0.00	99.17	11.80	0.00	4.15	0.03	0.04	0.00	0.17	3.94	0.00
AVE.		0.35	0.16	18.47	62.79	16.47	0.02	0.07	0.77	0.00	99.06	11.81	0.01	4.09	0.12	0.04	0.00	0.12	3.95	0.00

Digitised by the Department of Library Services in support of open access to information, University of Pretoria, 2021

RARE-EARTH MINERAL ANALYSES: KD01 SEQUENCE

APPENDIX 1.7

Samples KD111 and KD141

SAMPLE	CODE	SiO_2	CaO	FeO	SrO	Y_2O_3	La_2O_3	Ce_2O_3	Pr_2O_3	Nd_2O_3	Sm_2O_3	ThO_2	CO_2	TOTAL
KD111	FW29	0.69	9.15	2.85	0.65	1.52	13.34	20.02	2.13	9.25	1.73	1.48	30.18	62.81
KD111	FW30	0.00	11.48	3.55	0.75	0.00	11.59	17.78	1.83	9.16	1.38	1.14	28.57	58.66
KD111	FW31	0.49	8.08	2.27	1.03	1.32	14.86	22.15	1.59	7.92	1.37	1.96	29.49	63.04
AVE		0.39	9.57	2.89	0.81	0.95	13.26	19.98	1.85	8.78	1.49	1.53	29.41	61.50
KD141	FW70	0.00	18.04	0.00	0.00	2.13	7.14	23.74	3.34	12.85	1.59	0.00	34.81	68.83
KD141	FW71	0.00	6.20	0.00	0.00	0.00	25.35	31.60	1.35	4.49	0.00	0.00	30.14	68.99
AVE.		0.00	12.12	0.00	0.00	1.07	16.25	27.67	2.35	8.67	0.80	0.00	32.47	68.91

FORMULA: (analysis FW29, FW30 and FW31): $Ca(Ce,La)_2(CO_3)_3F_2$

NUMBER of oxygen equivalents: 4 (O)

SAMPLE	CODE	Si	Ca	Fe	Sr	Y	La	Ce	Pr	Nd	Sm	Th	TOTAL
KD111	FW29	0.07	0.95	0.08	0.04	0.08	0.48	0.71	0.08	0.32	0.06	0.03	3.04
KD111	FW30	0.00	1.26	0.00	0.05	0.00	0.44	0.67	0.07	0.34	0.05	0.03	3.19
KD111	FW31	0.05	0.86	0.07	0.06	0.07	0.54	0.81	0.06	0.28	0.05	0.04	3.01

FORMULA: (analysis FW70): $Ca(Ce,La)(CO_3)_2F$

NUMBER of oxygen equivalents: 2.5 (O)

FORMULA : (analysis FW71) $(Ce,La)CO_3F$

NUMBER of oxygen equivalents: 1.5 (O)

SAMPLE	CODE	Si	Ca	Fe	Sr	Y	La	Ce	Pr	Nd	Sm	Th	TOTAL
KD141	FW70	0.00	1.02	0.06	0.00	0.60	0.14	0.46	0.06	0.24	0.03	0.00	2.01
KD141	FW71	0.00	0.24	0.00	0.00	0.00	0.34	0.42	0.02	0.06	0.00	0.00	1.08

Digitised by the Department of Library Services in support of open access to information, University of Pretoria, 2021

APPENDIX 2: WHOLE ROCK MAJOR- AND TRACE, AND RARE-EARTH ELEMENTS

Digitised by the Department of Library Services in support of open access to information, University of Pretoria, 2021

APPENDIX 2.1

WHOLE ROCK ANALYSES: KD01 SEQUENCE

Samples KD011 to KD110

Oxides and L.O.I. in wt %; trace elements and rare-earth elements in ppm

Units: UAF = upper ash flow unit; PB = pyroclastic breccia unit

Sample	KD011	KD012	KD013	KD014	KD015	KD016	KD017	KD018	KD019	KD110
Unit	UAF	UAF	UAF	UAF	UAF	UAF	PB	PB	PB	PB
SiO_2	21.91	24.15	26.53	17.07	18.76	12.46	16.30	20.35	28.75	26.98
TiO_2	2.00	1.85	2.91	2.03	2.55	2.77	0.27	0.71	1.92	1.20
Al_2O_3	4.77	4.94	4.95	3.86	5.01	5.02	2.06	3.50	8.15	7.04
FeO	1.07	1.65	8.46	1.69	10.72	8.63	1.52	1.53	8.16	1.07
Fe_2O_3	7.35	6.45	1.04	8.20	0.90	3.45	5.85	6.30	5.92	9.00
MnO	0.84	0.76	0.71	0.98	0.80	0.89	2.87	3.01	1.59	3.01
MgO	8.41	8.20	7.99	8.62	2.13	5.62	8.66	7.91	5.55	5.16
CaO	20.65	19.93	17.62	22.72	29.25	29.93	30.55	23.55	14.80	19.68
Na_2O	0.06	0.08	0.16	0.07	0.03	0.13	0.07	0.08	0.10	0.08
K_2O	3.61	3.89	4.12	2.68	2.93	0.55	1.32	2.86	5.08	3.91
P_2O_5	1.28	1.51	0.75	1.30	1.00	1.72	0.94	1.02	1.92	1.10
BaO	0.24	0.27	0.15	0.09	0.33	0.88	1.08	0.32	0.70	0.78
SrO	0.11	0.14	0.18	0.14	0.10	0.39	0.19	0.08	0.20	0.14
PbO	<0.01	<0.01	<0.01	0.01	0.03	<0.01	0.08	0.02	0.04	0.02
ZnO	0.01	0.01	0.01	0.01	0.01	0.05	0.17	0.11	0.05	0.04
L.O.I.	26.44	24.14	25.16	29.16	25.13	27.22	26.59	27.42	17.70	19.29
TOTAL	98.72	98.96	100.72	98.63	99.68	99.70	98.51	98.78	100.64	98.50
H_2O^-	0.06	0.12	0.03	0.13	0.77	0.13	0.11	0.09	0.04	0.15
H_2O^+	0.43	0.33	0.46	0.28	1.95	2.39	0.15	0.18	1.05	1.35
CO_2	28.03	26.75	25.94	31.03	22.86	25.76	29.28	29.64	17.15	19.09
S	0.40	0.48	0.50	0.28	0.06	0.69	0.68	0.28	<0.001	0.25
F	0.33	0.20	0.20	0.20	0.20	0.30	0.35	0.69	0.49	2.90
Ba	2049	2355	1327	995	2716	7887	8960	3188	6410	6951
Cr	106	136	247	162	194	124	<5	32	49	59
Cu	<5	<5	<5	<5	6	<5	<5	<5	<5	<5
Ga	11	<5	<5	8	12	10	6	8	8	15
Hf	11	14	14	10	10	19	12	13	15	8
Mo	7	7	7	23	68	<2	401	42	<2	106
Nb	80	99	99	73	79	75	134	163	206	198
Ni	59	113	113	44	85	105	17	18	48	50
Pb	13	17	17	69	239	34	722	227	406	144
Rb	12	59	59	27	73	14	204	70	86	47
Sc	23	23	23	28	37	24	24	27	23	23
Sr	1237	1558	1558	1635	1087	3294	2012	961	1907	1366
Ta	<5	<5	<5	<5	<5	<5	<5	6	<5	<5
Th	<5	<5	<5	<5	7	7	48	37	74	57
U	15	25	25	22	21	19	51	37	15	13
V	263	409	409	294	337	472	200	202	577	275
W	<5	22	22	9	<5	26	<5	<5	17	<5
Y	56	51	51	49	54	68	336	235	374	360
Zn	64	75	75	74	117	417	1390	869	362	325
Zr	370	483	483	272	360	351	344	504	480	198
La	297	284	168	280	179	265	784	803	215	623
Ce	184	222	126	161	111	197	1053	912	315	672
Pr	49	49	37	53	17	31	58	98	50	173
Nd	118	115	92	141	70	97	262	304	239	449
Sm	14	13	11	17	11	13	53	59	62	65
Eu	4	4	3	5	3	3	15	18	17	15
Gd	11	11	9	14	8	9	45	51	47	38
Tb	1	1	1	2	1	1	6	7	6	4
Dy	8	8	7	9	6	7	40	37	32	27
Er	4	4	4	4	3	4	22	18	16	13
Tm	1	1	1	1	1	0	5	2	2	1
Yb	4	4	4	4	4	3	34	37	19	12

Digitised by the Department of Library Services in support of open access to information, University of Pretoria, 2021

APPENDIX 2.1

WHOLE ROCK ANALYSES: KD01 SEQUENCE

Samples KD111 to KD120

Oxides and L.O.I. in wt %; trace elements and rare-earth elements in ppm

Units: PB = pyroclastic breccia unit; FLT = ferruginous lapilli tuff unit

Sample	KD111	KD112	KD113	KD114	KD115	KD116	KD117	KD118	KD119	KD120
Unit	PB	PB	PB	FLT	FLT	FLT	FLT	FLT	FLT	FLT
SiO_2	13.19	23.74	18.46	28.75	21.38	27.03	30.69	42.73	38.49	37.97
TiO_2	1.19	2.05	1.36	1.64	1.96	1.55	2.55	2.33	2.66	1.81
Al_2O_3	7.34	6.19	7.17	9.18	7.31	7.12	9.66	11.09	13.18	8.85
FeO	11.19	0.74	10.89	7.54	7.48	11.09	13.32	5.47	4.77	8.33
Fe_2O_3	4.93	8.50	4.89	11.25	14.30	4.99	6.70	10.56	12.90	5.88
MnO	3.51	2.98	3.09	2.75	2.94	1.73	2.87	1.10	0.91	1.64
MgO	7.39	5.43	6.81	2.82	3.94	1.95	3.07	0.81	1.99	1.16
CaO	25.48	21.56	23.46	16.53	22.86	11.16	17.59	7.61	7.68	13.94
Na_2O	0.15	0.08	0.14	0.14	0.09	0.10	0.09	0.20	0.10	0.07
K_2O	2.38	3.65	3.12	2.74	0.94	4.06	2.89	9.17	8.07	6.71
P_2O_5	1.22	1.29	1.13	1.46	1.37	0.77	1.57	0.31	0.42	0.38
BaO	0.35	1.42	0.55	2.55	0.53	2.20	0.38	2.30	2.10	3.83
SrO	0.21	0.21	0.18	0.11	0.14	0.10	0.05	<0.01	0.10	0.07
PbO	0.01	0.04	0.13	0.01	0.02	0.03	0.01	0.01	0.01	0.01
ZnO	0.08	0.07	0.08	0.41	0.21	0.08	0.04	0.05	0.06	0.05
L.O.I.	20.34	20.60	17.50	10.96	12.43	27.10	7.21	5.85	7.10	8.36
TOTAL	98.97	98.55	98.92	98.84	97.91	101.03	98.69	99.59	100.52	99.05
H_2O^-	0.16	0.04	0.17	0.20	<0.01	0.02	0.26	0.03	0.05	0.07
H_2O^+	2.56	0.92	1.81	2.80	3.01	1.20	3.21	0.28	2.02	0.26
CO_2	19.24	21.11	17.18	6.30	7.69	7.40	5.35	4.43	3.26	5.68
S	0.17	0.36	0.47	0.3	0.26	0.37	0.57	0.32	0.32	0.69
F	5.5	2.3	5.2	>6.0	5.3	>6.0	3.3	3.5	3.5	5.7
Ba	3172	11800	4919	5827	6380	19790	22925	20956	18487	32.024
Cr	81	83	59	169	120	125	140	232	223	119
Cu	<5	<5	<5	<5	<5	<5	<5	<5	<5	<5
Ga	9	14	8	20	15	<5	16	<5	20	15
Hf	11	11	12	14	11	9	8	9	11	7
Mo	199	117	172	7	4	<2	26	<2	<2	<2
Nb	169	268	209	414	327	195	153	168	198	143
Ni	99	52	68	53	41	43	28	45	72	30
Pb	118	369	1163	128	174	247	79	96	67	71
Rb	35	108	44	43	55	81	30	131	134	27
Sc	19	28	26	23	23	22	11	10	19	20
Sr	1812	2118	1536	1022	1229	784	416	404	493	591
Ta	<5	<5	<5	<5	<5	<5	<5	7	<5	<5
Th	93	43	127	172	104	105	43	34	43	27
U	29	27	27	13	14	10	3	7	9	<2
V	285	394	320	660	452	444	576	452	544	404
W	17	5	12	9	<5	<5	<5	10	7	<5
Y	614	409	453	401	341	289	212	212	218	187
Zn	654	542	613	3298	1725	625	320	383	453	417
Zr	260	249	365	564	432	453	396	441	621	280
La	793	371	1200	1510	936	506	674	592	472	357
Ce	994	580	1624	2880	2253	920	1011	790	873	388
Pr	139	60	214	415	159	95	196	138	150	116
Nd	570	265	758	1337	758	471	890	564	414	279
Sm	114	64	135	162	103	90	158	72	41	27
Eu	26	16	36	32	21	22	36	12	7	5
Gd	73	41	100	71	51	52	72	33	17	12
Tb	12	6	11	8	7	6	8	5	3	2
Dy	61	37	62	45	31	30	32	27	20	12
Er	32	28	30	26	17	17	13	15	14	7
Tm	8	2	5	3	0	3	1	1	1	1
Yb	113	73	44	84	73	38	33	29	19	16

Digitised by the Department of Library Services in support of open access to information, University of Pretoria, 2021

WHOLE ROCK ANALYSES: KD01 SEQUENCE

APPENDIX 2.1

Samples KD121 to KD130

Oxides and L.O.I. in wt %; trace elements and rare-earth elements in ppm

Units: FLT = ferruginous lapilli tuff unit; LAF = lower ash flow unit; M = mineralised zones

Sample	KD121	KD122	KD123	KD124	KD125	KD126	KD127	KD128	KD129	KD130
Unit	FLT	FLT	FLT	FLT	FLT	LAF	LAF	LAF	LAF	M
SiO_2	31.67	46.00	41.87	45.29	36.87	0.82	36.29	38.11	32.51	13.56
TiO_2	3.10	2.10	1.98	2.06	1.55	0.05	1.57	1.84	1.89	1.05
Al_2O_3	11.08	9.27	9.07	9.89	8.83	1.51	7.95	9.44	7.90	3.75
FeO	13.13	11.59	9.73	6.27	7.22	3.45	8.24	8.27	4.86	11.54
Fe_2O_3	13.66	8.25	6.68	8.70	5.17	3.41	6.83	6.16	10.43	6.19
MnO	1.43	0.99	1.33	0.96	1.79	3.30	2.07	1.48	1.91	5.18
MgO	3.61	2.39	1.17	1.02	2.57	5.86	2.48	2.05	4.60	2.84
CaO	5.39	4.20	8.37	8.37	13.27	51.51	13.33	10.72	11.99	24.96
Na_2O	0.10	0.08	0.10	7.50	0.09	0.07	0.10	0.10	0.06	0.11
K_2O	4.63	4.76	6.91	7.91	6.58	0.04	5.81	6.47	3.20	2.11
P_2O_5	0.16	0.66	0.69	0.35	0.23	3.37	0.44	0.43	0.98	1.34
BaO	1.60	2.41	3.17	2.00	3.25	7.20	1.28	4.24	4.26	11.98
SrO	0.10	0.07	0.07	<0.01	0.09	0.31	0.08	0.08	0.14	0.14
PbO	0.01	0.04	0.04	0.07	0.03	0.95	0.01	0.01	<0.01	0.17
ZnO	0.10	0.08	0.09	0.05	0.04	0.28	0.07	0.07	0.07	0.07
L.O.I.	9.00	6.30	7.92	0.10	11.51	16.62	12.29	9.60	13.70	13.29
TOTAL	99.76	99.18	99.20	100.55	99.10	98.75	98.85	99.08	98.51	98.26
H_2O^-	0.13	0.03	0.04	0.01	0.02	0.11	0.05	0.05	<0.01	0.05
H_2O^+	2.65	0.32	0.38	0.39	0.28	0.64	0.44	0.69	1.89	0.60
CO_2	6.12	3.77	5.17	4.76	10.74	18.25	10.37	7.07	10.33	13.41
S	0.23	0.48	0.61	0.44	0.54	1.44	0.16	0.73	10.7	2.02
F	3.4	2.1	4.6	5.2	5.4	>6.0	5.6	4.3	2.9	>6.0
Ba	14290	21194	27819	18276	26371	62513	11141	37458	40845	107261
Cr	234	209	143	155	96	<5	130	139	125	10
Cu	<5	<5	22	<5	<5	<5	<5	<5	<5	<5
Ga	8	22	17	8	16	34	15	19	22	<5
Hf	13	9	8	8	7	8	7	9	11	7
Mo	<2	<2	<2	<2	<2	<2	7	<2	<2	<2
Nb	355	210	157	146	111	8	132	151	205	123
Ni	71	56	32	43	22	32	24	32	37	73
Pb	74	350	411	691	298	8838	55	52	45	1549
Rb	100	103	120	119	89	2400	23	22	20	40
Sc	18	14	19	12	17	50	18	19	19	22
Sr	576	569	576	384	864	2534	793	782	1338	1180
Ta	<5	<5	<5	<5	12	<5	<5	<5	<5	<5
Th	114	57	33	26	19	159	34	39	37	216
U	12	4	<2	3	5	5	4	<2	11	27
V	798	631	541	364	398	333	376	590	583	677
W	<5	<5	<5	12	<5	<5	<5	<5	<5	37
Y	208	132	202	131	123	408	111	128	144	810
Zn	780	635	761	430	315	2249	566	528	524	588
Zr	650	386	364	336	216	186	279	351	365	273
La	690	662	786	492	375	2372	664	666	679	1408
Ce	1207	1610	1166	816	365	3684	743	837	837	2503
Pr	221	151	184	101	65	568	121	132	138	412
Nd	624	706	610	338	220	1838	357	420	453	1558
Sm	81	96	54	32	24	179	43	42	69.3	223
Eu	16	18	9	7	5	37	10	11	19	60
Gd	39	41	29	17	14	84	23	20	42	158
Tb	5	5	5	3	3	8	4	3	4	17
Dy	28	24	22	13	12	40	18	13	16	78
Er	16	19	11	8	8	20	10	8	7	30
Tm	1	3	1	1	2	3	3	3	2	4
Yb	42	34	23	24	14	23	24	23	18	27

Digitised by the Department of Library Services in support of open access to information, University of Pretoria, 2021

APPENDIX 2.1

WHOLE ROCK ANALYSES: KD01 SEQUENCE
Samples KD131 to KD140
Oxides and L.O.I. in wt %; trace elements and rare-earth elements in ppm
Units: LAF = lower ash flow unit; M = mineralised zones

Sample	KD131	KD132	KD133	KD134	KD135	KD136	KD137	KD138	KD139	KD140
Unit	LAF	LAF	LAF	M	LAF	LAF	LAF	M	LAF	LAF
SiO_2	36.46	24.00	30.96	5.60	28.09	34.78	43.55	33.19	36.61	35.39
TiO_2	1.65	3.31	2.84	2.98	2.77	2.10	1.91	1.57	1.66	1.84
Al_2O_3	7.23	6.29	8.94	3.47	7.59	6.95	9.41	6.08	7.46	7.78
FeO	7.72	8.98	12.78	9.55	9.88	8.18	10.71	7.36	10.88	11.71
Fe_2O_3	10.29	12.70	7.30	3.22	9.43	7.44	6.91	5.10	6.76	5.83
MnO	1.48	3.01	1.64	4.72	2.13	2.07	0.61	2.19	1.69	1.45
MgO	3.09	3.88	4.08	4.87	5.08	3.57	1.90	2.28	1.61	1.50
CaO	12.83	12.57	10.70	31.83	11.41	12.30	10.29	21.58	14.21	16.90
Na_2O	0.07	0.08	0.10	0.24	0.08	0.08	0.07	0.15	0.07	0.06
K_2O	2.37	1.80	2.87	0.41	2.07	3.27	4.45	4.37	4.55	4.09
P_2O_5	0.71	3.05	2.37	8.62	2.52	0.63	0.42	1.23	0.97	0.67
BaO	2.64	3.73	2.60	4.52	2.57	2.21	0.54	2.88	1.99	1.96
SrO	0.15	0.25	0.20	0.67	0.26	0.10	0.05	0.15	0.09	0.08
PbO	0.01	0.22	0.11	0.66	0.01	0.01	0.01	0.01	0.01	0.01
ZnO	0.12	0.14	0.15	0.69	0.12	0.06	0.04	0.07	0.07	0.05
L.O.I.	12.05	14.52	12.40	17.62	14.51	15.23	8.17	11.41	10.33	9.65
TOTAL	98.88	98.53	100.04	99.67	98.52	98.99	99.05	99.61	98.95	98.97
H_2O^-	<0.01	0.01	0.19	0.08	0.20	<0.01	0.32	0.05	0.23	0.10
H_2O^+	2.08	1.94	2.24	1.14	2.70	1.27	2.24	0.56	0.89	1.12
CO_2	7.25	12.35	8.43	17.95	12.05	13.01	7.84	10.85	7.55	5.83
S	0.64	1.14	0.62	1.19	0.72	0.80	0.94	0.89	0.52	0.51
F	>6.0	2.00	4.20	5.70	2.50	3.00	4.30	>6.0	>6.0	>6.0
Ba	23925	36752	23087	40437	24927	19584	4943	25769	17291	16503
Cr	130	155	210	<5	165	136	157	141	123	132
Cu	<5	<5	<5	<5	<5	<5	<5	<5	<5	<5
Ga	18	23	7	20	17	14	18	<5	16	14
Hf	12	15	13	22	17	11	12	12	11	11
Mo	<2	<2	<2	<2	<2	<2	7	<2	<2	<2
Nb	164	330	237	253	280	219	195	139	185	198
Ni	32	33	42	16	32	26	33	30	20	26
Pb	132	2034	1034	6142	118	59	74	65	57	74
Rb	44	559	83	21	40	24	28	81	24	28
Sc	28	20	19	35	17	21	17	25	18	28
Sr	1434	2381	1649	5635	2496	1034	429	1283	844	709
Ta	<5	<5	<5	<5	<5	<5	<5	<5	<5	<5
Th	26	24	37	11	30	35	32	46	35	41
U	4	10	13	54	13	24	10	15	15	16
V	681	825	651	360	863	778	615	446	878	750
W	<5	<5	<5	15	<5	<5	<5	14	<5	<5
Y	104	149	139	192	147	142	105	137	110	140
Zn	932	1118	1226	5573	972	520	361	578	540	420
Zr	375	456	561	392	506	450	485	352	440	476
La	664	860	621	1650	694	782	551	754	596	942
Ce	1100	1275	950	2975	1303	1198	894	1206	1062	1527
Pr	116	158	123	385	140	128	89	110	124	144
Nd	359	503	420	1275	440	397	274	366	439	420
Sm	46	58	57	126	55	45	32	49	61	43
Eu	10	14	15	26	14	10	8	12	14	9
Gd	25	33	34	56	33	27	18	31	31	24
Tb	4	5	4	6	4	4	3	4	5	4
Dy	16	20	18	26	21	17	14	18	16	18
Er	10	11	9	12	11	11	8	10	9	11
Tm	2	1	1	2	1	2	2	2	5	3
Yb	28	27	11	17	26	26	25	27	28	29

Digitised by the Department of Library Services in support of open access to information, University of Pretoria, 2021

APPENDIX 2.1

WHOLE ROCK ANALYSES: KD01 SEQUENCE
Samples KD140 to KD150
Oxides and L.O.I. in wt %; trace elements and rare-earth elements in ppm
Units: LAF = lower ash flow unit; M = mineralised zones

Sample	KD141	KD142	KD143	KD144	KD145	KD146	KD147	KD148	KD149	KD150
Unit	M	M	M	LAF	LAF	LAF	LAF	LAF	LAF	LAF
SiO_2	3.89	30.45	13.07	34.98	25.66	33.56	28.56	28.10	29.70	29.12
TiO_2	3.69	0.12	2.20	1.99	2.63	2.23	2.10	2.37	2.13	1.72
Al_2O_3	0.69	0.88	4.80	9.07	11.80	9.55	8.04	10.00	8.92	6.51
FeO	9.05	1.29	4.80	8.19	8.97	9.20	9.45	11.87	10.86	4.05
Fe_2O_3	4.60	6.37	10.59	6.86	14.64	9.07	8.17	7.44	8.13	9.94
MnO	4.85	2.28	3.37	1.58	1.69	2.04	2.27	1.76	1.93	2.78
MgO	3.29	2.76	4.11	1.63	4.60	2.29	2.81	2.07	2.27	4.67
CaO	43.03	38.81	28.14	16.51	11.28	9.53	14.99	14.72	15.32	14.55
Na_2O	0.29	0.17	0.06	0.08	0.07	0.10	0.10	0.08	0.08	0.08
K_2O	<0.05	0.08	0.54	5.28	2.35	5.48	4.40	4.85	4.65	3.87
P_2O_5	6.99	0.18	3.69	0.71	0.67	0.79	1.09	1.31	0.99	0.70
BaO	3.77	3.93	7.04	2.85	2.31	4.80	5.00	5.05	3.92	2.36
SrO	0.29	0.13	0.30	0.11	0.08	0.10	0.10	0.13	0.13	0.11
PbO	0.63	0.04	0.50	0.01	0.01	0.04	0.04	0.02	0.03	0.09
ZnO	1.02	0.20	0.26	0.09	0.16	0.11	0.12	0.08	0.07	0.09
L.O.I.	13.01	11.34	14.41	8.89	11.20	11.10	12.50	8.80	9.44	17.87
TOTAL	99.09	99.03	97.89	98.82	98.12	99.98	99.73	98.64	98.56	98.51
H_2O^-	0.12	0.08	<0.01	<0.01	0.35	0.04	0.05	<0.01	<0.01	<0.01
H_2O^+	0.54	0.52	1.57	0.85	3.98	0.79	0.95	1.57	1.23	0.85
CO_2	14.55	10.44	15.02	5.72	5.53	10.44	8.68	6.08	7.04	18.54
S	1.61	1.26	2.84	0.57	0.59	0.95	0.98	1.01	0.77	0.50
F	>6.0	>6.0	>6	5.00	>6.0	>6.0	3.60	1.00	0.80	0.38
Ba	33729	35207	64694	24433	16254	43367	44775	46418	35288	21715
Cr	<5	<5	46	145	239	149	156	165	148	140
Cu	<5	<5	<5	<5	<5	<5	<5	<5	<5	<5
Ga	14	<5	26	17	21	6	8	23	23	17
Hf	8	5	9	11	16	12	11	15	14	14
Mo	4	<2	<2	<2	<2	<2	<2	<2	<2	<2
Nb	248	31	242	192	276	207	222	280	255	207
Ni	36	49	57	38	66	49	54	60	46	32
Pb	5885	356	4596	126	117	347	416	146	236	877
Rb	<5	12	1252	42	40	86	100	48	72	246
Sc	35	37	34	23	27	19	22	26	18	14
Sr	2455	1109	2579	902	747	923	756	1060	1111	1064
Ta	<5	<5	<5	<5	<5	<5	<5	<5	<5	<5
Th	10	248	52	60	75	76	96	107	90	56
U	194	36	71	10	17	19	15	18	11	6
V	343	279	661	485	911	628	608	762	645	442
W	81	22	<5	<5	<5	<5	11	<5	<5	<5
Y	306	630	214	179	227	200	212	321	279	174
Zn	8194	1611	2072	687	1294	844	957	614	590	692
Zr	298	82	271	456	706	582	604	690	599	577
La	1945	2580	6200	620	897	1018	1280	1650	1502	1385
Ce	3123	4550	9073	760	1083	1196	1515	1955	1994	1763
Pr	424	568	825	111	152	193	256	264	244	231
Nd	1181	1905	1955	409	533	645	900	856	794	687
Sm	93	198	143	55	80	90	147	152	129	102
Eu	17	44	29	13	17	20	34	34	31	25
Gd	42	114	59	34	42	48	75	90	79	58
Tb	5	11	10	4	5	5	7	1	9	6
Dy	30	52	40	22	26	27	33	54	48	30
Er	20	20	21	10	13	13	14	25	22	14
Tm	4	3	4	0	2	2	2	3	3	2
Yb	28	21	28	9	11	12	14	23	21	13

Digitised by the Department of Library Services in support of open access to information, University of Pretoria, 2021

WHOLE ROCK ANALYSES: DYKES

Samples S1 to S10

Oxides and L.O.I. in wt %; trace elements and rare-earth elements in ppm

APPENDIX 2.2

Sample	S1	S2	S3	S4	S5	S6	S7	S8	S9	S10
Unit	Sövite	Sövite	Sövite	Sövite	Sövite	Sövite	Sövite	Sövite	Sövite	Sövite
SiO_2	0.73	0.10	0.12	3.55	2.69	0.96	1.22	1.06	1.90	1.78
TiO_2	0.03	0.01	0.01	0.06	0.04	0.01	0.01	0.02	0.04	0.03
Al_2O_3	0.24	0.22	0.20	0.44	0.33	0.28	0.16	0.27	0.19	0.39
FeO	0.60	0.70	0.40	0.80	0.70	1.00	0.50	0.40	0.30	0.50
Fe_2O_3	0.05	0.06	0.45	0.48	2.02	0.60	1.30	0.80	0.38	0.48
MnO	0.70	0.66	0.73	0.64	1.27	1.02	1.17	0.79	0.60	0.90
MgO	0.20	0.23	0.28	0.40	0.41	1.43	0.78	0.37	0.43	0.56
CaO	54.27	53.08	53.63	50.37	49.80	52.83	58.96	58.13	62.04	60.81
Na_2O	0.08	0.03	0.03	0.04	0.04	0.02	0.02	0.02	0.02	0.04
K_2O	0.02	0.04	0.04	0.04	0.02	0.03	0.04	0.04	0.05	0.02
P_2O_5	0.16	0.18	0.08	0.66	0.50	0.09	0.11	0.22	0.03	0.11
BaO	0.03	0.04	0.04	0.89	1.11	0.04	0.03	0.03	0.05	0.05
SrO	0.33	0.28	0.13	0.16	0.98	0.16	0.18	0.13	0.31	0.28
PbO										
ZnO										
L.O.I.	40.51	42.84	42.44	39.38	37.52	39.63	33.32	35.40	31.06	31.17
TOTAL	98.01	98.52	98.63	97.99	97.50	98.22	97.85	97.72	97.42	97.17
H_2O^-	<0.05	<0.05	<0.05	<0.05	0.05	<0.05	0.05	0.05	<0.05	<0.05
H_2O^+	0.08	<0.05	0.15	0.23	0.19	0.14	0.31	0.14	0.10	0.11
CO_2	41.40	42.87	36.11	39.94	40.67	40.67	33.86	35.83	31.55	31.80
S	0.02	0.01	0.01	0.26	1.29	0.07	0.02	0.20	0.05	0.04
F	1.09	0.16	0.56	0.57	0.34	6.30	5.00	8.16	9.51	9.52
Ba	881	1057	920	7634	10268	841	352	757	1098	1019
Cr	<5	<5	<5	<5	<5	<5	<5	<5	<5	<5
Cu	<5	<5	<5	<5	<5	<5	<5	<5	<5	<5
Ga	6	<5	6	<5	9	6	5	5	6	7
Hf	13	9	5	5	34	6	6	<5	10	9
Mo	3	3	4	<2	73	14	38	80	3	8
Nb	6	5	3	17	31	11	10	23	12	11
Ni	3	<2	<2	3	3	4	6	15	5	5
Pb	17	84	76	43	352	27	30	49	13	20
Rb	5	7	6	6	8	7	6	7	7	7
Sc	42	39	42	39	37	37	41	41	48	55
Sr	2549	2220	1038	1232	7425	1283	1365	1020	2306	2109
Ta	11	<5	6	<5	<5	8	<5	<5	6	<5
Th	<5	<5	<5	<5	10	6	<5	12	<5	12
U	4	5	<2	<2	22	7	11	7	8	8
V	25	30	34	106	122	153	106	117	85	201
W	<5	<5	<5	6	<5	<5	<5	7	<5	<5
Y	66	56	52	65	138	89	105	166	122	121
Zn	270	156	339	654	531	18	32	25	18	20
Zr	57	47	27	42	301	32	32	28	53	49
La	719	778	666	628	942	794	733	855	820	890
Ce	982	1172	965	903	1351	1090	855	1152	1170	1200
Pr	89	102	78	78	122	88	56	90	99	99
Nd	274	358	272	231	371	288	175	292	331	308
Sm	41	47	38	37	50	39	29	43	45	46
Eu	12	12	9	10	13	10	7	13	12	14
Gd	29	27	22	26	33	29	28	34	32	35
Tb	4	3	2	3	4	3	4	4	4	4
Dy	16	12	11	14	21	17	25	23	20	20
Er	7	5	5	6	10	8	16	12	9	9
Tm	1	1	1	1	1	1	2	2	1	1
Yb	6	5	5	5	9	9	17	12	7	9

Digitised by the Department of Library Services in support of open access to information, University of Pretoria, 2021

APPENDIX 2.2

WHOLE ROCK ANALYSES: DYKES
Samples S11 and A1 to A5
Oxides and L.O.I. in wt %; trace elements and rare-earth elements in ppm

Sample	S11	A1	A2	A3	A4	A5
Unit	Sövite	Alvikite	Alvikite	Alvikite	Alvikite	Alvikite
SiO_2	0.27	0.91	1.08	1.36	2.36	1.75
TiO_2	0.15	0.06	0.03	0.06	0.04	0.01
Al_2O_3	0.30	0.23	0.25	0.33	0.33	0.27
FeO	1.45	0.50	<0.10	<0.10	<0.10	1.20
Fe_2O_3	1.06	2.03	4.88	4.50	5.57	0.37
MnO	1.00	1.46	1.90	1.71	2.30	1.03
MgO	0.91	0.85	3.46	3.37	4.06	1.45
CaO	52.90	52.20	49.38	50.02	50.31	52.71
Na_2O	0.03	0.01	0.02	0.02	0.04	0.02
K_2O	0.04	0.03	0.04	0.04	0.03	0.03
P_2O_5	0.43	0.02	0.12	0.20	0.26	0.07
BaO	0.03	0.25	0.05	0.07	0.06	0.03
SrO	0.23	0.09	0.06	0.06	0.07	0.16
PbO						
ZnO						
L.O.I.	38.56	39.58	36.64	36.40	31.84	38.88
TOTAL	97.52	98.30	97.91	98.15	97.27	98.13
H_2O^-	0.07	0.05	0.14	0.12	0.15	<0.05
H_2O^+	0.20	0.27	0.75	0.65	0.78	0.11
CO_2	36.93	41.04	37.37	37.01	32.68	39.57
S	0.23	0.21	0.03	0.03	0.04	0.06
F	3.53	1.16	4.18	5.24	3.89	2.90
Ba	1077	3794	2694	2382	3288	810
Cr	<5	<5	<5	<5	<5	<5
Cu	<5	<5	<5	<5	<5	<5
Ga	<5	5	<5	7	6	<5
Hf	8	<5	<5	<5	<5	<5
Mo	4	12	13	8	104	10
Nb	95	85	21	26	26	9
Ni	7	10	7	7	10	2
Pb	46	225	57	57	106	24
Rb	6	9	7	9	8	7
Sc	49	44	37	34	34	39
Sr	1751	659	458	454	563	1209
Ta	<5	<5	<5	<5	<5	<5
Th	10	25	42	36	44	6
U	18	13	6	8	24	7
V	131	145	178	185	205	132
W	9	15	7	7	<5	<5
Y	137	220	182	180	164	89
Zn	58	45	28	24	53	15
Zr	55	26	25	28	29	30
La	1020	1548	2270	2068	1713	820
Ce	1430	2910	3343	2760	4310	1146
Pr	130	239	243	212	320	97
Nd	379	614	564	577	760	293
Sm	54	63	64	73	68	42
Eu	15	17	17	20	15	11
Gd	40	46	45	50	36	29
Tb	5	5	4	5	4	3
Dy	25	29	21	25	19	17
Er	11	14	10	12	9	8
Tm	2	2	1	2	1	1
Yb	9	15	12	14	10	8

Digitised by the Department of Library Services in support of open access to information, University of Pretoria, 2021

APPENDIX 2.3A

Correlation matrix for major-element data of samples from borehole KD01

	SiO_2	TiO_2	Al_2O_3	Fe_2O_3	FeO	MnO	MgO	CaO	Na_2O	K_2O	P_2O_5	BaO	SrO	PbO	ZnO
Al_2O_3	0.7143	-0.0019	1.0000												
Fe_2O_3	0.6188	0.2739	0.7603	1.0000											
MgO	-0.7329	-0.2977	-0.5681	-0.7229	0.3298	0.2970	1.0000								
CaO	-0.7949	-0.0679	-0.7926	-0.6399	-0.0286	0.4945	0.5193	1.0000							
K_2O	0.7744	0.0844	0.6782	0.4769	-0.4006	-0.5393	-0.6004	-0.6723	0.1085	1.0000					
P_2O_5	-0.7023	0.0183	-0.4228	-0.2903	0.4112	0.4344	0.5213	0.5010	0.0487	-0.6030	1.0000				
SrO	-0.7158	0.0237	-0.6111	-0.5854	0.4103	0.4459	0.6664	0.5768	0.0717	-0.6720	0.7074	0.1179	1.0000		
ZnO	-0.2753	-0.0448	-0.1316	-0.0712	0.4774	0.5962	0.7688	0.1388	0.1914	-0.4789	0.3137	0.5007	0.3375	0.6186	1.0000

Digitised by the Department of Library Services in support of open access to information, University of Pretoria, 2021

APPENDIX 2.3B

Correlation matrix for trace-element data of samples from borehole KD01

	S	F	Ba	Cr	Cu	Ga	Mo	Nb	Ni	Pb	Rb	Sc	Sr	Th	U	V	Y	Zn	Zr
Ba	0.7970	0.3995	1.0000																
Mo	-0.4763	-0.2825	-0.6878	-0.2015	0.0933	-0.2734	1.0000												
U	0.1069	-0.0214	-0.1975	-0.3354	-0.0824	-0.3671	0.3669	0.0598	0.2913	0.1255	-0.2582	0.6364	0.5391	0.0484	1.0000				
V	0.3038	0.2067	0.3638	0.4763	-0.0882	0.3634	-0.5841	0.5450	0.0175	-0.0979	0.0740	-0.2906	-0.2391	0.1829	-0.1999	1.0000			
Y	0.0551	0.3161	0.2148	-0.3905	-0.1263	-0.0158	0.0988	0.3409	0.1603	0.5021	0.2332	0.2071	0.1173	0.7592	0.2720	-0.0955	1.0000		
Zn	0.3977	0.4075	0.4296	-0.1488	-0.0869	0.2609	-0.2319	0.5133	-0.1666	0.6220	0.2705	0.2019	0.2601	0.4594	0.1579	0.1676	0.4749	1.0000	
Zr	-0.0320	-0.1961	0.0121	0.6293	-0.0970	0.2006	-0.3193	0.6033	0.1073	-0.0540	0.2297	-0.3151	-0.3059	0.2376	-0.1169	0.5655	-0.0231	0.1999	1.0000

Digitised by the Department of Library Services in support of open access to information, University of Pretoria, 2021

APPENDIX 2.3C

Correlation matrix for major- and trace-element data of samples from borehole KD01

	SiO_2	TiO_2	Al_2O_3	Fe_2O_3	FeO	MnO	MgO	CaO	Na_2O	K_2O	P_2O_5	BaO	SrO	PbO	ZnO
S	-0.0837	0.0979	-0.2063	-0.0192	0.0739	0.3130	-0.0123	0.1189	-0.0353	-0.2962	0.1583	0.7738	0.2758	0.3037	0.3977
Cr	0.4408	0.5518	0.6398	0.5657	0.0988	-0.5910	-0.3087	-0.6336	0.0194	0.4095	-0.2306	-0.1102	-0.3850	-0.3114	-0.1488
Mo	-0.4096	-0.2046	-0.3214	-0.3743	-0.0870	0.1477	0.4641	0.4703	-0.0567	-0.2493	0.1965	-0.6943	0.0991	-0.1253	-0.2319
Nb	-0.0281	0.4116	0.3382	0.2837	0.6416	0.3179	-0.0153	-0.2746	0.0242	-0.0780	0.2604	0.2463	0.1525	0.2898	0.5133
Pb	-0.3340	-0.0432	-0.2361	-0.1612	0.2613	0.5876	0.0695	0.2194	0.1833	-0.3146	0.2952	0.4318	0.2956	0.9996	0.6220

Digitised by the Department of Library Services in support of open access to information, University of Pretoria, 2021